Synthetic Approaches to Metal-Organic Frameworks and Coordination Cages Incorporating Heterocycle-Based Linkers

Trinity College Dublin
Coláiste na Tríonóide, Baile Átha Cliath
The University of Dublin

A thesis submitted to Trinity College Dublin, the University of Dublin, for the degree of Doctor of Philosophy

Éadaoin Whelan

School of Chemistry,

Trinity College Dublin, the University of Dublin

2023

Declaration

I declare that this thesis has not been submitted as an exercise for a degree at this or any other university and it is entirely my own work.

I agree to deposit this thesis in the University's open access institutional repository or allow the Library to do so on my behalf, subject to Irish Copyright Legislation and Trinity College Library conditions of use and acknowledgement.

I consent to the examiner retaining a copy of the thesis beyond the examining period, should they so wish (EU GDPR May 2018).

Éadaoin Whelan

Summary

This thesis, entitled “Synthetic Approaches to Metal-Organic Frameworks and Coordination Cages Incorporating Heterocycle-Based Linkers”, focuses on the synthesis of metal-organic frameworks (MOFs) and coordination cages using linkers containing heterocyclic groups. This study aims to design, synthesise, and characterise stable photoactive metal-organic materials. The resulting materials were characterised using single crystal X-ray diffraction, and their potential application as porous and photoactive materials is explored.

Chapter 1 provides an overview of current literature in the field of metal-organic materials with a discussion on three key topics. Firstly, an introduction to coordination cages and metal-organic polyhedra is provided, with several interesting examples of coordination cages from the literature highlighted. The second topic explores the application of metal-organic frameworks as tunable photoluminescent materials, with examples including acting as tunable light-emitting materials and luminescence sensors. The final topic examines the use of MOFs as photocatalysts for water splitting, CO_2 reduction, or organic reactions. Throughout this chapter, an emphasis is placed on how the components used in the synthesis of metal-organic materials influence their structures and properties.

Chapter 2 explores the structural effects of integrating heterocycle-based ligands into coordination cages. The synthesis of a novel thienothiophene-based linker is reported, which was then utilised in the synthesis of a coordination cage with dinuclear $\{Cu_2\}$ paddlewheels. The resulting coordination cage is a rare example of a molecular hendecahedron and is the first example of a coordination cage with this geometry synthesised using a single organic linker. The coordination cage possesses a porous structure with a large solvent-accessible void volume, allowing the material to be used for the uptake of guest molecules, as demonstrated by studies using the dye methylene blue.

In Chapter 3, the synthesis of a novel tritopic heterocycle-based linker is reported. Two groups of three-dimensional Ln^{III}-based MOFs are reported using this ligand, with variations in the framework structure observed, which depend on the metal ion used to synthesise the MOF. Both groups of MOFs possess one-dimensional rod-shaped Ln^{III} SBUs, comprised of chains of Ln^{III} ions bridged by carboxylate groups. The Eu^{III}-based MOF is shown to be stable to a range of solvents, including water, and to thermal activation. Under UV light irradiation, the MOF showed bright red luminescence which was visible to the naked eye. This property was subsequently used to detect metal ions in water *via* "turn-off" luminescence sensing. The gas sorption properties of two of these new MOFs were also reported.

Chapter 4 expands upon the work carried out in chapter 3, by utilising the same organic linker in the construction of MOFs from Ln^{III} ions in the latter half of the lanthanide series. This highlights the structural dependence of MOFs incorporating the novel tritopic linker on the nature of the metal ion used. The four MOFs reported in this chapter are characterised by dinuclear $\{Ln^{III}_2\}$ SBUs and have extended two-dimensional structures.

Chapter 5 builds upon the previously discussed work by reacting a Cu^{I}-based photosensitiser with Eu^{III} ions, resulting in the synthesis of a stable three-dimensional MOF, with dinuclear $\{Eu_2\}$ SBUs. Preliminary photochemical studies were carried out, which indicate that the MOF can act as a visible light-harvesting material, with broad absorption of light across the visible region of the spectrum.

Chapter 6 provides the conclusions of this work, in addition to a discussion on possible directions for future work, based on the findings of this thesis. In Chapter 7 the details of the experimental procedures carried out in this work are described. Additional and supporting information can be found in the appendix of this thesis.

Acknowledgements

I would like to thank my supervisor, Prof. Wolfgang Schmitt, for the wonderful opportunity that carrying out this research has been. I am grateful for his guidance, and his support as I explored new ideas in the lab. I would also like to thank the European Research Council and Science Foundation Ireland for financial support in this degree.

I am grateful to the staff of the School of Chemistry, in particular: Dr. Manuel Rüther for training and help with a variety of techniques, and for his advice on integrating sphere measurements, Dr. Gary Hessman and Dr. Martin Feeney for measuring mass spectra. Thank you to Dr. John O'Brien for measuring NMR spectra, and for his wealth of knowledge on the subject, I'm particularly grateful for the weeks when he ran many spectra to help me search for my compounds in column fractions (the search was sometimes hopeless!). I am also grateful for the help and training I have received from Dr. Karsten Fleisher and Christopher Smith from the School of Physics. I also must thank Dr. Brendan Twamley for his training and advice (and patience!) when I was learning crystallography. Thank you so much also to the staff of AML for training and support for SEM and EDX analysis. Thank you to Rónán Crowley from UCD, for carrying out microanalysis.

One of the joys of my PhD has been teaching, both in the undergrad laboratories and in the academic writing clinics with TCD Student Learning Development. Thank you to everyone in SLD for making me feel so welcome during my time teaching there. Thank you to Patsy and Tom for the many Friday morning chats (and endless help) in the teaching labs, and to Peter, Gary and Noelle for all of your support.

I am so grateful for the Schmitt group, and all I have learnt from them in the last four years. A special mention for Friedrich, who helped me with when learning crystal structure refinement, answered all my questions, proofread this thesis in the roughest draft forms, and just genuinely had the HaHas for 4 years straight. We'll call it even for all the DRS samples I ran. And thank you Mariah, for being my PhD buddy, a title has never been so hard-earned. Thank you also to Jom, for crystallographic measurements and all his support, guidance and ideas that helped to shape this thesis. I am also grateful to have had, Justynne, wonderful student work with me on this project for 3 months. Thank you to Luana for all the help with lab management! Thank you to Sebastien for gas sorption and BET surface area measurements and calculations. Thank you to Joe, Guanghua and Kevin for always answering my questions! Thank you to other members of the Schmitt group: Amal, Ximo,

Aviral, Colm, Muhamed, Swetanshu, Debo, Zubair, Aneela, Greg, Rory, Paul, Ako. A big thank you to Nadia, Eleanor, June, Mariah, and Martha, for making Trinity feel like such a friendly place.

I would also like to thank my colleagues and friends at Viatris MDR for their support as I edited and proofread this thesis.

Thank you so very much to my last-minute proofreading dream team: Friedrich, Joe, June, Martha, and Emilio (my accountability buddy in the final months of this thesis!).

Thank you so much to my lovely, caring, funny and honest friends, who are kind to their cores. It is a joy to have you all in my life.

My family has been the most wonderful support to me for all my life, including during this PhD. I am thankful for the encouragement my parents have always given me to pursue my education, I would not be where I am today without this support. I'm also very thankful to have the very best siblings, Brian and Órfhlaith.

It is a privilege to feel as loved and supported as I do. I have never had to face anything alone.

Contents

List of Abbreviations

2,2'-DMBP	2,2’-dimethyl-4,4’-bipyridine
4,4’-bpy	4,4’-bipyridine
A	Acceptor
AF	Acriflavine
AMC	7-amino-4-methylcoumarin
AO7	Acid Orange 7
ATR	Attenuated Total Reflectance
BBTC	Benxo-(1,2;4,5)-bis(thiophene-2'-carboxylate)
BDC^{2-}	1,4-Benzenedicarboxylate
BET	Brunauer-Emmett-Teller
$BPDC^{2-}$	4,4'-Biphenyldicarboxylate
BPEE	1,2-Bipyridylethene
bpy	2,2’-Bipyridine
bpydc	2,2’-Bipyriine-5,5’-dicarboxylic acid
br	broad singlet
BTB^{3-}	4,4’,4’’-Benzene-1,3,5-triyl-tribenzoate
BUT	Beijing University of Technology
BVS	Bond Valence Sum
C-153	Coumarin-153
CB	Conduction band
CIF	Crystallographic Information File
Cp*	Pentamethylcyclopentadienyl
$CPNBP^{2-}$	4,4′-bis(carboxyphenyl)-2-nitro-1,1′-biphenyl
$CPTT^{2-}$	6-(4-Carboxyphenyl)thieno[3,2-*b*]thiophene-2-carboxylate
D	Donor
d	doublet
DCM	4-(Dicyanomethylene-2-methyl-6-(4-dimethylaminostyryl)-4H-pyran
dcppy	2-Phenylpyridine-5,4’-dicarboxylic acid
DEF	N,N-Diethylformamide
DMF	N,N-Dimethylformamide
DMNB	2,3-Dimethyl-2,3-dintrobutane
$DMTDC^{2-}$	3,4-Dimethylthieno[2,3-*b*]thiophene-2,5-dicarboxylate

DNA	Dioxyribonucleic Acid
DNT	2,4-dinitrotoluene
dppe	1,2-bis(diphenyl- phosphino)ethane
DSM	4-(*p*-dimethylaminestyryl-1-methylpyridinium)
EDX	Energy Dispersive X-Ray Spectroscopy
ET	Electron Transfer
FTIR	Fourier Transform Infrared
FTO	Fluorine-doped tin oxide
$H_2$2,2'-DMBP	6,6’-Dimethyl-2,2’-bipyridine-4,4’-dicarboxylic acid
H_2ADBA	4,4’-(9,10-anthracenediyl)dibenzoic acid
H_2BDT	1,4-benzenedi(1H-1,2,3-triazole)
HER	Hydrogen evolution reaction
HPLC	High Performace Liquid Chromotography
hxtt	5,5,10,10,15,15-Hexaalkyl-10,15-dihydro-5H-diindeno[1,2-a:1',2'-c]fluorene-2,7,12-tricarboxylic acid
IC	Internal conversion
IFMC	Institute of Funcitonal Materials Chemistry
IR	Infrared
IRMOF	Isoreticular metal-organic framework
ISC	Intersystem crossing
J	Coupling Constant
LED	Light emitting Diode
LLCT	Ligand-to-ligand chanrge transfer
LMCT	Ligand-to-metal charge transfer
Ln-MOF	Lanthanide-based metal-organic framework
m	multiplet
m	medium
MAF	Metal-azolate framework
m-BDC^{2-}	1,3-Benzenedicarboxylate
m-$BTEB^{3-}$	3,3’,3’’-(Benzene-1,3,5-triyltris(ethyne-2,2-diyl)tribenzoic acid
MIL	Matériaux de l'Institut Lavoisier
MLCT	Metal-to-ligand charge transfer
MMCT	Metal-to-metal charge transfer
MOF	Metal-organic framework

MOP	Metal-Organic Polyhedron
MUF	Massey University Framework
NAC	Nitroaromatic compounds
NDC^{2-}	naphthalene-2,6-dicarboxylate
NHE	Normal hydrogen electrode
NIR	Near infrared
NMR	Nuclear magnetic resonance
OEC	Oxygen evolving complex
OER	Oxygen evolution reaction
OLED	Organic light emitting diode
PCP	Porous coordination polymer
PET	Photoinduced electron transfer
phen	Phenanthroline
POM	Polyoxometalate
ppy	2-Phenylpyridine
PS	Persulfate
PT	*p*-phenanthroline dibenzoate
PXRD	Powder X-ray Diffraction
q	quartet
RCSR	Reticular Chemistry Strucuture Resource
RGB	Red green blue
S	Singlet
s	singlet
SBU	Secondary building unit
SEM	Scanning electron microscopy
SK	Supramolecular keplarate
st	strong
T	Triplet
t	triplet
$TATAB^{3-}$	4,4′,4″-s-Triazine-1,3,5-triyltri-p-aminobenzoate
TBP^{4-}	5,10,15,20-tetra(p-benzoate)porphyrin
TEOA	Triethanolamine
TGA	Thermogravimetric analysis
THF	Tetrahydrofuran
TLC	Thin Layer Chromotography

TOF	Turnover frequency
TON	Turnover number
TTMOP	Thienothiophene-based Metal-Organic Polyhedra
TTP	1′,1″-(2,4,6-Trimethylbenzene-1,3,5-triyl)tris(methylene)tris(pyridine-4(1*H*)-one)
TTT^{3-}	5,5’,5’’-(1,3,5-triazine-2,4,6-triyl)tris(thiophene-2-carboxylate)
UiO	Universitet I Oslo
UV	Ultraviolet
VB	Valence band
VOC	Volatile organic compound
w	weak
WOC	Water oxidation catalyst
XRD	X-ray diffraction
ZJU	Zhejiang University

A note on publications

Sections from chapter 1 were published in the peer-reviewed journal *Coord. Chem. Rev.*, in a review entitled "Tuning photoactive metal–organic frameworks for luminescence and photocatalytic applications".

É. Whelan*, F. W. Steuber, T. Gunnlaugsson and W. Schmitt*, Coord. Chem. Rev., 2021, 437, 213757.

Additional publications:

F. W. Steuber, J. J. Gough, É. Whelan, L. Burtnyak, A. L. Bradley and W. Schmitt*, Inorg. Chem., 2020, 59, 17244–17250.

Chapter 1 : Introduction to Metal-Organic Materials

1.1 Introduction to Metal-Organic Materials

Metal-organic frameworks (MOFs), or related porous coordination polymers (PCPs) can be regarded as a class of porous crystalline materials, which self-assemble from organic linkers and individual metal ions or coordination cluster nodes.[1,2] The organic linkers are multidentate species, which bridge metal ions or cluster moieties to form extended two- or three-dimensional structures. Early pioneering work demonstrated that through variation of the components used to construct MOFs, a wide range of structures were accessible.[3–9] Research into the control of the architecture of MOFs led to the development of reticular chemistry and related topological concepts.[10]

Reticular chemistry concepts are based on the realisation that a MOF can be reduced to the geometrical features of its subcomponents and categorised accordingly.[10] The inorganic node of the structure determines the relative orientation in which the organic linkers assemble. The organic linkers serve as geometrically defined connectors between the inorganic subunits. Both organic and inorganic components are often classified as secondary building units (SBUs), in analogy to zeolite topochemistry:[11,12] Reticular synthetic approaches take advantage of the specific geometries and chemical amiability of SBUs, producing extended network structures whose topologies relate to those of purely inorganic '*default'* structures. A key principle that governs the synthesis of MOFs stems from the realisation that MOFs whose components possess the same geometrical features form isoreticular structures that adopt analogous topologies, or the same nets.[13]

As reticular chemistry and related synthetic concepts gained increasing importance, and their applications resulted in the discovery of prodigious numbers of new structures, universal nomenclatures for structure classification and identification were developed, for instance through collaborative efforts between Blatov, O'Keeffe and Proserpio.[14] The Reticular Chemistry Structure Resource (RCSR) database categorises the structures according to their topologies[15]; the RCSR symbols are composed of three lower case bold letters with abbreviations either based on materials with that topology (e.g. **dia** for diamond or **pto** for platinum oxide) or geometrical shapes (e.g. **pcu** for primitive cubic lattice or **sql** for square lattice, etc.).

In addition to their tunable structures and pore volumes,[16,17] MOFs and related metal-organic materials offer an advantage over other conventional inorganic porous materials, such as zeolites, as their properties can be tuned for specific applications by varying the nature of the linkers and the metal ions in the structure.[18–20] Additionally, the porosity of MOFs allows incorporation of various guest molecules into their voids, which can influence the properties of the materials.[21] The chemical and structural versatility of MOFs, as well as their potentially high surface areas and porosity, have facilitated their application as catalysts,[22–24] materials for gas storage[25] and separation,[26,27] as chemical sensors,[28,29] as photosensitisers for photodynamic therapy[30] and other applications.[31]

The concepts of reticular synthesis can also be applied to the synthesis of MOPs and coordination cages.[32] A wide range of structures are possible through variation of the coordination geometry of the metal ions or clusters and the shape of the linkers used to construct MOPs. Ten basic polyhedral structures have been found for MOPs; tetrahedron (**tet**), octahedron (**oct**), cube (**cub**), icosahedron (**ico**), dodecahedron (**dod**), tricontahedron (**trc**), icosidodecahedron (**ido**), rhombic dodecahedron (**rdo**), cuboctahedron (**cuo**), and hendecahedron (**hen**).[32] For the hendecahedron structures, only two isostructural metal-organic hendecahedra have been reported using a mixture of ditopic ligands with bend angles of 90 and 120°.[33]

The ability to incorporate photosensitising ligands (e.g. organic chromophores, polyaromatic coordinating ligands, suitable coordination complexes, etc.) into MOFs and MOPs has led to their development as light-harvesting materials.[22,34] Significant research activities have been carried out to investigate how the choice of the organic linker and inorganic node used in the construction of MOFs, as well as interactions with guest molecules, allow their photochemical properties to be controlled.[35] Hence, by systematic variation of the individual MOF components, the light absorption characteristics, as well as the luminescence output can be tuned towards specific wavelengths.[36] Additionally, MOFs can be tailored towards photocatalytic applications by incorporation of the appropriate components or functional groups.[37–39]

Herein, the structures and applications of metal-organic materials are discussed, in the context of three key aspects. The first section discusses coordination cages. The second section of this chapter discusses the application of *MOFs as photoluminescent materials*, for example, as light-emitting materials with tunable emission characteristics, and as chemical sensors with luminescence responses. The third section explores the design of *MOFs as photocatalysts* for energy-conversion reactions such as water splitting, CO_2 reduction or for light-driven organic reactions, such as degradation of organic pollutants. Particular attention is given to how the choice of the constitutional components of MOFs influences the photoactivity of these materials. Selected examples of recent advancements in these three topics will be explored, to give context for the research carried out in this thesis. Organic linkers of the individual MOFs and coordination cages that are discussed, and their abbreviations are shown in **Fig. 1.1**.

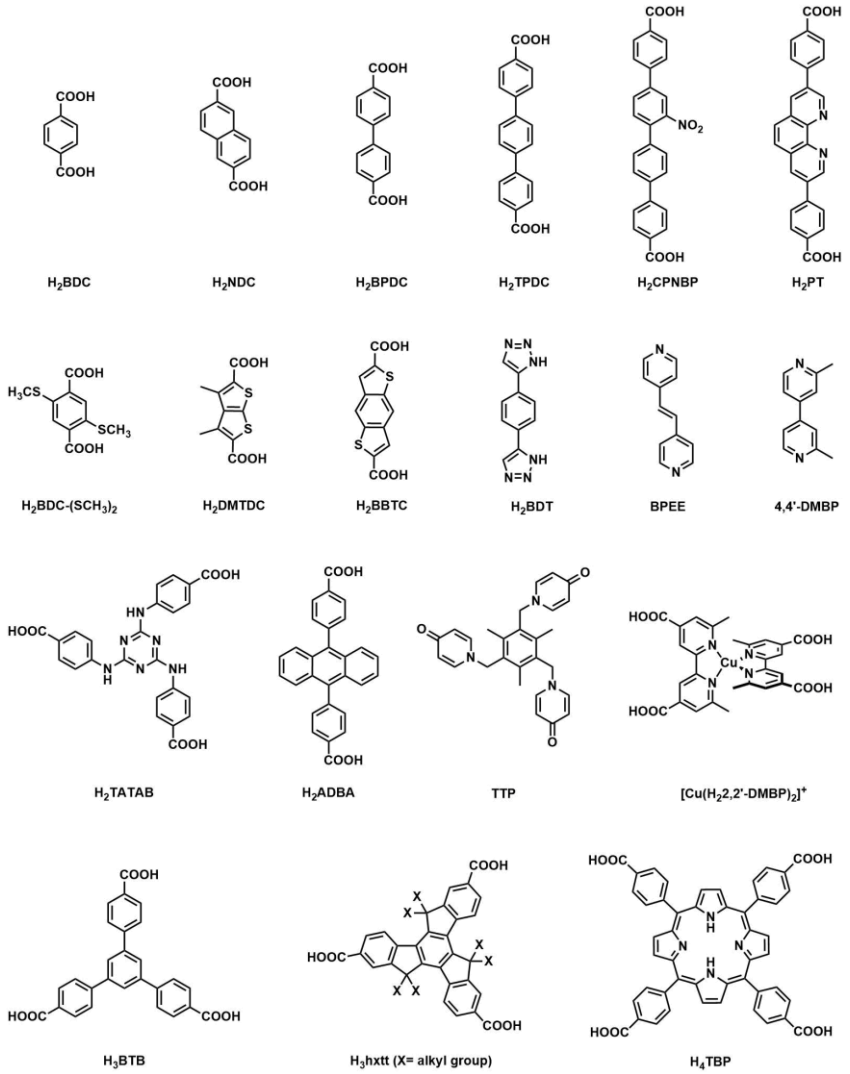

Fig. 1.1 A small selection of organic linkers used in the construction of photoactive MOFs, and corresponding abbreviations as they appear in this thesis.[40]

1.2 Introduction to coordination cages

Metal-organic polyhedra (MOPs) or coordination cages are discrete molecular structures which self-assemble from organic linkers and metal ions. Extensive research has been carried out on MOPs due to their promising applications, which include catalysis,[41–44] gas storage,[45–47] molecular sensing,[48–50] separation[51] and drug delivery.[52]

The term MOP was first used by Yaghi *et al.* in 2001.[53] Yaghi *et al.* reported the synthesis of a discrete metal-organic polyhedron (MOP-1) from copper (II) acetate and 1,3-benzenedicarboxylate (*m*-BDC^{2-}). The inorganic SBU of this MOP is a dinuclear copper paddlewheel, formed through binding of the deprotonated carboxylate moieties of *m*-BDC^{2-} to Cu^{II} ions. Each discrete molecule contains 12 dicopper paddlewheels bridged by 24 *m*-BDC^{2-} linkers to give a MOP with a cuboctahedron structure. The MOP contains a spherical cavity with a diameter of 15 Å.

Previous work by Schmitt *et al.* reported the synthesis of coordination cages with extremely large cross-sectional diameters of 48-50 Å (**Fig. 1.2**).[54] The coordination cage $[Cu_{36}(m\text{-}BTEB)_{24}(H_2O)_{28}(DMF)_8]\cdot$solv (SK-1) self-assembles from a solution of copper (II) nitrate and the

tritopic linker 3,3',3''-(benzene-1,3,5-triyltris(ethyne-2,2-diyl)tribenzoic acid (*m*-BTEB). The result was a molecular coordination cage with 96 components. The inorganic SBUs in SK-1 are dinuclear {Cu_2} paddlewheels, which are linked by the *m*-BTEB linkers.[54]

The name "Supramolecular Keplerate-1" (SK-1) was given to the coordination cage [Cu_{36}(*m*-BTEB)$_{24}$(H_2O)$_{28}$(DMF)$_8$]·solv. Keplerate is a structure with both Platonic and Archimedean solids arranged with one within the other. The structure of SK-1 molecular coordination cages consists of two shells, with an inner and outer shell present (**Fig. 1.2**). The topology of the outer shell of SK-1 can be described as a cuboctahedron (Archimedean solid), with centre of the Cu-Cu axis {Cu_2} paddlewheel forming the vertices of the cuboctahedron. The topology of the inner shell is best described as an octahedron (Platonic solid). Due to the flexibility of the *m*-BTEB linker, different arrangements of the octahedral shell are possible. Therefore, two structurally distinct isomers of SK-1 are possible; SK-1A and SK-1B (**Fig. 1.2**).

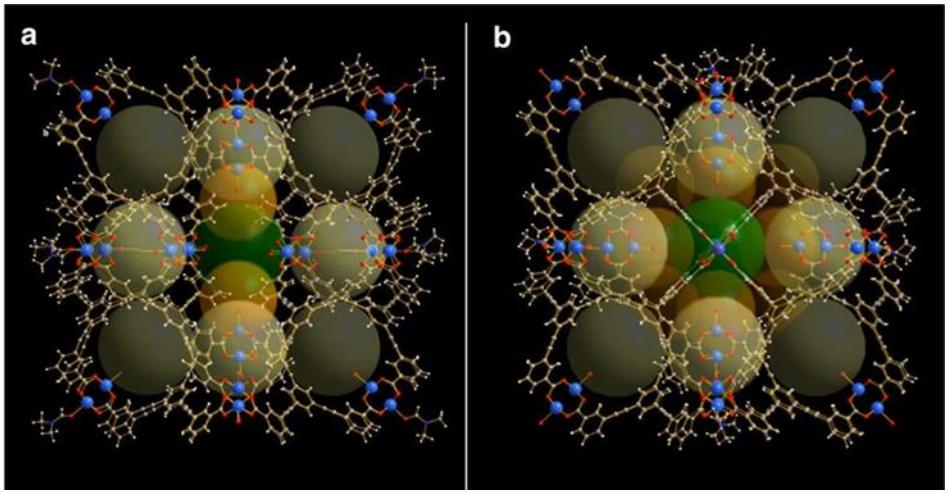

Fig. 1.2 Structures of SK-1A and SK-1B.[54]

SK-1 has large windows and a solvent accessible void volume of over 70%.[54] By functionalisation with 4-(3-phenylpropyl)pyridine, which binds to the {Cu_2} paddlewheels of SK-1, the cage could be dissolved in chloroform solution. Using fluorescence spectroscopy, the quenching of a solution of 7-amino-4-methylcoumarin (AMC) was observed upon introduction of AMC to a solution of SK-1. This indicates that AMC was absorbed by SK-1.

The uptake of guests by MOPs and coordination cages has also been explored. Previous work by Fujita *et al*. has reported the synthesis of a Pd_6L_4 (L = 2,4,6-tri(4-pyridyl)-1,3,5-triazine) coordination cage with 2,2'-bipyridine ancillary ligands and a roughly spherical geometry.[55] This coordination cage was shown to enclathrate guest molecules, including *o*-carborane, 1-adamantol and diphenyl methane. Single crystal X-ray diffraction analysis allowed the structure of these guests within the coordination cage pore to be obtained, allowing detailed study of the encapsulation of the guests. This has led to further research into using coordination cages and coordination networks as

"crystalline sponges", which can absorb target materials and allow single crystal X-ray diffraction analysis of the samples, even where single crystals of the target molecule cannot be obtained.[56,57]

1.3 Photochemistry of MOFs

1.3.1 Absorption of Light by MOFs

The design and synthesis of a photoactive MOF requires the incorporation of a light-harvesting unit into the structure. Typically, this is achieved by using an appropriate organic linker in the MOF structure, though light-harvesting guests can also be incorporated into the voids of the porous framework.[58] In some rarer cases, direct excitation of metal ions or metal clusters is also possible, for example, in Fe^{III}-based MOFs containing $\{Fe^{III}_3(\mu_3\text{-}O)\}^{7+}$ clusters.[59] By varying the organic linker, MOFs can be designed to absorb light in specific regions of the UV-visible spectrum.[60]

Many MOFs utilise aromatic organic linkers, which absorb light in either the UV or visible region of the spectrum.[61,62] Excitation of these organic linkers leads to n-π^*- or π-π^*-based transitions. The range of wavelengths in which these compounds absorb light can be varied by extending the conjugated aromatic system of the linker, or incorporating various functional groups on the backbone structure of the linker.[63,64] Alternatively, metalloligands can be employed as photosensitisers in MOFs. Of note are MOFs composed of metalloporphyrin ligands, which show great promise as photoactive materials, due to their ability to absorb visible light across a broad region of the spectrum. The photocatalytic properties of metalloporphyrin-based MOFs can be varied by changing the metal ion within the porphyrin cavity. For example, metallation of porphyrin linkers with high valent metal ions such as In^{III} and Sn^{IV} gives MOFs with oxidative photoexcited states that can facilitate organic reactions, for example, the Mannich reaction, aerobic amine coupling, and hydroxylation of arylboronic acids.[65] Thus, porphyrinic MOFs are being explored as promising and versatile photocatalytic materials.[66,67]

Furthermore, the use of polypyridyl ligands that can facilitate ligand-centred, metal-to-ligand and ligand-to-metal-based transitions can be used in the generation of photosensitisers in MOFs. MOFs based on Ru^{II} or Ir^{III} photosensitisers, which are well known as excellent photo-cleavage agents for nucleic acids such as DNA,[68,69] have been widely reported in recent times.[70,71] Ru^{II} polypyridyl-based photosensitisers offer advantages as linkers due to their ability to harvest visible light,[72] their long-lived excited states, and their ability to undergo photoinduced redox reactions.[73] Metalloligands employing earth-abundant metal ions have also been incorporated into MOF structures as photosensitisers, for example those based on Cu^{I} species.[74,75]

The diversity of ligands that can be used in the construction of MOFs can allow for further tuning of the optical band gaps of these materials. For example, by functionalisation of the ligand used in a MOF denoted as MIL-125 (MIL = Matériaux de l'Institut Lavoisier), the optical band gap of this material could be varied.[76] MIL-125 consists of 1,4-benzenedicarboxylate (BDC^{2-}) linkers that bridge octanuclear cyclic Ti-oxo clusters. Walsh and co-workers reported that the introduction of amine

functional groups onto the BDC^{2-} linker of MIL-125 led to a shift of the absorption onset of these MOFs from the UV region to the visible region of the electromagnetic spectrum. Furthermore, functional groups which impart weaker electron donating effects than amines revealed a reduced influence on the band gap, with smaller shifts observed for -Cl, $-CH_3$, and -OH substituents.

1.3.2 Luminescence processes of MOFs

Luminescence is defined as emission of light from a substance, which occurs following absorption of radiative energy, either directly or via sensitisation processes involving energy or electron transfer processes.[77] Two categories of luminescence exist, fluorescence and phosphorescence. Fluorescence occurs without a change in spin, when light is emitted from singlet excited states and fluorescence lifetimes are short, in the region of 10^{-12} to 10^{-6} seconds.[78] In contrast, phosphorescence occurs when spin-forbidden transitions occur resulting in the emission of a photon, for example, from triplet excited states to singlet ground-states. Phosphorescence lifetimes are longer than those observed for fluorescence processes, with typical values varying between 10^{-6} and 10^{2} seconds.[78] While not common for organic ligands (except at low temperatures), phosphorescence can be facilitated through intersystem crossing by the so-called heavy atom effect that is characteristic for many d- and f-block metal complexes (e.g. Ru^{II} polypyridyl complexes which normally emit from ^{3}MLCT states).

Generally, luminescence occurs following absorption of radiation of a specific wavelength, commonly, X-ray, UV or visible light, and emission of light at a different wavelength. The emitted light is usually lower in energy than the absorbed light, and the difference in energy between the maximum of the absorbed light and the maximum of the emitted light is known as the Stokes shift. Alternatively, upconversion may occur, a phenomenon in which absorption of two or more photons results in the emission of one photon of higher energy.[79] In this case, the energy difference is quantified by the anti-Stokes shift.

Due to the hybrid nature of MOF structures, luminescence in MOFs can arise from multiple different sources, as highlighted in **Fig. 1.3**. These include,

- Ligand-centred emission
- Ligand-to-ligand charge transfer (LLCT)
- Ligand-to-metal charge transfer (LMCT)
- Metal-to-ligand charge transfer (MLCT)
- Metal-to-metal charge transfer (MMCT)
- Metal-centred emission
- Interactions with guest molecules.

Combinations of more than one of these effects can also be observed in luminescent MOFs.

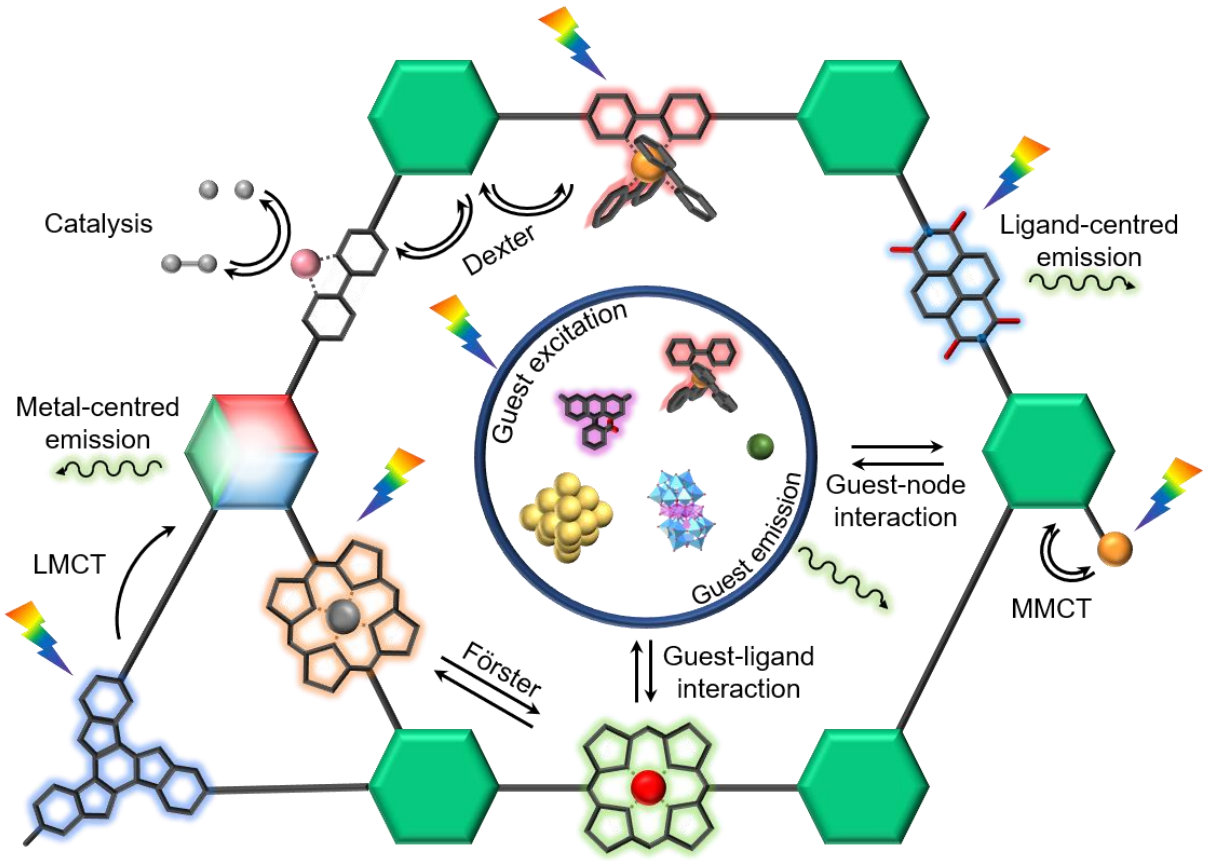

Fig. 1.3 Schematic representation of the absorption and emission processes in photoactive MOFs, showing examples of photoactive organic linkers and inorganic nodes are represented by hexagons. Polyoxometalate (POM) structure produced from Ref. [80].

Linkers in MOFs are constrained in ordered positions and as a result, the photochemical properties of the linkers differ from those of the free ligand in solution. In the rigid environment of MOFs, non-radiative processes from the linker excited state are less efficient, leading to enhancement of the linker fluorescence.[81–83] Ligand-centred emission is commonly observed in MOFs based on d^{10} metal ions such as Zn^{II} and Cd^{II} systems.[84] Due to their closed shell electron configuration, d-d transitions cannot occur, and the metal ions cannot be readily oxidised or reduced, leading to ligand-centred emission characteristics.

Luminescence can also occur via LMCT and MLCT interactions in MOFs. Charge-transfer luminescence occurs due to a transition from the charge-transfer excited state to the ground state. LMCT excited states occur via transfer of electrons from an orbital centred on a linker, to an orbital of a metal ion. The opposite effect is facilitated by MLCT, which involves electronic transitions from metal orbitals to orbitals of the linkers. MLCT is commonly observed in MOFs containing metal ions in low oxidation states, that can readily be oxidised further.

Metal-centred emissions are typically observed in lanthanide-based MOFs (Ln-MOFs).[85] In these systems the shielding of the 4f orbitals by the $5p^6 6s^2$ shells results in characteristic narrow-line emission, predominantly in the visible and near-infrared regions of the electromagnetic spectrum. The f-f transitions are Laporte forbidden, hence, the absorption coefficients for these transitions are

small, typically less than 3 M^{-1} cm^{-1}.[86] To excite lanthanide ions effectively, the antenna effect must be employed, in which a ligand coordinated to the Ln^{III} ion acts as a light harvesting chromophore which sensitises the excited state of the lanthanide ion. Absorption of energy by the ligand results in spin-allowed excitation from the ground state to the singlet excited state S_1 (S = singlet). Intersystem crossing (ISC) can then occur from the ligand-centred S_1 excited state to the triplet excited state, T_1 (T = triplet). Energy can then be transferred from the long-lived ligand triplet excited state to the Ln^{III} ion. Emission from the resulting Ln^{III} excited state occurs spontaneously, giving metal-centred luminescence in the absence of back energy transfer to the excited state of the ligand.[87] The latter may either reduce the efficiency of the emission process, or quench it entirely. The T_1 to Ln^{III} transfer may be facilitated by good overlap between the linker and metal orbitals, involving a double electron transfer, in line with an exchange or Dexter mechanism. More predominate in coordination compounds is a Förster mechanism, whereby the dipole moments of the 4f orbitals couple the dipole moment of the T_1 state. Similarly, dipole–multipole transfers and charge-transfer states can play a role in the sensitisation of Ln^{III} ions. In mixed-metal MOFs composed of transition metal-based linkers and Ln^{III} nodes, sensitisation of the Ln^{III} ions can occur via the ^{3}MLCT excited states of the transition metal. Metal-centred emission following sensitisation is also observed in actinide-based MOFs.[88] A simplified diagram for the energy migration pathways applicable to Ln-based MOFs is shown in **Fig. 1.4.**

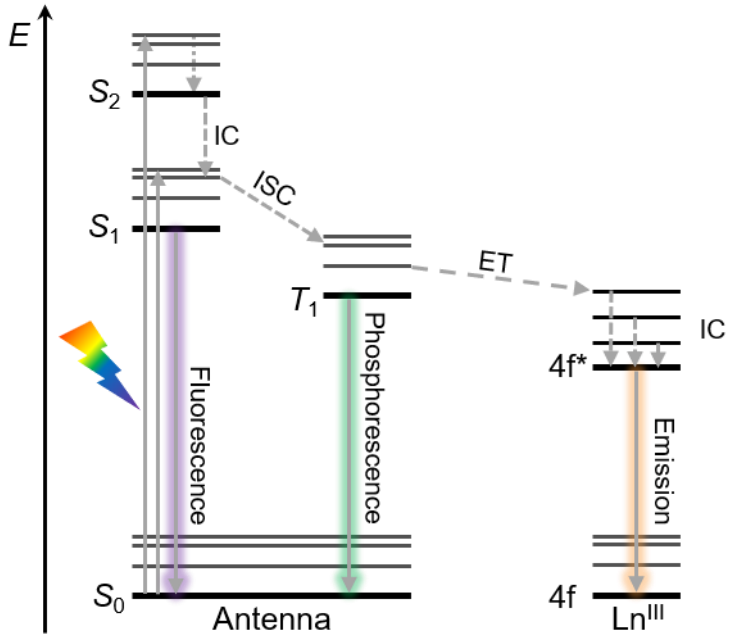

Fig. 1.4 A simplified diagram depicting the antenna effect in a Ln^{III} ion. The solid grey arrows represent absorption of a photon, which can be followed by fluorescence, intersystem crossing (ISC). After ISC occurs, phosphorescence can occur from the triplet excited state of the antenna, or energy transfer can occur, resulting in emission of a photon from the Ln^{III} ion. Internal conversion (IC) can occur as a non-radiative transition between excited states with the same spin.

The porous structures of MOFs allow the possibility of introducing luminescent guest molecules into their pores. The crystalline nature of MOFs allows guests in the pores of the material to be characterised in great detail.[89,90] Luminescence can arise from these guest molecules,[91] from both the

MOF and the guest molecule separately, or via interactions between these guest molecules and the framework structure.[92] The interactions between the guest molecule and the MOF can occur via weak intermolecular interactions, dipole interactions, or through coordination bonds between the guest and open coordination sites on the framework metal ion.[35]

1.3.3 Photocatalysis by MOFs

Fossil fuels are the world's primary energy source, accounting for over 80% of global energy consumption.[93] Combustion of fossil fuels results in emission of greenhouse gases, and consequently, the increase of global temperatures.[94] As emissions continue to rise, and fossil fuel reserves are depleted, the need for clean energy sources is increasingly urgent. Solar energy is a renewable and unlimited resource, and much research has focused on harnessing this energy to meet the world's energy demands in a sustainable way. Designing materials that can use light to carry out reactions such as H_2O splitting or CO_2 reduction is vital to provide a sustainable method of producing energy.

Photoactive MOFs have been shown to be promising photocatalysts for energy conversion due to their tunable structures and properties. MOFs can behave as heterogeneous catalysts, and offer an advantage over molecular photocatalysts, as their solid-state nature allows facile separation of catalyst from product, thus lowering the risk of contaminating products with toxic metals used for catalysis.[95] Heterogeneous catalysis also allows the catalyst to be recycled readily. Due to the crystalline nature of MOFs, the active sites are arranged in well-defined spatial sites, and the pores of MOFs can be tuned towards specific dimensions, which offers the potential for substrate selectivity.[96,97] Furthermore, porous MOFs are often characterised by a high number of active sites per volume and high diffusion coefficients, which are attractive properties in catalytic materials.[98]

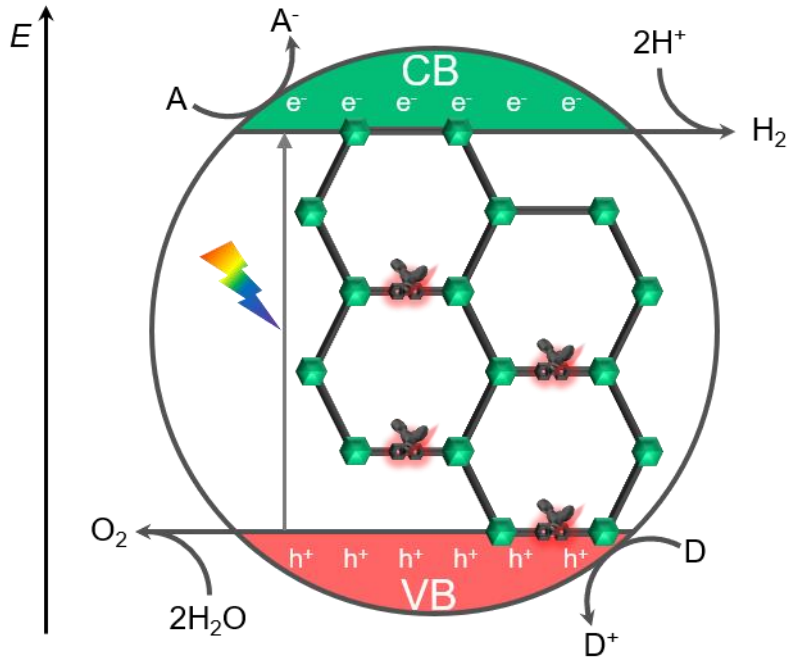

Fig. 1.5 Schematic representation of catalytic reactions after photoinduced charge transfer in a MOF. Excitation of electrons (e^-) from the valence band (VB) to the conduction band (CB) results in the formation of holes (h^+). Redox reactions can occur by oxidation of an electron donor (D) or reduction of an electron acceptor (A). Furthermore, photo-generated holes can lead to water oxidation, and photoexcited electrons can reduce H^+ to H_2.

To function as a photocatalyst, MOFs are required to efficiently separate charges within their structures upon light absorption by a chromophore and promotion of an electron to a higher energy level. This electron can then migrate from the chromophore to a nearby electron acceptor moiety within the structure. The resulting negative charges (electrons) and positive charges (holes) can be used to drive chemical reactions (**Fig. 1.5**).[99] Certain requirements are necessary for efficient photocatalysis, such as high molar absorption coefficients, excited state lifetimes that are long enough to allow catalytic conversion to compete with decay of the charge separated state, and finally, suitable redox potentials to drive the desired reactions.[100]

1.4 Utilising MOF Luminescence

1.4.1 MOFs as sensing materials

The ability to rapidly detect pollutants at low concentrations is vital to identify environmental risks and curtail pollution. The area of luminescent sensing focusing on small molecules and the *receptor-spacer-fluorophore* principles that govern the sensing process have recently been reviewed.[101] The underlying principles are transferable to MOFs, which offer some distinctive advantages over molecular sensors, associated with their intrinsic attributes including porosity and high surface areas. Luminescent MOFs can be used as sensors for a broad range of analytes, including gases,[102] explosive nitroaromatic compounds (NACs),[103,104] cations,[105,106] anions,[107,108] pesticides,[109] and other organic compounds.[110,111] The luminescence response from MOFs upon detection of analytes can result in luminescence quenching,[112] luminescence enhancing,[113,114] or a change in the colour of light

emitted.[115,116] Nanoscale MOFs have even been reported to be capable of pH sensing within living cells.[117]

Several mechanisms for luminescence sensing of analytes have been reported in MOFs. These include linker-analyte ion interaction, collapse of the MOF structure in response to the presence of an analyte, cation exchange between the analyte metal ions and framework metal ions, and competitive absorption of excitation wavelength due to overlap of absorption spectra of the MOF and analyte.[118] The advantage of using MOFs that display sensing through non-destructive mechanisms, such as linker-ion interactions, is that the sensor materials can be readily recycled.[119]

1.4.1.1 MOFs for sensing of organic compounds

The first example of a MOF capable of sensing explosive compounds was reported in 2009.[120] Li and co-workers demonstrated that the luminescent MOF $[Zn_2(BPDC)_2(BPEE)]$ ($BPDC^{2-}$ = 4,4'-biphenyldicarborboxylate, BPEE = 1,2-bipyridylethene) (**Fig. 1.6 a)**) is capable of fast, sensitive and reversible detection of explosive compounds. The structure of $[Zn_2(BPDC)_2(BPEE)]$ features one-dimensional channels which are approximately rectangular in shape (**Fig. 1.6 b)**). These channels contain DMF solvent molecules which can be removed to give a guest-free MOF. The luminescence quenching response of $[Zn_2(BPDC)_2(BPEE)]$ after solvent removal was tested for two analytes, 2,3-dimethyl-2,3-dinitrobutane (DMNB), a volatile aromatic compound (VOC) used as a taggant for explosives and 2,4-dinitrotoluene (DNT), a volatile impurity found in 2,4,6-trinitrotoluene. Thin layers of $[Zn_2(BPDC)_2(BPEE)]$ show solid-state ligand-based luminescence when irradiated under UV-light. This luminescence is quenched in response to DNT and DMNB vapours at concentrations of 0.18 ppm and 2.7 ppm respectively. The luminescence bands are also red-shifted in response to the presence of these analytes (**Fig. 1.6c)** and **d)**). Furthermore, the luminescence of solvent-free $[Zn_2(BPDC)_2(BPEE)]$ could be rapidly recovered after sensing, by heating the layers at 150 °C for one minute. The quenching mechanism involves photoinduced electron transfer (PET) from the excited state organic linker to the DNT and DMNB molecules.

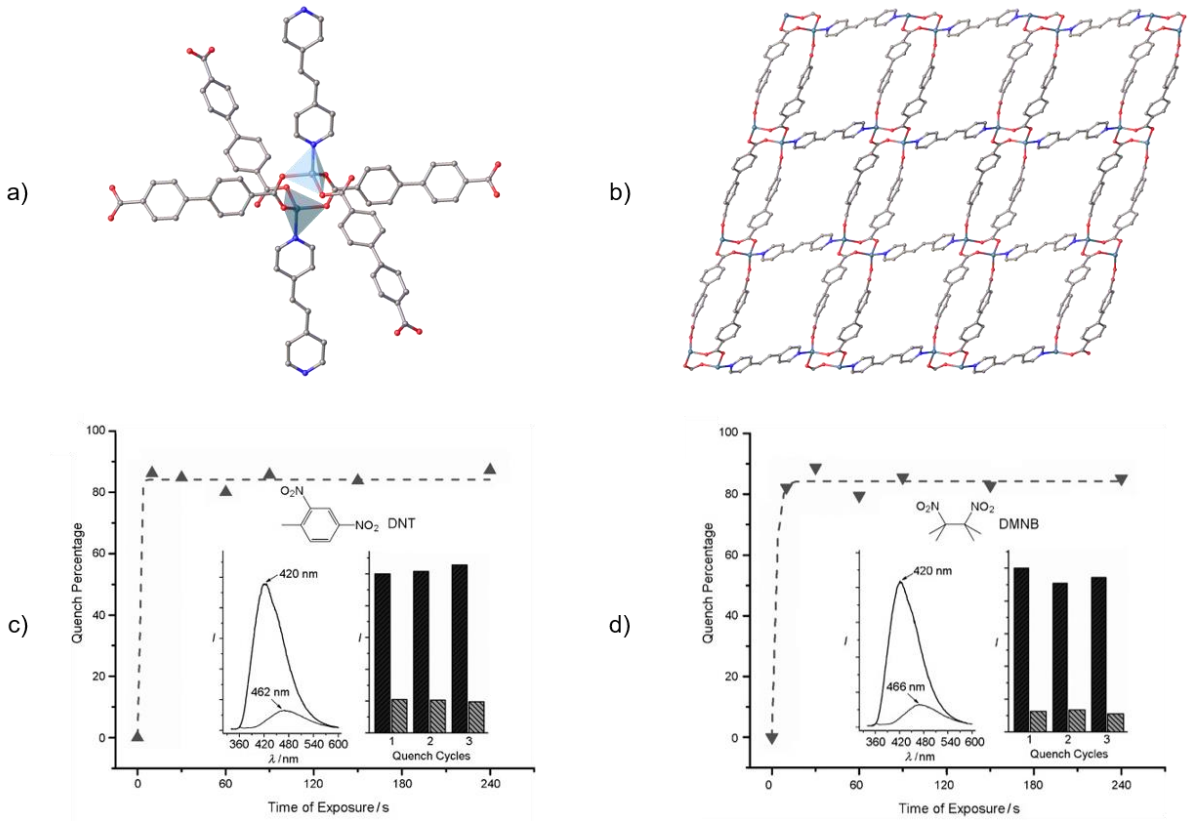

Fig. 1.6 a) The coordination environment of the dinuclear $\{Zn^{II}_2\}$ SBU in $[Zn_2(BPDC)_2(BPEE)]$ **b)** View of the structure of $[Zn_2(BPDC)_2(BPEE)]$ (DMF molecules removed for clarity) **c)** and **d)** Time-dependent fluorescence quenching by **c)** DNT and **d)** DMNB. Insets: Fluorescence spectra before and after exposure to vapours of the analytes for 10 s, and emission intensity after three cycles of quenching and regeneration. Reproduced with permission from Ref. [120]. Copyright 2009, Wiley-VCH Verlag GmbH & Co. KGaA, Weinheim.

Following this first report of MOFs being used for detection of explosives, MOFs have been reported to be applicable as efficient sensors for many explosive compounds, including picric acid, which also represents a well-known environmental pollutant used in the dye industry.[121] The use of luminescent MOF films for this purpose has been an area of much research. MOF thin films offer some advantages over MOFs which have been synthesised in bulk by solvothermal methods. Electrodeposition allows MOF films to be prepared under mild conditions, at room temperature, with short reaction times of as little as a few seconds.[122] Moreover, electrodeposition of MOFs can be used to selectively form MOFs in instances when more than one phase can be formed from the reagents, as reported by Dincă and co-workers for electrodeposition of MOF-5.[123,124] This method can be used to yield uniform, well-adhered films of MOFs. In terms of their use as sensors, MOF thin films can easily be separated from the analyte solution by removal of the film, and in many cases the material can then be washed and reused.[125]

An example of the use of an electrodeposited luminescent MOF was reported by Yang and co-workers, using the MOF $[Eu_4(NDC)_6(H_2O)_5]\cdot 3H_2O$ (Eu-NDC; NDC^{2-} = naphthalene-2,6-dicarboxylate).[126] Eu-NDC was first reported by Jin and co-workers in 2006.[127] The structure of Eu-NDC comprises channels with a compressed honeycomb-like shape, which run parallel to the crystallographic *a*-axis (**Fig. 1.7 a)**). Yang and co-workers reported the synthesis of Eu-NDC by

electrochemical methods on to the surface of fluorine-doped tin oxide (FTO) in 20 seconds.[126] Eu-NDC showed metal-centred luminescence under UV light irradiation (λ_{ex} = 355 nm). In response to the presence of picric acid dissolved in water samples, the MOF displayed luminescence quenching, with a detection limit of 0.67 μM. Furthermore, the MOF thin film could be washed and reused 5 times with no significant decrease in luminescence quenching (**Fig. 1.7 b)**).

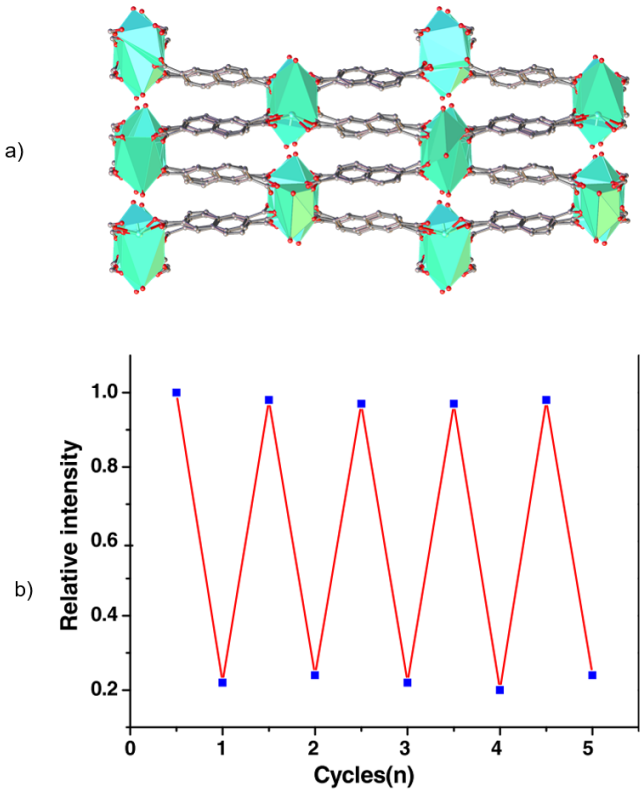

Fig. 1.7 a) Structure of Eu-NDC as viewed along the crystallographic *a*-axis.[127] **b)** Recyclability over 5 cycles of the Eu-NDC thin film immersed in 100 μM picric acid. Reproduced with permission from Ref. [126]. Copyright 2017, Springer Nature.

1.4.1.2 MOFs for sensing of metal ions

Many metal ions are toxic to human, plant, and animal life: and as a result the development of stable and reusable materials, which can rapidly detect the presence of metal ions at low concentration is desirable. Metal ions such as Li^{I}, Cr^{VI}, Hg^{II}, Cd^{II} and Pb^{II} are dangerous to the environment, livestock, and human health. Other ions are biologically essential, such as Cu^{II}, Zn^{II}, or Fe^{II}, but are harmful at higher concentrations. Luminescent MOFs have been reported to function as effective sensors for a wide range of metal ions. In some cases, selective sensing of specific metal ions over other analytes is possible.[128] Selective sensing of ions has also been accomplished, in fact, MOFs have been reported to be capable of discriminating between Fe^{II} and Fe^{III} ions.[129]

As previously mentioned, a common mechanism for luminescence sensing of metal ions by MOFs is through interactions between the analyte metal ions and the organic linker of the MOF structure. This interaction can lead to quenching or enhancement of the MOF luminescence, or a shift in the wavelength at which the MOF emits light. In some rarer cases, the luminescence response can even be observed by the naked eye.[130,131] One approach which can increase the ability of MOFs to sense

metal cations involves the functionalisation of organic linkers, for example, through introduction of functional groups containing Lewis-basic N, O or S atoms.

Nitrogen- and sulfur-containing linkers have been reported as promising linkers for selective detection of Hg^{II} ions, which is desirable due to the toxicity of these ions, and their potential for bioaccumulation. One example was reported by Wang and co-workers.[132] Reaction of $Cd(NO_3)_2 \cdot 6H_2O$ and the organic ligand, 4,4′,4″-s-triazine-1,3,5-triyltri-p-aminobenzoate ($TATAB^{3-}$) gave a porous, luminescent MOF (Cd-TATAB) (**Fig. 1.8**). The organic linker features two kinds of Lewis-basic functional moieties, involving the central triazine ring and the surrounding amino functionalities (**Fig. 1.8**). Due to the high affinity of Hg^{II} ions for nitrogen donors, and the spatial orientation of the nitrogen atoms in $TATAB^{3-}$, this MOF facilitates selective detection of Hg^{II} ions (**Fig. 1.8c)**), even in the presence of several other transition metal ions. In this case, the characteristic luminescence response arises from LMCT effects, which are influenced by $Hg^{II} \cdot\cdot N$ interactions between the metal ions and the framework structure, leading to luminescence quenching and a red shift of the MOF-derived luminescence (**Fig. 1.8 d)**).

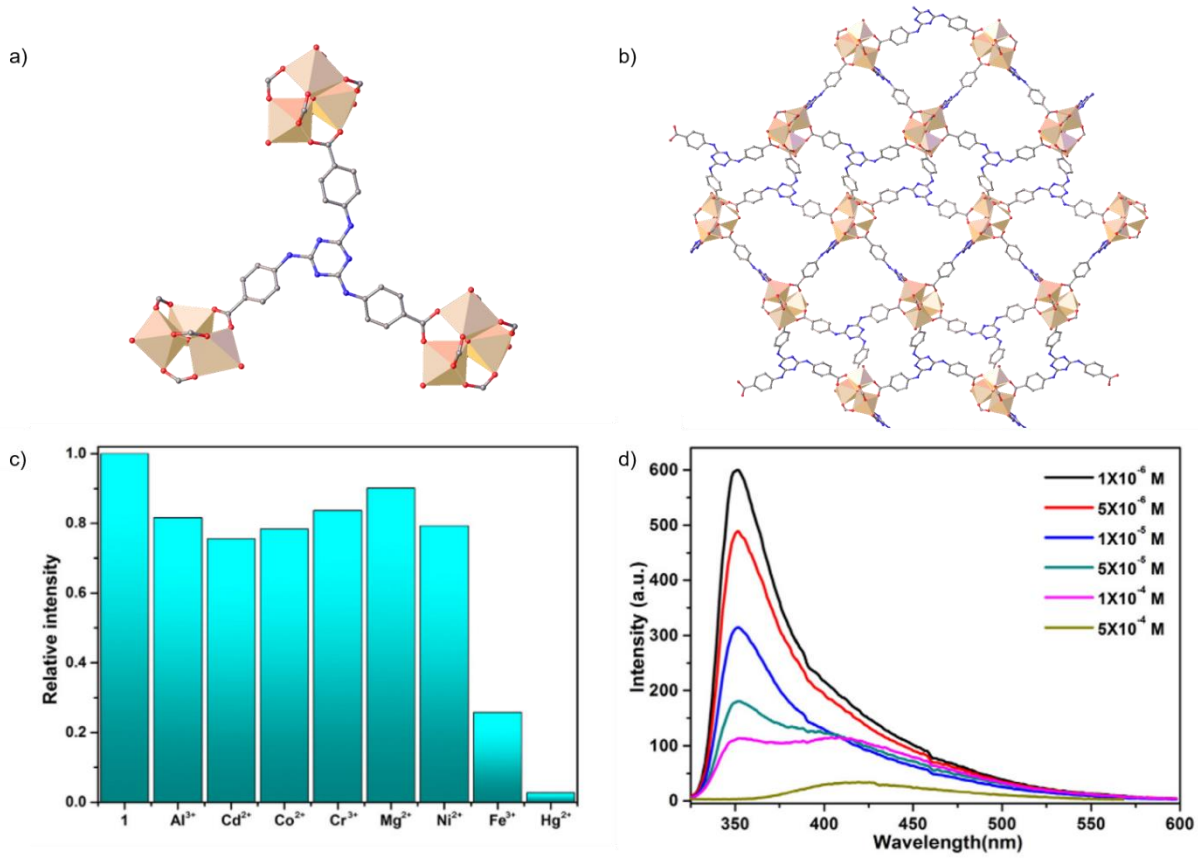

Fig. 1.8 a) Ligand and inorganic SBU of Cd^{II}-based MOF, Cd-TATAB **b)** Structure of the MOF **c)** relative fluorescence intensity of Cd-TATAB (1) MOF in response to the presence of metal ions **d)** Changes in fluorescence spectra of Cd^{II}-MOF in response to increasing Hg^{II} concentration. Reproduced with permission from Ref. [132]. Copyright 2018, Elsevier B.V..

In 2013, Su and co-workers reported a Zn-containing MOF, IFMC-28 (IFMC = Institute of Functional Materials Chemistry), using 3,4-dimethylthieno[2,3-*b*]thiophene-2,5-dicarboxylate ($DMTDC^{2-}$) as a linker (**Fig. 1.9**).[133] The Lewis-basic sulfur sites of the thienothiophene linker were

identified as potential coordination sites for the selective chelation of metal ions. IFMC-28 showed selective adsorption of Cu^{II} ions over other metal ions, such as Pb^{II}, Ni^{II}, Co^{II}, Mn^{II}, Mg^{II} and Cd^{II} ions (**Fig. 1.9 b)**). This selective adsorption behaviour was not observed in experiments using the isoreticular MOFs, MOF-5 or IRMOF-3, as controls (**Fig. 1.9 c)**) and was therefore attributed to favourable binding energies between sulfur atoms and metal ions. This selective absorption behaviour could be applied to the use of IFMC-28 as an ion chromatographic column, which selectively favoured adsorption of Cu^{II} ions over Co^{II} ions, giving an efficient method of separating Co^{II} ions from Cu^{II} ions (inset, **Fig. 1.9 c)**).

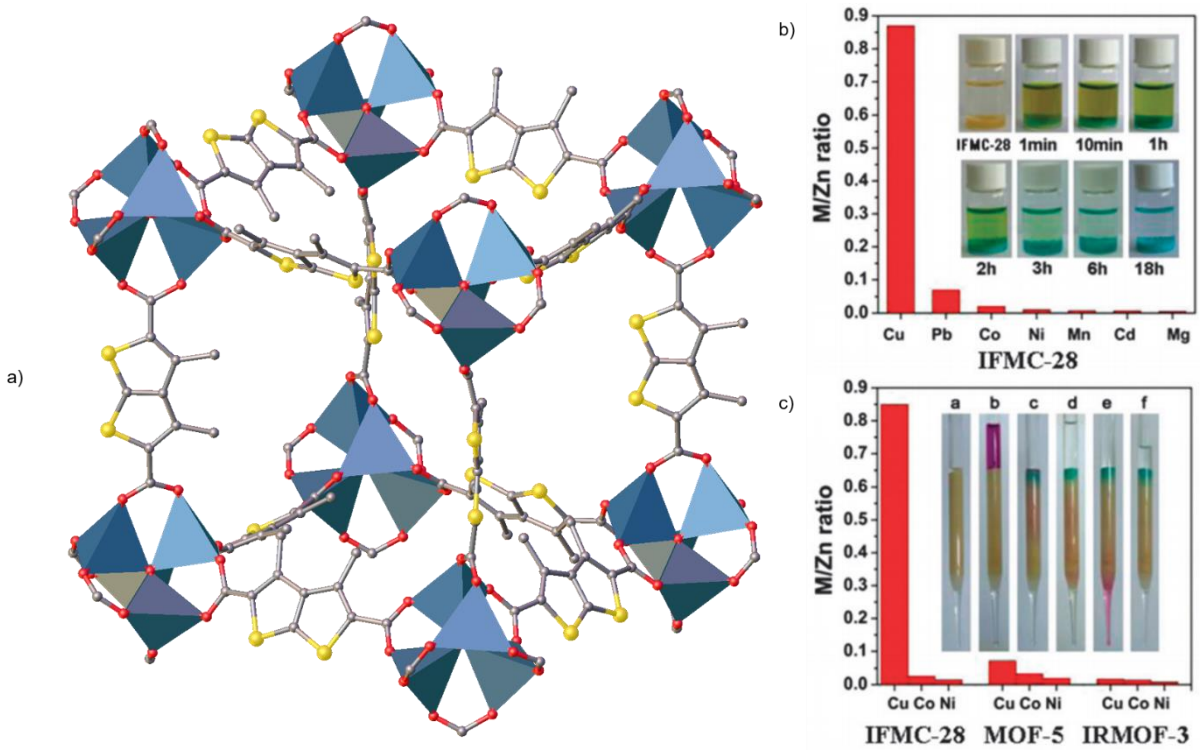

Fig. 1.9 a) Structure of IFMC-28 **b)** Metal ion absorption selectivity (graph) and Cu^{II} sorption over time when IFMC-28 was immersed in $CuCl_2$ solution (inset) **c)** Comparison of absorption of metal ions by IFMC-28, MOF-5 and IRMOF-3 and separation of Cu^{II} and Co^{II}ions by the MOF-based chromatography column (inset). Reproduced with permission from Ref. [133]. Copyright, Royal Society of Chemistry, 2013.

Many MOFs based on d^{10} metal ions have been reported to display luminescence sensing as a result of interactions between functionalised ligands and analyte metal ions. For example, Zhang and co-workers reported two Zn-based MOFs which can efficiently sense a range of transition metal ions.[134] These MOFs incorporate the ligand benzo-(1,2;4,5)-bis(thiophene-2′-carboxylate) ($BBTC^{2-}$), and two different ancillary ligands. Both MOFs display luminescence quenching effects in response to Hg^{II}, Cu^{II} and Cr^{VI} ions. These ions can be detected selectively by the MOFs from aqueous solutions containing other analytes. Luminescence quenching was also observed in response to the presence of the organic molecule salicylaldehyde in ethanol solution. Furthermore, in the case of Cr^{VI}, Hg^{II} and salicylaldehyde, the sensing behaviour could be reproduced after washing the MOFs, demonstrating facile recyclability of the system.

The detection of toxic anions in wastewater is important to prevent environmental contamination, and MOFs have been reported that can detect harmful pollutants such as $Cr_2O_7^{2-}$ and CrO_4^{2-}.[108,135] These ions present a serious risk to human health, causing DNA damage and cancer.[136] Li and co-workers have reported the synthesis of a luminescent Zr-based MOF, BUT-39 (BUT = Beijing University of Technology) which contains a tritopic imidazole ligand.[137] The luminescence in the MOF arises from ligand-centred emission. BUT-39 could selectively detect Hg^{II} and Fe^{III} ions through luminescence quenching effects. In terms of anion sensing, BUT-39 showed a selective sensing ability towards $Cr_2O_7^{2-}$, as the MOF luminescence was quenched by 99 % in response to this anion. In addition to this luminescence sensing response, the MOF also facilitated rapid removal of $Cr_2O_7^{2-}$ from water. This dual potential of sensing and absorbing harmful ions from aqueous solutions demonstrates some of the advantages of utilising porous, luminescent MOFs as sensor materials.

1.4.2 MOFs as tunable light emitting devices

The emission of MOFs can be tuned using several different methods, including by linker variation, incorporation of dopant metal ions into the SBU of MOFs,[138,139] and absorption of guests which alter the luminescence properties of the MOFs.[140]

A strategy that has been effective in designing MOFs that are characterised by tunable light emission involves the synthesis of Ln-MOFs using multiple different lanthanide ions, to give mixed-lanthanide MOFs.[141,142] Every Ln^{III} ion, except La^{III} and Lu^{III}, is photoluminescent. This luminescence can be observed in the UV region (Gd^{III}), in the visible region (Pr^{III}, Sm^{III}, Eu^{III}, Tb^{III}, Dy^{III}, Ho^{III}, Tm^{III}) or in the near-infrared (NIR) region (Pr^{III}, Nd^{III}, Ho^{III}, Er^{III}, Yb^{III}).[87] These ions can be categorised as triplet state emitters whereby the emission is often referred to as ‘metal-centred’ or as ‘lanthanide delayed luminescence’; as crystal field effects are minimal and the emission generally arises from the deactivation of the lanthanide’s excited state. Due to their visible, ‘bright’ luminescence (which is due to their long-lifetimes in the millisecond time range, which overcomes autofluorescence from other shorter lived emitters and from light scattering), Eu^{III} (red emission) and Tb^{III} (green emission) ions in particular have been studied with great interest. Further, the use of most conventional and commercially available spectrometers allows for their emission to be recorded without the need of special detectors (as is the case for some of the NIR emitting ions). However, a drawback to the use of the lanthanides is that their excited states can easily be quenched by O-H oscillators of coordinating solvent molecules, particularly water and alcohols, as their narrow energy gaps can be quenched. The often observed on and off emission characteristics associated with binding or displacement of solvent molecules is often exploited in functional materials including MOFs.[143]

In some cases it is possible to dope different lanthanide ions into a MOF without changing the framework structure.[144] Facile synthesis of mixed-lanthanide MOFs with varying ratios of lanthanide ions can be achieved by controlling the stoichiometry of the reactant lanthanide ions during synthesis.[145–147] In mixed-lanthanide MOFs, multiple luminescence emission bands are observed from the different lanthanide ions in the structure, allowing modulation of overall emission colour.[148–

[151] Thus, strategic combination of lanthanide ions that emit light in different regions of the visible spectrum allows the luminescence output of the MOFs to be specifically tuned, depending on the desired application; particularly significant work has been dedicated to the use of lanthanide-based MOFs or related soft materials as white light emitters.[152–154]

A vast majority of known luminescent materials only show emission in one part of the visible region of the electromagnetic spectrum. Su and co-workers reported a series of isostructural mixed-lanthanide MOFs, which can be tuned towards a range of emission colours.[155] The MOFs in this series have the general formula $[Ln_nLn'_{1-n}(TTP)_2 \cdot H_2O]Cl_3 \cdot$solvent (TTP = 1′,1″-(2,4,6-trimethylbenzene-1,3,5-triyl)tris(methylene)tris(pyridine-4(1H)-one)). Mixed-metal MOFs were synthesised using three combinations of two different ions; Eu^{III} and Tb^{III}, Eu^{III} and Gd^{III}, Gd^{III} and Tb^{III} ions. The structure of the MOF consists of seven-coordinate Ln^{III} ions, with pentagonal-bipyramidal geometry. Each Ln^{III} is coordinated by six oxygen atoms from six different TTP ligands and one water molecule. The MOF forms one-dimensional chains with channels within (**Fig. 1.10 a)**). The TTP ligand behaves as an antenna for photosensitisation of the Eu^{III} (red emission) and Tb^{III} (green emission) ions in the MOF (**Fig. 1.10 b)**). The presence of methylene groups linking the pyridone groups to the core benzene rings allows each pyridone group to function as an independent sensitising antenna. Coordination of a pyridine group to Gd^{III}, which is non-emissive in the visible region, results in ligand-centred blue emission from the pyridone group. Changing the ratios of the lanthanide ions in the structure allowed the colour of the MOF luminescence to be varied across the RGB triangle.

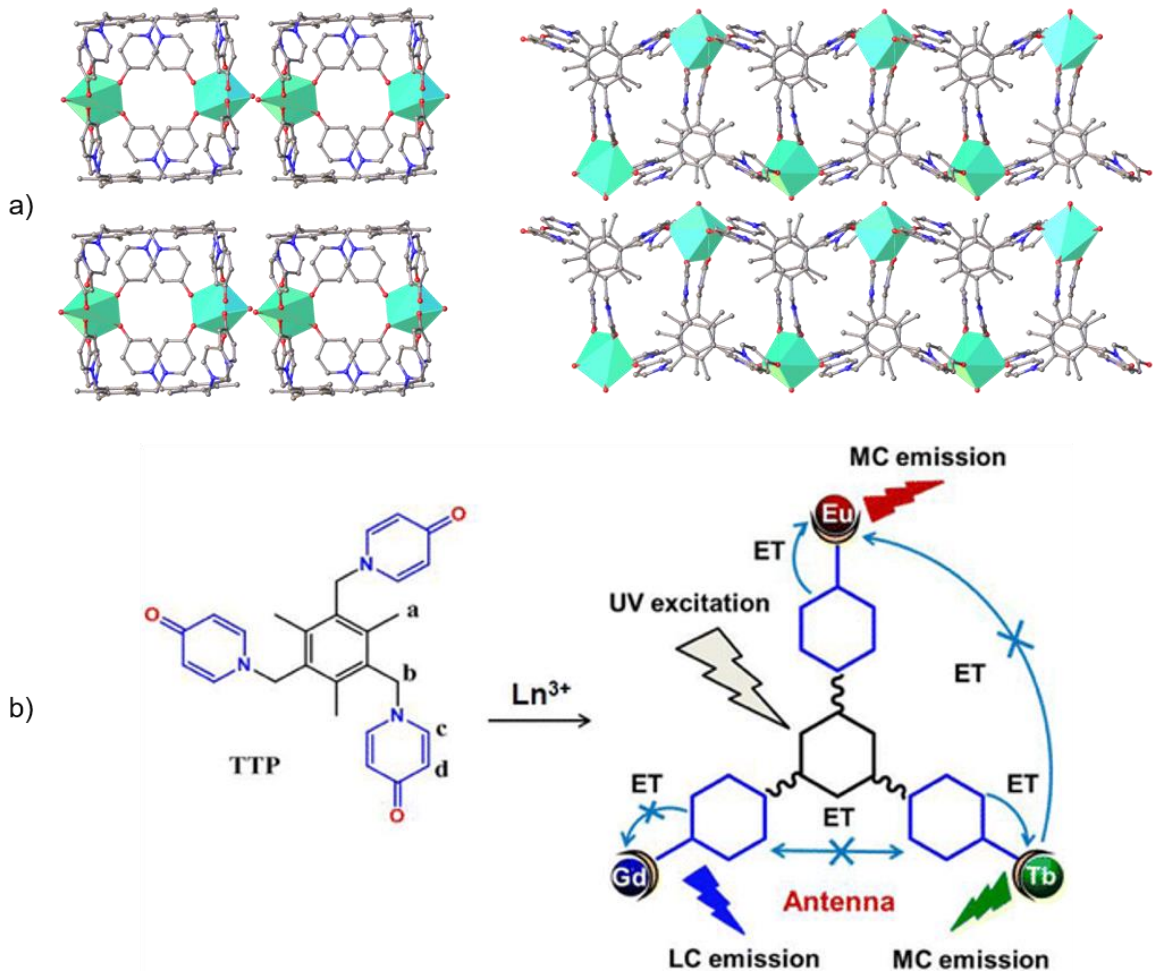

Fig. 1.10 a) Crystal structure of isostructural MOFs with the general formula $[Ln_nLn'_{1-n}(TTP)_2 \cdot H_2O]Cl_3 \cdot$solvent, showing their packing mode. **b)** Synthesis of the MOFs from TTP, showing energy transfer processes. Reproduced with permission from Ref. [155]. Copyright 2015, American Chemical Society.

Materials that exhibit white light emission are desirable due to their applications in displays and solid-state lighting.[156,157] Often, sources of white light are achieved by combining light sources, however this has drawbacks due to high costs and variations in colour.[158] Therefore the design of materials which can emit white light is a current topic of much research in the field of luminescent materials.[159]

In multicomponent MOFs, which contain more than one type of linker molecule, the emission of the MOF can be tuned by variation of each of the linkers in the structure independently, affording great control over the luminescence output of the material. For example, Telfer and co-workers have reported a multicomponent MOF composed of three structurally different linkers, and demonstrated that the luminescence properties of this MOF can be controlled both by linker modification and guest binding (**Fig. 1.11**).[160] The constitutional composition of this MOF, abbreviated as MUF-77 (MUF; Massey University Framework) is given by the formula $[Zn_4O(hxtt)_{4/3}(BPDC)_{1/2}(BDC)_{1/2}]$ (hxtt = 5,5,10,10,15,15-hexaalkyl-10,15-dihydro-5H-diindeno[1,2-a:1',2'-c]fluorene-2,7,12-tricarboxylic acid (alkyl = methyl, butyl, hexyl or octyl) , $BPDC^{2-}$ = 4,4'-biphenyldicarboxylate). Prior to modification of the linkers, the MOF showed blue emission. Introduction of a guanidine functional

group to the $BPDC^{2-}$ linker moiety resulted in yellow emission from the MOF, while addition of a $-NH_2$ functional group to the BDC^{2-} linker gave blue fluorescence. Combining the guanidine functionalised $BPDC^{2-}$ and the amine functionalised BDC^{2-} group gave a white light emitting MOF. Additionally, the luminescence of MUF-77 could be tuned by interactions with guest molecules in the framework. In response to the presence of nitrobenzene, which interacts with the MOF through hydrogen bonding, the emission of the MOF was quenched. Interestingly, this quenching effect was stronger for the yellow emission band of the MOF, causing the luminescence output of the MOF to shift to a blue colour.

As demonstrated by some previously mentioned examples, the inclusion of guest molecules in MOFs also provides a method of tuning their photochemistry. The porosity of MOFs allows for incorporation of guest molecules which can influence the luminescence output of the material. For example, Qian and co-workers have reported that encapsulation of dye molecules into the structure of MOFs gives a method of modulating the colour of the luminescence output of the material.[161] Two cationic dyes, acriflavine (AF), which emits green light, and 4-(*p*-dimethylaminestyryl-1-methylpyridinium (DSM), which emits red light, were encapsulated in the anionic framework ZJU-28 (ZJU = Zhejiang University). ZJU-28 is an anionic MOF, with the formula $(Me_2NH_2)_3[In_3(BTB)_4]\cdot 12DMF\cdot 22H_2O$ (BTB^{3-} = 4,4',4''-benzene-1,3,5-triyl-tribenzoate).[162] Prior to encapsulation of dyes, ZJU-28 emits blue light upon excitation with UV light (λ = 365 nm). Incorporation of the DSM dye into the structure of ZJU-28 gives tunable light emission, with blue emission observed at low dye concentration, and purple emission at high dye concentration.[161] A similar effect is observed when AF is encapsulated into the MOF, with green emission observed at high AF concentration. Encapsulation of the two dyes, AF and DSM, into ZJU-28, gives a mixed-dye exchanged MOF which emits white light. The potential of this material in white light emitting devices was also demonstrated by coating a UV-LED (LED = light emitting diode) with the mixed-dye-encapsulated MOF, resulting in warm white light emission from the MOF-coated LED.

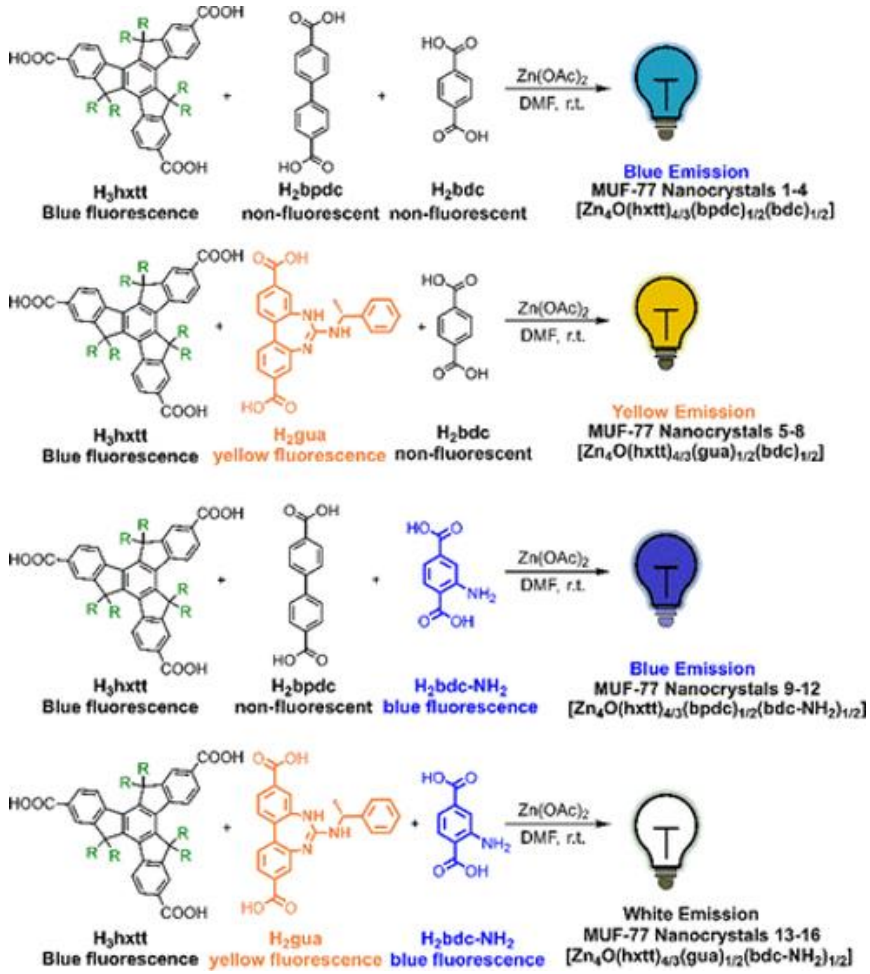

Fig. 1.11 Synthesis of luminescent MUF-77 nanocrystals and their luminescence output colours (R= methyl, butyl, hexyl or octyl groups). Reproduced with permission from Ref. [160]. Copyright 2018, American Chemical Society.

Recently, MOFs have been reported for their application as organic light emitting diodes (OLEDs). OLEDs and LEDs are materials which generate light in response to an electric current. LEDs are typically constructed from semiconductors such as GaN or AlGaN, with the colour of light emitted depending on the band gap of the material. The emissive components of OLEDs are films of organic compounds or polymers. Compared to LEDs, which are typically rigid, OLEDs can possess increased flexibility, which, in principle, allows for displays that can be bent and rolled up.[163] Furthermore, OLEDs can be designed to be transparent materials.[164]

In 2018, Douhal and co-workers reported OLEDs based on a Zr-based MOF, Zr-NDC.[165] The structure of Zr-NDC is composed of $[Zr_6(\mu_3\text{-}O)_4(\mu_3\text{-}OH)_4(\mu\text{-}COO)_{12}]$ SBUs, which are 12-fold connected by the NDC^{2-} organic linkers. This MOF displays electroluminescence, a property which is relatively rare in MOFs. Incorporation of dye molecules as guests into the MOF pores can effectively tune the optoelectronic properties of this material. Two different dye molecules were encapsulated into the MOF pores, Coumarin 153 (C153) and 4-(dicyanomethylene-2-methyl-6-(4-dimethylaminostyryl)-4H-pyran (DCM). In the MOFs with encapsulated dyes, C153@Zr-NDC and DCM@Zr-NDC, two different emission bands are observed in the photoluminescence spectra, blue luminescence originating from the Zr-NDC MOF, and red luminescence from the encapsulated dye

molecules. The photoluminescence bands of both dyes are shifted in the MOF environment compared to the pure dyes in the solid state, indicating that interaction occurs between the MOF and the dyes in their pores.

To investigate the electroluminescence of Zr-NDC and the dye-encapsulated analogues, Douhal and co-workers designed light emitting devices with the MOF as a light emitting layer in a polymer matrix. The MOF displayed electroluminescence that could be modified by dye encapsulation. The dye encapsulated MOFs did not show a change in colour of electroluminescence, however, the electroluminescence intensity was increased in C153@Zr-NDC and DCM@Zr-NDC.

1.5 MOFs as Photocatalysts

1.5.1 Introduction to Photocatalytic MOFs

In view of sociologically important sustainable energy-related applications, MOF-based research activities can be directed towards artificial photosynthetic systems. Artificial photosynthetic systems that convert light into chemical energy, producing molecular O_2 and H_2, provide arguably the most attractive approach to green and renewable energy technologies. Photosynthesis is the process by which plants, algae and some bacteria use light energy to split water, and use the electrons and protons produced for the reduction of CO_2 to produce sugars. The process stores energy in chemical bonds. Insights into molecular details of these conversions can guide us towards employing solar energy to produce fuels, whereby the term ‘fuel’ in a broader sense can be thought of as a reduced molecule that can be oxidised, to produce desired compounds or energy as required. The replication in any artificial photosynthetic analogue is scientifically highly challenging but can be rendered more manageable when the overall process is separated into distinct sequential, partial processes: a) light harvesting, b) charge separation, c) reaction involving the positive cation ‘hole’ at the catalytic centre to oxidise a suitable electron donor molecule (water or other donor molecules) and d) reactions involving the mobilised electrons to produce a desired compound via the reductive process. Thus, by conceptualizing ‘artificial photosynthesis’ into these modular processes, catalytic oxidative and reductive processes may be developed and combined to give a highly efficient, optimised overall redox system.

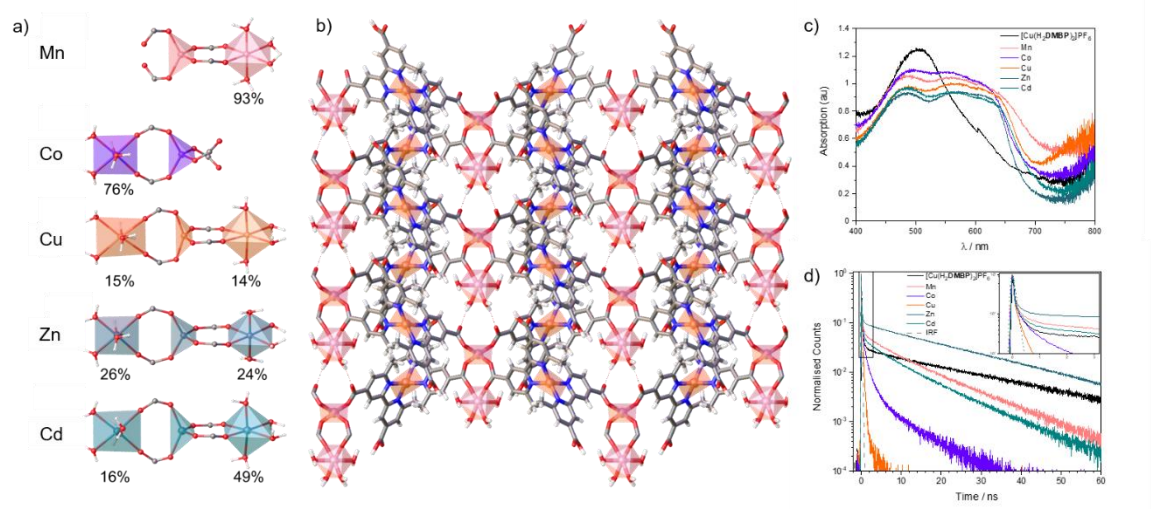

Fig. 1.12 a) Coordination environments of metal ions in $[Cu(H_{1-x}2,2'\text{-DMBP})_2M_{0.5}][M(OH_2)_4]_x$ (M = Mn^{II}, Co^{II}, Cu^{II}, Zn^{II}, or Cd^{II}), and the occupancies of the $[M^{II}(OH_2)]$ moieties. Only one of the chemically equivalent (though crystallographically distinct) $[M(OH_2)_4]$ moieties can be occupied per SBU. **b)** Layers of Mn^{II}-based MOF featuring $[Cu^{I}(H_2 2,2'\text{-DMBP})_2]PF_6$ metallolinker **c)** Absorption spectra and **d)** normalised photoluminescence decay of $[Cu^{I}(H_2 2,2'\text{-DMBP})_2]PF_6$ and MOFs (inset: initial decay characteristics) (IRF= instrument response function). Adapted with permission from Ref. [166]. Copyright 2020, American Chemical Society.

The effect of variation of inorganic SBUs on the optoelectronic properties of MOFs was investigated by Schmitt and co-workers.[166] Five isostructural two-dimensional MOFs were reported, which incorporate a Cu^{I} metallolinker, $[Cu^{I}(H_2 2,2'\text{-DMBP})_2]PF_6$ ($H_2 2,2'$-DMBP = 6,6'-dimethyl-2,2'-bipyridine-4,4'-dicarboxylic acid) (**Fig. 1.12**). The isostructural MOFs have the formula $[Cu(H_{1-x}2,2'\text{-DMBP})_2M_{0.5}][M(OH_2)_4]_x$ (M = Mn^{II}, Co^{II}, Cu^{II}, Zn^{II}, or Cd^{II}) and feature mixed mono- and dinuclear SBUs (**Fig. 1.12 a)**). The MOFs exhibit broad absorption in the visible region (**Fig. 1.12 c)**) and emission centred at 728 nm. Compared to the parent PS, these MOFs' rigidity enhances ISC from the singlet to the triplet state and enables higher radiative decay rates, which depend on the nuclearity of the SBU via O-H oscillations of coordinated water molecules. Quantum yields depend on the chemical nature of the SBU, and are up to six times higher for the Zn^{II}-MOF than $[Cu^{I}(H_2 2,2'\text{-DMBP})_2]PF_6$. The shortest triplet excited state lifetimes are observed in the Cu^{II}- and Co^{II}- MOFs, as the excited states are quenched by rapid ET to the SBU (**Fig. 1.12 d)**). Due to the known importance of PETs in photocatalytic processes, this series of MOFs demonstrates the potential for tuning photochemical properties by variation of inorganic SBUs.

1.5.2 MOFs as catalysts for CO_2 reduction

Due to rising levels of atmospheric CO_2 from fossil fuel combustion, and the need to curb the associated rise in global temperatures, research into technologies that can capture CO_2 and convert it to value-added products is a source of high scientific and societal interest. Fixation of CO_2 to form valuable products such as CO and methanol has the potential to replace or alter current methods of synthesising these products, which use conventional fossil fuels as a feedstock.[167,168] However, the thermodynamic energy barriers associated with the conversion of CO_2 currently present a major challenge in implementing these new sustainable and cost-effective technologies.

MOFs have been explored as materials that can catalyse the reduction of CO_2 using visible light as an energy source.[169,170] Early catalysts for CO_2 reduction involved various metals or metal oxides such as TiO_2,[171] followed by the development of molecular homogenous catalysts.[172] However, the use of heterogenous photocatalysts for CO_2 reduction offers several advantages over homogenous catalysts.

The advantages of MOFs as heterogenous catalysts arise from their intrinsic properties and their ordered and well-defined nature, whereby associated reticular synthesis concepts offer some degree of synthetic control during assembly of the materials. This approach may allow the preparation of materials in which the components for photocatalysis, for example the photosensitiser, catalyst and sacrificial electron donor, can be oriented in an ordered and well-defined manner, thus optimising electron transfer to the active site. The dimensions of the components determine the porosity and diffusion characteristics in the materials. Catalytic transformations may occur in confined spaces of molecular-sized cavities, involving structural intermediates and moieties that may relate to those of molecular catalysts, or which may not be attainable in condensed liquid phases. Hence, MOFs may provide synthetic avenues to bio-inspired materials that replicate some of the key features of enzymatic catalysts.

The development of photocatalytic MOFs for CO_2 reduction represents an area of intense research, and as a result, different generations of photoactive MOFs have emerged.[173] First generation MOFs for photocatalytic CO_2 reduction employ the strategy of immobilising molecular photocatalysts in MOFs. First generation MOFs overcome some issues that arise when using homogenous catalysts, preventing dimerization of catalysts and the resulting loss of catalytic activity. Additionally, the environment within MOFs offers advantages for photocatalytic reactions, such as high densities of catalytic active sites and good light penetration into their crystalline structures.[173]

Second generation photoactive MOFs are those which are capable of absorbing light in the visible region of the spectrum.[173] This characteristic is important in order to carry out photocatalysis efficiently using solar light as an energy source. Absorption of light by MOFs is typically tuned by variation of the organic linker in the system, emphasising the advantages of the tunable optical properties of MOFs. Third generation photocatalytic MOFs focus on electronic efficiency, by aiming to optimise the transfer of energy from the photosensitiser to the catalytic active site.[173] These materials should have charge separated states with lifetimes that are long enough to facilitate transfer of electrons to the CO_2 substrate.

In 2011, Lin and co-workers reported the first example of MOFs that could perform as heterogenous catalysts for H_2O oxidation, photocatalytic CO_2 reduction and light-driven organic reactions.[174] A series of stable, porous heterogenous catalysts were prepared by incorporating various catalytically active complexes as metalloligands into the UiO-67[175] (UiO = University of Oslo) framework, $[Zr_6O_4(OH)_4(BPDC)_6]$ (**Fig. 1.13**). Varying the molecular dyes used as metalloligands changed the

catalytic behaviour of the MOF. For example, using $[Re^{I}(CO)_3(bpydc)Cl]$ (bpydc = 2,2'-bipyriine-5,5'-dicarboxylic acid) as a metalloligand enabled the MOF to perform as a heterogeneous photocatalyst for reduction of CO_2. A turnover number (TON) of 10.9 was recorded for the Re-doped MOF over a 20 hour reaction period, which is over three times higher than that recorded for $[Re^{I}(CO)_3(bpydc)Cl]$ in solution over the same time period. Incorporating linkers which were previously established as molecular water oxidation catalysts (WOCs), such as $[Ir^{III}(Cp^*)(dcppy)Cl]$ (Cp^{*-} = pentamethylcyclopentadienyl, dcppy = 2-phenylpyridine-5,4'-dicarboxylic acid), $[Ir^{III}(Cp^*)(bpydc)Cl]^+$ and $[Ir^{III}(dcppy)_2(H_2O)_2]^+$, led to MOFs which were capable of performing as H_2O oxidation catalysts. The highest turnover frequency was observed for the MOF which incorporates $[Ir^{III}(Cp^*)(dcppy)Cl]$, with a turnover frequency (TOF) of 4.8 h^{-1} recorded over the first 3 hours. In addition, the MOFs synthesised with $[Ir^{III}(ppy)_2(bpydc)]^+$ (ppy = 2-phenylpyridine) and $[Ru^{II}(bpy)_2(bpydc)]^{2+}$ (bpy = 2,2'-bipyridine) were capable of catalysing photochemical aza-Henry reactions, aerobic amine coupling and sulfide photo-oxidations.[174]

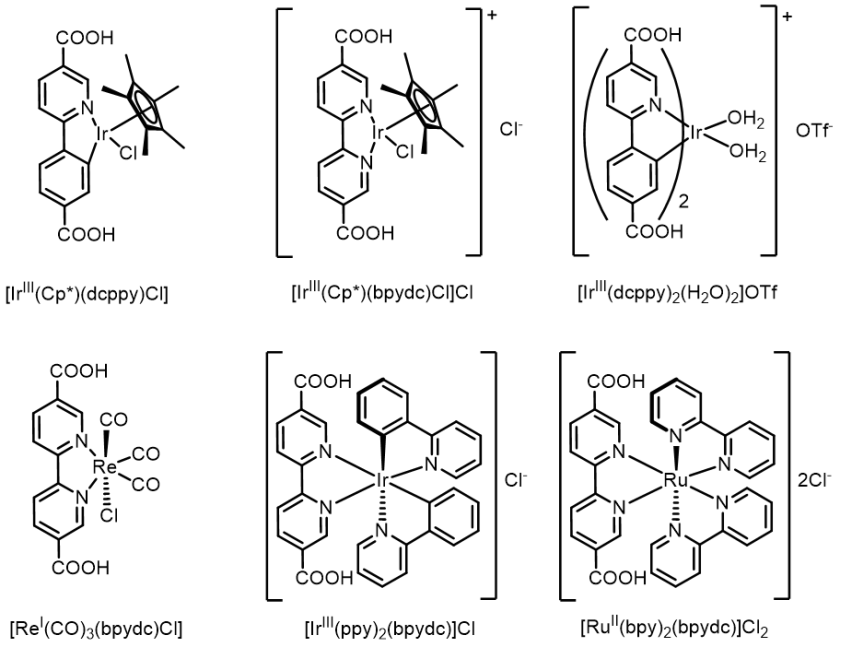

Fig. 1.13 Ir^{III}, Re^{I} and Ru^{II} metalloligands used by Lin and co-workers in the synthesis of doped UiO-67 frameworks.[174]

In 2018, Zheng and co-workers reported the synthesis of a novel Eu-based MOF with a $\{Ru(phen)_3\}$-derived (phen = phenathroline) ligand, [Ru(4-(1H-imidazo[4,5-*f*][1,10]phenanthrolin-2-yl)benzoate)$_3$] and dinuclear $\{Eu^{III}_2\}$ SBUs (**Fig. 1.14**).[73] Europium was chosen due to the favourable reduction potential of Eu^{II} for catalytic reduction reactions,[176,177] while the rationale for use of the $Ru(phen)_3$-derived ligand was the redox activity and excited state lifetime of ruthenium polypyridine complexes.[178] Zheng and co-workers report the synthesis of a Ru^{II}/Eu^{III} MOF, in which the carboxylate-bearing Ru^{II}-metalloligands bridge dinuclear $\{Eu^{III}_2\}$ moieties, to give a MOF with large channels that penetrate the material (**Fig. 1.14**)).[73] Each Eu^{III} ion in the structure is nine-coordinate, and one μ_2-H_2O bridges the two ions in each dinuclear $\{Eu^{III}_2\}$ unit. This MOF efficiently catalyses the reduction CO_2 to formate upon photoirradiation with visible light (λ_{ex} = 420-800 nm). Upon

irradiation, the Ru^{II} metalloligand is excited to its ^{3}MLCT excited state, followed by PET from the ligand excited state to the [Eu^{III}-H_2O-Eu^{III}] unit. Transfer of two electrons results in the reduction of this unit to a photogenerated dinuclear [Eu^{II}-H_2O-Eu^{II}] species, which reduces CO_2 to formate. The catalytic cycle is completed by reduction of the Ru^{III} ion back to Ru^{II} by a sacrificial electron donor. The same metalloligand was also employed for the formation of a Co^{II}-based MOF that is characterised by hexagonal accessible helical one-dimensional channels (**Fig. 1.14**). Its structural characteristics facilitate relatively high CO_2 uptake capacities and selectivity over N_2. The photoactive porous material retains the photophysical properties of the Ru^{II} nodes giving rise to emission centred at 620 nm and photoactivity associated with the ^{3}MLCT states.[72] It is further noteworthy that the bifunctional phenanthroline-carboxylate ligand itself can be applied for the synthesis of photoluminescent Zn- and Mn-based MOFs displaying high CO_2 adsorption capacities associated with structural framework flexibility.[179]

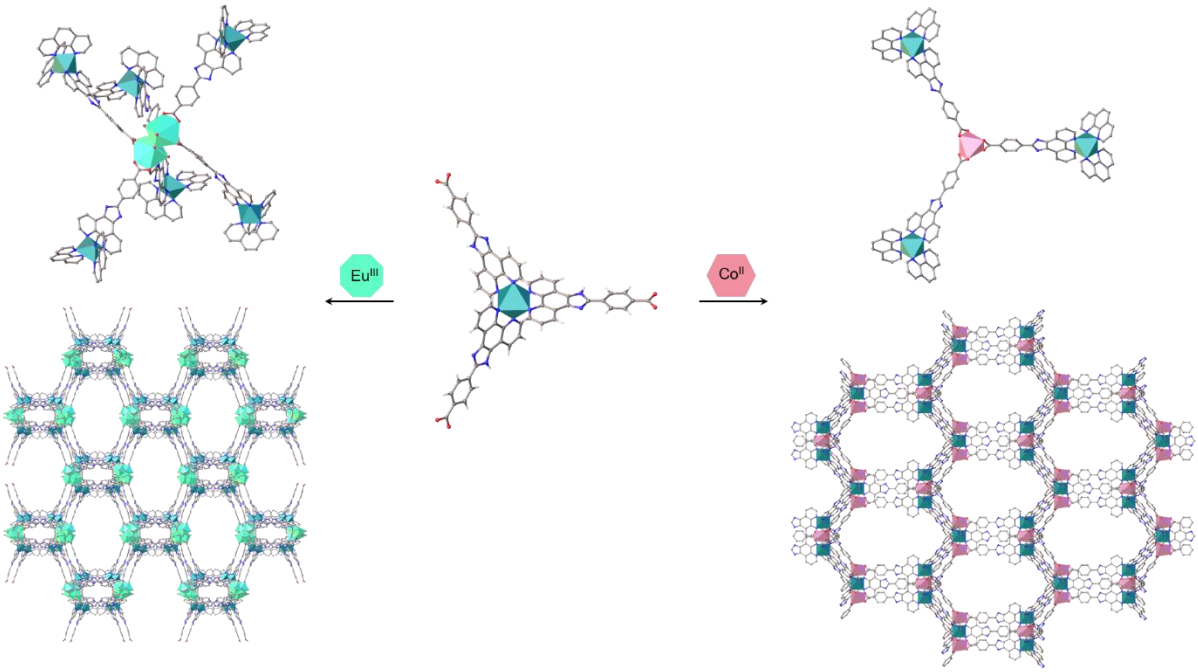

Fig. 1.14 Structures of MOFs formed upon reaction of {$Ru(phen)_3$}-derived ligand with Eu^{III} salts (left)[73] and Co^{II} salts (right).[72]

Though Ru^{II}-based linkers have shown great potential as photosensitising ligands in photoactive MOFs, the development of catalysts using earth abundant metals is desirable. Fe-containing MOFs fulfil the criteria of containing earth abundant metals and have the added advantage that it is possible to use visible light to excite the Fe oxo-clusters of these MOFs directly. Excitation of the Fe oxo-clusters can lead to transfer of an electron from the bridging O^{2-} to Fe^{III} ions, forming Fe^{II}, which can facilitate the reduction of CO_2. A series of Fe-containing MOFs, MIL-101(Fe), MIL-53(Fe) and MIL-88B(Fe), have been reported as photocatalysts for reduction of gaseous CO_2 to formate in the presence of triethanolamine (TEOA) as a sacrificial electron donor.[180] Each of these MOFs contains the linker BDC^{2-}, however the structures of the MOFs differ (**Fig. 1.15**). The structure of MIL-53(Fe) is composed of chains of -OH corner-sharing Fe^{III} octahedra, which are connected by BDC^{2-} linkers.

In contrast, both MIL-88B(Fe) and MIL-101(Fe) have oxo-centred $\{Fe^{III}_3(\mu_3\text{-}O)\}^{7+}$ SBUs. In MIL-88B(Fe), BDC^{2-} linkers connect Fe_3O units to form a porous three-dimensional framework with microporous channels. However, the structure of MIL-101(Fe) contains mesoporous cages.

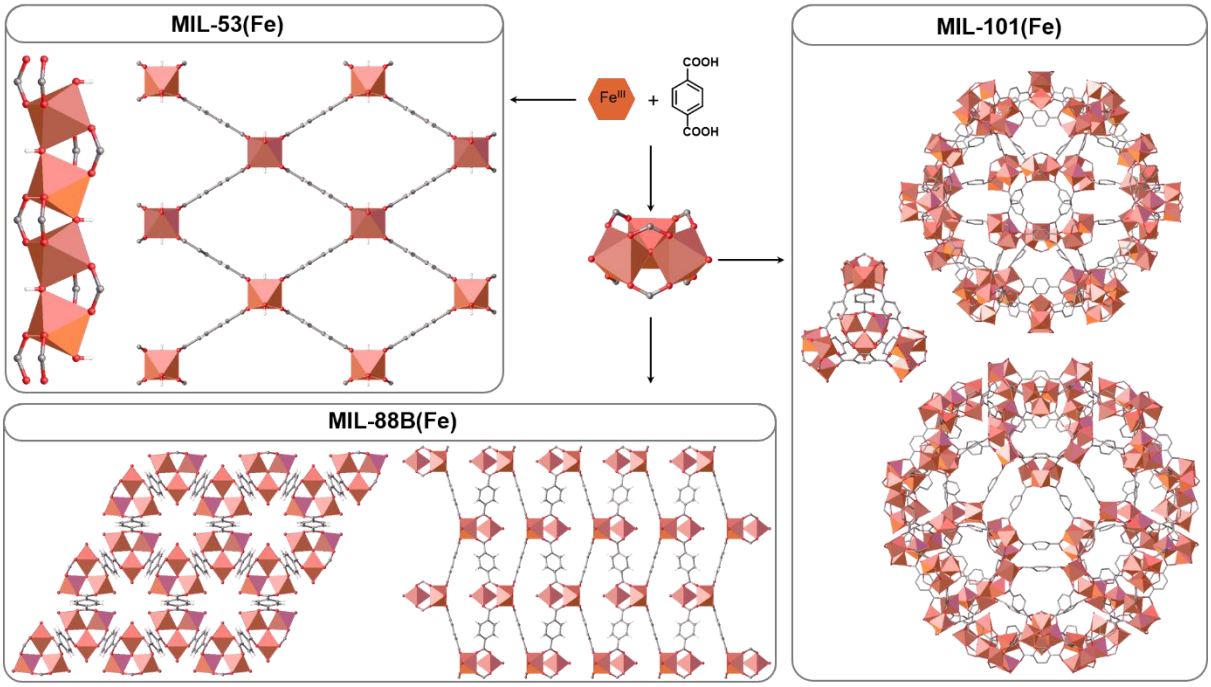

Fig. 1.15 Structural differences between MIL-53(Fe),[181] MIL-88B(Fe)[182] and MIL-101(Fe).[183]

These structural differences lead to different catalytic activities for each material.[180] The best activity for photocatalytic reduction of CO_2 was recorded in MIL-101(Fe), due to the presence of a labile water molecule, which, when removed, leads to an unsaturated coordination site, allowing direct chemical adsorption of CO_2 onto the metal centre. Direct adsorption of CO_2 at the Fe sites was not observed for MIL-88B(Fe) or MIL-53(Fe). The difference in activity between these three MOFs shows the effect of the inorganic SBU structure on the photocatalytic activity of MOFs.

Further, modification of the organic linker can lead to enhancement of the catalytic activity for each of these Fe-containing MOFs. The catalytic activity of each of these three MOFs was enhanced by functionalisation of the BDC^{2-} linker by an amine group, to give three amino-substituted MOFs, NH_2-MIL-101(Fe), NH_2-MIL-53(Fe) and NH_2-MIL-88B(Fe).[180] This improvement in catalytic activity was attributed to two factors. Firstly, the presence of a polar amino functionality increases the interaction with CO_2 molecules, leading to enhanced absorption capacity. Additionally, the amino group enables the absorption of visible light, thus providing an additional pathway for the excitation of the Fe oxo-cluster through energy transfer from the excited ligand. The ability to tune the photocatalytic activity of MOFs by linker and node modification demonstrates the advantage MOFs can provide as molecularly-tunable catalytically active scaffolds.

Amine-functionalised Ti-based MOFs have also been reported as promising photocatalysts for CO_2 reduction. For example, Li and co-workers have reported that introduction of an amine group on to the BDC^{2-} ligand in a previously reported titanium-based MOF with octanuclear Ti units, MIL-125,[184] gave the isostructural MOF NH_2-MIL-125.[185] Under visible light irradiation, NH_2-MIL-125 can reduce CO_2 to formate. This photocatalytic activity was not observed in the unfunctionalized MIL-125 MOF under the same conditions.

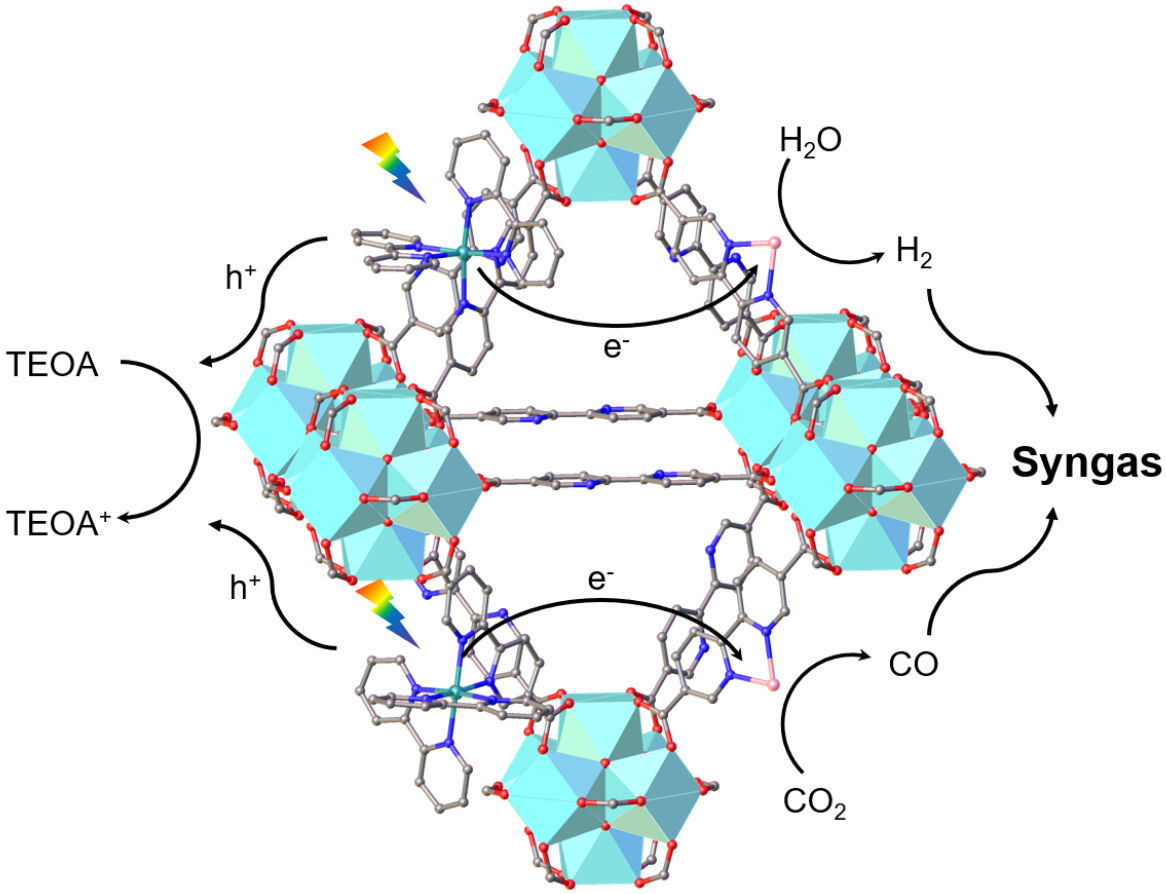

Fig. 1.16 Proposed mechanism of photocatalytic syngas production by $(Co/Ru)_{2.4}$-UiO-67(bpydc).[186]

MOFs have been explored as catalysts for selective reduction of CO_2 to CO. For example, Lu and co-workers have reported a MOF which utilises visible light to reduce CO_2 to syngas,[186] a mixture consisting primarily of CO and H_2, which is used in a diverse range of industrial reactions for the synthesis of hydrocarbons, ammonia for fertiliser production and methanol.[187] Current industrial methods of producing syngas rely on fossil fuel sources. Hence, photocatalytic reduction of CO_2 offers a potentially sustainable method of producing syngas under mild conditions. Lu and co-workers designed a photoactive MOF, $(Co/Ru)_{2.4}$-UiO-67(bpydc).[186] The photoactive MOF, $(Co/Ru)_{2.4}$-UiO-67(bpydc), was synthesised by functionalising the Zr-based UiO-67(bpydc) structure with a Ru^{II}-based photosensitiser, and a Co^{II} single site catalyst (**Fig. 1.16**). The ratio of Co:Ru could be controlled during the synthesis; and in a saturated solution of CO_2 in CH_3CN and H_2O, containing TEAO as an electron donor, $(Co/Ru)_{2.4}$-UiO-67(bpydc) produced both CO, by reduction of CO_2, and H_2, by H_2O reduction, when irradiated by visible light (**Fig. 1.16**). The yield obtained for syngas

production by the MOF was 13,600 μmol g^{-1}, which was 29.2 times higher than that obtained using the corresponding homogenous system. The relative composition of the CO:H_2 mixture could be controlled by variation of the H_2O content of the solvent system. Furthermore, systematically varying the Co:Ru ratio in the MOF allowed the CO:H_2 product ratio to be influenced, thus rendering this MOF system a tunable photocatalyst for syngas production.

1.5.3 Photocatalytic water splitting by MOFs

Using solar energy to carry out photocatalytic water splitting to produce H_2 and O_2 is a promising energy conversion and storage approach, providing a potentially sustainable alternative energy source to replace fossil fuels. The advantage that H_2 fuel sources possess over fossil fuels is that no emissions are generated from using H_2 as fuel.[188] Applications are severely hampered by the high production costs and lack of H_2 storage solutions for automotive and transport applications. Electrolysis of water is an energetically uphill process, and research is rapidly progressing to find catalysts for the two half reactions in H_2O splitting, the oxygen evolution reaction (OER) (Reaction 1, Scheme 1) and the hydrogen evolution reaction (HER) (Reaction 2, Scheme 1).[189] A major challenge is developing catalysts for the highly endergonic OER reaction, as the potential required for each electron transferred at pH 0 is 1.23 eV versus NHE (NHE = normal hydrogen electrode).

$$\mathbf{2H_2O \rightarrow O_2 + 4H^+ + 4e^-} \qquad \mathbf{E^0 = -1.23\ eV\ (1)}$$

$$\mathbf{4H^+ + 4e^- \rightarrow 2H_2} \qquad \mathbf{E^0 = 0.00\ eV\ (2)}$$

Scheme 1: Half reactions for water splitting, and their respective standard potentials at pH 0 versus NHE.

To design efficient H_2O oxidation catalysts, research activities may take inspiration from the oxygen-evolving complex (OEC) of photosystem II. From a molecular point of view, the 4-electron H_2O oxidation half-equation, coupled to a transfer of 4 protons and the formation of an O-O bond, is one of the most challenging catalytic transformations and insights into this process can guide the development of highly efficient oxidation catalysts. The complexity and energy demand of this reaction is illustrated by large overpotentials associated with the individual reaction steps. Thus, an energetically favoured catalysed pathway relies on concerted processes in which the substrate and catalyst adopt geometrically constrained conformations. Whilst artificial photosynthetic systems are severely hampered by a lack of active catalysts, nature uses a {Mn_4CaO_5} oxo-cluster to oxidize water at efficiencies far exceeding those of any synthetic system. Recent X-ray, spectroscopic, and computational studies resulted in new mechanistic insights into the oxidation process.[190–193] Active synthetic molecular oxidation catalysts that relate or mimic the naturally occurring process should be compatible with processes of the Kok cycle,[194] and enable multiple electron transfer (ET) or proton-coupled processes within a narrow potential range. In addition, they should be composed of abundant elements and should be amenable to structural modifications which allow them to interface with sensitisers.

MOFs have been explored as photocatalysts for H_2O splitting due to their tunable photoactivity, large surface areas, favourable diffusion coefficients and high density of active sites per volume, as previously indicated.[31,195] The SBUs of MOFs can incorporate active sites for catalysis, including open metal sites, which have labile coordinating solvent molecules that can be exchanged for substrates during catalytic reactions.[196] The fundamental requirement of such labile coordination sites is exemplified in highly efficient biological or bio-inspired oxidation catalysts including dioxygenases, catalases, or the oxygen-evolving complex of photosystem II. In addition, dynamic structures and multiple conformations that are typical for MOFs are widely recognised to be key characteristics, responsible for the performances of biocatalysts. MOFs may impart the principal advantages of heterogeneous catalysts compared to corresponding homogeneous phases, whereby enhanced stability or facile processability in photochemical systems can potentially lead to unique materials.

Cobalt-based MOFs have been reported as effective heterogeneous catalysts for light-driven water oxidation. In 2019, Chen and co-workers reported the synthesis of MAF-48 (MAF = metal-azolate framework), a cobalt-based MOF with the formula $[Co_8(OH)_4(H_2O)_2(BDT)_6]$ (H_2BDT = 1,4-benzenedi(1H-1,2,3-triazole)), which functions as a stable heterogenous catalyst for water oxidation.[197] The structure of MAF-48 consists of octanuclear hydroxide-bridged $\{Co^{II}_8(\mu_4\text{-}OH)_6\}$ SBUs, linked by BDT linkers (**Fig. 1.17**). Each face of the octanuclear cobalt cluster features four coplanar Co^{II} ions, coordinated to hydroxide ions which adopt μ_4-bridging modes. In the presence of a photosensitiser, $[Ru(bpy)_3]SO_4$, and a sacrificial electron acceptor, $Na_2S_2O_8$, MAF-48 demonstrates photodriven water oxidation when irradiated with visible light. A TOF of 3.05 s^{-1} and a TON of 1.2 x 10^6 was recorded, demonstrating the high catalytic activity of MAF-48. In fact, this MOF demonstrates the highest activity of any heterogenous catalyst, except for photosystem II. This study demonstrates the influence of specific SBUs on the activity of MOFs as photocatalysts, as the high activity of MAF-48 was attributed to the structure of the octanuclear Co^{II} hydroxo-cluster. The presence of four Co^{II} ions that coordinate to a central μ_4-OH^- group leads to a stabilising effect on the reacting hydroxyl radical during the water oxidation cycle, thus enhancing the activity of the MOF.

Due to their ability to absorb visible light, porphyrins represent promising ligands for designing photocatalytic MOFs. For example, the MOF Ru-TBP (TBP^{-4} = 5,10,15,20- tetra(*p*-benzoate)porphyrin) and its zinc-metallated analogue, Ru-TBP-Zn, have been shown to be effective at photochemical evolution of H_2.[198] Ru-TBP-Zn was a better photocatalyst than Ru-TBP or TBP^{4-} alone. The MOF is constructed from dinuclear $\{Ru^{II}_2\}$ paddlewheel SBUs linked by tetratopic porphyrin linkers. The mechanism for H_2 evolution involved photochemical excitation of the TBP-Zn linker, and subsequent electron transfer to the $\{Ru^{II}_2\}$ SBU. The electrons transferred to the paddlewheel SBU consequently drive the proton reduction to generate H_2.

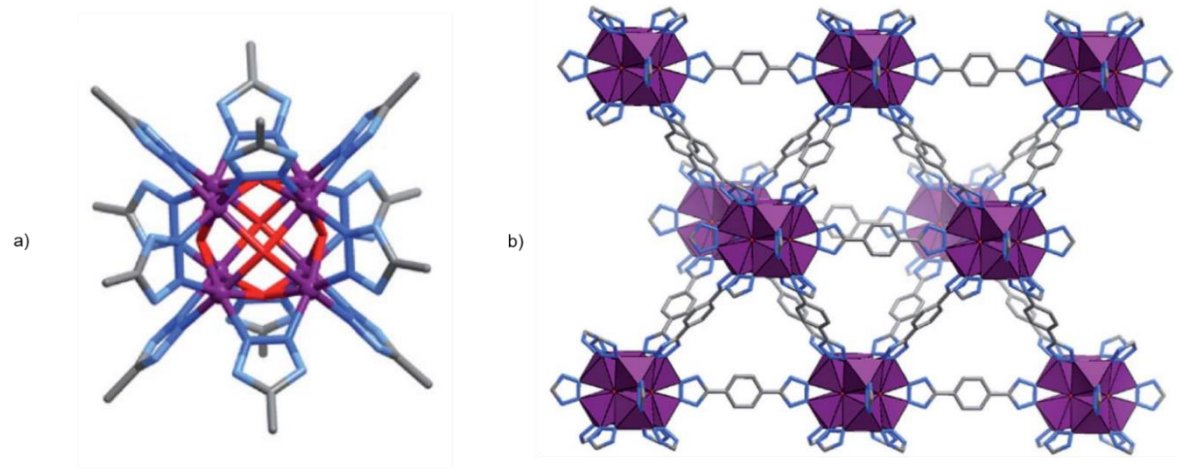

Fig. 1.17 a) SBU of MAF, showing $\{Co^{II}_8(\mu_4\text{-}OH)_6\}$ cluster. **b)** Structure of MAF-48. Reproduced with permission from Ref. [197]. Copyright 2019, The Royal Society of Chemistry.

While MAF-48 utilises $[Ru(bpy)_3]^{2+}$ as a photosensitiser,[197] other MOFs incorporate photosensitising ligands into the structure of the MOF. For example, Lin and co-workers recently reported photocatalytic proton or CO_2 reduction using a series of MOFs with Cu^I photosensitisers as metalloligands (**Fig. 1.18**).[74] Two different postsynthetic modification approaches were chosen for these MOFs, which are isostructural to UiO-69 and comprised of $Zr_6(\mu_3\text{-}O)_4(\mu_3\text{-}OH)_4$ SBUs, connected by *p*-phenanthroline dibenzoate (PT) and 4,4′-bis(carboxyphenyl)-2-nitro-1,1′-biphenyl ($CPNBP^{2-}$) linkers. In the initial study,[75] both the Cu^I-PS as well as the catalytically active site (Re^I or Co^{II} for CO_2 or proton reduction, respectively) were sequentially installed at the PT ligands, respectively yielding mPT-Cu/Re (**Fig. 1.18 b)**) and mPT-Cu/Co (**Fig. 1.18 c)**). For the follow-up study,[75] FeX@mPT-Cu (X= Br, Cl, OAc, BF_4) were obtained by sequential instalment of the Cu-PS at the PT-ligands (**Fig. 1.18 f)**), followed by transformation of the inert SBUs into catalytic centres by addition of Fe^{II} salts (**Fig. 1.18 g)**). The photocatalytic cycle in all cases is initiated by photoexcitation of the Cu-PS to [Cu-(PS)]*, followed by reductive quenching pathway, yielding $[Cu(PS)]^-$ and oxidized sacrificial electron donor (1,3-dimethyl-2-phenyl-2,3-dihydro-1*H*-benzo[*d*]imidazole). Electron transfer from $[Cu(PS)]^-$ to the catalytic centre initiates the reductive transformation of the chosen substrate. When compared to the Cu-PS and Re^I- or Co^{II}-catalysts in solution, the spatial proximity of both in the framework as well as the stabilising effect of the MOF, mPT-Cu/Re and mPT-Cu/Co exhibit enhanced catalytic activity by almost two orders of magnitude, with respective CO_2 reduction reaction and HER TONs of 1328 and 18700 (**Fig. 1.18 c)** and **e)**). The latter is exceeded further by FeX@mPT-Cu, which display HER TONs of up to 33700 for $FeBF_4@Zr_6$-Cu (**Fig. 1.18 h)**). Further, it was found that the activity of FeX@mPT-Cu is dependent on the coordination strength of the counterion to the Fe^{II}, with the weakest coordination resulting in the highest catalytic activity.

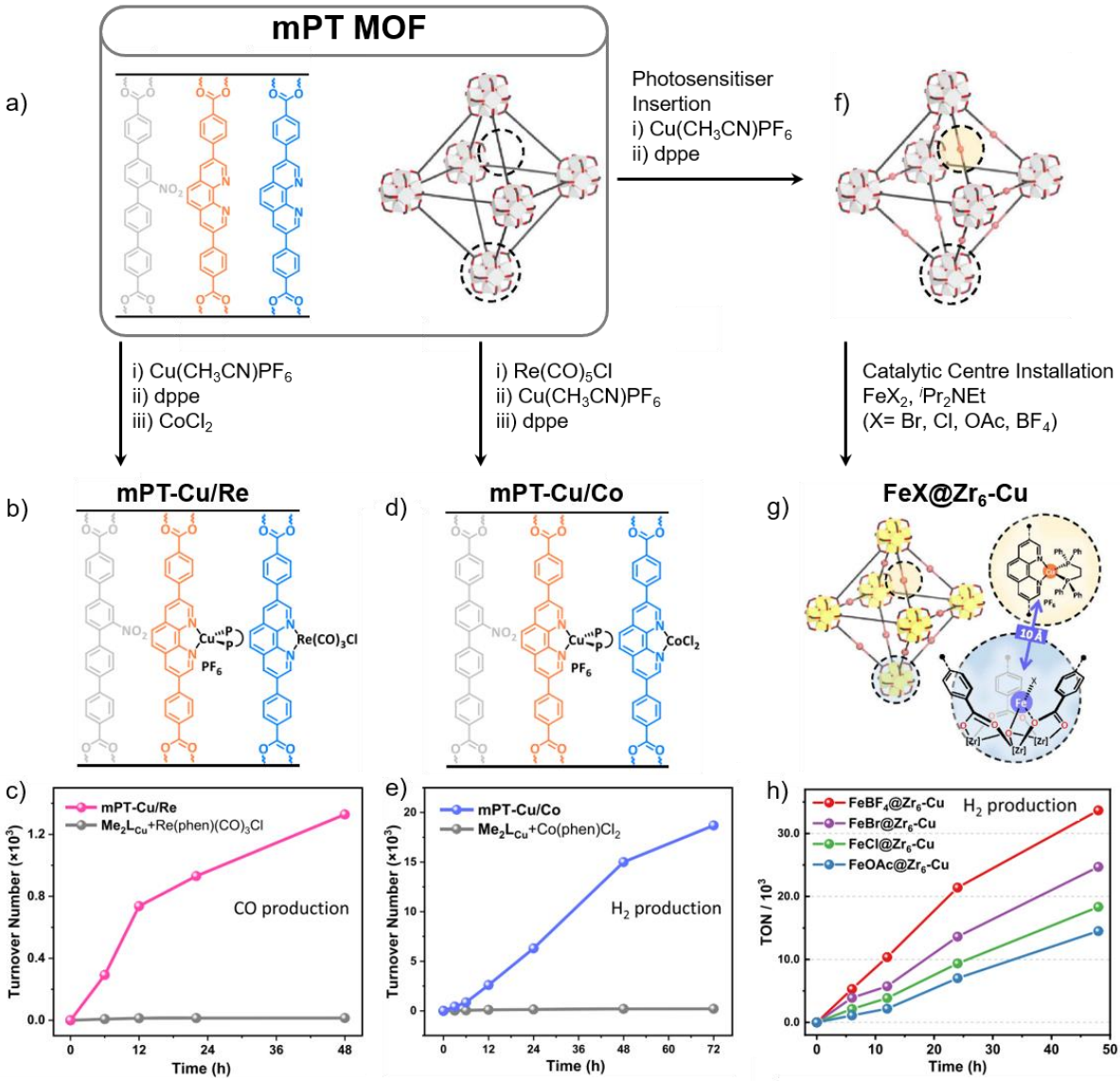

Fig. 1.18. a) Schematic representation of mPT-MOF **b)** Postsynthetic modification of mPT-MOF, giving mPT-Cu/Re (dppe = 1,2-bis(diphenyl- phosphino)ethane) **c)** Time dependent CO_2 reduction reaction TONs of mPT-Cu/Re, compared to the homogeneous control **d)** Postsynthetic modification of mPT-MOF, giving mPT-Cu/Co **e)** Time dependent HER TONs of mPT-Cu/Co, compared to the homogeneous control **f)** Installation of Cu^{I} photosensitisers in mPT-MOF **g)** Installation of Fe^{II} catalytic centres, giving FeX@Zr_6Cu (X = Br, Cl, OAc, BF_4) **h)** Time-dependent H_2 evolution TONs of FeX@Zr_6Cu (X = Br, Cl, OAc, BF_4). Adapted with permission from Ref. [74] and Ref. [75]. Copyright 2020, American Chemical Society.

Encapsulation of catalytically active guests into the pores of MOFs can enhance their performance of as photocatalysts for water splitting. For example, Kögerler and co-workers reported the encapsulation of two Co-based POMs into a MIL-100 (Fe) MOF,[199] an Fe^{III} carboxylate MOF.[200] The two POMs encapsulated in the MOF, $[Co^{II}Co^{III}W_{11}O_{39}(H_2O)]^{7-}$ (Co2) and $[Co_4(PW_9O_{34})_2(H_2O)_2]^{10-}$ (Co4) had previously been reported to display excellent activities as homogenous catalysts for water oxidation.[201,202] The water oxidation activities of the two composite materials Co2@MIL-100 (Fe) and Co4@MIL-100 (Fe) were studied at pH = 9 and 8 respectively, using NaS_2O_8 as a sacrificial electron donor and $Ru(bpy)_3^{2+}$ as a photosensitiser (**Fig. 1.19**). Both POMs demonstrated higher catalytic activity when encapsulated into the MOF structure, compared to the POM alone, due to cooperative electrostatic interactions between the MOF and the POM guest. Furthermore, the activity

of the catalysts did not significantly decrease when the catalyst was recycled, as the POMs did not leach from the host framework.

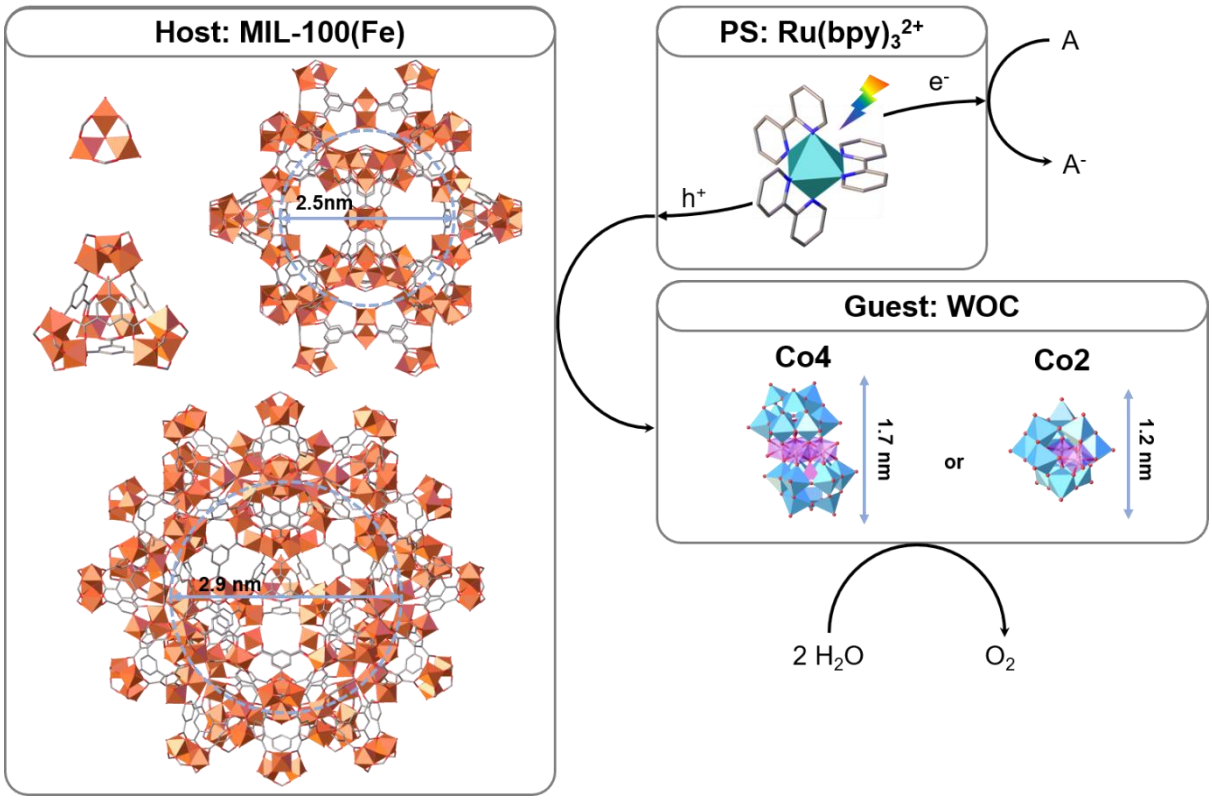

Fig. 1.19 Schematic representation of photocatalytic water oxidation by composite materials Co2@MIL-100 (Fe) and Co4@MIL-100 (Fe).[199]

Lin and co-workers encapsulated a Wells-Dawson type POM, $[P_2W_{18}O_{62}]^{6-}$, into the pores of a $[Ru(bpy)_3]^{2+}$-derived UiO-type MOF.[203] Visible light irradiation leads to excitation of the Ru-based ligands to the ^{1}MLCT excited state, followed by intersystem crossing to the ^{3}MLCT state. Subsequent multielectron transfer from the excited metalloligand to the encapsulated POMs facilitates the latter to act as a proton reduction catalyst (**Fig. 1.20**). A series of POM@UiO materials were synthesised by variation of the quantity of POM in the reaction mixture, yielding highest activity at low POM loading. The materials were recycled thrice with only a minor loss of activity.

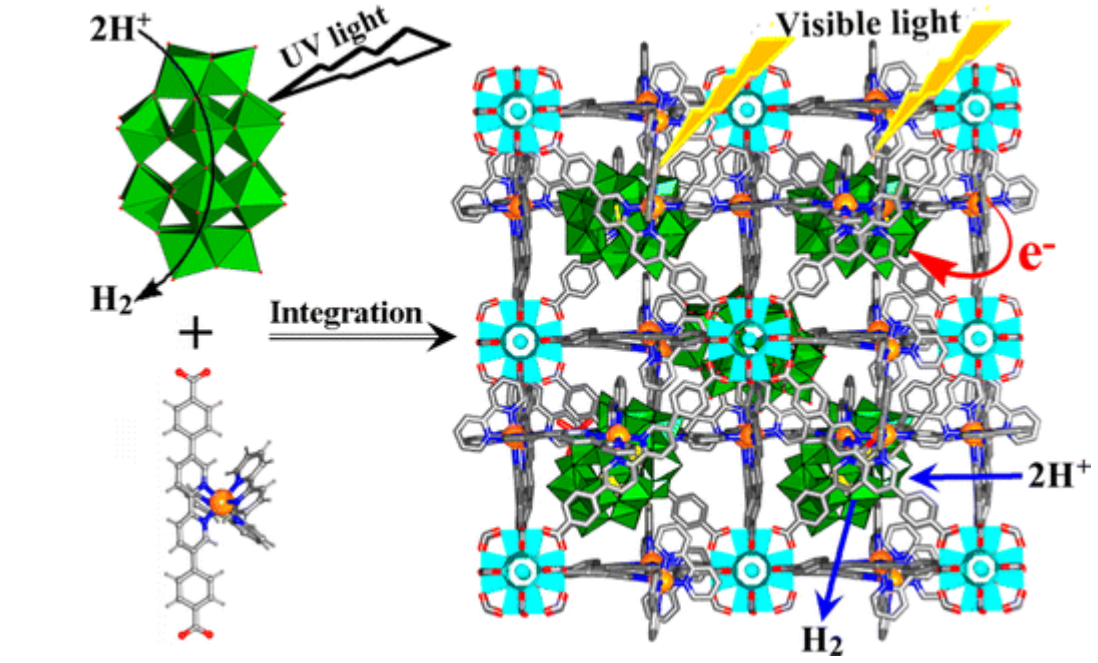

Fig. 1.20 Schematic representation of the mechanism of visible-light-driven proton reduction by the POM@UiO system. Reproduced with permission from Ref. [203]. Copyright 2015, American Chemical Society.

Incorporation of functional groups can also enhance the photocatalytic H_2 evolution activity of MOFs. For example, introducing a methylthio group (-SCH_3) onto the BDC^{2-} linker of MIL-125 gave a MOF which was highly active for light driven H_2 evolution.[37] Direct synthesis of MIL-125 with the methylthio-functionalised BDC^{2-} (BDC-$(SCH_3)_2^{2-}$) linker was unsuccessful, and therefore the methylthio-functionalised MOF was synthesised by solvent-assisted ligand-exchange of BDC-$(SCH_3)_2^{2-}$ into the structure of MIL-125. The resulting MOFs, 20%-MIL-125-$(CH_3)_2$, containing 20% BDC-$(SCH_3)_2^{2-}$ and 50%-MIL-125-$(CH_3)_2$, containing BDC-$(SCH_3)_2^{2-}$ showed visible light absorption and lower band gaps of 2.69 eV and 2.61 eV respectively, than that of MIL-125, which has a band gap of 3.8 eV. Additionally, in the presence of Pt as a co-catalyst, and TEOA as a sacrificial electron donor, the MOFs perform well as catalysts for H_2 evolution from water. The highest H_2 evolution activity was observed for Pt/20%-MIL-125-$(SCH_3)_2$ which had a H_2 evolution rate of 3814.0 μmol g^{-1} h^{-1}. The enhanced ability of Pt/20%-MIL-125-$(SCH_3)_2$ over Pt/50%-MIL-125-$(SCH_3)_2$ was attributed to the higher stability of Pt/20%-MIL-125-$(SCH_3)_2$.

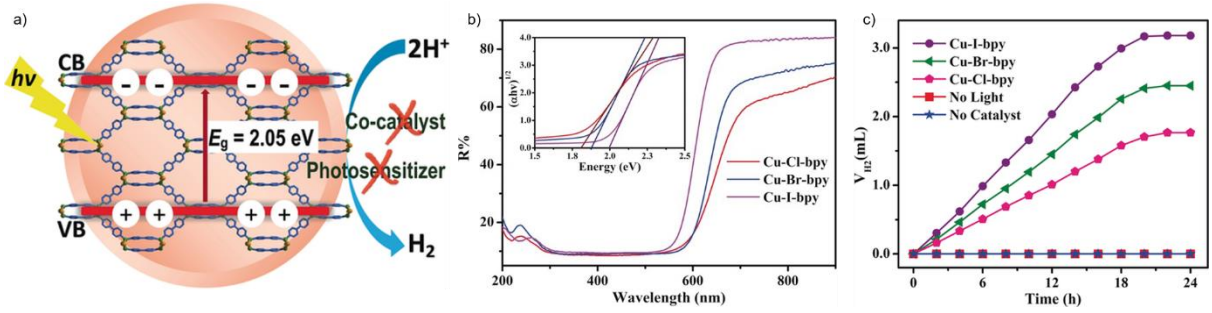

Fig. 1.21 a) Semiconductive MOFs Cu-X-4,4'-bpy as H_2 evolution photocatalysts**. b)** Reflectance spectra and Tauc plot inset. **c)** Photocatalytic hydrogen evolution in aqueous TEOA (5% v/v, pH 11.5) under UV light irradiation. Reproduced with permission from Ref. [204]. Copyright 2017, Wiley-VCH Verlag GmbH & Co. KGaA, Weinheim.

Recently, the groups of Liu and Du reported that the MOFs Cu-X-4,4'-bpy ($[Cu_2X_2(4,4'\text{-bpy})_2]$, X=Cl, Br, I), (4,4'-bpy= 4,4'-bipyridine) (**Fig. 1.21**), whose structure had been known for 20 years prior and can be easily obtained from cheap earth abundant reagents,[205,206] are in fact semiconductors with narrow optical band gaps ranging from 1.85 eV for Cu-Cl-4,4'-bpy to 2.00 eV for Cu-I-4,4'bpy (**Fig. 1.21**).[204] Here, the $Cu^{I}_2(\mu_2\text{-X})_2$ clusters are linked by four 4,4'-bpy ligands, resulting in orthogonally interpenetrating layers of (3,6)-connected honeycomb nets. Moreover, they found Cu-X-4,4'bpy to be an active hydrogen evolution photocatalysts under visible light irradiation, that did not require any additional photosensitiser or co-catalyst, with particularly high activity and recyclability of Cu-I-4,4'-bpy using TEOA as a sacrificial electron donor.

1.6 Degradation of organic pollutants by MOFs

Organic dyes, in addition to other pollutants, are the by-product of many industrial processes, and many are toxic to humans and to plant and animal life.[207,208] The ability to degrade organic pollutants into less toxic or even harmless compounds is essential for wastewater treatment technologies. MOFs can be designed to photocatalytically degrade organic dyes under various different conditions, including using samples of contaminated wastewater.[209]

In 2016, Zhang and co-workers reported that MIL-53(Fe) could be used as a heterogeneous catalyst containing earth-abundant metal ions for the photochemical degradation of the organic dye Acid Orange 7 (AO7) under visible light irradiation.[210] The catalytic activity originates from charge separated sites which form upon photoexcitation of the structure. However, the catalytic performance of MIL-53(Fe) was hindered by fast recombination of electron-hole pairs after excitation. This deficiency could be overcome by addition of an electron acceptor, sodium persulfate (PS = persulfate), which was necessary in order to prevent electron-hole recombination, thus enhancing the catalytic activity of the system. In the presence of PS, MIL-53(Fe) could effectively decolourise a 0.05 mM aqueous solution of AO7 within 90 minutes of irradiation with a visible light LED (**Fig. 1.22**). No substantial difference in activity was recorded after five successive cycles of photocatalytic AO7 degradation, demonstrating that MIL-53(Fe) is a stable and reusable catalyst.

MOF thin films have also been reported as effective photocatalysts for photocatalytic waste treatment. A manganese-based MOF film composed of metalloporphyrin linkers was reported by Zhao and co-workers.[211] The MOF, which is constructed from the metalloporphyrin [5,10,15,20-tetra(4-carboxyphenyl)porphyrin]Mn^{III}, 2,2'-dimethyl-4,4'-bipyridine (4,4'-DMBP) and zinc acetate, was synthesised by layer-by-layer deposition onto a quartz glass substrate. The structure of the MOF consists of sheets of dinuclear $\{Zn^{II}_2\}$ SBUs connected by the tetratopic metalloporphyrin linker. The layers form parallel to the quartz substrate, and consecutive layers are linked by 4,4'-DMBP pillars. The MOF film was applied to the photocatalytic degradation of an aqueous solution of methylene blue with H_2O_2 under irradiation with visible light (400 – 700 nm). The MOF is stable, and can be recycled by washing and drying, and still performs as an effective catalyst after 5 catalytic cycles.

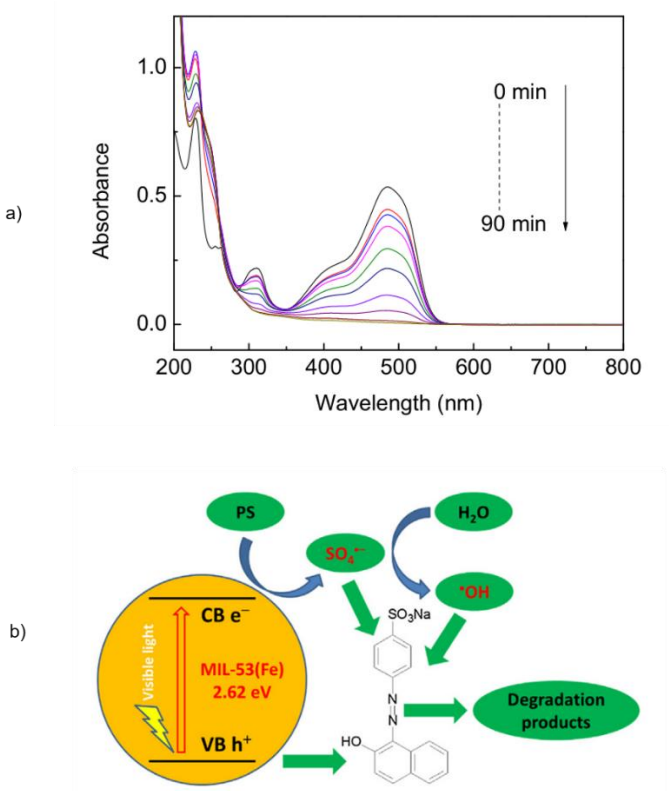

Fig. 1.22 a) UV–vis spectra changes during AO7 decolorization by the MIL-53(Fe)/PS/Vis process with the following reaction conditions: AO7 (0.05 mM); MIL-53(Fe) (0.6 g L^{-1}); PS (2.0 mM); initial pH 6.0. **b)** Proposed mechanism of photocatalytic AO7 degradation by MIL-53(Fe). Reproduced with permission from Ref. [210]. Copyright 2016, Elsevier B.V..

MOFs can also be employed in using visible light for photocatalytic degradation of antibiotics in aqueous solutions. Pollution of water systems by antibiotics can occur due to treatment of livestock with antibiotics.[212] As the incidence of antibiotic resistance increases,[213] the need to treat wastewater to remove antibiotics is vitally important. A europium-based MOF, with the formula $[(CH_3)_2NH_2]_2[Eu_6(OH)_8(ADBA)_6(H_2O)_6]\cdot(DMF)_{15}$ (H_2ADBA = 4,4'-(9,10-anthracenediyl)dibenzoic acid), abbreviated as Eu-ADBA, has been reported to be effective in using visible light to catalyse photodegradation of the antibiotic tetracycline.[214] The linker in this MOF was chosen for the interesting optical attributes of its conjugated anthracene moiety. Eu-ADBA was capable of absorbing organic molecules into the MOF structure and using visible light to catalyse the degradation of two organic dyes, methylene blue and rhodamine B, and tetracycline in water.

1.7 Conclusion

In recent years, MOFs have been explored as promising materials for a wide range of applications, some of which centre on their performance as photoactive materials. Here, characteristics of selected photoactive MOFs have been highlighted considering two broad areas, MOFs as luminescent materials, and photocatalytic MOFs.

The design principles of MOFs, that take advantage of self-assembly approaches and which are governed by the geometrical considerations of their sub-components, impart a degree of synthetic

control which is somewhat rare within the area of synthetic materials science. The hybrid nature of the systems results in structural and physico-chemical amenability through both their organic and inorganic building units. Further, the porosity of MOFs often facilitates an extended interface enabling reversible interactions with analytes, substrates or other functionalising molecules which can locate in the cavities. The influence of these tenable features of MOFs are highlighted by the selected examples demonstrating how optical and electronic attributes can be influenced. Of particular note are emerging lanthanide-based MOFs or MOFs containing highly luminescent organic moieties. Through strategic selection of components, MOFs have been reported to be efficient and reusable sensors for a wide range of analytes.

The underlying design principles allow for the preparation of complex photocatalytic systems, that incorporate efficient molecular catalysts within extended frameworks and that operate in the heterogeneous phase. Some prominent examples have the potential to function as artificial photosynthetic systems, using synergistic effects between photosensitisers, catalysts and sacrificial electron donor/acceptors and which find inspiration from biological systems. The extended systems can lead to charge separations whereby a coordination cluster entity can accumulate oxidation/reduction equivalents. The network structures generally enable the required charge transport characteristics, whilst deactivations arising from hydrolytic and oxidative degradation require further investigation. In general, MOFs have shown promising turnover characteristics as photocatalysts in energy conversion/storage systems that promote H_2O splitting to form O_2 and H_2 or CO_2 reduction. These and other examples point towards intriguing future areas of study and potential applications of photoactive MOFs.

1.8 Aims and Objectives

This chapter has outlined how the structure and properties of metal-organic materials can be tuned through variation in the organic linkers and inorganic components utilised in their construction. As described above, heterocycle-based linkers possess many promising properties such as interesting bend and twist angles, flexible coordination geometries, electron-rich π-conjugated systems, and the presence of Lewis-basic heteroatoms, offering potential interaction sites for analytes in sensing applications. Furthermore, incorporating heterocyclic pyridyl groups onto organic linkers provides binding sites for ions such as Cu^{I}, allowing metallolinkers to be synthesised.

The primary objective of the research presented in this thesis was to develop stable, photoactive metal-organic materials using heterocycle-based linkers to study the potential applications of these materials. To achieve this goal, two novel organic linkers will firstly be synthesised, 6-(4-carboxyphenyl)thieno[3,2-*b*]thiophene-2-carboxylic acid (H_2**CPTT**) and 5,5',5''-(1,3,5-triazine-2,4,6-triyl)tris(thiophene-2-carboxylic acid) (H_3**TTT**) (**Fig. 1.23**). Synthetic pathways to these compounds will be developed, and the compounds will be characterised using single crystal X-ray diffraction studies (XRD), in addition to analysis of their photochemical properties.

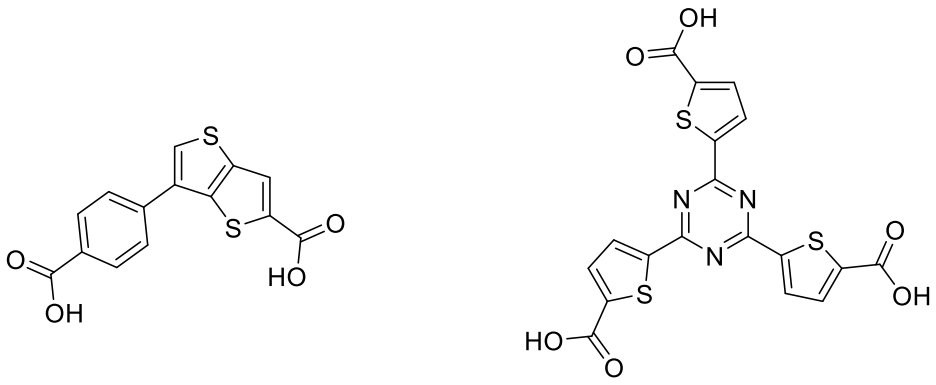

H_2**CPPT** H_3**TTT**

Fig. 1.23 The two novel heterocycle-based linkers this work aims to synthesise.

Following the successful synthesis of the organic linkers shown in **Fig. 1.23**, focus will then be directed to the synthesis of metal-organic materials. This will be achieved by reacting the linkers with transition metal and lanthanide salts under various solvothermal conditions. Due to the flexible coordination geometries of Ln^{III} ions, in addition to their known photoactive properties, and their tendency to form stable MOFs it is expected that the Ln-MOFs will possess attractive properties that may be utilised for a range of potential applications. As the target metal-organic materials in this thesis are solid-state materials, a particular focus of this work will be to study the structures of these materials through single crystal XRD.

This work will also expand on previously reported work on the earth-abundant photosensitiser $[Cu^{I}(H_2$2,2'-DMBP$)_2]PF_6$,[166] by reacting this metallolinker with Eu^{III}, with the aim of synthesising a stable, photoactive three-dimensional Ln-MOF incorporating these components.

References

1 S. R. Batten, N. R. Champness, X.-M. Chen, J. Garcia-Martinez, S. Kitagawa, L. Öhrström, M. O'Keeffe, M. Paik Suh and J. Reedijk, *Pure Appl. Chem.*, 2013, **85**, 1715–1724.

2 A. C. Sudik, A. R. Millward, N. W. Ockwig, A. P. Côté, J. Kim and O. M. Yaghi, *J. Am. Chem. Soc.*, 2005, **127**, 7110–7118.

3 S. Subramanian and M. J. Zaworotko, *Angew. Chemie Int. Ed. English*, 1995, **34**, 2127–2129.

4 B. F. Hoskins and R. Robson, *J. Am. Chem. Soc.*, 1990, **112**, 1546–1554.

5 B. F. Abrahams, B. F. Hoskins, D. M. Michail and R. Robson, *Nature*, 1994, **369**, 727–729.

6 M. Munakata, L. P. Wu, T. Kuroda-Sowa, M. Maekawa, K. Moriwaki and S. Kitagawa, *Inorg. Chem.*, 1997, **36**, 5416–5418.

7 D.-L. Long, A. J. Blake, N. R. Champness and M. Schröder, *Chem. Commun.*, 2000, 1369–1370.

8 B. Chen, S. Ma, F. Zapata, F. R. Fronczek, E. B. Lobkovsky and H.-C. Zhou, *Inorg. Chem.*, 2007, **46**, 1233–1236.

9 C. Livage, N. Guillou, J. Marrot and G. Férey, *Chem. Mater.*, 2001, **13**, 4387–4392.

10 O. M. Yaghi, M. O'Keeffe, N. W. Ockwig, H. K. Chae, M. Eddaoudi and J. Kim, *Nature*, 2003, **423**, 705–714.

11 J. V. Smith, *Chem. Rev.*, 1988, **88**, 149–182.

12 D. W. Breck, *Zeolite Molecular Sieves: Structure, Chemistry, and Use*, John Wiley & Sons, New York, 1973.

13 J. Kim, B. Chen, T. M. Reineke, H. Li, M. Eddaoudi, D. B. Moler, M. O'Keeffe and O. M. Yaghi, *J. Am. Chem. Soc.*, 2001, **123**, 8239–8247.

14 V. A. Blatov, M. O'Keeffe and D. M. Proserpio, *CrystEngComm*, 2010, **12**, 44–48.

15 M. O'Keeffe, M. A. Peskov, S. J. Ramsden and O. M. Yaghi, *Acc. Chem. Res.*, 2008, **41**, 1782–1789.

16 S. Jeoung, S. Kim, M. Kim and H. R. Moon, *Coord. Chem. Rev.*, 2020, 420, 213377.

17 D. Aulakh, T. Islamoglu, V. F. Bagundes, J. R. Varghese, K. Duell, M. Joy, S. J. Teat, O. K. Farha and M. Wriedt, *Chem. Mater.*, 2018, **30**, 8332–8342.

18 M.-H. Zeng, Q.-X. Wang, Y.-X. Tan, S. Hu, H.-X. Zhao, L.-S. Long and M. Kurmoo, *J. Am. Chem. Soc.*, 2010, **132**, 2561–2563.

19 F. Chen, Y.-M. Wang, W. Guo and X.-B. Yin, *Chem. Sci.*, 2019, **10**, 1644–1650.

20 M. C. Wasson, C. T. Buru, Z. Chen, T. Islamoglu and O. K. Farha, *Appl. Catal. A Gen.*, 2019, **586**, 117214.

21 A. M. Ullman, J. W. Brown, M. E. Foster, F. Léonard, K. Leong, V. Stavila and M. D. Allendorf, *Inorg. Chem.*, 2016, **55**, 7233–7249.

22 J.-L. Wang, C. Wang and W. Lin, *ACS Catal.*, 2012, **2**, 2630–2640.

23 J. Baek, B. Rungtaweevoranit, X. Pei, M. Park, S. C. Fakra, Y.-S. Liu, R. Matheu, S. A. Alshmimri, S. Alshehri, C. A. Trickett, G. A. Somorjai and O. M. Yaghi, *J. Am. Chem. Soc.*, 2018, **140**, 18208–18216.

24 Y. Li, H. Xu, S. Ouyang and J. Ye, *Phys. Chem. Chem. Phys.*, 2016, **18**, 7563–7572.

25 D. Sensharma, N. Zhu, S. Tandon, S. Vaesen, G. W. Watson and W. Schmitt, *Inorg. Chem.*, 2019, **58**, 9766–9772.

26 P. Vervoorts, A. Schneemann, I. Hante, J. Pirillo, Y. Hijikata, T. Toyao, K. Kon, K. Shimizu, T. Nakamura, S. Noro and R. A. Fischer, *ACS Appl. Mater. Interfaces*, 2020, **12**, 9448–9456.

27 B. Chen, C. Liang, J. Yang, D. S. Contreras, Y. L. Clancy, E. B. Lobkovsky, O. M. Yaghi and S. Dai, *Angew. Chemie Int. Ed.*, 2006, **45**, 1390–1393.

28 J. Wang, J. Wang, Y. Li, M. Jiang, L. Zhang and P. Wu, *New J. Chem.*, 2016, **40**, 8600–8606.

29 M.-L. Gao, X.-M. Cao, Y.-Y. Zhang, M.-H. Qi, S.-M. Wang, L. Liu and Z.-B. Han, *RSC Adv.*, 2017, **7**, 45029–45033.

30 K. Lu, C. He and W. Lin, *J. Am. Chem. Soc.*, 2014, **136**, 16712–16715.

31 H. Furukawa, K. E. Cordova, M. O'Keeffe and O. M. Yaghi, *Science (80-.).*, 2013, **341**, 1230444–1230444.

32 D. J. Tranchemontagne, Z. Ni, M. O'Keeffe and O. M. Yaghi, *Angew. Chem. Int. Ed.*, 2008, **47**, 5136–5147.

33 J. R. Li and H. C. Zhou, *Angew. Chem.*, 2009, **48**, 8465–8468.

34 C. Y. Lee, O. K. Farha, B. J. Hong, A. A. Sarjeant, S. T. Nguyen and J. T. Hupp, *J. Am. Chem. Soc.*, 2011, **133**, 15858–15861.

35 E. P. McCarney, C. S. Hawes, J. A. Kitchen, K. Byrne, W. Schmitt and T. Gunnlaugsson, *Inorg. Chem.*, 2018, **57**, 3920–3930.

36 C.-X. Chen, Q.-F. Qiu, M. Pan, C.-C. Cao, N.-X. Zhu, H.-P. Wang, J.-J. Jiang, Z.-W. Wei and C.-Y. Su, *Chem. Commun.*, 2018, **54**, 13666–13669.

37 S.-Y. Han, D.-L. Pan, H. Chen, X.-B. Bu, Y.-X. Gao, H. Gao, Y. Tian, G.-S. Li, G. Wang, S.-L. Cao, C.-Q. Wan and G.-C. Guo, *Angew. Chemie Int. Ed.*, 2018, **57**, 9864–9869.

38 Z. Wu, X. Huang, H. Zheng, P. Wang, G. Hai, W. Dong and G. Wang, *Appl. Catal. B Environ.*, 2018, **224**, 479–487.

39 U. J. Ryu, S. J. Kim, H.-K. Lim, H. Kim, K. M. Choi and J. K. Kang, *Sci. Rep.*, 2017, **7**, 612.

40 É. Whelan, F. W. Steuber, T. Gunnlaugsson and W. Schmitt, *Coord. Chem. Rev.*, 2021, **437**, 213757.

41 C. Tan, D. Chu, X. Tang, Y. Liu, W. Xuan and Y. Cui, *Chem. Eur. J.*, 2019, **25**, 662–672.

42 W. Cullen, A. J. Metherell, A. B. Wragg, C. G. P. Taylor, N. H. Williams and M. D. Ward, *J. Am. Chem. Soc.*, 2018, **140**, 2821–2828.

43 M. D. Pluth, R. G. Bergman and K. N. Raymond, *Acc. Chem. Res.*, 2009, **42**, 1650–1659.

44 W. Lu, D. Yuan, A. Yakovenko and H. C. Zhou, *Chem. Commun.*, 2011, **47**, 4968–4970.

45 E. J. Gosselin, G. R. Lorzing, B. A. Trump, C. M. Brown and E. D. Bloch, *Chem. Commun.*, 2018, **54**, 6392–6395.

46 C. A. Rowland, G. R. Lorzing, E. J. Gosselin, B. A. Trump, G. P. A. Yap, C. M. Brown and E. D. Bloch, *J. Am. Chem. Soc.*, 2018, **140**, 11153–11157.

47 H. D. Mai, P. Kang, J. K. Kim and H. Yoo, *Sci. Rep.*, 2017, **7**, 1–7.

48 Y. Liu, X. Wu, C. He, Y. Jiao and C. Duan, *Chem. Commun.*, 2009, **0**, 7554–7556.

49 K. I. Yamashita, M. Kawano and M. Fujita, *Chem. Commun.*, 2007, **1**, 4102–4103.

50 S. Tashiro, M. Tomínaga, M. Kawano, B. Therrien, T. Ozeki and M. Fujita, *J. Am. Chem. Soc.*, 2005, **127**, 4546–4547.

51 Y.-C. He, J. Yang, W.-Q. Kan and J.-F. Ma, *CrystEngComm*, 2013, **15**, 848–851.

52 F. Kaiser, A. Schmidt, W. Heydenreuter, P. J. Altmann, A. Casini, S. A. Sieber and F. E. Kühn, *Eur. J. Inorg. Chem.*, **2016**, 5181–5196.

53 M. Eddaoudi, J. Kim, J. B. Wachter, H. K. Chae, M. O'Keeffe and O. M. Yaghi, *J. Am. Chem. Soc.*, 2001, **123**, 4368–4369.

54 K. Byrne, M. Zubair, N. Zhu, X.-P. Zhou, D. S. Fox, H. Zhang, B. Twamley, M. J. Lennox, T. Düren and W. Schmitt, *Nat. Commun.*, 2017, **8**, 15268.

55 T. Kusukawa and M. Fujita, *J. Am. Chem. Soc.*, 2002, **124**, 13576–13582.

56 Y. Inokuma, S. Yoshioka, J. Ariyoshi, T. Arai, Y. Hitora, K. Takada, S. Matsunaga, K.

Rissanen and M. Fujita, *Nature*, 2013, **495**, 461–466.

57 M. Hoshino, A. Khutia, H. Xing, Y. Inokuma and M. Fujita, *IUCrJ*, 2016, **3**, 139–151.

58 C. R. McKeithan, L. Wojtas and R. W. Larsen, *Dalt. Trans.*, 2018, **47**, 9250–9256.

59 K. G. M. Laurier, F. Vermoortele, R. Ameloot, D. E. De Vos, J. Hofkens and M. B. J. Roeffaers, *J. Am. Chem. Soc.*, 2013, **135**, 14488–14491.

60 C.-K. Lin, D. Zhao, W.-Y. Gao, Z. Yang, J. Ye, T. Xu, Q. Ge, S. Ma and D.-J. Liu, *Inorg. Chem.*, 2012, **51**, 9039–9044.

61 G. Tobin, S. Comby, N. Zhu, R. Clérac, T. Gunnlaugsson and W. Schmitt, *Chem. Commun.*, 2015, **51**, 13313–13316.

62 C. S. Hawes, G. M. Ó Máille, K. Byrne, W. Schmitt and T. Gunnlaugsson, *Dalt. Trans.*, 2018, **47**, 10080–10092.

63 W. Yin, C. Tao, F. Wang, J. Huang, T. Qu and J. Wang, *Sci. China Mater.*, 2018, **61**, 391–400.

64 E. Flage−Larsen, A. Røyset, J. H. Cavka and K. Thorshaug, *J. Phys. Chem. C*, 2013, **117**, 20610–20616.

65 J. A. Johnson, J. Luo, X. Zhang, Y.-S. Chen, M. D. Morton, E. Echeverría, F. E. Torres and J. Zhang, *ACS Catal.*, 2015, **5**, 5283–5291.

66 S. Nakagaki, G. Ferreira, G. Ucoski and K. Dias de Freitas Castro, *Molecules*, 2013, **18**, 7279–7308.

67 C. Pereira, M. Simões, J. Tomé and F. Almeida Paz, *Molecules*, 2016, **21**, 1348.

68 J. Weynand, A. Moreno-Betancourt, F. Loiseau, N. Berthet, E. Defrancq and B. Elias, *Inorg. Chem.*, 2020, **59**, 2426–2433.

69 A. Hergueta-Bravo, M. E. Jiménez-Hernández, F. Montero, E. Oliveros and G. Orellana, *J. Phys. Chem. B*, 2002, **106**, 4010–4017.

70 K. Fan, S.-S. Bao, W.-X. Nie, C.-H. Liao and L.-M. Zheng, *Inorg. Chem.*, 2018, **57**, 1079–1089.

71 A. M. Rasero-Almansa, A. Corma, M. Iglesias and F. Sánchez, *Green Chem.*, 2014, **16**, 3522–3527.

72 L. Martins, L. K. Macreadie, D. Sensharma, S. Vaesen, X. Zhang, J. J. Gough, M. O'Doherty, N.-Y. Zhu, M. Rüther, J. E. O'Brien, A. L. Bradley and W. Schmitt, *Chem. Commun.*, 2019, **55**, 5013–5016.

73 Z.-H. Yan, M.-H. Du, J. Liu, S. Jin, C. Wang, G.-L. Zhuang, X.-J. Kong, L.-S. Long and L.-S. Zheng, *Nat. Commun.*, 2018, **9**, 3353.

74 Y. Pi, X. Feng, Y. Song, Z. Xu, Z. Li and W. Lin, *J. Am. Chem. Soc.*, 2020, **142**, 10302–10307.

75 X. Feng, Y. Pi, Y. Song, C. Brzezinski, Z. Xu, Z. Li and W. Lin, *J. Am. Chem. Soc.*, 2020, **142**, 690–695.

76 C. H. Hendon, D. Tiana, M. Fontecave, C. Sanchez, L. D'Arras, C. Sassoye, L. Rozes, C. Mellot-Draznieks and A. Walsh, *J. Am. Chem. Soc.*, 2013, **135**, 10942–10945.

77 J. R. Lakowicz, *Principles of Fluorescence Spectroscopy*, Springer US, Boston, MA, 2006.

78 B. Wardle, *Principles and Applications of Photochemistry*, John Wiley & Sons, 2009.

79 J.-C. G. Bünzli and S. V. Eliseeva, *Chem. Sci.*, 2013, **4**, 1939.

80 J. Soriano-López, D. G. Musaev, C. L. Hill, J. R. Galán-Mascarós, J. J. Carbó and J. M. Poblet, *J. Catal.*, 2017, **350**, 56–63.

81 X. Zhou, B. Li, G. Li, Q. Zhou, Z. Shi and S. Feng, *CrystEngComm*, 2012, **14**, 4664.

82 T.-G. Qu, X.-M. Hao, H. Wang, X.-G. Cui, F. Chen, Y.-B. Wu, D. Yang, M. Zhang and W.-L. Guo, *Polyhedron*, 2018, **156**, 208–217.

83 M.-N. Zhang, T.-T. Fan, Q.-S. Wang, H.-L. Han and X. Li, *J. Solid State Chem.*, 2018, **258**, 744–752.

84 Y.-J. Yang, D. Liu, Y.-H. Li and G.-Y. Dong, *Polyhedron*, 2019, **159**, 32–42.

85 G.-X. Wen, Y.-P. Wu, W.-W. Dong, J. Zhao, D.-S. Li and J. Zhang, *Inorg. Chem.*, 2016, **55**, 10114–10117.

86 W. T. Carnall, *Handbook on the Physics and Chemistry of Rare Earths*, North Holland Publishing Co., Amsterdam, Vol. 3., 1979.

87 J.-C. G. Bünzli and S. V. Eliseeva, in *Springer Series on Fluorescence*, 2010, vol. 13, pp. 1–45.

88 J. A. Ridenour, R. G. Surbella, A. V. Gelis, D. Koury, F. Poineau, K. R. Czerwinski and C. L. Cahill, *Angew. Chemie - Int. Ed.*, 2019, **58**, 16508–16511.

89 S. Lee, E. A. Kapustin and O. M. Yaghi, *Science (80-.).*, 2016, **353**, 808–811.

90 T. L. Easun, F. Moreau, Y. Yan, S. Yang and M. Schröder, *Chem. Soc. Rev.*, 2017, **46**, 239–274.

91 M. Müller, A. Devaux, C.-H. Yang, L. De Cola and R. A. Fischer, *Photochem. Photobiol. Sci.*, 2010, **9**, 846.

92 X. Zhao, X. Song, Y. Li, Z. Chang and L. Chen, *ACS Appl. Mater. Interfaces*, 2018, **10**, 5633–5640.

93 F. Johnsson, J. Kjärstad and J. Rootzén, *Clim. Policy*, 2019, **19**, 258–274.

94 H. Le Treut, R. Somerville, U. Cubasch, Y. Ding, C. Mauritzen, A. Mokssit, T. Peterson and M. Prather, in *Climate Change 2007: The Physical Science Basis. Contribution of Working Group I to the Fourth Assessment Report of the Intergovernmental Panel on Climate Change*, eds. S. Solomon, D. Qin, M. Manning, Z. Chen, M. Marquis, K. B. Averyt, M. Tignor and H. L. Miller, Cambridge University Press, Cambridge, United Kingdom and New York, NY, USA, 2007, pp. 95–127.

95 A. H. Chughtai, N. Ahmad, H. A. Younus, A. Laypkov and F. Verpoort, *Chem. Soc. Rev.*, 2015, **44**, 6804–6849.

96 J. Liu, L. Chen, H. Cui, J. Zhang, L. Zhang and C.-Y. Su, *Chem. Soc. Rev.*, 2014, **43**, 6011–61.

97 J. Pang, Z. Di, J.-S. Qin, S. Yuan, C. T. Lollar, J. Li, P. Zhang, M. Wu, D. Yuan, M. Hong and H.-C. Zhou, *J. Am. Chem. Soc.*, , DOI:10.1021/jacs.0c05758.

98 T. Zhang and W. Lin, *Chem. Soc. Rev.*, 2014, **43**, 5982–5993.

99 H.-Q. Xu, J. Hu, D. Wang, Z. Li, Q. Zhang, Y. Luo, S.-H. Yu and H.-L. Jiang, *J. Am. Chem. Soc.*, 2015, **137**, 13440–13443.

100 J. G. Santaclara, F. Kapteijn, J. Gascon and M. A. van der Veen, *CrystEngComm*, 2017, **19**, 4118–4125.

101 D. Wu, A. C. Sedgwick, T. Gunnlaugsson, E. U. Akkaya, J. Yoon and T. D. James, *Chem. Soc. Rev.*, 2017, **46**, 7105–7123.

102 J. Zhang, T. Xia, D. Zhao, Y. Cui, Y. Yang and G. Qian, *Sensors Actuators B Chem.*, 2018, **260**, 63–69.

103 J. A. Smith, M. A. Singh-Wilmot, K. P. Carter, C. L. Cahill and J. A. Ridenour, *Cryst. Growth Des.*, 2019, **19**, 305–319.

104 W.-H. Huang, J. Ren, Y.-H. Yang, X.-M. Li, Q. Wang, N. Jiang, J.-Q. Yu, F. Wang and J. Zhang, *Inorg. Chem.*, 2019, **58**, 1481–1491.

105 Y.-L. Gai, Q. Guo, X.-Y. Zhao, Y. Chen, S. Liu, Y. Zhang, C.-X. Zhuo, C. Yao and K.-C. Xiong, *Dalt. Trans.*, 2018, **47**, 12051–12055.

106 F. Guo, C. Su, Y. Fan, W. Shi and X. Zhang, *J. Solid State Chem.*, 2020, **284**, 121183.

107 Y.-J. Yang, Y.-H. Li, D. Liu and G.-H. Cui, *CrystEngComm*, 2020, **22**, 1166–1175.

108 X. Zhang, Z. Zhan, X. Liang, C. Chen, X. Liu, Y. Jia and M. Hu, *Dalt. Trans.*, 2018, **47**, 3272–3282.

109 N. Xu, Q. Zhang, B. Hou, Q. Cheng and G. Zhang, *Inorg. Chem.*, 2018, **57**, 13330–13340.

110 M. Zhang, G. Feng, Z. Song, Y.-P. Zhou, H.-Y. Chao, D. Yuan, T. T. Y. Tan, Z. Guo, Z. Hu, B. Z. Tang, B. Liu and D. Zhao, *J. Am. Chem. Soc.*, 2014, **136**, 7241–7244.

111 Y.-Q. Wang, Q.-H. Tan, H.-T. Liu, W. -Sun and Z.-L. Liu, *RSC Adv.*, 2015, **5**, 86614–86619.

112 W. Liu, Y. Wang, L. Song, M. A. Silver, J. Xie, L. Zhang, L. Chen, J. Diwu, Z. Chai and S. Wang, *Talanta*, 2019, **196**, 515–522.

113 A. Legrand, A. Pastushenko, V. Lysenko, A. Geloen, E. A. Quadrelli, J. Canivet and D. Farrusseng, *ChemNanoMat*, 2016, **2**, 866–872.

114 K. Zheng, Z.-Q. Liu, Y. Huang, F. Chen, C.-H. Zeng, S. Zhong and S. W. Ng, *Sensors Actuators B Chem.*, 2018, **257**, 705–713.

115 S. Khatua, S. Goswami, S. Biswas, K. Tomar, H. S. Jena and S. Konar, *Chem. Mater.*, 2015, **27**, 5349–5360.

116 T. Gong, P. Li, Q. Sui, J. Chen, J. Xu and E.-Q. Gao, *J. Mater. Chem. A*, 2018, **6**, 9236–9244.

117 C. He, K. Lu and W. Lin, *J. Am. Chem. Soc.*, 2014, **136**, 12253–12256.

118 M. Pamei and A. Puzari, *Nano-Structures & Nano-Objects*, 2019, **19**, 100364.

119 S. A. A. Razavi and A. Morsali, *Coord. Chem. Rev.*, 2020, **415**, 213299.

120 A. Lan, K. Li, H. Wu, D. H. Olson, T. J. Emge, W. Ki, M. Hong and J. Li, *Angew. Chemie Int. Ed.*, 2009, **48**, 2334–2338.

121 Y. Zhang, B. Li, H. Ma, L. Zhang and W. Zhang, *J. Mater. Chem. C*, 2017, **5**, 4661–4669.

122 W.-J. Li, M. Tu, R. Cao and R. A. Fischer, *J. Mater. Chem. A*, 2016, **4**, 12356–12369.

123 M. Li and M. Dincă, *Chem. Mater.*, 2015, **27**, 3203–3206.

124 M. Li and M. Dincă, *J. Am. Chem. Soc.*, 2011, **133**, 12926–12929.

125 F. Zhang, Y. Wang, T. Chu, Z. Wang, W. Li and Y. Yang, *Analyst*, 2016, **141**, 4502–4510.

126 F. Zhang, G. Zhang, H. Yao, Y. Wang, T. Chu and Y. Yang, *Microchim. Acta*, 2017, **184**, 1207–1213.

127 X. Zheng, C. Sun, S. Lu, F. Liao, S. Gao and L. Jin, *Eur. J. Inorg. Chem.*, 2004, **2004**, 3262–3268.

128 C.-H. Chen, X.-S. Wang, L. Li, Y.-B. Huang and R. Cao, *Dalt. Trans.*, 2018, **47**, 3452–3458.

129 B. Wang, Q. Yang, C. Guo, Y. Sun, L.-H. Xie and J.-R. Li, *ACS Appl. Mater. Interfaces*, 2017, **9**, 10286–10295.

130 C. Qiao, X. Qu, Q. Yang, Q. Wei, G. Xie, S. Chen and D. Yang, *Green Chem.*, 2016, **18**, 951–956.

131 J. Zhang, J. Ouyang, Y. Ye, Z. Li, Q. Lin, T. Chen, Z. Zhang and S. Xiang, *ACS Appl. Mater. Interfaces*, 2018, **10**, 27465–27471.

132 B.-H. Liu, D.-X. Liu, K.-Q. Yang, S.-J. Dong, W. Li and Y.-J. Wang, *Inorg. Chem. Commun.*, 2018, **90**, 61–64.

133 G.-S. Yang, Z.-L. Lang, H.-Y. Zang, Y.-Q. Lan, W.-W. He, X.-L. Zhao, L.-K. Yan, X.-L. Wang and Z.-M. Su, *Chem. Commun.*, 2013, **49**, 1088.

134 Y. Zhao, X. Xu, L. Qiu, X. Kang, L. Wen and B. Zhang, *ACS Appl. Mater. Interfaces*, 2017, **9**, 15164–15175.

135 W. Wu, B. Li, C. Gu, J. Wang, A. Singh and A. Kumar, *J. Mol. Struct.*, 2017, **1148**, 531–536.

136 A. Zhitkovich, *Chem. Res. Toxicol.*, 2005, **18**, 3–11.

137 T. He, Y.-Z. Zhang, X.-J. Kong, J. Yu, X.-L. Lv, Y. Wu, Z.-J. Guo and J.-R. Li, *ACS Appl. Mater. Interfaces*, 2018, **10**, 16650–16659.

138 S. Mohapatra, S. Adhikari, H. Riju and T. K. Maji, *Inorg. Chem.*, 2012, **51**, 4891–4893.

139 J. F. S. do Nascimento, A. M. U. de Araújo, J. Kulesza, A. F. de Farias Monteiro, S. A. Júnior and B. S. Barros, *New J. Chem.*, 2018, **42**, 5514–5522.

140 H. He, F. Sun, T. Borjigin, N. Zhao and G. Zhu, *Dalt. Trans.*, 2014, **43**, 3716–3721.

141 Y. Gai, Q. Guo, K. Xiong, F. Jiang, C. Li, X. Li, Y. Chen, C. Zhu, Q. Huang, R. Yao and M. Hong, *Cryst. Growth Des.*, 2017, **17**, 940–944.

142 X. Mi, D. Sheng, Y. Yu, Y. Wang, L. Zhao, J. Lu, Y. Li, D. Li, J. Dou, J. Duan and S. Wang, *ACS Appl. Mater. Interfaces*, 2019, **11**, 7914–7926.

143 Y. Yu, J. P. Ma and Y. Bin Dong, *CrystEngComm*, 2012, **14**, 7157–7160.

144 L. K. Cadman, M. F. Mahon and A. D. Burrows, *Dalt. Trans.*, 2018, **47**, 2360–2367.

145 Q. Tang, S. Liu, Y. Liu, D. He, J. Miao, X. Wang, Y. Ji and Z. Zheng, *Inorg. Chem.*, 2014,

53, 289–293.

146 J. Liu, W. Sun and Z. Liu, *RSC Adv.*, 2016, **6**, 25689–25694.

147 D. K. Singha, P. Majee, S. K. Mondal and P. Mahata, *RSC Adv.*, 2015, **5**, 102076–102084.

148 S. Zou, Q. Li and S. Du, *RSC Adv.*, 2015, **5**, 34936–34941.

149 P. R. Matthes, C. J. Höller, M. Mai, J. Heck, S. J. Sedlmaier, S. Schmiechen, C. Feldmann, W. Schnick and K. Müller-Buschbaum, *J. Mater. Chem.*, 2012, **22**, 10179.

150 S. Wang, L. Shan, Y. Fan, J. Jia, J. Xu and L. Wang, *J. Solid State Chem.*, 2017, **245**, 132–137.

151 S. Wang, J. Xu, J. Wang, K.-Y. Wang, S. Dang, S. Song, D. Liu and C. Wang, *J. Mater. Chem. C*, 2017, **5**, 6620–6628.

152 M. Martínez-Calvo, O. Kotova, M. E. Möbius, A. P. Bell, T. McCabe, J. J. Boland and T. Gunnlaugsson, *J. Am. Chem. Soc.*, 2015, **137**, 1983–1992.

153 V. K. Praveen, C. Ranjith and N. Armaroli, *Angew. Chemie - Int. Ed.*, 2014, **53**, 365–368.

154 H. Kim and J. Young Chang, *RSC Adv.*, 2013, **3**, 1774–1780.

155 Q.-Y. Yang, M. Pan, S.-C. Wei, K. Li, B.-B. Du and C.-Y. Su, *Inorg. Chem.*, 2015, **54**, 5707–5716.

156 K. T. Kamtekar, A. P. Monkman and M. R. Bryce, *Adv. Mater.*, 2010, **22**, 572–582.

157 M. Shang, C. Li and J. Lin, *Chem. Soc. Rev.*, 2014, **43**, 1372–1386.

158 C.-H. Huang, W.-R. Liu and T.-M. Chen, *J. Phys. Chem. C*, 2010, **114**, 18698–18701.

159 J. Qiao, J. Zhao, Q. Liu and Z. Xia, *J. Rare Earths*, 2019, **37**, 565–572.

160 J. Cornelio, T.-Y. Zhou, A. Alkaş and S. G. Telfer, *J. Am. Chem. Soc.*, 2018, **140**, 15470–15476.

161 Y. Cui, T. Song, J. Yu, Y. Yang, Z. Wang and G. Qian, *Adv. Funct. Mater.*, 2015, **25**, 4796–4802.

162 J. Yu, Y. Cui, C. Wu, Y. Yang, Z. Wang, M. O'Keeffe, B. Chen and G. Qian, *Angew. Chemie Int. Ed.*, 2012, **51**, 10542–10545.

163 S. R. Forrest, *Org. Electron.*, 2003, **4**, 45–48.

164 M. Aleksandrova, *Adv. Mater. Sci. Eng.*, 2016, **2016**, 1–8.

165 M. Gutiérrez, C. Martin, K. Kennes, J. Hofkens, M. Van der Auweraer, F. Sánchez and A. Douhal, *Adv. Opt. Mater.*, 2018, **6**, 1701060.

166 F. W. Steuber, J. J. Gough, É. Whelan, L. Burtnyak, A. L. Bradley and W. Schmitt, *Inorg. Chem.*, 2020, **59**, 17244–17250.

167 A. S. Agarwal, E. Rode, N. Sridhar and D. Hill, in *Handbook of Climate Change Mitigation and Adaptation*, eds. W.-Y. Chen, T. Suzuki and M. Lackner, Springer International Publishing, Cham, 2016, pp. 2487–2526.

168 J. Kothandaraman, A. Goeppert, M. Czaun, G. A. Olah and G. K. S. Prakash, *J. Am. Chem. Soc.*, 2016, **138**, 778–781.

169 A. Kidanemariam, J. Lee and J. Park, *Polymers (Basel).*, 2019, **11**, 2090.

170 I. I. Alkhatib, C. Garlisi, M. Pagliaro, K. Al-Ali and G. Palmisano, *Catal. Today*, 2020, **340**, 209–224.

171 A. Fujishima and K. Honda, *Nature*, 1972, **238**, 37–38.

172 A. J. Morris, G. J. Meyer and E. Fujita, *Acc. Chem. Res.*, 2009, **42**, 1983–1994.

173 C. S. Diercks, Y. Liu, K. E. Cordova and O. M. Yaghi, *Nat. Mater.*, 2018, **17**, 301–307.

174 C. Wang, Z. Xie, K. E. DeKrafft and W. Lin, *J. Am. Chem. Soc.*, 2011, **133**, 13445–13454.

175 J. H. Cavka, S. Jakobsen, U. Olsbye, N. Guillou, S. Bordiga, K. P. Lillerud, C. Lamberti, S. Bordiga and K. P. Lillerud, *J. Am. Chem. Soc.*, 2008, **130**, 1–19.

176 K. A. Vincent, G. J. Tilley, N. C. Quammie, I. Streeter, B. K. Burgess, M. R. Cheesman and F. A. Armstrong, *Chem. Commun.*, 2003, **3**, 2590.

177 C. C. Lee, Y. Hu and M. W. Ribbe, *Proc. Natl. Acad. Sci.*, 2012, **109**, 6922–6926.

178 S. Zhang, L. Li, S. Zhao, Z. Sun and J. Luo, *Inorg. Chem.*, 2015, **54**, 8375–8379.

179 L. Macreadie, C. J. Setter, M. B. Price, L. Conte, W. Schmitt, S. R. Batten, C. Richardson, M. R. Hill and R. Babarao, *Chem. Commun.*, , DOI:10.1039/D0CC05715K.

180 D. Wang, R. Huang, W. Liu, D. Sun and Z. Li, *ACS Catal.*, 2014, **4**, 4254–4260.

181 S. Bauer, C. Serre, T. Devic, P. Horcajada, J. Marrot, G. Férey and N. Stock, *Inorg. Chem.*, 2008, **47**, 7568–7576.

182 P. Horcajada, F. Salles, S. Wuttke, T. Devic, D. Heurtaux, G. Maurin, A. Vimont, M. Daturi, O. David, E. Magnier, N. Stock, Y. Filinchuk, D. Popov, C. Riekel, G. Férey and C. Serre, *J. Am. Chem. Soc.*, 2011, **133**, 17839–17847.

183 O. I. Lebedev, F. Millange, C. Serre, G. Van Tendeloo and G. Férey, *Chem. Mater.*, 2005, **17**, 6525–6527.

184 M. Dan-Hardi, C. Serre, T. Frot, L. Rozes, G. Maurin, C. Sanchez and G. Férey, *J. Am. Chem. Soc.*, 2009, **131**, 10857–10859.

185 Y. Fu, D. Sun, Y. Chen, R. Huang, Z. Ding, X. Fu and Z. Li, *Angew. Chemie - Int. Ed.*, 2012, **51**, 3364–3367.

186 M. Liu, Y.-F. Mu, S. Yao, S. Guo, X.-W. Guo, Z.-M. Zhang and T.-B. Lu, *Appl. Catal. B Environ.*, 2019, **245**, 496–501.

187 K. Aasberg-Petersen, I. Dybkjær, C. V. Ovesen, N. C. Schjødt, J. Sehested and S. G. Thomsen, *J. Nat. Gas Sci. Eng.*, 2011, **3**, 423–459.

188 J. H. Kim, D. Hansora, P. Sharma, J.-W. Jang and J. S. Lee, *Chem. Soc. Rev.*, 2019, **48**, 1908–1971.

189 H. Ahmad, S. K. Kamarudin, L. J. Minggu and M. Kassim, *Renew. Sustain. Energy Rev.*, 2015, **43**, 599–610.

190 E. M. Sproviero, J. A. Gascón, J. P. McEvoy, G. W. Brudvig and V. S. Batista, *Coord. Chem. Rev.*, 2008, **252**, 395–415.

191 Y. Kato, F. Akita, Y. Nakajima, M. Suga, Y. Umena, J. R. Shen and T. Noguchi, *J. Phys. Chem. Lett.*, 2018, **9**, 2121–2126.

192 M. Suga, F. Akita, K. Hirata, G. Ueno, H. Murakami, Y. Nakajima, T. Shimizu, K. Yamashita, M. Yamamoto, H. Ago and J. R. Shen, *Nature*, 2015, **517**, 99–103.

193 Y. Umena, K. Kawakami, J. R. Shen and N. Kamiya, *Nature*, 2011, **473**, 55–60.

194 B. Kok, B. Forbush and M. McGloin, *Photochem. Photobiol.*, 1970, **11**, 457–475.

195 E. M. Miner and M. Dincă, *Nat. Energy*, 2016, **1**, 16186.

196 Ü. Kökçam-Demir, A. Goldman, L. Esrafili, M. Gharib, A. Morsali, O. Weingart and C. Janiak, *Chem. Soc. Rev.*, 2020, **49**, 2751–2798.

197 N.-Y. Huang, J.-Q. Shen, Z.-M. Ye, W.-X. Zhang, P.-Q. Liao and X.-M. Chen, *Chem. Sci.*, 2019, **10**, 9859–9864.

198 G. Lan, Y.-Y. Zhu, S. S. Veroneau, Z. Xu, D. Micheroni and W. Lin, *J. Am. Chem. Soc.*, 2018, **140**, 5326–5329.

199 W. A. Shah, A. Waseem, M. A. Nadeem and P. Kögerler, *Appl. Catal. A Gen.*, 2018, **567**, 132–138.

200 P. Horcajada, S. Surblé, C. Serre, D.-Y. Hong, Y.-K. Seo, J.-S. Chang, J.-M. Grenèche, I. Margiolaki and G. Férey, *Chem. Commun.*, 2007, **100**, 2820–2822.

201 F. Song, Y. Ding, B. Ma, C. Wang, Q. Wang, X. Du, S. Fu and J. Song, *Energy Environ. Sci.*, 2013, **6**, 1170.

202 Q. Yin, J. M. Tan, C. Besson, Y. V Geletii, D. G. Musaev, A. E. Kuznetsov, Z. Luo, K. I. Hardcastle and C. L. Hill, *Science (80-.).*, 2010, **328**, 342–345.

203 Z.-M. Zhang, T. Zhang, C. Wang, Z. Lin, L. Long and W. Lin, *J. Am. Chem. Soc.*, 2015, **137**, 3197–3200.

204 D. Shi, R. Zheng, M. J. Sun, X. Cao, C. X. Sun, C. J. Cui, C. Sen Liu, J. Zhao and M. Du, *Angew. Chemie - Int. Ed.*, 2017, **56**, 14637–14641.

205 O. M. Yaghi and G. Li, *Angew. Chemie Int. Ed. English*, 1995, **34**, 207–209.

206 S. R. Batten, J. C. Jeffery and M. D. Ward, *Inorganica Chim. Acta*, 1999, **292**, 231–237.

207 D. A. Yaseen and M. Scholz, *Int. J. Environ. Sci. Technol.*, 2019, **16**, 1193–1226.

208 B. Lellis, C. Z. Fávaro-Polonio, J. A. Pamphile and J. C. Polonio, *Biotechnol. Res. Innov.*, 2019, **3**, 275–290.

209 Y. Pan, Q. Ding, H. Xu, C. Shi, A. Singh, A. Kumar and J. Liu, *CrystEngComm*, 2019, **21**, 4578–4585.

210 Y. Gao, S. Li, Y. Li, L. Yao and H. Zhang, *Appl. Catal. B Environ.*, 2017, **202**, 165–174.

211 Y. Zhou, W. Yang, M. Qin and H. Zhao, *Appl. Organomet. Chem.*, 2016, **30**, 188–192.

212 M. J. García-Galán, T. Garrido, J. Fraile, A. Ginebreda, M. S. Díaz-Cruz and D. Barceló, *J. Hydrol.*, 2010, **383**, 93–101.

213 B. Aslam, W. Wang, M. I. Arshad, M. Khurshid, S. Muzammil, M. H. Rasool, M. A. Nisar, R. F. Alvi, M. A. Aslam, M. U. Qamar, M. K. F. Salamat and Z. Baloch, *Infect. Drug Resist.*, 2018, **Volume 11**, 1645–1658.

214 X. Liu, B. Liu, G. Li and Y. Liu, *J. Mater. Chem. A*, 2018, **6**, 17177–17185.

Chapter 2 Thienothiophene-based coordination cage with rare hendecahedron geometry

2.1 Introduction

2.1.1 Coordination Cages

Aspects of the reticular chemistry concept can be applied to coordination cages, in a similar manner to MOFs, allowing the structures and applications of coordination cages to be varied through rational selection of components.[1] A wide range of different structures and geometries can be obtained by variation of the structure of the inorganic units and organic linkers in coordination cages.[2–5] It is possible to synthesise isoreticular series of coordination cages using different organic linkers, thus allowing internal pore sizes to be tuned.[6,7] Furthermore, the reaction conditions, such as temperature,[8,9] concentration,[9,10] solvent system,[8,9,11,12] reaction duration,[9] the presence of templating guests[10,13] and pH[14] can influence the structure of the materials formed. The desire to understand the range of structures that are possible for coordination cages has led to the synthesis of many fascinating structures.[15,16] Coordination cages have been reported for a range of applications, such as gas adsorption,[17,18] separations,[19,20] chemical sensing,[21,22] drug delivery,[23–25] guest uptake and release,[26–28] and catalysis,[29–32] including asymmetric catalysis.[33] Coordination cages can also be included as guests in the pores of MOFs to form hybrid solid systems.[34] Additionally, MOFs can be synthesised from coordination cages, for example by pillaring cages into two- or three-dimensional frameworks, resulting in fascinating structures.[35–39]

Though reticular chemistry principles have led to synthetic pathways for many different coordination cage structures, some geometries are very rare in coordination cages. In particular, geometries in which coordination cages have an odd number of faces and vertices are unusual, and are rarely reported. For example, only one previous report has been made of the synthesis of metal-organic hendecahedra. Zhou and co-workers utilised ligands with two different bend angles, 90° and 120°, to synthesise metal-organic hendecahedra composed of dinuclear {Cu_2} paddlewheel SBUs.[40]

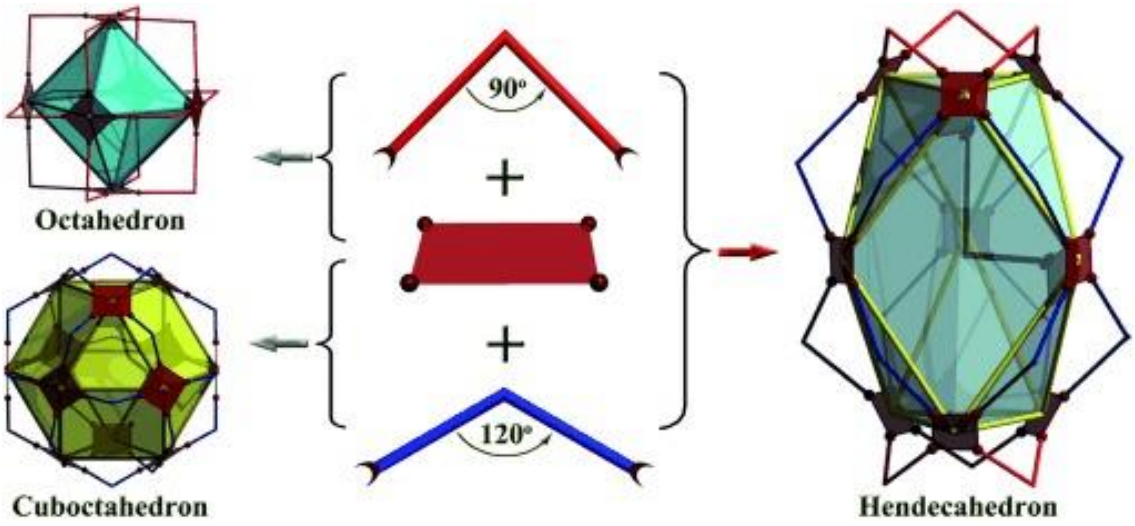

Scheme 2.1 Schematic representation of the self-assembly of coordination cages from organic linkers with 90° and 120° bend angles.[40]

Two mixed-linker coordination cages were reported by Zhou and coworkers.[40] In the first coordination cage, 9*H*-carbazole-3,6-dicarboxylate (9*H*-3,6-cdc^{2-}), a linker with a 90° bend angle, was used in combination with 4,4'-pyridine-2,6-diyldibenzoate (pddb^{2-}), a linker which has a bend angle of 120°. Reacting ligands with 120° bend angles with {Cu_2} paddlewheels gives metal-organic cuboctahedra[41,42] (**Scheme 2.1**), while linkers with a 90° bend angle, such as 9*H*-3,6-cdc^{2-}, form metal-organic octahedra (**Scheme 2.1**) when combined with {Cu_2} paddlewheels.[43,44] However, when 9*H*-3,6-cdc^{2-} and pddb^{2-} were used in combination, the result was a coordination cage with rare hendecahedron geometry (Scheme 2.2). The pddb^{2-} ligand leads to a nitrogen rich interior of this coordination cage. A second coordination cage could be synthesised by combining 9*H*-3,6-cdc^{2-} another linker with a 120° bend angle, 3,4'-dicarboxylate (3,4'-bpdc^{2-}), giving the same hendecahedron geometry (Scheme 2.2). Thus, utilizing a mixture of two different organic linkers, with different bend angles, allowed the synthesis of coordination cages with a hendecahedron geometry that was previously synthetically inaccessible using a single organic linker. This work by Zhou and coworkers also illustrates the concepts of reticular chemistry in coordination cages, as this rare geometry could be reproduced using different linkers with the same structural properties.

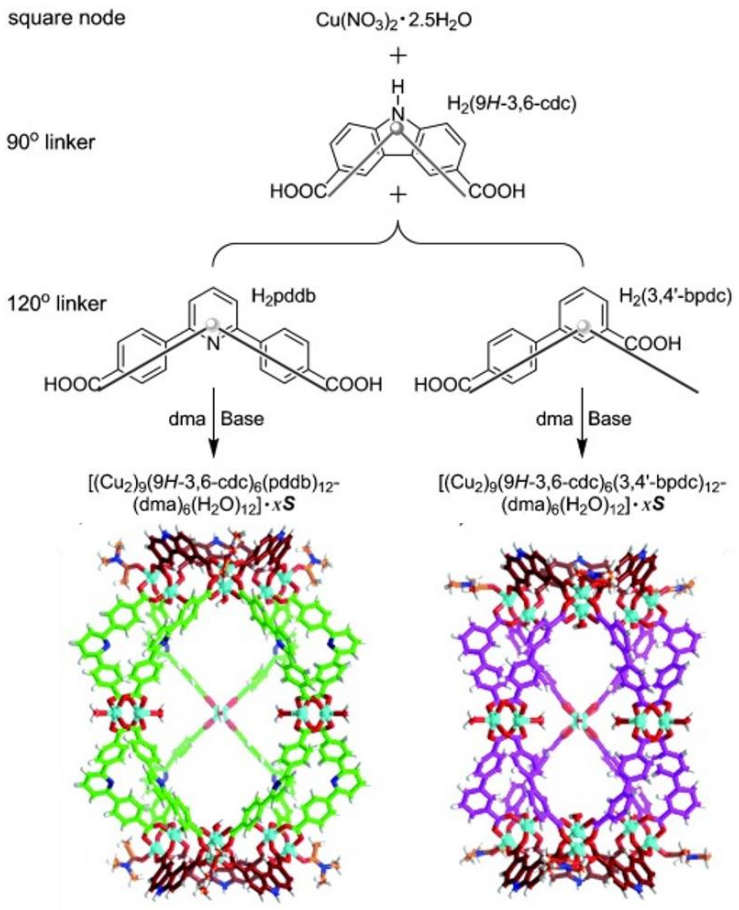

Scheme 2.2 Synthetic pathway to two different coordination cages with hendecahedral geometry.

2.1.2 Thienothiophene-based linkers

Incorporation of organic linkers based on heterocyclic ring systems into metal-organic frameworks and coordination cages has led to many interesting materials. Of particular interest to this work are linkers based on thiophene and thienothiophene rings.

Thiophene rings can impart interesting structural properties into molecules. When compared with linkers with multiple phenyl groups, thiophene-based linkers have increased flexibility, as phenyl groups have little conformational flexibility about the C-C bond due to steric bulk.[45] In contrast, rotation is possible about thiophene-phenyl bonds, leading to increased conformational flexibility, which can facilitate the formation of interesting coordination compounds.[46] Furthermore, the structure of thiophene rings allows variable and unusual angles between coordinating groups to be formed, resulting in bent molecules with interesting angles.[47] Interestingly, as sulfur atoms possess lower electronegativity than oxygen or nitrogen atoms, thiophene rings are more π-electron rich than their oxygen (furan) or nitrogen (pyrrole) analogues.[48]

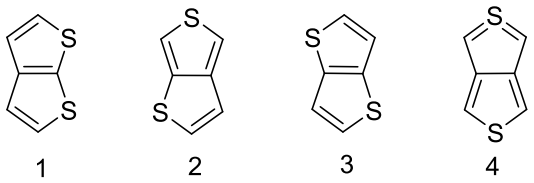

Fig. 2.1 Thienothiophene isomers.

Thienothiophenes are the simplest fused thiophene heterocycles, containing two fused thiophene rings. The first example of a thienothiophene was reported by Biedermann and Jacobson in 1886.[49] By heating citric acid and P_2S_3, they obtained thieno[2,3-*b*]thiophene (**1**) (Fig. 2.1) at a yield of less than 1%. Three other thienothiophene isomers are now known, thieno[3,4-*b*]thiophene (**2**), thieno[3,2-*b*]thiophene (**3**), and thieno[3,4-*c*]thiophene (**4**) (Fig. 2.1). With the exception of the unstable thienothiophene isomer thieno[3,4-*c*]thiophene, the efficient synthesis of all thienothiophene isomers is possible through cyclisation reactions of substituted thiophenes.[47] Due to their fused ring systems and rigid structure, thienothiophenes have extended π-conjugation compared to thiophene. Extending the conjugation of π-systems in this way leads to a lower band gap.[50] Isomers thieno[2,3-*b*]thiophene and thieno[3,4-*b*]thiophene have conjugated systems with low band gaps, while thieno[3,2-*b*]thiophene possesses a cross-conjugated system with a larger band gap.[47]

Due the presence of two sulphur atoms in their bicyclic ring systems, thienothiophenes and thienothiophene derivatives have been used as electron rich units in semiconducting polymers.[51] Current research has shown that these molecules have promising applications as organic dyes for dye sensitised solar cells[52], as polymers for polymer solar cells,[53] and as thin film transistors.[54]

In MOFs, thienothiophene-based linkers have been reported to improve the sensing capabilities,[55–57] and lower the band gaps of MOFs.[58] For example, in 2016, Bai and coworkers reported the synthesis of two lanthanide MOFs which incorporated a thienothiophene-based linker.[59] The MOFs are isostructural and have the structural formula $[Ln_2(DMTDC)_3(DEF)_4]\cdot DEF\cdot 6H_2O$ (Ln^{III} = Eu^{III} and Tb^{III}) (H_2DMTDC = 3,4-dimethylthieno[2,3-*b*]thiophene-2,5-dicarboxylic acid). The MOFs have 3D framework structures, and feature both rectangular and diamond-shaped channels, depending on the axis the MOF is viewed along. The electron rich sulfur atoms in the thienothiophene rings of the linker improve the capabilities of the MOF for luminescence sensing, by providing electron rich sites for interactions with analytes such as small molecules and metal ions. These MOFs demonstrated luminescence sensing in response to the presence of nitrobenzene and Fe^{III} ions. Furthermore, these sensing materials could be reused 5 times by washing the MOF samples with DMF. The proposed mechanism of luminescence quenching in response to the presence of nitrobenzene was attributed to PET from the photoexcited MOF to the electron deficient nitrobenzene molecules. However, luminescence quenching in response to detection of Fe^{III} ions arose from weak interactions between the sulfur atoms of the $DMTDC^{2-}$ linkers in the MOF and the Fe^{III} ions, which reduces the sensitisation of the lanthanide ions by the organic linker *via* the antenna effect.

To date, no examples of thienothiophene-based coordination cages have been reported.

2.1.3 Aims and objectives

Here, we propose that incorporating thienothiophene groups into organic SBUs will facilitate the design of novel bent linkers with interesting structural properties, such as bend angles and twist angles. We aimed to design a novel thienothiophene linker, and to explore the metal-organic materials that can be synthesised from this linker. We anticipated that the resulting materials would have interesting structures and geometries that may not have been synthetically accessible using known linkers.

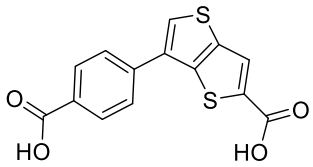

H_2**CPTT**

Fig. 2.2 The novel thienothiophene-based linker, 6-(4-carboxyphenyl)thieno[3,2-*b*]thiophene-2-carboxylic acid (H_2**CPTT**).

In this chapter, it is demonstrated that the novel thienothiophene-based linker, 6-(4-carboxyphenyl)thieno[3,2-*b*]thiophene-2-carboxylic acid (H_2**CPTT**) (Fig. 2.2), can be used to synthesise a coordination cage with rare hendecahedral geometry. This represents the first example of a metal-organic hendecahedron synthesised using a single organic linker. It is demonstrated that the open channels with large cross-sectional aperture of this coordination compound can be used for efficient uptake of organic dye molecules.

2.2 Synthesis of novel thienothiophene-based linker

2.2.1 Synthesis of H_2CPTT and crystal structures of intermediates

In this chapter, the design and synthesis of an organic linker with interesting optical and structural properties is described. H_2**CPTT** was selected as an organic linker for the construction of coordination cages for several key features. Bent ditopic linkers have been shown to be suitable linkers for the synthesis of coordination cages[5] and the unusual geometry and bend angles in the asymmetric linker H_2**CPTT** were expected to yield interesting structures. The carboxylate moieties provide a coordination site for binding to metal ions. Furthermore, the thienothiophene ring provides a rigid backbone, with electron rich sulfur atoms. After H_2**CPTT** was identified as a linker candidate, a synthetic strategy was outlined for the synthesis of this linker.

The novel linker, H_2**CPTT**, was synthesised in three synthetic steps (Scheme 2.3), starting from the commercially available compound 3,4-dibromothiophene.

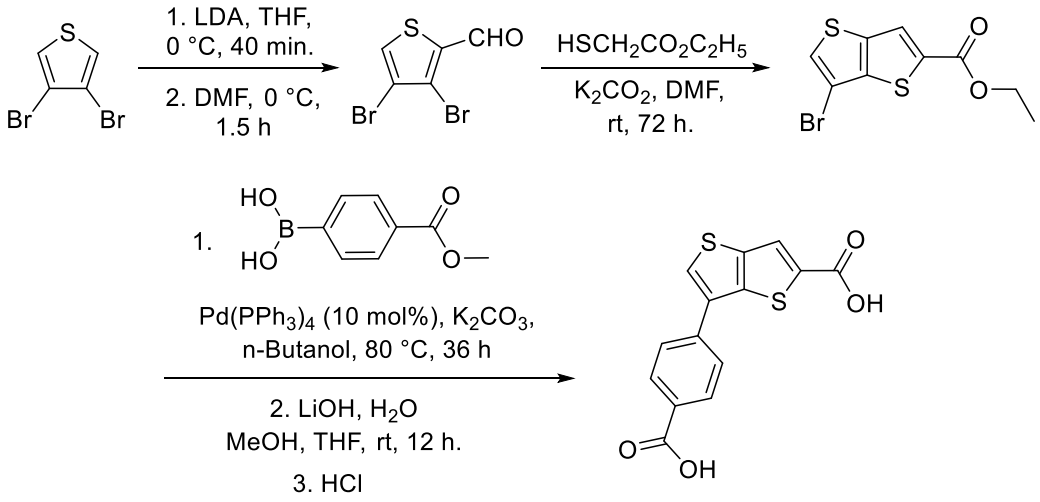

Scheme 2.3 Synthesis of 6-(4-carboxyphenyl)thieno[3,2-*b*]thiophene-2-carboxylic acid (H_2**CPTT**).

2.2.1.1 Synthesis of 3,4-dibromothiophene-2-carbaldehyde

In the first synthetic step in the synthesis of H_2**CPTT**, 3,4-dibromothiophene-2-carbaldehyde was prepared from 3,4-dibromothiophene, via a formylation reaction, using a modified version of the procedure previously reported by Chu *et al.*.[60] Lithium diisopropylamine (LDA) was synthesised *in situ* from diisopropyl amine and *n*-butyllithium (*n*-BuLi) in THF at 0 °C. Addition of 3,4-dibromothiophene-2-carbaldehyde to a solution of LDA resulted in lithiation of the 2-position of the thiophene ring. Electrophilic quenching this organolithium intermediate with DMF gave formylation of the 2-position. The reaction was washed with ammonium chloride solution, and extracted with ethyl acetate. The product was purified by flash column chromatography (SiO_2, hexane:ethyl acetate, 19:1, v/v), affording the product as a pale yellow powder. A yield of 65% was obtained. ^{1}H NMR was in good agreement with the literature.[60] Dark yellow crystals of 3,4-dibromothiophene-2-carbaldehyde were obtained by slow evaporation of the solvent from a solution of 3,4-dibromothiophene-2-carbaldehyde in dichloromethane (DCM).

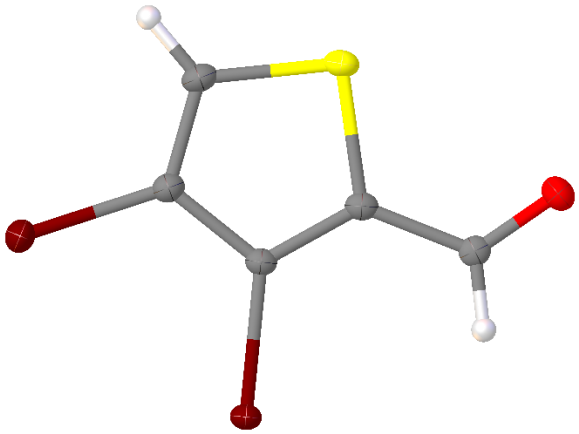

Fig. 2.3 Asymmetric unit of 3,4-dibromothiophene-2-carbaldehyde (thermal displacement ellipsoids are shown at the 50% probability level). Atom colour scheme: C, dark grey, O, red, S, yellow, Br, brown, H, white.

Table 2.1 Crystal data and refinement results for 3,4-dibromothiophene-2-carbaldehyde.

Compound name	3,4-dibromothiophene-2-carbaldehyde
Empirical formula	$C_5H_2Br_2OS$
Formula weight	269.944
Temperature (K)	105.15
Crystal description	Dark yellow plate
Crystal size (mm^3)	0.13 × 0.1 × 0.08
Crystal system	Orthorhombic
Space group	*Pnma*
a (Å)	11.524(3)
b (Å)	6.4297(13)
c (Å)	9.556(2)
α (°)	90
β (°)	90
γ (°)	90
V ($Å^3$)	708.1(3)
Z	4
ρ_{calc} (g/cm^3)	2.532
μ (mm^{-1})	11.649
F(000)	503.0
Radiation	Mo Kα (λ = 0.71073)
2θ range for data collection (°)	5.54 to 71.36
Reflections collected	8446
Independent reflections	1749 [R_{int} = 0.0351, R_{sigma} = 0.0296]
Data/restraints/parameters	1749/0/55
Goodness-of-fit on F^2	1.009
R_1 [I≥2σ (I)], all	0.0307, 0.0486
wR_2 [I≥2σ (I)], all	0.0696, 0.0773
Largest diff. peak/hole (e $Å^{-3}$)	1.47/-1.25

The structure of 3,4-dibromothiophene-2-carbaldehyde was solved and refined in the orthorhombic space group *Pnma* (Table 2.1). The asymmetric unit contains one 3,4-dibromothiophene-2-carbaldehyde molecule. All atoms are coplanar with the *b*-face of the molecule. The packing of molecules of 3,4-dibromothiophene-2-carbaldehyde along the crystallographic *b*-axis is presented in **Fig. 2.4**. Molecules of 3,4-dibromothiophene-2-carbaldehyde pack in layers, with the orientation of molecules alternating in successive layers, giving an *ABAB* stacking pattern. No π-π stacking was observed between 3,4-dibromothiophene-2-carbaldehyde molecules.

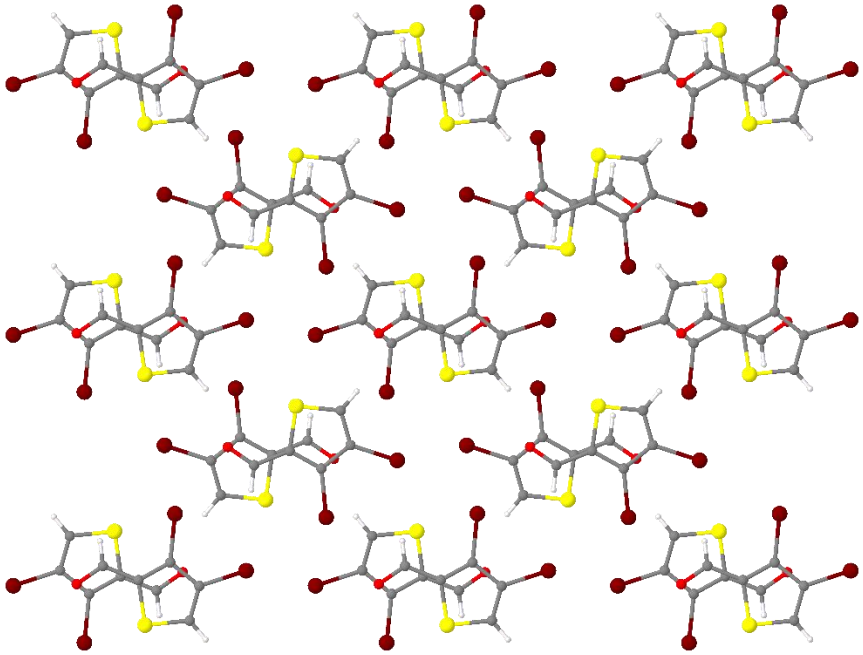

Fig. 2.4 Packing of molecules of 3,4-dibromothiophene-2-carbaldehyde, viewed along the crystallographic *b*-axis. Atom colour scheme: C, dark grey, O, red, S, yellow, Br, brown, H, white.

2.2.1.2 Synthesis and crystal structure of ethyl 6-bromothieno[3,2-b]thiophene-2-carboxylate

Ethyl 6-bromothieno[3,2-b]thiophene-2-carboxylate was synthesised by a cyclisation reaction between 3,4-dibromothiophene-2-carbaldehyde and ethyl thioglycolate, in the presence of K_2CO_3 in DMF suspension, using a modified version of the procedure reported by Chu *et al*. (**Scheme 2.3**).[60] The crude product was washed with brine and lithium chloride solution, extracted with ethyl acetate and concentrated. Subsequently, purification was carried out by flash column chromatography (SiO_2, hexane:ethyl acetate, 19:1, v/v), furnishing the product as a yellow crystalline solid with 93 % yield. ^{1}H and ^{13}C NMR spectra were in good agreement with the literature.[60]

Crystals of ethyl 6-bromothieno[3,2-*b*]thiophene-2-carboxylate were obtained by dissolving the compound in dichloromethane in a round bottom flask and allowing the solvent to evaporate slowly. Upon evaporation, yellow-brown crystals of ethyl 6-bromothieno[3,2-*b*]thiophene-2-carboxylate formed as large needles. The crystal structure of the compound was measured using single crystal XRD analysis, and was solved and refined in the monoclinic space group $P2_1/n$.

The asymmetric unit of ethyl 6-bromothieno[3,2-*b*]thiophene-2-carboxylate contains two molecules (**Fig. 2.5**). The -Br and ester groups in each molecule extend coplanar to the thienothiophene fused ring system (**Fig. 2.6**).

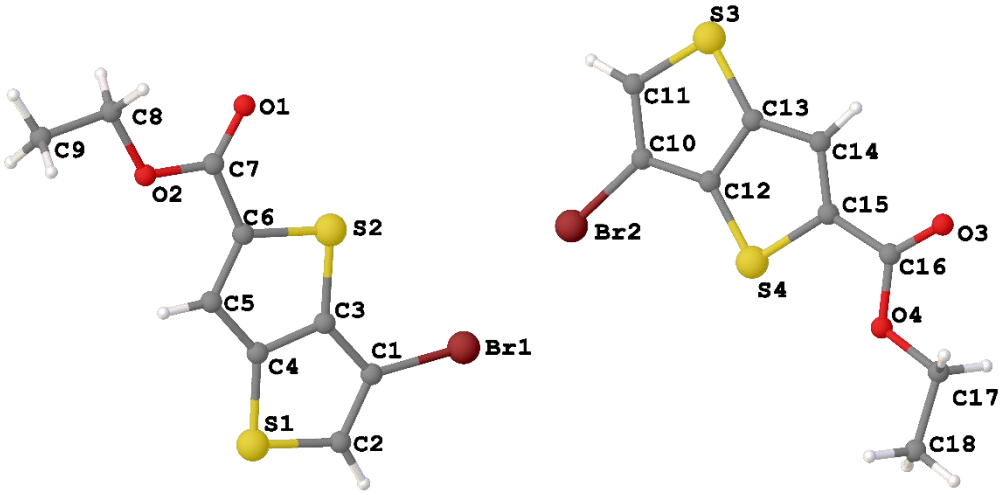

Fig. 2.5 Asymmetric unit of ethyl 6-bromothieno[3,2-*b*]thiophene-2-carboxylate, viewed along the crystallographic *a*-axis, showing non-H atom labels. Thermal ellipses are shown at 50% probability level. Atom colour scheme: C, dark grey, O, red, S, yellow, Br, brown, H, white.

Table 2.2 Crystal data and refinement results for ethyl 6-bromothieno[3,2-*b*]thiophene-2-carboxylate

Compound name	Ethyl 6-bromothieno[3,2-*b*]thiophene-2-carboxylate
Empirical formula	$C_9H_7BrO_2S_2$
Formula weight	291.18
Temperature (K)	100.15
Crystal description	Brown needle
Crystal system	Monoclinic
Space group	$P2_1/n$
a (Å)	3.9559(4)
b (Å)	38.703(2)
c (Å)	13.4187(2)
α (°)	90
β (°)	92.090(7)
γ (°)	90
V (Å^3)	2053.1(3)
Z	8
ρ_{calc} (g/cm^3)	1.884
μ (mm^{-1})	9.025
F(000)	1152
Radiation	c
2θ range for data collection (°)	4.566 to 124.956
Reflections collected	20696
Independent reflections	3210 [R_{int} = 0.2321, R_{sigma} = 0.1346]
Data/restraints/parameters	3210/21/255
Goodness-of-fit on F^2	1.066
R_1 [I≥2σ (I)], all	0.0922, 0.1376
wR_2 [I≥2σ (I)], all	0.2017, 0.2262
Largest diff. peak/hole (e Å^{-3})	0.98/ -1.06

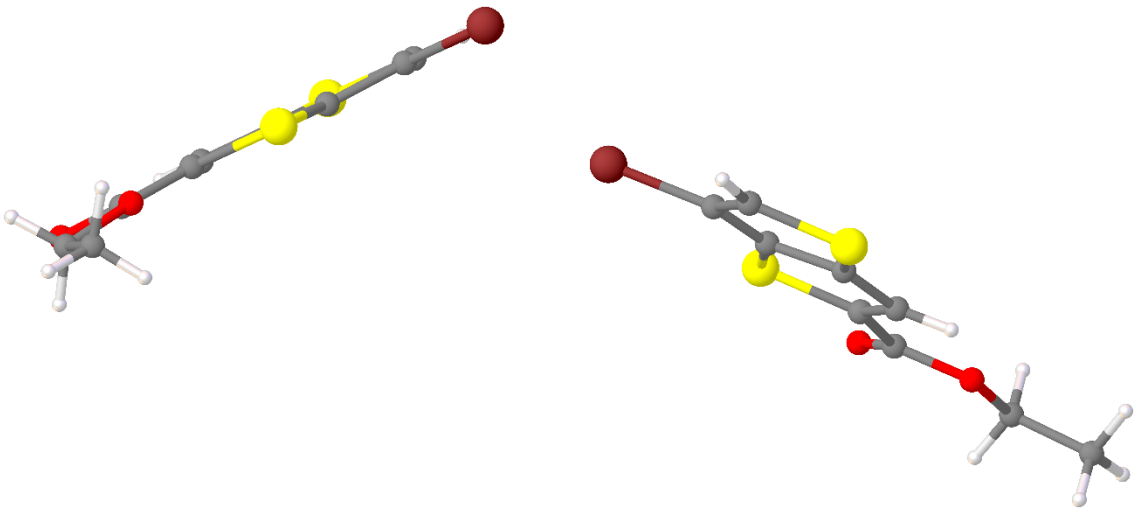

Fig. 2.6 Asymmetric unit of ethyl 6-bromothieno[3,2-*b*]thiophene-2-carboxylate viewed along the crystallographic *c*-axis. Atom colour scheme: C, dark grey, O, red, S, yellow, Br, brown, H, white.

Molecules of ethyl 6-bromothieno[3,2-*b*]thiophene-2-carboxylate are aligned parallel to the crystallographic *a*-axis. The distances between ethyl 6-bromothieno[3,2-*b*]thiophene-2-carboxylate molecules in consecutive layers is approximately 4 Å. Interestingly, the Br atoms in each molecule are aligned to face a second Br atom, resulting in pairs of ethyl 6-bromothieno[3,2-*b*]thiophene-2-carboxylate molecules with Br atoms oriented towards one another. As a result, investigations were carried out to determine if structure-influencing intermolecular Br···Br interactions occur in this structure.

Fig. 2.7 Types of intermolecular halogen···halogen interactions, showing type I (left) where $\theta_1 \approx \theta_2$ and type II (right) where $\theta_1 \approx 90°$ and $\theta_1 \approx 180°$.[61]

Several criteria have been outlined for determining the presence of attractive intermolecular C-Br··· Br-C interactions in crystals.[62] The first is that the interatomic distance between the halogen atoms must not exceed the sum of the van der Waals radii of the halogen atoms. The second criteria relates to the C-Br···Br' angles. Type I interactions occur when the C-Br···Br' angles θ_1 and θ_2 are close to identical ($\theta_1 \approx \theta_2$), whereas Type II interactions are characterised by the corresponding angles, $\theta_1 \approx 180°$ and $\theta_2 \approx 90°$ (**Fig. 2.7**).[61,63,64] A recent classification identifies three types of interactions, based on the difference between θ_1 and θ_2, $|\theta_1 - \theta_2|$. Type I interactions can be defined as those with 0°

$\leq \left| \theta_1 - \theta_2 \right| \leq 15°$, type II interactions have $30° \leq \left| \theta_1 - \theta_2 \right|$, and quasi type I/type II interactions are those with $15° \leq \left| \theta_1 - \theta_2 \right| \leq 30°$.[65]

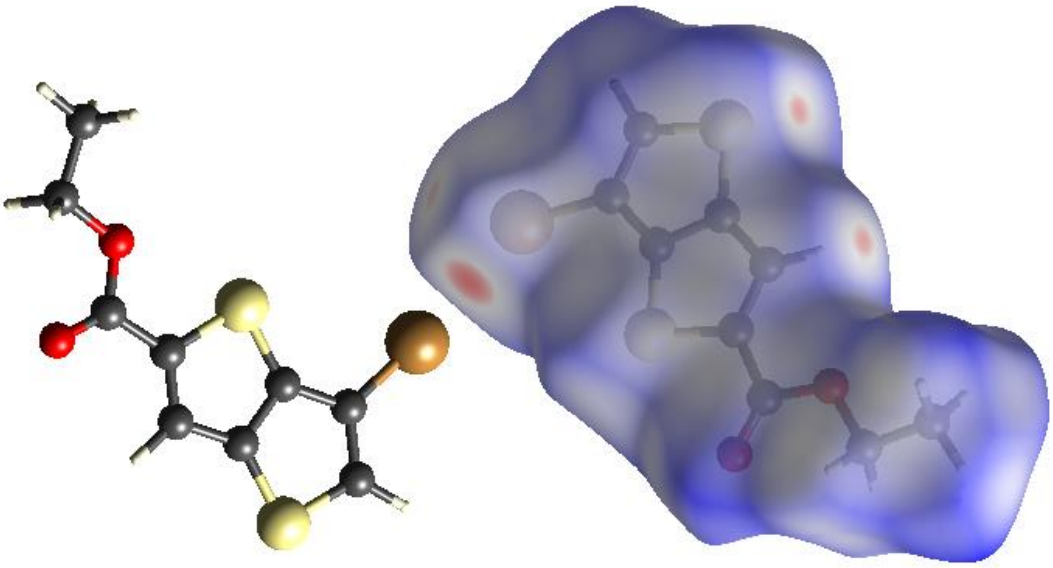

Fig. 2.8 Hirshfeld surface of ethyl 6-bromothieno[3,2-*b*]thiophene-2-carboxylate molecules, viewed along the crystallographic *a*-axis, indicating close contacts between Br atoms on adjacent molecules. The red colour represents the area on the surface where intermolecular contacts between atoms are closer than the sum of their van der Waals radii. Atom colour scheme: C, dark grey, O, red, S, yellow, Br, brown, H, white.

Intermolecular interactions in the crystal structure of ethyl 6-bromothieno[3,2-*b*]thiophene-2-carboxylate were investigated using the CrystalExplorer17 software package.[66] Analysis of the Hirshfeld surface[67] of ethyl 6-bromothieno[3,2-*b*]thiophene-2-carboxylate confirms these close contacts between Br atoms on adjacent molecules (**Fig. 2.8**). Two Br-Br distances occur between molecules, 3.4941(19) Å and 3.6671(19) Å, which are both less than the sum of van der Waals radii (3.7 Å for Br), indicating a strong interaction between Br atoms.

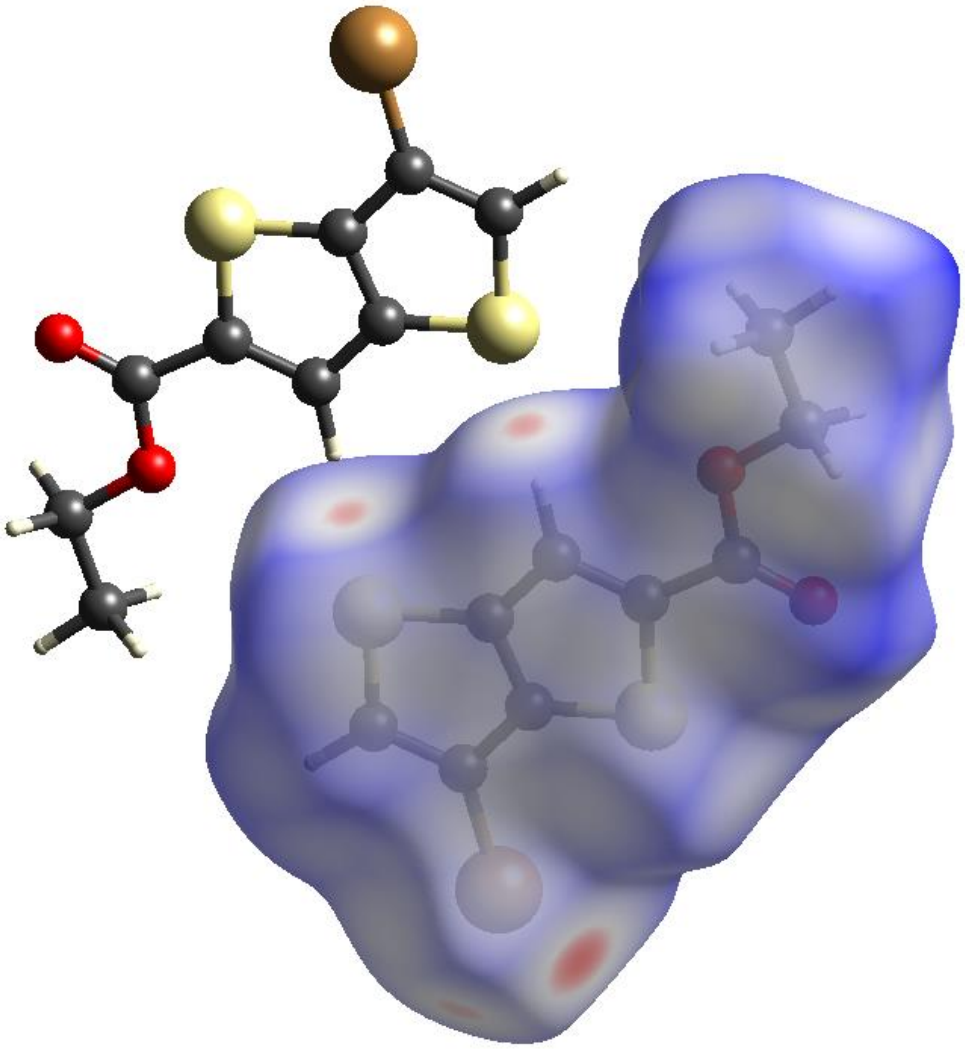

Fig. 2.9 Hirshfeld surface of ethyl 6-bromothieno[3,2-*b*]thiophene-2-carboxylate molecules, viewed along the crystallographic *a*-axis, indicating close contacts between S atoms and H-C atoms on adjacent molecules. The red colour represents the area on the surface where intermolecular contacts between atoms are closer than the sum of their van der Waals radii. Atom colour scheme: C, dark grey, O, red, S, yellow, Br, brown, H, white.

Close contacts also occur between thienothiophene S atoms and hydrogen atoms on adjacent molecules (**Fig. 2.9**), indicating possible hydrogen bonding between thienothiophene molecules. These close contacts occur between the ethyl 6-bromothieno[3,2-*b*]thiophene-2-carboxylate molecule containing Br1 and its inversion symmetry equivalent. The C-S distance for the S1···H-C5 interaction is 3.770(12) Å. Though S atoms and C-H bonds are not typical H bond acceptors or donors respectively, investigations into C-H···S interactions have shown that this interaction has the same characteristics as conventional hydrogen bonds.[68]

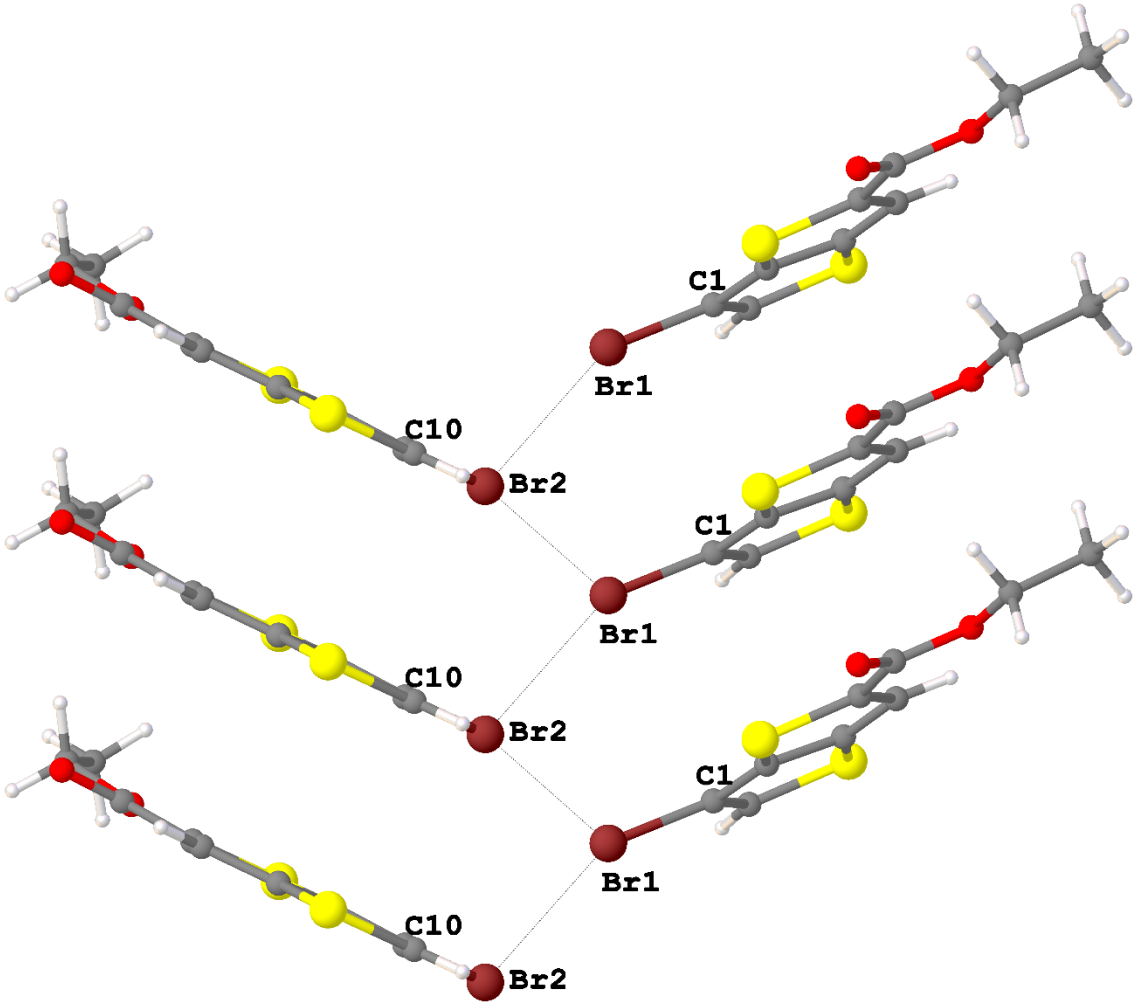

Fig. 2.10 Chains of Br···Br interactions between ethyl 6-bromothieno[3,2-*b*]thiophene-2-carboxylate molecules, viewed along the crystallographic *c*-axis, showing labelled atoms. Atom colour scheme: C, dark grey, O, red, S, yellow, Br, brown, H, white.

The Br···Br interactions in crystals of ethyl 6-bromothieno[3,2-*b*]thiophene-2-carboxylate form a zig-zag chain of interactions extending parallel to the crystallographic *a*-axis (**Fig. 2.10**). As a result, two sets of C-Br···Br' angles occur (**Table 2.3**). In one set C-Br···Br' angles of θ_1 = 124.2(5)° and θ_2 = 148.0(4)° are observed, therefore $|\theta_1 - \theta_2| \approx 23.8°$. Hence, this interaction between Br atoms in the crystal structure of ethyl 6-bromothieno[3,2-*b*]thiophene-2-carboxylate can be defined as a quasi type I/type II interaction. In the second set of C-Br···Br' angles, θ_1 = 119.3(4)° and θ_2 = 167.5(5)°, and $|\theta_1 - \theta_2| \approx 48.2°$. This interaction can therefore be identified as a type II interaction.

Table 2.3 Br···Br distances, θ_1 and θ_2 angles, $|\theta_1 - \theta_2|$ and interaction types in ethyl 6-bromothieno[3,2-*b*]thiophene-2-carboxylate

Br···Br distance (Å)	θ_1 atoms	θ_1 (°)	θ_2 atoms	θ_2 (°)	$\lvert\theta_1 - \theta_2\rvert$ (°)	Interaction type
3.4941(19)	C1-Br1···Br2	119.3(4)	C10-Br2···Br1	167.5(5)	48.2	Type II
3.6671(19)	C10-Br2···Br1	124.2(5)	C1-Br1···Br2	148.0(4)	23.8	Quasi type I/type II

The result of these Br···Br and S···H-C interactions is a packing arrangement in which ethyl 6-bromothieno[3,2-*b*]thiophene-2-carboxylate molecules align in layers extending parallel to the

crystallographic *b*- and *c*-axis. This arrangement leads to interacting S1 and H-C5 atoms, and Br1 and Br2 atoms pointing towards one another (**Fig. 2.11**).

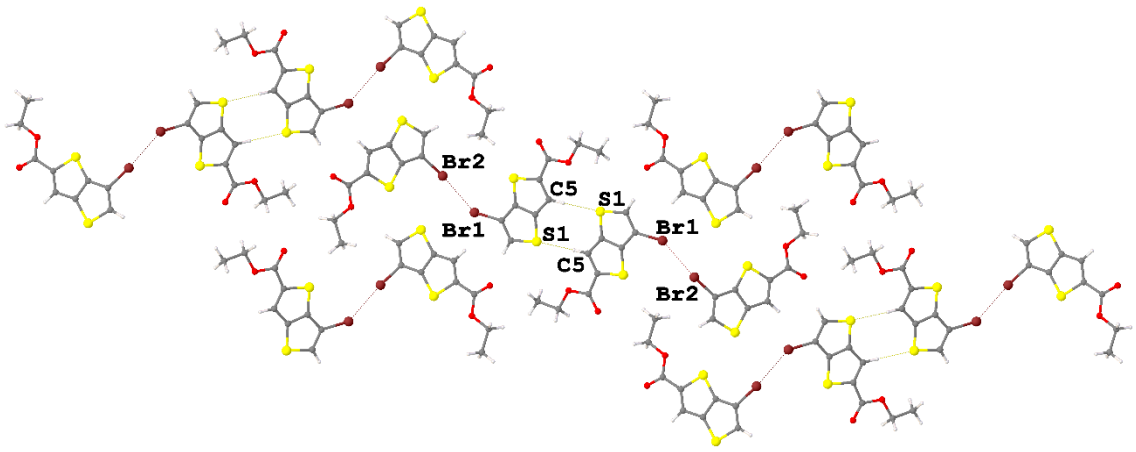

Fig. 2.11 Packing diagram of ethyl 6-bromothieno[3,2-*b*]thiophene-2-carboxylate molecules as viewed along the crystallographic *a*-axis, showing intermolecular interactions, with selected interacting atoms labelled. Atom colour scheme: C, dark grey, O, red, S, yellow, Br, brown, H, white.

2.2.1.4 Synthesis and crystal structure of 6-(4-carboxyphenyl)thieno[3,2-b]thiophene-2-carboxylic acid (H_2CPTT)

The final synthetic step in the synthesis of 6-(4-carboxyphenyl)thieno[3,2-b]thiophene-2-carboxylic acid (H_2**CPTT**) consisted of a Suzuki coupling reaction between ethyl 6-bromothieno[3,2-b]thiophene-2-carboxylate and (4-(methoxycarbonyl)phenyl)boronic acid. This reaction was followed by base-catalysed hydrolysis of the ester groups and subsequent acidification, to give carboxylic acid groups.

Initial attempts to synthesise ethyl 6-(4-(methoxycarbonyl)phenyl)thieno[3,2-b]thiophene-2-carboxylate via a Suzuki coupling reaction between ethyl 6-bromothieno[3,2-b]thiophene-2-carboxylate and (4-(methoxycarbonyl)phenyl)boronic acid in the presence of K_2CO_3, using 1,4-dioxane as a solvent, at 80 °C for 36 hours were not successful. NMR spectroscopy of the crude reaction mixture showed only starting materials, with no evidence of successful coupling between ethyl 6-bromothieno[3,2-b]thiophene-2-carboxylate and (4-(methoxycarbonyl)phenyl)boronic acid.

Palladium-catalysed cross-coupling reactions are known to be sensitive to solvent effects.[69] The reaction was therefore re-attempted under the same reaction conditions, using *n*-butanol as a solvent. This afforded the synthesis of butyl 6-(4-(butoxycarbonyl)phenyl)thieno[3,2-b]thiophene-2-carboxylate at 58% yield. The use of *n*-butanol as a solvent, in the presence of base, resulted in the butylation of both esters on the molecule. Though this was initially seen as a disadvantage of this synthesis, the presence of butyl chains on the molecule increased the solubility of 6-(4-(butoxycarbonyl)phenyl)thieno[3,2-b]thiophene-2-carboxylate in non-polar organic solvents, such as hexane. This allowed facile purification of this intermediate product by washing with brine, extraction with DCM, followed by flash column chromatography (SiO_2, hexane:ethyl acetate, 19:1,

v/v), giving butyl 6-(4-(butoxycarbonyl)phenyl)thieno[3,2-b]thiophene-2-carboxylate as a pale yellow oil, at a yield of 58%.

NMR studies were used to characterise the intermediate, butyl 6-(4-(butoxycarbonyl)phenyl)thieno[3,2-b]thiophene-2-carboxylate. The ^{1}H NMR and ^{13}C NMR spectra both displayed overlapping signals of the two butyl chains of the molecule. Base-catalysed hydrolysis of the butyl esters of butyl 6-(4-(butoxycarbonyl)phenyl)thieno[3,2-b]thiophene-2-carboxylate followed by acidification to pH 1 and filtration, gave the product 6-(4-carboxyphenyl)thieno[3,2-b]thiophene-2-carboxylic acid (H_2**CPTT**), as a white solid at 90% yield with respect to the butyl ester intermediate, and an overall yield of ~53 % for this final step.

Single crystals of H_2**CPTT** were obtained while attempting to form Zr-based coordination compounds with this linker. Heating a solution of H_2**CPTT** (30 mg), $ZrCl_4$ and benzoic acid (300 mg) in DMF (1 mL) at 120 °C for c.a. 16 hrs, gave colourless needle-shaped crystals upon cooling of the solution. The structure of H_2**CPTT** was determined by single-crystal XRD analysis. H_2**CPTT** was solved and refined in the monoclinic space group $P2_1/c$.

Table 2.4 Crystal data and refinement results for H_2**CPTT.**

Compound name	H_2**CPTT**
Empirical formula	$C_{14}H_8O_4S_2$
Formula weight	304.32
Temperature (K)	215(2)
Crystal description	Colourless needle
Crystal system	Monoclinic
Space group	$P2_1/c$
a (Å)	3.8037(7)
b (Å)	24.729(4)
c (Å)	13.155(3)
α (°)	90
β (°)	95.50(2)
γ (°)	90
V (Å^3)	1231.6(4)
Z	4
ρ_{calc} (g/cm^3)	1.641
μ (mm^{-1})	4.034
F(000)	624.0
Radiation	CuKα (λ = 1.54184)
2θ range for data collection (°)	7.15 to 125.354
Reflections collected	8184
Independent reflections	1942 [R_{int} = 0.0374, R_{sigma} = 0.0337]
Data/restraints/parameters	1942/0/189
Goodness-of-fit on F^2	1.197
R_1 [I≥2σ (I)], all	0.0606,0.0653
wR_2 [I≥2σ (I)], all	0.1593,0.1632
Largest diff. peak/hole (e Å^{-3})	0.51/-0.37

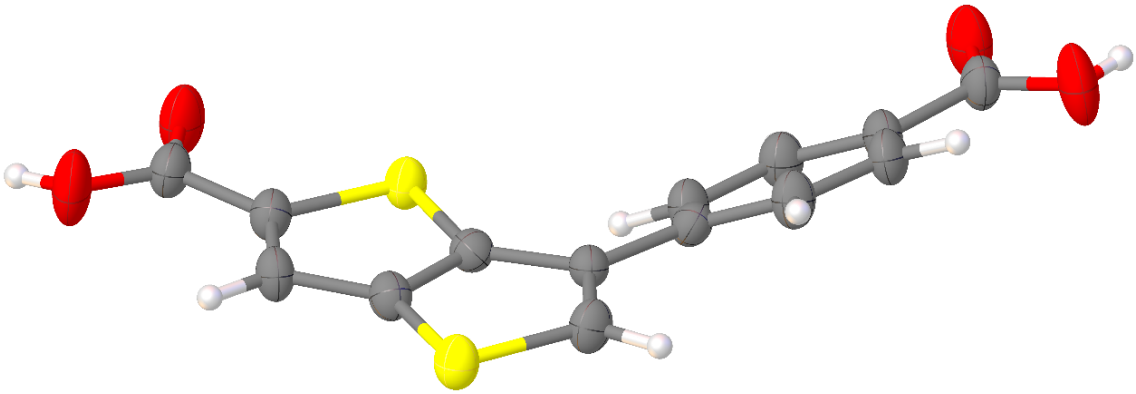

Fig. 2.12 Thermal displacement ellipsoid plot of H_2**CPTT**, viewed along the crystallographic c-axis (thermal ellipsoids are shown at the 50% probability level). Atom colour scheme: C, dark grey, O, red, S, yellow, H, white.

The thermal displacement ellipsoid plot of the asymmetric unit in H_2**CPTT** is presented in **Fig. 2.12**. Molecules of H_2**CPTT** are non-planar in structure, with a dihedral angle of 25.81(19)° between the plane of the phenyl ring and the plane of the thienothiophene rings. The carboxylic acid moieties are almost coplanar with their respective aromatic rings. The bend angle between the carboxylic acid moieties in H_2**CPTT**, calculated as the angle between the two carboxylate C-C bonds in the molecule is 102.3(3)°.

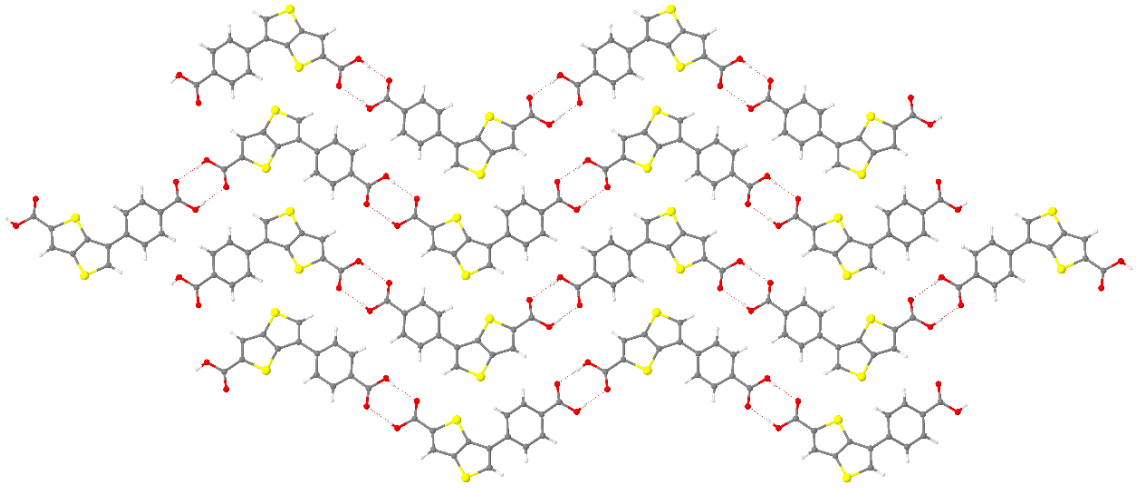

Fig. 2.13 View of the packing of H_2**CPTT** along the crystallographic *a*-axis. Atom colour scheme: C, dark grey, O, red, S, yellow, H, white.

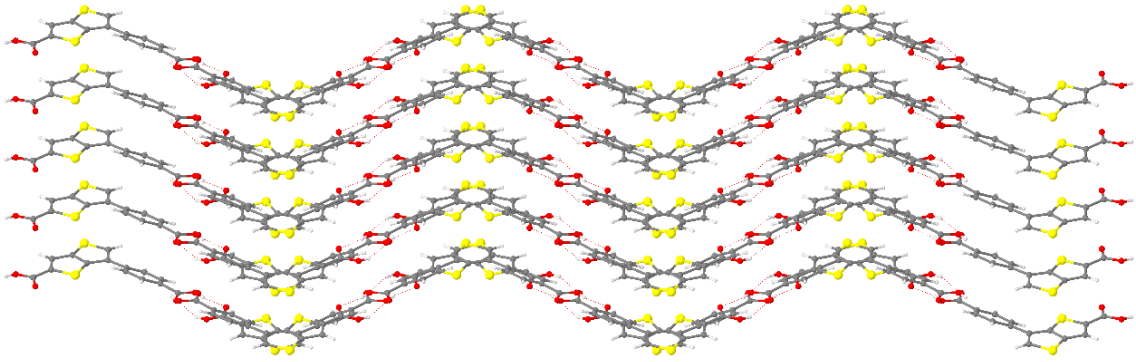

Fig. 2.14 View of the packing of H_2**CPTT** along the crystallographic *c*-axis. Atom colour scheme: C, dark grey, O, red, S, yellow, H, white.

Carboxylic acids have the ability to self-associate through hydrogen bonding as they are both strong hydrogen bond acceptors (C=O) and hydrogen bond donors (O-H).[70] Intermolecular O-H···O hydrogen bonding occurs between the carboxylic acids of H_2**CPTT** molecules (**Fig. 2.13**). The O···O distances between carboxylic acids of adjacent molecules are 2.675(5) Å and 2.6163(50) Å, the O···H distances are *ca.* 1.93 Å. It should be noted that hydrogen bonds form between heterofunctional carboxylic acids. These intermolecular hydrogen bonding interactions leads to the self-assembly of H_2**CPTT**, to form well-defined one-dimensional polymeric assemblies which propagate along the *b*-axis (**Fig. 2.14**). The bent shape of H_2**CPTT** molecules leads to the hydrogen bonded polymer chains of H_2**CPTT** forming a zig-zag pattern along both the *a* and *c*-axes.

2.2.2 Nuclear Magnetic Resonance (NMR) studies of H_2CPTT

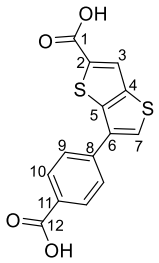

Fig. 2.15 H_2**CPTT** showing labelled carbon atoms.

NMR studies were used to characterise H_2**CPTT**, and the numbering scheme used for assigning C atoms is shown in **Fig. 2.15**. The H-atoms were numbered using the same number as the carbon atom to which they are attached. The aromatic region of the ^{1}H NMR spectrum showed 4 signals, consisting of two doublets at 8.47 and 8.24 ppm, and two singlets at 8.10 and 7.95 ppm (**Fig. 2.16**). Selective rotating frame Overhauser enhancement spectroscopy (ROESY) was used to assign the H-atoms to their respective signals. A clear NOE correlation occurs between the signals at 8.47 and 7.95 ppm, which, when considered with the multiplicity of the signals (n=1 and n=2 respectively), allows for the assignment of H7 to the singlet at 8.47 ppm and H9 to the doublet at 7.95 ppm. Due to their proximity, a NOE correlation is also observed between the signals at 7.95 and 8.10 ppm (corresponding to H10). The H9 and H10 signals each arise from two chemically equivalent H-atoms,

thus giving integration values of 2 compared to a relative integration value of 1 for H3 and H7. The remaining singlet, at 8.24 ppm can be assigned to H3. The ^{1}H NMR spectrum also shows two broad singlets at 13.05 and 13.38 ppm, which can be assigned to the carboxylic acid H-atoms.

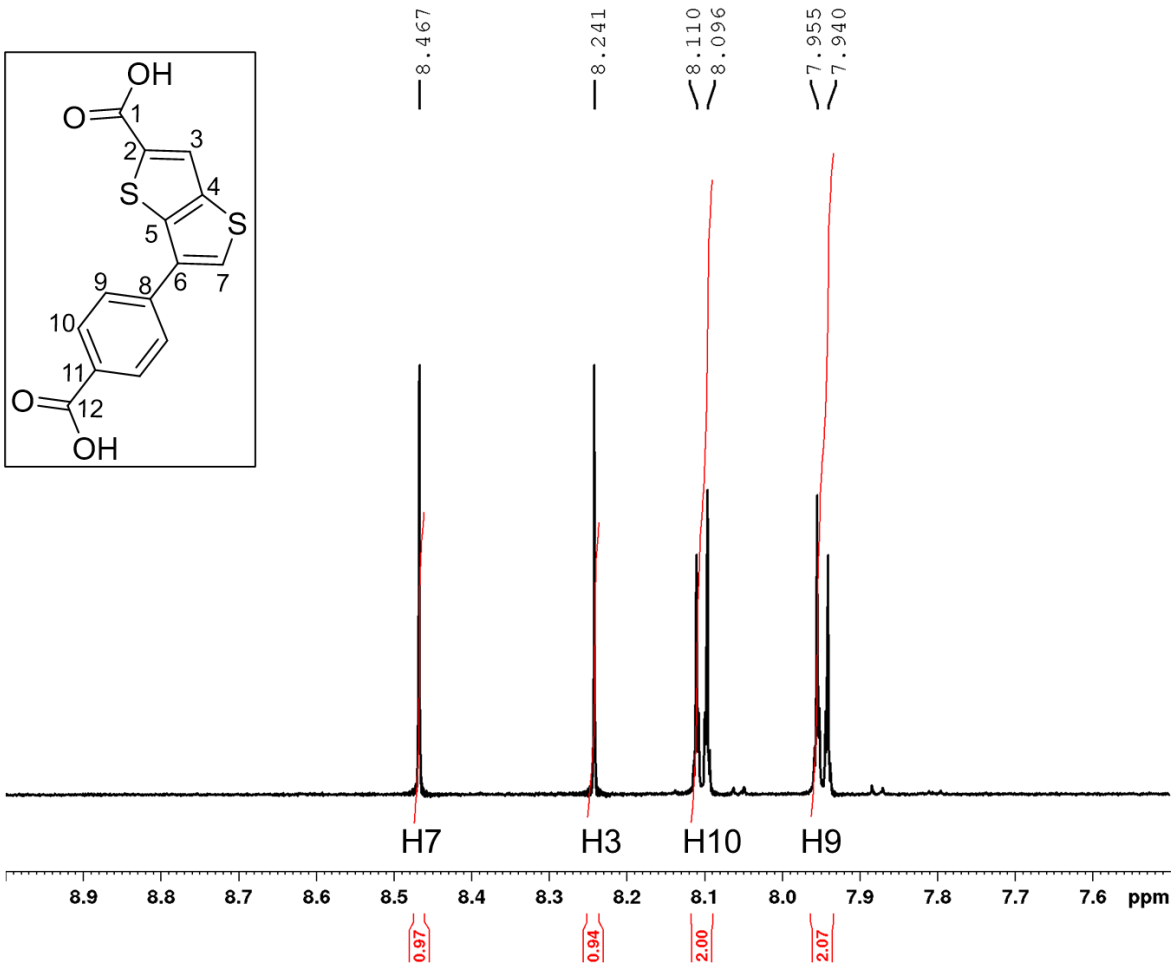

Fig. 2.16 Close up view of the aromatic region of the ^{1}H NMR spectrum of H_2**CPTT** (600 mHz, d_6-DMSO), showing H_2**CPTT** as an inset, and with labelled H-atoms.

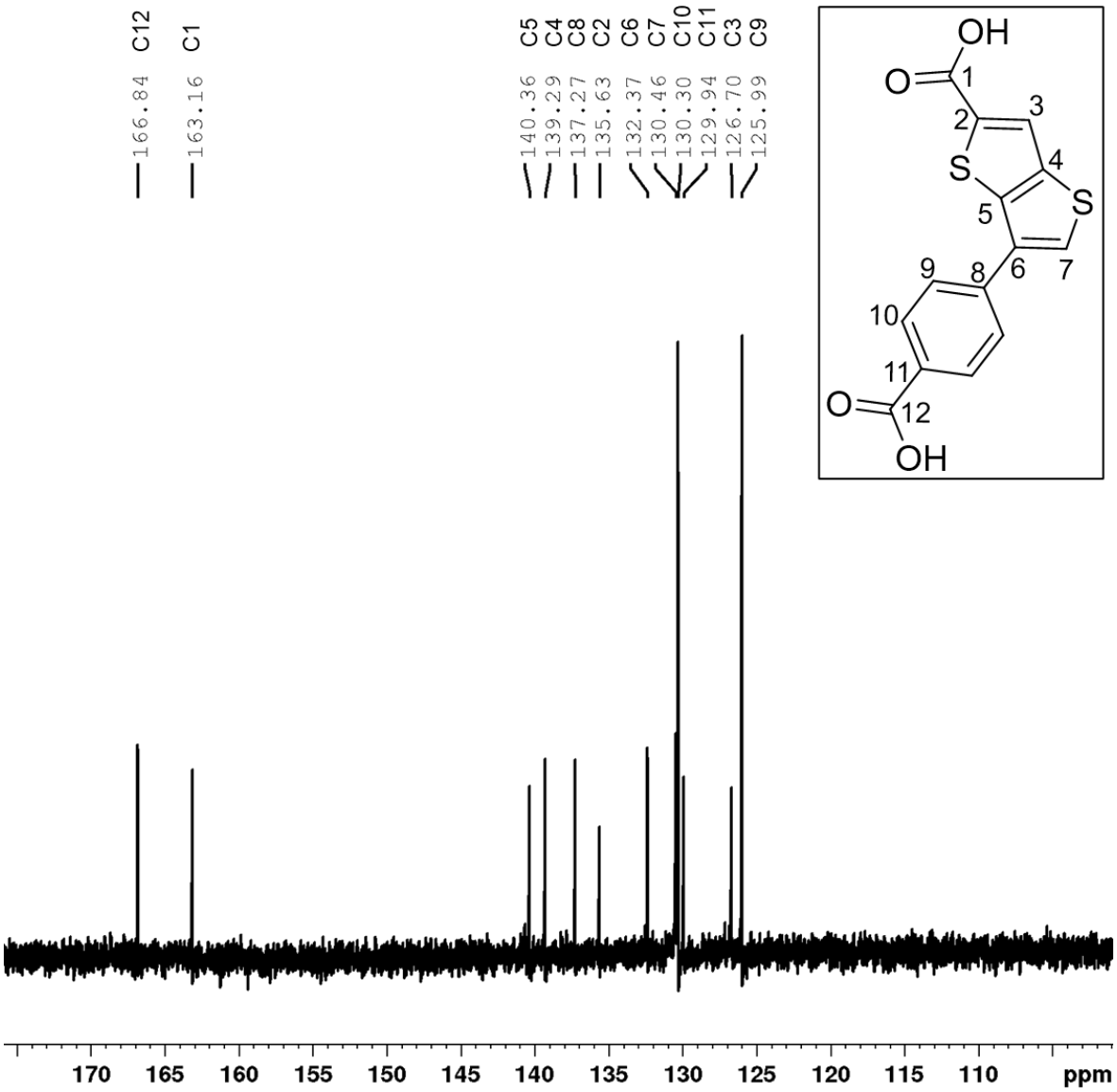

Fig. 2.17 Close up view of the ^{13}C NMR spectrum of H_2**CPTT** (150 mHz, d_6-DMSO), showing H_2**CPTT** as an inset, and with labelled C-atoms.

The ^{13}C NMR spectrum of H_2**CPTT** features 12 carbon signals (**Fig. 2.17**). The heteronuclear single quantum coherence (HSQC) spectrum facilitated the assignment of the C atoms with bonds to H atoms. Two-dimensional NMR spectroscopy allow resonances on two axes to be correlated with one another, which gives information on how the spins in molecules are related to each other. HSQC experiments are used to correlate the chemical shift of a proton to a heteroatom nucleus (usually ^{13}C or ^{15}N) which is separated from the proton by one bond. In a HSQC experiment, polarisation transfer occurs from a more sensitive nucleus (e.g. ^{1}H) to a less sensitive nucleus (e.g. ^{13}C), followed by transfer of the polarisation back to the more sensitive nucleus. The spectrum is detected at the frequency of the more sensitive nucleus.

Analysis of the HSQC interactions observed in the spectrum (**Fig. 2.18**) allowed assignment of the ^{13}C signals at 125.99 ppm to C9, 126.70 ppm to C3, 130.3 ppm to C10, 130.46 ppm to C7.

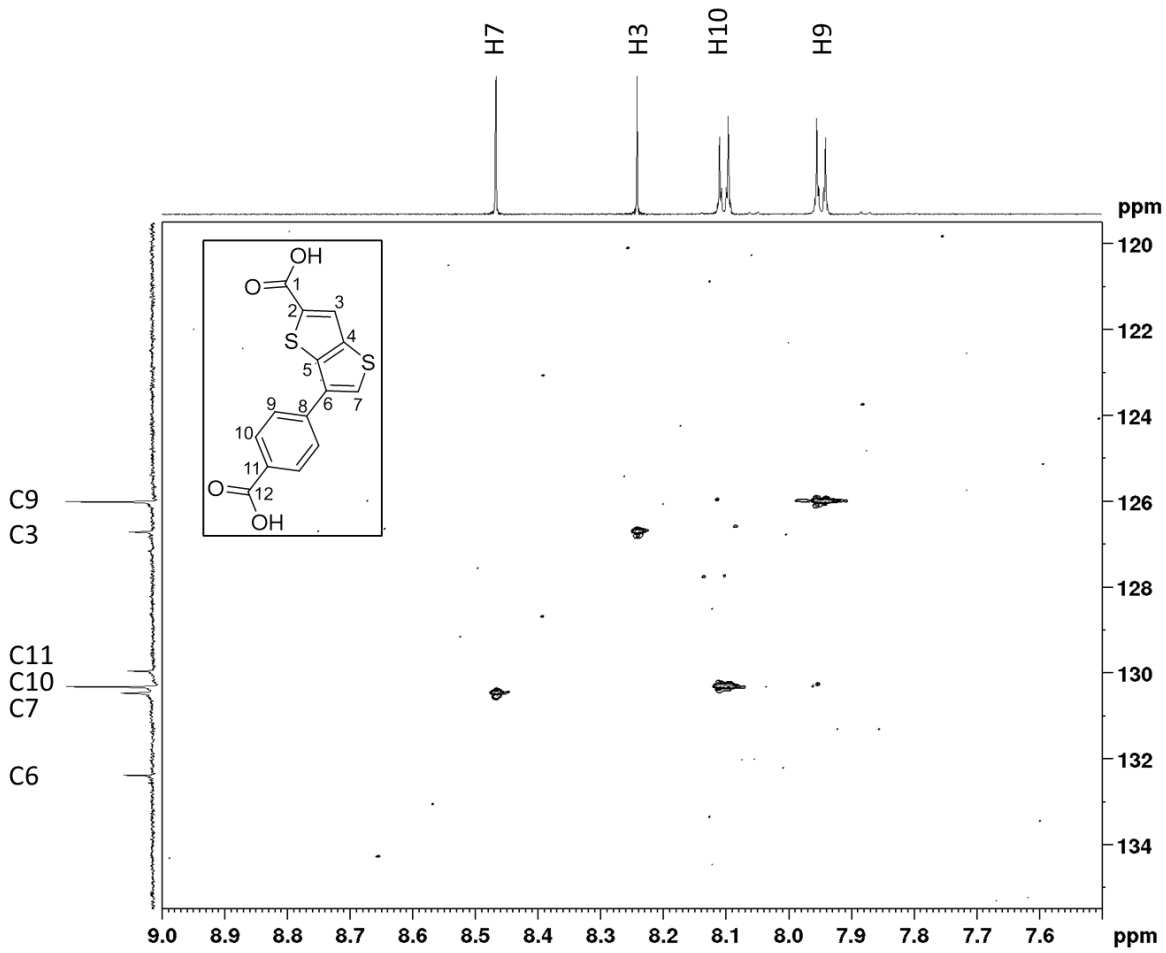

Fig. 2.18 HSQC spectrum of H_2**CPTT**, showing H_2**CPTT** as an inset, and with labelled H-atoms and C-atoms.

The heteronuclear multiple bond correlation (HMBC) spectrum could be used to assign the remaining signals to the quaternary carbon atoms in H_2**CPTT** (**Fig. 2.19**). HMBC experiments are 2D NMR experiments that give correlations between heteroatoms (usually ^{1}H and ^{13}C) that are separated by two, three, or multiple bonds.

An interaction between the ^{1}H signal at 8.10 ppm (H10) and the ^{13}C signal at 166.84 ppm, along with the deshielded nature of this ^{13}C signal, facilitated the assignment of this signal to the carboxylic carbon atom, C12. The other highly deshielded ^{13}C signal in this spectrum, at 163.16 ppm can therefore be assigned to the other carboxylic carbon atom, C1.

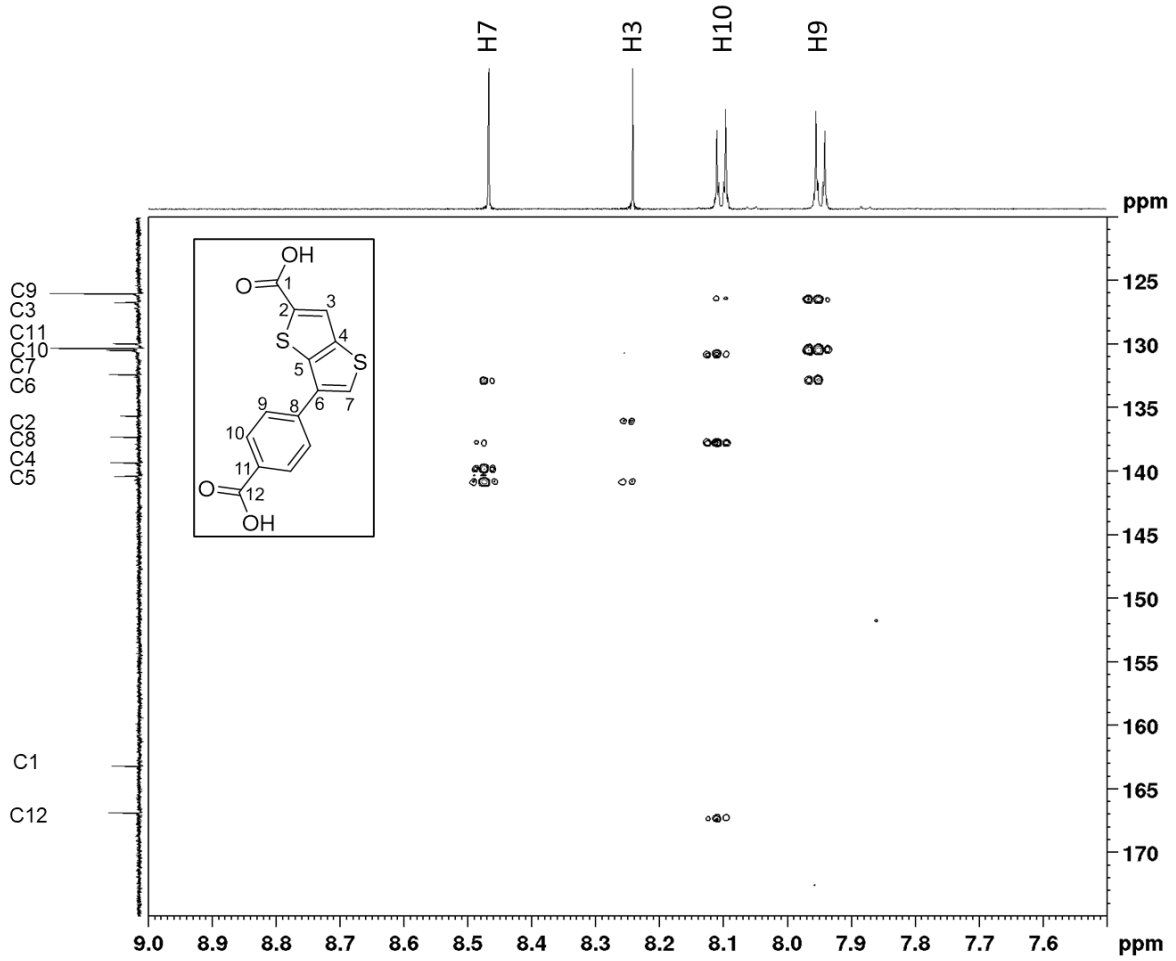

Fig. 2.19 HMBC spectrum of H_2**CPTT,** showing H_2**CPTT** as an inset, and with labelled H-atoms and C-atoms.

The ^{13}C signal at 135.63 ppm shows a correlation only with the H3 signal (8.24 ppm) in the HMBC spectrum. As no other correlations are observed with this ^{13}C signal, this signal can be assigned to C2, due to the lack of proximity between this carbon atom and other H-atoms. Similarly, the ^{13}C signal at 129.94 ppm can be assigned to C11, as this carbon atom only shows a correlation with the H9 signal (7.95 ppm).

The ^{13}C signals at 140.36 and 139.29 ppm both show correlations with the ^{1}H signals at 8.47 ppm (H7) and 8.24 ppm (H3), indicating that these signals correspond to C4 and C5. To assign the correct carbon atom to each signal, the relative strengths of the correlations were compared. A stronger correlation was observed between H3 (8.24 ppm) and the carbon signal at 140.36 ppm than the signal at 139.29 ppm. In HMBC spectra, correlations through two bonds are often weaker than correlations through three bonds particularly in aromatic rings. Thus, larger cross signals are often observed for correlations through three bonds. Therefore the ^{13}C signal at 140.36 ppm can be assigned to C5.

Finally, the ^{13}C signal at 132.37 ppm has cross signals with both the ^{1}H signal at 8.47 ppm (H7) and 7.95 ppm (H9), therefore can be assigned to C6. The ^{13}C signal at 137.27 ppm also shows a correlation with the 8.47 ppm (H7), in addition to 8.10 ppm (H10) signals, and therefore arises from C8.

2.2.3 Fourier Transform Infrared spectroscopy (FTIR) spectroscopy of H_2CPTT

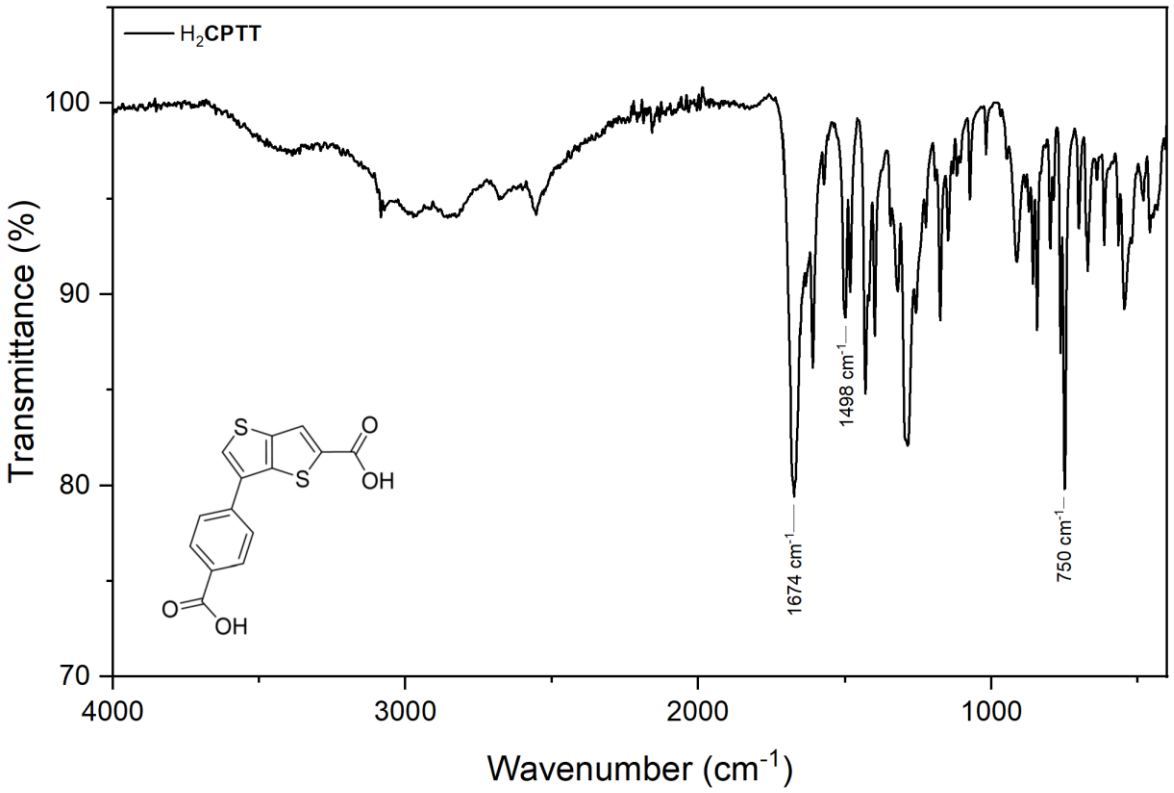

Fig. 2.20 FTIR spectrum of H_2**CPTT**, with characteristic vibrational bands labelled.

The FTIR spectrum of H_2**CPTT** is shown in **Fig. 2.20**. The spectrum shows stretching modes associated with the carboxylate C=O stretching mode at 1674 cm^{-1}, in addition to vibrations associated with stretching of the C-S-C bonds at 750 cm^{-1}. A broad band from 3250 to 2450 cm^{-1} can be attributed to stretching of the carboxylate O-H bonds and the C-H bonds on aromatic rings in the molecule. Ring stretching of the C=C bonds in the aromatic rings leads to a band at 1498 cm^{-1}. The FTIR spectrum of H_2**CPTT** is in good agreement with spectra previously reported for thienothiophene-based organic compounds.[71]

2.3 Synthesis and crystal structure of hendecahedron coordination cage

Following the successful synthesis of H_2**CPTT**, investigations were carried out into the coordination chemistry of this ligand. Initial efforts focussed on the reaction of this linker with Cu^{II} salts, due to the vast array of previously reported MOFs and coordination cages based on Cu^{II} SBUs.[15,17,72–74]

The syntheses of supramolecular systems are influenced by their reaction conditions, such as the nature of the solvent, temperature, pH, reaction time and counterions present in the reaction system. In order to screen for the formation of supramolecular materials incorporating H_2**CPTT**, a series of reactions were carried out under varying conditions of reaction temperature (80 °C, 100 °C), reaction duration (1 day, 2 days, 5 days), H_2**CPTT** ligand concentration (0.1 M, 0.2 M), ligand:metal ion ratio (1:1, 1:2, 1:4) and solvent system (DMF, N,N-dimethylacetamide (DMA)).

Through these experiments, it was found that heating a solution of $Cu(NO_3)_2 \cdot 3H_2O$ and H_2**CPTT** (1:1 ligand:metal ratio, 0.01 M concentration) in DMF at 80 °C for 5 days gave green crystals (**Fig. 2.21** and **Fig. 2.22**). The crystals form as square-shaped plates, which vary in size. In some cases, several crystals assemble in clusters or form intergrown assemblies. The crystal structure of one of these crystals was measured using single-crystal XRD analysis.

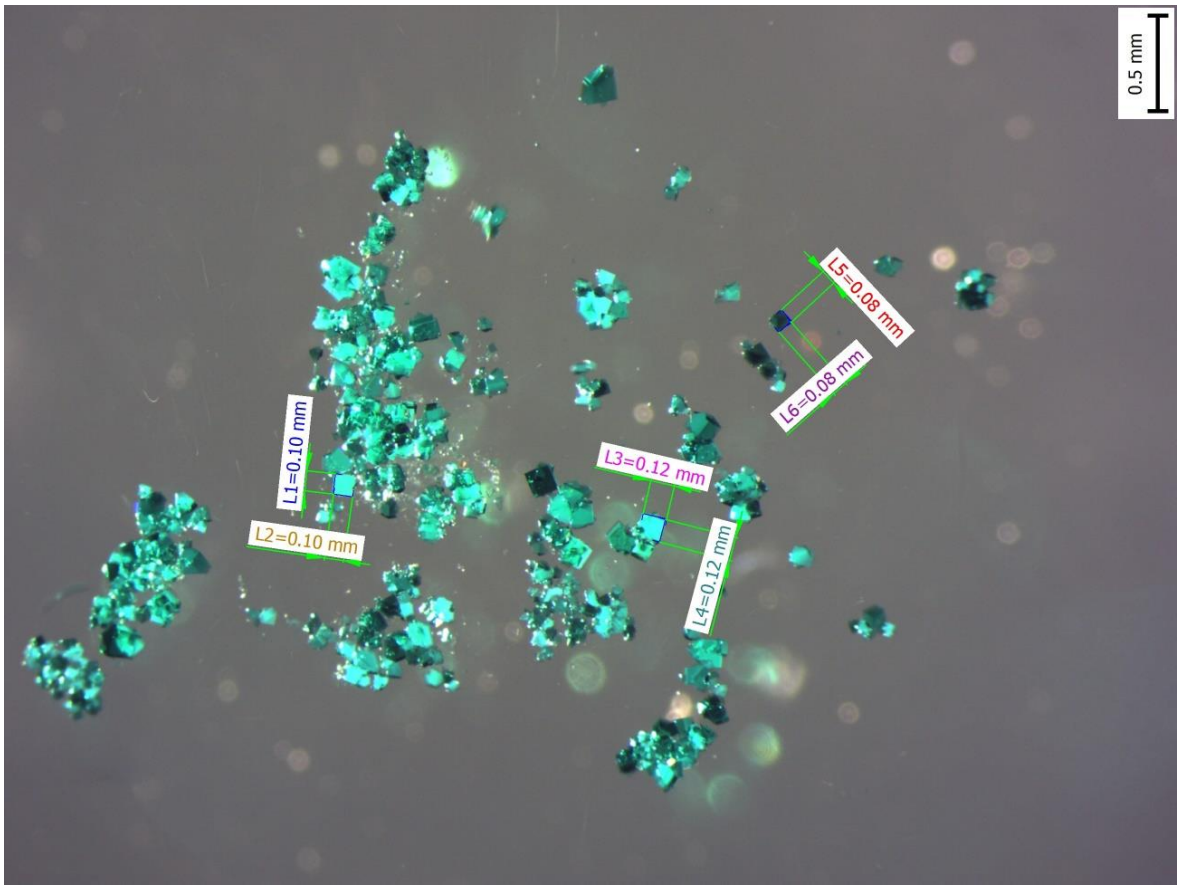

Fig. 2.21 Optical microscope image of **Cu-TTMOP** crystals showing the dimensions of several different crystals.

The structure was identified as a thienothiophene-based coordination cage, **Cu-TTMOP** (TT = thienothiophene), with the molecular formula, $[(Cu_2)_9(\mathbf{CPTT})_{18}(H_2O)_{18}] \cdot x$DMF. The structure of **Cu-TTMOP** was solved and refined in the trigonal space group $R\bar{3}c$. A Cu^{II}:H_2**CPTT** ratio of 1:1 was found to favour formation of this coordination cage. A 4:1 Cu^{II}:H_2**CPTT** ratio gave polycrystalline materials, the structure of which could not be measured. Higher temperatures (100 °C) also favoured the formation of this polycrystalline material. The crystal data and refinement results for **Cu-TTMOP** are summarised in **Table 2.5**.

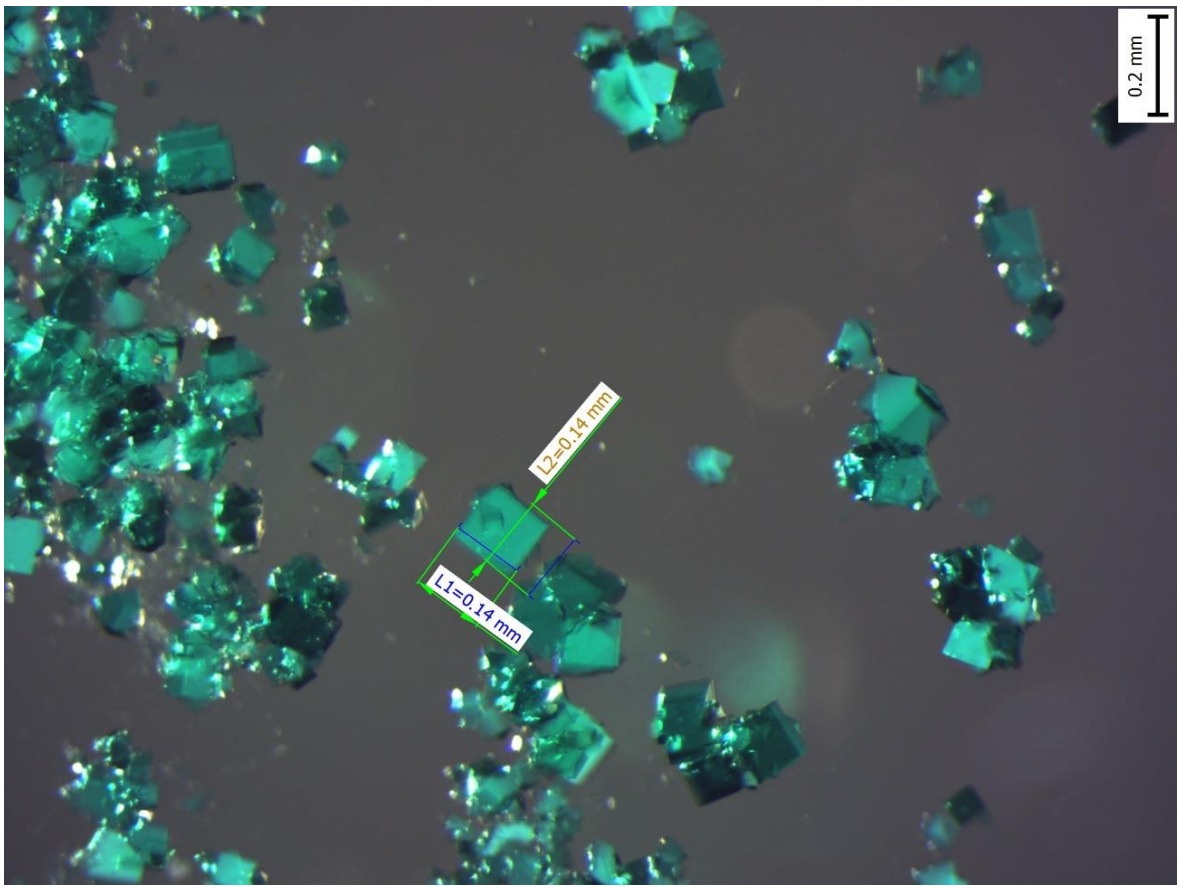

Fig. 2.22 Optical microscope image of **Cu-TTMOP** crystals showing the dimensions of several different crystals.

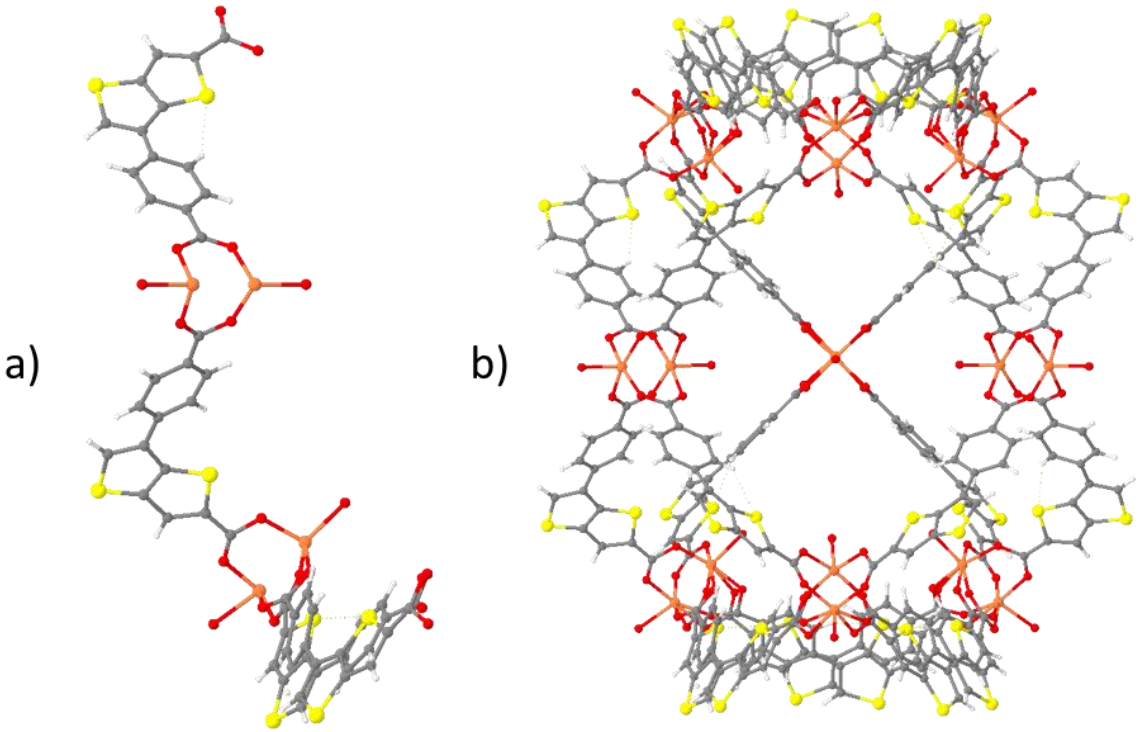

Fig. 2.23 a) Asymmetric unit of **Cu-TTMOP**, viewed along the crystallographic *b*-axis, showing flip-disorder in one of the **CPTT**$^{2-}$ linkers. **B)** Structure of **Cu-TTMOP**, viewed along the crystallographic *b*-axis, showing flip disorder in 6 of the 18 **CPTT**$^{2-}$ linkers in the structure. Atom colour scheme: Cu, orange, C, dark grey, O, red, S, yellow, H, white.

Table 2.5 Crystal data and refinement results for **Cu-TTMOP**

Compound name	**Cu-TTMOP**
Empirical formula	$C_{42}H_{24}Cu_3O_{15}S_6$
Formula weight	1151.59
Temperature (K)	215(2)
Crystal description	Blue-green block
Crystal system	Trigonal
Space group	$R\bar{3}c$
a (Å)	39.265(4)
b (Å)	39.265(4)
c (Å)	104.711(10)
α (°)	90
β (°)	90
γ (°)	120
V (Å^3)	139805(31)
Z	36
ρ_{calc} (g/cm^3)	0.492
μ (mm^{-1})	1.405
F(000)	20844.0
Radiation	CuKα (λ = 1.54178)
2θ range for data collection (°)	3.098 to 76.62
Reflections collected	91892
Independent reflections	8293 [R_{int} = 0.0616, R_{sigma} = 0.322]
Data/restraints/parameters	8293/449/652
Goodness-of-fit on F^2	1.080
R_1 [I≥2σ (I)], all	0.0825, 0.1062
wR_2 [I≥2σ (I)], all	0.2767, 0.2926
Largest diff. peak/hole (e Å^{-3})	0.35/-0.29

The asymmetric unit of **Cu-TTMOP** contains three **CPTT**$^{2-}$ linkers and four Cu^{II} ions (**Fig. 2.23**). Each of the four Cu^{II} ions is coordinated by a water molecule. One of the **CPTT**$^{2-}$ linkers in the asymmetric unit shows flip disorder across two positions (**Fig. 2.23**). In each coordination cage, flip-disorder is observed in 6 of the **CPTT**$^{2-}$ linkers in the structure, as shown in **Fig. 2.23**, however, for clarity, this disorder was omitted from figures showing the cage structure in this chapter. The ORTEP (Oak Ridge Thermal Ellipsoid Plot) of the asymmetric unit with this flip disorder omitted is shown in **Fig. 2.24**.

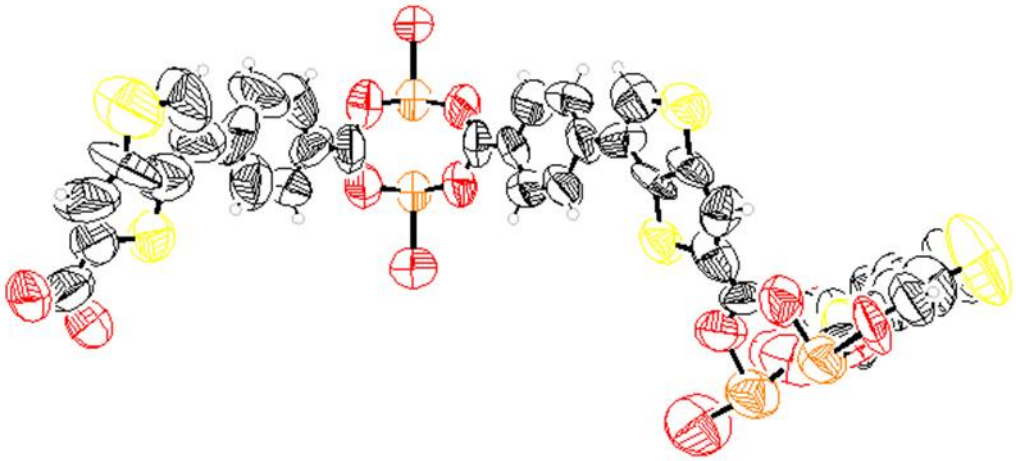

Fig. 2.24 ORTEP plot of the asymmetric unit of **Cu-TTMOP**, with flip disorder omitted, viewed along the crystallographic *b*-axis. Thermal probabilities are shown at the 50 % probability level. Atom colour scheme: Cu, orange, C, dark grey, O, red, S, yellow, H, white.

Crystals of **Cu-TTMOP** are composed of discrete coordination cages, each with the molecular formula $[(Cu_2)_9(\mathbf{CPTT})_{18}(H_2O)_{18}]\cdot x$DMF. The inorganic SBUs of **Cu-TTMOP** are dinuclear $\{Cu_2\}$ 'paddlewheel' units, which are formed by binding of the carboxylate moieties of the deprotonated $\mathbf{CPTT}^{2-}$ molecules to Cu^{II} ions. Coordinating water molecules bind to apical positions of the copper paddlewheels. Each dinuclear $\{Cu_2\}$ paddlewheel is coordinated by four $\mathbf{CPTT}^{2-}$ linkers, which bridge the $\{Cu_2\}$ paddlewheel units.

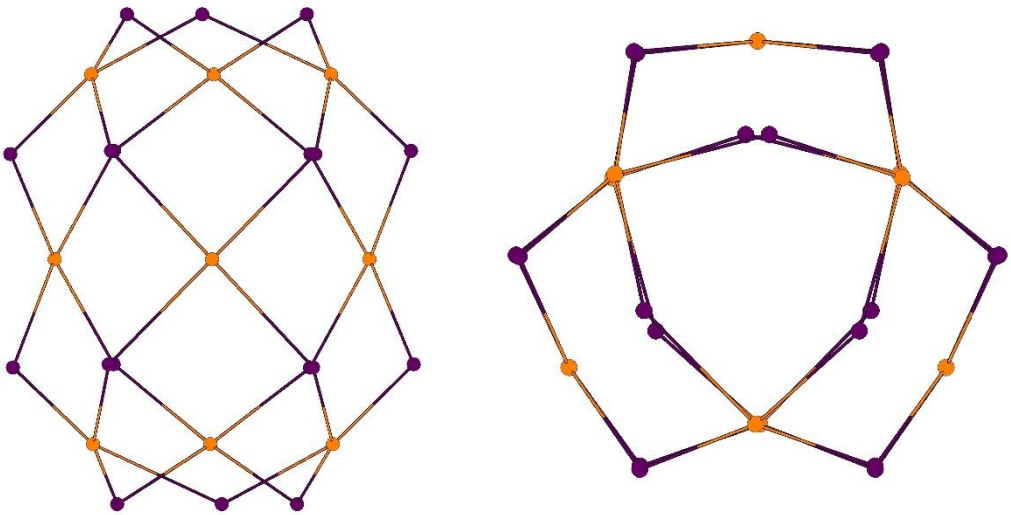

Fig. 2.25 Topological representation of **Cu-TTMOP** a) along the crystallographic *b*-axis and b) along the crystallographic *c*-axis. Colour scheme: orange, $\{Cu_2\}$ paddlewheel SBU, purple, H_2**CPTT** linker.

Topological analysis was carried out on **Cu-TTMOP** using Topos-Pro software.[75] The $\{Cu_2\}$ paddlewheel SBUs can be mapped as square vertices, and the $\mathbf{CPTT}^{2-}$ as bent 2-connected edges. The structure forms a 2,2,4,4-connected 4-nodal net with point symbol $\{6^2.8^2.10^2\}\{6^3.8^3\}_2\{6\}_6$.

When considering the dinuclear {Cu_2} paddlewheel SBUs as vertices, and the **CPTT**$^{2-}$linkers as edges, **Cu-TTMOP** can be described as a hendecahedron, with 11 faces, 9 vertices and 18 edges (**Fig. 2.27**). As previously highlighted, this molecular hendecahedron structure is extremely rare, and only one previous example of this geometry- a mixed-linker metal-organic hendecahedron, has been reported previously.[40] **Cu-TTMOP** is therefore the first example of a metal-organic hendecahedron synthesised using a single organic linker. Thus, the crystal structure of **Cu-TTMOP** was examined in detail, to understand the role of the SBUs in the construction of this fascinating structure.

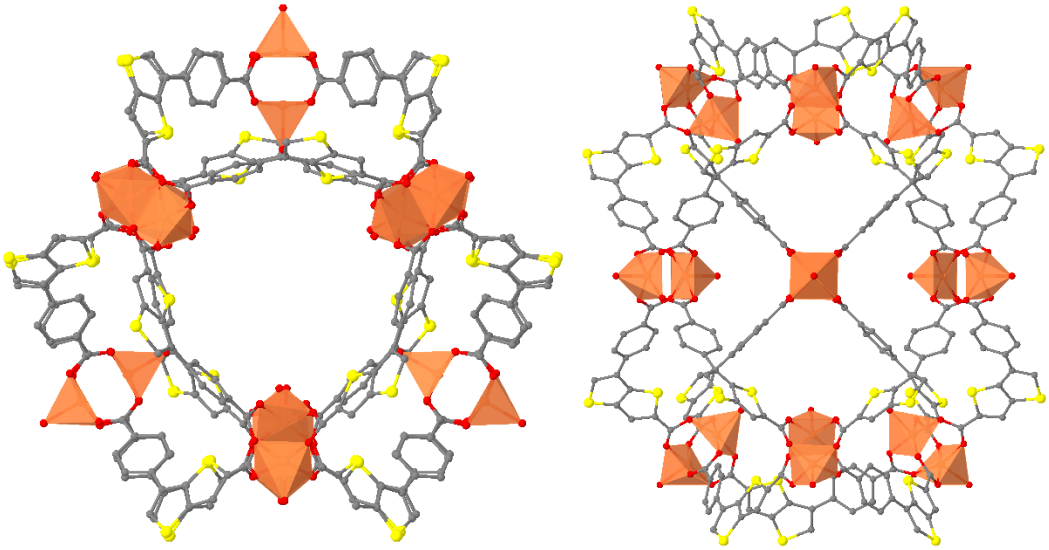

Fig. 2.26 Structure of **Cu-TTMOP** as viewed along the crystallographic a) *a*-axis and b) *b*-axis. Atom colour scheme: Cu, orange, C, dark grey, O, red, S, yellow. H-atoms are omitted for clarity.

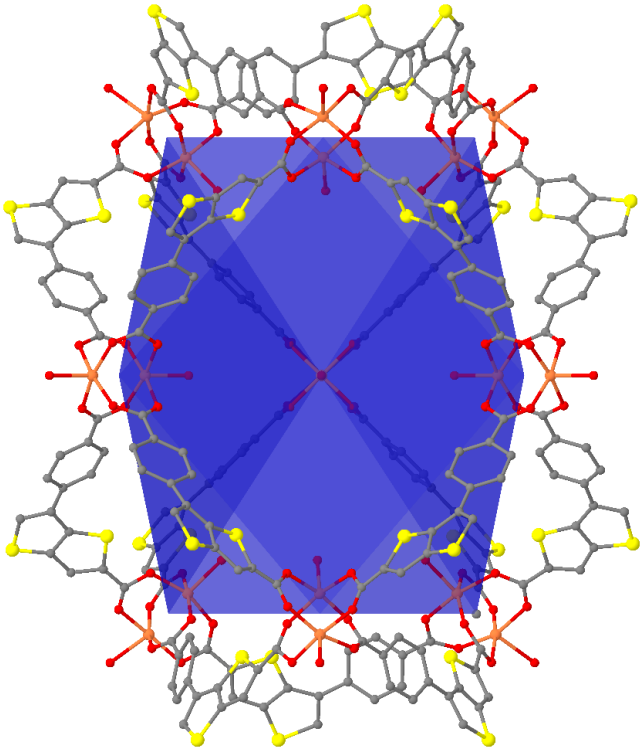

Fig. 2.27 Schematic diagram of the polyhedron when considering the metal clusters of **Cu-TTMOP** as vertices. Atom colour scheme: Cu, orange, C, dark grey, O, red, S, yellow. H-atoms are omitted for clarity.

Topologically, **Cu-TTMOP** is composed of 8 triangular windows and 3 larger quadrilateral windows. The dimensions of the sides of these windows can be measured as the distance between the centroids of the {Cu_2} paddlewheels which form the corners of the windows. The quadrilateral windows have two sides of 13.742(2) Å, and two sides of 13.835(2) Å in length. Among the remaining eight windows, two distinct types of triangular windows are present, of which two windows form equilateral triangles, and six are scalene triangles. The scalene triangular windows have sides of lengths of 13.835(2) Å, 13.742(2) Å and 13.327(3) Å, and while the sides of the two equilateral triangles measure 13.327(3) Å.

In order to determine the coordination environment of the Cu^{II} atoms in **Cu-TTMOP**, continuous shape measurements were carried out using Shape 2.1 software.[76] This software analyses the coordination environment of metal ions by calculating the distortion of that metal ion from ideal angles in known coordination environments. Smaller values indicate less deviation from ideal values for that coordination environment, with a value of zero indicating a perfect fit to a particular geometry. The results of these calculations for **Cu-TTMOP** are shown in **Table 2.6**. Continuous shape calculations confirm that the Cu1 and Cu2 atoms in **Cu-TTMOP** form square pyramidal coordination environments as expected for dinuclear {Cu_2} paddlewheels.

Table 2.6 Continuous shape measurement values for Cu^{II} atoms in **Cu-TTMOP**. The lowest values (indicating closest fit) are highlighted in bold for each metal centre.

ML_5 structure	**Pentagon**	**Vacant octahedron (Johnson square pyramid J1)**	**Trigonal bipyramid**	**Square pyramid**	**Johnson trigonal bipyramid (J12)**
Symmetry	D_{5h}	C_{4v}	D_{3h}	C_{4v}	D_{3h}
Cu1	28.302	14.633	15.290	**12.032**	17.922
Cu2	28.360	14.681	16.369	**12.2380**	20.097
Cu3	**7.797**	12.918	17.497	12.757	17.844
Cu4	12.464	**9.775**	13.724	10.710	14.356

Continuous shape measurements indicated that Cu3 and Cu4 may be described as pentagonal and vacant octahedral coordination environments respectively in **Cu-TTMOP**. This deviation from the square pyramid coordination environment, which is common for {Cu_2} dinuclear paddlewheels can be attributed to the position of the apical water molecules on Cu3 and Cu4. These coordinated water molecules show distortion from the ideal positions of a square pyramidal coordination environment. This distortion is exemplified by the O_{apical}-Cu-O angles in **Table 2.7**.

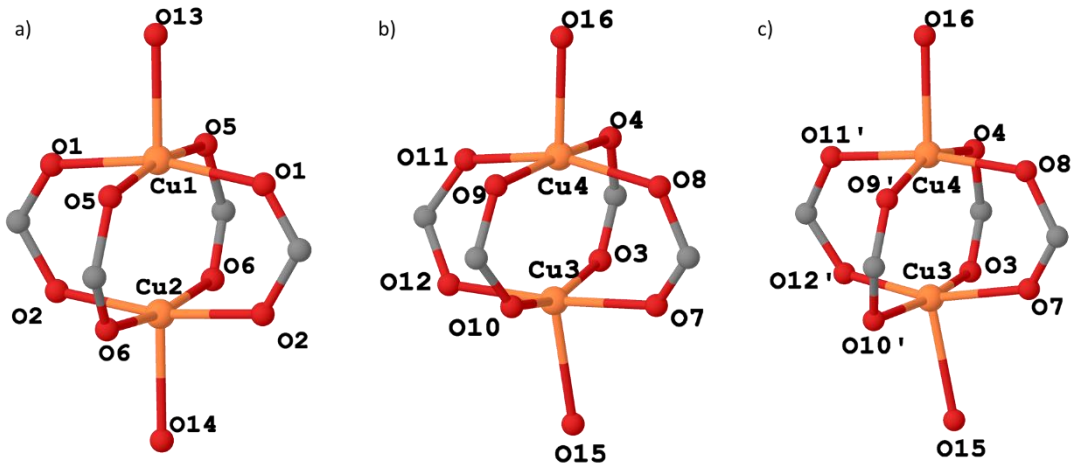

Fig. 2.28 Inorganic SBUs of **Cu-TTMOP**. Atom colour scheme: Cu, orange, C, dark grey, O, red.

In the structure of **Cu-TTMOP**, the Cu-Cu distances in the paddlewheel SBUs are 2.634(3) Å and 2.624(3) Å. The bonds between Cu^{II} and the coordinating water molecules in the apical positions have Cu-O bond lengths varying between 2.143(8) and 2.292(7) Å. The bond angles (**Table 2.7**) and bond lengths (**Table 2.8**) are in good agreement with those previously reported for dinuclear $\{Cu_2\}$ paddlewheel units.[77] The structures of the inorganic SBUs in **Cu-TTMOP** are shown in **Fig. 2.28**.

Table 2.7 Selected O-Cu-O angles (°) in **Cu-TTMOP**.

Angle	Bond Angle (°)
O1-Cu1-O5	88.5(3)
O2-Cu2-C6	88.3(4)
O3-Cu3-O12	83.7(3)
O3-Cu3-O12’	78.2(7)
O4-Cu4-O11	84.3(3)
O4-Cu4-O11’	94(3)

Table 2.8 Bond lengths (Å) in **Cu-TTMOP**.

Bond	Distance	Bond Length (Å)
Cu1-O	Cu1-O1	1.955(8)
	Cu1-O5	1.977(9)
	Cu1-O13	2.145(9)
Cu2-O	Cu2-O2	1.954(9)
	Cu2-O6	1.941(10)
	Cu2-O14	2.163(10)
Cu3-O	Cu3-O3	1.901(12)
	Cu3-O7	2.000(11)
	Cu3-O10	1.930(18)
	Cu3-O10’	1.928(18)
	Cu3-O12	1.862(15)
	Cu3-O12’	1.883(15)
	Cu3-O15	2.293(8)
Cu4-O	Cu4-O4	1.942(10)
	Cu4-O8	1.988(11)
	Cu4-O9	1.946(18)
	Cu-O9’	1.975(18)
	Cu4-O11	1.875(16)
	Cu4-O11’	1.871(16)
	Cu4-O16	2.183(10)

According to studies by Yaghi, O’Keeffe and co-workers, coordination cages can be characterised by two important angles.[1] The first angle, η, is the angle between the links extending from the SBU. Examples illustrating this angle, η, for previously reported SBUs are shown in **Fig. 2.29**. For example, in a $\{Cu_2\}$ paddlewheel SBU, $\eta = 90°$.

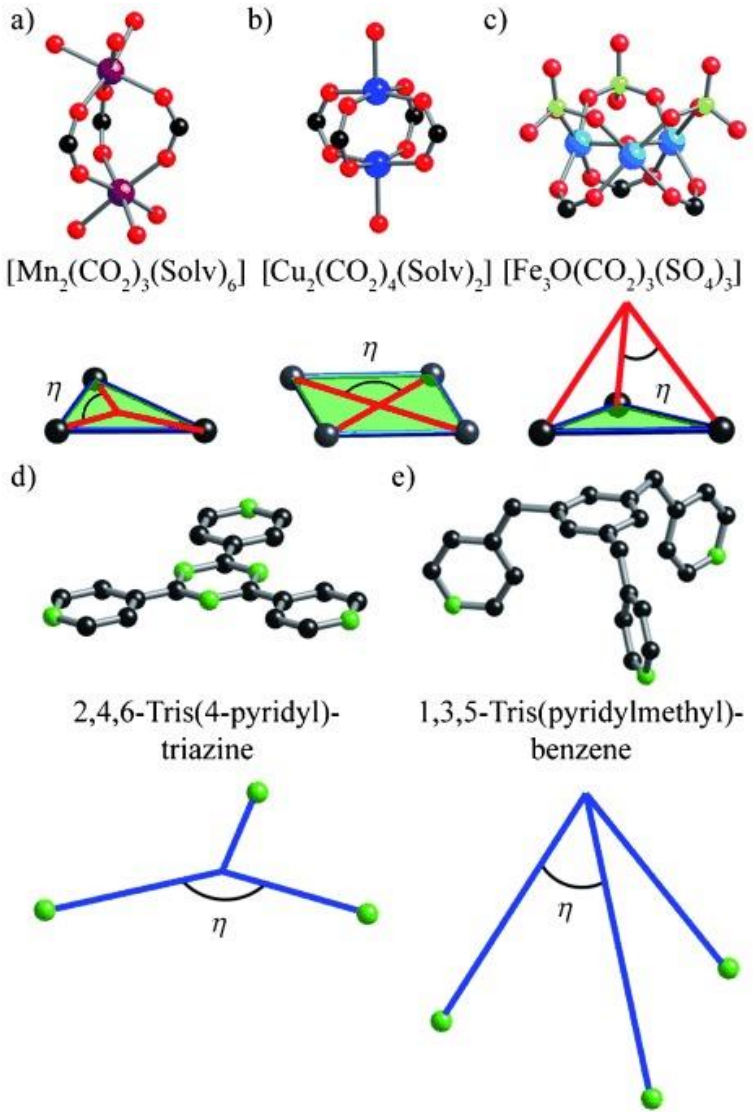

Fig. 2.29 Examples of SBUs and their corresponding angles η. Figure adapted from reference.[1]

The second angle, θ, is the bend angle between the links of a ditopic linker. Examples of this angle in previously reported linkers are shown in **Fig. 2.29**. For example, for the linker 1,3-benzene-dicarboxylate, the bend angle θ = 120°.

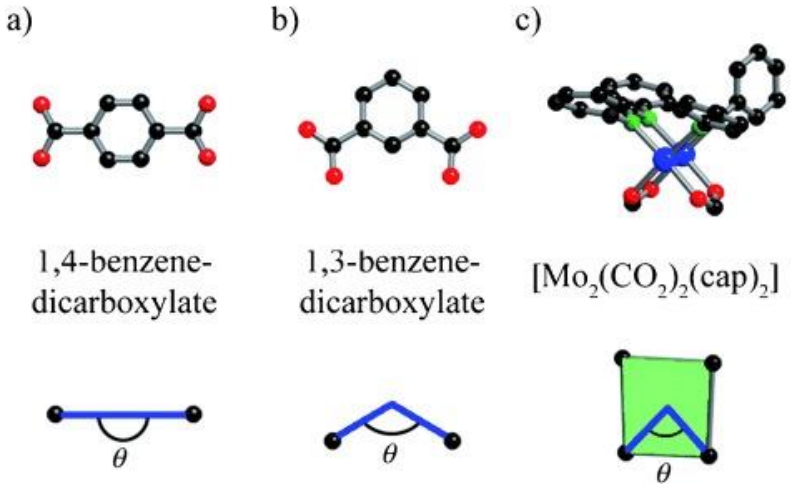

Fig. 2.30 Examples of linkers, and their corresponding angles θ. Figure adapted from reference.[1]

In the case of H_2**CPTT**, additional angles are needed to describe the molecule. In addition to featuring a bend in the structure, molecules of H_2**CPTT** are also non-planar. Therefore, H_2**CPTT** can be described using a fold angle of the carboxylates towards one another, and a twist angle between the planes of the carboxylate planes relative to one another. These additional angles have been described by Yaghi and co-workers (**Fig. 2.31**),[78] and studies have been carried out to understand how angles such as bend and twist angles in linkers influence the structures of the resulting MOFs[79] and MOPs.[1,7]

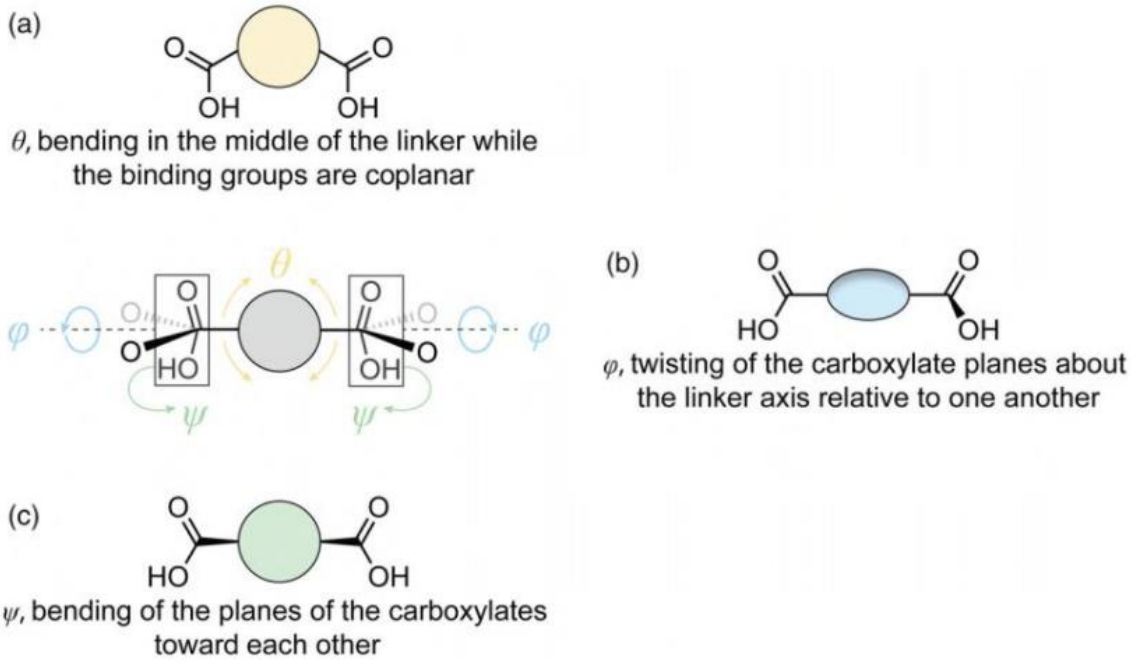

Fig. 2.31 Schematic diagram showing the different angles on a ditopic linker. a) The bend angle θ between the two binding groups b) the twist angle φ between non coplanar binding groups and c) the fold angle Ψ between two binding groups that bend towards one another. Figure adapted from reference.[78]

To estimate the angle θ, the angle between the two C-C bonds extending from the carboxylate moieties of **CPTT**$^{2-}$ was measured using the Olex2 software package.[80] The asymmetric unit of **Cu-TTMOP** contains three **CPTT**$^{2-}$ linkers, each of which features a slightly different θ angle. The θ angles measured were 107.9(15)°, 121.2(15)°, and for the third linker, 109(3)° and 100(4)°. Two θ angles were measured for the third linker, due to the flip disorder observed for this **CPTT**$^{2-}$ linker. For comparison, the θ angle between the two carboxylate bonds in the crystal structure of the free linker, H_2**CPTT** is 102.3(3)°. The larger bend angles for **CPTT**$^{2-}$ linkers in **Cu-TTMOP** highlight that these linkers are restricted in their positions by the rigidity of the cage structure.

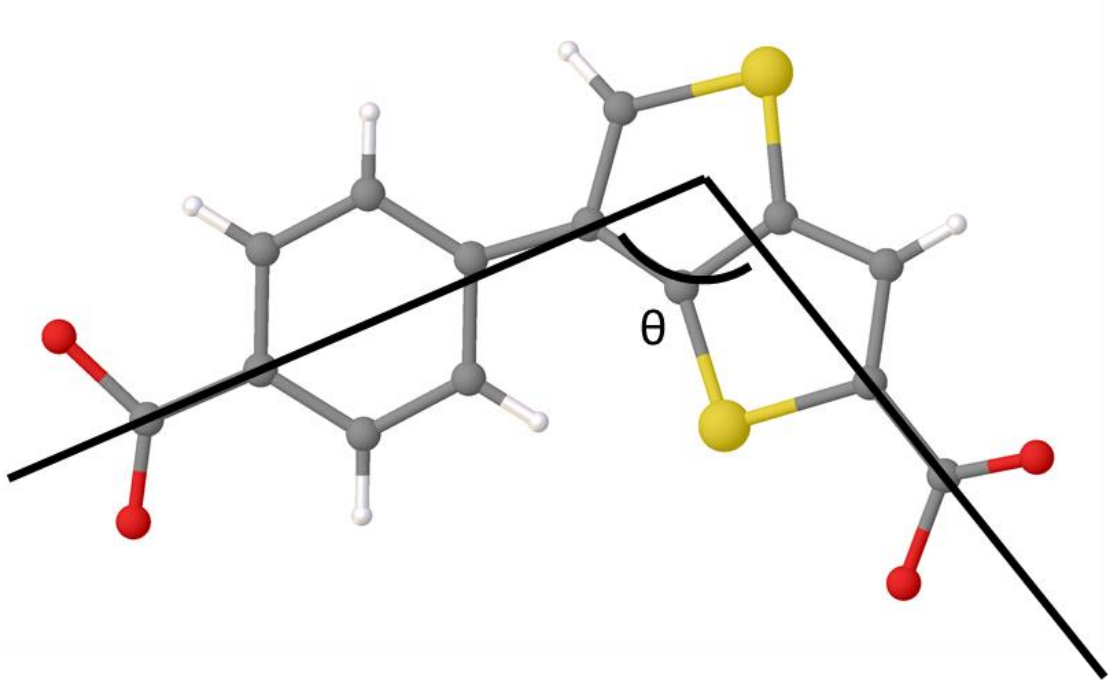

Fig. 2.32 Asymmetric unit of **Cu-TTMOP,** showing the angle θ between the C-C bonds extending from the carboxylate moieties of **CPTT**$^{2-}$ linkers. Atom colour scheme: C, dark grey, O, red, S, yellow, H, white.

In the crystal structure of **Cu-TTMOP**, the angles φ and Ψ can be calculated as the twist (dihedral angle) and fold angles respectively between the planes of the carboxylate binding groups in **CPTT**$^{2-}$ linkers, using Olex2 software.[80] Each of the three linkers in the asymmetric unit of **Cu-TTMOP** features slightly different Ψ and φ angles, indicating nonplanarity in the **CPTT**$^{2-}$ linkers. These angles are similar in both the **CPTT**$^{2-}$ linkers in **Cu-TTMOP** and the free linker H_2**CPTT**. The θ, Ψ and φ angles, in the crystal structure of H_2**CPTT** and the **CPTT**$^{2-}$ linker in **Cu-TTMOP** are summarised in **Table 2.9**. Larger errors were present on the calculations of the Ψ and φ angles in linker 3. These larger errors are as a result of difficulties modelling the disorder in this linker. Due to the low certainty in these values, these angles were omitted from **Table 2.9**.

Table 2.9 Bend (θ), fold (Ψ) and twist (dihedral angle, φ) angles in H_2**CPTT** and **Cu-TTMOP.**

Linker	**θ**	**Ψ**	**φ**
H_2**CPTT**	102.3(3)°	17.6(7)°	7.0(5)°
Cu-TTMOP linker 1 (C1)	121.2(15)°	16(3)°	12(2)°
Cu-TTMOP linker 2 (C15)	107.9(15)°	18(2)°	9.9(19)°
Cu-TTMOP linker 3 (C29)	100(4)°	-	-
Cu-TTMOP linker 3' (C29')	109(3)°	-	-

The highly asymmetric, bent and nonplanar structure of H_2**CPTT** makes straightforward comparison with other linkers in coordination cages difficult. However, it is clear that this linker possesses a unique structure that has provided a previously inaccessible synthetic pathway to a hendecahedron geometry, forming a novel type of coordination cage.

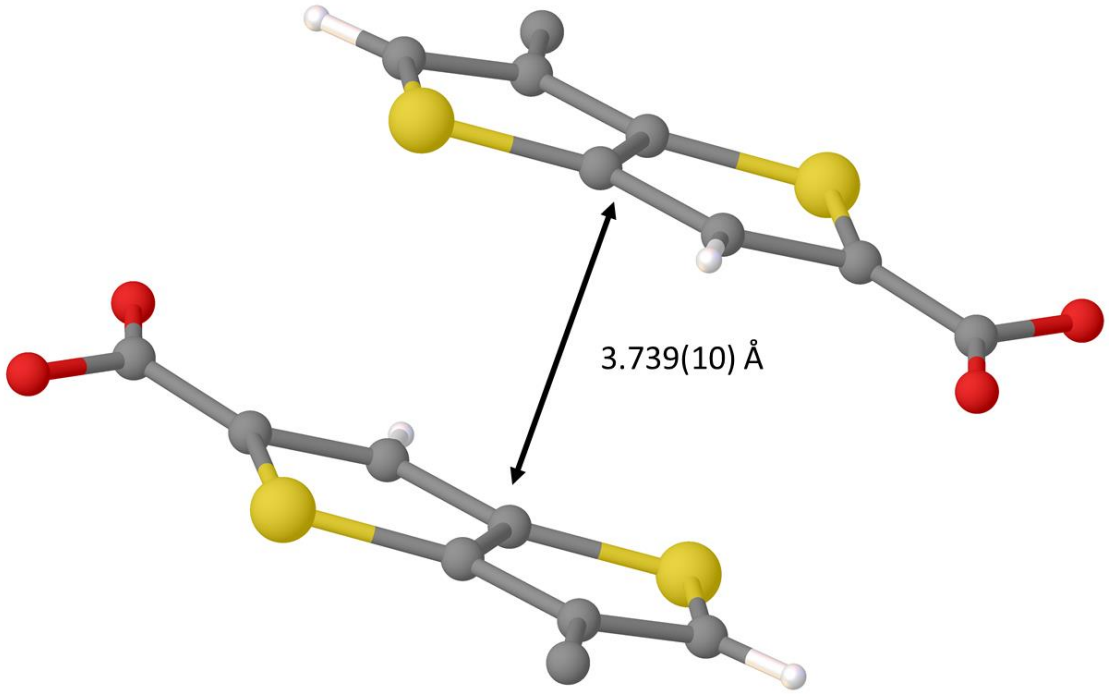

Fig. 2.33 Schematic diagram showing π-π interactions between thienothiophene ring systems on adjacent **Cu-TTMOP** molecules. Atom colour scheme: C, dark grey, O, red, S, yellow, H, white.

In crystals of **Cu-TTMOP**, π-π stacking interactions can be observed through the thienothiophene moiety of **CPTT**$^{2-}$ linkers on adjacent **Cu-TTMOP** molecules. The distance between the planes of the thienothiophene rings on adjacent cages is 3.739(10) Å (**Fig. 2.33**). This π-π interaction between adjacent **Cu-TTMOP** molecules influences the molecular packing to form an open framework structure (**Fig. 2.34**). The packing gives rise to channels which extend parallel to the crystallographic *c*-axis. The structure has a void volume of 77.1% of the unit cell volume, as calculated by PLATON.[81] The volume of the largest spherical void in the structure is 1987.80 Å^3, and this void has a radius of 7.80 Å. The PLATON squeeze routine was applied for the structure refinement to account for disordered solvent molecules in the structure.[82]

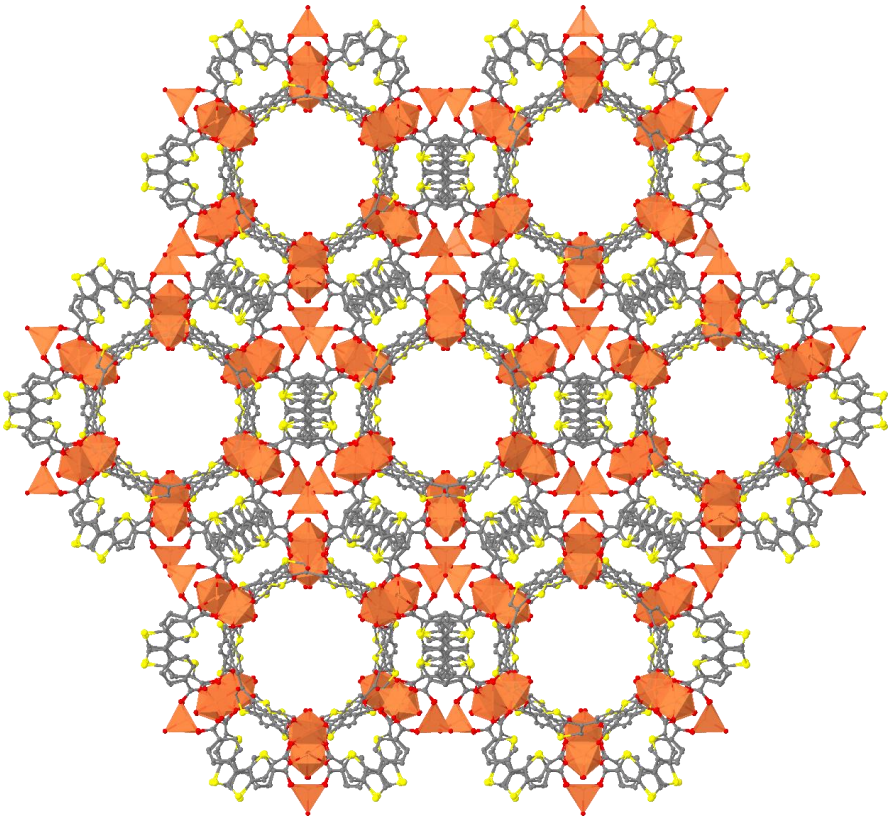

Fig. 2.34 Packing structure of **Cu-TTMOP** with view in the direction of the crystallographic *c*-axis. Atom colour scheme: Cu, orange, C, dark grey, O, red, S, yellow. H-atoms are omitted for clarity.

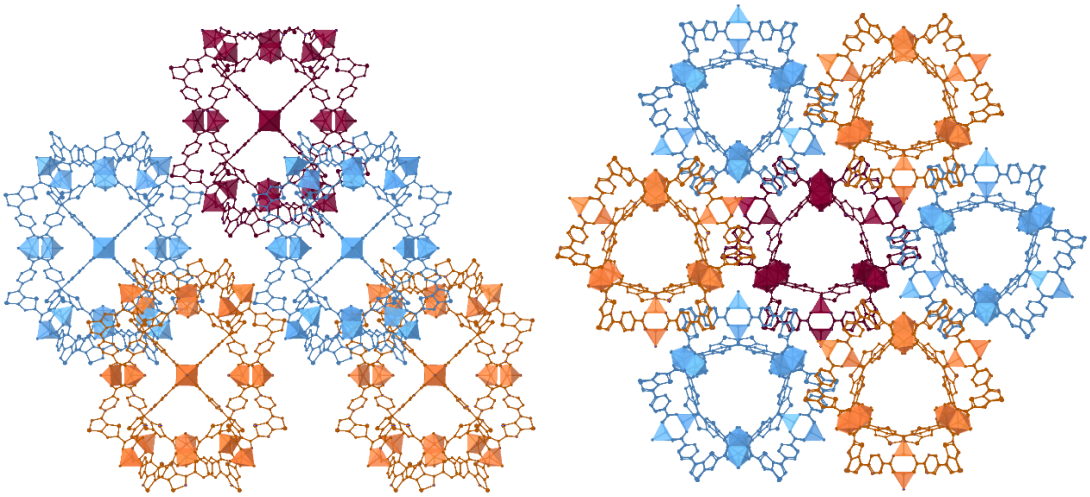

Fig. 2.35 Packing diagram of **Cu-TTMOP** viewed along the crystallographic **a)** *a*-axis and **b)** *c*-axis, showing cages in different layers in different colours. H-atoms are omitted for clarity.

In crystals of **Cu-TTMOP**, individual molecules stack in layers, with an ABC packing arrangement in the [0 0 1] direction. This leads to a face-centred cubic packing arrangement in the crystals (**Fig. 2.35**). Individual molecules of **Cu-TTMOP** pack along 3-fold helical screw axes extending parallel to the crystallographic *c*-axis (**Fig. 2.36**).

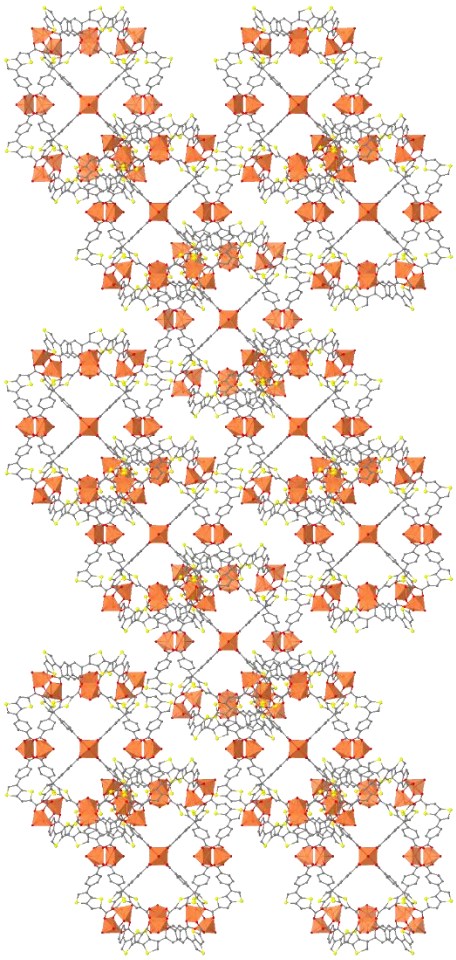

Fig. 2.36 Packing diagram of **Cu-TTMOP** molecules. Atom colour scheme: Cu, orange, C, dark grey, O, red, S, yellow. H-atoms are omitted for clarity.

To confirm that the Cu metal centres in **Cu-TTMOP** are present in the +II oxidation state, BVS calculations were used. The BVS method can be used to estimate the oxidation state of a metal ion, using the metal-ligand bond distances. The expressions for this relationship are:[83]

$$BV_j = e^{(R_0 - R)/0.37}$$

$$Oxidation\ state\ estimate = \sum_j BV_j$$

Where R is the experimental bond length, R_0 is an empirical parameter associated with the metal in a given oxidation state, and BV_j is the bond valence value for the j^{th} bonded atom to the metal. The R_0 value for Cu^{II}-O bonds is 1.679.[84] In carrying out BVS analysis for **Cu-TTMOP**, only one part of the disordered **CPTT**$^{2-}$ linker in the structure was taken into consideration for the Cu atoms connected to the disordered linker (Cu3 and Cu4). The Cu-O distances used in these calculations are shown in **Table 2.8**. The distances used in the case of the disordered linker were Cu3-O10', Cu3-

O11', Cu4-O9', Cu4-O11'. Good agreement with the metal oxidation state estimated by BVS calculations are values within the range of ± 0.25 units from the metal oxidation state. As all the values calculated for **Cu-TTMOP** are within the range 2 ± 0.25, BVS calculations confirm that Cu atoms in **Cu-TTMOP** are present in the +II oxidation state (**Table 2.10**) as expected.

Table 2.10 BVS analysis of Cu atoms in **Cu-TTMOP**.

Metal ion	R_0 (Å)	BVS	Oxidation state
Cu1	1.679	2.13	+II
Cu2	1.679	2.21	+II
Cu3	1.679	2.25	+II
Cu4	1.679	2.23	+II

Following the success in accessing a molecule with a rare and fascinating structure using the linker H_2**CPTT**, attempts were made to react H_2**CPTT** with several other metal salts, including Zr^{IV}, Zn^{II}, Cd^{II}, Co^{II} and Eu^{III} salts. However, these reactions were unsuccessful, yielding either insoluble amorphous materials, or crystals of poor quality, which were not suitable for single crystal XRD analysis. In the case of the reaction between Zn^{II} salts and H_2**CPTT**, several attempts were made at synthesising single crystals, however, the structure could not be obtained due to a combination of poor crystal diffraction and high levels of disorder in the structure.

2.4 Characterisation of hendecahedron coordination cage

2.4.1 Powder X-ray diffraction (PXRD) studies of Cu-TTMOP

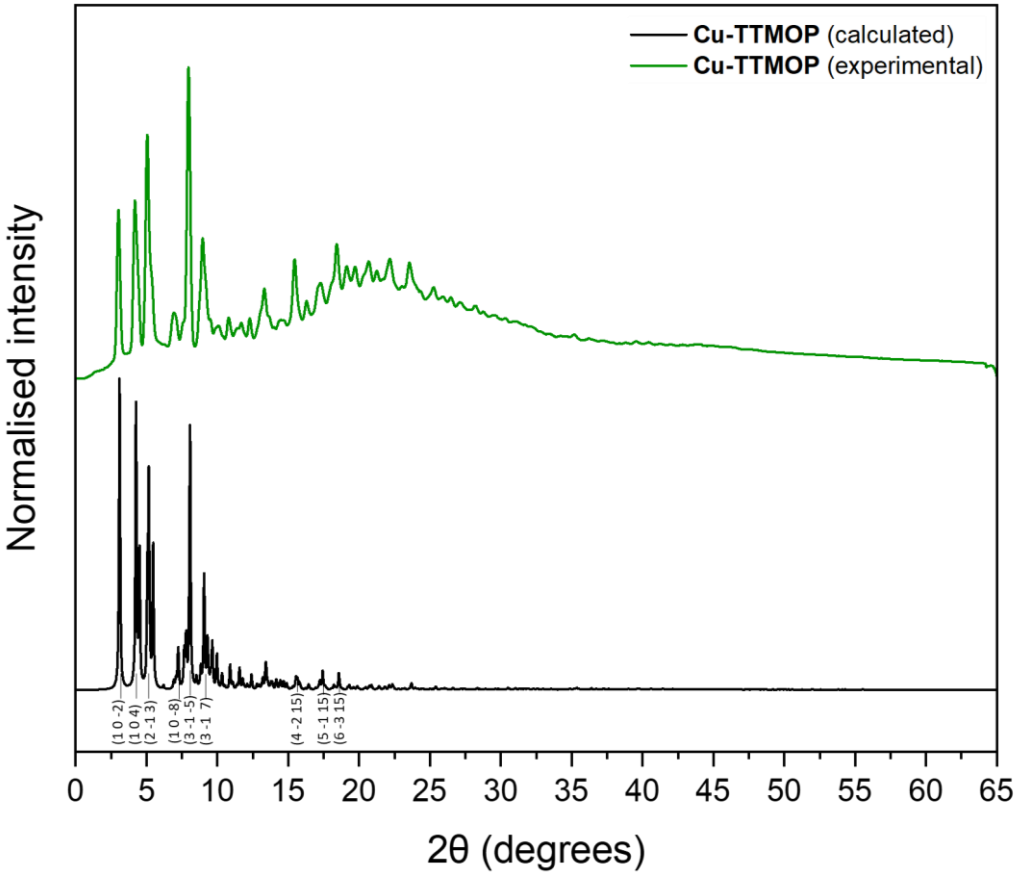

Fig. 2.37 Calculated (black) and experimental (green) PXRD pattern of **Cu-TTMOP**, showing indexed diffraction peaks. The experimental powder pattern was recorded in a polyamide capillary.

The phase-purity of bulk **Cu-TTMOP** was confirmed using PXRD measurements. Crystals of **Cu-TTMOP** desolvate rapidly upon removal from solutions, as will be demonstrated later in this chapter by thermogravimetric analysis (TGA). Therefore, PXRD measurements were carried out in polyamide capillaries. The PXRD patterns of the sample as synthesised is in good agreement with the pattern calculated from the single crystal XRD data, indicating that the **Cu-TTMOP** sample is phase pure (**Fig. 2.37**). However, preferential orientation was observed, and therefore the experimental powder pattern (prior to background correction) was fitted using the Le Bail method[85] within the Expo2014 software package (**Fig. 2.38**).[86] The final *R* values obtained were R_p = 2.116 and R_{wp} = 3.498, which indicate excellent agreement between the experimental and calculated patterns.

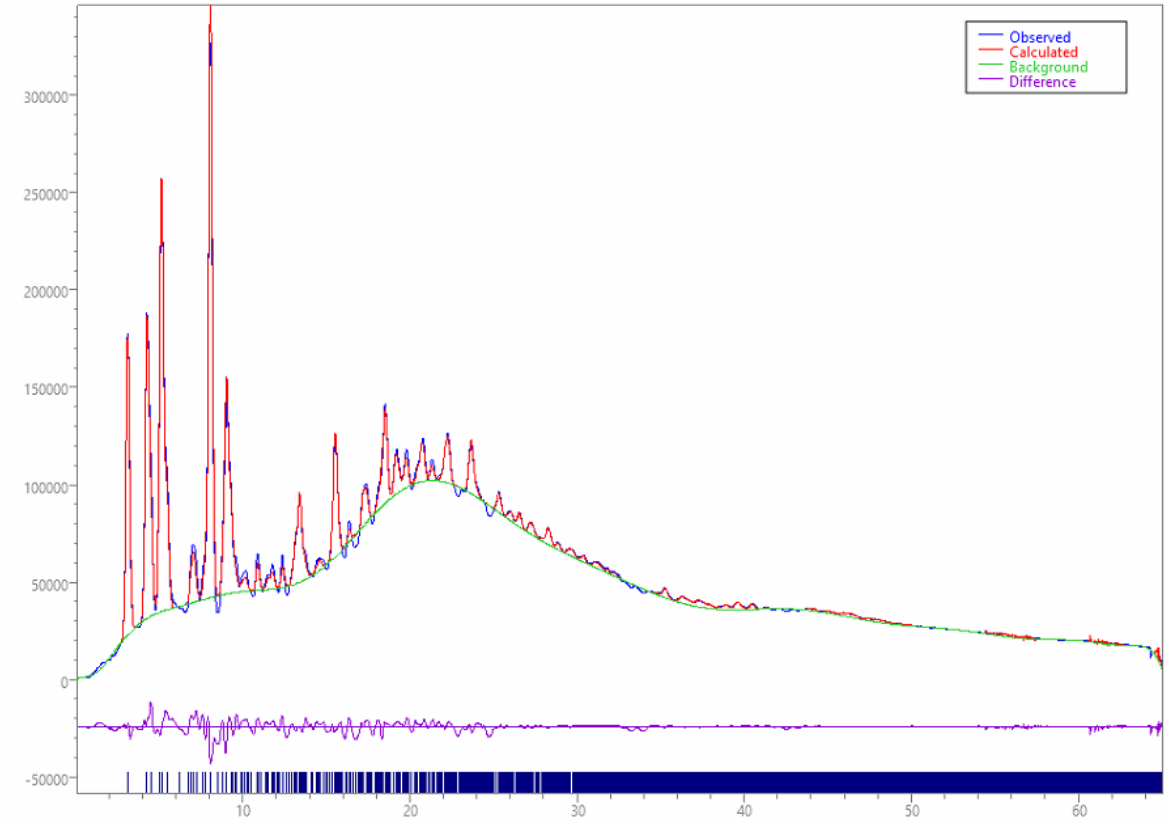

Fig. 2.38 Le Bail fits of PXRD patterns of **Cu-TTMOP**, showing observed (blue) and calculated (red) data, and their difference (violet). The background is shown in green, and the dark blue lines indicate the positions of reflections predicted from the unit cell. The experimental powder pattern was measured in a polyamide capillary containing the mother liquor.

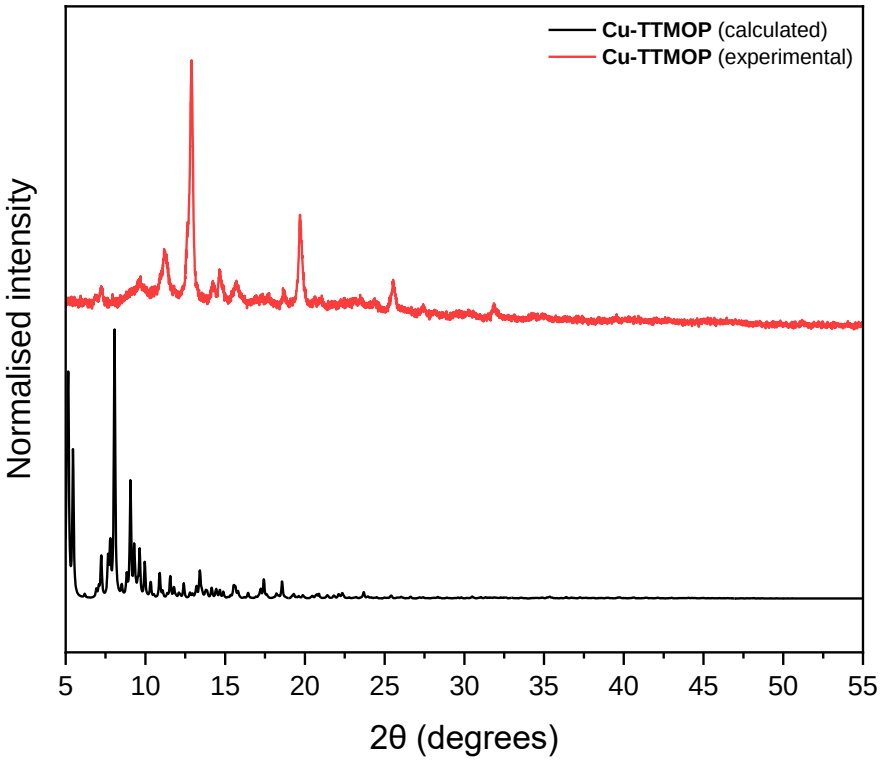

Fig. 2.39 Calculated (black) and experimental (red) PXRD pattern of **Cu-TTMOP**. The experimental PXRD pattern was recorded in air at room temperature.

The stability of the 3D structure of **Cu-TTMOP** in air at room temperature was tested by removing crystals of **Cu-TTMOP** from DMF solution, drying them in air, and measuring the PXRD pattern immediately (**Fig. 2.39**). The sample retained crystallinity for the duration of the measurement. Comparison of the experimental and calculated PXRD patterns was difficult due to thermal effects and preferential orientation. Fitting the pattern using the Le Bail method, as above, indicated that good agreement was present between the pattern calculated from the single crystal data and the experimental PXRD pattern (**Fig. 2.40**). The final *R* values obtained were $R_p = 4.008$ and $R_{wp} = 5.153$.

These results indicate that **Cu-TTMOP** forms as a phase pure sample, and the sample can be handled in air at room temperature for short periods of time without destruction of the structure of the material.

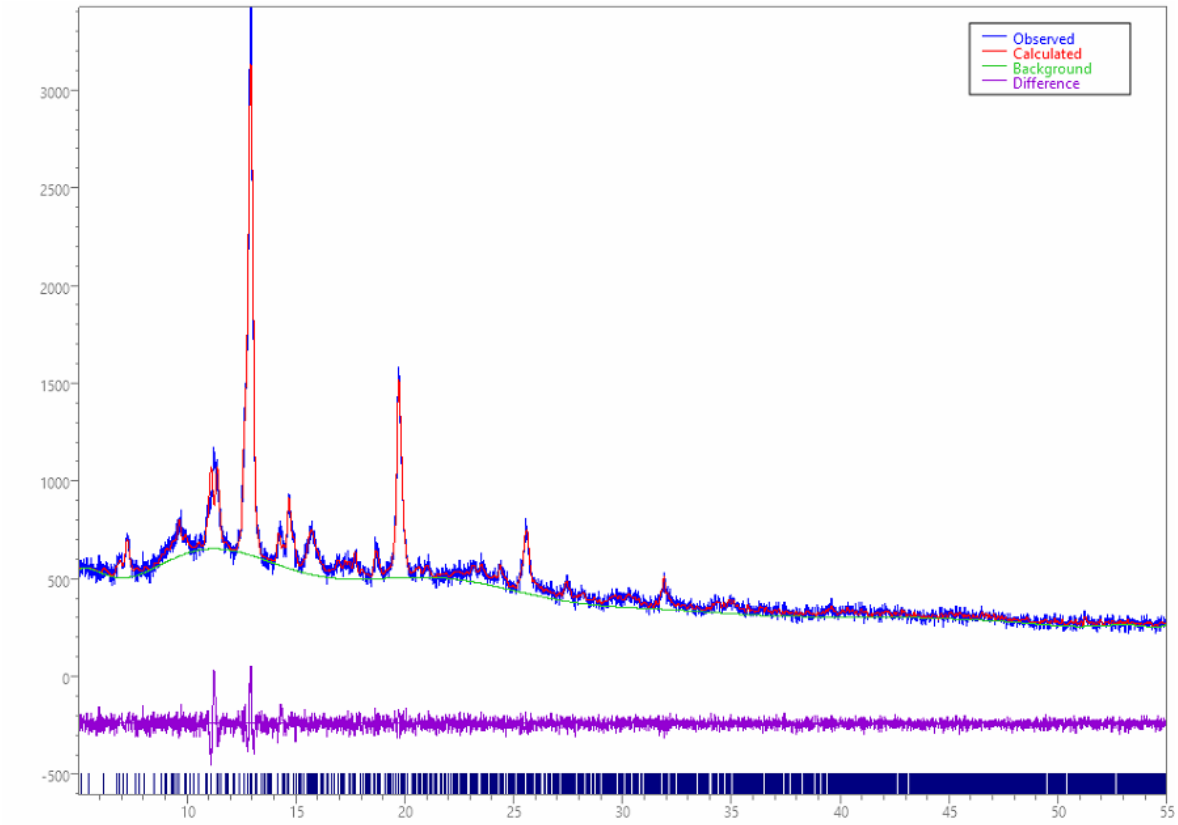

Fig. 2.40 Le Bail fits of PXRD patterns of **Cu-TTMOP**, showing observed (blue) and calculated (red) data, and their difference (violet). The background is shown in green, and the dark blue lines indicate the positions of reflections predicted from the unit cell. Experimental PXRD pattern was recorded in air at room temperature.

2.4.2 Thermogravimetric analysis (TGA) of Cu-TTMOP

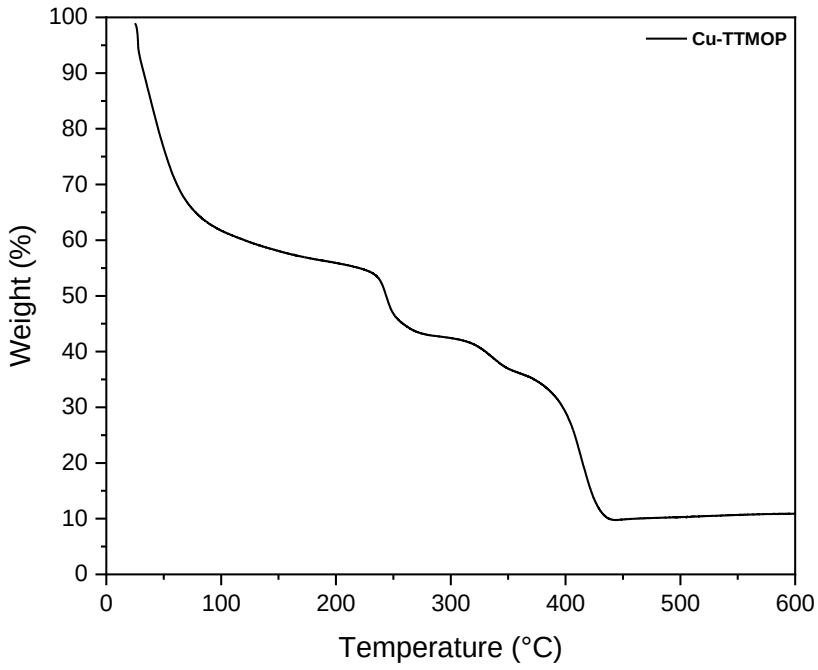

Fig. 2.41 TGA of Cu-TTMOP crystals carried out under air gas flow (20 mL min^{-1}).

The thermal stability of a crystalline sample of **Cu-TTMOP** was investigated using TGA measurements. The sample was prepared by immersing a freshly synthesised sample of **Cu-TTMOP** in DMF for 24 hours, then removing the crystals from solution, and removing excess solvent by placing the crystals on filter paper, before adding the sample to the TGA crucible. The measurement was carried out under air gas flow (20 mL min^{-1}), in the temperature range of 30 to 600 °C. The heating rate was 5 °C per minute. The sample was initially held at an isothermal temperature of 30 °C for 1 minute. Crystals of the **Cu-TTMOP** immediately began to desolvate when removed from DMF solution. The TGA of **Cu-TTMOP** is characterised by three thermogravimetric steps. The first thermogravimetric step is seen between 30 and 100 °C. This step is accompanied by a mass loss of ca. 40%, and can be attributed to loss of solvent guest molecules within the pores of **Cu-TTMOP**. Between 235 and 260 °C a mass loss of ca. 8% occurs, corresponding to loss of coordinated solvent molecules from the structure. Between approximately 320 and 435 °C, the decomposition of the organic linker is observed over two steps, with an overall mass loss of ca. 31%. The remaining mass is expected to stem from the formation of copper oxide from the dinuclear {Cu_2} paddlewheel SBUs of **Cu-TTMOP**. The large loss of mass that can be attributed to the loss of uncoordinated solvent molecules in the pores of the **Cu-TTMOP** structure and is consistent with the open-framework structure and crystallographic analysis using PLATON.[81]

2.4.3 Fourier-Transform Infrared (FTIR) spectroscopy of Cu-TTMOP

FTIR was used to characterise **Cu-TTMOP** (**Fig. 2.42**), and the spectrum obtained was compared to the FTIR spectrum of the linker, H_2**CPTT** (**Fig. 2.20**). The FTIR spectrum of **Cu-TTMOP** featured signals corresponding to the H_2**CPTT** linker, the coordination modes of the carboxylate moieties to the Cu^{II} ions, as well as DMF solvent molecules. Clear similarities were observed between the FTIR spectra of H_2**CPTT** and **Cu-TTMOP**. Stretching of the C-S-C bonds can be assigned to the vibration at 765 cm^{-1}. The signals at 1507 cm^{-1} and 1655 cm^{-1} stem from the C=O symmetric and asymmetric stretching modes respectively. The broad band between ~3700 and ~2700 cm^{-1} arises from C-H stretching vibrations and the O-H stretching of solvent water and DMF molecules. A signal associated with constitutional DMF solvent molecules in the structure can also be observed at 1606 cm^{-1}, corresponding to the asymmetric C=O stretching vibration. These DMF molecules are present in the pores of the structure of **Cu-TTMOP**.

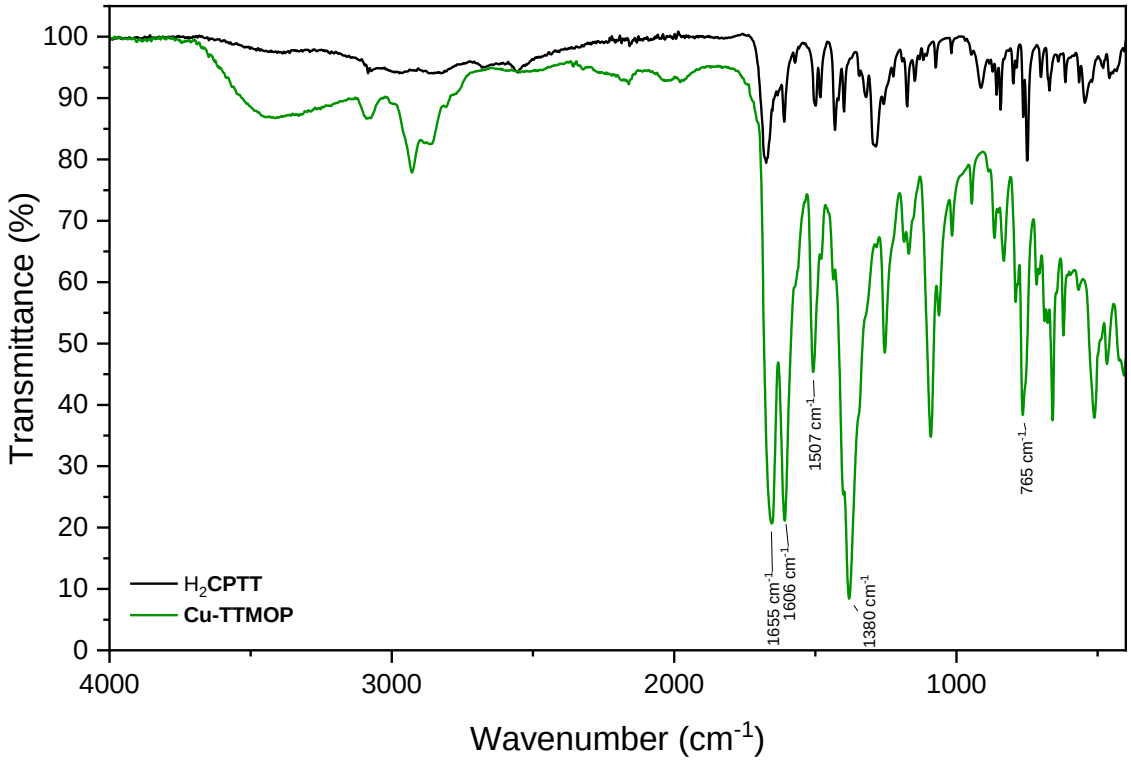

Fig. 2.42 FTIR spectra of H_2**CPTTT** and **Cu-TTMOP**, with characteristic vibrational bands labelled.

In molecules of **Cu-TTMOP**, the carboxylate moieties of H_2**CPTT** bind to the Cu^{II} ions in a *syn,syn*-η^1:η^1:μ^2 binding mode. The symmetric and asymmetric carboxylate stretches appear at 1507 and 1655 cm^{-1} respectively, allowing $\Delta_{asy\text{-}sym}$ to be calculated as 148 cm^{-1}. Deacon and Phillips have reported relationships between $\Delta_{asy\text{-}sym}$ and the carboxylate binding mode.[87] The value of $\Delta_{asy\text{-}sym}$ in **Cu-TTMOP** is in good agreement with values reported for bridging bidentate carboxylate ligands that adopt a *syn-syn* configuration.

2.4.4 Scanning electron microscopy (SEM) and energy dispersive X-ray (EDX) spectroscopy of Cu-TTMOP

Crystals of **Cu-TTMOP** were soaked in DMF, dried in air and analysed using scanning electron microscopy (SEM). The SEM images show that **Cu-TTMOP** forms as square-shaped crystals (**Fig. 2.43**).

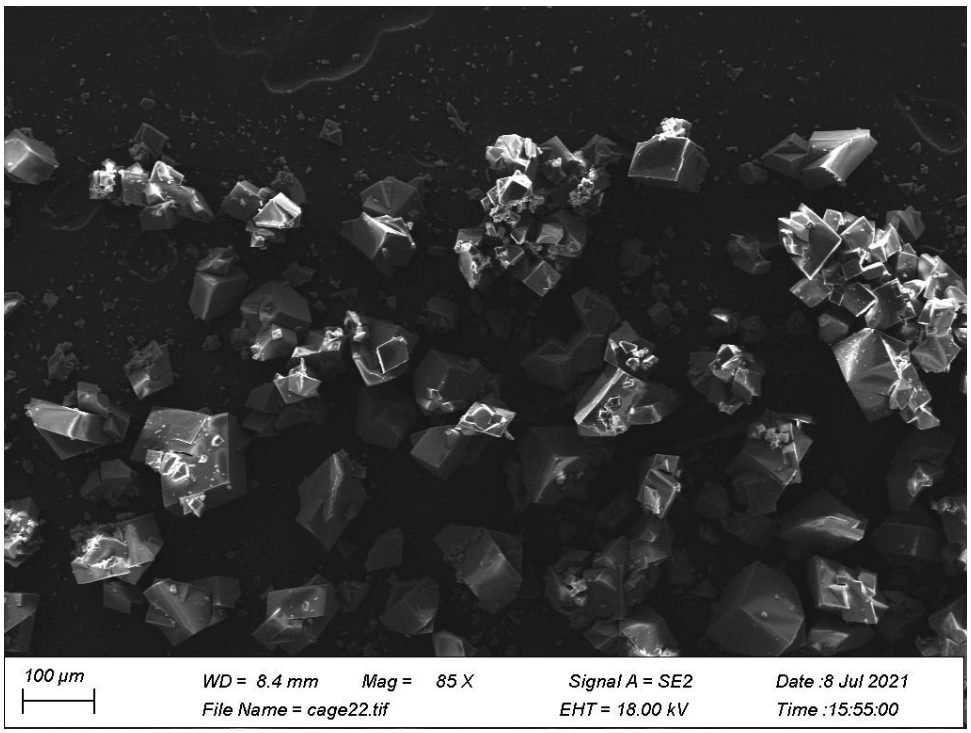

Fig. 2.43 SEM images of **Cu-TTMOP** on a carbon tab.

Table 2.11 Expected and experimentally observed atomic ratios for **Cu-TTMOP**. The expected atomic ratios were calculated from the molecular formula of **Cu-TTMOP**, $[(Cu_2)_9(\mathbf{CPTT})_{18}(H_2O)_{18}]\cdot x$DMF.

Compound	Expected ratio Cu:S	Observed ratio Cu:S from EDX spectrum
Cu-TTMOP	1:2	1:2:14

Energy dispersive X-ray spectroscopy (EDX) of **Cu-TTMOP** crystals on a carbon tab was used to determine the elemental composition of the crystals. EDX analysis confirmed the presence of copper and sulfur in the expected ratios (**Table 2.11**).

2.5 Further studies of Cu-TTMOP

2.5.1 Pore size distribution and surface area of Cu-TTMOP

Due the open framework structure of the **Cu-TTMOP**, the potential of this material for gas sorption purposes was explored, however, the poor stability of the framework structure of **Cu-TTMOP** hindered its use for these purposes. No significant uptake of the gas was observed after activation of **Cu-TTMOP**, suggesting collapse of the open 3D structure under the conditions used for activation. However, theoretical calculations could be used to gain insight into the surface area of the structure.

Using the PoreBlazer software package,[88] theoretical calculations of the pore size distribution and solvent accessible surface area could be obtained for **Cu-TTMOP**. The calculated pore size distribution can be seen in **Fig. 2.44**, and shows that the coordination cage possesses defined pores. The calculations indicated that if the constitutional solvent molecules in the pores of the compound were removed, the structure would have a He pore volume of 1.623 cm^3/g, a maximum pore diameter of 15.22 Å and limiting pore diameter of 9.70 Å. The accessible surface area of **Cu-TTMOP** was calculated as 4101.04 m^2/g.

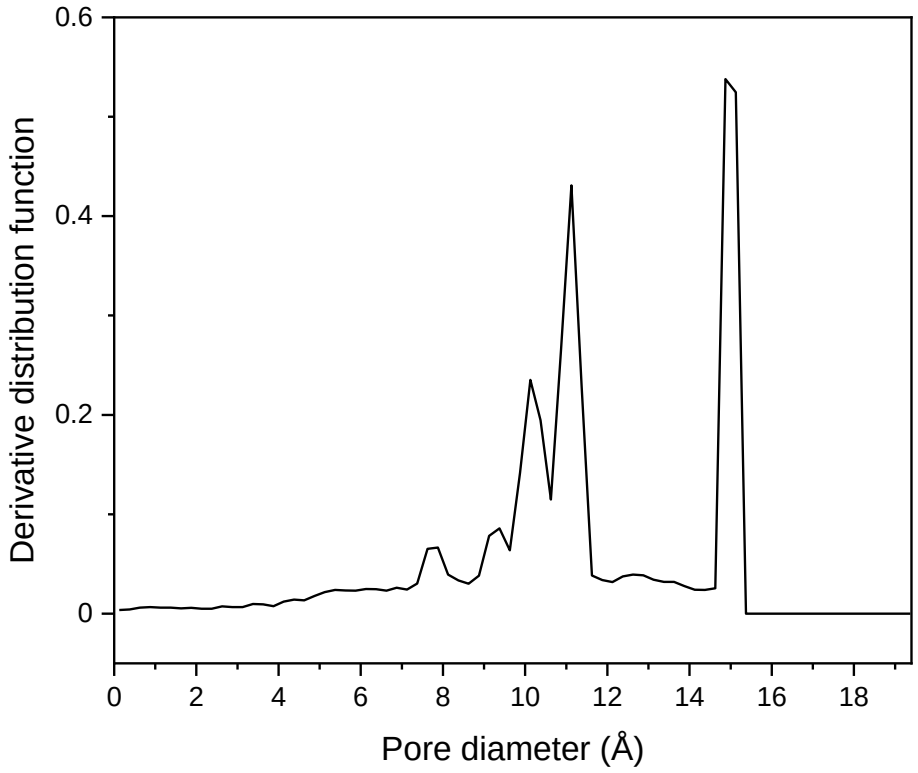

Fig. 2.44 Simulated pore size distribution of **Cu-TTMOP**.

2.5.2 Uptake of dyes from solution

Though the poor 3D framework stability of **Cu-TTMOP** in air prevented the application of this material for gas sorption purposes, the presence of large solvent accessible channels in the structure of **Cu-TTMOP** suggested that this material could be a promising candidate for uptake of guest molecules in a condensed phase. Copper-based MOPs are known to be poorly soluble in both polar and non-polar solvents,[16] which hinders their potential for applications as molecular species in liquid phases, however, presents an advantage for their use as solid state materials for uptake and subsequent removal of pollutants from solution.

The pores of coordination cages can be used to encapsulate guest molecules. Coordination cages have been reported as materials for uptake of organic dye molecules from solution. For example, Ma and co-workers reported the synthesis of a {Cu_2}-based coordination cage which showed efficient adsorption of four organic dyes from aqueous solution: methylene blue (MB), rhodamine B, methyl orange and congo red.[89] The {Cu_2} paddlewheel-based coordination cage used in this study has a rhombic dodecahedral structure, with the formula $[Cu_{12}(CPMM)_8(H_2O)_{12}]\cdot 37DMA\cdot 18H_2O$ (H_3CPMM = 2,4,6-tris[1-(3-carboxylphenoxy)ylmethyl]mesitylene).

In order to investigate if the structure of **Cu-TTMOP** can be used for uptake of guest molecules, the dye molecule methylene blue (MB) was chosen as an analyte. Dye molecules are common environmental pollutants,[90,91] and uptake of dye molecules from water can help to reduce the

environmental harm caused by these compounds. For this reason, the solvent chosen for this study was deionised water. The size of MB molecules is also compatible with the windows to the inner cavity of **Cu-TTMOP**. Additionally, investigations into guest uptake in coordination cages and MOFs have indicated that small dye molecules with higher ionic strength are adsorbed more quickly and effectively, making MB an ideal compound for this study.[89] The structure of MB is shown in **Fig. 2.45**.

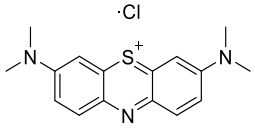

Fig. 2.45 Chemical structure of methylene blue, the dye chosen for guest uptake studies with **Cu-TTMOP**.

In order to investigate the dye uptake behaviour of **Cu-TTMOP**, a solution of MB (2.8×10^{-5} M) in deionised water was prepared, and the UV-vis spectrum of this solution was recorded. A sample of **Cu-TTMOP** crystals as synthesised were washed with water and dried on filter paper. The **Cu-TTMOP** crystals (16.3 mg) were added to the aqueous MB solution, and the UV-vis spectrum of the solutions were measured at a series of time intervals after addition of the **Cu-TTMOP** crystals. The spectra recorded are shown in **Fig. 2.46**.

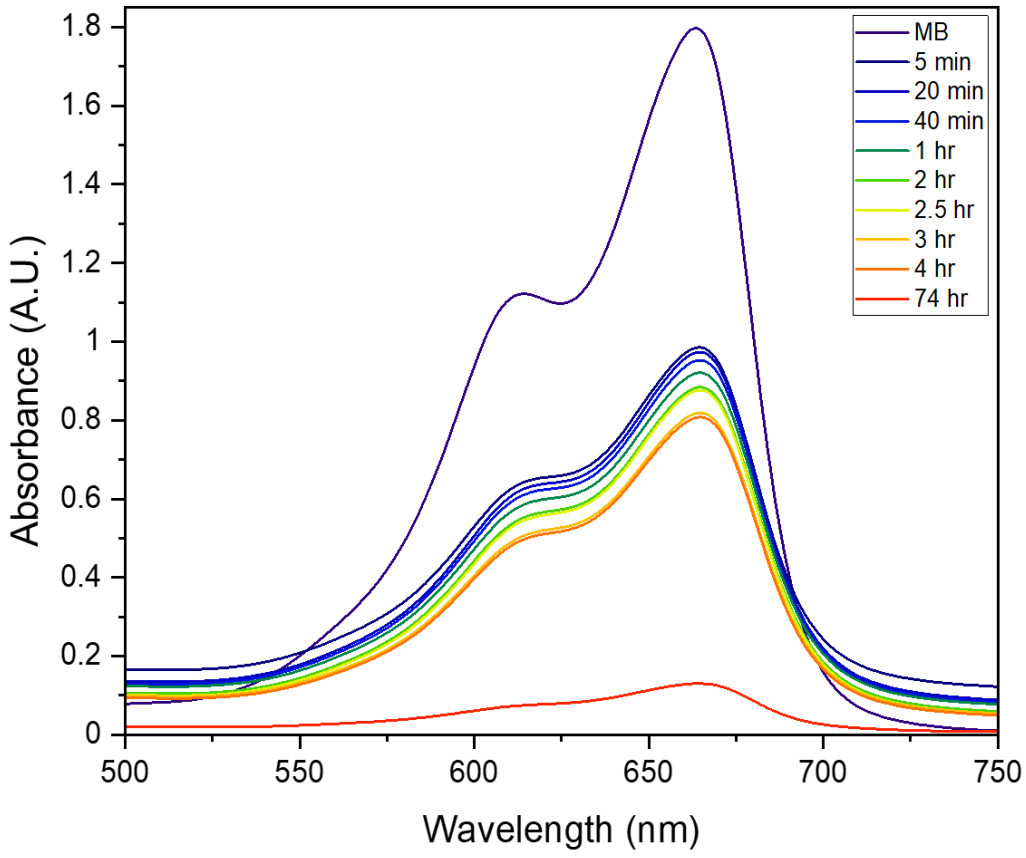

Fig. 2.46 Change in UV-vis absorption spectrum of MB over time after addition of **Cu-TTMOP** crystals to 3 mL of dye solution in water.

The decrease in dye concentration was monitored by comparing the change over time in intensity of the MB absorption band at λ_{max} = 664 nm. Rapid uptake of the dye molecules occurred after addition of **Cu-TTMOP** crystals. In the first 5 minutes after addition of **Cu-TTMOP** to the dye solution, 45.2 % of the initial dye was adsorbed by the material. After this initial drop in the concentration of **MB**, the concentration of the dye gradually decreased at a much slower rate over several hours. After 4 hours, 55.1 % of the dye initially present in solution was absorbed by **Cu-TTMOP** crystals, corresponding to uptake of 6.96×10^{-5} mmol of MB.

Table 2.12 Relative absorbance changes over time of the MB dye solutions after addition of **Cu-TTMOP**. A_0 corresponds to the absorption value at 664 nm (in AU) of the initial 2.8×10^{-5} M MB solution, while A indicates the absorbance value recorded at the selected time intervals after addition of **Cu-TTMOP** above. The MB concentration remaining was calculated by multiplying the original MB concentration ($C_0 = 2.8 \times 10^{-5}$ M) by A/A_0.

Time after addition of **Cu-TTMOP**	A/A_o
0 min	1
5 min	0.548
20 min	0.541
40 min	0.530
1 hr	0.512
2 hr	0.492
2.5 hr	0.488
3 hr	0.455
4 hr	0.449
74 hr	0.0725

The change in concentration of MB in the solution due to uptake by **Cu-TTMOP** can be seen using the naked eye (**Fig. 2.47**). After 5 hours, the solution to which **Cu-TTMOP** was added showed a less intense blue colour than the same solution without **Cu-TTMOP**. The colour of the **Cu-TTMOP** crystals also changed from green to dark blue after immersion in the **MB** solution (**Fig. 2.47**).

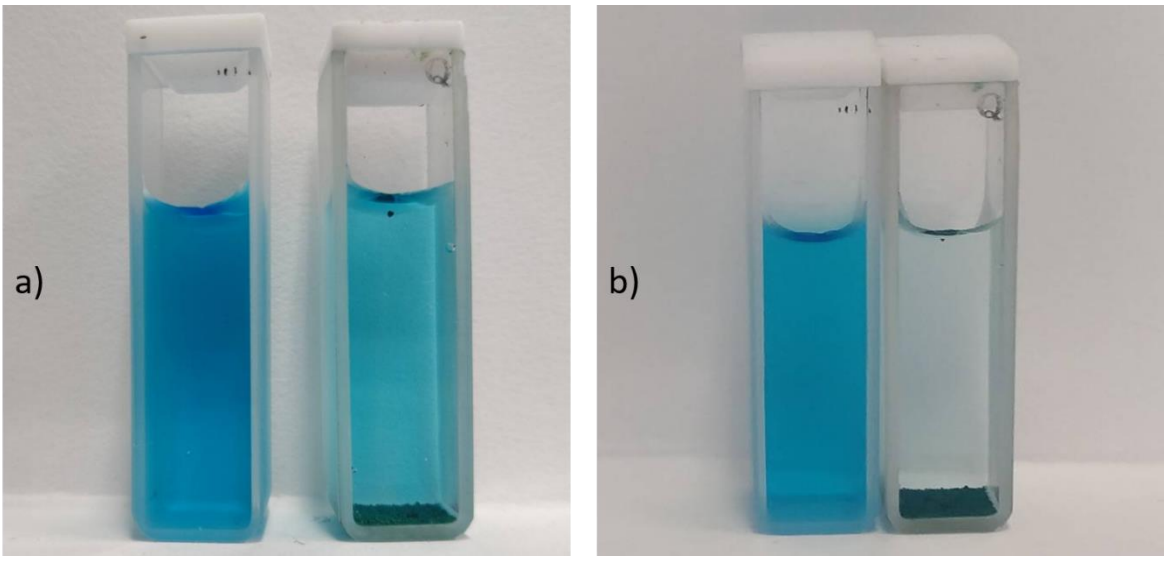

Fig. 2.47 a) Photograph showing the colour change of aqueous MB solutions before (left) and 5 hours after addition of **Cu-TTMOP** (right) **b)** Photograph showing the colour change of aqueous MB solutions before (left) and 74 hours after addition of **Cu-TTMOP** (right).

The absorption spectrum of the dye solution was measured once again at 3 days (74 hours) after addition of **Cu-TTMOP** (**Fig. 2.46**). After this time period, the intensity of the MB absorption band decreased significantly compared to the spectrum taken at 4 hours after adding **Cu-TTMOP**. This can also be seen in the photographs of the cuvettes in **Fig. 2.47**. By comparing the intensity of the initial absorption band of the initial 2.8×10^{-5} M MB solution at 664 nm (A_0 = 1.79718) with the intensity at the same wavelength at 74 hours (A_{74} = 0.13029), it can be estimated that approximately 93 % of the dye in the MB solution was adsorbed.

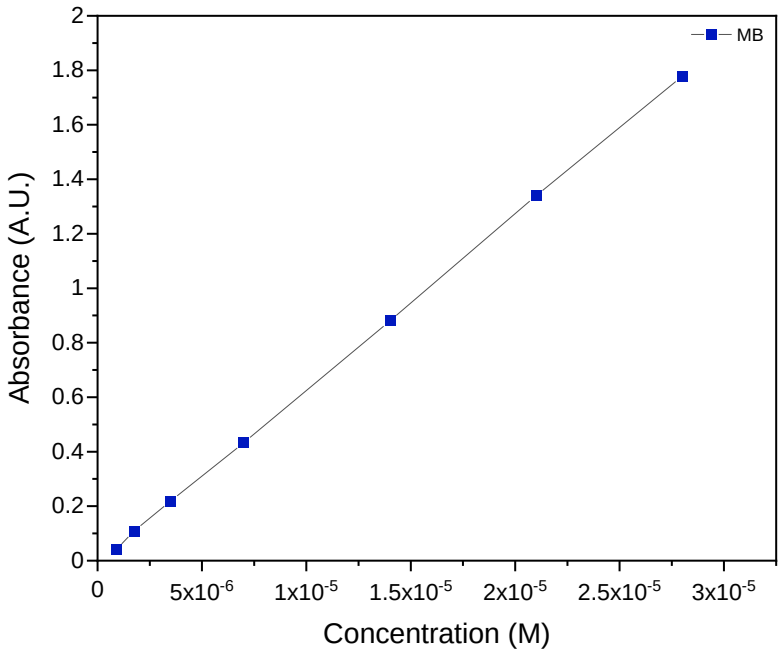

Fig. 2.48 Calibration curve showing the linear relationship between the intensity of the absorption band of MB at 664 nm and the concentration of MB solutions. The blue line represents the calibration curve for solutions of known MB concentration.

In order to prepare a calibration curve, a series of aqueous MB solutions were prepared, and the UV-vis spectra of these solutions was recorded. The calibration curve was used to confirm the linear relationship between the intensity of the absorption band at 664 nm and the concentration of MB dye in solution (**Fig. 2.48**).

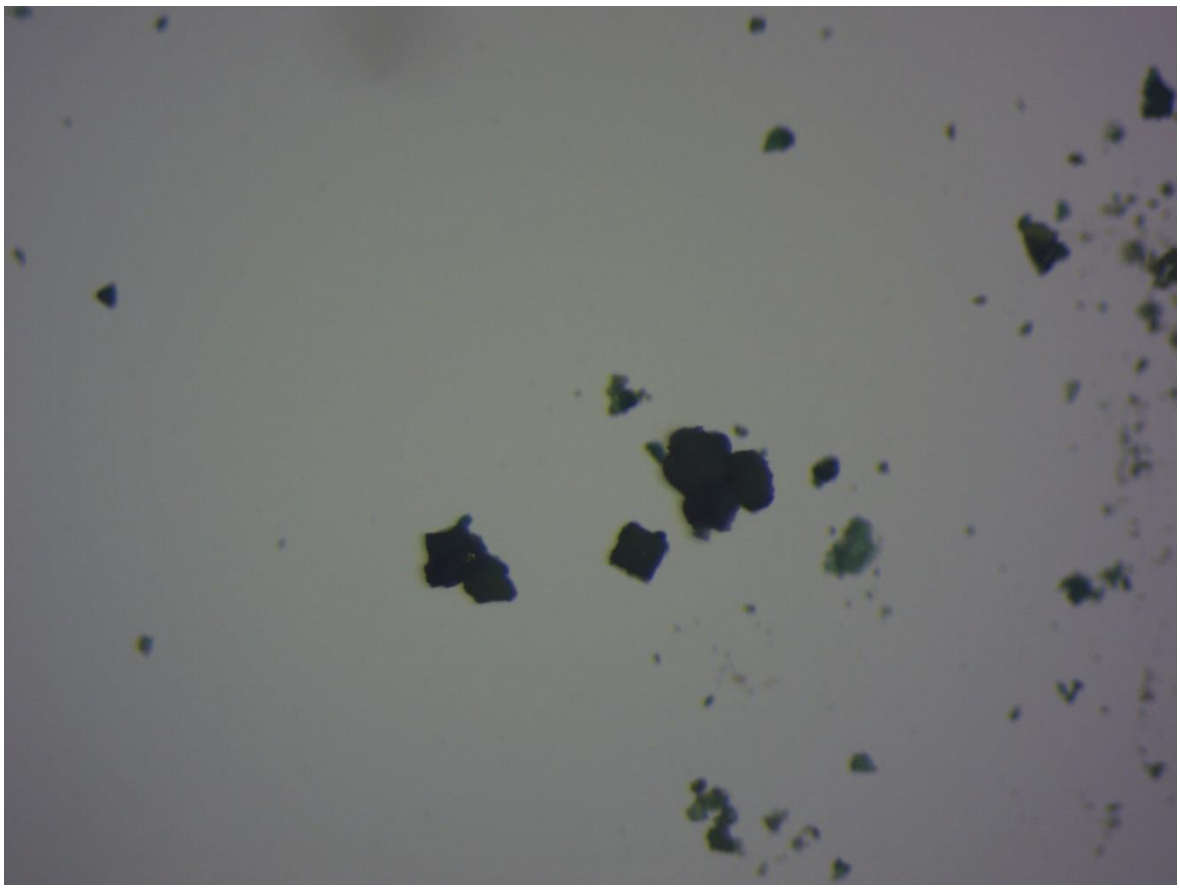

Fig. 2.49 Microscope images of **Cu-TTMOP** after soaking in MB solution for 74 hours

Microscope images also show that MB was successfully adsorbed by crystals of **Cu-TTMOP** (**Fig. 2.49**). Comparison with the microscope images of **Cu-TTMOP** prior to soaking in MB solution (**Fig. 2.21** and **Fig. 2.22**) show that a clear colour change from green to blue was observed in **Cu-TTMOP** crystals after immersion in aqueous MB solution for 74 hours, indicating the presence of MB in the crystals. Examination of the crystals under a microscope with a polarised light source suggested that loss of crystallinity had occurred in the **Cu-TTMOP** crystals after soaking in MB solution.

FTIR spectroscopy was used in an attempt to investigate the presence of the dyes in the **Cu-TTMOP** crystals (**Fig. 2.50**). A sample of crystals was removed from the MB solution, dried on filter paper and rinsed with a few drops of deionised water, to remove any MB solution on the surface of the crystals. Following this, the FTIR spectrum was recorded. The similarity in the chemical bonds in the organic linker H_2**CPTT** and MB made identification of any MB-derived vibrations in the FTIR spectrum difficult, as both MB and H_2**CPTT** possess C-S bonds and phenyl rings. Additionally, C-N bonds are present in the FTIR spectrum of **Cu-TTMOP** due to the presence of DMF solvent molecules. Though FTIR spectroscopy was not useful in identifying MB in the sample, the close agreement between the FTIR spectrum of **Cu-TTMOP** before and after soaking in MB solution for 74 hours (with the exception of solvent peaks) indicated that no significant chemical change had occurred in the **Cu-TTMOP** sample, as the same key bonds were present in both spectra.

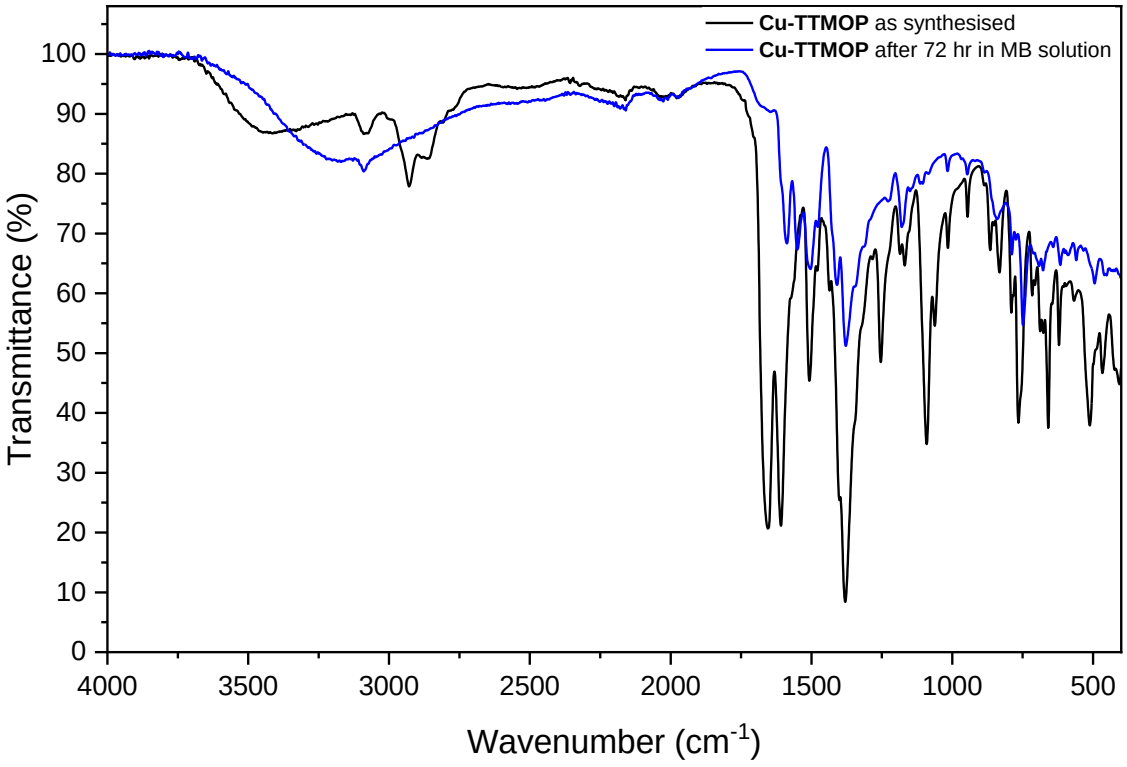

Fig. 2.50 FTIR spectra of **Cu-TTMOP** crystals soaked in MB solution for 72 h, MB and **Cu-TTMOP**.

Due to the presence of sulfur atoms in MB molecules, EDX spectroscopy could be used to confirm the presence of MB dye in crystals of **Cu-TTMOP** after the dye uptake experiment. An increase in the ratio of S:Cu atoms in the crystals was expected upon successful encapsulation of MB. The sample was prepared by drying the MB-soaked crystal on filter paper to remove MB solution on the surface of the crystals. The results of the EDX measurements are shown in **Table 2.13**. A clear increase was observed in the S:Cu ratio after the MB dye uptake experiments, confirming encapsulation of the dye into the **Cu-TTMOP** crystals.

Table 2.13 Experimentally observed S:Cu atomic ratios for **Cu-TTMOP** as synthesised and **Cu-TTMOP**.

Compound	Observed ratio S:Cu from EDX spectrum
Cu-TTMOP	2.14.1
Cu-TTMOP soaked in aqueous MB solution for 74 hrs.	2.64:1

SEM imaging of the **Cu-TTMOP** crystals that had been soaked in aqueous MB solution also showed evidence that the crystals had degraded while in the MB solution (**Fig. 2.51**). Comparison of the SEM images in **Fig. 2.51** with those of **Cu-TTMOP** as synthesised (**Fig. 2.43**) show that the crystals of **Cu-TTMOP** began to degrade while immersed in aqueous MB solution. When compared with the **Cu-TTMOP** crystals as synthesised, the crystals of **Cu-TTMOP** which had been soaked in aqueous MB solution showed rougher surfaces and less defined edges, suggesting loss of crystallinity in the sample. Thus, investigations into the stability of the coordination cage under the experimental

conditions were carried out, to assess if the material could be washed and reused multiple times for dye uptake.

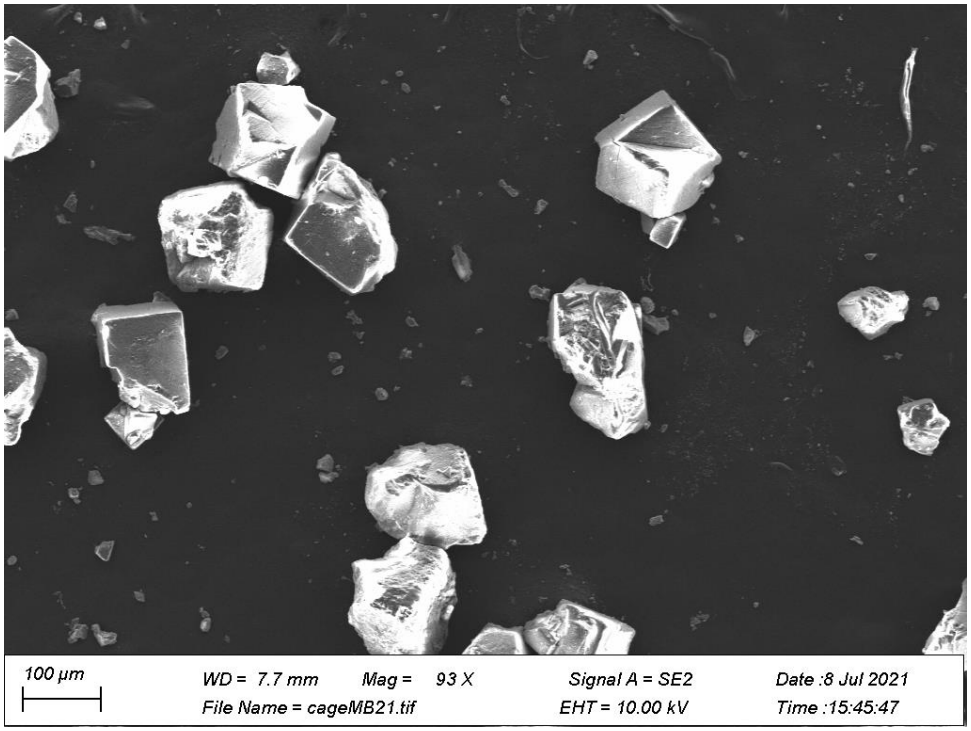

Fig. 2.51 SEM images of **Cu-TTMOP** after soaking in MB solution for 74 hours.

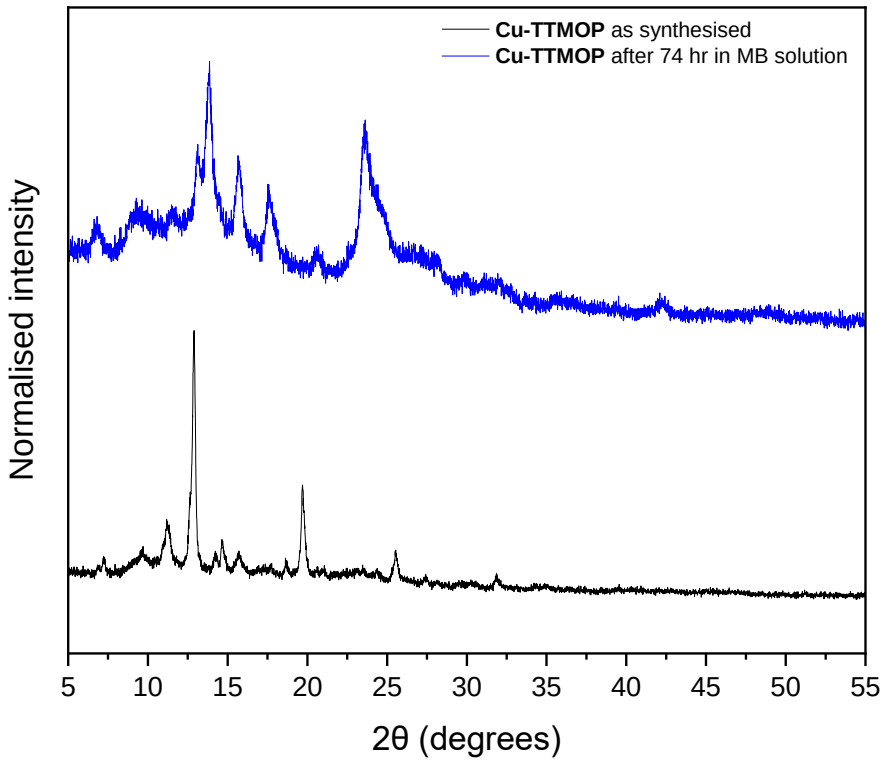

Fig. 2.52 PXRD of **Cu-TTMOP** after immersion in aqueous dye solution for 74 h, compared to experimental PXRD pattern for **Cu-TTMOP** as synthesised. Both patterns were recorded in air, at room temperature.

PXRD was used to assess if any changes occurred in the structure of **Cu-TTMOP** after immersion of the crystals in the aqueous dye solution for 3 days (74 hr). A sample of crystals was removed from the MB solution and dried on filter paper prior to PXRD analysis. This PXRD pattern was compared to cage crystals as synthesised in DMF and dried on filter paper. Both of these PXRD patterns were recorded in air, at room temperature. The PXRD pattern of **Cu-TTMOP** after 74 hr immersed in MB solution shows that a change in the crystallinity of the sample had occurred (**Fig. 2.52**). To account for any effects of preferred orientation or thermal effects on the PXRD pattern, the experimental powder pattern (background uncorrected) was fit using Le Bail methods[85] within the Expo2014 software package (**Fig. 2.53**).[86]. The final *R* values were R_p= 5.735, R_{wp}= 7.242. When compared to the fits previously obtained, poorer agreement was observed between the experimental and calculated patterns, indicating that the sample had lost crystallinity over the 74 hours of the dye uptake experiment.

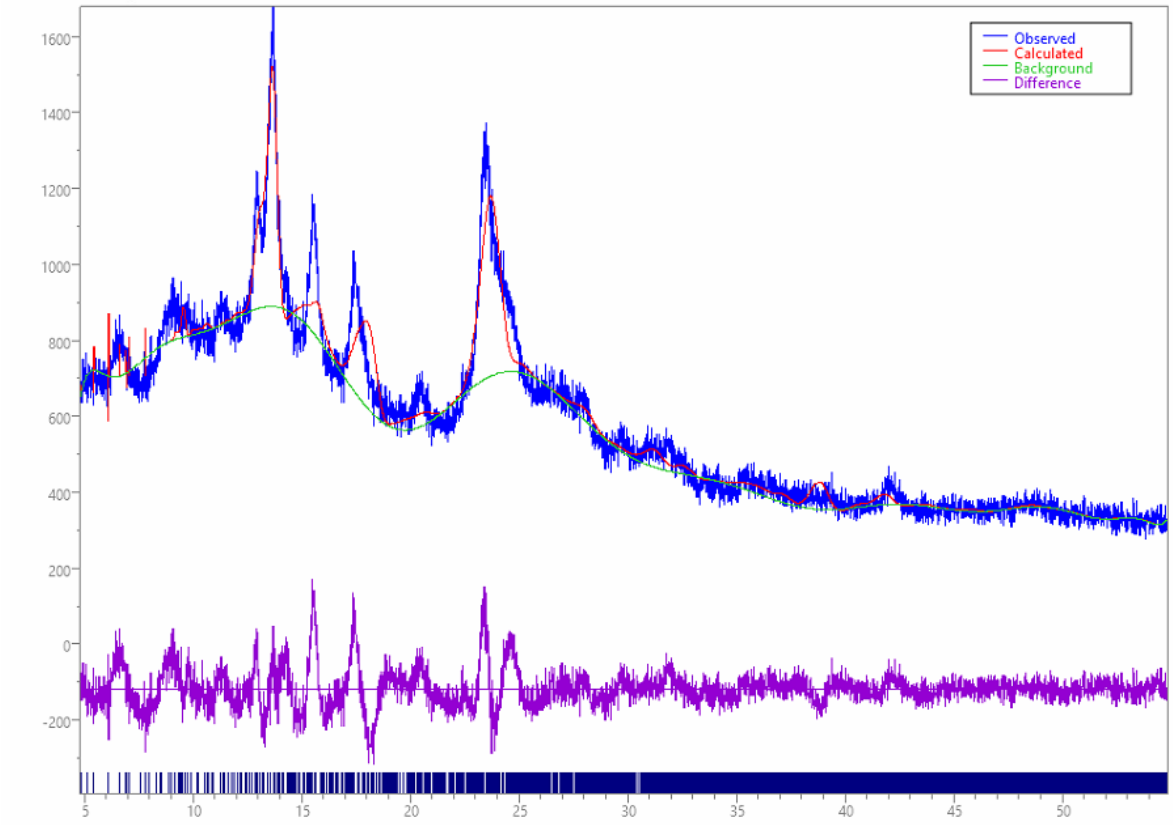

Fig. 2.53 Le Bail fits of PXRD patterns of **Cu-TTMOP**, showing observed (blue) and calculated (red) data, and their difference (violet). The background is shown in green, and the dark blue ticks indicate the positions of reflections predicted from the unit cell. Experimental PXRD pattern was measured after soaking **Cu-TTMOP** crystals in MB solution for 74 hours. The PXRD pattern was recorded in air, at room temperature.

The rapid uptake of **MB** dye molecules as guests into the pores of **Cu-TTMOP** demonstrates that this coordination cage has solvent accessible channels and pores which facilitate uptake of guest molecules from water.

2.6 Conclusion

In this chapter, the design and synthesis of a novel linker, H_2**CPTT** was described. The crystal structures of two intermediates in the synthesis of H_2**CPTT** were measured; 3,4-dibromothiophene-2-carbaldehyde, and ethyl 6-bromothieno[3,2-b]thiophene-2-carboxylate. Intermolecular interactions in crystals of ethyl 6-bromothieno[3,2-b]thiophene-2-carboxylate were investigated, and it was found that intermolecular Br···Br interactions occur, leading to an interesting packing arrangement.

Following the successful synthesis of H_2**CPTT**, this linker was characterised by NMR and FTIR spectroscopy. Furthermore, the crystal structure of H_2**CPTT**, demonstrating that individual molecules assemble in the solid-state into one-dimensional chains of H_2**CPTT** linked by hydrogen bonds.

This novel thienothiophene-based linker, H_2**CPTT**, was used in the synthesis of a Cu^{II}-based coordination cage, **Cu-TTMOP**. The result was a coordination cage with rare hendecahedral geometry, which had previously only been reported once, for coordination cages featuring two ligands. The crystal structure of **Cu-TTMOP** revealed a porous packing structure with a calculated surface area of 4101 m^2/g

This study contributes to the field of coordination cages by outlining a previously unknown synthetic pathway to a metal-organic hendecahedron, using a single organic linker. Detailed analysis of the structure of the novel linker H_2**CPTT**, as well as that of **Cu-TTMOP**, allowed for insight into the assembly of organic and inorganic SBUs. It is clear from this work that linkers incorporating heterocyclic ring systems, particularly thienothiophene rings, present great opportunities to synthesise novel and rare structures due to the unusual angles and binding geometries that can be accessed using these molecules.

Cu-TTMOP was characterised by FTIR spectroscopy, PXRD measurements, TGA, SEM and EDX spectroscopy. Furthermore, theoretical calculations were carried out to gain insight into the pore structure and theoretical surface area of the material. The solvent accessible pores and channels of **Cu-TTMOP** were used for uptake of dye molecules from solution, which was confirmed by UV-vis and EDX spectroscopy.

However, the applications of this coordination cage, **Cu-TTMOP** were limited by the poor solubility of the material, and poor framework stability for gas sorption measurements, two known features of Cu^{II} coordination cages and related molecular species.[92] Additionally, immersion in water for 3 days led to loss of crystallinity of the material. The next step in this search for photoactive materials was to design more stable 3D MOFs, to enable a broader range of applications to be pursued. This goal of utilising organic linkers featuring heterocyclic functional groups to synthesise photoactive metal-organic materials with enhanced stability is the focus of subsequent chapters.

References

1 D. J. Tranchemontagne, Z. Ni, M. O'Keeffe and O. M. Yaghi, *Angew. Chem. Int. Ed.*, 2008, **47**, 5136–5147.

2 H. Vardhan and F. Verpoort, *Aust. J. Chem.*, 2015, **68**, 707–730.

3 J.-R. Li and H.-C. Zhou, *Nat. Chem.*, 2010, **2**, 893–898.

4 M. D. Young, Q. Zhang and H. C. Zhou, *Inorganica Chim. Acta*, 2015, **424**, 216–220.

5 R. J. Li, F. Fadaei-Tirani, R. Scopelliti and K. Severin, *Chem. - A Eur. J.*, 2021, 1–8.

6 A. C. Sudik, A. R. Millward, N. W. Ockwig, A. P. Côté, J. Kim and O. M. Yaghi, *J. Am. Chem. Soc.*, 2005, **127**, 7110–7118.

7 S. Lee, H. Jeong, D. Nam, M. S. Lah and W. Choe, *Chem. Soc. Rev.*, 2021, **50**, 528–555.

8 S. Zarra, J. K. Clegg and J. R. Nitschke, *Angew. Chemie Int. Ed.*, 2013, **52**, 4837–4840.

9 W. Cullen, C. A. Hunter and M. D. Ward, *Inorg. Chem.*, 2015, **54**, 2626–2637.

10 S. Tashiro, M. Tominaga, T. Kusukawa, M. Kawano, S. Sakamoto, K. Yamaguchi and M. Fujita, *Angew. Chemie Int. Ed.*, 2003, **42**, 3267–3270.

11 K. Suzuki, M. Kawano and M. Fujita, *Angew. Chemie Int. Ed.*, 2007, **46**, 2819–2822.

12 C.-P. Li and M. Du, *Chem. Commun.*, 2011, **47**, 5958.

13 K. Umemoto, K. Yamaguchi and M. Fujita, *J. Am. Chem. Soc.*, 2000, **122**, 7150–7151.

14 X. Hang, S. Wang, X. Zhu, H. Han and W. Liao, *CrystEngComm*, 2016, **18**, 4938–4943.

15 K. Byrne, M. Zubair, N. Zhu, X.-P. Zhou, D. S. Fox, H. Zhang, B. Twamley, M. J. Lennox, T. Düren and W. Schmitt, *Nat. Commun.*, 2017, **8**, 15268.

16 E. G. Percástegui, T. K. Ronson and J. R. Nitschke, *Chem. Rev.*, 2020, **120**, 13480–13544.

17 C. A. Rowland, G. R. Lorzing, E. J. Gosselin, B. A. Trump, G. P. A. Yap, C. M. Brown and E. D. Bloch, *J. Am. Chem. Soc.*, 2018, **140**, 11153–11157.

18 P. C. Shi, X. Lin, J. Liang, X. X. Li, Y. B. Huang and R. Cao, *Inorg. Chem. Commun.*, 2017, **78**, 28–31.

19 M. A. Andrés, A. Carné-Sánchez, J. Sánchez-Laínez, O. Roubeau, J. Coronas, D. Maspoch and I. Gascón, *Chem. – A Eur. J.*, 2020, **26**, 143–147.

20 S. M. Xie, N. Fu, L. Li, B. Y. Yuan, J. H. Zhang, Y. X. Li and L. M. Yuan, *Anal. Chem.*, 2018, **90**, 9182–9188.

21 K. I. Yamashita, M. Kawano and M. Fujita, *Chem. Commun.*, 2007, **1**, 4102–4103.

22 J. Dong, Y. Zhou, F. Zhang and Y. Cui, *Chem. - A Eur. J.*, 2014, **20**, 6455–6461.

23 A. Casini, B. Woods and M. Wenzel, *Inorg. Chem.*, 2017, **56**, 14715–14729.

24 J. E. M. Lewis, E. L. Gavey, S. A. Cameron and J. D. Crowley, *Chem. Sci.*, 2012, **3**, 778–784.

25 N. P. E. Barry, O. Zava, P. J. Dyson and B. Therrien, *Chem. - A Eur. J.*, 2011, **17**, 9669–9677.

26 M. Han, R. Michel, B. He, Y. S. Chen, D. Stalke, M. John and G. H. Clever, *Angew. Chemie - Int. Ed.*, 2013, **52**, 1319–1323.

27 R. Küng, T. Pausch, D. Rasch, R. Göstl and B. M. Schmidt, *Angew. Chemie - Int. Ed.*, 2021, **60**, 13626–13630.

28 D. Zhang, T. K. Ronson, S. Güryel, J. D. Thoburn, D. J. Wales and J. R. Nitschke, *J. Am. Chem. Soc.*, 2019, **141**, 14534–14538.

29 S. Chen, K. Li, F. Zhao, L. Zhang, M. Pan, Y. Z. Fan, J. Guo, J. Shi and C. Y. Su, *Nat. Commun.*, 2016, **7**, 1–8.

30 X. Qi, R. Zhong, M. Chen, C. Sun, S. You, J. Gu, G. Shan, D. Cui, X. Wang and Z. Su, *ACS Catal.*, 2021, 7241–7248.

31 C. Mozaceanu, C. G. P. Taylor, J. R. Piper, S. P. Argent and M. D. Ward, *Chemistry (Easton).*, 2020, **2**, 22–32.

32 M. D. Ward, C. A. Hunter and N. H. Williams, *Chem. Lett.*, 2017, **46**, 2–9.

33 C. Tan, D. Chu, X. Tang, Y. Liu, W. Xuan and Y. Cui, *Chem. Eur. J.*, 2019, **25**, 662–672.

34 J. Lee, D. W. Lim, S. Dekura, H. Kitagawa and W. Choe, *ACS Appl. Mater. Interfaces*, 2019, **11**, 12639–12646.

35 E. J. Gosselin, G. R. Lorzing, B. A. Trump, C. M. Brown and E. D. Bloch, *Chem. Commun.*, 2018, **54**, 6392–6395.

36 J. Li, D. J. Timmons and H. Zhou, 2009, 6368–6369.

37 H. Chun, H. Jung and J. Seo, *Inorg. Chem.*, 2009, **48**, 2043–2047.

38 H. Chun, *J. Am. Chem. Soc.*, 2008, **130**, 800–801.

39 N. Ahmad, H. A. Younus, A. H. Chughtai, K. Van Hecke, M. Danish, Z. Gaoke and F. Verpoort, *Sci. Rep.*, 2017, **7**, 1–8.

40 J. R. Li and H. C. Zhou, *Angew. Chem.*, 2009, **48**, 8465–8468.

41 H. Furukawa, J. Kim, N. W. Ockwig, M. O'Keeffe and O. M. Yaghi, *J. Am. Chem. Soc.*,

2008, **130**, 11650–11661.

42 B. Moulton, J. Lu, A. Mondal and M. J. Zaworotko, *Chem. Commun.*, 2001, **2**, 863–864.

43 Z. Ni, A. Yassar, T. Antoun and O. M. Yaghi, *J. Am. Chem. Soc.*, 2005, **127**, 12752–12753.

44 J. R. Li, D. J. Timmons and H. C. Zhou, *J. Am. Chem. Soc.*, 2009, **131**, 6368–6369.

45 E. L. Eliel and S. H. Wilen, *Stereochemistry of Organic Compounds*, Wiley, New York, 1994.

46 N. N. Ji, Z. Q. Shi and H. L. Hu, *J. Solid State Chem.*, 2018, **267**, 68–75.

47 M. E. Cinar and T. Ozturk, *Chem. Rev.*, 2015, **115**, 3036–3140.

48 J. W. Jung, J. W. Jo, E. H. Jung and W. H. Jo, *Org. Electron.*, 2016, **31**, 149–170.

49 P. Jacobson, *Berichte der Dtsch. Chem. Gesellschaft*, 1886, **19**, 1067–1077.

50 J. Roncali, *Chem. Rev.*, 1997, **97**, 173–206.

51 D. Zhu, L. Sun, X. Bao, S. Wen, L. Han, C. Gu, J. Guo and R. Yang, *RSC Adv.*, 2015, **5**, 62336–62342.

52 S.-L. Li, K.-J. Jiang, K.-F. Shao and L.-M. Yang, *Chem. Commun.*, 2006, **2**, 2792.

53 C. Zhang and S. Holdcroft, *J. Mater. Res.*, 2018, **33**, 1879–1890.

54 J. Y. Kim, D. S. Yang, J. Shin, D. Bilby, K. Chung, H. A. Um, J. Chun, S. Pyo, M. J. Cho, J. Kim and D. H. Choi, *ACS Appl. Mater. Interfaces*, 2015, **7**, 13431–13439.

55 G.-S. Yang, Z.-L. Lang, H.-Y. Zang, Y.-Q. Lan, W.-W. He, X.-L. Zhao, L.-K. Yan, X.-L. Wang and Z.-M. Su, *Chem. Commun.*, 2013, **49**, 1088.

56 R. Dalapati, Ü. Kökçam-Demir, C. Janiak and S. Biswas, *Dalt. Trans.*, 2018, **47**, 1159–1170.

57 S. K. Mostakim, M. Grzywa, D. Volkmer and S. Biswas, *J. Solid State Chem.*, 2015, **232**, 221–227.

58 H. Q. Pham, T. Mai, N. N. Pham-Tran, Y. Kawazoe, H. Mizuseki and D. Nguyen-Manh, *J. Phys. Chem. C*, 2014, **118**, 4567–4577.

59 A. N. Dou, L. B. Yang, X. D. Fang, Q. Yin, M. D. Li, J. Li, M. Y. Wang, A. X. Zhu and Q. Q. Xu, *CrystEngComm*, 2018, **20**, 3609–3619.

60 S. Sun, P. Zhang, J. Li, Y. Li, J. Wang, S. Zhang, Y. Xia, X. Meng, D. Fan and J. Chu, *J. Mater. Chem. A*, 2014, **2**, 15316–15325.

61 P. Metrangolo and G. Resnati, *IUCrJ*, 2014, **1**, 5–7.

62 M. Capdevila-Cortada and J. J. Novoa, *CrystEngComm*, 2015, **17**, 3354–3365.

63 T. Sakurai, M. Sundaralingam and G. A. Jeffrey, *Acta Crystallogr.*, 1963, **16**, 354–363.

64 N. Ramasubbu, R. Parthasarathy and P. Murray-Rust, *J. Am. Chem. Soc.*, 1986, **108**, 4308–4314.

65 S. Tothadi, S. Joseph and G. R. Desiraju, *Cryst. Growth Des.*, 2013, **13**, 3242–3254.

66 M. J. Turner, J. J. McKinnon, S. K. Wolff, D. J. Grimwood, P. R. Spackman, D. Jayatilaka and M. A. Spackman, 2017.

67 M. A. Spackman and D. Jayatilaka, *CrystEngComm*, 2009, **11**, 19–32.

68 S. Ghosh, P. Chopra and S. Wategaonkar, *Phys. Chem. Chem. Phys.*, 2020, **22**, 17482–17493.

69 J. Sherwood, J. H. Clark, I. J. S. Fairlamb and J. M. Slattery, *Green Chem.*, 2019, **21**, 2164–2213.

70 A. Bajpai, M. S. Krishna and J. N. Moorthy, *J. Indian Inst. Sci.*, 2014, **94**, 25–34.

71 W. J. Bae, C. Scilla, V. V. Duzhko, W. Ho Jo and E. B. Coughlin, *J. Polym. Sci. Part A Polym. Chem.*, 2011, **49**, 3260–3271.

72 F. W. Steuber, J. J. Gough, É. Whelan, L. Burtnyak, A. L. Bradley and W. Schmitt, *Inorg. Chem.*, 2020, **59**, 17244–17250.

73 H. Vardhan, M. Yusubov and F. Verpoort, *Coord. Chem. Rev.*, 2016, **306**, 171–194.

74 V. Brega, M. Zeller, Y. He, H. Peter Lu and J. K. Klosterman, *Chem. Commun.*, 2015, **51**, 5077–5080.

75 V. A. Blatov, A. P. Shevchenko and D. M. Proserpio, *Cryst. Growth Des.*, 2014, **14**, 3576–3586.

76 S. Alvarez, P. Alemany, D. Casanova, J. Cirera, M. Llunell and D. Avnir, *Coord. Chem. Rev.*, 2005, **249**, 1693–1708.

77 G. M. Brown and R. Chidambaram, *Acta Crystallogr. Sect. B Struct. Crystallogr. Cryst. Chem.*, 1973, **29**, 2393–2403.

78 O. M. Yaghi, M. J. Kalmutzki and C. S. Diercks, *Introduction to Reticular Chemistry*, Wiley, 2019.

79 V. Guillerm and D. Maspoch, *J. Am. Chem. Soc.*, 2019, **141**, 16517–16538.

80 O. V. Dolomanov, L. J. Bourhis, R. J. Gildea, J. A. K. Howard and H. Puschmann, *J. Appl. Crystallogr.*, 2009, **42**, 339–341.

81 A. L. Spek, *J. Appl. Crystallogr.*, 2003, **36**, 7–13.

82 A. L. Spek, *Acta Crystallogr. Sect. C Struct. Chem.*, 2015, **71**, 9–18.

83 I. D. Brown and D. Altermatt, *Acta Crystallogr. Sect. B Struct. Sci.*, 1985, **41**, 244–247.

84 W. Liu and H. H. Thorp, *Inorg. Chem.*, 1992, **31**, 1585–1588.

85 A. Le Bail, *Powder Diffr.*, 2005, **20**, 316–326.

86 A. Altomare, C. Cuocci, C. Giacovazzo, A. Moliterni, R. Rizzi, N. Corriero and A. Falcicchio, *J. Appl. Crystallogr.*, 2013, **46**, 1231–1235.

87 G. B. Deacon and R. J. Phillips, *Coord. Chem. Rev.*, 1980, **33**, 227–250.

88 L. Sarkisov and A. Harrison, *Mol. Simul.*, 2011, **37**, 1248–1257.

89 Y.-C. He, J. Yang, W.-Q. Kan and J.-F. Ma, *CrystEngComm*, 2013, **15**, 848–851.

90 D. A. Yaseen and M. Scholz, *Int. J. Environ. Sci. Technol.*, 2019, **16**, 1193–1226.

91 B. Lellis, C. Z. Fávaro-Polonio, J. A. Pamphile and J. C. Polonio, *Biotechnol. Res. Innov.*, 2019, **3**, 275–290.

92 S. Mollick, S. Fajal, S. Mukherjee and S. K. Ghosh, *Chem. - An Asian J.*, 2019, **14**, 3096–3108.

Chapter 3 : Ln-MOFs with One-Dimensional Ln^{III} SBUs Based on La^{III}, Ce^{III}, Pr^{III}, Nd^{III}, Sm^{III} and Eu^{III}

3.1 Introduction

In chapter 2, it is demonstrated that the structural properties of thiophene-based linkers can be exploited to synthesise supramolecular structures with fascinating geometries. However, use of the **Cu-TTMOP** for further applications, such as gas sorption, was hindered by the poor stability of the material under certain conditions. Further efforts were therefore applied to designing materials with enhanced stability. In this chapter, supramolecular design principles have been applied, with the aim of synthesising a stable series of photoactive MOFs.

3.1.1 Lanthanide-based Metal-Organic Frameworks

Lanthanide-based MOFs (Ln-MOFs) have been shown to possess excellent potential for a wide range of applications, due to their unique photochemical properties,[1,2] versatile coordination geometry of the lanthanide ions,[3,4] and high stability of the frameworks.[5–8] For example, Ln-MOFs have been reported to show excellent thermal stability,[9–11] in addition to stability to various solvents,[10,12] including water[13–15] and a wide pH range.[16–18] The luminescence properties of Ln-MOFs, arising from the sharp and well-defined *f-f* transitions of the Ln^{III} ions, make them promising candidates as photocatalysts[19] and luminescence sensors.[20] In order to enhance the luminescence of lanthanide ions, the antenna effect can be employed,[21] in which the use of electron-rich chromophores as ligands in Ln-MOFs leads to photosensitisation of Ln^{III} ions, through ligand to metal energy transfer.[22] In particular, Ln-MOFs based on europium and terbium are considered to be excellent candidates as chemical sensors and photocatalysts, due to their visible fluorescence which is observable with the naked eye.[23,24]

In addition to the use of Ln-MOFs for their optical properties, these materials have also been used for other applications, such as gas uptake and separation,[25,26] and lanthanide MOFs have also been demonstrated to possess fascinating magnetic properties.[27,28]

3.1.2 Aims and Objectives

In this chapter, we continue to explore the effect of incorporating heterocyclic ring systems into metal-organic materials on the structures and properties of these materials. To this end, the design and synthesis of a novel linker, 5,5',5''-(1,3,5-triazine-2,4,6-triyl)tris(thiophene-2-carboxylic acid) (H_3**TTT**) is reported. This novel linker is an electron-rich carboxylate-based compound, allowing for a potential coordination site to inorganic SBUs. The presence of thiophene rings allows this linker to adopt a highly planar conformation, while the Lewis-basic nitrogen atoms of the triazine ring give a potential interaction site for analytes,[29] making this a promising linker for synthesis of MOFs for

luminescent sensing applications. A further advantage of this linker is its synthetic accessibility, as the synthetic pathway to this linker features only two synthetic steps, the first of which had previously been reported in the literature with excellent yield.[30] Following successful synthesis of H_3**TTT**, the optical and structural properties of this linker will be explored.

This chapter will also investigate the reaction of H_3**TTT** with Ln^{III} ions in the early lanthanide series, with the aim of synthesising a series of Ln-MOFs, and characterising these MOFs by single crystal XRD to gain insight into their structures. Furthermore, this work aims to investigate the stability and photochemical properties of the MOFs, and to examine their potential as materials for gas sorption and luminescence sensing applications.

3.2 Ligand Synthesis

3.2.1 Organic Synthesis of Synthesis of 5,5',5''-(1,3,5-triazine-2,4,6-triyl)tris(thiophene-2-carboxylic acid) (H_3TTT)

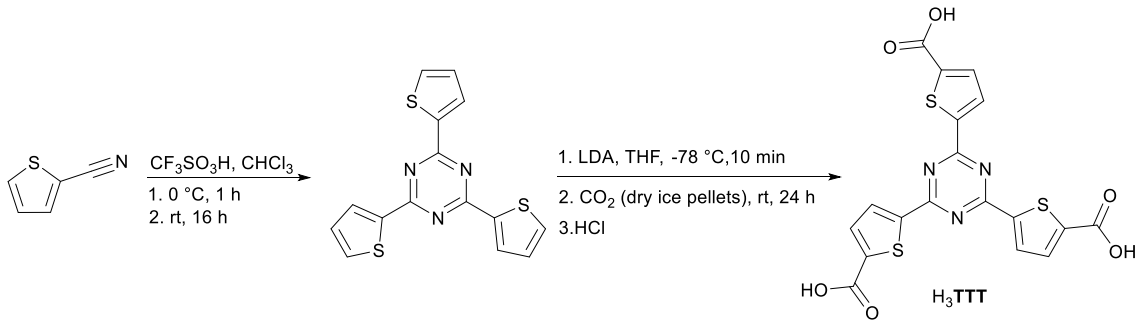

Scheme 3.1 Synthesis of 5,5',5''-(1,3,5-triazine-2,4,6-triyl)tris(thiophene-2-carboxylic acid) (H_3**TTT**).

The synthesis of 5,5',5''-(1,3,5-triazine-2,4,6-triyl)tris(thiophene-2-carboxylic acid) (H_3**TTT**) was accomplished out in two synthetic steps, which are presented in **Scheme 3.1**. The first step of the synthesis, acid-catalysed cyclisation of three equivalents of thiophene-2-carbonitrile to give 2,4,6-tri(thiophen-2-yl)-1,3,5-triazine was carried out using a modified version of a synthesis previously reported by Yu et *al.*.[30] The work-up of this reaction involved subsequent washing of the crude product with water, acetone and methanol, instead of column chromatography as carried out by Yu *et al.*. A yield of 91 % was achieved for 2,4,6-tri(thiophen-2-yl)-1,3,5-triazine. The pure compound had a pale pink colour. The ^{1}H and ^{13}C NMR spectra were in good agreement with those previously reported in the literature.[30]

The second synthetic step involved addition of carboxylate moieties to 2,4,6-tri(thiophen-2-yl)-1,3,5-triazine to give the novel ligand, H_3**TTT** (**Scheme 3.1**). The first step of the reaction required *in situ* synthesis of lithium diisopropylamine (LDA) by adding n-butyllitium dropwise to a solution of diisopropylamine in tetrahydrofuran (THF) at -78 °C. Addition of 2,4,6-tri(thiophen-2-yl)-1,3,5-triazine to the LDA solution resulted in lithiation at the 5-position of the three thiophene rings. Dry ice was then added to the solution, quenching the lithiated product and resulting in addition of

carboxylate groups to the thiophene rings. Subsequent acidification, filtration, washing with H_2O, and recrystallisation from THF gave the product, H_3**TTT** as a pale-yellow powder with 53% yield.

3.2.2 Crystal Structure of H_3TTT

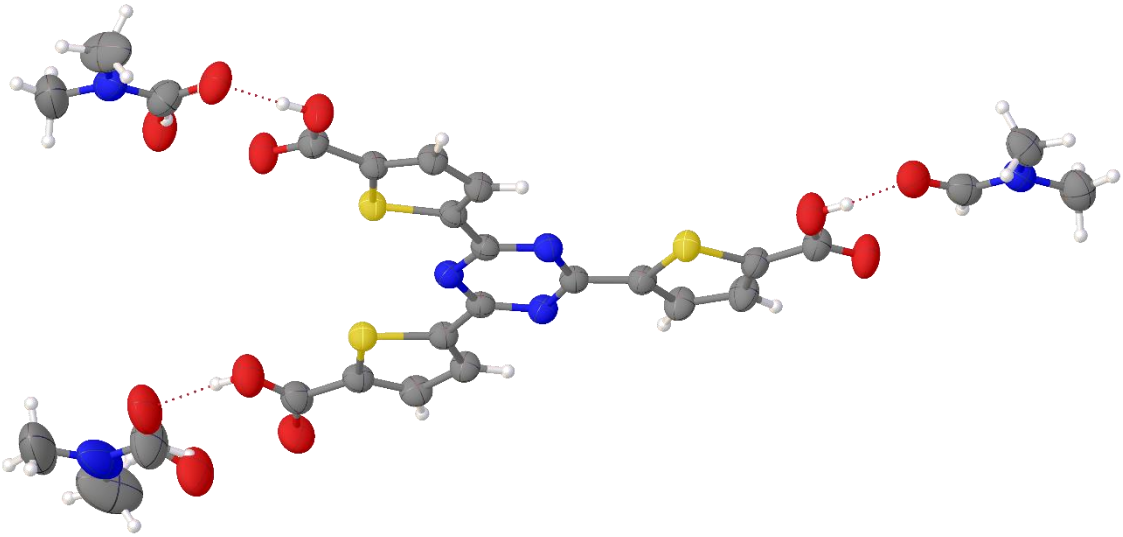

Fig. 3.1 Thermal displacement ellipsoid plot of asymmetric unit of H_3**TTT**, as viewed along the crystallographic *c*-axis (thermal displacement ellipsoids are shown at the 50 % probability level). Three cocrystallised DMF solvent molecules are shown, two of which show flip disorder over two positions. Atom colour scheme: C, dark grey; O, red; S, yellow; N, blue; H, white.

Heating a solution of H_3**TTT** in DMF solution at 100 °C for 24 hours gave colourless plate-shaped crystals of H_3**TTT** of a suitable size and quality for single crystal XRD analysis. H_3**TTT** was solved and refined in the monoclinic space group *C2/c*. It is interesting to note that H_3**TTT** does not display C_3 symmetry, as the sulphur atoms of two thiophene groups face each other.

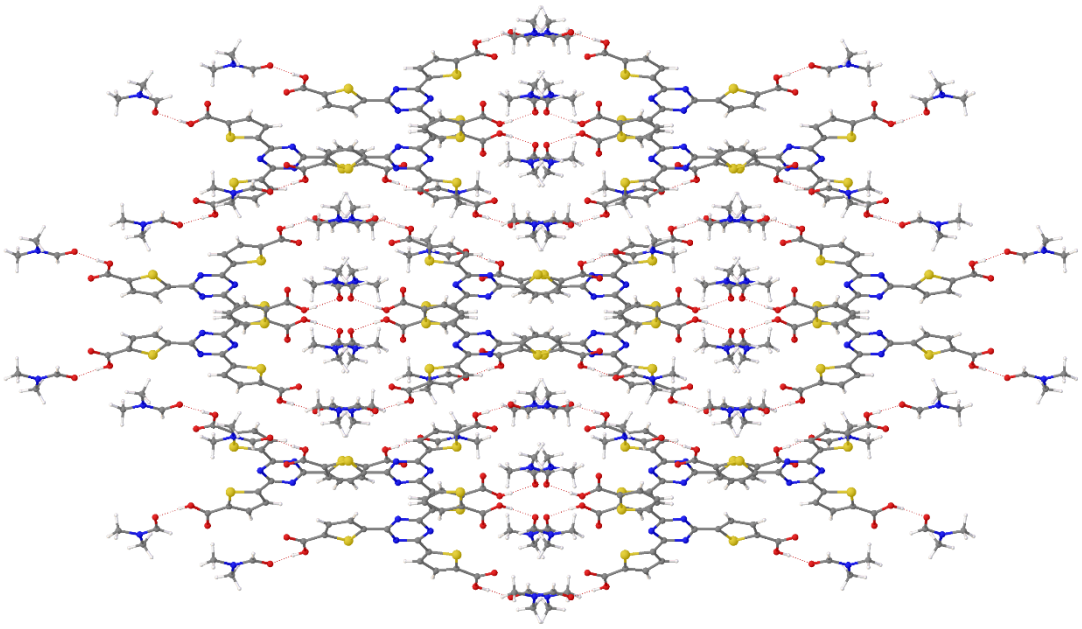

Fig. 3.2 Packing diagram of H_3**TTT**, viewed along the crystallographic *c*-axis with co-crystallised DMF solvent molecules shown. Only one part of the disordered DMF molecules was shown for clarity. Atom colour scheme: C, dark grey; O, red; S, yellow; N, blue; H, white.

The thermal displacement ellipsoid of the asymmetric unit in H_3**TTT** is shown in **Fig. 3.1**. The asymmetric unit contains one H_3**TTT** molecule and three DMF solvent molecules. Two of the DMF molecules and the carboxylate moieties of H_3**TTT** show flip-disorder over two positions. Carboxylic acids have the ability to self-associate through hydrogen bonding as they are both strong hydrogen bond acceptors (C=O) and hydrogen bond donors (O-H).[31] The oxygen atom of each DMF molecule forms a hydrogen bond to the adjacent carboxylate -OH group atom.

The packing diagram of H_3**TTT** is shown in **Fig. 3.2**. H_3**TTT** packs as two-dimensional layers of molecules. The distance between the centroids of triazine rings in consecutive layers is 3.649 Å, indicating that π-π interactions exist between H_3**TTT** molecules in different layers.

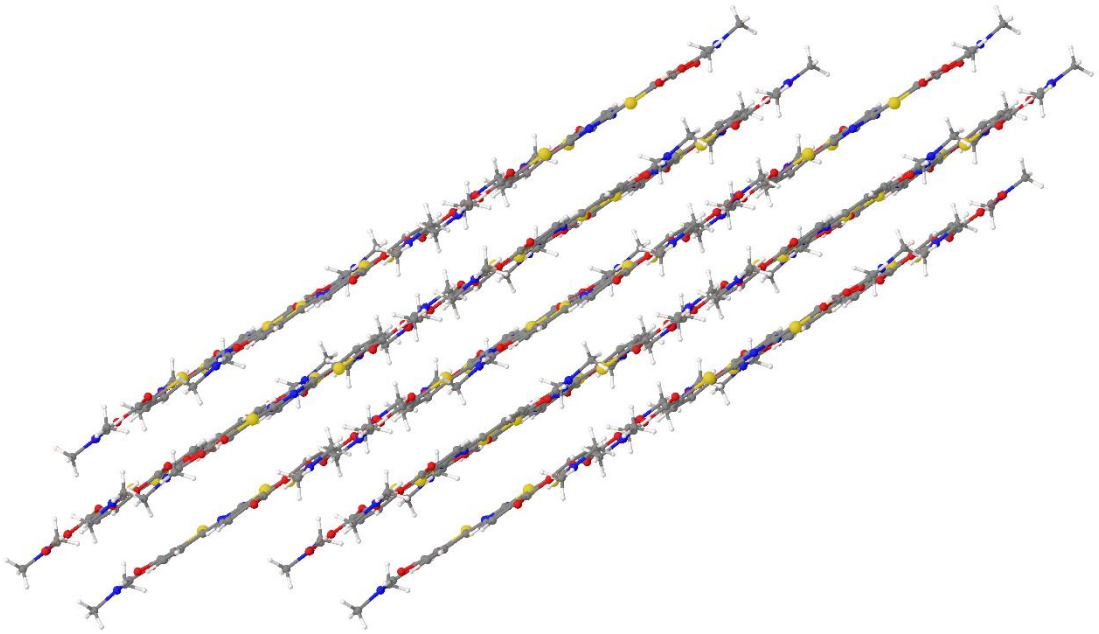

Fig. 3.3 Packing diagram of H_3**TTT**, viewed along the crystallographic *b*-axis with co-crystallised DMF solvent molecules shown. Only one part of the disordered DMF molecules was shown for clarity. Atom colour scheme: C, dark grey; O, red; S, yellow; N, blue; H, white.

Molecules of H_3**TTT** are almost planar in structure. A table of dihedral angles between the plane of the triazine ring and the plane of the three thiophene rings is shown in **Table 3.1.** The dihedral angles are between 3.61° and 6.24°. Each carboxylate moiety is coplanar with the thiophene ring to which it is attached.

Table 3.1 Dihedral angles between triazine ring and thiophene rings in H_3**TTT**.

Angle between:	Thiophene ring atoms	Angle between planes
Triazine ring, thiophene ring 1	S1, C2, C3, C4, C5	6.24°
Triazine ring, thiophene ring 2	S2, C8, C9, C10, C11	3.61°
Triazine ring, thiophene ring 3	S3, C14, C15, C16, C17	6.20°

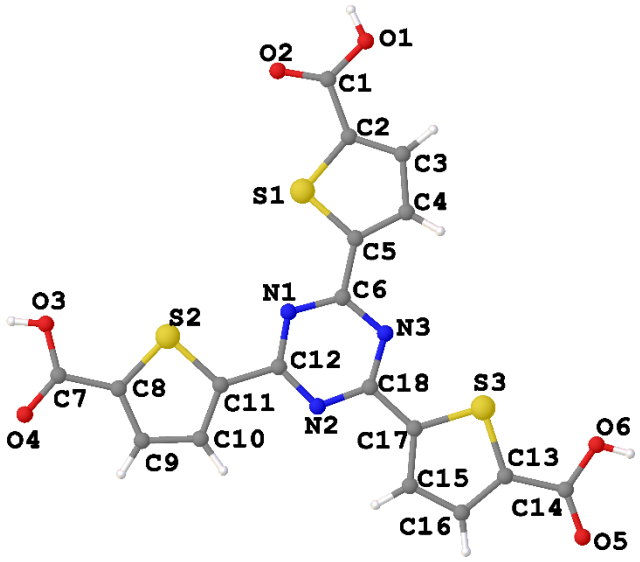

Fig. 3.4 Structure of H_3**TTT** showing atom labels. Atom colour scheme: C, dark grey; O, red; S, yellow; N, blue; H, white.

Table 3.2 Crystal data and refinement results for H_3**TTT**.

Compound name	H_3**TTT**
Empirical formula	$C_{27}H_{30}O_9N_6S_3$
Formula weight	678.75
Temperature (K)	215(2)
Crystal description	Colourless needles
Crystal system	Monoclinic
Space group	*C*2/*c*
a (Å)	25.0325(7)
b (Å)	24.1288(7)
c (Å)	11.6551(3)
α (°)	90
β (°)	133.7560(10)
γ (°)	90
V (Å^3)	6443.2(3)
Z	8
ρ_{calc} (g/cm^3)	1.399
μ (mm^{-1})	2.624
F(000)	2832.0
Radiation	CuKα (λ = 1.54178)
2θ range for data collection (°)	7.328 to 137.736
Reflections collected	40741
Independent reflections	5946 [R_{int} = 0.0321, R_{sigma} = 0.0248]
Data/restraints/parameters	5946/6/429
Goodness-of-fit on F^2	1.059
R_1 [I≥2σ (I)], all	0.0467, 0.0514
wR_2 [I≥2σ (I)], all	0.1404, 0.1441
Largest diff. peak/hole (e Å^{-3})	0.37/-0.37

3.2.3 Nuclear Magnetic Resonance (NMR) spectroscopy of H_3TTT

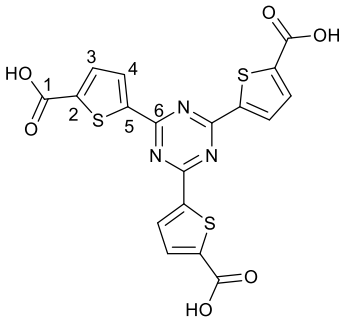

Fig. 3.5 H_3**TTT**, showing labelled carbon atoms.

H_3**TTT** was characterised by ^{1}H NMR and ^{13}C NMR spectroscopy. Three proton signals were observed in the ^{1}H NMR spectrum (**Fig. 3.6**), one broad signal at 13.71 ppm, corresponding to the carboxylic acid proton, and two aromatic proton signals at 8.27 and 7.86 ppm, both of which possess doublet multiplicity. The peak at 8.27 ppm can be assigned to H3, the proton bonded to C3, the carbon in thiophene 3-position. This proton is expected to appear at a deshielded position in the spectrum due to its proximity to the carboxylic acid moiety. The peak at 7.86 ppm can be assigned to the proton bonded to C4, the carbon in the thiophene 4-position. Each ^{1}H NMR peak arises from three chemically identical protons in the structure of H_3**TTT** due to the symmetry in the molecule.

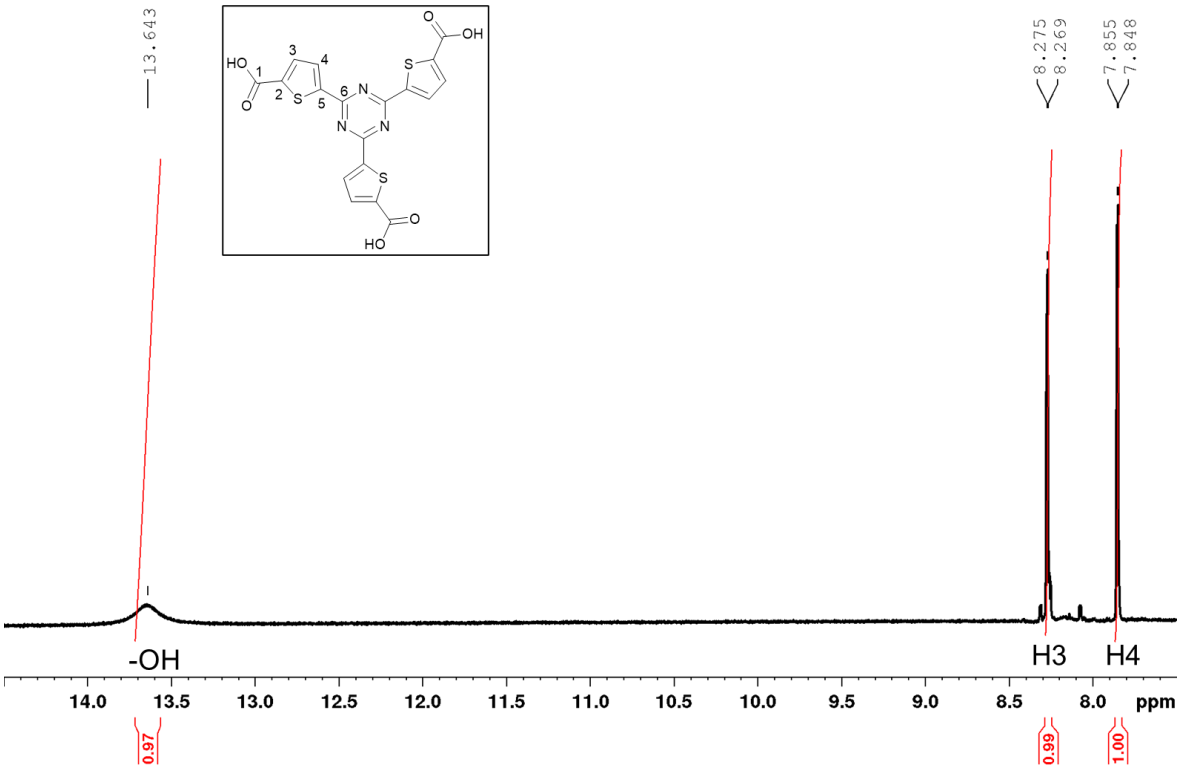

Fig. 3.6 The aromatic region of the ^{1}H NMR spectrum of H_3**TTT** (600 mHz, d_6-DMSO), with inset of H_3**TTT**, showing labelled H-atoms.

The ^{13}C NMR spectrum of H_3**TTT** (**Fig. 3.7**) and features 6 carbon atoms, with each peak arising from three chemically identical carbon atoms in H_3**TTT**. The ^{13}C NMR signal at 166.90 ppm can be assigned to C1, as this carbon peak is expected to be highly deshielded as it is a carboxylate carbon.

The HSQC spectrum (**Fig. 3.8**) could be used to identify the peaks corresponding to C3 and C4, the carbon atoms with attached protons. Clear correlation can be observed between H3 and the ^{13}C peak at 132.54 ppm, and H4 and the ^{13}C peak at 133.96 ppm, allowing these peaks to be assigned to C3 and C4 respectively.

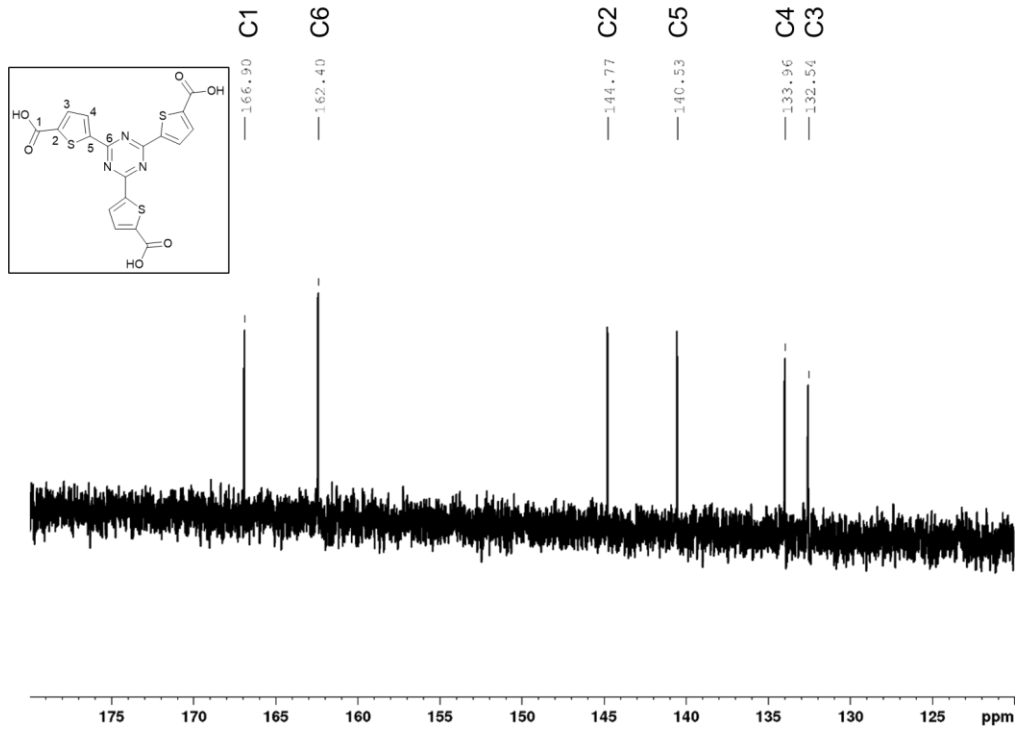

Fig. 3.7 ^{13}C NMR spectrum of H_3**TTT** (150 mHz, d_6-DMSO), with inset of H_3**TTT**, showing labelled C-atoms.

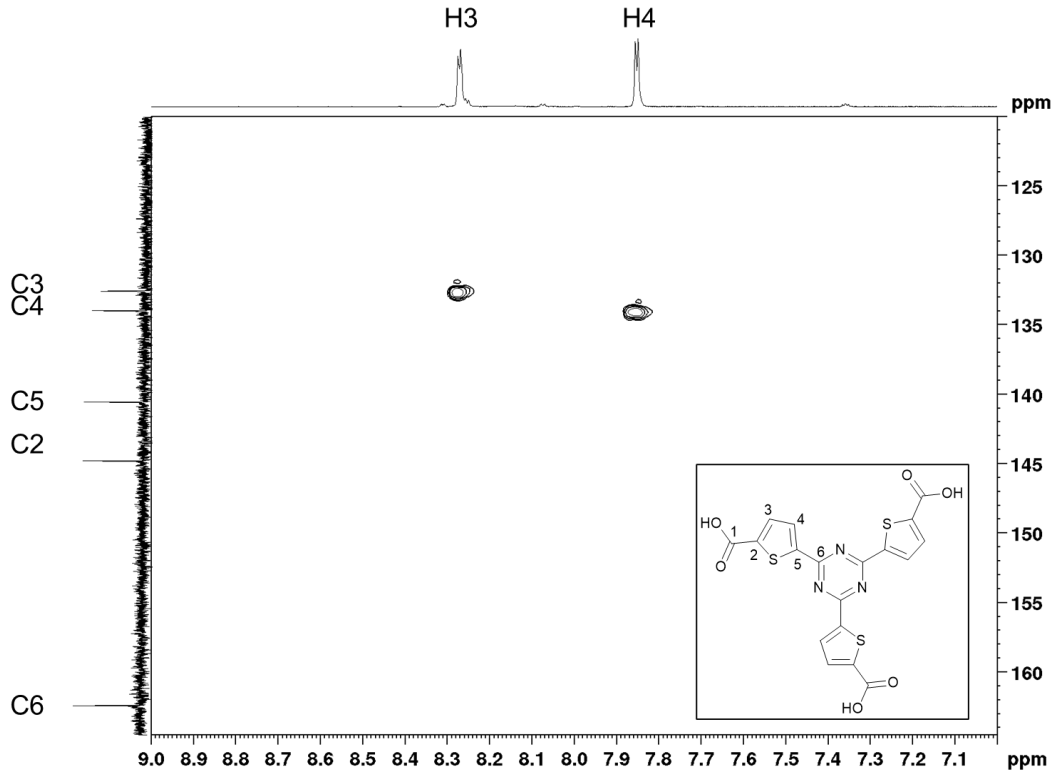

Fig. 3.8 HSQC spectrum of H_3**TTT** with inset of H_3**TTT**, showing labelled H-atoms and C atoms.

Finally, the HMBC spectrum of H_3**TTT** (**Fig. 3.9**) could be used to assign C2, C5 and C6 to the correct values. In HMBC spectra, correlations that occur through three bonds are often stronger than correlations that occur through two bonds, especially in aromatic systems. Cross peaks occur between H3 and the ^{13}C peaks at 144.77 and 140.53 ppm. Cross peaks can also be seen between H4 and these two protons. However stronger interactions can be observed between H3 and the ^{13}C peak at 140.53 and H4 and the ^{13}C peak at 144.77 ppm. The ^{13}C peaks at 144.77 ppm and 140.53 ppm can therefore be assigned to C2 and C5 respectively. Correlations can also be observed between H3 and the ^{13}C peak at 166.90 ppm, confirming that this peak can be assigned to C1. The ^{13}C peak at 162.40 ppm can be assigned to the triazine carbon atoms, C6.

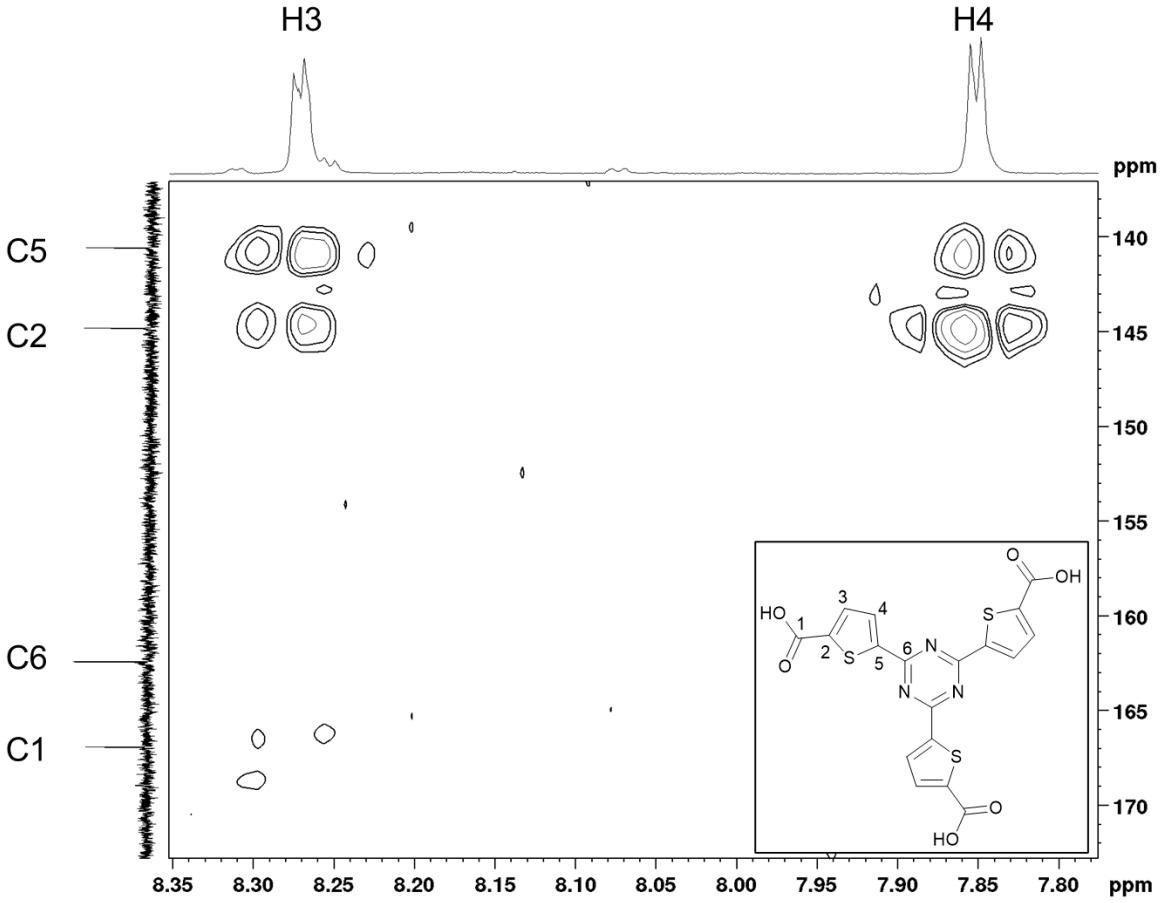

Fig. 3.9 HMBC spectrum of H_3**TTT,** with inset of H_3**TTT**, showing labelled H-atoms and C atoms.

3.2.4 Fourier-Transform Infrared (FTIR) spectroscopy of H_3TTT

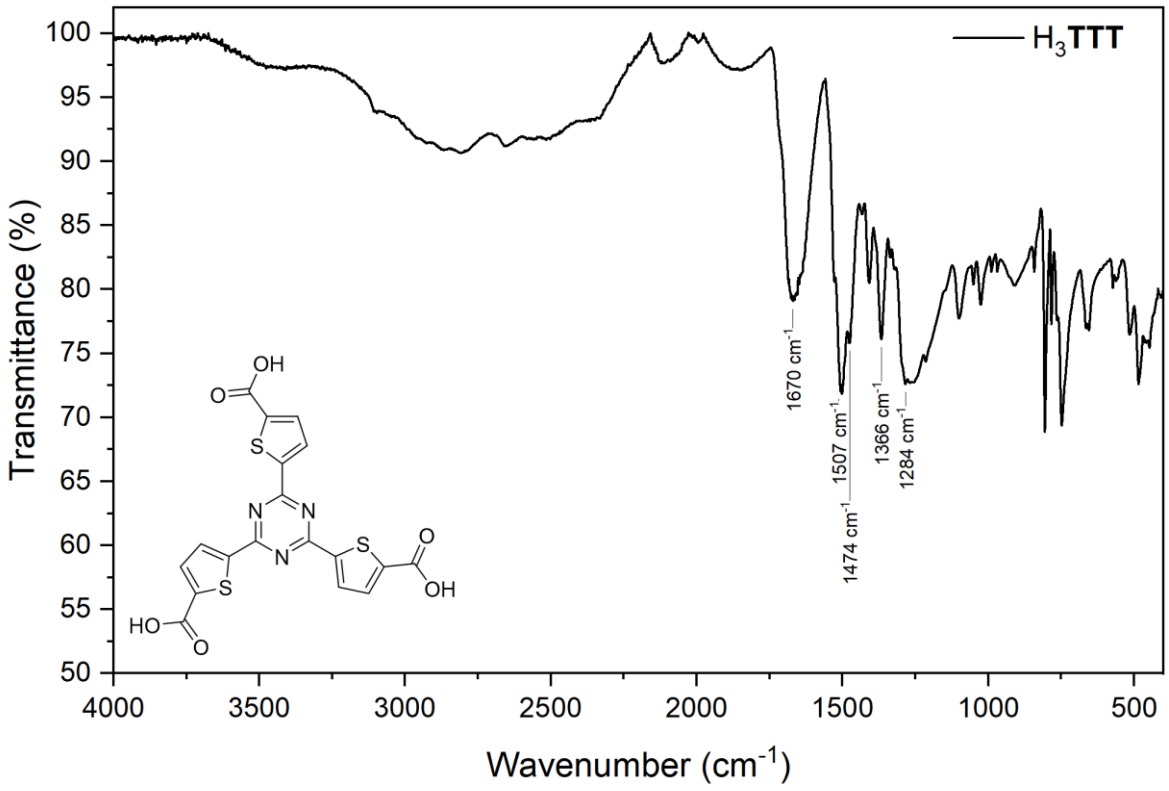

Fig. 3.10 FTIR spectrum of H_3**TTT**, with characteristic vibrational bands labelled.

The FTIR spectrum of H_3**TTT** is shown in **Fig. 3.10**. The broad band from approximately 3200 to 2150 cm^{-1} arises from the O-H vibration of the carboxylate moieties of H_3**TTT**, in addition to C-H bond stretching arising from the thiophene rings in the molecule.

Comparison of the FTIR spectra of H_3**TTT** and 2,4,6-tri(thiophen-2-yl)-1,3,5-triazine allows identification of the vibrational bands associated with the carboxylic acid moieties in H_3**TTT** (**Fig. 3.11**), confirming successful synthesis of H_3**TTT**. The strong vibrational band at 1670 cm^{-1} can be assigned to the asymmetric C=O stretching vibration in H_3**TTT**, as this vibration is absent in the FTIR spectrum of 2,4,6-tri(thiophen-2-yl)-1,3,5-triazine. The band which appears as a shoulder at 1507 cm^{-1} in the FTIR spectrum of H_3**TTT** corresponds to the symmetric C=O stretch (ν_{sym}) and Δ, the difference between ν_{asym} and ν_{sym} is 163 cm^{-1}. The vibrational band at 1284 cm^{-1} can be assigned to the carboxylate C-O stretch. The vibrations of the bonds in the triazine ring can be observed at 1474 and 1366 cm^{-1} in the FTIR spectrum of H_3**TTT**, and 1500 and 1372 cm^{-1} in 2,4,6-tri(thiophen-2-yl)-1,3,5-triazine.

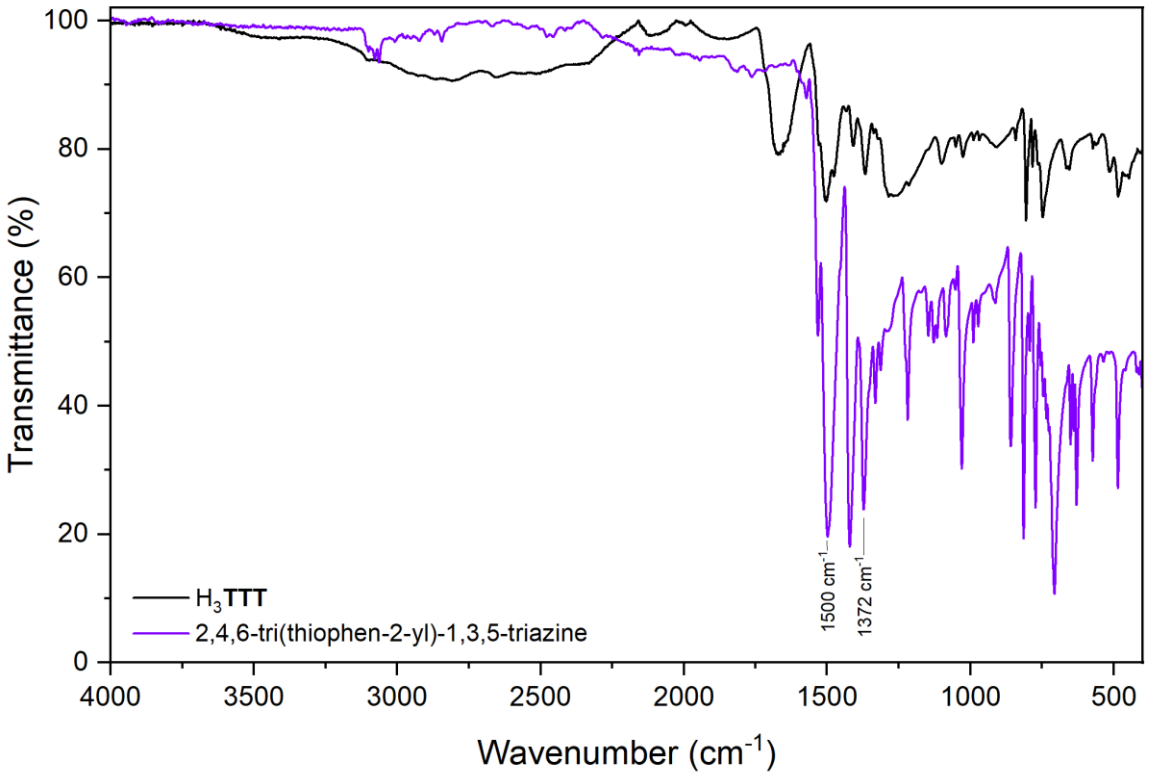

Fig. 3.11 Comparison of FTIR spectra of 2,4,6-tri(thiophen-2-yl)-1,3,5-triazine and H_3**TTT**, with triazine vibrational bands in 2,4,6-tri(thiophen-2-yl)-1,3,5-triazine labelled.

3.2.5 Photochemistry

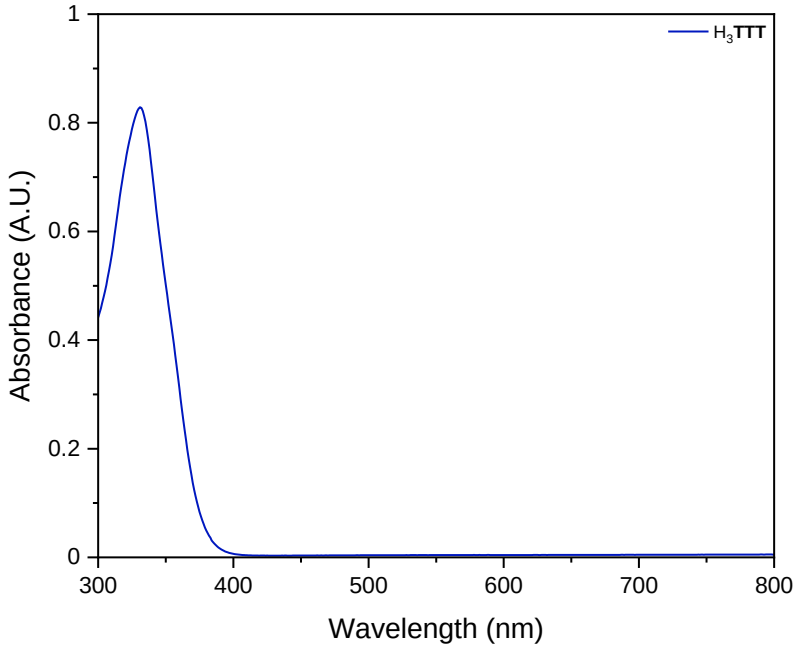

Fig. 3.12 UV-Vis spectrum of H_3**TTT** in DMF solution.

Photochemical studies of H_3**TTT** in degassed DMF solution were carried out at room temperature. The UV-vis absorption spectrum of H_3**TTT** in DMF solution shows a λ_{max} of 330 nm (**Fig. 3.12**). These correspond to π-π* transitions in the conjugated system of H_3**TTT**.

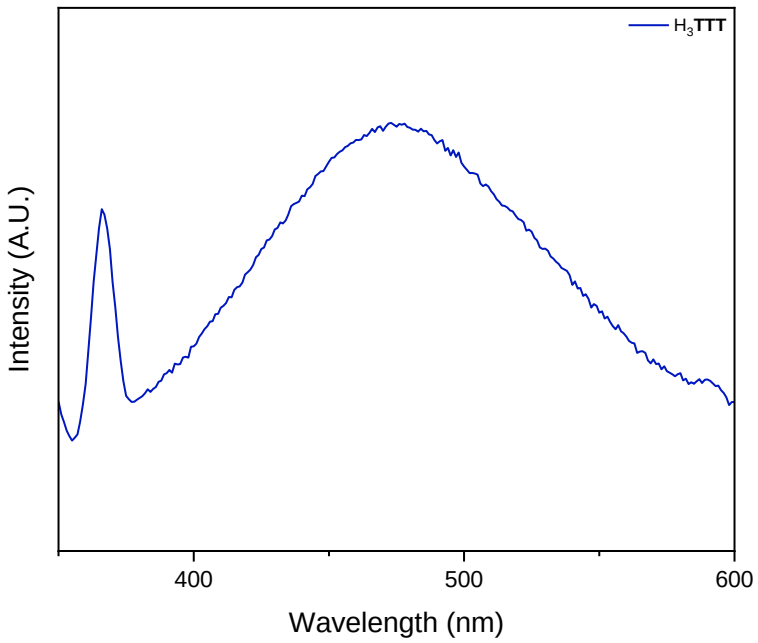

Fig. 3.13 Photoluminescence spectrum of a solution of H_3**TTT** in DMF (λ_{ex} = 330 nm).

When a solution of H_3**TTT** in DMF is excited at 330 nm, two emission bands can be observed in the photoluminescence spectrum (**Fig. 3.13**). The first, sharper emission band has a λ_{max} of 366 nm. The emission spectrum of H_3**TTT** also shows a broad emission band in the visible region of the spectrum, with a maximum at ca. 475 nm. This can also be observed with the naked eye when a solution of H_3**TTT** is irradiated with UV light (365 nm).

3.3 Synthesis of MOFs Based on La^{III}, Ce^{III}, Pr^{III} and Nd^{III}

3.3.1 Solvothermal Synthesis of MOFs

Following the successful synthesis of H_3**TTT** and investigation of the photophysical properties of the ligand, work commenced on synthesis of Ln-MOFs based on this ligand. Initially, reaction with the first four metals in the lanthanide series was investigated; La, Ce, Pr and Nd. In order to determine what conditions were required to obtain phase pure crystalline MOFs with sizes appropriate for single crystal XRD analysis, systematic screening across a range of parameters were investigated, as the structures formed by MOFs are known to be dependent on a range of conditions.[32] The parameters varied in this work were: temperature, reaction duration, reactant concentration and metal:ligand ratio.

Reaction of H_3**TTT** with Ln^{III} salts in a 1:1 ligand:metal ratio at 100 °C gave crystals gave a series of isostructural Ln-MOFs with the formula [Ln(**TTT**)(DMF)]·2DMF (Ln= La (**La-MOF**), Ce (**Ce-**

MOF), Pr (**Pr-MOF**), Nd (**Nd-MOF**)). The synthesis of each MOF required different reaction durations. In the case of **La-MOF** and **Ce-MOF**, H_3**TTT** was reacted with $La(NO_3)_3{\cdot}6H_2O$ or $CeCl_3{\cdot}7H_2O$ respectively for 24 hours. A reaction duration of 48 hours between H_3**TTT** and $Pr(NO_3)_3{\cdot}6H_2O$ was required for synthesis of **Pr-MOF**. Crystals of **Nd-MOF** formed after reacting H_3**TTT** and $Nd(NO_3)_3{\cdot}6H_2O$ for 72 hours. Crystals of the Ln-MOFs (Ln= La, Ce, Pr and Nd) formed as dense clusters of needle-shaped crystals. Cutting a single needle crystal from the cluster gave single crystals of a sufficient size and quality for single crystal XRD analysis.

3.3.2 Crystal Structure Description

Each of the isostructural MOFs **La-MOF**, **Ce-MOF**, **Pr-MOF** and **Nd-MOF** have been studied by single crystal XRD, and the unit cell parameters are summarised in **Table 3.3** for each MOF. **Ce-MOF** was chosen as a representative strucure for detailed discussion in this section. The full crystal data and refinement results for **Ce-MOF** are summarised in **Table 3.4**.

Table 3.3 Unit cell parameters of **La-MOF**, **Ce-MOF**, **Pr-MOF** and **Nd-MOF**.

Compound name	**La-MOF**	**Ce-MOF**	**Pr-MOF**	**Nd-MOF**
Empirical formula	$LaC_{21}H_{13}N_4O_7$	$CeC_{21}H_{13}N_4O_7$	$PrC_{21}H_{13}N_4O_7$	$NdC_{21}H_{13}N_4O_7$
Crystal system	Monoclinic	Monoclinic	Monoclinic	Monoclinic
Space group	*Cc*	*Cc*	*Cc*	*Cc*
a (Å)	22.037(9)	21.7213(9)	21.866(3)	21.8299(11)
b (Å)	16.187(8)	16.0617(9)	16.0713(18)	16.0694(8)
γ (Å)	8.254(5)	8.1106(3)	8.1472(11)	8.0522(4)
α (°)	90	90	90	90
β (°)	93.17(2)	94.906(4)	93.84(4)	94.074(4)
γ (°)	90	90	90	90
V (Å^3)	2938(3)	2819.3(2)	2856.7(6)	2817.5(2)

The structure of **Ce-MOF** was solved and refined in the monoclinic space group *Cc*, and has the structural formula [Ce(**TTT**)(DMF)]·DMF. The asymmetric unit of **Ce-MOF** contains one Ce^{III} ion, one $\mathbf{TTT}^{3-}$ ligand, one coordinated DMF solvent molecule and one non-coordinating DMF molecule in the pores of the MOF (**Fig. 3.14**). ORTEP-3 software[33] was used to generate the ORTEP of **Ce-MOF**, shown in **Fig. 3.15**.

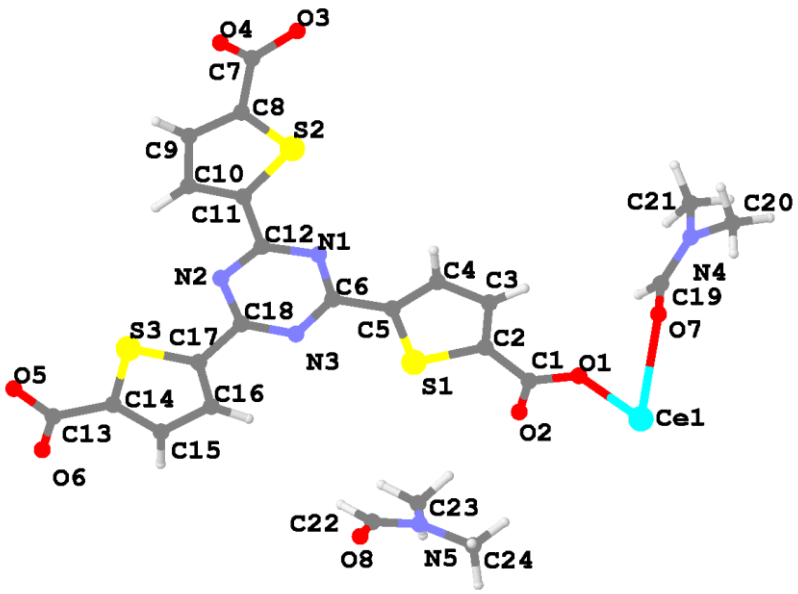

Fig. 3.14 Asymmetric unit of **Ce-MOF** with selected atoms labelled. Atom colour scheme: Ce, turquoise, S, yellow, C, dark grey, N, blue, O, red, H, white.

Table 3.4 Crystal data and refinement results for **Ce-MOF**.

Compound name	**Ce-MOF**
Empirical formula	$CeC_{21}H_{13}N_4O_7$
Formula weight	614.78
Temperature (K)	100.01
Crystal description	Colourless needles
Crystal system	Monoclinic
Space group	*Cc*
a (Å)	21.7213(9)
b (Å)	16.0617(9)
c (Å)	8.1106(3)
α (°)	90
β (°)	94.906(4)
γ (°)	90
V (Å^3)	2819.3(2)
Z	4
ρ_{calc} (g/cm^3)	1.448
μ (mm^{-1})	14.862
F(000)	1181.0
Radiation	CuKα (λ = 1.54178)
2θ range for data collection (°)	6.854 to 108.628
Reflections collected	24657
Independent reflections	3396
Data/restraints/parameters	3396/107/374
Goodness-of-fit on F^2	1.086
R_1 [I≥2σ (I)], all	0.0665, 0.0787
wR_2 [I≥2σ (I)], all	0.1608, 0.1693
Largest diff. peak/hole (e Å^{-3})	1.34/ -1.68

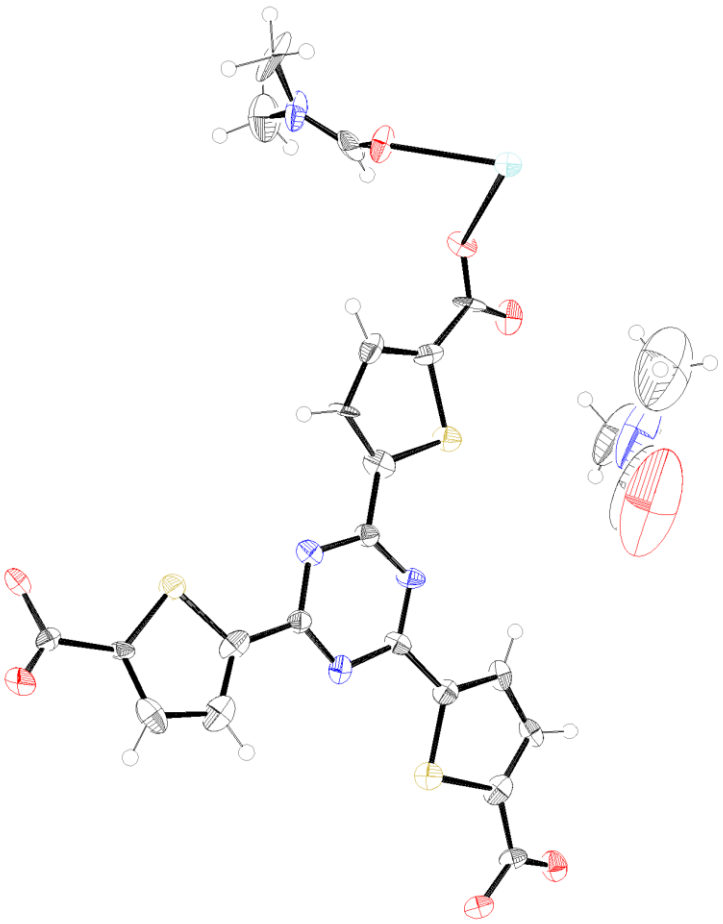

Fig. 3.15 ORTEP of the asymmetric unit of **Ce-MOF,** viewed along the crystallographic *c*-axis. Thermal probabilities are shown at the 50% probability level. Atom colour scheme: Ce, turquoise, S, yellow, C, dark grey, N, blue, O, red, H, white.

In **Ce-MOF** the Ce^{III} ions form an infinite rod shaped SBU, in which a chain of Ce^{III} ions extends parrallel to the crystallographic *c* axis (**Fig. 3.16**). Each Ce^{III} ion in **Ce-MOF** is ten-coordinate, with one bond to the oxygen atom of a coordinated DMF molecule and nine bonds to the carboxylate oxygen atoms of the $\mathbf{TTT}^{3-}$ ligand. Each carboxylate moeity of $\mathbf{TTT}^{3-}$ adopts a chelating bridging μ_2-η^2:η^1 coordination mode. The infinite rod-shaped SBU consists of a zig-zag chain of Ln^{III} ions, in which the metal cations are linked by the bridging carboxylates of $\mathbf{TTT}^{3-}$. The Ln-Ln distance in **Ce-MOF** is 4.0896(3) Å. An interesting feature of **Ce-MOF** is that the coordinated DMF molecules on successive Ce^{III} ions bind from the same direction, giving a chain of DMF molecules **Fig. 3.17**. The chains of Ln^{III} ions in **Ce-MOF** are close to linear with Ce-Ce-Ce angles of 165.15(6) °, giving a slight zig-zag shape in the SBU.

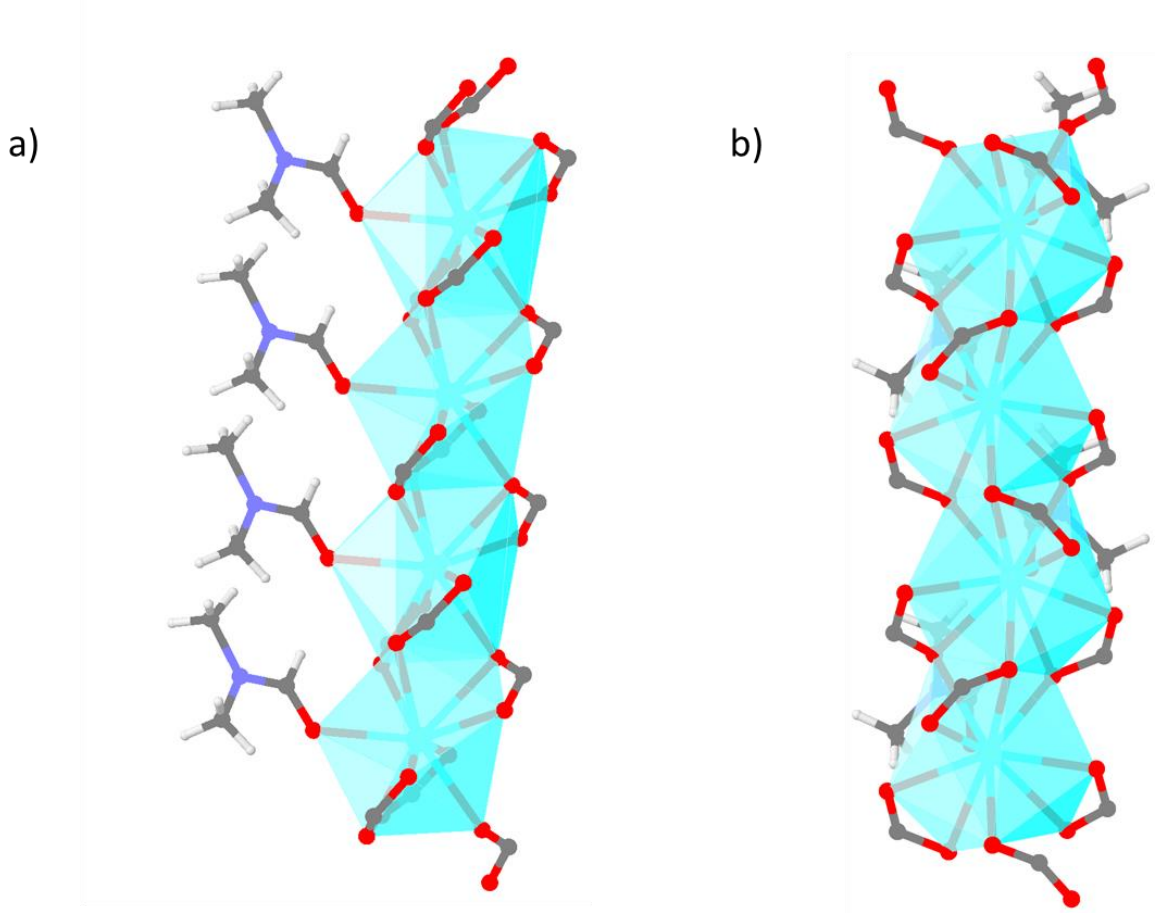

Fig. 3.16 The coordination environment of the Ce^{III} ions in the infinite one-dimensional rod-shaped SBUs of **Ce-MOF a)** along the crystallagraphic *b*-axis and **b)** along the crystallographic *a*-axis. Atom colour scheme: Ce, turquoise, S, yellow, C, dark grey, N, blue, O, red, H, white.

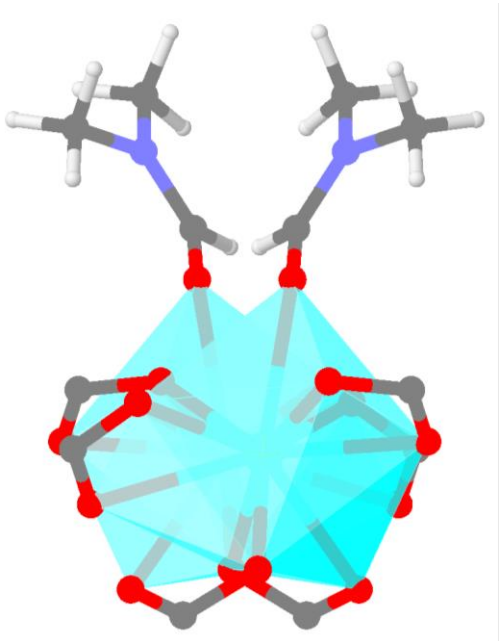

Fig. 3.17 The Ce^{III} rod-shaped SBU in **Ce-MOF**, as viewed along the crystallographic *c*-axis. Atom colour scheme: Ce, turquoise, C, dark grey, N, blue, O, red, H, white.

Table 3.5 Ln^{III}-O bond lengths (Å) in **Ce-MOF**.

Bond	Distance	**Ce-MOF** Bond Length (Å)
Ce^{III}-O	Ce^{III}-O1	2.738(14)
	Ce^{III}-O1	2.456(16)
	Ce^{III}-O2	2.514(17)
	Ce^{III}-O3	2.588(17)
	Ce^{III}-O3	2.693(17)
	Ce^{III}-O4	2.522(16)
	Ce^{III}-O5	2.670(14)
	Ce^{III}-O5	2.644(14)
	Ce^{III}-O6	2.586(17)
	Ce^{III}-O7	2.505(16)

Olex2 software was used to measure the Ce^{III}-O bond distances in **Ce-MOF**.[34] The Ce^{III}-O distances are displayed in **Table 3.5**. The Ce^{III}-O distances bond lengths range from 2.456(16) to 2.738(14) Å. These values are in good agreement with the ranges previously reported for Ce^{III} ions.[35]

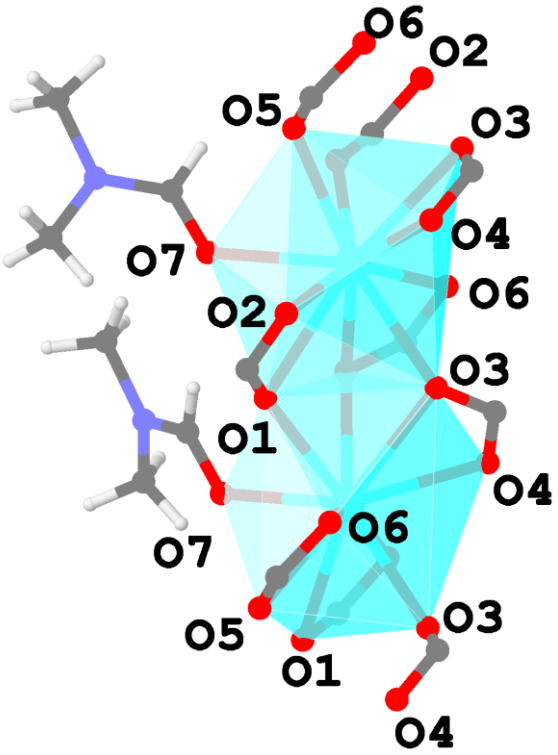

Fig. 3.18 Coordination environment of Ce^{III} ions in **Ce-MOF**, with O atoms labelled. Atom colour scheme: Ce, turquoise, C, dark grey, N, blue, O, red, H, white.

Shape 2.1 software[36] was used to further study the coordination environment of the Ce^{III} ions in **Ce-MOF**. The continuous shape measurement values for **Ce-MOF** are presented in **Table 3.6.** The lowest value was obtained for sphenocorona coordination geometry, indicating that the Ce^{III} have the closest fit to that coordination geometry.

Table 3.6 Continuous shape measurement values for Ce^{III} atoms in **Ce-MOF**. The lowest value (indicating closest fit) is highlighted in bold.

Shape	**Symmetry**	**Continuous shape measurement value**
Decagon	D_{10h}	34.067
Enneagonal pyramid	C_{9v}	20.494
Octagonal bipyramid	D_{8h}	19.071
Pentagonal prism	D_{5h}	12.080
Pentagonal antiprism	D_{5d}	11.408
Bicapped cube (J15)	D_{4h}	11.634
Bicapped square antiprism (J17)	D_{4d}	4.742
Metabidiminished icosahedron (J62)	C_{2v}	6.241
Augmented tridiminished icosahedron (J64)	C_{3v}	15.532
Sphenocorona (J87)	**C_{2v}**	**3.052**
Staggered Dodecahedron (2:6:2)	D_2	6.551
Tetradecahedron (2:6:2)	C_{2v}	5.710
Hexadecahedron (2:6:2) or (1:4:4:1)	D_{4h}	10.386

BVS calculations[37] were used to confirm the oxidation state of Ce^{III} ions in **Ce-MOF**, using the bond lengths shown in **Table 3.5**. The BVS results obtained (**Table 3.7**) confirm that the Ce ions in **Ce-MOF** are present in the +III oxidation state, as expected. The R_0 value used for ten-coordinate Ce-O bonds is 2.121 Å.[38]

Table 3.7 BVS analysis of metal centres in **Ce-MOF**.

Metal ion	R_0 (Å)	BVS	Oxidation state
Ce1	2.121	2.88	+III

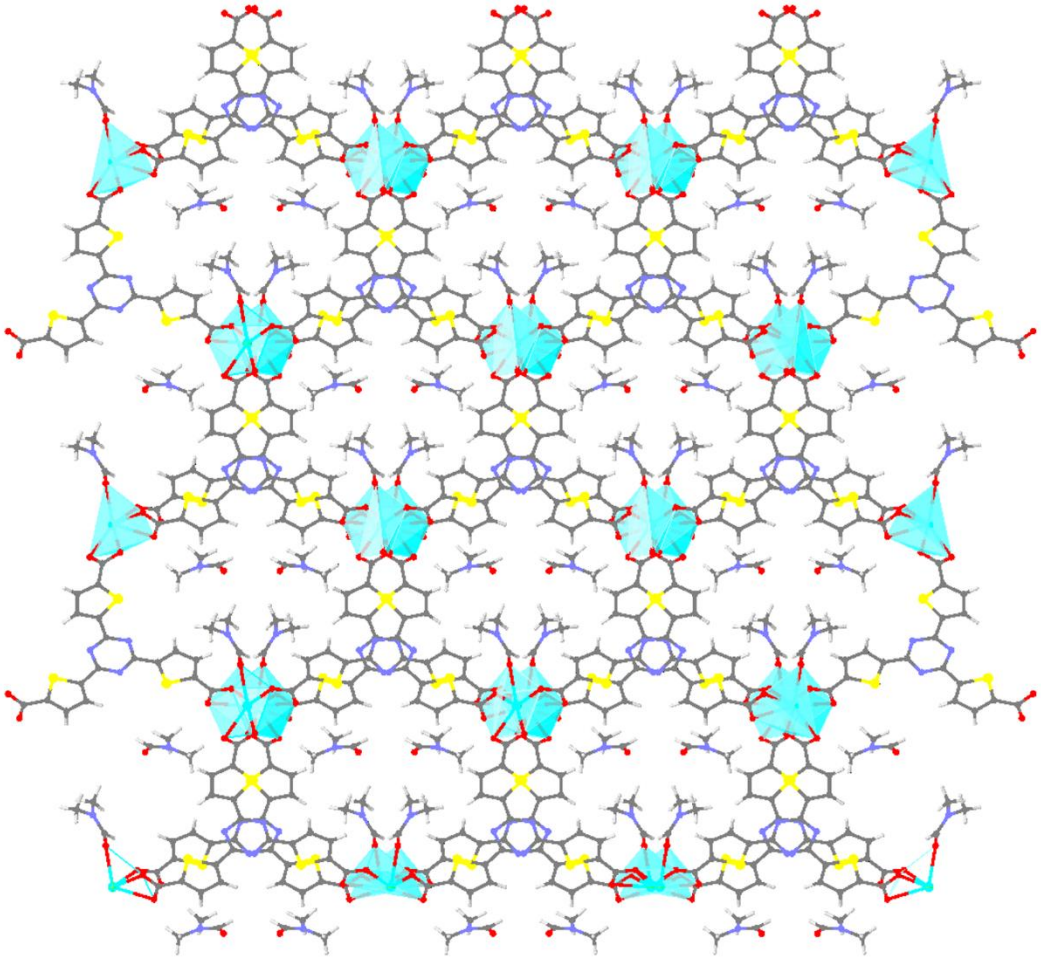

Fig. 3.19 Crystal structure of **Ce-MOF** viewed along the crystallographic *c*-axis Atom colour scheme: Ce, turquoise, S, yellow, C, dark grey, N, blue, O, red, H, white.

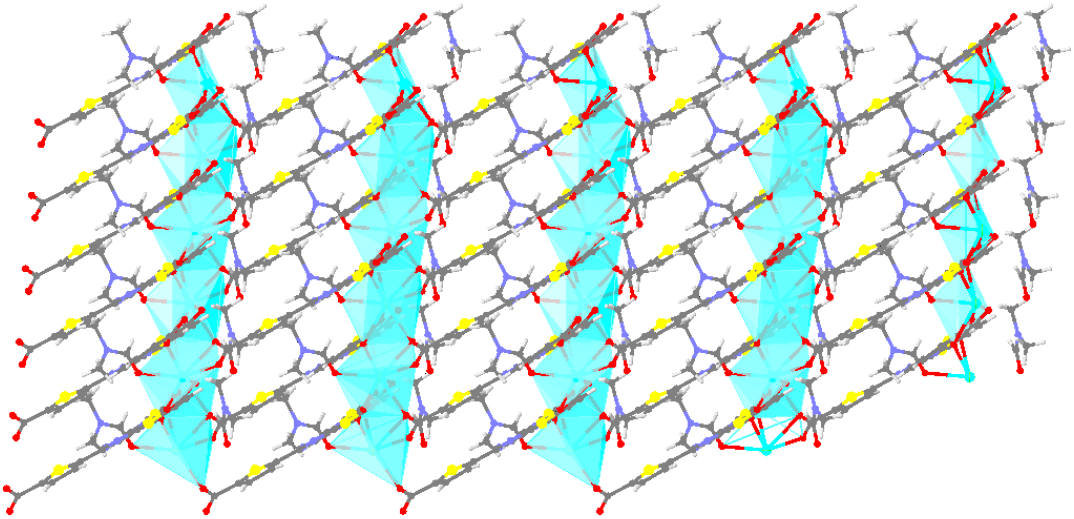

Fig. 3.20 Crystal structure of **Ce-MOF** viewed along the crystallographic b-axis Atom colour scheme: Ce, turquoise, S, yellow, C, dark grey, N, blue, O, red, H, white.

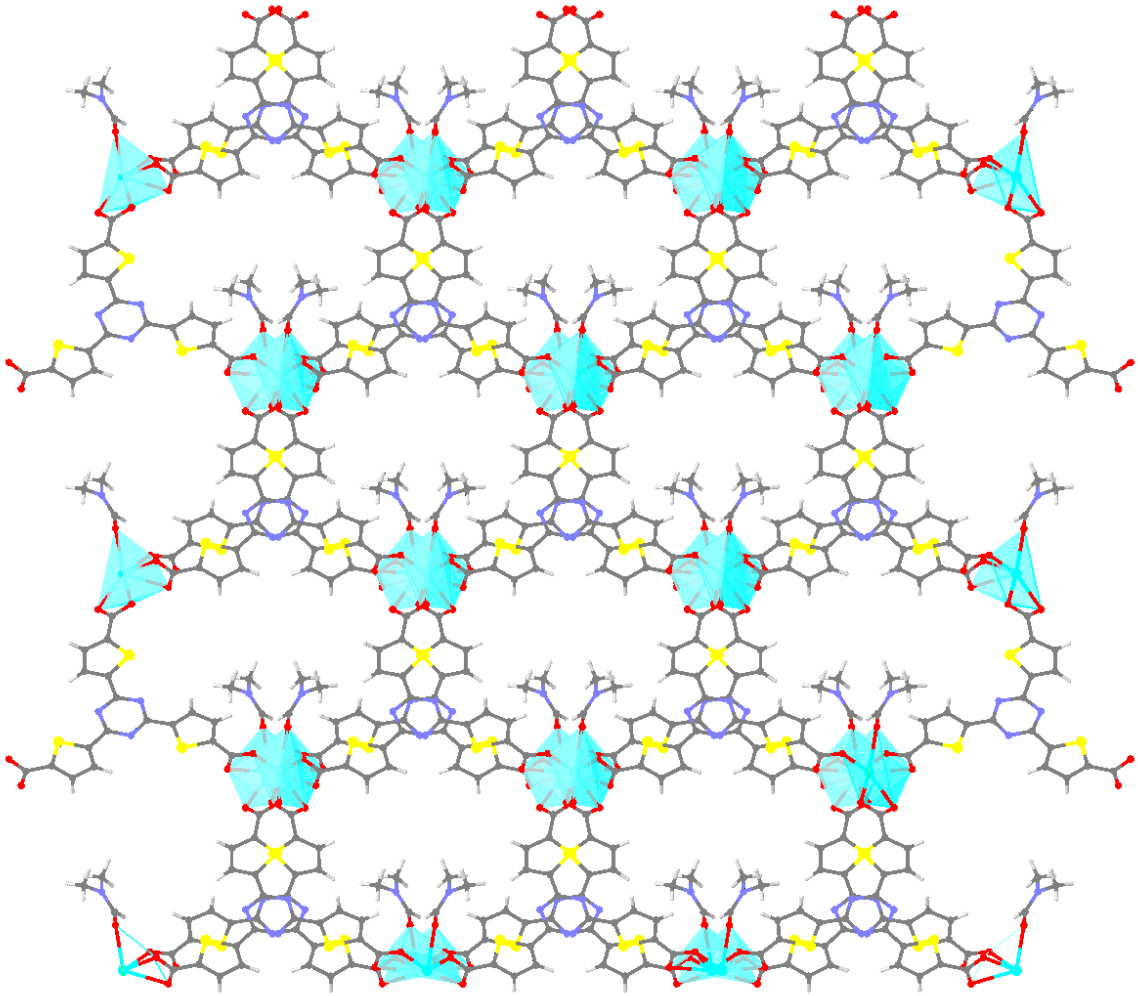

Fig. 3.21 Crystal structure of **Ce-MOF** viewed along the crystallographic *c*-axis, with non-coordinating DMF molecules removed for clarity. Atom colour scheme: Ce, turquoise, S, yellow, C, dark grey, N, blue, O, red, H, white.

In crystals of **Ce-MOF** (as well as in the isostructural **La-MOF**, **Pr-MOF** and **Nd-MOF**), the MOF forms a three-dimensional structure, with channels along the crystallographic *c*-axis that are approximately hexagonal in shape.

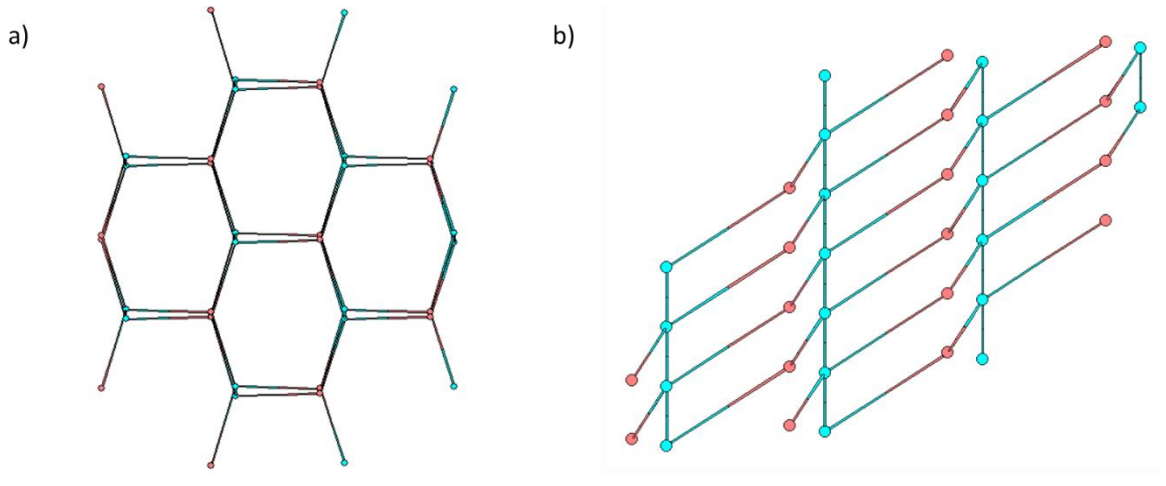

Fig. 3.22 Topological representation of **Ce-MOF**, as viewed along the crystallographic **a)** *c*-axis and **b)** *b*-axis. Colour scheme: turquoise (Ce^{III} ions), pink ($\mathbf{TTT}^{3-}$ ligand).

The topology of **Ce-MOF** was analysed using the the ToposPro software.[39] The MOF forms a binodal 3,5-connected net with **hms** topology (**Fig. 3.22**). The stoichiometry of this net is (3-c)(5-c), and the net has point symbol $\{6^3\}\{6^9.8\}$. Each Ce^{III} ion acts as a 5-connected node, as it is coordinated to three $\mathbf{TTT}^{3-}$ linkers and two other Ce^{III} ions, and each $\mathbf{TTT}^{3-}$ linker as a 3-connected node.

The unit cell parameters of the Ln-MOFs are summarised in **Table 3.3**. A plot of unit cell volume in **La-MOF**, **Ce-MOF**, **Pr-MOF** and **Nd-MOF** is shown in **Fig. 3.23**. Due to lanthanide contraction, a steady decrease in unit cell volume was expected with increasing atomic number of the Ln^{III} ion in this series of isostructural MOFs, has been observed in other isostructural series of Ln-MOFs.[40] Interestingly, a large drop in unit cell volume occurs between **La-MOF** and **Ce-MOF**, followed by an increase from **Ce-MOF** to **Pr-MOF**, and a further decrease between **Pr-MOF** and **Nd-MOF**.

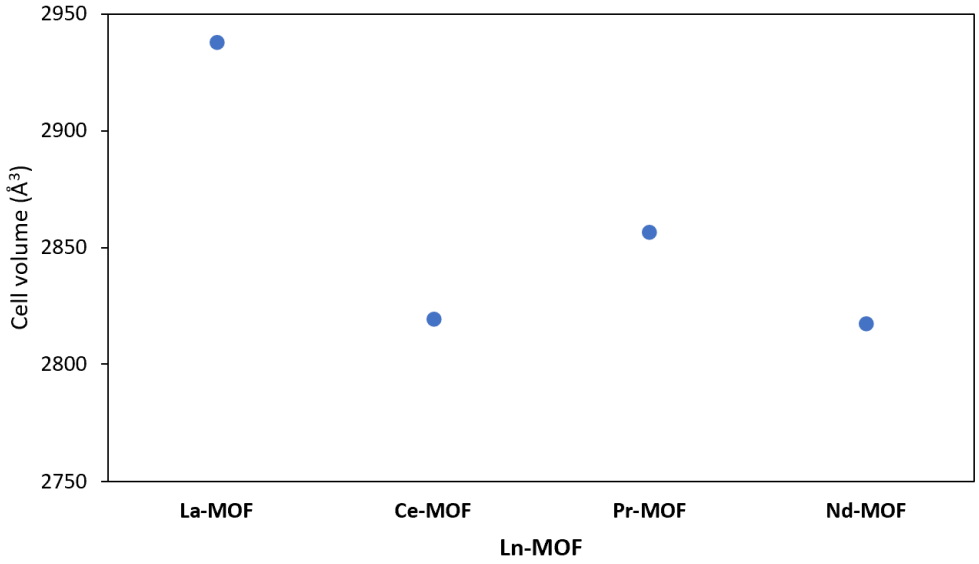

Fig. 3.23 Plot of unit cell volume for each **Ln-MOF** in this isostructural series.

The structure of **Ce-MOF** was studied using the **calcvoid** routine in Olex2 software,[34] in order to understand the voids and channels within the framework. These calculations indicate that **Ce-MOF** occupies 64.89% of the cell volume. The radius of the largest spherical void in the structure is 1.6 Å, and the largest channel in the structure is in the crystallographic *c*-direction, which can be penetrated by a sphere with 0.8 Å radius.

When the non-coordinating DMF molecules are removed from the structure, the voids and channels become larger. The largest spherical void in the structure is 2.20 Å upon removal of DMF, and the *c*-direction can be penetrated by a sphere with radius 1.8 Å.

Previously, a series of Ln-MOFs (Ln= La, Ce, Pr) have been reported by Kitagawa and coworkers, using the organic linker benzene-1,3,5-tris(2-thiophene-carboxylate) ($BTTc^{3-}$).[41] The MOFs synthesised with $BTTc^{3-}$, La-BTTc, Ce-BTTc and Pr-BTTc, are isostructural with this series of MOFs reported here, using $\mathbf{TTT}^{3-}$ as a linker. Kitagawa and coworkers reported that the removal of

the coordinated solvent molecules from the La^{III} ions in La-BTTc lead to a series of alligned open metal sites, which behaved as Lewis acid sites. La-BTTc can be used as a Lewis acid catalyst for cyanosilylation reactions. The optical and gas sorption properties of La-BTTc were not reported by Kitagawa and coworkers.

3.3.3 Scanning Electron Microscopy and Energy Dispersive X-Ray Spectroscopy of Ln-MOFs

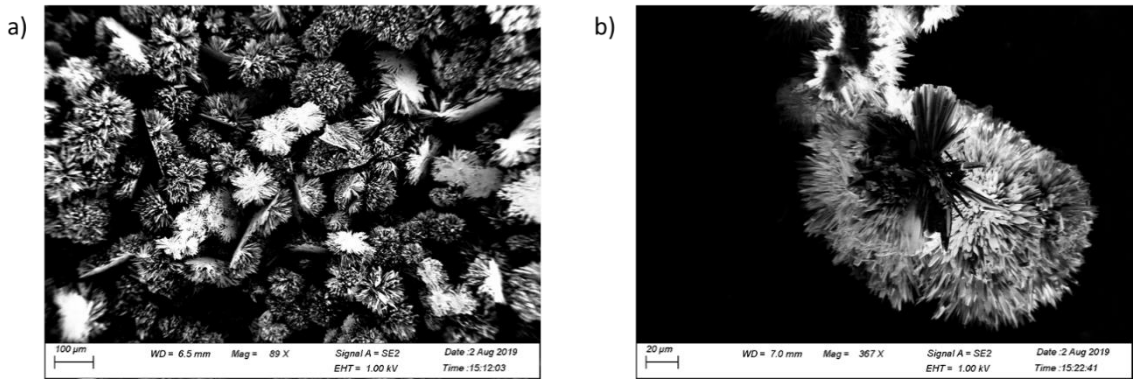

Fig. 3.24 SEM images of **a) La-MOF** crystals and **b) Nd-MOF** crystals.

Scanning electron microscopy (SEM) was used to image crystals of **La-MOF** and **Nd-MOF**. The crystals form as dense clusters of acicular crystals, which radiate from a central point (**Fig. 3.24**).

3.3.4 Fourier-Transform Infrared (FTIR) spectra of La-MOF, Ce-MOF, Pr-MOF and Nd-MOF

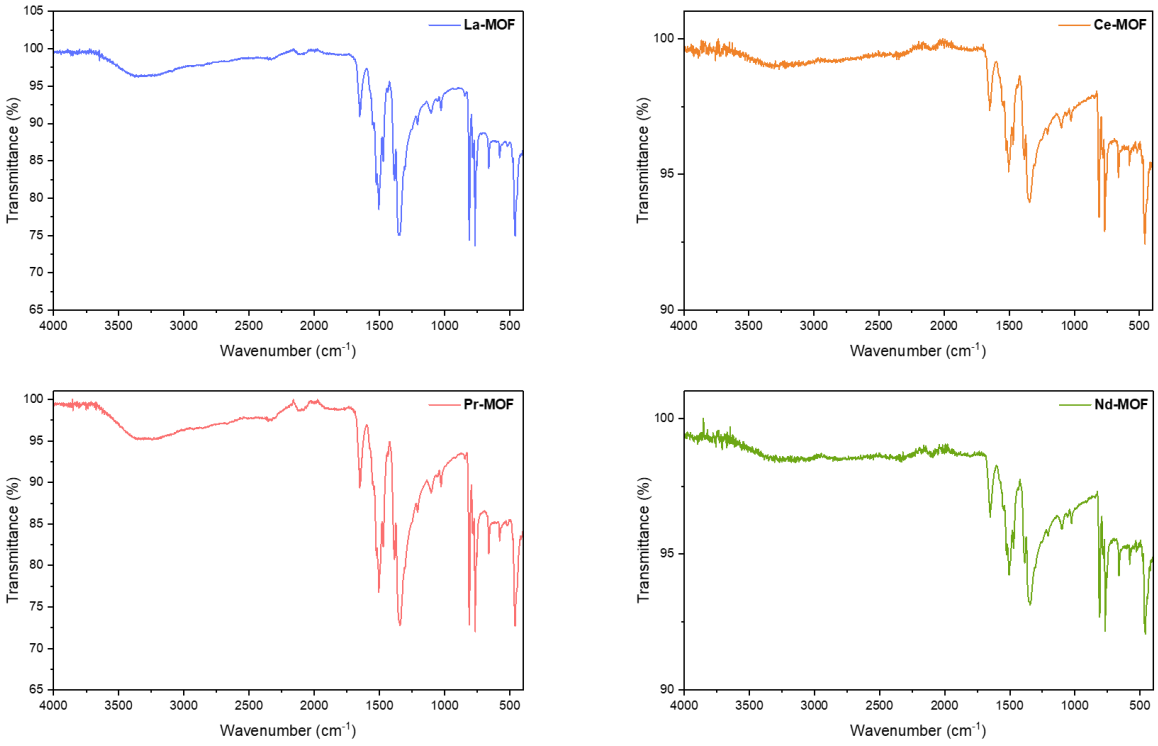

Fig. 3.25 FTIR spectra of **La-MOF** (top left), **Ce-MOF** (top right), **Pr-MOF** (bottom left) and **Nd-MOF** (bottom right)

FTIR spectroscopy was used to analyse the series of Ln-MOFs (**Fig. 3.25**). The FTIR spectra of **La-MOF**, **Ce-MOF**, **Pr-MOF** and **Nd-MOF** are largely identical. Broad bands between approximately 3700 cm^{-1} and 2500 cm^{-1} arise from C-H stretching vibrations from the $\mathbf{TTT^{3-}}$ linkers in the MOF, as well C-H stretching and O-H stretching in co-crystallised DMF molecules. Comparison of the FTIR spectra of the Ln-MOFs (**Fig. 3.25**) with that of the linker, H_3**TTT** (**Fig. 3.10**) allowed the vibrational bands in the MOFs that correspond to the linker to be identified.

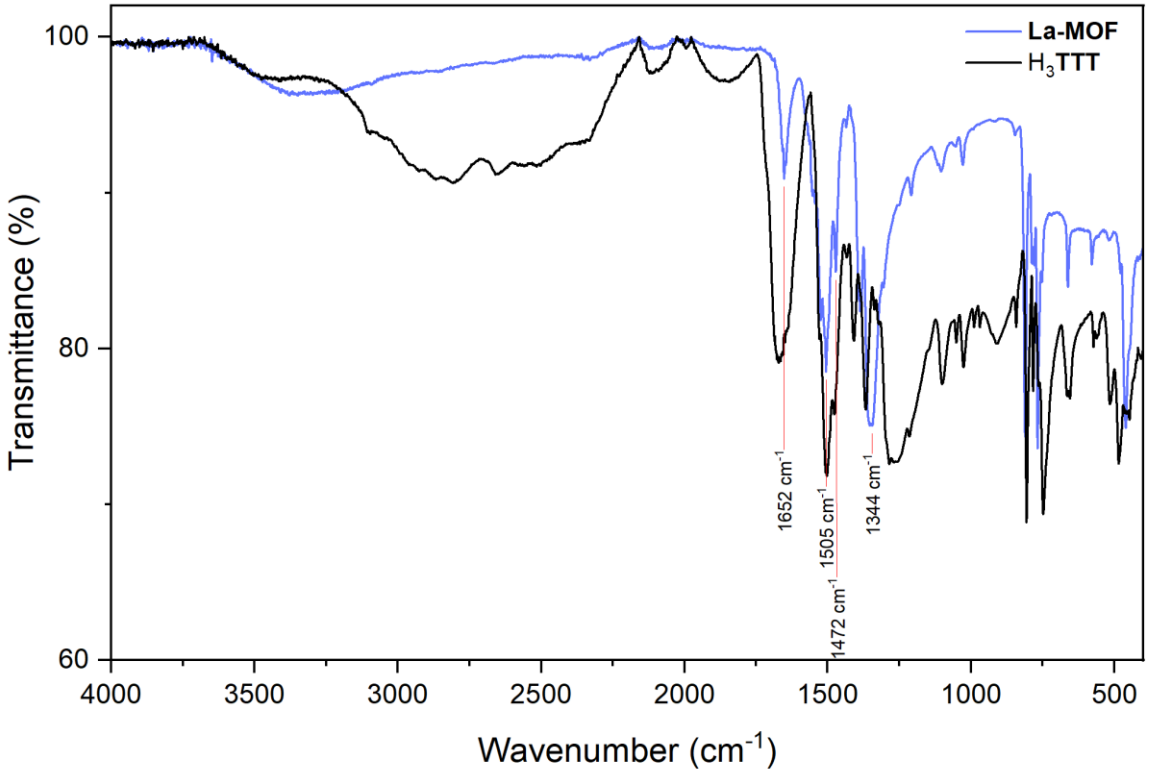

Fig. 3.26 Comparison of FTIR spectra of **La-MOF** and H_3**TTT**, characteristic peaks on the FTIR spectrum of **La-MOF** are labelled.

A comparison between the FTIR spectra of H_3**TTT** and **La-MOF** is shown in **Fig. 3.26**. In **La-MOF**, the coordinating carboxylates in the $\mathbf{TTT^{3-}}$ linker lead to an asymmetric stretching vibration at 1652 cm^{-1} and, as well as a symmetric stretching vibrational band at 1472 cm^{-1}. The difference between the average of the wavenumber of the symmetric and asymmetric C=O vibrations, Δ,[42] was calculated for each Ln-MOF. These values are summarised in **Table 3.8.** The triazine vibrational bands appear at 1505 cm^{-1} and 1344 cm^{-1} in **La-MOF**, and at very similar wavenumbers in the spectra of **Ce-MOF**, **Pr-MOF** and **Nd-MOF** (see chapter 2 for assignment of key vibrational bands in each of these MOFs).

Table 3.8 Asymmetric C=O stretch (ν_{asym}), symmetric C=O stretch (ν_{sym}), and the difference (Δ) between ν_{asym} and ν_{sym} for each MOF.

Compound	ν_{asym} (cm^{-1})	ν_{sym} (cm^{-1})	Δ (cm^{-1})
La-MOF	1652	1472	180
Ce-MOF	1652	1471	181
Pr-MOF	1652	1471	181
Nd-MOF	1652	1471	181

3.4 Stability of La-MOF, Ce-MOF, Pr-MOF and Nd-MOF

3.4.1 Thermogravimetric Analysis (TGA)

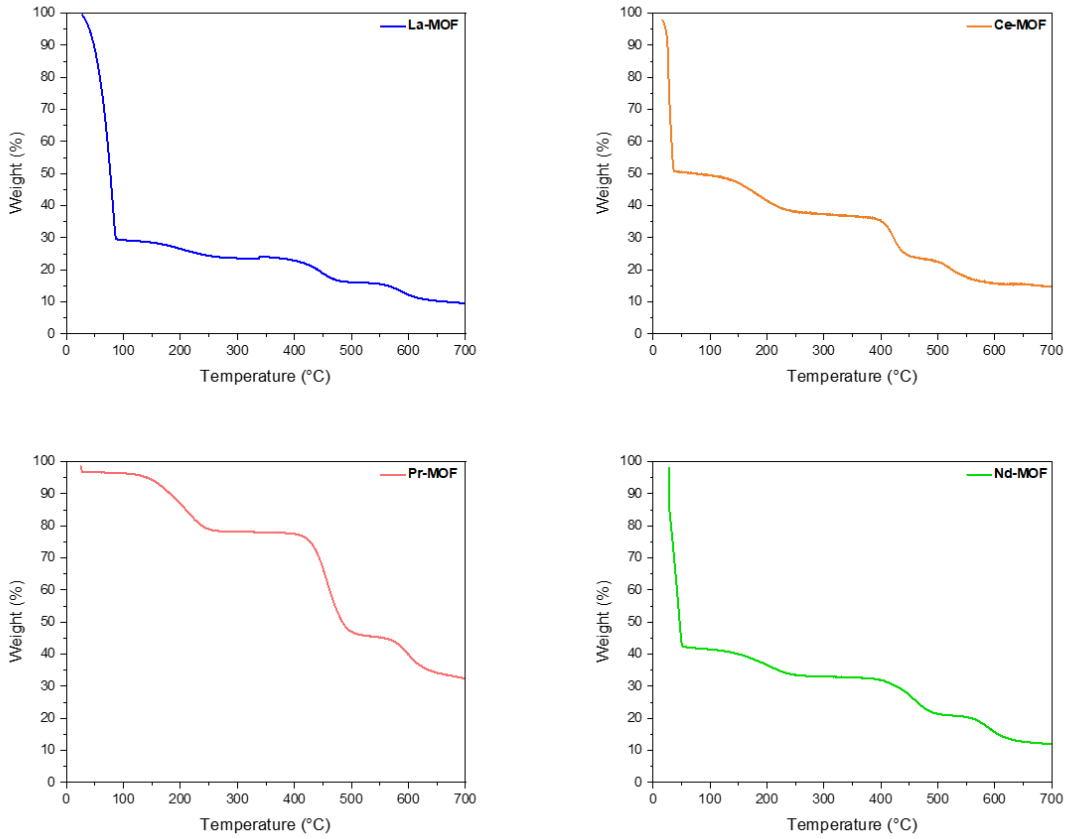

Fig. 3.27 Thermogravimetric analysis (TGA) curves of **La-MOF** (top left), **Ce-MOF** (top right), **Pr-MOF** (bottom left) and **Nd-MOF** (bottom right) samples as synthesised, under air flow (20 mL min^{-1}).

TGA measurements were used to assess the thermal stability of the MOFs (**Fig. 3.27**) as synthesised, under air flow. Three key steps are seen in the TGA curve of the MOFs, the first occurs below 100 °C and can be attributed to the loss of guest solvent molecules in the pores of the MOFs. The second step (between approximately 120 and 240 °C) can be attributed to loss of coordinated solvent molecules from the Ln^{III} ions in the structure. In air, the decomposition of the organic linker occurs over two decomposition steps, between approximately 400 and 650 °C. The remaining weight above this 650 °C is the remaining Ln metal from the inorganic SBUs. Thus, TGA measurements reveal that these MOFs are thermally stable to 400 °C.

3.4.2 PXRD Stability Tests

The phase purity of all MOFs was confirmed by powder XRD diffraction experiments. Visual comparison of the position of the experimental diffractions peaks with those in the calculated pattern for **Ce-MOF** confirmed that for all four Ln-MOFs, the powder XRD patterns of the MOFs as synthesised in good agreement with patterns simulated from the single crystal XRD data (**Fig. 3.28**). This indicates that the samples are phase pure, and do not lose crystallinity when stored in air, at room temperature.

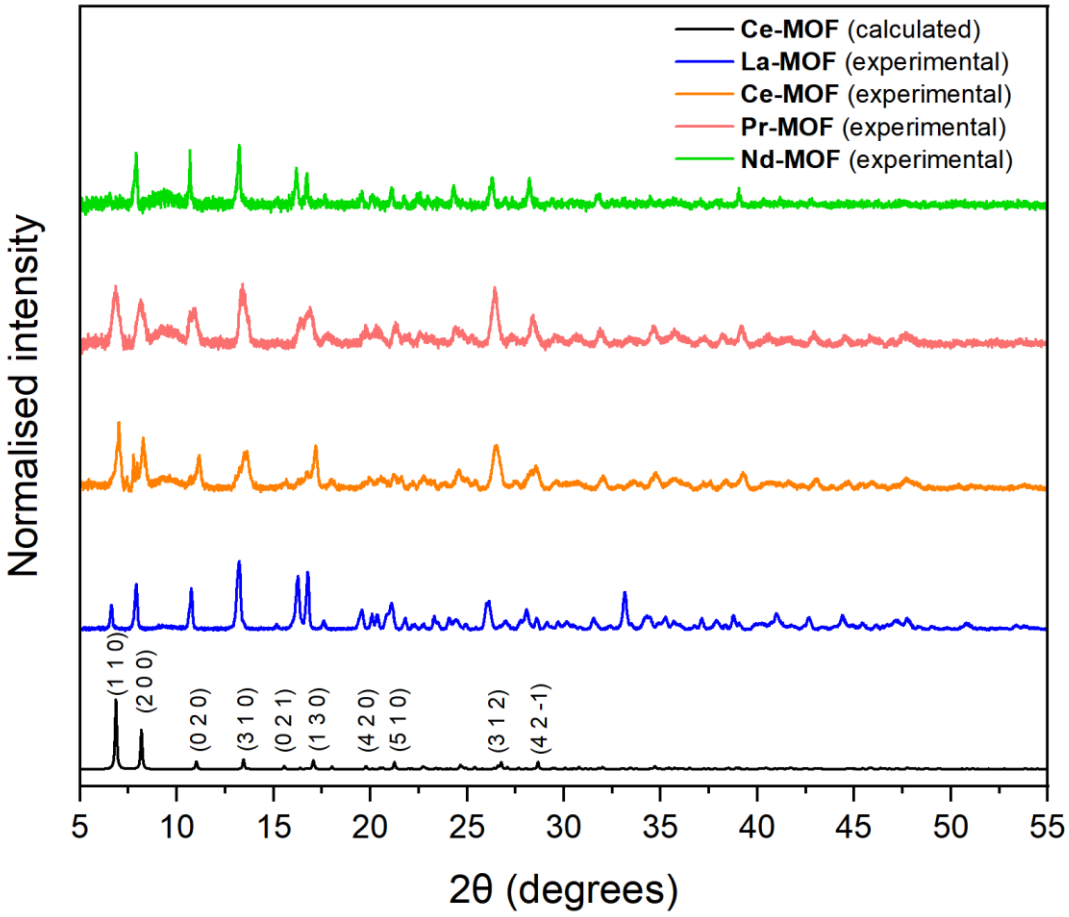

Fig. 3.28 Powder XRD patterns of **Ce-MOF** simulated from single crystal XRD experiments (with indexed diffraction peaks) compared to bulk samples of **La-MOF**, **Ce-MOF**, **Pr-MOF** and **Nd-MOF** as synthesised. Both the simulated and experimental patterns were normalised to facilitate comparison of the patterns. The experimental PXRD patterns were measured in air, at room temperature.

Powder XRD experiments were used to investigate whether a sample of **La-MOF** maintained its crystallinity after thermal activation (**Fig. 3.29**). A sample of **La-MOF** was heated to a temperature of 250 °C under vacuum. When compared to the TGA graph for this material, it was clear that at this temperature, all coordinated DMF would be removed, leaving a vacant coordination site on the La^{III} metal ion. The powder XRD pattern of **La-MOF** after thermal activation is in good agreement with the pattern of the MOF as synthesised, indicating that the MOF is stable to thermal activation, and maintains its structure after removal of coordinated solvent.

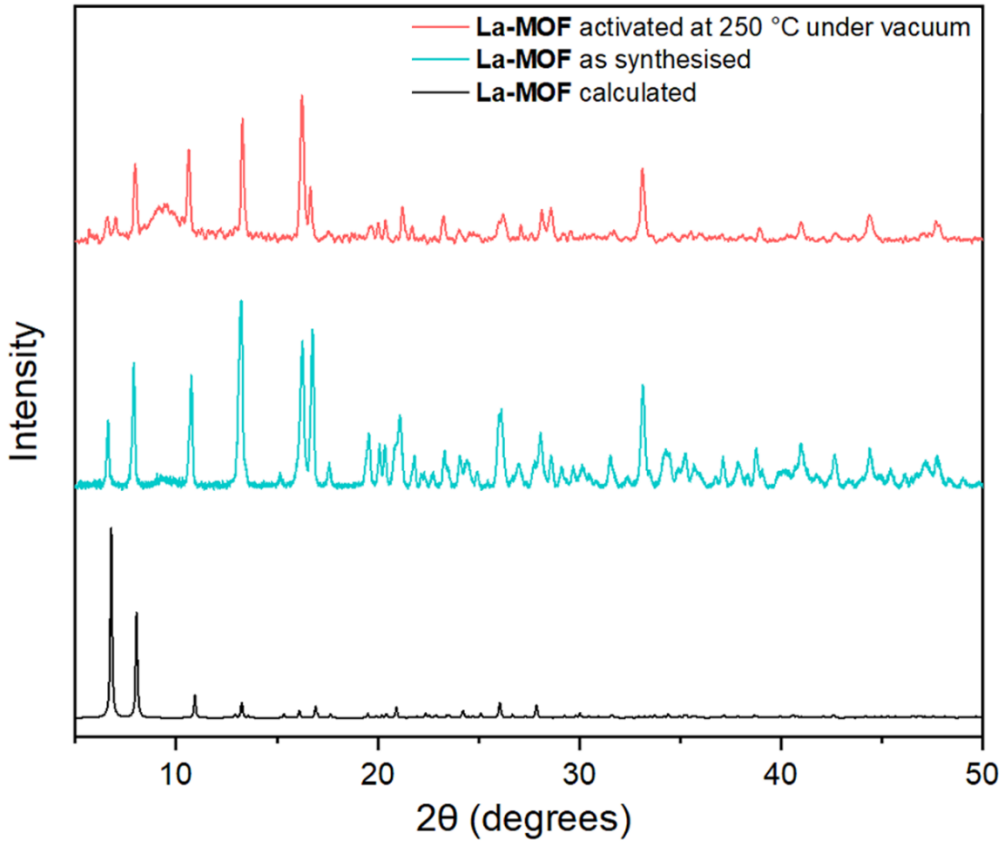

Fig. 3.29 Comparison of PXRD patterns of **La-MOF** as synthesised and after heating at 250 °C under vacuum, with the pattern calculated from single crystal XRD experiments. Both the simulated and experimental patterns were normalised to facilitate comparison of the patterns. Experimental PXRD patterns were measured at room temperature in air.

3.6 Synthesis of Sm- and Eu-based MOFs

Following successful synthesis of the series of isostructural MOFs based on La^{III}, Ce^{III}, Pr^{III} and Nd^{III} using **TTT**$^{3-}$, this novel linker was then reacted with Sm^{III} and Eu^{III} salts, in order to study the versatility of H_3**TTT** as a linker. Furthermore, we aimed to understand how the supramolecular materials synthesised using H_3**TTT** would vary as the Ln^{III} series progressed. Synthesis of a Eu^{III}-based MOF using H_3**TTT** was of particular interest, due to the known photoluminescent properties of Eu^{III} ions.[22] This section describes the synthesis and characterisation of two new MOFs, **Sm-MOF** and **Eu-MOF**, which were synthesised as crystalline materials following reactions to screen for optimal temperature, linker and metal salt concentrations and ratios, and reaction duration.

3.6.1 Solvothermal synthesis of Sm-MOF and Eu-MOF

Reaction of H_3**TTT** with Ln^{III} salts (Ln=Sm, Eu) with a 1:1 ratio of metal to ligand in DMF solution at 100 °C for 72 hours gave dense clusters of pale yellow needle-shaped crystals. Optical microscope images of these clusters in a sample of **Sm-MOF** are shown in **Fig. 3.31** and **Fig. 3.31**. Single crystals of **Eu-MOF** and **Sm-MOF** could be obtained by carefully breaking these clusters to give small single needle-shaped crystals. Using single crystal X-ray diffraction analysis, the structure of the MOFs was identified as a porous three-dimensional framework structure, with the constitutional formula

[Ln(**TTT**)(DMF)]·*x*DMF (Ln= Eu (**Eu-MOF**), Sm (**Sm-MOF**)). The images shown in this section use **Eu-MOF** as a structure representative of both isostructural MOFs, unless otherwise stated.

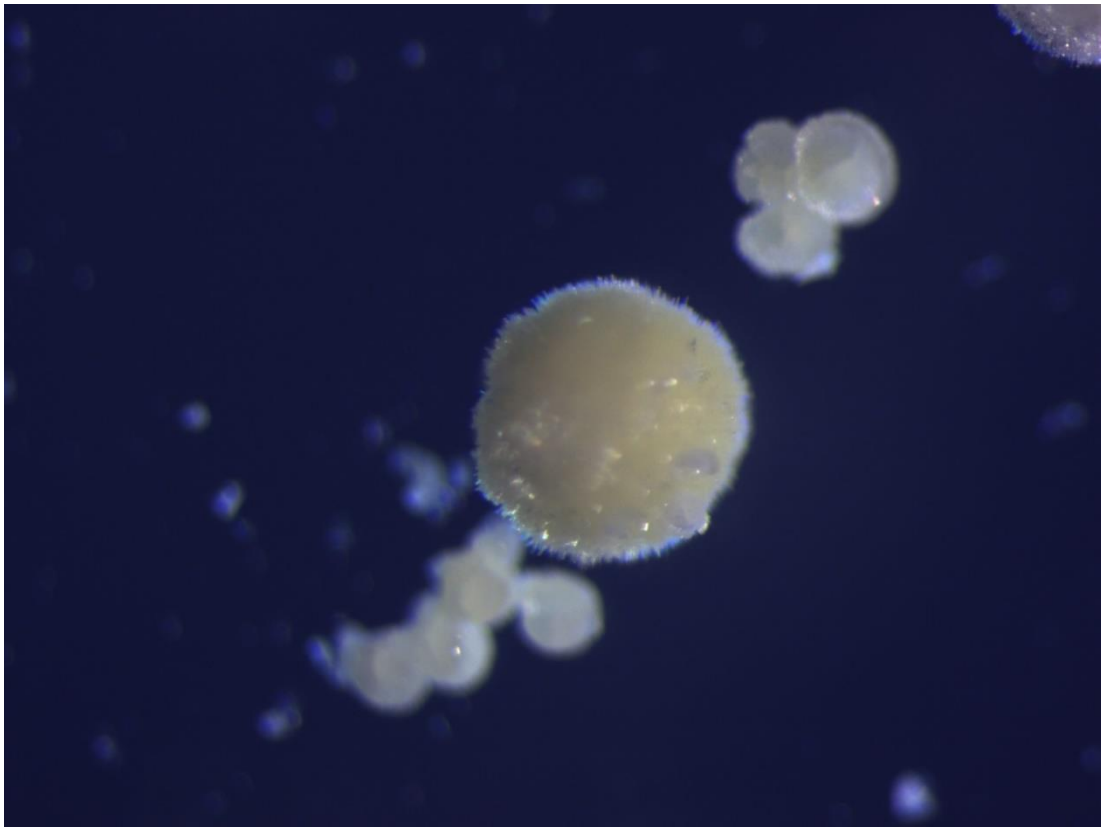

Fig. 3.30 Microscope images of Sm-MOF crystals, showing dense clusters of needle shaped crystals.

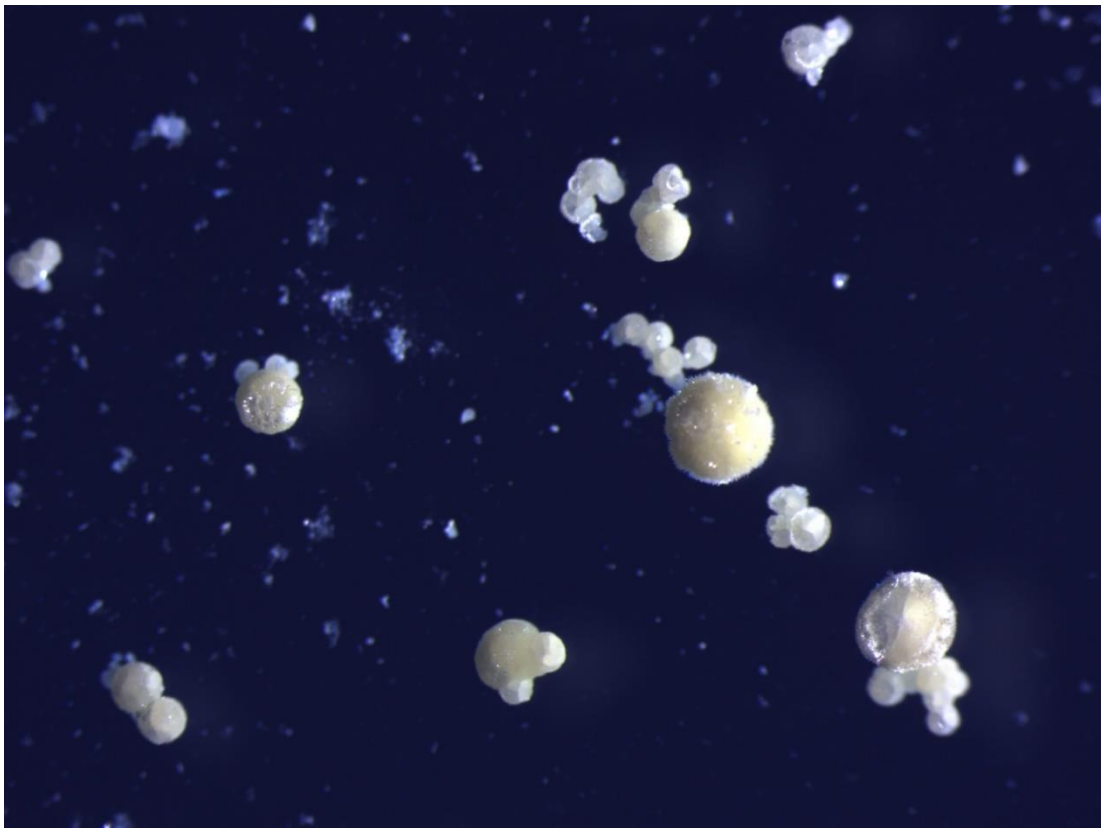

Fig. 3.31 Microscope images of Sm-MOF crystals, showing dense clusters of needle shaped crystals.

3.6.2 Crystal structure description: Sm-MOF and Eu-MOF

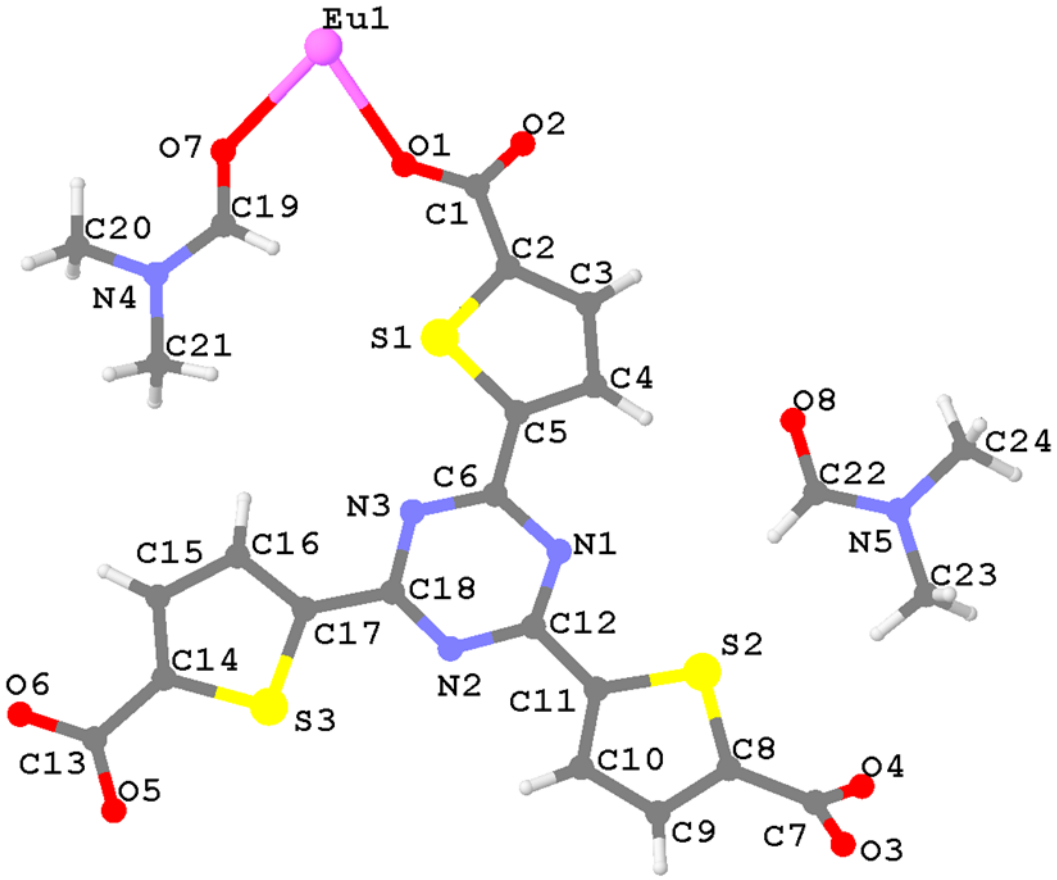

Fig. 3.32 Asymmetric unit of **Eu-MOF**, viewed along the crystallographic *c*-axis, with atoms labelled. Atom colour scheme: Eu, purple, S, yellow, C, dark grey, N, blue, O, red, H, white.

Eu-MOF crystallises in the monoclinic spacegroup *Cc*. Each asymmetric unit of **Eu-MOF** consists of one Eu^{III} ion, one fully deprotonated $\mathbf{TTT}^{3-}$ ligand molecule and one coordinated DMF solvent molecule (**Fig. 3.32**). There are two DMF guest solvent molecules in the pores of the structure, within **Eu-MOF**. ORTEP-3 software[33] was used to generate the ORTEP plot of **Eu-MOF** (**Fig. 3.33**). The crystal data and refinement results for both **Sm-MOF** and **Eu-MOF** are summarised in **Table 3.9**.

Each Eu^{III} ion **Eu-MOF** is eight-coordinate and is coordinated to seven oxygen atoms from the carboxylate groups of five different $\mathbf{TTT}^{3-}$ ligands, and one oxygen atom from a coordinated DMF solvent molecule (**Fig. 3.34**). The $\mathbf{TTT}^{3-}$ ligand has one chelating η^2, one bridging μ_2-η^1:η^1, and one chelating bridging μ_2-η^2:η^1 coordination mode. The bridging coordination modes of the carboxylate groups of $\mathbf{TTT}^{3-}$ links each Eu^{III} ion in **Eu-MOF** to two adjacent Eu^{III} ions, forming an infinite one-dimensional rod SBU, which extends parallel to the crystallographic *c*-axis (**Fig. 3.35**).

Table 3.9 Crystal data and refinement results for **Sm-MOF** and **Eu-MOF**

Compound name	**Sm-MOF**	**Eu-MOF**
Empirical formula	$SmC_{21}S_3N_4O_7H_{13}$	$EuC_{24}S_3N_5O_8H_{20}$
Formula weight	672.83	754.59
Temperature (K)	100.0	100.00
Crystal description	Pale yellow needles	Pale yellow needles
Crystal system	Monoclinic	Monoclinic
Space group	*Cc*	*Cc*
a (Å)	25.810(9)	25.8127(16)
b (Å)	15.987(4)	16.1287(9)
c (Å)	7.041(2)	7.0693(4)
α (°)	90	90
β (°)	95.128(19)	95.744(4)
γ (°)	90	90
V (Å^3)	2893.7(15)	2928.4(3)
Z	4	4
ρ_{calc} (g/cm^3)	1.544	1.712
μ (mm^{-1})	17.642	17.809
F(000)	1304.9	1496.0
Radiation	CuKα (λ = 1.54178)	CuKα (λ = 1.54178)
2θ range for data collection (°)	6.51 to 106.154	6.47 to 118.682
Reflections collected	7929	11181
Independent reflections	2686	3774
Data/restraints/parameters	2686/59/33	3774/312/374
Goodness-of-fit on F^2	0.997	1.114
R_1 [I≥2σ (I)], all	0.1055, 0.1724	0.0878, 0.1027
wR_2 [I≥2σ (I)], all	0.2408,0.2894	0.2266, 0.2602
Largest diff. peak/hole (e Å^{-3})	1.34/-1.43	2.08/-1.79

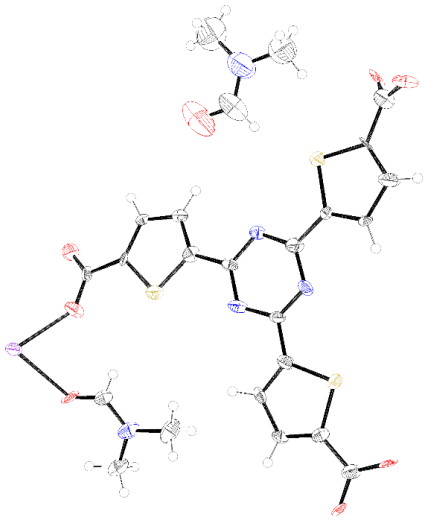

Fig. 3.33 ORTEP of the asymmetric unit of **Eu-MOF,** viewed along the crystallographic *c*-axis. Thermal probabilities are shown at the 50 % probability level. Atom colour scheme: Eu, purple, S, yellow, C, dark grey, N, blue, O, red, H, white.

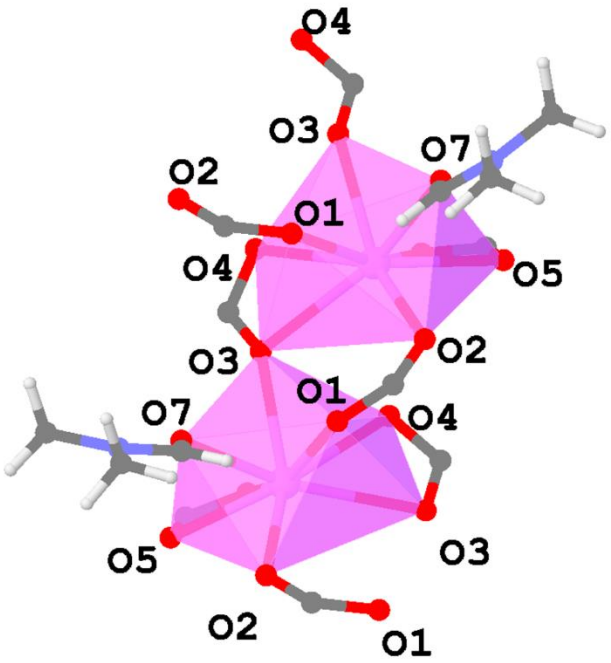

Fig. 3.34 Coordination environment of Eu^{III} ions in **Eu-MOF**, with O atoms labelled. Atom colour scheme: Eu, purple, S, yellow, C, dark grey, N, blue, O, red, H, white.

In **Eu-MOF**, the Eu-Eu distance in the rod SBU is 4.3266(15) Å, while in **Sm-MOF**, the Sm-Sm distance is 4.302(3) Å. The alternate stacking of $\mathbf{TTT}^{3-}$ ligands along the *c* axis leads to a zigzag arrangement of Ln^{III} ions within the rod SBU (**Fig. 3.35**). The Ln-Ln-Ln angles within **Sm-MOF** and **Eu-MOF** are 109.83(11)° and 109.56(6)° respectively. A notable feature of the structure of **Eu-MOF**, as well as the isostructural **Sm-MOF**, is that the DMF molecules on consecutive Ln^{III} ions coordinate from different directions (**Fig. 3.36**). The Eu^{III}-O and Sm^{III}-O angles in **Eu-MOF** and **Sm-MOF** are shown in **Table 3.10**. The Ln^{III}-O distances in both **Sm-MOF** and **Eu-MOF** are all typical of those previously reported.[35]

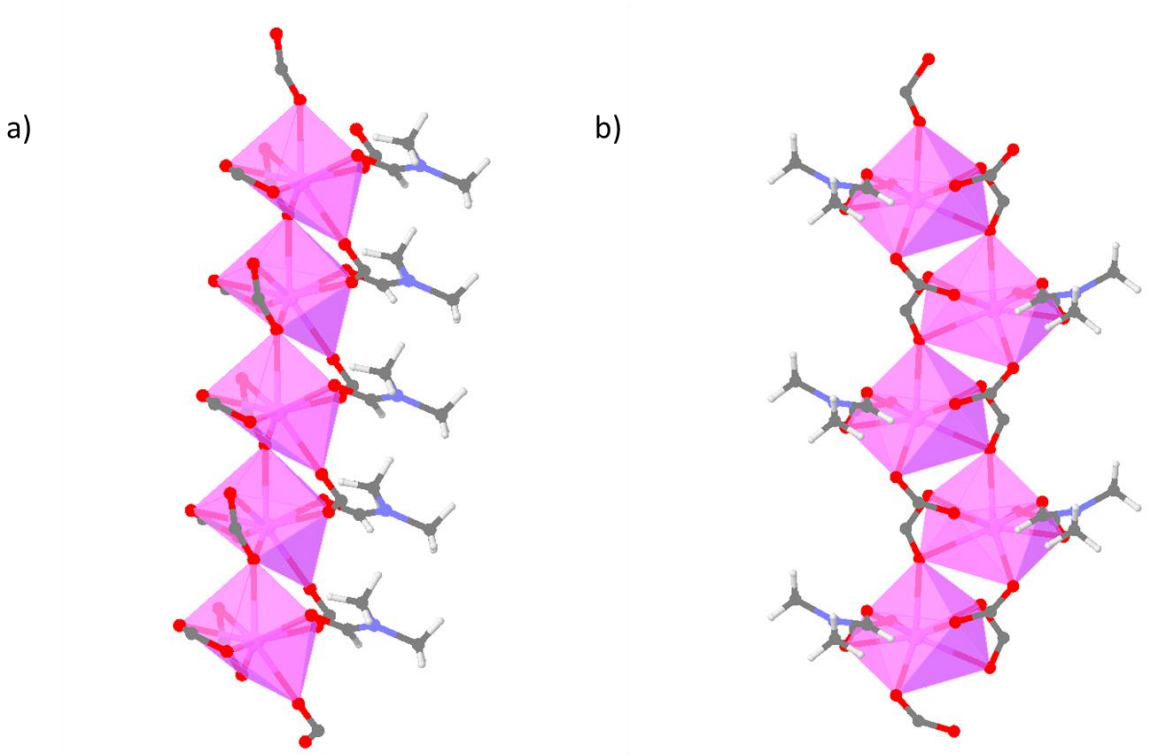

Fig. 3.35 The coordination environment of the Eu^{III} ions in the infinite one-dimensional rod-shaped SBUs of **Eu-MOF a)** along the crystallagraphic *b*-axis and **b)** along the crystallographic *a*-axis. Atom colour scheme: Eu, purple, S, yellow, C, dark grey, N, blue, O, red, H, white.

Table 3.10 Ln^{III}-O bond lengths (Å) in **Eu-MOF** and **Sm-MOF**.

Bond	Distance	Bond Length (Å)	Bond	Distance	Bond Length (Å)
Eu^{III}-O	Eu^{III}-O1	2.337(18)	Sm^{III}-O	Sm^{III}-O1	2.25(4)
	Eu^{III}-O2	2.414(18)		Sm^{III}-O2	2.24(5)
	Eu^{III}-O3	2.614(15)		Sm^{III}-O3	2.50(4)
	Eu^{III}-O3	2.504(16)		Sm^{III}-O3	2.60(3)
	Eu^{III}-O4	2.567(18)		Sm^{III}-O4	2.55(3)
	Eu^{III}-O5	2.438(15)		Sm^{III}-O5	2.41(3)
	Eu^{III}-O6	2.472(17)		Sm^{III}-O6	2.41(3)
	Eu^{III}-O7	2.485(16)		Sm^{III}-O7	2.42(3)

In order to understand the coordination environment of the Ln^{III} in **Sm-MOF** and **Eu-MOF**, continuous shape measurement were carried out on these structures, using Shape 2.1 software.[36] The results of these calculations are shown in **Table 3.11**. The lowest values, indicating the least deviation from the ideal values for each geometry, are highlighted in bold. These measurements indicate that the metal centres in both **Sm-MOF** and **Eu-MOF** are in biaugmented trigonal prism geometry.

Each rod SBU in **Eu-MOF** is connected to six other rod SBUs through $\mathbf{TTT}^{3-}$ linkers (**Fig. 3.37**). This leads to the formation of approximately hexagonal pores within the structure of **Eu-MOF**, and

the isostructural **Sm-MOF**. Along the crystallographic *c* axis, the **TTT**$^{3-}$ ligands stack in an alternate pattern. Non-coordinating guest DMF molecules are present in the hexagonal channels of the MOF.

Table 3.11 Continuous shape measurement values for Ln^{III} atoms in **Sm-MOF** and **Eu-MOF**. The lowest value (indicating closest fit) is highlighted in bold.

Shape	**Symmetry**	**Continuous shape measurement value (Sm-MOF)**	**Continuous shape measurement value (Eu-MOF)**
Octagon	D_{8h}	27.717	26.949
Heptagonal pyramid	C_{7v}	17.763	17.414
Hexagonal bipyramid	D_{6h}	13.012	13.460
Cube	O_h	12.673	13.193
Square antiprism	D_{4d}	7.433	7.499
Triangular dodecahedron	D_{2d}	6.288	6.356
Johnson – Gyrobifastigium (J26)	D_{2d}	8.723	9.517
Johnson – Elongated triangular bipyramid (J14)	D_{3h}	24.755	23.930
Johnson – Biaugmented trigonal prism (J50)	C_{2v}	5.297	5.202
Biaugmented trigonal prism	**C_{2v}**	**4.357**	**4.279**
Snub disphenoid (J84)	C_{2v}	6.896	7.202
Triakis tetrahedron	T_d	13.426	13.771
Elongated trigonal bipyramid	D_{3h}	19.644	19.589

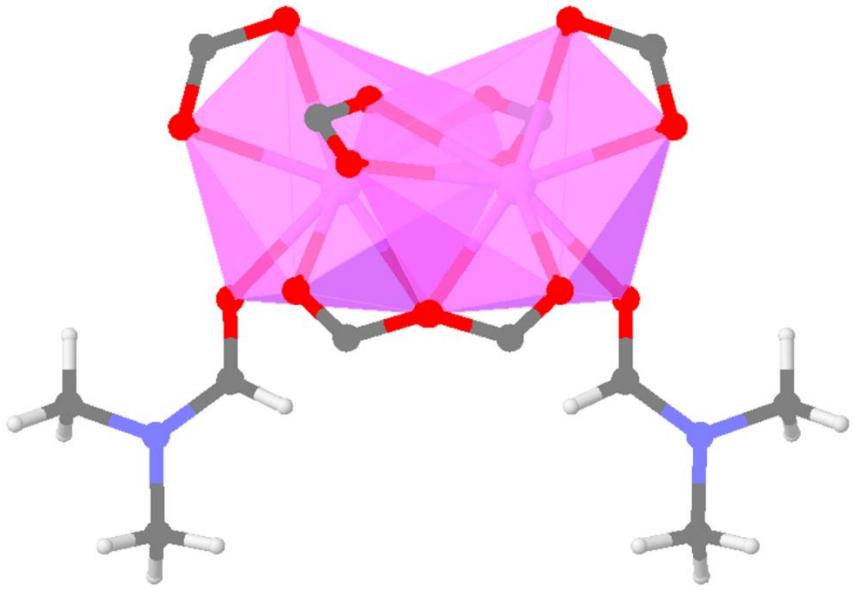

Fig. 3.36 The Eu^{III} rod-shaped SBU in **Eu-MOF**, as viewed along the crystallographic *c*-axis. Atom colour scheme: Eu, purple, S, yellow, C, dark grey, N, blue, O, red, H, white.

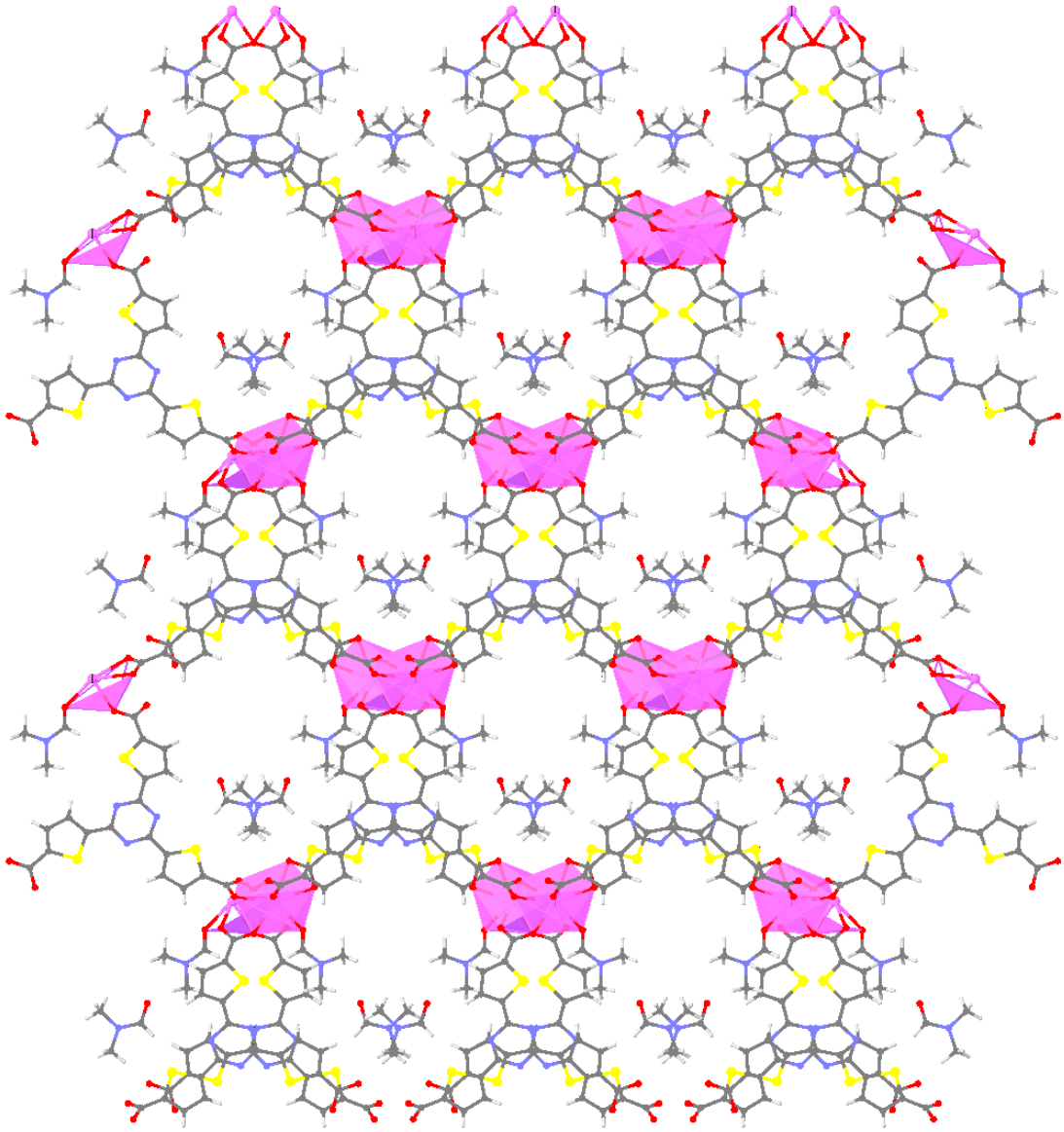

Fig. 3.37 Crystal structure of **Eu-MOF** viewed along the crystallographic *c*-axis. Atom colour scheme: Eu, purple, S, yellow, C, dark grey, N, blue, O, red, H, white.

To facilitate comparison of the structure of **Eu-MOF** to that of **Ce**-MOF, the **calcvoid** routine in Olex2 software[34] was used to study the structure of **Eu-MOF**. **Eu-MOF** occupies 53.46 % of the cell volume. The radius of the largest spherical void within the framework structure is 2.4 Å, and the crystallographic *c*-direction can be penetrated by a sphere with a radius of 2.00 Å.

Upon removal of the non-coordinating guest DMF molecules are removed from the structure of **Eu-MOF**, the voids and channels become larger (**Fig. 3.38**). The **calcvoid** routine in Olex2 software[34] then gives the largest spherical void in the structure is 3.00 Å upon removal of DMF, and the *c*-direction can be penetrated by a sphere with radius 2.60 Å.

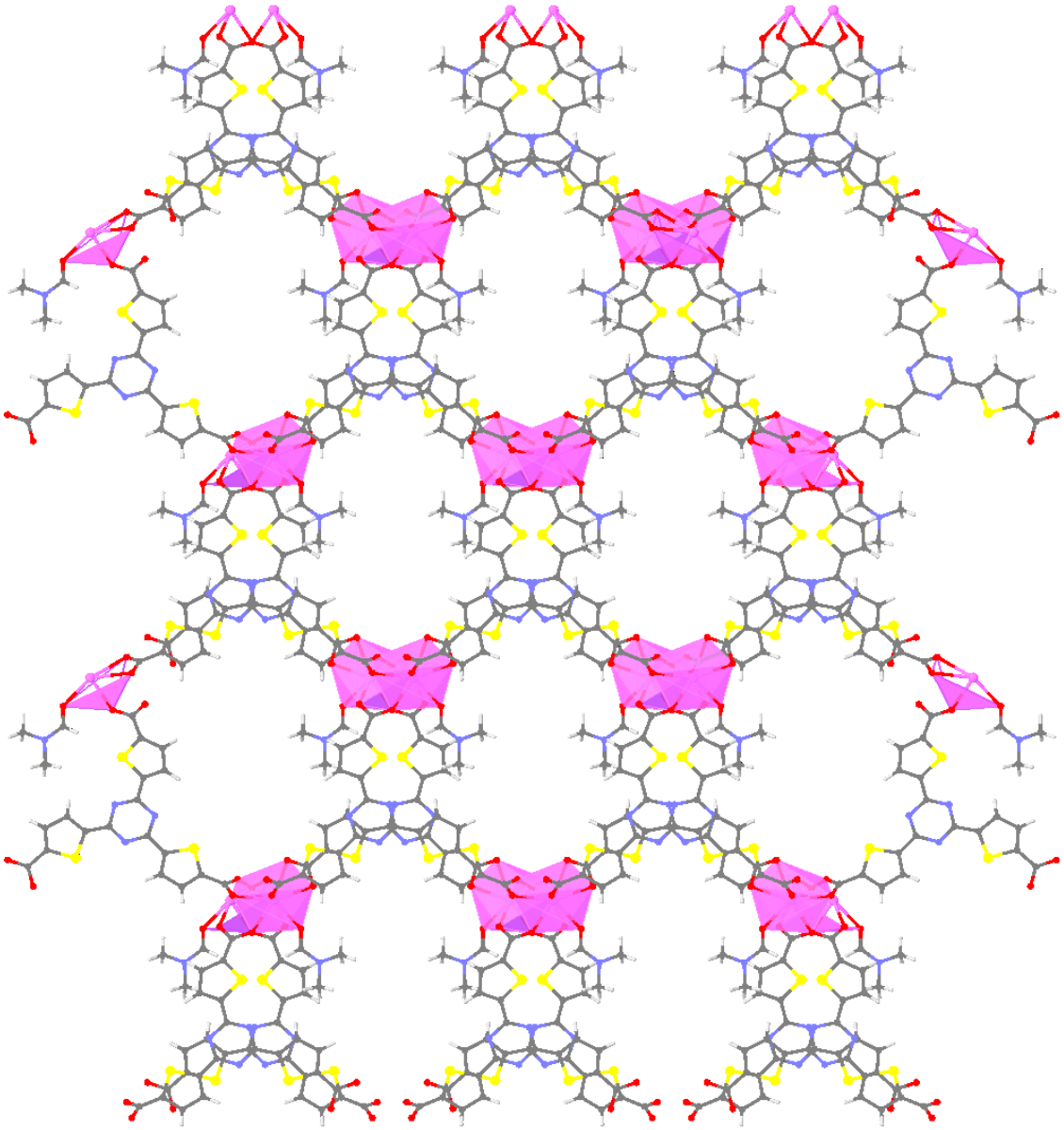

Fig. 3.38 Crystal structure of **Eu-MOF** viewed along the crystallographic *c*-axis, with non-coordinating DMF molecules removed for clarity. Atom colour scheme: Eu, purple, S, yellow, C, dark grey, N, blue, O, red, H, white

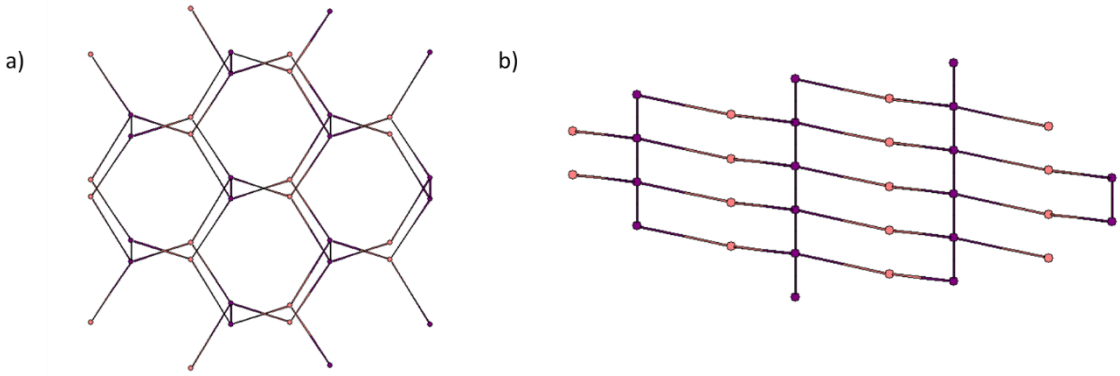

Fig. 3.39 Topological representation of **Eu-MOF**, as viewed along the crystallographic **a)** *c*-axis and **b)** *b*-axis. Colour scheme: purple (Eu^{III} ions), pink (**TTT**$^{3-}$ ligand).

The topology of **Eu-MOF** was analysed using ToposPro software.[39] **Eu-MOF** forms a three-dimensional binodal 3,5-connected net with (3-c)(5-c) stoichiometry (**Fig. 3.39**). The MOF has **hms** topology and point symbol $\{6^3\}\{6^9.8\}$. Each Eu^{III} ion in **Eu-MOF** is connected to three different **TTT**$^{3-}$ linkers, and two other Eu^{III} ions, thus forming 5-connected nodes. The **TTT**$^{3-}$ linkers act as 3-connected nodes.

Bond valence sum analysis[37] was carried out for **Sm-MOF** and **Eu-MOF** to confirm that the Ln ions in the structures are present in the +III oxidation state (**Table 3.12**). The R_0 values used for eight-coordinate Sm-O and Eu-O bonds were 2.050 and 2.036 respectively.[43] The bond lengths used in these calculations are shown in **Table 3.10**.

Table 3.12 BVS analysis of metal centres in **Sm-MOF** and **Eu-MOF**

MOF	Metal ion	R_0 (Å)	BVS	Oxidation state
Sm-MOF	Sm1	2.050	3.1	+III
Eu-MOF	Eu1	2.036	2.5	+III

3.6.3 Comparison of Sm-MOF and Eu-MOF structures

Though the structures of Sm-MOF and Eu-MOF are similar in many ways, several minor but interesting differences are present in the structures. One difference is that the Ln^{III}-Ln^{III} distances in the MOFs differ, with a longer distance of 4.302(3) Å present in Sm-MOF, compared to 4.075 Å in Eu-MOF.

Table 3.13 Ln^{III}-Ln^{III} distances in **Sm-MOF** and **Eu-MOF**.

Lanthanide ion	Ln^{III}-Ln^{III} distance (Å)
Sm	4.302(3)
Eu	4.075(3)

3.6.4 Scanning Electron Microscopy and Energy Dispersive X-ray Spectroscopy

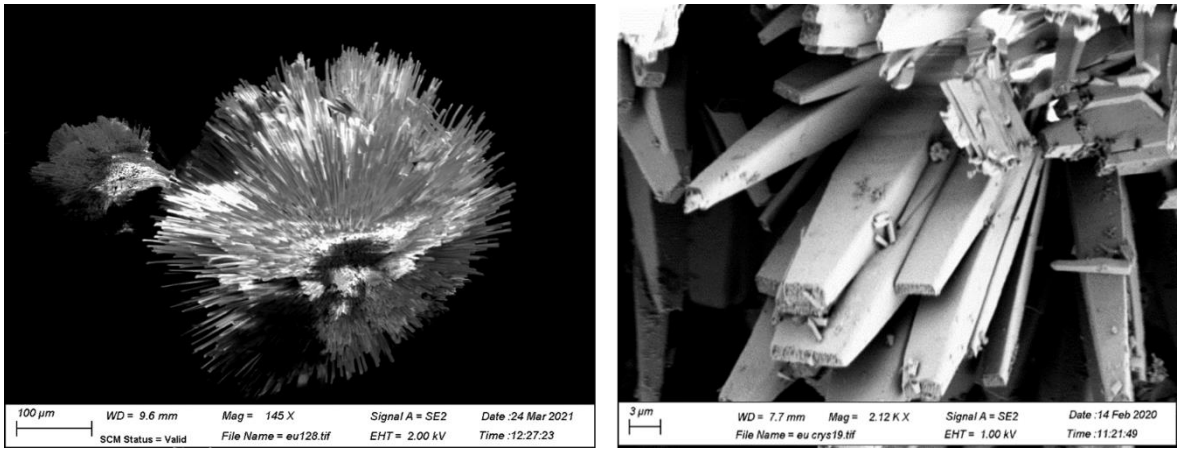

Fig. 3.40 SEM images of **Eu-MOF** crystals.

SEM images of **Sm-MOF** and **Eu-MOF** are shown in **Fig. 3.40**, **Fig. 3.41**. The crystals form as dense clusters of acicular crystals, which radiate outwards from a central point in the cluster. Energy dispersive X-ray (EDX) spectroscopy showed that the ratio of Eu:S in crystals of **Eu-MOF** was consistent with that expected from the formula [Eu(**TTT**)(DMF)]. The expected ratio was 1:3 Eu:S, and the experimentally obtained ratio was 1:2.8.

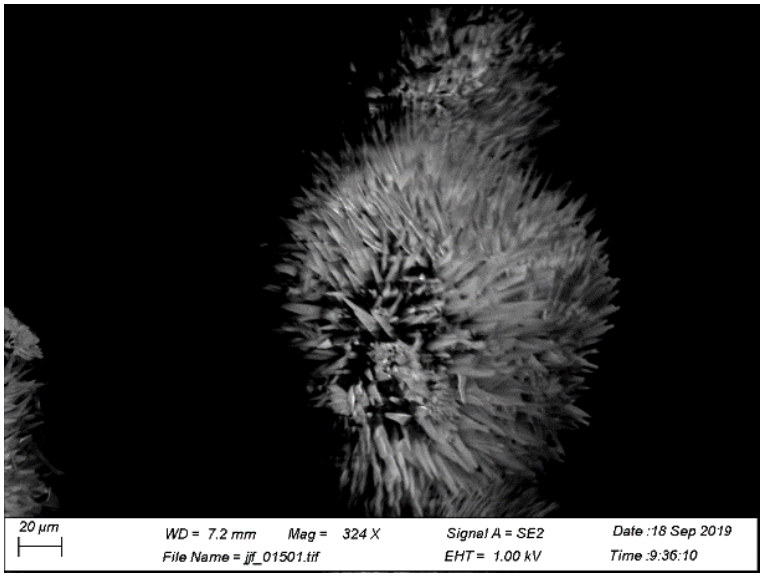

Fig. 3.41 SEM image of **Sm-MOF** crystals.

3.6.5 Fourier-Transform Infrared spectroscopy of Sm-MOF and Eu-MOF

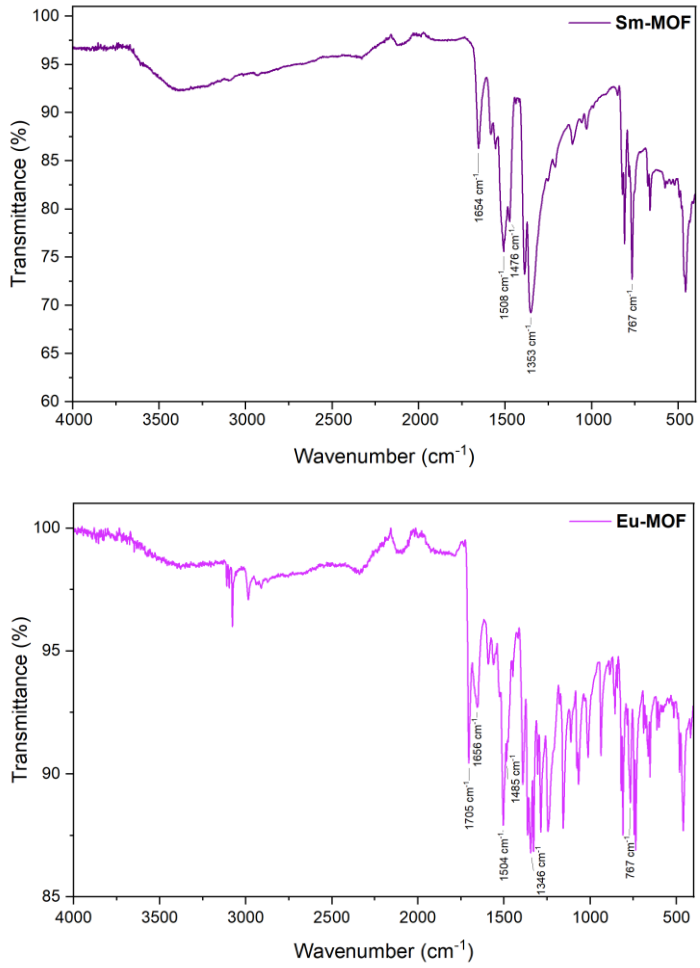

Fig. 3.42 FTIR spectra of **Sm-MOF** and **Eu-MOF,** with key vibrational bands labelled.

The FTIR spectra of **Sm-MOF** and **Eu-MOF** show similarities in the key vibrational bands expected in these materials. Additional vibrational bands are visible in the FTIR spectrum of **Eu-MOF** due to incomplete drying of the sample prior to measurement of the FTIR spectrum of the sample, leading to vibrational bands in the spectrum that correspond to DMF solvent molecules.

Characteristic bands for the $\mathbf{TTT^{3-}}$ linker can be observed in the FTIR spectrum of **Eu-MOF** and **Sm-MOF**. A broad band between approximately 3700 cm^{-1} and 2200 cm^{-1} originate from the linker C-H vibration, the DMF solvent molecule O-H vibration, as well as C-H stretching vibrations in the $\mathbf{TTT^{3-}}$ linkers in the structure. In **Sm-MOF**, the asymmetric C=O stretch ν_{asym} is observed at 1654 cm^{-1} and ν_{sym} is observed at 1476 cm^{-1}. In **Eu-MOF**, the ν_{asym} can be observed at 1656 cm^{-1}, and ν_{sym} appears at 1485 cm^{-1}. The values for Δ, the difference between the asymmetric and symmetric C=O stretch in each MOF, are shown in **Table 3.14**. The triazine rings lead to vibrational bands at 1508 cm^{-1} and 1352 cm^{-1} in **Sm-MOF**, and 1504 cm^{-1} and 1346 cm^{-1} in **Eu-MOF**.

In the FTIR spectrum of **Eu-MOF**, the DMF solvent molecules lead to C-H stretching vibrations appear at 3111, 3097, 3078 and 2986 cm^{-1}, in addition to C=O vibrational bands at 1705 cm^{-1}.

Table 3.14 Asymmetric C=O stretch (ν_{asym}), symmetric C=O stretch (ν_{sym}), and the difference (Δ) between ν_{asym} and ν_{sym} for each MOF.

Compound	ν_{asym} (cm^{-1})	ν_{sym} (cm^{-1})	Δ (cm^{-1})
Sm-MOF	1655	1476	179
Eu-MOF	1656	1485	171

3.7 Comparison of La-MOF and Eu-MOF

When Ln^{III} ions are employed in the synthesis of MOFs, it is possible for an isoreticular series of MOFs to be formed, incorporating different Ln^{III} ions from across the series.[44] However, other studies show a variation in the MOF structures depending on the Ln^{III} ion used,[45] as is seen for H_3**TTT**.

Although the two series of isostructural MOFs (**Ln1-MOF**, Ln1 = La, Ce, **Ln2-MOF**, Ln2 = Sm, Eu) reported in this chapter incorporate the same organic linker, H_3**TTT**, and are synthesised under the same conditions (solvent, temperature, concentration, metal to ligand ratio), the two MOFs series differ in structure, highlighting the strong effect of the Ln^{III} ion on the structure of these MOFs. Comparison of these two series of MOFs indicates several key differences, namely, the coordination environment of Ln^{III} ion and the alignment of open coordination sites on the MOF (**Fig. 3.43**). However, the underlying topology of the two MOF series are the same.

In terms of the coordination environment of Ln^{III} ions, in the **Ln1-MOF** series, each Ln^{III} ion is ten-coordinate, with an overall sphenocorona coordination geometry. In **Ln2-MOF** the Ln^{III} ions are eight-coordinated, and the coordination geometry of the Ln^{III} ions can be classified as a biaugmented trigonal prism.

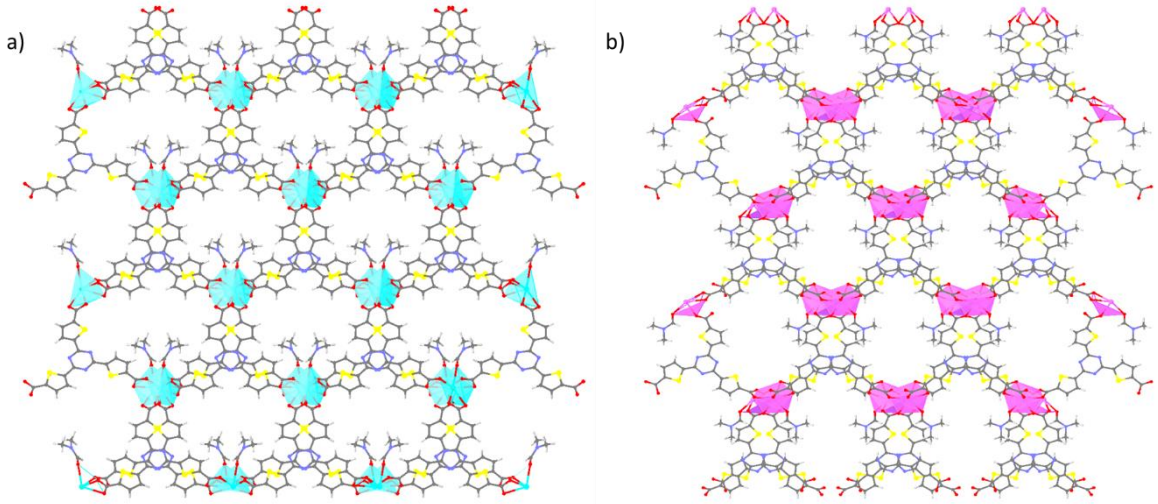

Fig. 3.43 Comparison of the structures of **a) Ce-MOF** and **b) Eu-MOF**, as viewed along the crystallographic *c*-axis. Guest DMF molecules were removed for clarity. Atom colour scheme: Ce, turquoise, Eu, purple, S, yellow, C, dark grey, N, blue, O, red, H, white.

The two MOF series also show key differences in their inorganic SBUs (**Fig. 3.44**). Though both MOF series feature one-dimensional rod-shaped SBUs, the SBU of the **Ln1-MOF** series has a more linear alignment of Ln^{III} ions in the structure. In comparison, the structures of **Sm-MOF** and **Eu-MOF** feature a more pronounced zig-zag orientation of the corresponding Ln^{III} ions. These differences can be examined in more detail by comparing the angles between Ln^{III} ions along the SBU in each structure. These Ln^{III}-Ln^{III}-Ln^{III} angles, as well as the distances between consecutive Ln^{III} ions in the rod SBUs, are listed for **Ce-MOF** and **Eu-MOF**, as representative structures for each series, in **Table 3.15**. As expected from the pronounced bends in the **Sm-MOF** and **Eu-MOF** rod SBU, the Ln^{III}-Ln^{III}-Ln^{III} angle, 109.83(11)° and 109.56(6)° respectively, is smaller than those observed in the **Ln1-MOF** series, which is more linear by comparison. The corresponding Ln^{III}-Ln^{III}-Ln^{III} angle in **Ce-MOF** is 165.15(6)°. Despite the differences in the SBUs between the two series, the Ln^{III}-Ln^{III} distances do not vary substantially, due to the presence of bridging linker carboxylates in both structures.

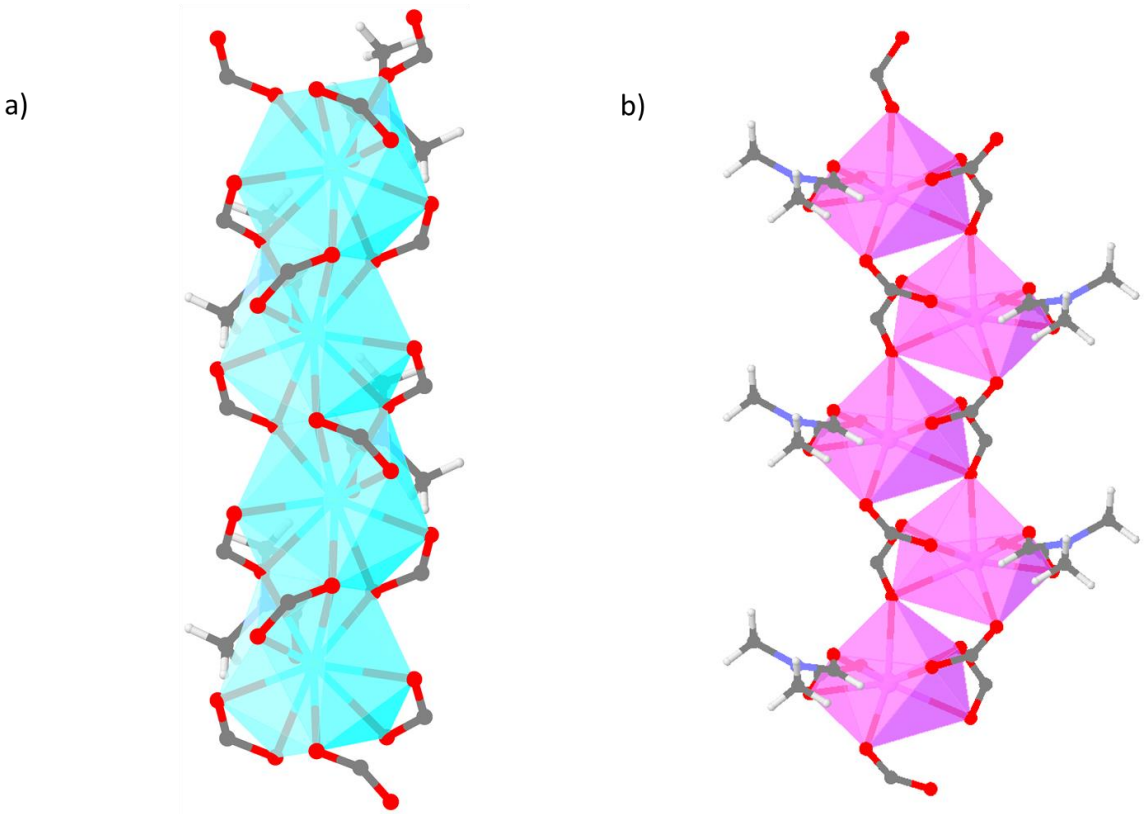

Fig. 3.44 Comparison of the Ln^{III} SBUs in **a) Ce-MOF** and **b) Eu-MOF**, as viewed along the crystallographic *a*-axis. Atom colour scheme: Ce, turquoise, Eu, purple, C, dark grey, N, blue, O, red, H, white.

Table 3.15 Comparison of Ln^{III}-Ln^{III} distances in the MOFs

Lanthanide ion	Ln^{III}-Ln^{III} distance (Å)	Ln^{III}-Ln^{III}-Ln^{III} angle
Ce	4.0896(3)	165.15(6)°
Eu	4.075(3)	109.56(6)°

The alignment of Ln^{III} open coordination sites is influenced by the relative positions of the Ln^{III} ions in both series of MOFs. In the **Ln1-MOF** series, the DMF molecules are oriented further into the

porous channel of the MOFs, giving a more linear alignment of DMF molecules along the crystallographic *c*-axis, compared to that observed in **Sm-MOF** and **Eu-MOF**.

Overall, analysis of the differences between the **Ln1-MOF** series and the **Ln2-MOF** series indicate that the structures of MOFs incorporating H_3**TTT** are strongly influenced by the Ln^{III} metal ion.

3.8 Stability of Sm- and Eu-MOFs

3.8.1 Thermogravimetric Analysis (TGA) of Sm-MOF and Eu-MOF

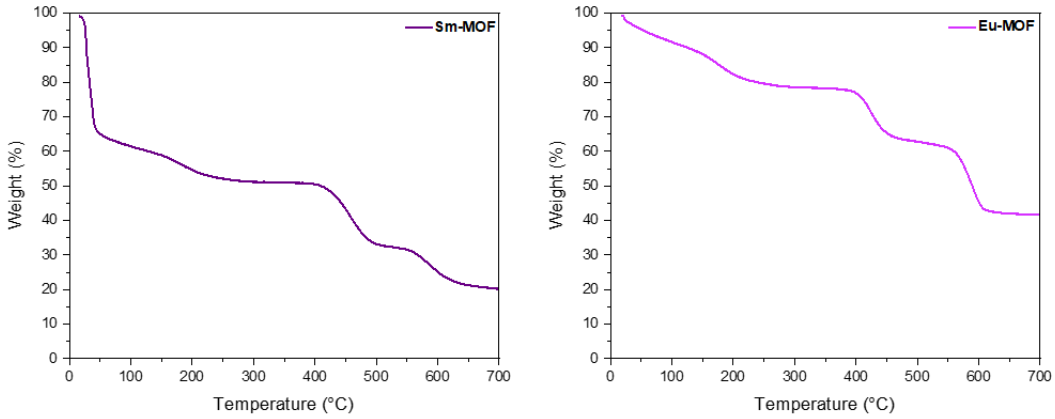

Fig. 3.45 Thermogravimetric analysis of **Sm-MOF** (left) and **Eu-MOF** (right) samples as synthesised, under air flow (20 mL min^{-1}).

Thermogravimetric analysis measurements reveal that **Eu-MOF** and **Sm-MOF** show good thermal stability to approximately 400 °C (**Fig. 3.45**). Two weight loss steps can be attributed to removal of solvent molecules from the material. The first weight loss step below 100 °C, can be attributed to loss of non-coordinated DMF solvent molecules from the pores of the framework. The second weight loss occurs gradually between 140 °C and 240 °C corresponds to removal of the DMF molecules coordinated to the Ln^{III} ions in the material. Decomposition of the $\mathbf{TTT}^{3-}$ ligand in the framework occurred between approximately 400 °C and 650 °C, in two thermal decomposition steps. Overall, the TGA curves of **Sm-MOF** and **Eu-MOF** are very similar to those observed for **La-MOF**, **Ce-MOF**, **Pr-MOF** and **Nd-MOF** (**Fig. 3.27**), indicating that the materials share similar properties, as expected from their closely related structures.

3.8.2 PXRD measurements

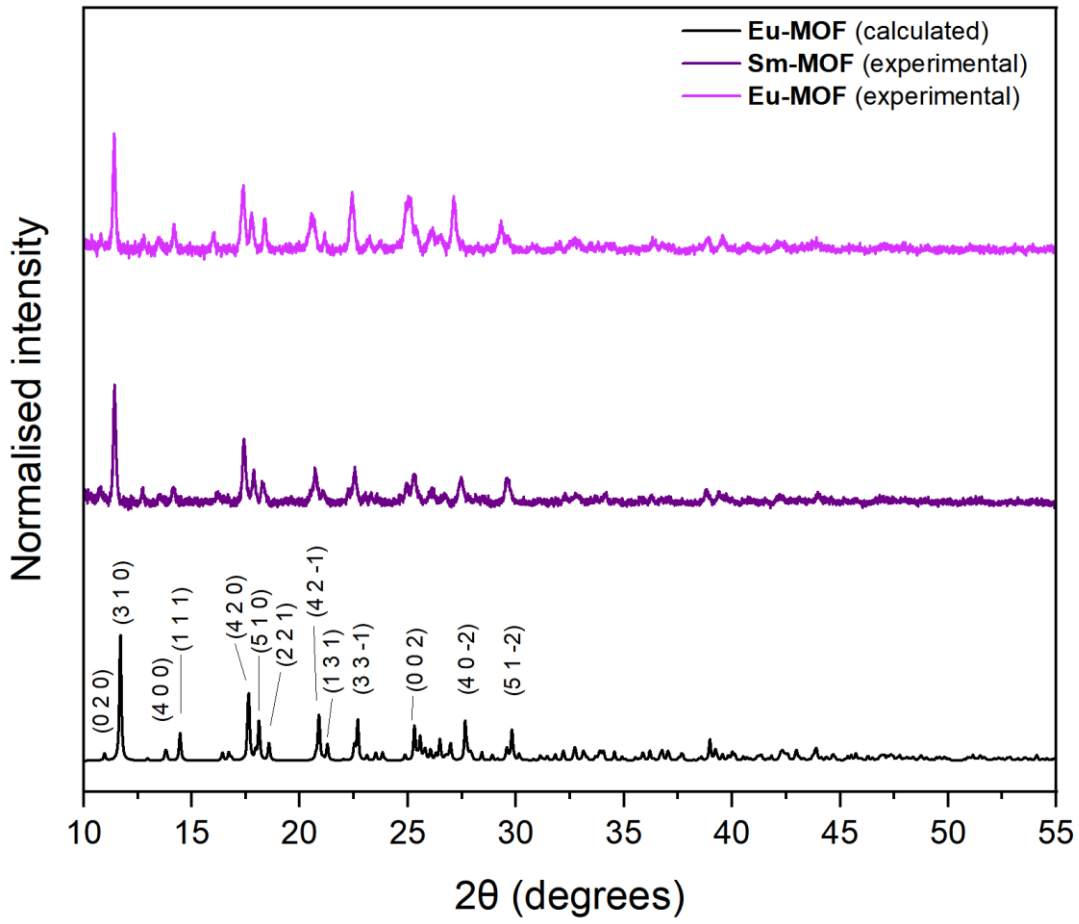

Fig. 3.46 PXRD patterns of **Eu-MOF** simulated from single crystal XRD experiments (showing indexed diffraction peaks) compared to the bulk sample of **Eu-MOF** and **Sm-MOF** as synthesised. Both the simulated and experimental patterns were normalised to facilitate comparison of the patterns. The experimental PXRD patterns were measured in air, at room temperature.

The phase purity of both **Sm-MOF** and **Eu-MOF** were confirmed by powder X-ray diffraction methods (**Fig. 3.46)**. For both MOFs, the powder XRD pattern of a sample of the MOFs as synthesised was in good agreement with the powder XRD pattern calculated using the single crystal XRD data.

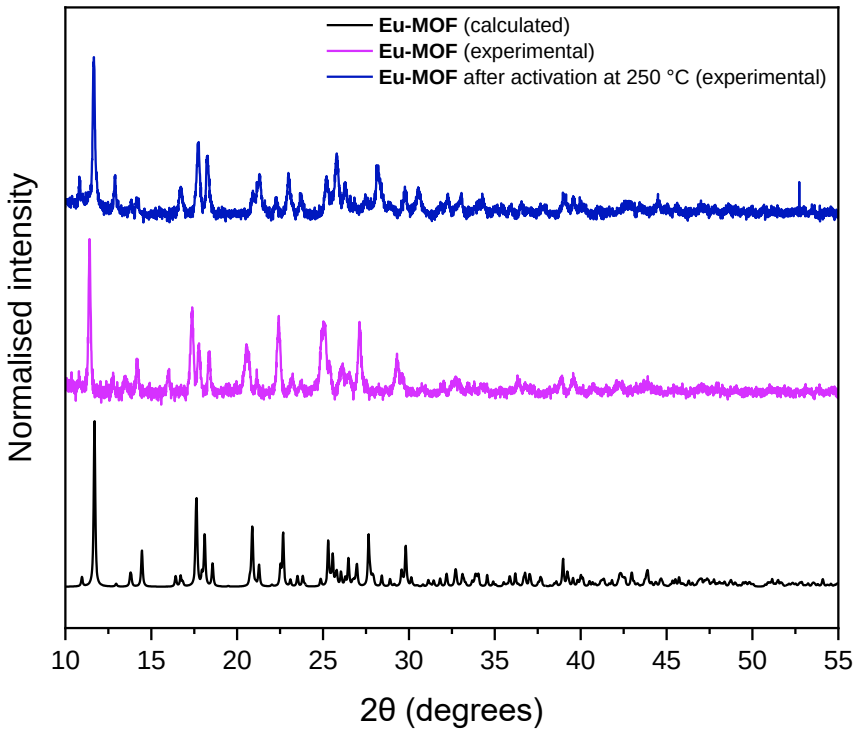

Fig. 3.47 Comparison of the PXRD pattern of **Eu-MOF** as synthesised with the PXRD pattern of **Eu-MOF** after activating the sample at 250 °C, under vacuum. Both the simulated and experimental patterns were normalised to facilitate comparison of the patterns. The experimental PXRD patterns were measured in air, at room temperature.

In order to understand the thermal stability behaviour of **Eu-MOF**, a crystalline sample was activated at 250 °C under vacuum (**Fig. 3.47**). Comparison of the PXRD pattern of the **Eu-MOF** as synthesised, and after thermal activation, showed that the sample retained its crystallinity after activation. An activation temperature of 250 °C was selected based of examination of the TGA curve of **Eu-MOF**, as at this temperature, coordinated DMF is expected to be removed from the structure. PXRD studies therefore indicate that **Eu-MOF** is stable upon removal of coordinated solvent (DMF) from the Eu^{III} ions.

In addition, powder XRD experiments could be used to show that **Eu-MOF** is stable to water, methanol and toluene. Three samples of **Eu-MOF** were synthesised, washed with DMF, dried on filter paper, then the samples were soaked in water, methanol or toluene for 16 hours. After 16 hours, the crystals were filtered, and the PXRD pattern of the sample was measured. The PXRD pattern of the **Eu-MOF** samples after soaking in each solvent showed close similarity to the PXRD pattern of **Eu-MOF** as synthesised (**Fig. 3.48**), indicating that the MOF does not lose crystallinity in the presence of these solvents.

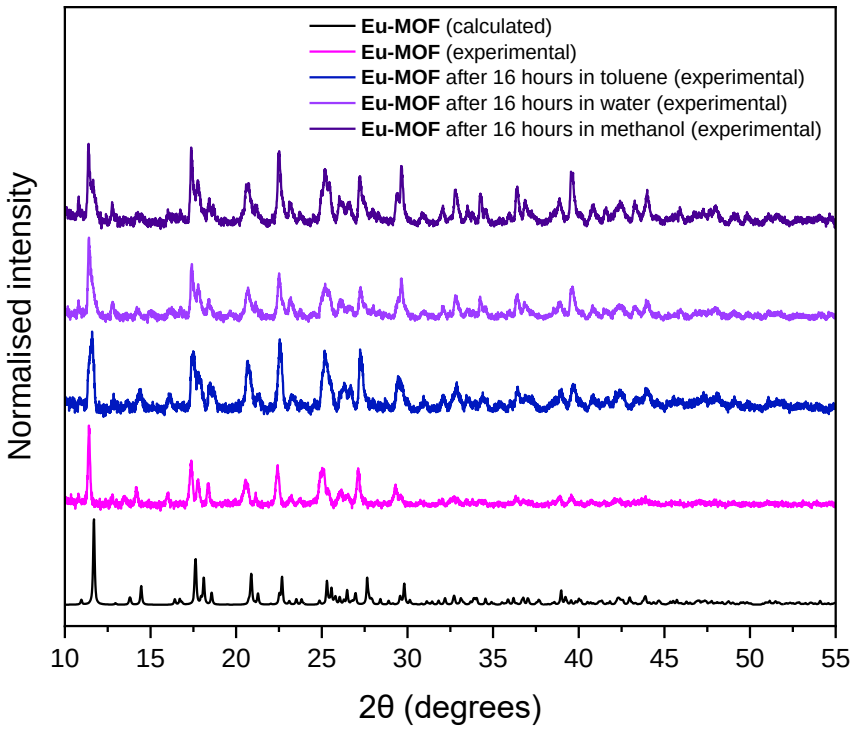

Fig. 3.48 Comparison of the PXRD pattern of **Eu-MOF** as synthesised with the PXRD pattern of **Eu-MOF** after soaking a sample of the crystals in water, methanol or toluene for 16 hours. Both the simulated and experimental patterns were normalised to facilitate comparison of the patterns. The experimental PXRD patterns were measured in air, at room temperature.

Thus, PXRD studies of **Sm-MOF** and **Eu-MOF** indicate that both samples are phase-pure, and that **Eu-MOF** shows excellent thermal stability, in addition to stability in water, and organic solvents (toluene, methanol).

3.9 Gas Sorption Measurements

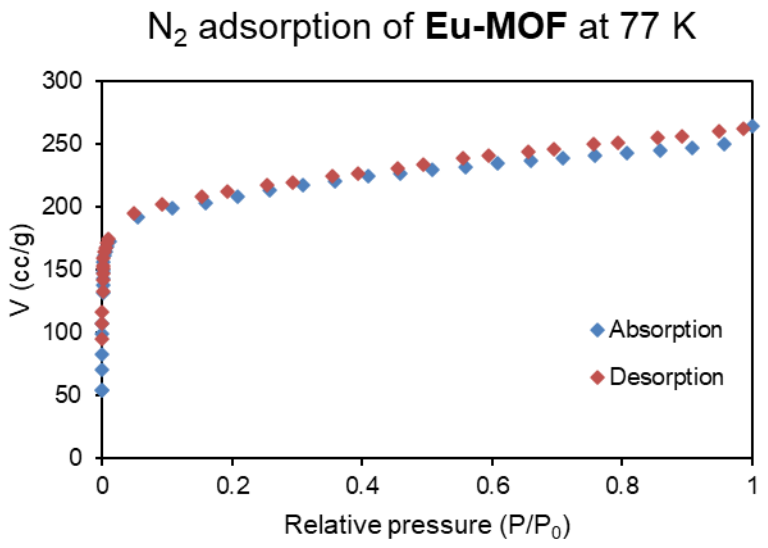

Fig. 3.49 N_2 absorption plot of **Eu-MOF** at 77 K. The sample was activated at 200 °C, under secondary vacuum.

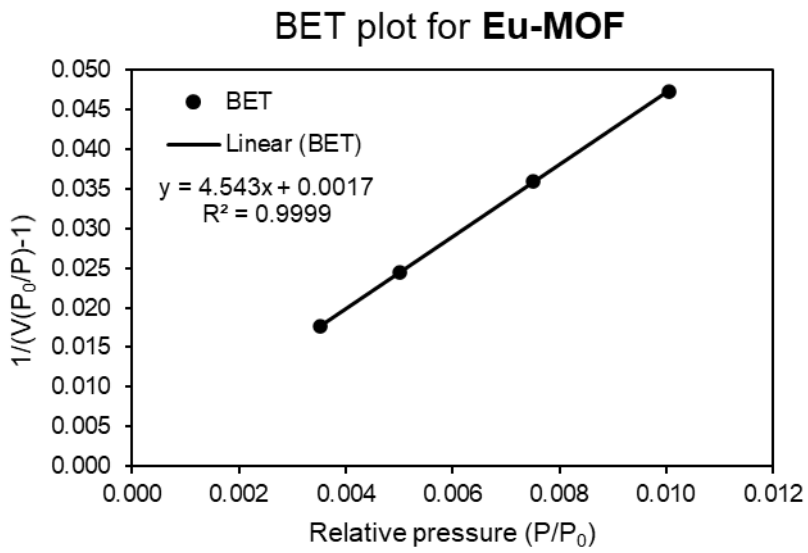

Fig. 3.50 BET plot of **Eu-MOF.** The sample was activated at 200 °C, under secondary vacuum.

Following confirmation of the thermal stability of **Eu-MOF**, gas sorption analysis was carried out on a sample of **Eu-MOF** crystals which had been washed with DMF. **Eu-MOF** was activated at two different temperatures under secondary vacuum; 120 °C and 200 °C. N_2 gas adsorption showed that **Eu-MOF** maintained porosity upon activation. No significant difference in gas uptake was observed in the sample when activated at 200 °C compared to activation at 120 °C. The Brunner-Emmett-Teller (BET) surface area of **Eu-MOF** was calculated to be 766.28 $m^2 g^{-1}$ and a total pore volume of 0.408 $cm^3 g^{-1}$ was found. These experimental values can be compared to the theoretical calculations performed using the single crystal XRD data and RASPA,[46] which gave a surface area of 929 $m^2 g^{-1}$ and a total pore volume of 0.325 $cm^3 g^{-1}$.

Similar values were obtained for **La-MOF** with an experimental BET surface area of 798.89 $m^2 g^{-1}$ and total pore volume of 0.516 $cm^3 g^{-1}$. This compares to the values calculated using the single crystal XRD data and RASPA,[46] which gave a surface area of 941 $m^2 g^{-1}$. The BET plot for **La-MOF**, as well as the additional supporting data for both **La-MOF** and **Eu-MOF** can be found in the appendix of this thesis.

3.10 Eu-MOF and Sm-MOF: Photochemistry

To evaluate the role of H_3**TTT** as a photosensitising ligand, UV-vis absorption, diffuse reflectance spectroscopy and photoluminescence studies were carried out using H_3**TTT**, **Sm-MOF** and **Eu-MOF**. The UV-vis absorption spectrum of H_3**TTT** shows a λ_{max} of 365 nm. When excited at 365 nm, H_3**TTT** shows a broad emission band in the visible region of the spectrum, with a maximum at ca. 430 nm.

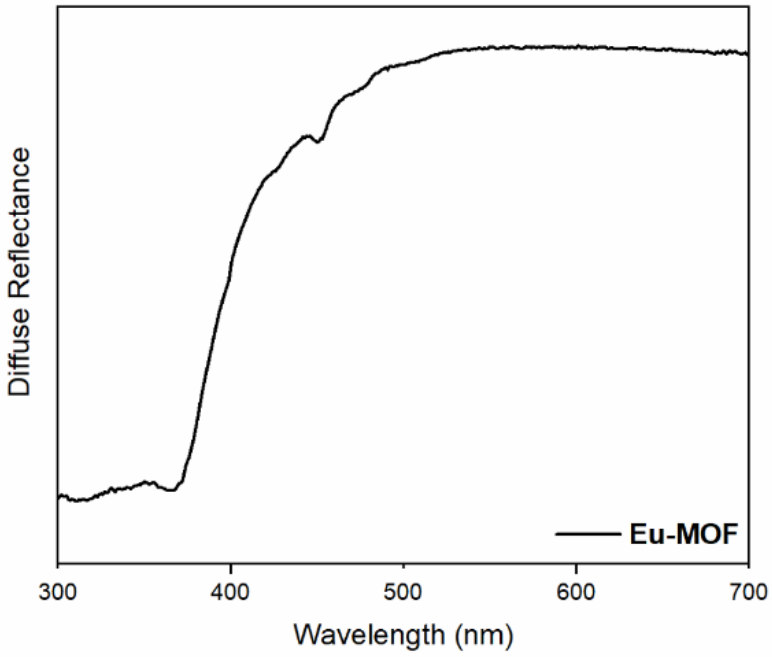

Fig. 3.51 Diffuse reflectance spectrum of **Eu-MOF** in the solid state.

Diffuse reflectance spectroscopy of solid-state samples of **Eu-MOF** show that this material has an absorption onset at ca. 400 nm.

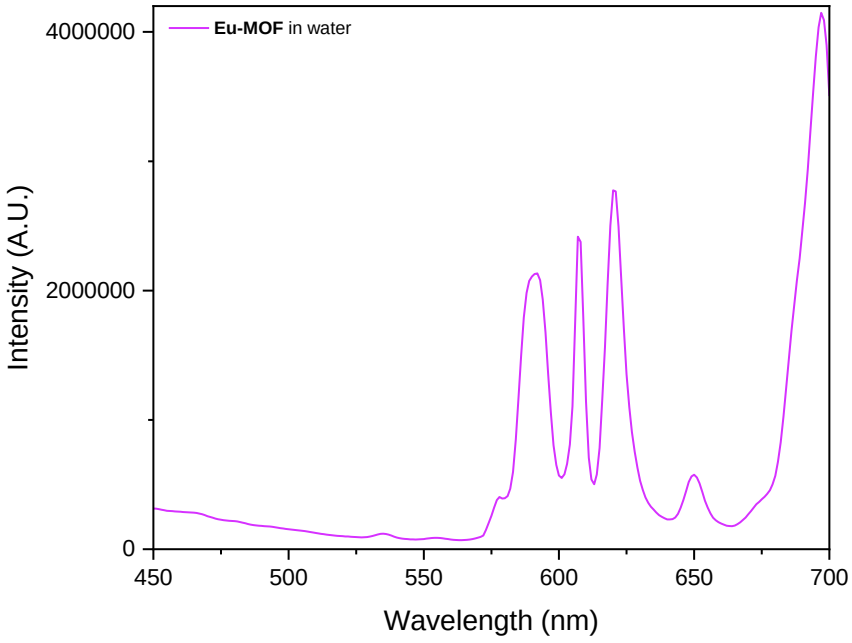

Fig. 3.52 Photoluminescence spectrum of a suspension of **Eu-MOF** crystals in acetonitrile (λ_{ex} = 365 nm).

Fig. 3.53 Photograph of **Eu-MOF** irradiated under UV light (λ_{ex} = 365 nm).

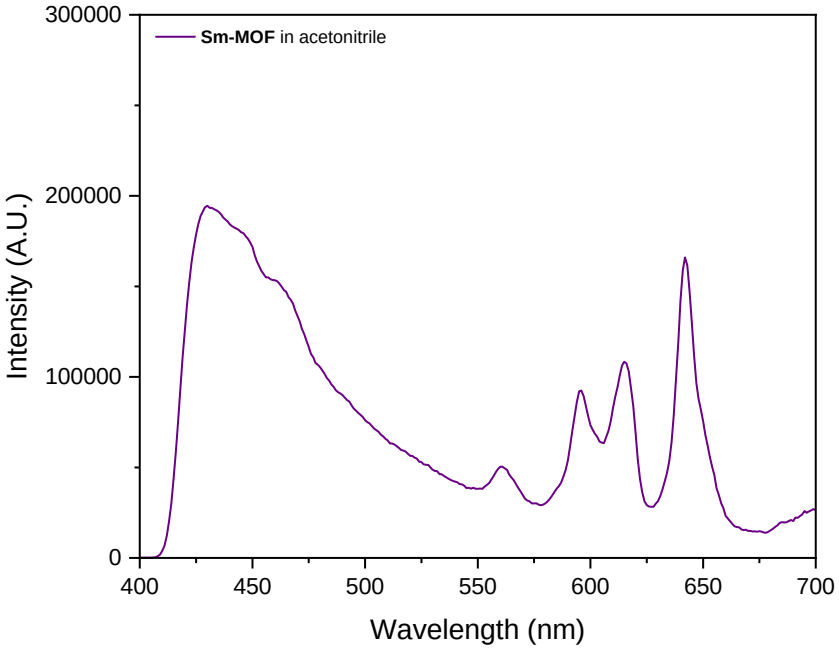

Fig. 3.54 Photoluminescence spectrum of a suspension of **Sm-MOF** crystals in acetonitrile (λ_{ex} = 365 nm).

Fig. 3.52 shows the photoluminescence spectrum of a suspension of **Eu-MOF** in water solution. Upon excitation of **Eu-MOF** (λ_{ex} = 365 nm), strong red photoluminescence is observed, which originates from Eu^{III} centered $^7F_J \leftarrow ^5D_0$ (J =0-4) transitions. Characteristic emission bands are observed for the Eu^{III} f-f transitions, which indicates that Eu^{III} ions in **Eu-MOF** are sensitized by the electron-rich

TTT ligands in the structure. The most intense transition in the photoluminescence spectrum of **Eu-MOF** is the hypersensitive $^7F_2 \leftarrow\!\!- {}^5D_0$ emission band, which is split into two peaks at 607 and 0nm. Another strong transition occurs at 592 nm, arising from the $^7F_1 \leftarrow\!\!- {}^5D_0$ transitions. Two weaker emission bands occur at 650 nm and 697 nm, which correspond to the $^7F_3 \leftarrow\!\!- {}^5D_0$ and $^7F_4 \leftarrow\!\!- {}^5D_0$ transitions respectively.

Comparison with the emission spectrum of H_3**TTT** shows that the broad emission band observed from the ligand emission spectrum is absent in the emission spectrum of **Eu-MOF**. This suggests that energy transfer from the **TTT** excited states to Eu^{III} ions in **Eu-MOF** occurs efficiently.

The photoluminescence spectrum of **Sm-MOF** (λ_{ex}=365 nm) shows four emission bands at 561, 596, 615 and 642 nm, arising from the $^6H_{5/2} \leftarrow\!\!- {}^4G_{5/2}$, $^6H_{7/2} \leftarrow\!\!- {}^4G_{5/2}$, $^6H_{9/2} \leftarrow\!\!- {}^4G_{5/2}$ and $\mathbf{^6H_{11/2} \leftarrow\!\!- {}^4G_{5/2}}$ transitions of the Sm^{III} metal centre respectively. In addition to the photoluminescence bands originating from Sm^{III} ions in **Sm-MOF**, a broad emission band is observed. Comparison with the UV-Vis photoluminescence spectrum of the free H_3**TTT** ligand confirms that this emission band originated from ligand-centred emission. For this reason, it can be concluded that the sensitisation of the Sm^{III} ions in **Sm-MOF** by $\mathbf{TTT^{3-}}$ linkers is not as efficient as in **Eu-MOF**.

Table 3.16 Summary of *f-f* transitions in **Sm-MOF** and **Eu-MOF** luminescence spectra.

Sm-MOF		**Eu-MOF**	
Transition	**Wavelength (nm)**	**Transition**	**Wavelength (nm)**
$^6H_{5/2} \leftarrow\!\!- {}^4G_{5/2}$	561	$^7F_1 \leftarrow\!\!- {}^5D_0$	592
$^6H_{7/2} \leftarrow\!\!- {}^4G_{5/2}$	596, 615	$^7F_2 \leftarrow\!\!- {}^5D_0$	607, 620
$^6H_{9/2} \leftarrow\!\!- {}^4G_{5/2}$	642	$^7F_3 \leftarrow\!\!- {}^5D_0$	650
$^6H_{11/2} \leftarrow\!\!- {}^4G_{5/2}$	699	$^7F_4 \leftarrow\!\!- {}^5D_0$	697

3.12 Eu-MOF Photoluminescence Quenching Behaviour

The pollution of water by metal ions has the potential to have environmental and health impacts. Notable ions which can trigger environmental damage, as well as adverse human health effects are Pb^{II}, Cd^{II}, and Cu^{II}.[47] For this reason, sensing of pollutant metal ions has been an attractive application of new materials, including MOFs, which have been shown to exhibit changes in photoluminescence in response to the presence of various ions.[48–50]

Eu-MOF possesses several key characteristics which suggest that this material is a promising candidate for photoluminescence quenching in response to the presence of pollutants. **Eu-MOF** demonstrates bright red photoluminescence which is visible to the naked eye. The MOF is stable in multiple solvents, including water. Furthermore, the presence of channels in the structure of **Eu-MOF** provides a large solvent accessible surface area which may increase the potential for interactions between the structure of **Eu-MOF** and ions in solution. Finally, the presence of S- and N-atoms in the structure may provide interaction sites which increase the potential of **Eu-MOF** as a sensing material.

In order to investigate the response of **Eu-MOF** photoluminescence to the presence of analytes, a suspension of **Eu-MOF** was prepared by sonicating crystal of **Eu-MOF** in deionised water (1 mg per mL). Solutions of metal salts ($Cu(NO_3)_2{\cdot}3H_2O$, $Fe(NO_3)_3{\cdot}9H_2O$, $Cd(NO_3)_2{\cdot}4H_2O$, $Ni(NO_3)_2{\cdot}6H_2O$, $Pb(NO_3)_2$, $Co(NO_3)_2{\cdot}6H_2O$) in deionised water (4 mM) were also prepared. Combining 1.5 mL of the **Eu-MOF** aqueous suspension with 1.5 mL of the analyte solution gave final concentration of 2 mM of the analytes and 0.5 mg per mL of **Eu-MOF**.

The photoluminescence spectrum (λ_{ex} = 365 nm) of **Eu-MOF** was measured 2 minutes after addition of analyte solutions to the **Eu-MOF** suspensions. The change in luminescence intensity was compared to a control (addition of 1.5 mL deionised water alone to 1.5 mL of the **Eu-MOF** suspension). The luminescence spectra of **Eu-MOF** 2 minutes after addition of the analyte solutions are shown in **Fig. 3.55**. Due to the close similarities between the intensity of the bands in their spectra, the plot of **Eu-MOF** in the presence of Cd^{II} is shown separately for clarity in **Fig. 3.56.**

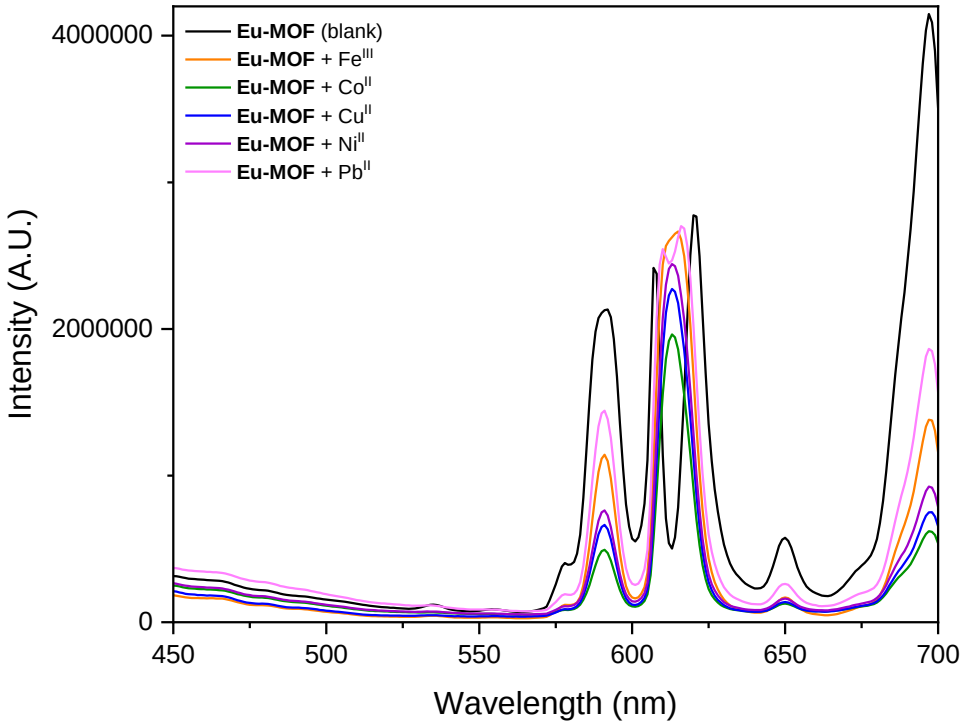

Fig. 3.55 Luminescence spectra of a suspension of **Eu-MOF** in water upon addition of metal ion analytes (λ_{ex} = 365 nm).

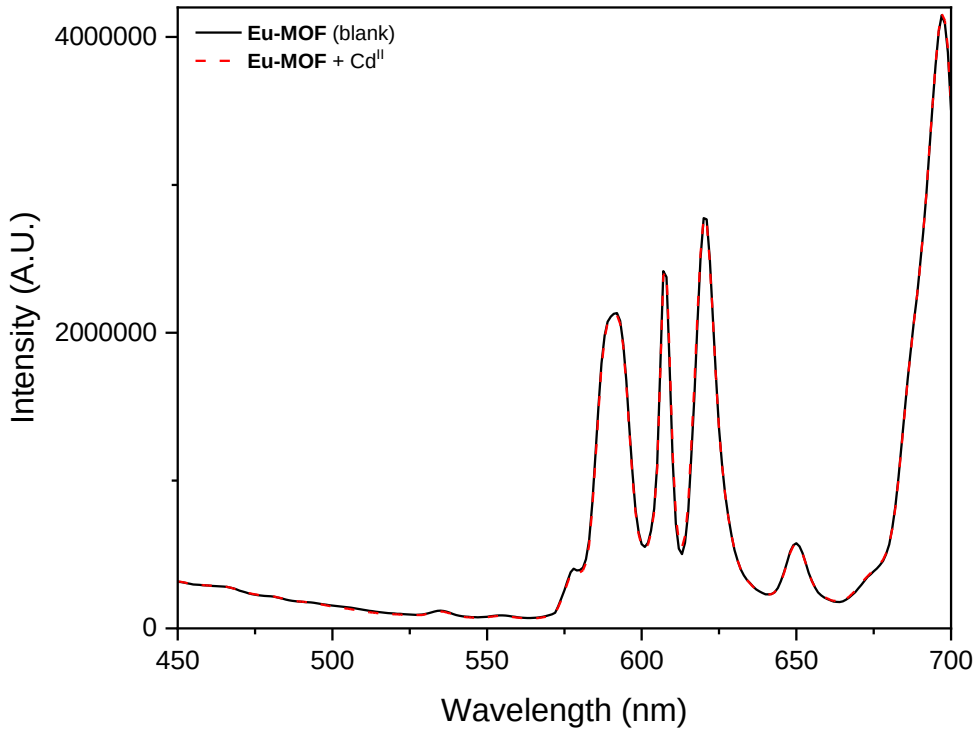

Fig. 3.56 Luminescence spectra of a suspension of **Eu-MOF** in water upon addition of Cd^{II} solution (λ_{ex} = 365 nm).

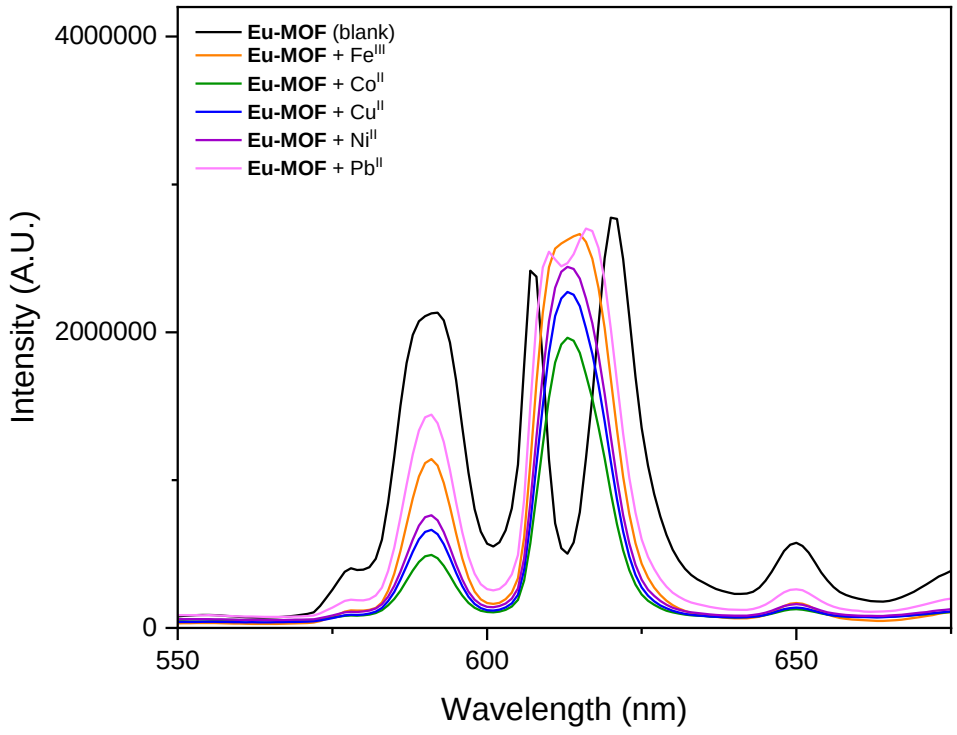

Fig. 3.57 Luminescence spectra of a suspension of **Eu-MOF** in water upon addition of metal ion analytes, showing the change in the hypersensitive $^7F_2 \leftarrow {}^5D_0$ emission band of **Eu-MOF** (λ_{ex} = 365 nm).

It is notable that the presence of metal ions caused a change in the shape of the hypersensitive $^7F_2 \leftarrow {}^5D_0$ emission band of **Eu-MOF** (**Fig. 3.57**). In the emission spectrum of **Eu-MOF** alone, the band is split into two components, however in the presence of metal ion salts, the emission band is seen to have one component, with a maximum of 614 nm. In some of the spectra, two emission bands are observed for this transition, however the emission bands are closer together than in the case of **Eu-MOF** alone.

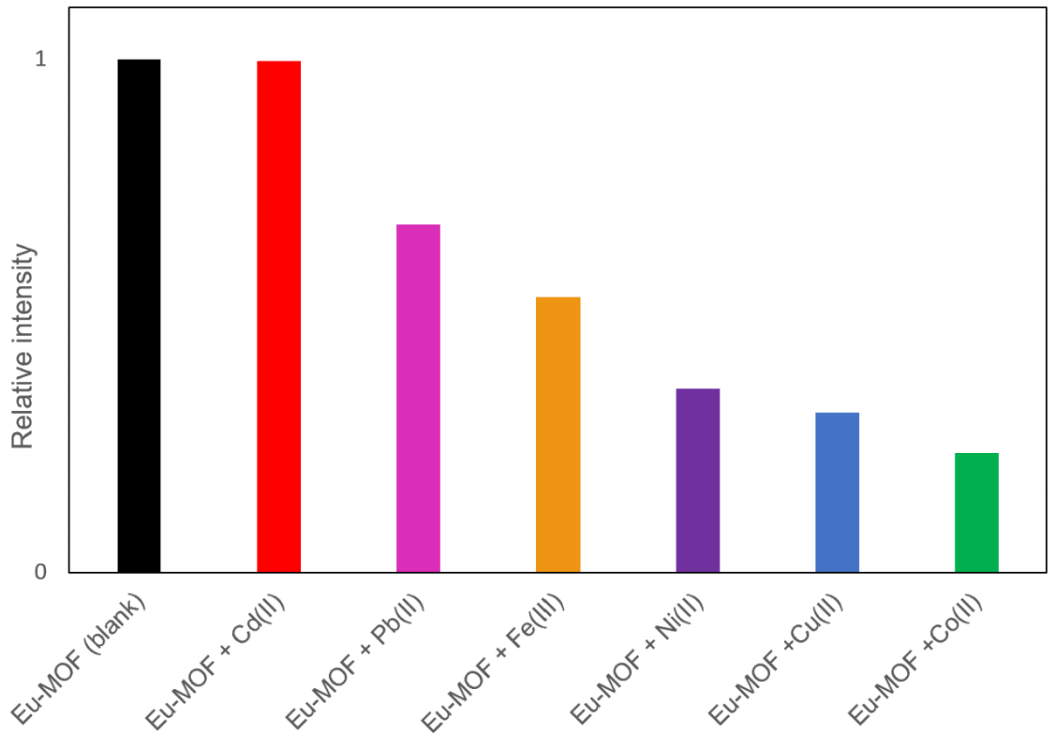

Fig. 3.58 Relative change in luminescence intensity of **Eu-MOF** $^7F_1 \leftarrow {}^5D_0$ transition in response to various metal ions (λ_{ex} = 365 nm, emission intensity monitored at 592 nm).

Table 3.17 Relative intensity of $^7F_1 \leftarrow {}^5D_0$ in **Eu-MOF** spectra after addition of analyte solutions, as compared to blank **Eu-MOF** sample.

Sample	**Relative intensity ($I_{sample}/I_{Eu\text{-}MOF}$)**
Eu-MOF (blank)	1
Eu-MOF + Cd^{II}	0.996
Eu-MOF + Pb^{II}	0.678
Eu-MOF + Fe^{III}	0.537
Eu-MOF + Ni^{II}	0.358
Eu-MOF + Cu^{II}	0.312
Eu-MOF + Co^{II}	0.232

A turn-off quenching effect in **Eu-MOF** photoluminescence was observed in response to the presence of metal ion analytes. Due to the changes in the splitting of the $^7F_2 \leftarrow {}^5D_0$ emission band, the decrease in the photoluminescence intensity was monitored at the $^7F_1 \leftarrow {}^5D_0$ band (591 nm), as

no changes in the features of this band were observed. The quenching effect depends on the nature of the ions, indicating that **Eu-MOF** is a selective sensor. The largest quenching effect was observed in response to Co^{II} ions.

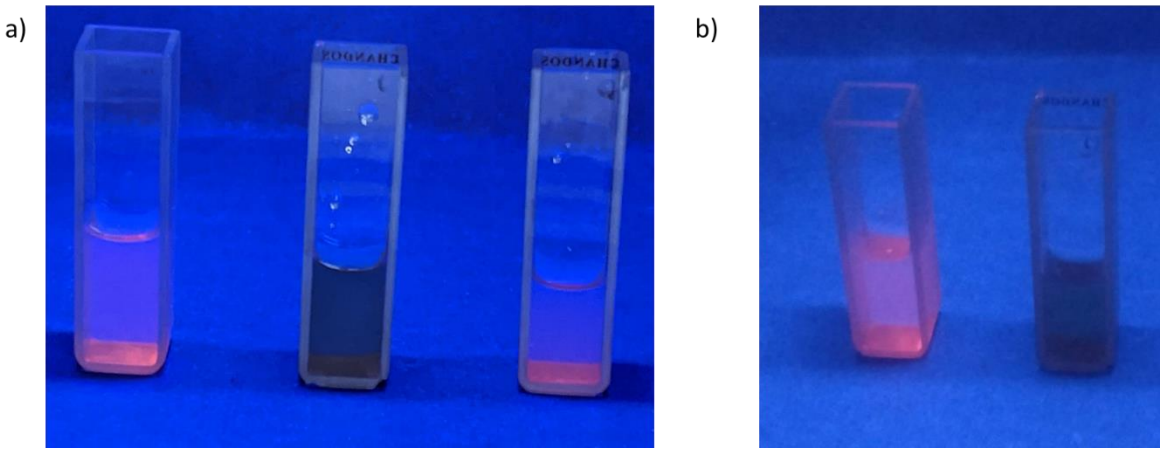

Fig. 3.59 Photograph showing the change in photoluminescence of **Eu-MOF** suspensions under UV light irradiation (365 nm) in response to the presence of analytes. **a)** Left: **Eu-MOF** in water (reference sample), middle: in response to the presence of Fe^{III} ions, right: in response to the presence of Cd^{II} ions. **b)** Left: **Eu-MOF** in water (reference sample), right: in response to the presence of Cu^{II} ions. The photographs were taken 16 hours after addition of the analyte solutions.

The photoluminescence quenching of **Eu-MOF** in the presence of metal ions could be observed under UV light irradiation with the naked eye (**Fig. 3.59** and **Fig. 3.60**). The visibility of the photoluminescence quenching to the naked eye presents an excellent property in this material, as this allows the MOF to be used for facile detection of metal ions in aqueous solution.

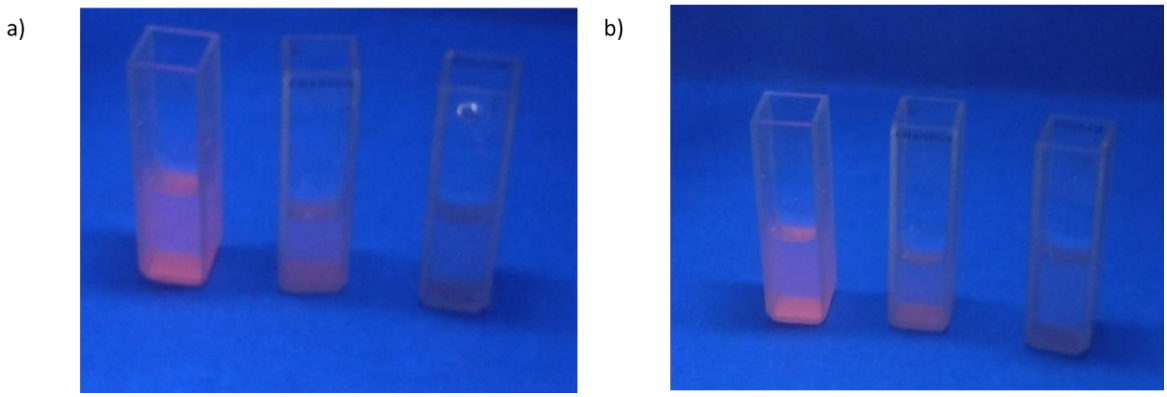

Fig. 3.60 Photograph showing the change in photoluminescence of **Eu-MOF** suspensions under UV light irradiation (365 nm) in response to the presence of analytes. **a)** Left: **Eu-MOF** in water (reference sample), middle: in response to the presence of Pb^{II} ions, right: in response to the presence of Cd^{II} ions. **b)** Left: **Eu-MOF** in water (reference sample), middle: in response to the presence of Pb^{II} ions, right: in response to the presence of Ni^{II} ions. The photographs were taken 16 hours after addition of the analyte solutions.

3.13 Conclusions

In this chapter, the synthesis of a new organic linker H_3**TTT** was reported, and this compound was studied by NMR spectroscopy and single crystal XRD analysis. The linker shows blue light luminescence when excited at 365 nm.

Two series of isostructural MOFs were synthesised using H_3**TTT**, both of which contain one-dimensional rod-shaped SBUs. The first series, incorporating **La-MOF**, **Ce-MOF**, **Pr-MOF** and **Nd-MOF**, has an inorganic SBU comprising ten-coordinate Ln^{III} ions. In the inorganic SBU of the second MOF series, **Sm-MOF** and **Eu-MOF**, eight-coordinate Ln^{III} ions form a zig zag chain within the SBU. Both MOF series have the same underlying **hms** topology. The structure of the MOFs synthesised using $\mathbf{TTT}^{3-}$ was demonstrated to be highly dependent on the nature of the Ln^{III} ion used, with a change in the structure observed as the lanthanide series progressed.

The MOFs were characterised by single crystal XRD, in addition to PXRD, FTIR spectroscopy, SEM and EDX analysis. Each of the MOFs were synthesised as phase-pure crystals with good yield. In terms of the stability of the MOFs, each of the MOFs were stable to air, as demonstrated by PXRD, and TGA indicated that the MOFs were thermally stable to 400 °C. PXRD experiments showed that **La-MOF** and **Eu-MOF** were shown to be stable to thermal activation at 250 °C under secondary vacuum. **Eu-MOF** was also shown to be water-stable, as well as stable in methanol and in toluene.

Both **Eu-MOF** and **Sm-MOF** show emission bands characteristic of Ln^{III} ions when the materials are excited into the ligand absorption band, indicating that H_3**TTT** effectively sensitises the metal ions in the Ln-MOFs. In the case of **Eu-MOF**, bright red luminescence can be observed using the naked eye when the material is excited under UV light irradiation. **Eu-MOF** has also been shown to behave as a luminescence sensor, exhibiting a turn-off luminescence response in the presence metal cations in water. The response depends on the nature of the metal ion and shows the highest level of quenching for Co^{II} ions. The luminescence response can be observed with the naked eye, a very promising feature for this MOF.

When compared to **Cu-TTMOP** discussed in chapter 2, the metal-organic materials synthesised and characterised in this chapter had more promising characteristics, such as improved stability to solvents and air, in addition to posessing 3D porous frameworks with high surface areas, and in the case of **Sm-MOF** and **Eu-MOF**, interesting photoluminescence properties.

However, one disadvantage of the novel materials reported in this chapter is that none of these MOFs possess the ability to absorb visible light, which would present an advantage in the search for light-harvesting photoactive materials. Chapter 5 will build on the work reported in this chapter, by discussing the design of a MOF constructed from a heterocycle-based metallolinker, with the aim of constructing a stable MOF which can act as a visible light harvesting material.

References

1 E. P. McCarney, C. S. Hawes, J. A. Kitchen, K. Byrne, W. Schmitt and T. Gunnlaugsson, *Inorg. Chem.*, 2018, **57**, 3920–3930.

2 G. Tobin, S. Comby, N. Zhu, R. Clérac, T. Gunnlaugsson and W. Schmitt, *Chem. Commun.*, 2015, **51**, 13313–13316.

3 K. Liu, X. Zhang, X. Meng, W. Shi, P. Cheng and A. K. Powell, *Chem. Soc. Rev.*, 2016, **45**, 2423–2439.

4 K. Liu, H. Li, X. Zhang, W. Shi and P. Cheng, *Inorg. Chem.*, 2015, **54**, 10224–10231.

5 L. Song, W. Liu, Y. Wang, L. Chen, X.-F. Wang and S. Wang, *CrystEngComm*, 2019, 3471–3477.

6 Y.-L. Gai, Q. Guo, X.-Y. Zhao, Y. Chen, S. Liu, Y. Zhang, C.-X. Zhuo, C. Yao and K.-C. Xiong, *Dalt. Trans.*, 2018, **47**, 12051–12055.

7 S.-L. Yang, Y.-Y. Yuan, P.-P. Sun, T. Lin, C.-X. Zhang and Q.-L. Wang, *New J. Chem.*, 2018, **42**, 20137–20143.

8 R. Liu, Q.-Y. Liu, R. Krishna, W. Wang, C.-T. He and Y.-L. Wang, *Inorg. Chem.*, 2019, **58**, 5089–5095.

9 Y. Pan, H. Q. Su, E. L. Zhou, H. Z. Yin, K. Z. Shao and Z. M. Su, *Dalt. Trans.*, 2019, **48**, 3723–3729.

10 D. Bejan, L. G. Bahrin, S. Shova, N. L. Marangoci, Ü. Kökçam-Demir, V. Lozan and C. Janiak, *Molecules*, 2020, **25**, 3055.

11 L. Xu, Y. Li, Q. Pan, D. Wang, S. Li, G. Wang, Y. Chen, P. Zhu and W. Qin, *ACS Appl. Mater. Interfaces*, 2020, **12**, 18934–18943.

12 Q.-R. Liu, B. Liu, M.-M. Qiu, W.-N. Miao and L. Xu, *J. Solid State Chem.*, 2022, 123138.

13 H. Li, Y. Han, Z. Shao, N. Li, C. Huang and H. Hou, *Dalt. Trans.*, 2017, **46**, 12201–12208.

14 X. Han, J. Liu, K. Yu, Y. Lu, W. Xiang, D. Zhao and Y. He, *Inorg. Chem.*, 2022, **61**, 5067–5075.

15 Y. Yang, L. Chen, F. Jiang, M. Wu, J. Pang, X. Wan and M. Hong, *CrystEngComm*, 2019, **21**, 321–328.

16 H. Yu, Q. Liu, J. Li, Z. M. Su, X. Li, X. Wang, J. Sun, C. Zhou and X. Hu, *J. Mater. Chem. C*, 2021, **9**, 562–568.

17 Y. Zhang, Y. Wang, L. Liu, N. Wei, M. L. Gao, D. Zhao and Z. B. Han, *Inorg. Chem.*, 2018,

57, 2193–2198.

18 H. H. Yu, J. Li, Y. Yang, X. Li, Z. M. Su and J. Sun, *J. Solid State Chem.*, 2021, **294**, 121789.

19 J. R. Choi, T. Tachikawa, M. Fujitsuka and T. Majima, *Langmuir*, 2010, **26**, 10437–10443.

20 G.-X. Wen, Y.-P. Wu, W.-W. Dong, J. Zhao, D.-S. Li and J. Zhang, *Inorg. Chem.*, 2016, **55**, 10114–10117.

21 A. J. Savyasachi, D. F. Caffrey, K. Byrne, G. Tobin, B. D'Agostino, W. Schmitt and T. Gunnlaugsson, *Front. Chem. Sci. Eng.*, 2019, **13**, 171–184.

22 J.-C. G. Bünzli and S. V. Eliseeva, in *Springer Series on Fluorescence*, 2010, vol. 13, pp. 1–45.

23 N. Campagnol, E. Rezende Souza, D. E. De Vos, K. Binnemans and J. Fransaer, *Chem. Commun.*, 2014, **50**, 12680–12683.

24 S. Mohapatra, S. Adhikari, H. Riju and T. K. Maji, *Inorg. Chem.*, 2012, **51**, 4891–4893.

25 Y. N. Gong, P. Xiong, C. T. He, J. H. Deng and D. C. Zhong, *Inorg. Chem.*, 2018, **57**, 5013–5018.

26 R. Liu, Q. Y. Liu, R. Krishna, W. Wang, C. T. He and Y. L. Wang, *Inorg. Chem.*, 2019, **58**, 5089–5095.

27 V. Zeleňák, M. Almáši, A. Zeleňáková, P. Hrubovčák, R. Tarasenko, S. Bourelly and P. Llewellyn, *Sci. Rep.*, 2019, **9**, 1–9.

28 F. Luo, X. Feng, Y. Li, G. Zheng, A. Zhou, P. Xie, Z. Wang, T. Tao, X. Long and J. Wan, *Colloids Surfaces A Physicochem. Eng. Asp.*, 2021, **611**, 125906.

29 Y.-Q. Wang, Q.-H. Tan, H.-T. Liu, W. -Sun and Z.-L. Liu, *RSC Adv.*, 2015, **5**, 86614–86619.

30 Z. Wang, J. Liu, Y. Fu, C. Liu, C. Pan, Z. Liu and G. Yu, *Chem. Commun.*, 2017, **53**, 4128–4131.

31 A. Bajpai, M. S. Krishna and J. N. Moorthy, *J. Indian Inst. Sci.*, 2014, **94**, 25–34.

32 R. Seetharaj, P. V. Vandana, P. Arya and S. Mathew, *Arab. J. Chem.*, 2019, **12**, 295–315.

33 L. J. Farrugia, *J. Appl. Crystallogr.*, 2012, **45**, 849–854.

34 O. V. Dolomanov, L. J. Bourhis, R. J. Gildea, J. A. K. Howard and H. Puschmann, *J. Appl. Crystallogr.*, 2009, **42**, 339–341.

35 O. C. Gagné, *Acta Crystallogr. Sect. B Struct. Sci. Cryst. Eng. Mater.*, 2018, **74**, 49–62.

36 S. Alvarez, P. Alemany, D. Casanova, J. Cirera, M. Llunell and D. Avnir, *Coord. Chem. Rev.*,

2005, **249**, 1693–1708.

37 I. D. Brown and D. Altermatt, *Acta Crystallogr. Sect. B Struct. Sci.*, 1985, **41**, 244–247.

38 A. Trzesowska, R. Kruszynski and T. J. Bartczak, *Acta Crystallogr. Sect. B Struct. Sci.*, 2004, **60**, 174–178.

39 V. A. Blatov, A. P. Shevchenko and D. M. Proserpio, *Cryst. Growth Des.*, 2014, **14**, 3576–3586.

40 Y. W. Ren, J. X. Liang, J. X. Lu, B. W. Cai, D. Bin Shi, C. R. Qi, H. F. Jiang, J. Chen and D. Zheng, *Eur. J. Inorg. Chem.*, 2011, 4369–4376.

41 T. Kajiwara, M. Higuchi, A. Yuasa, H. Higashimura and S. Kitagawa, *Chem. Commun.*, 2013, **49**, 10459.

42 G. B. Deacon and R. J. Phillips, *Coord. Chem. Rev.*, 1980, **33**, 227–250.

43 A. Trzesowska, R. Kruszynski and T. J. Bartczak, *Acta Crystallogr. Sect. B Struct. Sci.*, 2004, **60**, 174–178.

44 L. Zhai, W. W. Zhang, X. M. Ren and J. L. Zuo, *Dalt. Trans.*, 2015, **44**, 5746–5754.

45 A. R. K. Chatenever, B. Ehlke, P. Le Maguerès, E. W. Reinheimer, X. Song, H. Fei and S. R. J. Oliver, *CrystEngComm*, 2021, **23**, 1388–1397.

46 D. Dubbeldam, S. Calero, D. E. Ellis and R. Q. Snurr, *Mol. Simul.*, 2016, **42**, 81–101.

47 L. Joseph, B. M. Jun, J. R. V. Flora, C. M. Park and Y. Yoon, *Chemosphere*, 2019, **229**, 142–159.

48 Y. Z. Chen and H. L. Jiang, *Chem. Mater.*, 2016, **28**, 6698–6704.

49 S. A. A. Razavi and A. Morsali, *Coord. Chem. Rev.*, 2020, **415**, 213299.

50 W. Wu, B. Li, C. Gu, J. Wang, A. Singh and A. Kumar, *J. Mol. Struct.*, 2017, **1148**, 531–536.

Chapter 4 : Ln-MOFs with Dinuclear SBUs Based on Gd^{III}, Dy^{III}, Er^{III} and Yb^{III}

4.1 Introduction

The previous chapter pertained to the synthesis and characterisation of the novel tritopic linker H_3**TTT**. Reactions between H_3**TTT** and Ln^{III} salts resulted in two series of isostructural MOFs with infinite rod-shaped SBUs. The structure of the MOFs formed was dependent on the location of the Ln^{III} in the lanthanide series, with one structure formed for La^{III}, Ce^{III}, Pr^{III} and Nd^{III}, and a different structure for Sm^{III} and Eu^{III}. The MOFs formed using H_3**TTT** had many desirable properties, such as high yield, phase purity, in addition to thermal stability. In this chapter, investigations into the coordination chemistry of the novel linker H_3**TTT** will be expanded by examining the structures of MOFs formed by reacting H_3**TTT** with Ln^{III} ions from the latter half of the lanthanide series.

The lanthanide ions used in the synthesis of MOFs in this chapter, Gd^{III}, Dy^{III}, Er^{III} and Yb^{III}, have many interesting properties, both in terms of their photochemistry,[1] and magnetic properties.[2] These inherent properties of later-lanthanide series ions, in addition to the excellent stability properties of Ln-MOFs, such as thermal stability,[3–5] water stability,[4,6,7] and stability to pH,[8–10] make MOFs based on later lanthanide series ions very interesting materials to study.

Ln-MOFs which are based on ions in the second half of the lanthanide series have been used in a broad range of applications. Gd-MOF nanoparticles have been studied as potential alternatives to small molecule contrast agents in magnetic resonance imaging (MRI). The use of hydrotropes in the synthesis of these nanoscale Gd^{III}-based MOFs allowed control of the nanoparticle size in these MOFs, offering another example of the degree to which MOF properties can be tuned towards specific applications.[11]

The photochemical properties of Ln-MOFs have been exploited in a range of applications. An Er-based MOF, which uses terphenyl-3,4",5-tricarboxylate as a linker, has been used to encapsulate thioflavine T (ThT), giving **ThT@Er-MOF**, a MOF which can behave as fluorescent sensor to detect the presence of three biomarkers for Alzheimer's disease, presenilin 1, amyloid β-protein and acetylcholine in cerebrospinal fluid solution.[12] Additionally, Yb^{III}- and Dy^{III}-based MOFs display NIR luminescence,[13,14] and Yb-MOFs have been studied for luminescence sensing applications.[15,16]

The magnetic properties of MOFs based on later-lanthanide series ions have been studied. For example, a series of Ln^{III}-MOFs (Ln = Nd^{III}, Gd^{III}, Dy^{III}, Er^{III} and Yb^{III}) have been reported by Rodriguez-Diéguez and co-workers, based on a 9,10-anthracenedicarboxylate linker.[17] A study of the magnetic relaxation of these MOFs revealed that the Nd^{III}- and Yb^{III}-based MOFs demonstrated slow relaxation of magnetisation, which represent the first MOFs to be reported with this property.

In this chapter, we report a series of four MOF structures based on H_3**TTT**. Each of these MOFs features dinuclear {Ln^{III}_2} SBUs (Ln^{III} = Gd^{III}, Dy^{III}, Er^{III} and Yb^{III}}, with coordinated solvent

molecules. The Ln-MOFs are similar in structures, all featuring Ln^{III} dimer SBUs connected by **TTT**$^{3-}$ linkers to form two-dimensional sheets which pack in layers. Physicochemical characterisation of these MOFs will be carried out to further understand the properties of these novel materials.

4.2 Synthesis and crystal structures of Later Lanthanide Series MOFs

4.2.1 Solvothermal synthesis of MOFs

In many cases, Ln-MOFs have been observed to form isostructural series of MOFs featuring metals across the lanthanide series.[18–20] Therefore, initial attempts at crystallisation of MOFs using metals later in the lanthanide series (Gd to Yb) utilised the same reaction conditions as those used in the synthesis of MOFs previously reported in this work.

Under the conditions in which the previously described MOFs were synthesised, (1:1 metal to ligand ratio, 0.0125 M concentration of each reactant in DMF, heated in a seal vial at 100 °C for between 24 and 72 hours), reaction of H_3**TTT** and Gd^{III}, Tb^{III}, Dy^{III}, Er^{III} and Yb^{III} salts gave large quantities of precipitate, and no crystalline material. The reaction was repeated at different reactant concentrations and ratios, as well as over different reaction durations. Heating a solution of Ln^{III} salts (Ln = Gd, Dy, Er and Yb) and H_3TTT with concentrations of 0.05 M in DMF at 100 °C gave pale yellow plate-shaped crystals, which formed after 24-72 hours depending on the Ln^{III} salt. The metals salts used were $Gd(NO_3)_3{\cdot}5H_2O$, $Dy(NO_3)_3{\cdot}5H_2O$, $Er(NO_3)_3{\cdot}5H_2O$, $Yb(NO_3)_3{\cdot}6H_2O$. The solutions were heated for a duration of either 24 hours (**Er-MOF**, **Yb-MOF**) or 72 hours (**Gd-MOF**, **Dy-MOF**). The MOFs formed as thin, plate-shaped crystals, which either grew in stacks, or formed as clusters, with plate-shaped crystals radiating from a central point. Despite numerous attempts under different reaction conditions, reaction with Tb^{III} salts and H_3TTT gave no MOF formation. Instead, the ligand repeatedly crystallised from the reaction mixture, in addition to large quantities of insoluble amorphous precipitate.

4.2.2 Crystal Structure Description of MOFs

Attempts to carry out single crystal XRD measurements of **Ln-MOF** crystals (Ln = Gd, Dy, Er, Yb) were hindered both by the small and thin crystal dimensions, in addition to their crystal habit, as plates of **Ln-MOF** crystals formed as clusters or stacks of plate-shaped crystals. In order to measure single crystal data, it was necessary to cut a single plate-shaped crystal from clusters or stacks of plate-shaped crystals which had formed during the reaction. Due to their size, the crystals did not diffract readily, however, the crystal structure of **Gd-MOF** could be solved and refined. The structure of **Gd-MOF** will be discussed in detail in this section, and later in this chapter demonstrate that **Dy-MOF**, **Er-MOF** and **Yb-MOF** are isostructural to **Gd-MOF**.

Gd-MOF crystallises in the monoclinic space group $P2_1/c$, and has the structural formula $[Gd_4(\mathbf{TTT})_3(DMF)_2(NO_3)(H_2O)_7(OH)_2]$. The asymmetric unit of **Ln-MOFs** consists of four crystallographically independent Gd^{III} ions, three **TTT**$^{3-}$ ligands, 7 coordinating OH^- ions or water

molecules and 2 coordinating DMF molecules (**Fig. 4.1**). Furthermore, each **Gd-MOF** structure also features three counter anions to balance the charge per asymmetric unit. One of these counterions is a chelating nitrate ion, while the remaining charge is balanced by OH^- ions. It was not possible to distinguish between the coordinating water molecules and OH^- ions. The crystal data and refinement results for **Gd-MOF** are presented in **Table 4.1**.

Table 4.1 Crystal data and refinement results for Ln-MOFs

Compound name	**Gd-MOF**
Empirical formula	$C_{30}H_{16}Gd_2N_6O_{16}S_{4.5}$
Formula weight	1175.26
Temperature (K)	100.0
Crystal description	Colourless plate
Crystal system	Monoclinic
Space group	$P2_1/c$
a (Å)	22.8462(11)
b (Å)	25.8299(14)
c (Å)	23.3623(12)
α (°)	90
β (°)	97.559(3)
γ (°)	90
V (Å^3)	13666.6(12)
Z	8
ρ_{calc} (g/cm^3)	1.142
μ (mm^{-1})	14.106
F(000)	4528
Radiation	CuKα (λ = 1.54178 nm)
2θ range for data collection (°)	3.902 to 109.548
Reflections collected	89851
Independent reflections	16617
Data/restraints/parameters	16617/ 482/ 1058
Goodness-of-fit on F^2	1.112
R_1 [I≥2σ (I)], all	0.1233, 0.2305
wR_2 [I≥2σ (I)], all	0.3313, 0.3952
Largest diff. peak/hole (e Å^{-3})	1.88/ -0.89

The four crystallographically independent Gd^{III} ions in **Gd-MOF** form two different dinuclear {Gd_2} SBUs, which differ in the coordination environment of the Gd^{III} ions. In the {Gd_2} dimer containing Gd1 and Gd2, (**Fig. 4.2a**)), both Gd^{III} ions are eight-coordinate. Four carboxylates from four different **TTT**$^{3-}$ molecules bridge the two Gd^{III} ions, with a μ^2-η^1:η^1 coordination mode. A fifth **TTT**$^{3-}$ linker coordinates this SBU through a carboxylate moiety which chelates Gd1 in a η^2 coordination mode. Gd1 is also coordinated by a chelating nitrate ion. In addition to the O atoms from the bridging **TTT**$^{3-}$ carboxylate moieties, Gd2 is coordinated by O atoms from two DMF molecules and two coordinating water or OH^- ions. The Gd-Gd distance in this dimer is 4.3628(2) Å.

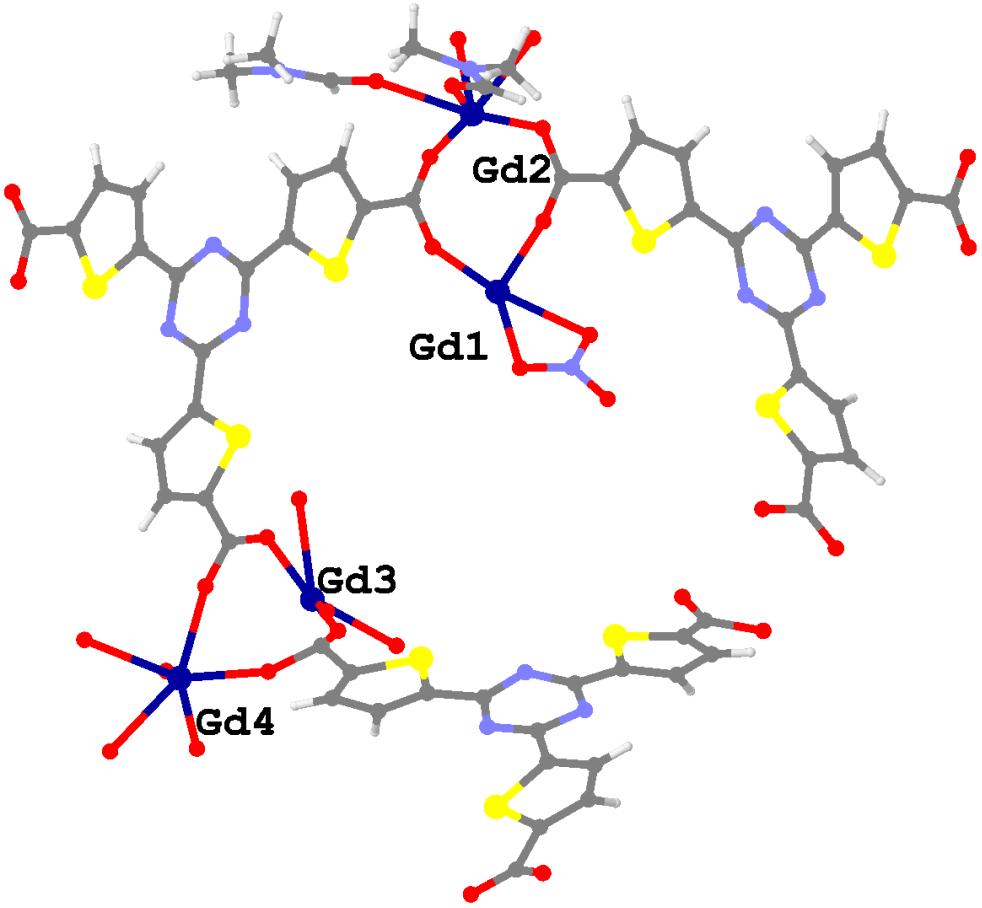

Fig. 4.1 Asymmetric unit of **Gd-MOF**, viewed along the crystallographic *c*-axis, with the Gd ions labelled. Atom colour scheme: Gd, dark blue, C, dark grey, S, yellow, O, red, N, light blue, H, white. H-atoms on coordinating O atoms are omitted for clarity.

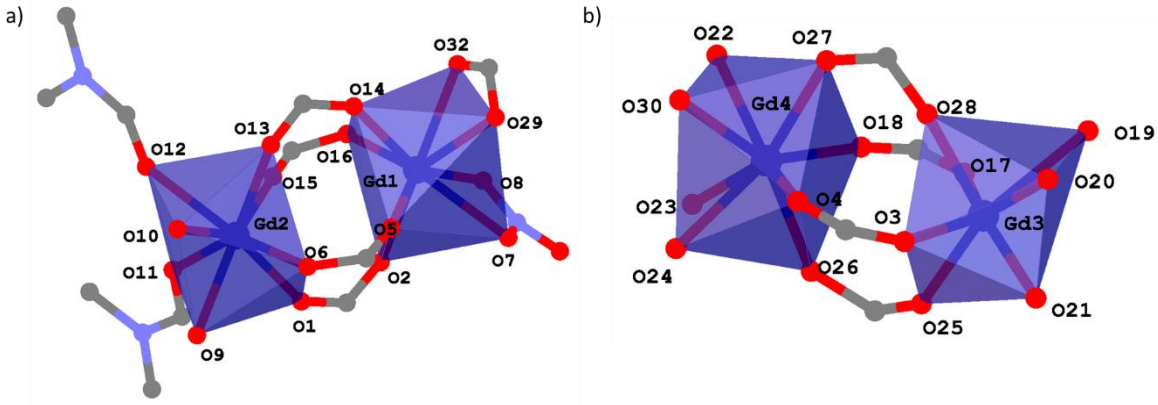

Fig. 4.2 The {Gd_2} dimer SBUs in **Gd-MOF**, with Gd and O atom labels shown. Atom colour scheme: Gd, dark blue, C, dark grey, O, red, N, light blue. H-atoms are omitted for clarity.

The second dinuclear Gd^{III} SBU, containing Gd3 and Gd4, also features two Gd^{III} ions bridged by four bridging μ^2-η^1:η^1 carboxylate moieties (**Fig. 4.2b)**). Gd3 has a coordination number of seven, while Gd4 is eight-coordinate, and these Gd^{III} ions are coordinated by three and four water molecules or OH^- ions respectively. The Gd-Gd distance in this SBU is 4.30526(15) Å.

Table 4.2 Selected bond lengths (Å) in **Gd-MOF**.

Bond	Distance	Bond Length (Å)	Bond	Distance	Bond Length (Å)
Gd1-O	Gd1-O2	2.36(2)	Gd2-O	Gd2-O1	2.32(2)
	Gd1-O5	2.26(2)		Gd2-O6	2.333(19)
	Gd1-O7	2.47(3)		Gd2-O9	2.40(2)
	Gd1-O8	2.40(3)		Gd2-O10	2.44(3)
	Gd1-O14	2.35(2)		Gd2-O11	2.40(2)
	Gd1-O15	2.37(2)		Gd2-O12	2.48(3)
	Gd1-O29	2.436(18)		Gd2-O13	2.32(2)
	Gd1-O32	2.487(19)		Gd2-O15	2.31(2)
Gd3-O	Gd3-O3	2.30(2)	Gd4-O	Gd4-O4	2.37(2)
	Gd3-O17	2.37(3)		Gd4-O18	2.32(3)
	Gd3-O19	2.68(6)		Gd4-O22	2.55(3)
	Gd3-O20	2.48(3)		Gd4-O23	2.64(5)
	Gd3-O21	2.62(7)		Gd4-O24	2.40(4)
	Gd3-O25	2.234(17)		Gd4-O26	2.32(3)
	Gd3-O28	2.242(17)		Gd4-O27	2.40(3)
				Gd4-O31	2.61(5)

Shape 2.1 software[21] was used to carry out continuous shape measurements, to determine the coordination environment of the Gd^{III} ions in **Gd-MOF**. The results of these calculations are shown in **Fig. 4.3** for the eight-coordinate ions Gd1, Gd2 and Gd4, and the results for the seven-coordinate Gd3 ion are displayed in **Table 4.4**. The lowest values, indicating the best fit to the geometry for that coordination environment, are highlighted in bold for each ion. The calculations show that each of the three eight-coordinate Gd^{III} ions in **Gd-MOF** are present in square antiprism coordination environments. The results calculated for Gd3 indicate that this ion has a distorted capped trigonal prism coordination environment.

Table 4.3 Continuous shape measurement values for Gd1, Gd2 and Gd4 atoms in **Gd-MOF**. The lowest value (indicating closest fit) is highlighted in bold.

Shape	**Symmetry**	**Gd1 Continuous shape measurement value**	**Gd2 Continuous shape measurement value**	**Gd4 Continuous shape measurement value**
Octagon	D_{8h}	32.917	29.498	30.549
Heptagonal pyramid	C_{7v}	20.359	23.153	20.838
Hexagonal bipyramid	D_{6h}	17.165	17.125	14.730
Cube	O_h	10.434	10.282	10.241
Square antiprism	D_{4d}	**1.540**	**0.250**	**1.454**
Triangular dodecahedron	D_{2d}	2.933	2.207	2.752
Johnson – Gyrobifastigium (J26)	D_{2d}	15.540	16.368	15.317
Johnson – Elongated triangular bipyramid (J14)	D_{3h}	27.222	28.513	25.985
Johnson – Elongated triangular bipyramid (J50)	C_{2v}	2.730	2.666	3.419
Biaugmented trigonal prism	C_{2v}	1.866	2.008	2.904
Snub disphenoid (J84)	C_{2v}	5.564	4.966	5.083
Tetrakis tetrahedron	T_d	11.230	11.051	11.057
Elongated trigonal bipyramid	D_{3h}	22.794	23.902	21.287

Table 4.4 Continuous shape measurement values for Gd3 atoms in **Gd-MOF**. The lowest value (indicating closest fit) is highlighted in bold.

Shape	**Symmetry**	**Gd3 Continuous shape measurement value**
Heptagon	D_{7h}	26.446
Hexagonal pyramid	C_{6v}	12.277
Pentagonal bipyramid	D_{5h}	10.567
Capped octahedron	C_{3v}	5.617
Capped trigonal prism	C_{2v}	**4.340**
Johnson pentagonal bipyramid (J13)	D_{5h}	13.009
Elongated triangular pyramid (J7)	C_{3v}	13.901

BVS calculations could be used to confirm the oxidation state of the Ln ions in these MOFs.[22] The results of these calculations are shown in **Table 4.5**. The BVS values indicate that all four of the Gd ions in **Gd-MOF** are present in the +III oxidation state. The R_0 values used in this calculation were 2.034 for the seven coordinate Gd3 ion, and 2.029 for the three eight coordinate ions.[23] The bond distances used in the BVS calculations are displayed in **Table 4.2**, and all distances were calculated using using Olex2 software.[24] The Gd^{III}-O distances are in good agreement with the ranges previously reported for Gd^{III} ions.[25]

Table 4.5 BVS values calculated for **Gd-MOF**.

MOF	Metal ion	R_0 (Å)	BVS	Oxidation state
Gd-MOF	Gd1	2.029	3.05	+III
	Gd2		3.17	+III
	Gd3		2.72	+III
	Gd4		2.69	+III

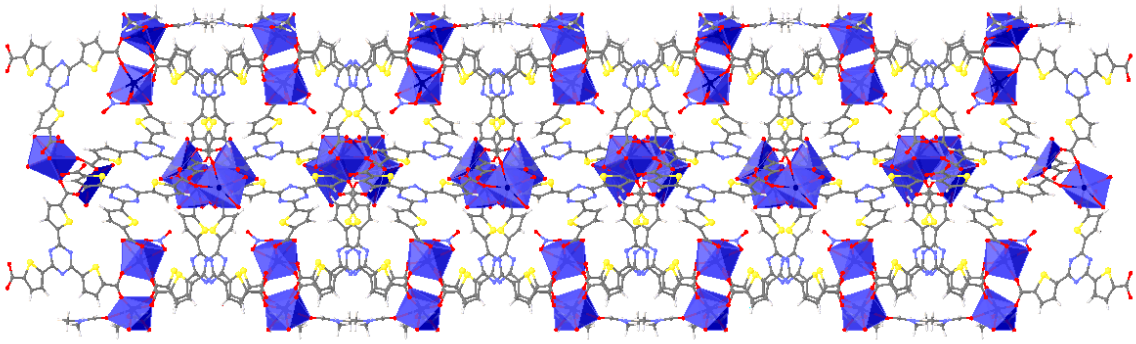

Fig. 4.3 Structure of **Gd-MOF**, viewed along the crystallographic *c*-axis, showing layer structure. Atom colour scheme: Gd, dark blue, C, dark grey, S, yellow, O, red, N, light blue. H-atoms are omitted for clarity.

The structure of **Gd-MOF** is determined by the connectivity of the two {Gd_2} SBUs in the structure, as well as the geometry and carboxylate binding mode of the **TTT**$^{3-}$ linker. The MOF forms as two-dimensional sheets (**Fig. 4.3**, **Fig. 4.4**, **Fig. 4.5**), which pack densely in layers in crystals of **Gd-MOF**. The sheets stack in layers along crystallographic *a*-axis, as demonstrated by **Fig. 4.6**, in which sheets of **Gd-MOF** are shown in different colours. No H-bonding or π-π stacking occurs between sheets of **Gd-MOF**.

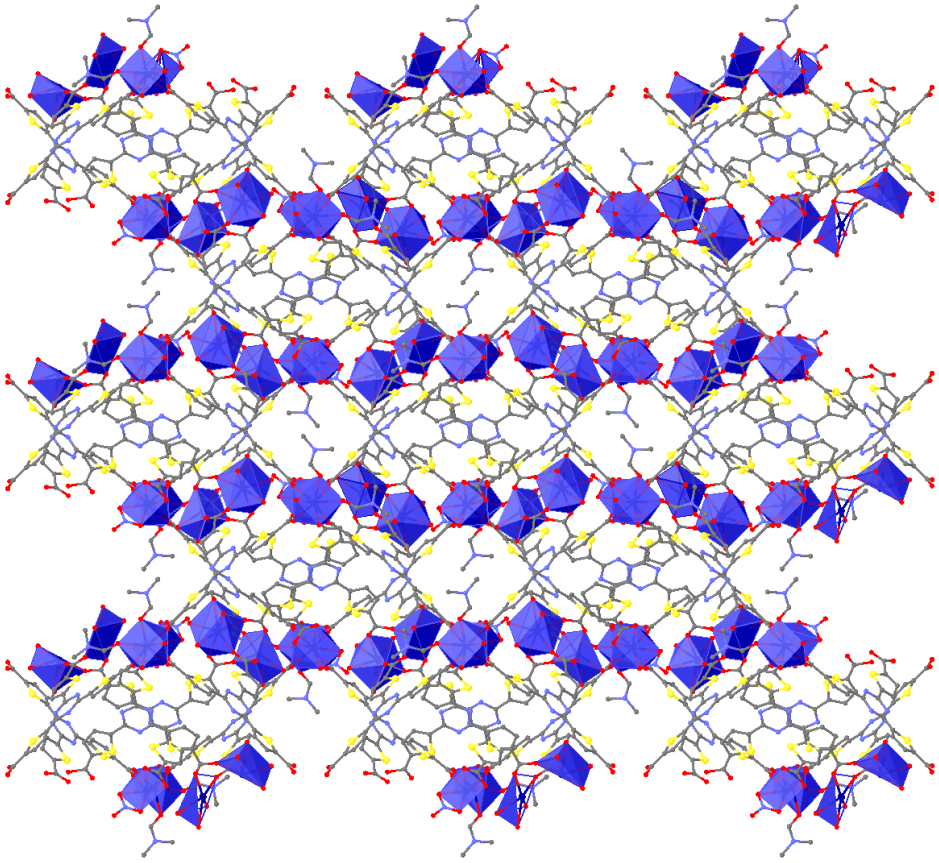

Fig. 4.4 Structure of **Gd-MOF**, viewed along the crystallographic *a*-axis. Atom colour scheme: Gd, dark blue, C, dark grey, S, yellow, O, red, N, light blue. H-atoms are omitted for clarity.

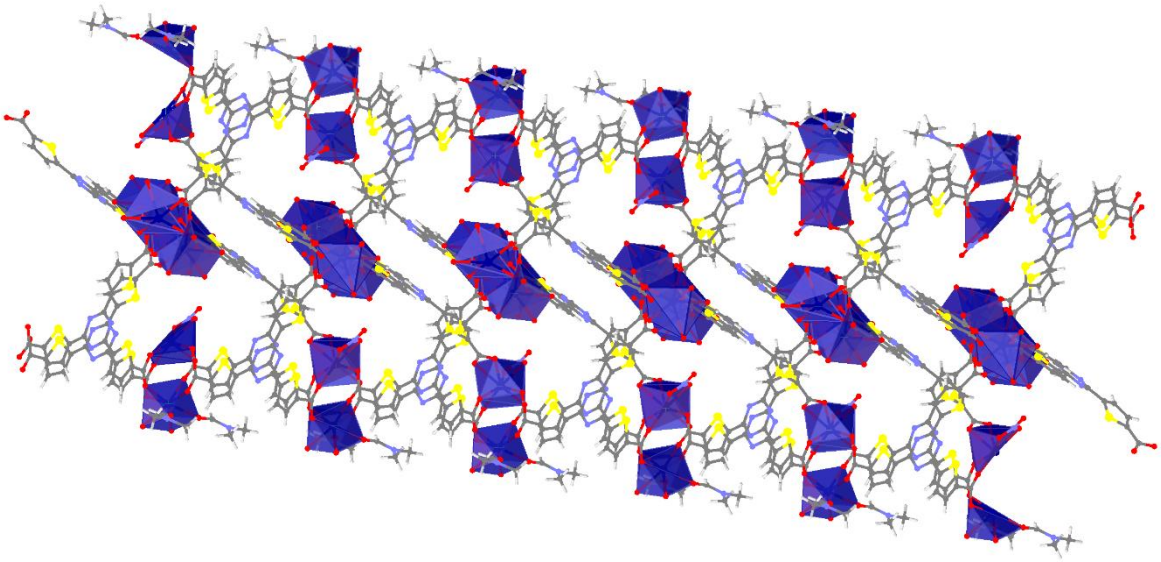

Fig. 4.5 Structure of **Gd-MOF**, viewed along the crystallographic *b*-axis. Atom colour scheme: Gd, dark blue, C, dark grey, S, yellow, O, red, N, light blue. H-atoms are omitted for clarity.

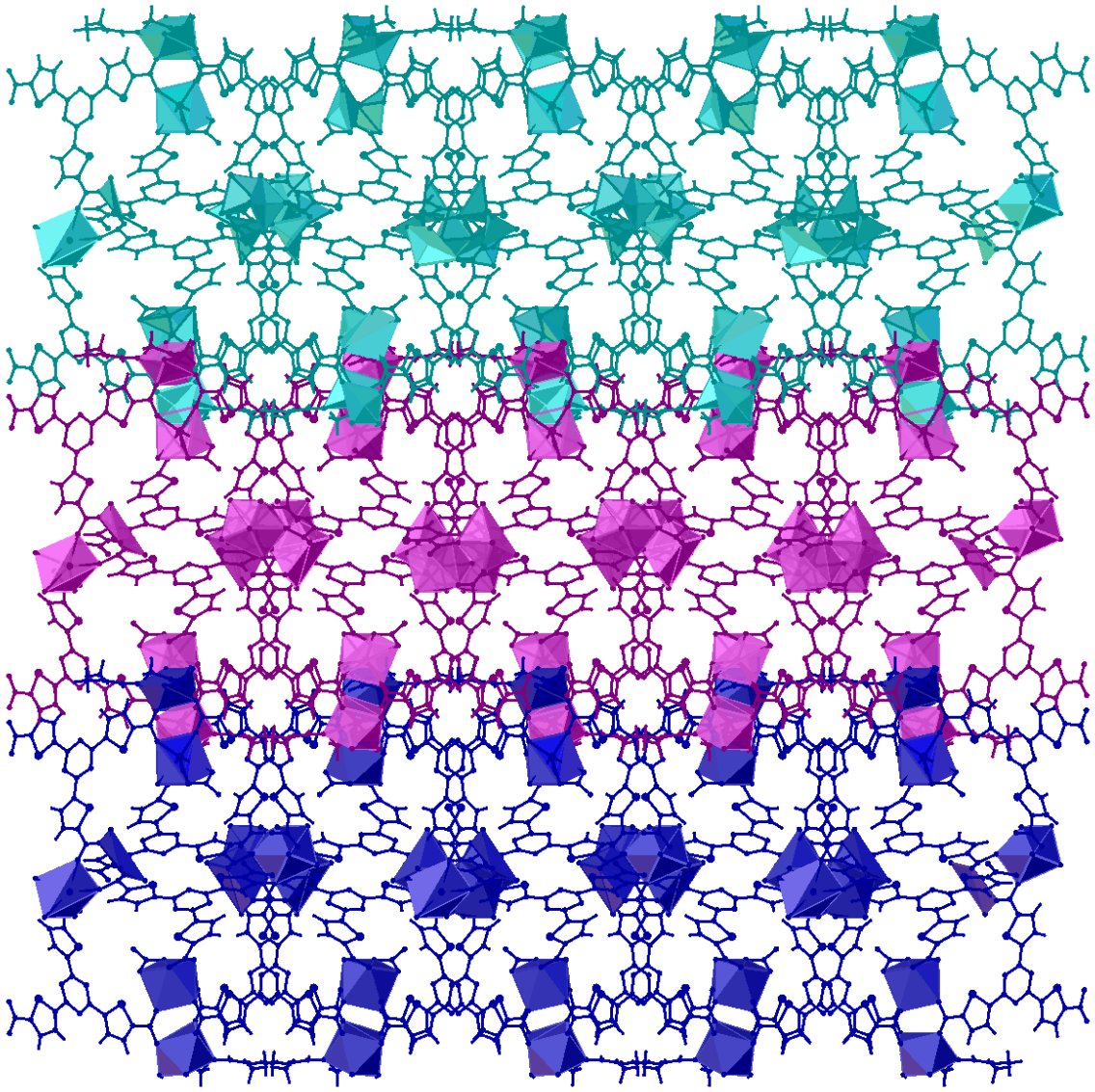

Fig. 4.6 Structure of **Gd-MOF**, viewed along the crystallographic *c*-axis showing sheets of the MOF in different colours.

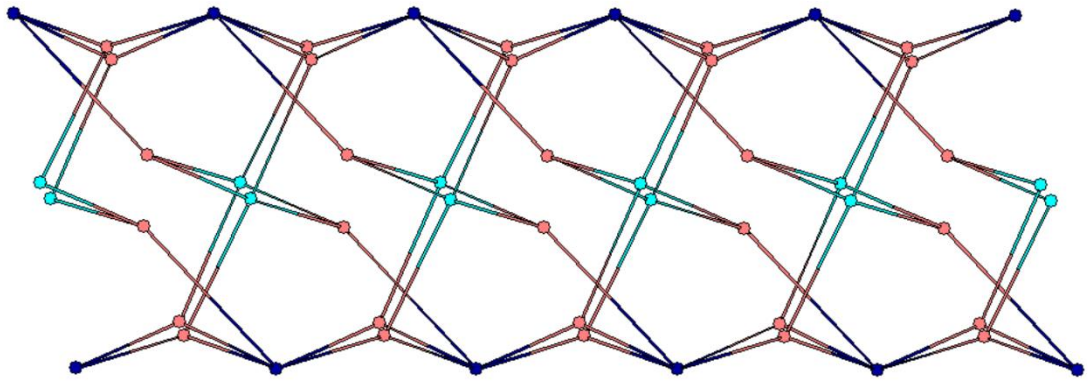

Fig. 4.7 Topological representation of **Gd-MOF** as viewed along the crystallographic *b*-axis. Colour scheme: pink, **TTT**$^{3-}$ linker, turquoise, four-connected {Gd_2} node, navy, five-connected {Gd_2} node.

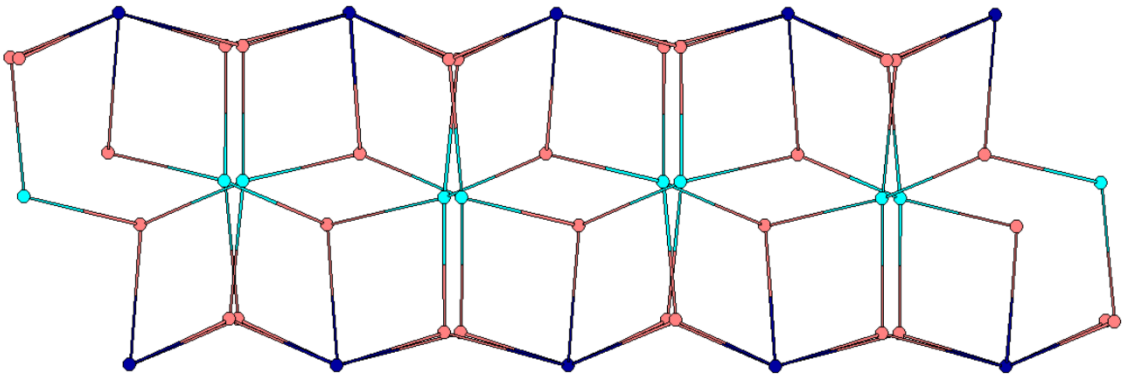

Fig. 4.8 Topological representation of **Gd-MOF** as viewed along the crystallographic *c*-axis. Colour scheme: pink, **TTT**$^{3-}$ linker, turquoise, four-connected {Gd_2} node, navy, five-connected {Gd_2} node.

To study the packing of **Gd-MOF** in detail, topological analysis of the framework was carried out using ToposPro software (**Fig. 4.7**, **Fig. 4.8**).[26] The structure of **Gd-MOF** consists of as a series of two-dimensional sheets, which pack in layers in the crystals. The structure of the MOF is a 4-nodal 3,3,4,5-connected net with $(3\text{-c})_2(3\text{-c})(4\text{-c})(5\text{-c})$. The **TTT**$^{3-}$ linkers act as three-connected nodes, linking the {Gd_2} dimer SBUs. There are two different types of {Gd_2} nodes in **Gd-MOF**. The {Gd_2} node containing Gd1 and Gd2 acts as a five-connected node, linking five different **TTT**$^{3-}$ linkers. The {Gd_2} node containing Gd3 and Gd4 forms a four-connected node, linking four different **TTT**$^{3-}$ linkers *via* bridging μ_2-η^1:η^1 carboxylates. The point symbol for the net of **Gd-MOF** is $\{6^3\}_3\{6^4.8^2\}\{6^6.8^4\}$.

Yb-MOF formed in poor yield, with large amounts of precipitate forming in the vials. As a result, samples of **Yb-MOF** were not obtained for bulk characterisation.

4.2.3 Powder X-Ray Diffraction (PXRD) analysis

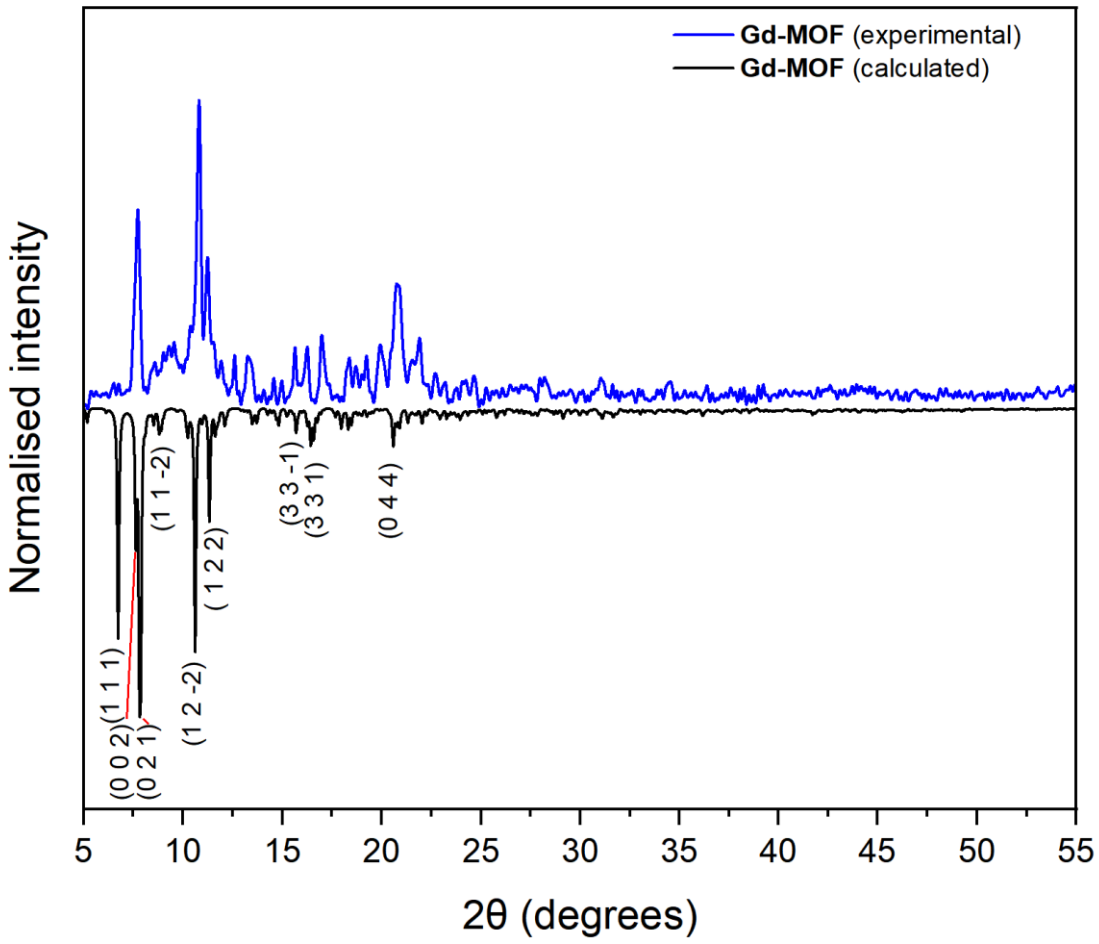

Fig. 4.9 Calculated (black) and experimental (blue) PXRD pattern of **Gd-MOF**, showing indexed diffraction peaks. The experimental powder pattern was recorded in air, at room temperature.

PXRD was used to investigate the phase purity of **Gd-MOF**, in addition to confirming that **Gd-MOF**, **Dy-MOF**, **Er-MOF** and **Yb-MOF** are isostructural. Comparison of the experimental powder pattern for **Gd-MOF** and the pattern calculated from the single crystal XRD data is shown in **Fig. 4.9**. Differences between the experimental and calculated PXRD patterns can be observed as the experimental PXRD pattern was recorded at room temperature, while the single crystal XRD measurement from which the calculated pattern was simulated was measured at 215 K. Additionally, preferred orientation of crystals was observed in the experimental PXRD pattern. Therefore the experimental powder pattern (prior to background correction) was fit using the Le Bail method[27] within the Expo2014 software package (**Fig. 4.10**).[28] The R_p and R_{wp} values for **Gd-MOF** are 3.786 and 4.903 respectively, indicating good agreement between the calculated and experimental PXRD pattern. These results show that the bulk samples of **Gd-MOF** are phase pure.

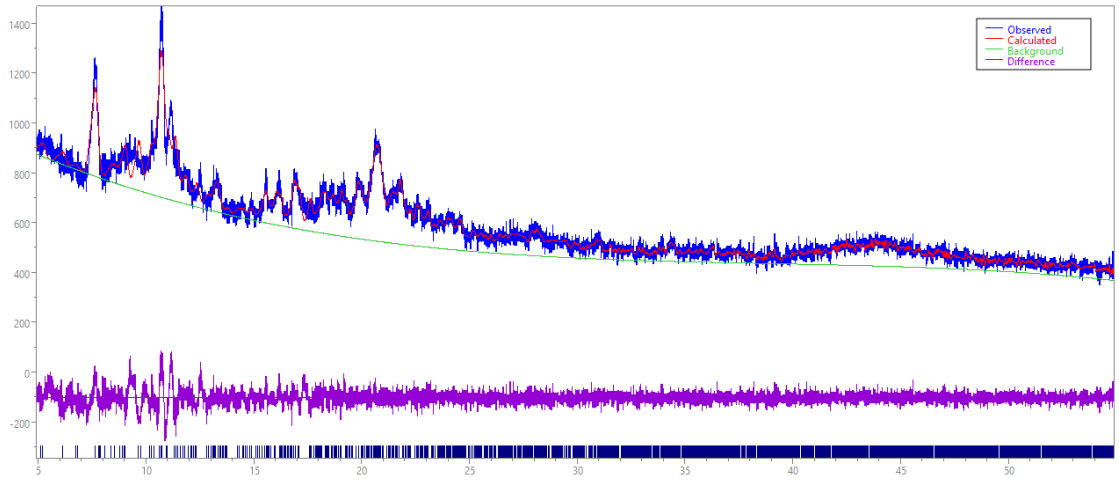

Fig. 4.10 Le Bail fits of PXRD patterns of **Gd-MOF**, showing observed (blue) and calculated (red) data, and their difference (violet). The background is shown in green, and the dark blue lines indicate the positions of reflections predicted from the unit cell. The experimental powder pattern was recorded in air, at room temperature.

PXRD measurements were also used to confirm that **Gd-MOF**, **Dy-MOF**, **Er-MOF** and **Yb-MOF** are isostructural (**Fig. 4.11**). The PXRD patterns of the four MOFs are in good agreement with each other, and with the pattern calculated for **Gd-MOF**. This indicated that bulk samples of **Dy-MOF**, **Er-MOF**, and **Yb-MOF** are phase pure. Note that preferred orientation and thermal expansion lead to differences in intensity and minor differences in peak position between the calculated pattern and experimental patterns.

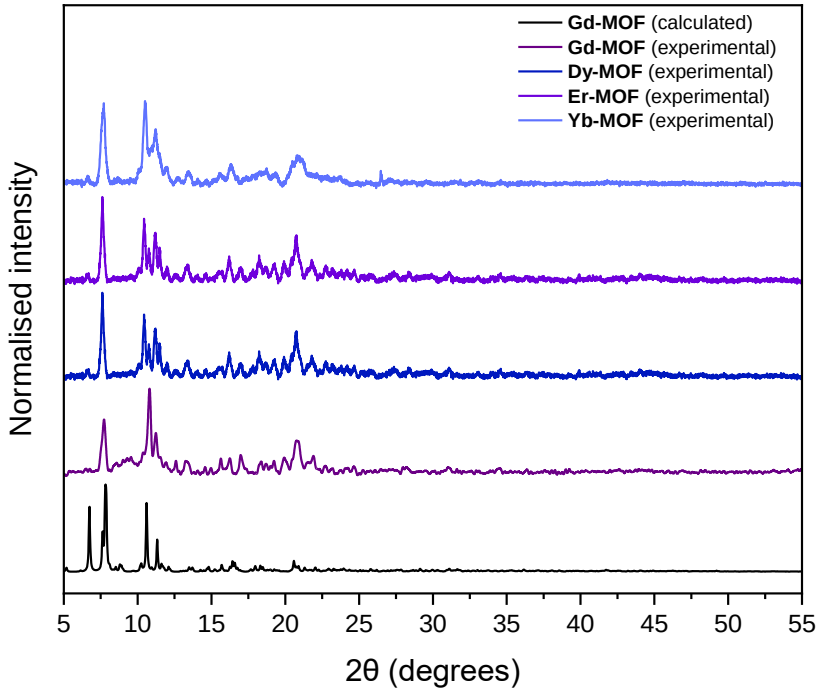

Fig. 4.11 Comparison of the PXRD patterns of MOFs as synthesised and the calculated PXRD patterns for **Gd-MOF**, **Dy-MOF**, **Er-MOF** and **Yb-MOF**. The experimental PXRD patterns were recorded in air, at room temperature.

Unfortunately, though single crystal data was obtained for **Ho-MOF**, the poor yield of crystals of this MOF, as well as the quantity of amorphous precipitate that formed in addition to the MOF crystals for this material, hindered attempts to obtain a sample for PXRD measurements.

4.2.4 Scanning Electron Microscopy and Energy Dispersive X-Ray Spectroscopy

SEM imaging was carried out on **Dy-MOF**, to examine the morphology of the crystals. As can be seen in **Fig. 4.12**, individual crystals of **Dy-MOF** have a thin plate crystal habit, and vary in size. Crystals of **Dy-MOF** form dense clusters of radiating plates, which illustrates the difficulty in obtaining a single crystal of these materials for single crystal XRD analysis.

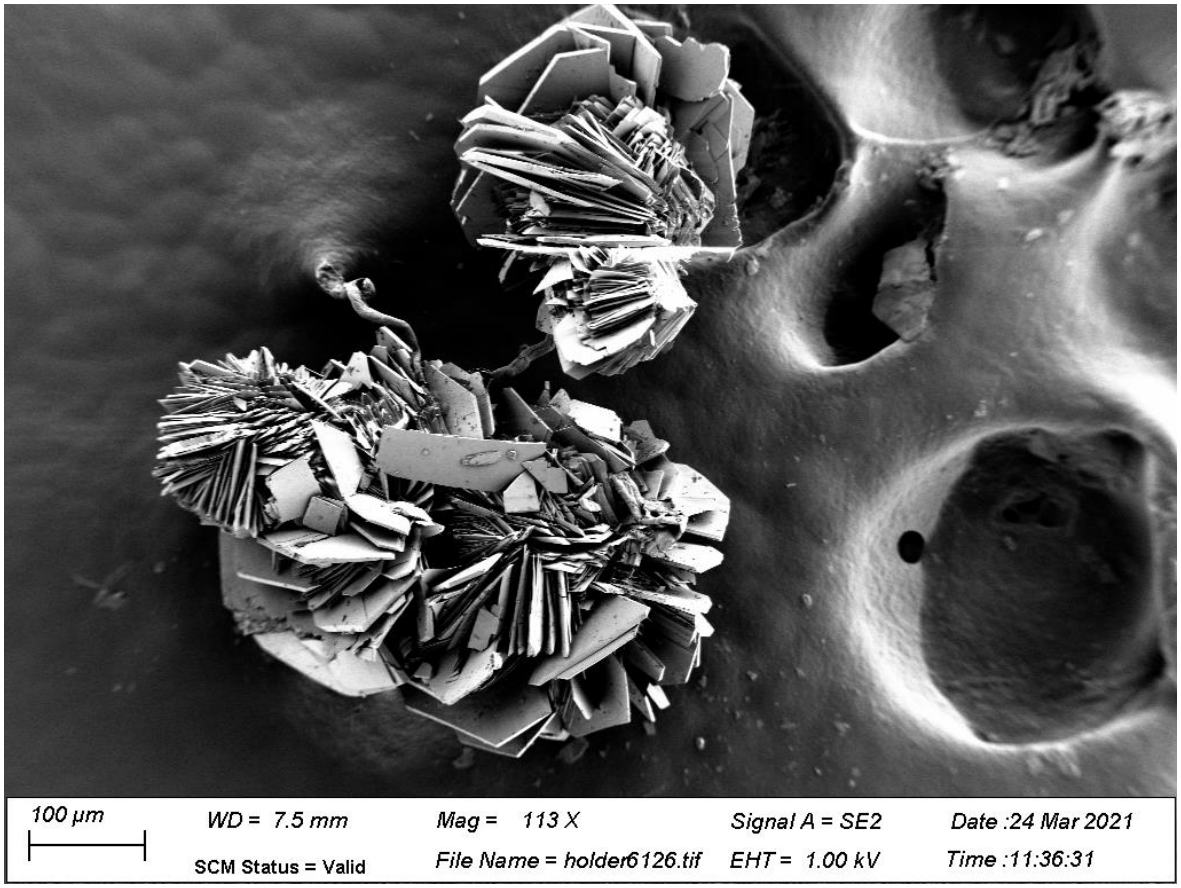

Fig. 4.12 SEM image of **Dy-MOF** crystals.

4.2.5 Fourier Transform Infrared Spectroscopy of Ln-MOFs

FTIR spectroscopy was used to analyse **Gd-MOF**, **Dy-MOF**, **Er-MOF** and **Yb-MOF**, and the FTIR spectra for these MOFs are shown in **Fig. 4.13.**. The FTIR spectra for each MOF in this chapter are largely identical, as expected due to their chemical similarities. A broad vibrational band between approximately 3680 cm^{-1} and 2100 cm^{-1} in the spectrum of each MOF arises from vibrations of coordinated water molecules in the structure of the MOFs, the O-H and C-H vibrations of co-crystallised DMF molecules, and C-H stretching vibrations, arising from the linker $\mathbf{TTT^{3-}}$ molecules.

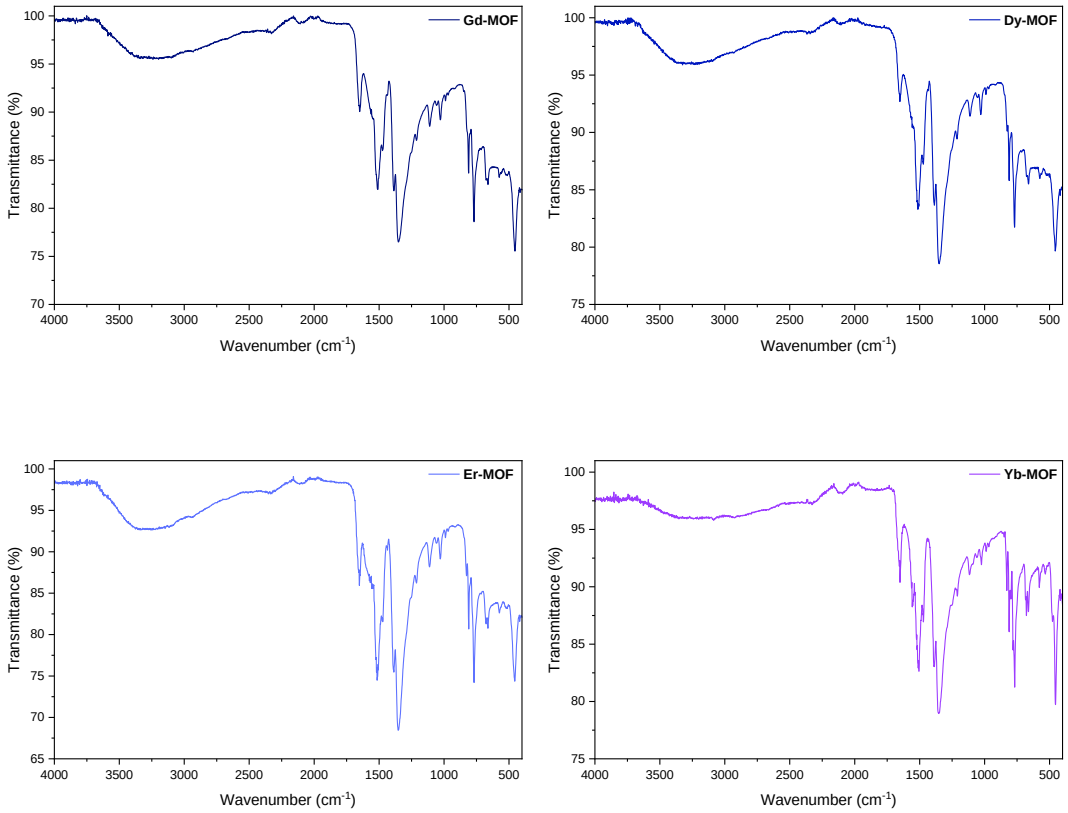

Fig. 4.13 FTIR spectra of **a) Gd-MOF**, **b) Dy-MOF**, **c) Er-MOF** and **d) Yb-MOF**.

Comparison of the FTIR spectra of **Gd-MOF**, **Dy-MOF**, **Er-MOF** and **Yb-MOF** with the FTIR spectrum of the linker, H_3**TTT** (see Section 3.2.4), allowed identification of the vibrational bands which arise from the H_3**TTT** linker in each MOF. In **Gd-MOF**, the asymmetric C=O stretch (ν_{asym}) appears at 1649 cm^{-1}, while the symmetric C=O stretch (ν_{sym}) leads to a vibrational band at 1473 cm^{-1}. The difference between ν_{asym} and ν_{sym} in **Gd-MOF**, Δ,[29] is 176 cm^{-1}. The values for ν_{asym}, ν_{sym}, and Δ in **Gd-MOF**, **Dy-MOF**, **Er-MOF** and **Yb-MOF** are shown in **Table 4.6**. These values are in good agreement with typical values for bridging carboxylates.

Table 4.6 Asymmetric C=O stretch (ν_{asym}), symmetric C=O stretch (ν_{sym}), and the difference (Δ) between ν_{asym} and ν_{sym} for each MOF.

Compound	ν_{asym} (cm^{-1})	ν_{sym} (cm^{-1})	Δ (cm^{-1})
Gd-MOF	1649	1473	176
Dy-MOF	1652	1472	180
Er-MOF	1652	1475	177
Yb-MOF	1652	1471	181

Other characteristic bands which appear in the FTIR spectrum of **Gd-MOF**, **Dy-MOF**, **Er-MOF** and **Yb-MOF** are vibrations from the triazine ring. In **Gd-MOF**, these bands appear at 1510 cm^{-1} and 1351 cm^{-1}. For detailed assignment of the bands in each spectrum, refer to Chapter 7.

4.3 Stability

4.3.1 Thermogravimetric Analysis

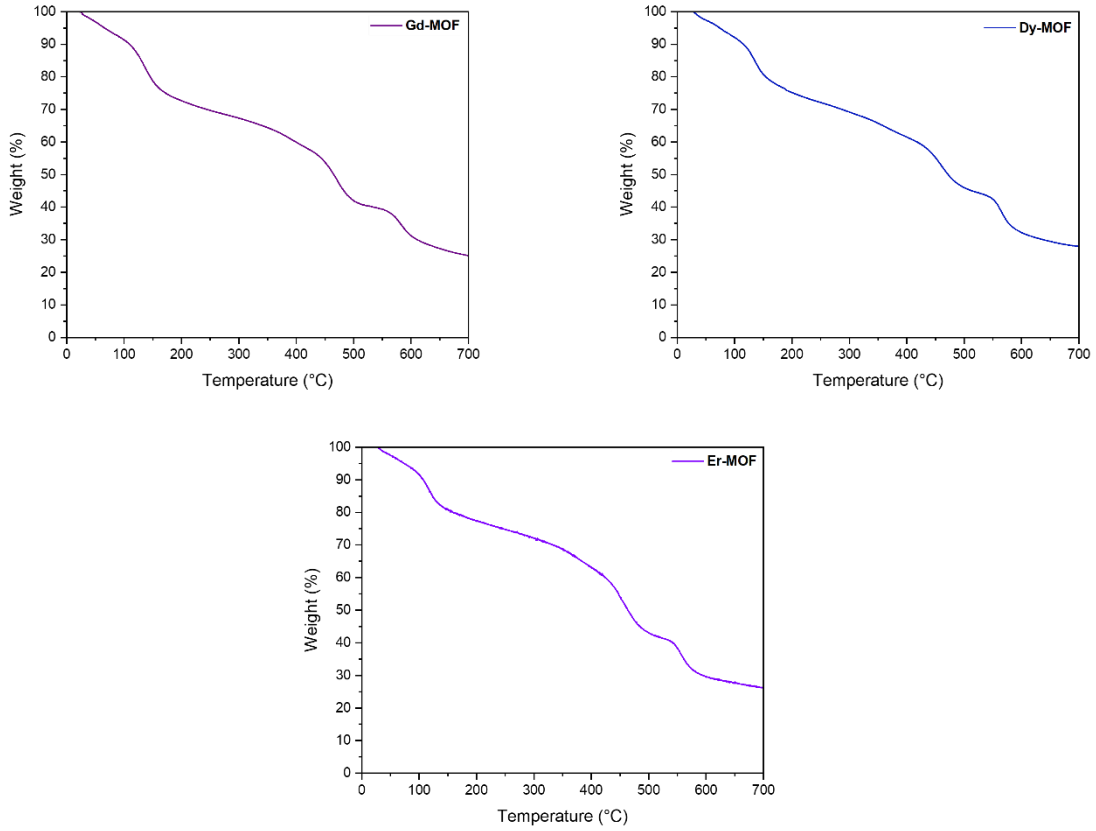

Fig. 4.14 TGA curves of **Gd-MOF**, **Dy-MOF** and **Er-MOF**

Following synthesis of phase pure samples of **Gd-MOF**, **Dy-MOF** and **Er-MOF** with good yield, the thermal stability of the MOFs was examined by TGA (**Fig. 4.14**). To prepare the samples for this measurement, the MOF crystals were first removed from the solutions in which they were synthesised and rinsed with DMF. To remove excess and surface solvent, the crystals were placed on filter paper, prior to transferring them to the TGA crucible for measuring. The samples were measured in air atmosphere, while heating at a rate of 5°C per minute.

The TGA curves were very similar across all of the MOFs measured from this series (**Fig. 4.14**). Mass loss occurred over three thermogravimetric steps. The initial weight loss, a steady decline from approximately 30°C to 120°C could be attributed to loss of uncoordinated DMF solvent in the pores of the MOF, followed by loss of coordinated solvent molecules (water, DMF) between approximately 110°C and 160°C. Decomposition of the linker occurred under air in two steps, the first occurred between approximately 435°C and 500°C. The second step occurred between approximately 560°C and 590°C. The remaining weight (c.a. 30%) could be attributed to the remaining Ln metal.

4.4 Conclusions

In this chapter, we report four MOFs formed by reaction the novel linker H_3**TTT** with later-lanthanide series ions. Each of the MOFs in this series feature dinuclear {Ln^{III}_2} SBUs (Ln^{III} = Gd^{III}, Dy^{III}, Er^{III} and Yb^{III}), with labile solvent molecules coordinating the Ln^{III} ions in the SBUs. The MOFs form as two-dimensional sheets. PXRD studies show that **Gd-MOF**, **Dy-MOF** and **Er-MOF** form as phase-pure materials with reasonable yields, while TGA measurements reveal that these materials are thermally stable to approximately 300 °C. Physicochemical characterisation of **Yb-MOF** was limited by the poor yield of the materials, in addition to the formation of large amounts of amorphous precipitate in the reaction systems for these MOFs. Additionally, SEM imaging was used to study the morphology of crystals of these MOFs, and FTIR spectroscopy was used to characterise these novel materials.

The structures of the MOFs formed using Ln^{III} ions and H_3**TTT** shows a clear dependence on the Ln^{III} ion used, with numerous structures accessible using this linker. Through studying the structure of the MOFs reported in this chapter, further understanding of the versatility of H_3**TTT** as an organic SBU for the synthesis of supramolecular materials.

Future studies could build on the work reported in this chapter by exploring the magnetic properties of these Ln-MOFs. In particular, **Dy-MOF** and **Yb-MOF** may have interesting magnetic behaviour and studying these materials would further the understanding of the magnetic properties of MOFs which incorporate later-lanthanide series ions. However, these studies may be limited by the poor yield so far achieved for **Yb-MOF**, and future work would require optimisation of the synthesis of this material.

References:

1 J.-C. G. Bünzli and S. V. Eliseeva, in *Springer Series on Fluorescence*, 2010, vol. 13, pp. 1–45.

2 D. N. Woodruff, R. E. P. Winpenny and R. A. Layfield, *Chem. Rev.*, 2013, **113**, 5110–5148.

3 J. Rong, W. Zhang and J. Bai, *CrystEngComm*, 2016, **18**, 7728–7736.

4 Q. Yu, H. Dong, X. Zhang, Y. X. Zhu, J. H. Wang, F. M. Zhang and X. J. Sun, *CrystEngComm*, 2018, **20**, 3228–3233.

5 K. Zheng, Z.-Q. Liu, Y. Huang, F. Chen, C.-H. Zeng, S. Zhong and S. W. Ng, *Sensors Actuators B Chem.*, 2018, **257**, 705–713.

6 D. L. Burnett, R. Oozeerally, R. Pertiwi, T. W. Chamberlain, N. Cherkasov, G. J. Clarkson, Y. K. Krisnandi, V. Degirmenci and R. I. Walton, *Chem. Commun.*, 2019, **55**, 11446–11449.

7 C. Wang, X. Liu, N. Keser Demir, J. P. Chen and K. Li, *Chem. Soc. Rev.*, 2016, **45**, 5107–5134.

8 G. Tan, R. Q. Jia, W. L. Wu, B. Li and L. Y. Wang, *Cryst. Growth Des.*, 2022, **22**, 323–333.

9 F. M. Wang, B. X. Hu, W. P. Lustig, L. Zhou, J. Xiang, L. Z. Chen and J. Li, *Inorg. Chem.*, 2021, **60**, 17926–17932.

10 L. Liu, Y. Wang, R. Lin, Z. Yao, Q. Lin, L. Wang, Z. Zhang and S. Xiang, *Dalt. Trans.*, 2018, **47**, 16190–16196.

11 W. Hatakeyama, T. J. Sanchez, M. D. Rowe, N. J. Serkova, M. W. Liberatore and S. G. Boyes, *ACS Appl. Mater. Interfaces*, 2011, **3**, 1502–1510.

12 X. Z. Wang, J. Du, N. N. Xiao, Y. Zhang, L. Fei, J. D. Lacoste, Z. Huang, Q. Wang, X. R. Wang and B. Ding, *Analyst*, 2020, **145**, 4646–4663.

13 G. Collet, A. Hrvat, S. V. Eliseeva, C. Besnard, A. Kovalenko and S. Petoud, *Chem. Commun.*, 2021, **57**, 3351–3354.

14 Y. Yang, X. Liu, Z. Guo and H. Zhan, *Inorg. Chem. Commun.*, 2018, **92**, 18–21.

15 H. Li, Y. Li, X. Zhang, P. Liu, M. He, C. Li and Y. Wang, *Nanoscale*, 2021, **13**, 9757–9765.

16 X. Z. Wang, X. R. Wang, Y. Y. Liu, J. Z. Huo, Y. Li, Q. Wang, K. Liu and B. Ding, *Ultrason. Sonochem.*, 2019, **59**, 104734.

17 A. J. Calahorro, I. Oyarzabal, B. Fernández, J. M. Seco, T. Tian, D. Fairen-Jimenez, E. Colacio and A. Rodríguez-Diéguez, *Dalt. Trans.*, 2016, **45**, 591–598.

18 L. Zhou, Z. G. Wang, H. Y. Dong, K. Zhao, Y. J. Hu, Z. J. Gao, S. N. Tie and H. G. Zheng,

Inorg. Chem. Commun., 2017, **78**, 1–4.

19 L. J. Zhou, W. H. Deng, Y. L. Wang, G. Xu, S. G. Yin and Q. Y. Liu, *Inorg. Chem.*, 2016, **55**, 6271–6277.

20 D. H. Chen, L. Lin, T. L. Sheng, Y. H. Wen, X. Q. Zhu, L. T. Zhang, S. M. Hu, R. B. Fu and X. T. Wu, *New J. Chem.*, 2018, **42**, 2830–2837.

21 S. Alvarez, P. Alemany, D. Casanova, J. Cirera, M. Llunell and D. Avnir, *Coord. Chem. Rev.*, 2005, **249**, 1693–1708.

22 I. D. Brown and D. Altermatt, *Acta Crystallogr. Sect. B Struct. Sci.*, 1985, **41**, 244–247.

23 A. Trzesowska, R. Kruszynski and T. J. Bartczak, *Acta Crystallogr. Sect. B Struct. Sci.*, 2004, **60**, 174–178.

24 O. V. Dolomanov, L. J. Bourhis, R. J. Gildea, J. A. K. Howard and H. Puschmann, *J. Appl. Crystallogr.*, 2009, **42**, 339–341.

25 O. C. Gagné, *Acta Crystallogr. Sect. B Struct. Sci. Cryst. Eng. Mater.*, 2018, **74**, 49–62.

26 V. A. Blatov, A. P. Shevchenko and D. M. Proserpio, *Cryst. Growth Des.*, 2014, **14**, 3576–3586.

27 A. Le Bail, *Powder Diffr.*, 2005, **20**, 316–326.

28 A. Altomare, C. Cuocci, C. Giacovazzo, A. Moliterni, R. Rizzi, N. Corriero and A. Falcicchio, *J. Appl. Crystallogr.*, 2013, **46**, 1231–1235.

29 G. B. Deacon and R. J. Phillips, *Coord. Chem. Rev.*, 1980, **33**, 227–250.

Chapter 5 : Europium-based MOF incorporating an earth abundant Cu^{I} photosensitiser

5.1 Introduction

The work reported to this point in this thesis has explored the synthesis of MOFs and coordination cages based on linkers with heterocyclic backbones. By systematic variation of the organic linker and inorganic SBU of these metal-organic materials, we have succeeded in synthesising materials with varying structural and photochemical properties. However, the two linkers used until this point, H_2**CPTT** and H_3**TTT**, have shown a lack of absorption of visible light, and instead absorb light in the UV region of the electromagnetic spectrum. Efficient absorption of visible light is an important property in MOFs for many applications, including photocatalysis.[1–5] Visible light comprises approximately 44.7% of sunlight, with the remaining portion arising from infrared (c.a. 48.7%) and only a small fraction, at approximately 6.6% arising from UV light.[6] Thus, designing materials that can harvest light from broad regions of the electromagnetic spectrum, including visible light, is an important area of research.

This final chapter builds upon the work carried out in other chapters, and previous work in the literature, by designing and synthesising a stable MOF, which forms with excellent yield and features desirable photochemical properties, such as broad absorption in the visible region. This MOF incorporates a Cu^{I} metallo-linker and features a Eu^{III}-based inorganic SBU. The advantages of utilising Cu^{I} photosensitisers as an alternative to Ru^{II} photosentisers have previously been demonstrated.[7–14] These advantages include the lower cost and increased earth abundance of Cu compared to Ru salts.[15] As discussed in Chapter 1 of this thesis, Cu^{I} photosensitisers can be used to impart interesting photochemical properties into MOFs.[16–18]

The Cu^{I} photosensitiser selected for this work, $[Cu\text{-}^{I}(H_2$2,2'-DMBP$)_2]PF_6$ ($H_2$2,2'-DMBP = 6,6'-dimethyl-2,2'-bipyridine-4,4'-dicarboxylic acid), is a tetratopic ligand, which has previously been integrated into a series of coordination polymers by Schmitt and co-workers.[18] A series of isostructural coordination polymers with SBUs based on Mn^{II}, Co^{II}, Cu^{II}, Zn^{II}, or Cd^{II} were synthesised. The photochemical properties, such as quantum yield and excited state lifetimes, vary depending on the nature of the inorganic SBU. The photosensitiser has also previously been utilised in dye-sensitised solar cells (DSCs), where it was adsorbed onto TiO_2.[19]

In this chapter, $[Cu^{I}(H_2$2,2'-DMBP$)_2]PF_6$ was reacted with Eu^{III} salts, due to the interesting luminescence properties of Eu^{III}-based MOFs, and the potential to form stable porous materials using lanthanide-based SBUs. The result was a MOF which showed many desirable properties, such as good stability, high yield, broad absorption in the visible region of the electromagnetic spectrum and open coordination sites on the Eu^{III} ion. These properties suggest that this MOF has excellent potential as a compound for future photocatalytic studies.

5.2 Synthesis and crystal structure description of Cu-Eu-MOF

Cu-Eu-MOF was synthesised using a modified version of a procedure previously reported by Schmitt and co-workers for the synthesis of transition metal-based coordination polymers using $[Cu^{I}(H_2$2,2'-DMBP$)_2]^{+}$.[18] $[Cu^{I}(H_2$2,2'-DMBP$)_2]PF_6$ was first synthesised by combining $[Cu(MeCN)_4]PF_6$ and H_2DMBP in 1:2 molar ratio in DMF at room temperature. Immediate colour change to dark red was observed, indicating that formation of $[Cu^{I}(H_2$2,2'-DMBP$)_2]PF_6$ had occurred. A solution of $Eu(NO_2)_3{\cdot}5H_2O$ (2:1 Eu:Cu ratio) was prepared in DMF:H_2O (2:1 *v/v*), to which trifluoroacetic acid was added (0.43 M concentration). These two solutions were combined and heated at 80 °C for 16 hours. The crystals formed during this reaction were a mixture of large red-orange needle-shaped crystals, and clusters of smaller red-purple needle-shaped crystals (**Fig. 5.1**). Due to their small size, poor diffraction was observed from the red-purple crystals. One of the larger, red-orange crystals was analysed using single-crystal XRD. The structure was revealed to be a MOF with a three-dimensional framework, with the sum formula $[Eu(Cu($2,2'-DMBP$)_2)(H_2O)_2]$ (**Cu-Eu-MOF**). The crystal structure of **Cu-Eu-MOF** was solved and refined in the monoclinic space group *C*2/*c*. The crystal data and refinement results for this compound, (**Cu-Eu-MOF**) are presented in **Table 5.1**.

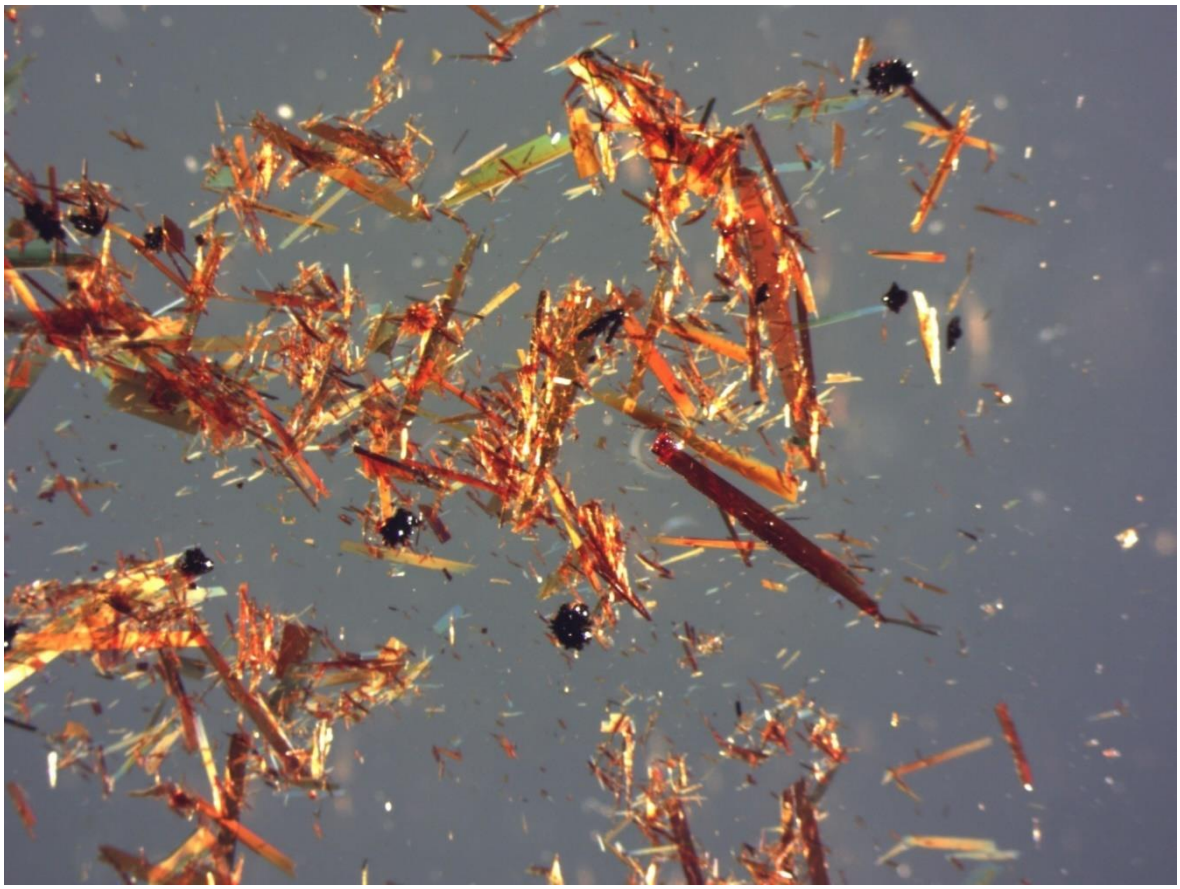

Fig. 5.1 Optical microscope images of **Cu-Eu-MOF**, showing red-orange plate crystals, and clusters of smaller, darker red-purple crystals.

Table 5.1 Crystal data and refinement results for **Cu-Eu-MOF**.

Compound name	**Cu-Eu-MOF**
Empirical formula	$CuEuC_{28}N_4O_{10}H_{23}$
Formula weight	791.00
Temperature (K)	215 K
Crystal description	Red-orange plate
Crystal system	Monoclinic
Space group	*C*2/*c*
a (Å)	26.7959(10)
b (Å)	14.1418(5)
c (Å)	19.4029(7)
α (°)	90
β (°)	93.573(3)
γ (°)	90
V (Å^3)	7338.3(5)
Z	8
ρ_{calc} (g/cm^3)	1.432
μ (mm^{-1})	13.271
F(000)	3128.0
Radiation	CuKα (λ = 1.54178)
2θ range for data collection (°)	17.106 to 136.568
Reflections collected	17303
Independent reflections	6570 [R_{int} = 0.0649, R_{sigma} = 0.0742]
Data/restraints/parameters	6570/28/422
Goodness-of-fit on F^2	1.002
R_1 [I≥2σ (I)], all	0.0566, 0.0670
wR_2 [I≥2σ (I)], all	0.1480, 0.1559
Largest diff. peak/hole (e Å^{-3})	3.01/ -1.56

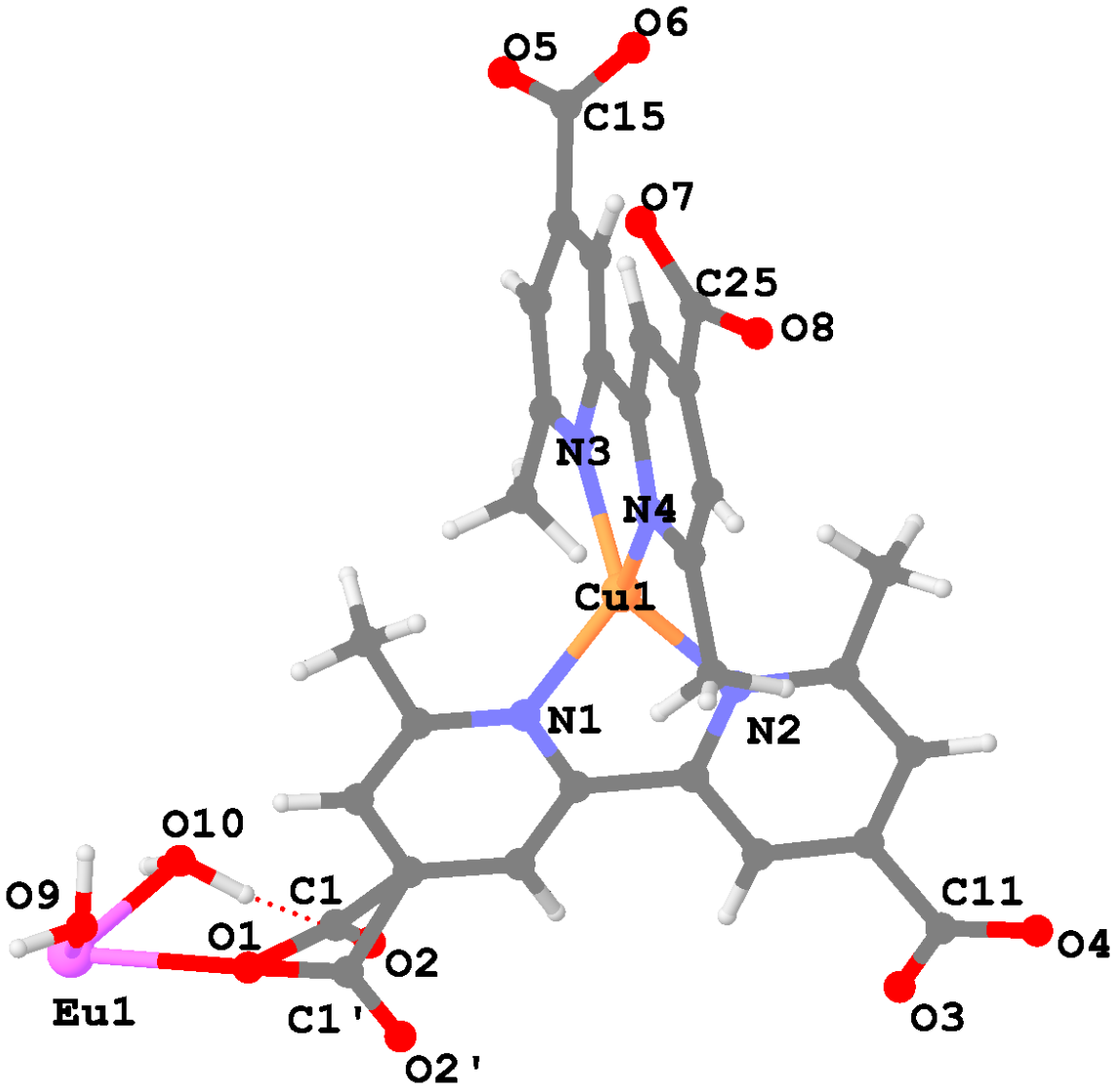

Fig. 5.2 Asymmetric unit of **Cu-Eu-MOF** with selected atoms labelled. Atom colour scheme: Eu, purple, Cu, orange, C, dark grey, O, red, H, white.

The asymmetric unit of **Cu-Eu-MOF** contains one $[Cu^{I}(2,2'\text{-DMBP})_2]^{3-}$ metallo-linker and one Eu^{III} ion, which has two coordinated water molecules. The ORTEP of the asymmetric unit of **Cu-Eu-MOF** is shown in **Fig. 5.3**, and was generated using ORTEP-3 software.[20]

The inorganic SBUs of **Cu-Eu-MOF** are $\{Eu_2\}$ dimers, which are connected by bridging carboxylate moieties from $[Cu^{I}(2,2'\text{-DMBP})_2]^{3-}$ metallo-linkers to form a three-dimensional framework. Each Eu^{III} metal centre in the structure of **Cu-Eu-MOF** is eight-coordinate, and is coordinated by six oxygen atoms from $[Cu^{I}(2,2'\text{-DMBP})_2]^{3-}$ carboxylate groups, and two water molecules. The $[Cu^{I}(2,2'\text{-DMBP})_2]^{3-}$ metallo-linker is fully deprotonated, and coordinates six different Eu^{III} ions through carboxylate oxygen atoms.

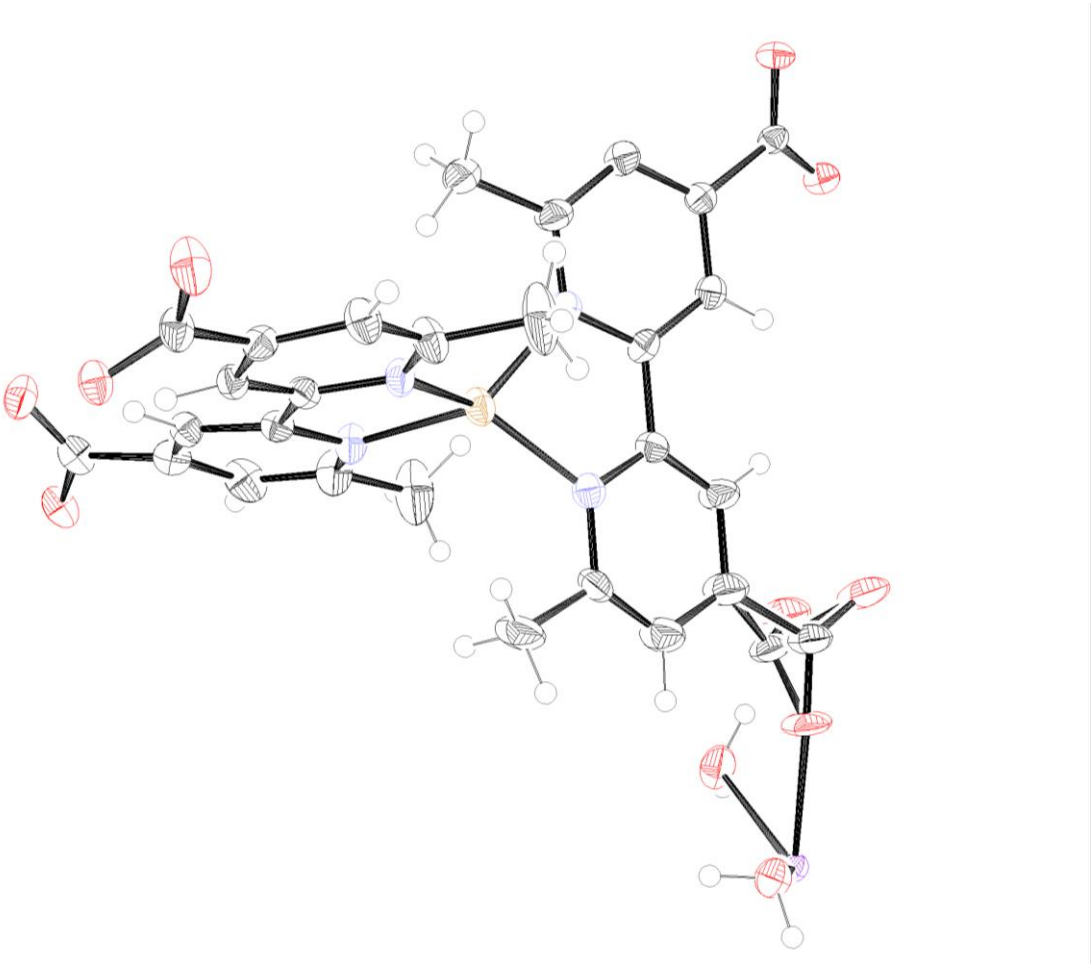

Fig. 5.3 ORTEP of the asymmetric unit of **Cu-Eu-MOF**, viewed along the crystallographic *a*-axis. Thermal probabilities are shown at the 50 % probability level. Atom colour scheme: Eu, purple, Cu, orange, C, dark grey, O, red, H, white.

The $[Cu^{I}(2,2'\text{-DMBP})_2]^{3-}$ linkers in **Cu-Eu-MOF** are fully deprotonated, giving a charge balanced structure. The C atom and one of the O atoms of one coordinating carboxylate group of the $[Cu^{I}(2,2'\text{-DMBP})_2]^{3-}$ linker is disordered over two orientations (**Fig. 5.4**), with occupancies of 35.8% and 64.2%. The coordinating O atom, O1, is not disordered. In the disordered carboxylate group with an occupancy of 0.642, all atoms of the carboxylate moiety (O1, C1', O2') are approximately coplanar with the adjacent pyridine ring.

The second part of the disordered carboxylate, which has an occupancy of 0.358, is not coplanar with the adjacent pyridine ring. Hydrogen bonding can be observed between one of the coordinated water molecules on each Eu^{III} ion (water molecule containing O10) and deprotonated carboxylate oxygen atom (O2) (**Fig. 5.4**). The O-O distance in the O10-H···O2 interaction is 2.630(18) Å, which is within the range of expected values for O·O hydrogen bonds,[21] and is shorter than the sum of the two oxygen atom van der Waals radii.[22] The O2···H distance is 1.805(17) Å. The O10-H···O2 angle is 148.0(6)° which is also consistent with previously reported ranges for A-H···A angles (A = hydrogen bond acceptor).[23]

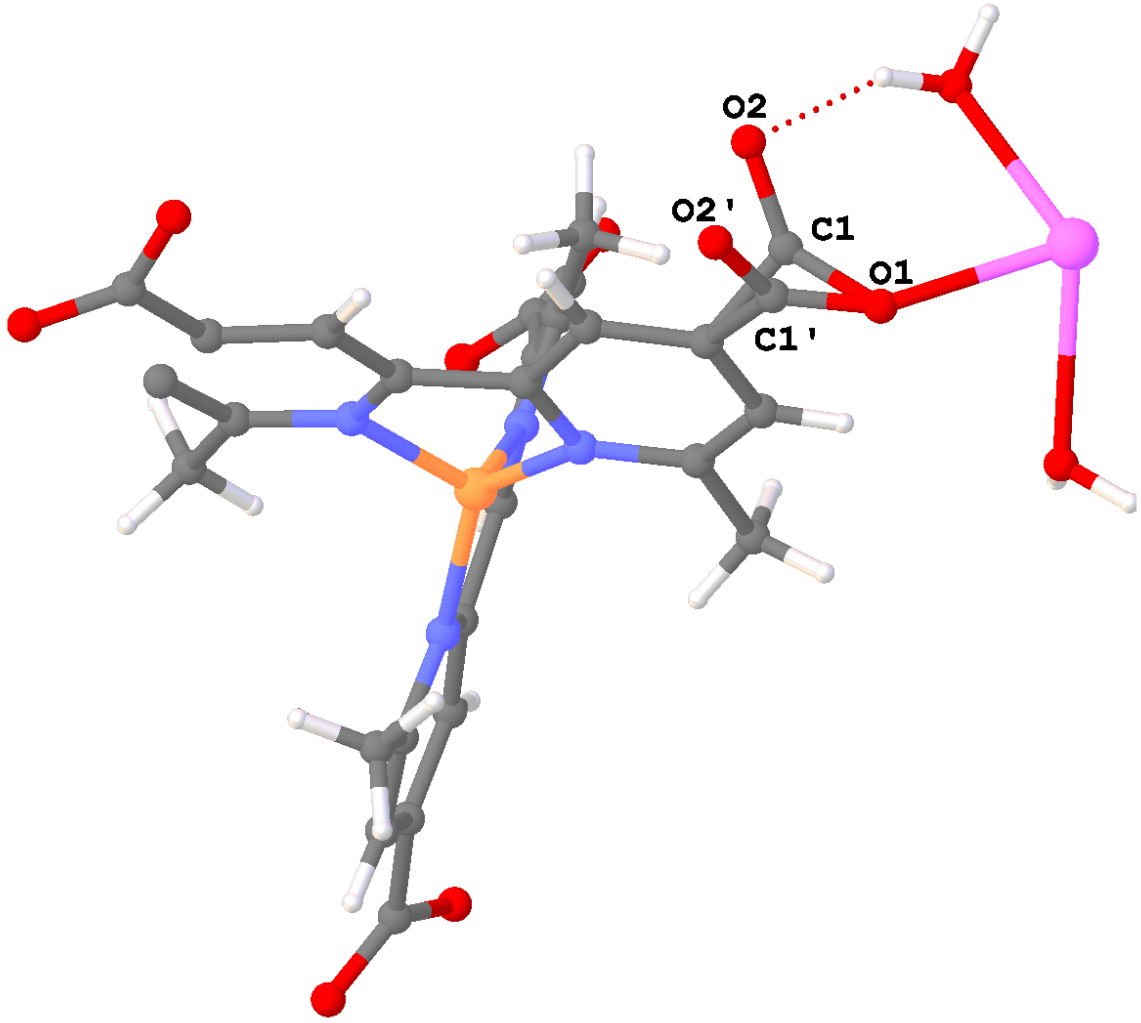

Fig. 5.4 Disorder over two orientations of C and O in carboxylate group of $[Cu^{I}(2,2'\text{-DMBP})_2]^{3-}$ linker, as viewed along the crystallographic *c*-axis. The occupancies for O2 and C1 are both 0.358, while the occupancy of O2' and C1' are 0.642. Atom colour scheme: Eu, purple, Cu, orange, C, dark grey, O, red, H, white.

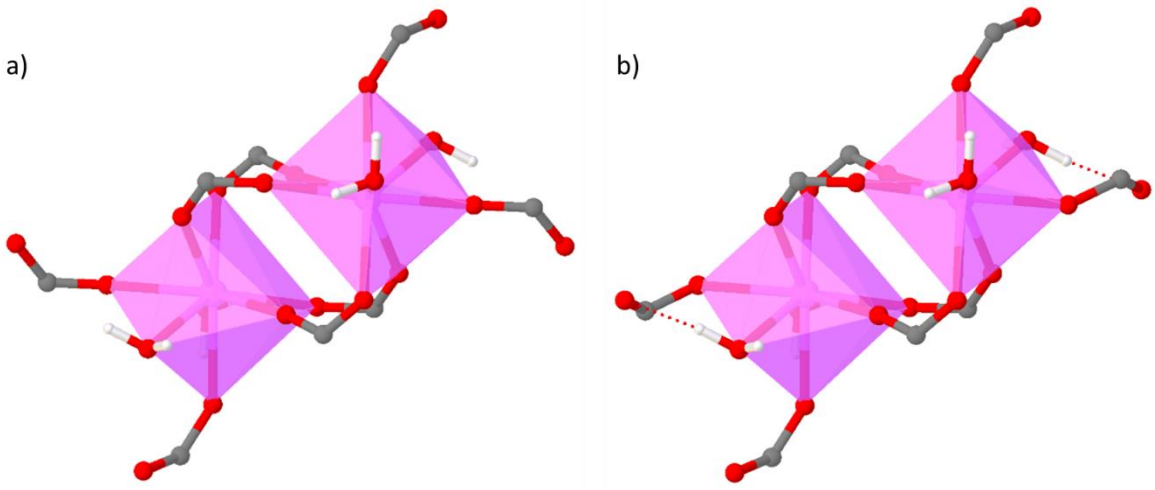

Fig. 5.5 The coordination environment of the Eu^{III} ions in the $\{Eu_2\}$ SBU of **Cu-Eu-MOF**, showing a) the disordered part containing C1' and O2', with chemical occupancy of 0.642, and b) the disordered part containing C1 and O2, with chemical occupancy 0.358. Atom colour scheme: Eu, purple polyhedra, C, dark grey, O, red, H, white.

The coordination environments of the Eu^{III} ions in the $\{Eu_2\}$ SBUs in **Cu-Eu-MOF** are shown in **Fig. 5.5**, for both parts of the disorder in C1 and O2. Within the $\{Eu_2\}$ SBUs, the symmetry equivalent Eu^{III} ions, which are related by inversion, are coordinated by one oxygen atom each from four bridging μ_2-η^1:η^1 carboxylates and two monodentate carboxylates in the η^1 binding mode (**Fig. 5.5**). The Eu-Eu distance in the $\{Eu^{III}\}_2$ SBU is 4.2803(6) Å. In total, each dinuclear $\{Eu_2\}$ SBU coordinates 8 carboxylates from 8 different $[Cu^I(2,2'\text{-DMBP})_2]^{3-}$ metallo-linkers. The Eu-O bond lengths are shown in **Table 4.2**. The Eu-O distances in **Cu-Eu-MOF** are in the range 2.312(4) to 2.567(4) Å. These bond lengths are in good agreement with those previously reported for Eu-O bonds in the literature.[24]

Table 5.2 Selected bond lengths (Å) in **Cu-Eu-MOF**.

Bond	Distance	Bond Length (Å)
Eu^{III}-O	Eu^{III}-O1	2.312(4)
	Eu^{III}-O3	2.380(4)
	Eu^{III}-O4	2.371(4)
	Eu^{III}-O5	2.350(4)
	Eu^{III}-O6	2.454(5)
	Eu^{III}-O7	2.340(4)
	Eu^{III}-O9	2.567(4)
	Eu^{III}-O10	2.485(5)
Cu^I-N	Cu^I-N1	2.021(5)
	Cu^I-N2	2.036(5)
	Cu^I-N3	2.050(5)
	Cu^I-N4	2.009(5)

The Cu^I atom in the $[Cu^I(2,2'\text{-DMBP})_2]^{3-}$ metallo-linkers of **Cu-Eu-MOF** is coordinated by four N atoms, from the two bipyridyl groups of the $DMBP^{2-}$ moieties, (**Fig. 5.4**). The dihedral angle between the 2,2'-$DMBP^{2-}$ moieties in $[Cu^I(2,2'\text{-DMBP})_2]^{3-}$ is 78.28(7)° (plane normal-plane normal angle). This is a larger deviation from orthogonality than was reported in the crystal structure of $[Cu^I(H_2 2,2'\text{-DMBP})_2]PF_6$,[25] indicating that the ligand is constrained in this position by the rigid framework of **Cu-Eu-MOF**. The Cu-N bond distances in **Cu-Eu-MOF** are shown in **Table 4.2**, and the N-Cu-N bond angles are shown in **Table 5.3**. All bond lengths and angles were measured using Olex2 software,[26] and are in good agreement with values expected for Cu^I-N bonds. The symmetry-inequivalent ligands express identical ligand bite angles of approx. 82°, which is in good agreement with previously reported values for this linker.[18]

Table 5.3 Bond angles (°) in **Cu-Eu-MOF**

	Bond angle
N1-Cu1-N2	81.9(2)°
N3-Cu1-N4	81.8(2)°

Continuous shape analyses were used to determine the coordination environment of the Cu^{I} and Eu^{III} metal centres in **Cu-Eu-MOF**. These calculations were carried out using Shape 2.1 software.[27] The results of the continuous shape analyses in **Cu-Eu-MOF** are shown in **Fig. 5.4** and **Fig. 5.5**. Smaller continuous shape measurement values indicate less deviation from ideal values for that coordination environment. A continuous shape measurement value of zero indicates a perfect fit to a particular geometry. Continuous shape calculations indicate that Cu^{I} ions in **Cu-Eu-MOF** are present in a distorted tetrahedral coordination environment. The coordination environment of the Cu^{I} atoms in **Cu-Eu-MOF** is in good agreement with that observed in previously reported coordination polymers containing this metallo-linker.[18] In **Cu-Eu-MOF,** the eight-coordinate Eu^{III} ions have a biaugmented triangular prism coordination environment.

Table 5.4 Continuous shape measurement values for Cu^{I} atoms in **Cu-Eu-MOF**. The lowest value (indicating closest fit) is highlighted in bold.

Shape	**Symmetry**	**Continuous shape measurement value**
Octagon	D_{8h}	28.604
Heptagonal pyramid	C_{7v}	24.700
Hexagonal bipyramid	D_{6h}	16.051
Cube	O_h	11.954
Square antiprism	D_{4d}	1.696
Triangular dodecahedron	D_{2d}	1.813
Johnson – Gyrobifastigium (J26)	D_{2d}	12.602
Johnson – Elongated triangular bipyramid (J14)	D_{3h}	27.698
Johnson – Biaugmented triangular prism (J50)	C_{2v}	0.996
Biaugmented trigonal prism	**C_{2v}**	**0.637**
Snub disphenoid (J84)	C_{2v}	3.253
Tetrakis tetrahedron	T_d	12.365
Elongated trigonal bipyramid	D_{3h}	24.011

Table 5.5 Continuous shape measurement values for Eu^{III} atoms in **Cu-Eu-MOF**. The lowest value (indicating closest fit) is highlighted in bold.

Shape	Symmetry	Continuous shape measurement value
Square	D_{3h}	20.678
Tetrahedron	**C_{3v}**	**6.181**
Seesaw	C_{3v}	7.277
Vacant trigonal bipyramid	$C2_v$	8.769

The three-dimensional structure of the **Cu-Eu-MOF** is densely packed, and is determined by the connectivity of both the $\{Eu_2\}$ SBU and the connectivity and geometry of the $[Cu^{I}(2,2'\text{-DMBP})_2]^{3-}$ metallo-linker (**Fig. 5.6, Fig. 5.7, Fig. 5.8**). Disordered solvent molecules were removed during the refinement using the Platon SQUEEZE routine, as implemented in Olex2.[26]

The structure of **Cu-Eu-MOF** was studied using the **calcvoid** routine in Olex2 software.[26] These calculations indicate that this MOF does not feature large voids or channels. The largest spherical void in **Cu-Eu-MOF** has a radius of 2.4 Å and a volume of 57.9 $Å^3$. The structure occupies 50.92% of the unit cell volume, a low occupancy, considering the overall high packing density of the MOF. The radii of the largest spherical channels along the crystallographic *a*-, *b*- and *c*-axis are 0.6 Å, 1.0 Å and 0.6 Å respectively. It can be concluded from these values that this material would not be suitable for gas sorption applications.

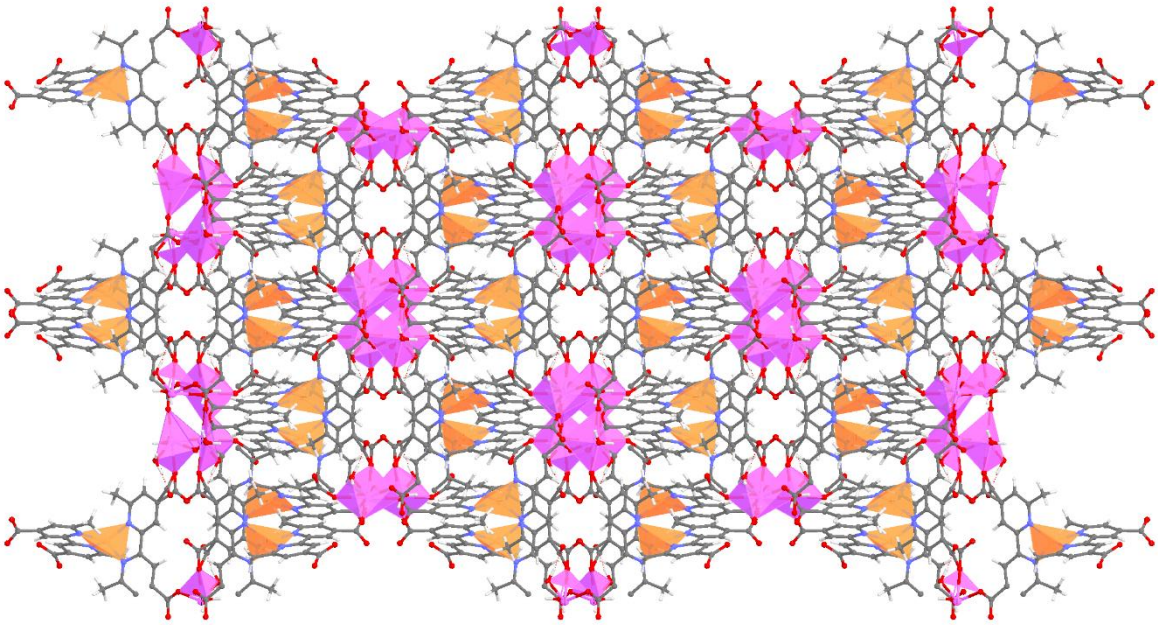

Fig. 5.6 Structure of **Cu-Eu-MOF** as viewed along the crystallographic *c*-axis. Atom colour scheme: Eu, purple polyhedra, Cu, orange polyhedra, C, dark grey, O, red, N, blue, H, white.

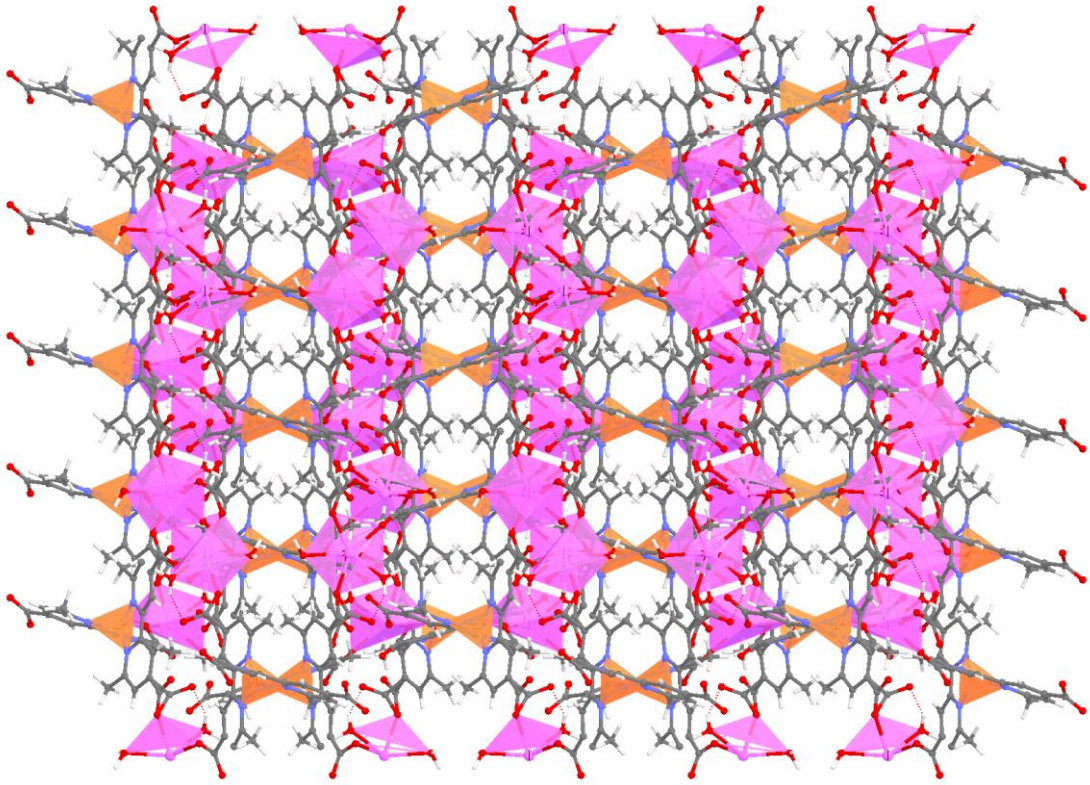

Fig. 5.7 Structure of **Cu-Eu-MOF** as viewed along the crystallographic *a*-axis. Atom colour scheme: Eu, purple polyhedra, Cu, orange polyhedra, C, dark grey, O, red, N, blue, H, white.

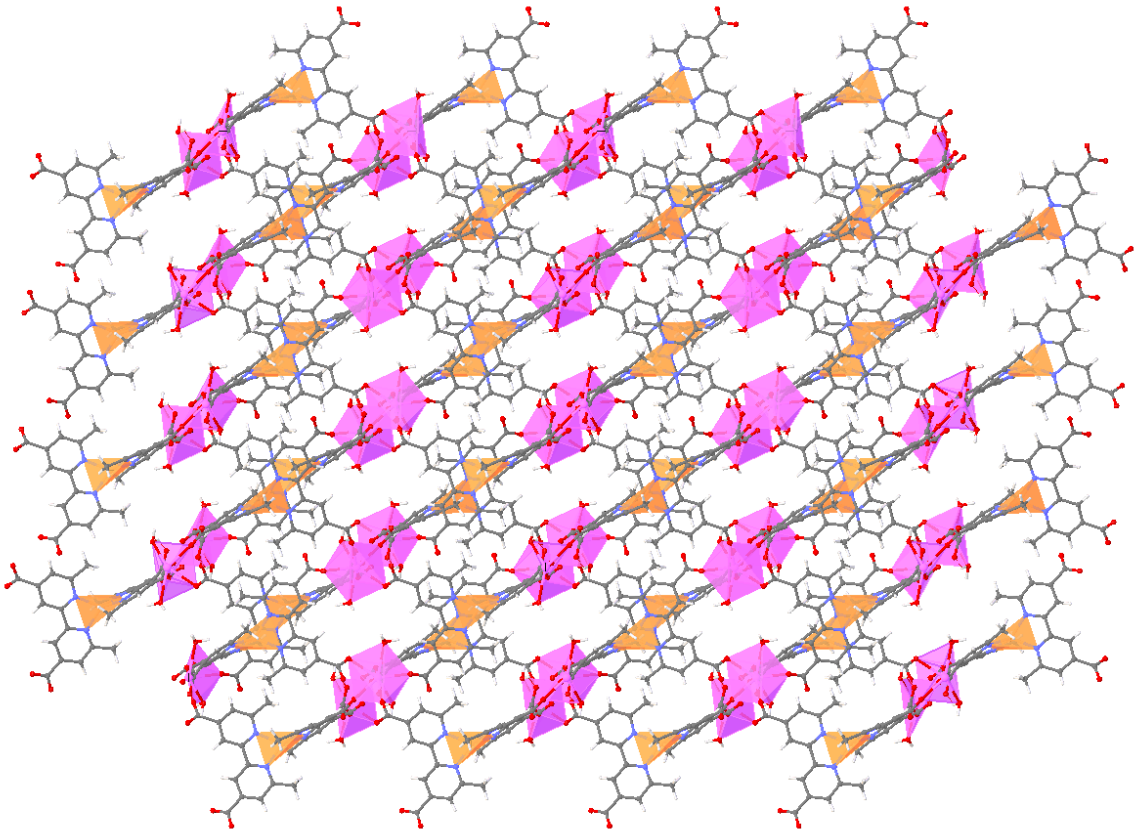

Fig. 5.8 Structure of **Cu-Eu-MOF** as viewed along the crystallographic *b*-axis. Atom colour scheme: Eu, purple polyhedra, Cu, orange polyhedra, C, dark grey, O, red, N, blue, H, white.

As the structure of **Cu-Eu-MOF** is very dense, as shown in **Fig. 5.7**, **Fig. 5.8**, further insight into the packing in **Cu-Eu-MOF** can be gained by studying the topology of this framework. Topological analysis was carried out on the structure of **Cu-Eu-MOF** using the ToposPro software.[28] The structure forms a three-dimensional binodal 4,8-connected net with $(4\text{-c})_2(8\text{-c})$ stoichiometry, and **flu** (fluorite) topology (**Fig. 5.9**, **Fig. 5.10**). Each $[Cu^{I}(2,2'\text{-DMBP})_2]^{2-}$ linker is connected to 6 Eu^{III} ions in four different $\{Eu_2\}$ SBUs, thus forming a four-connected node, while each dinuclear $\{Eu_2\}$ SBU are considered as an eight-connected node. The point symbol for this net is $\{4^{12}.6^{12}.8^4\}\{4^6\}_2$.

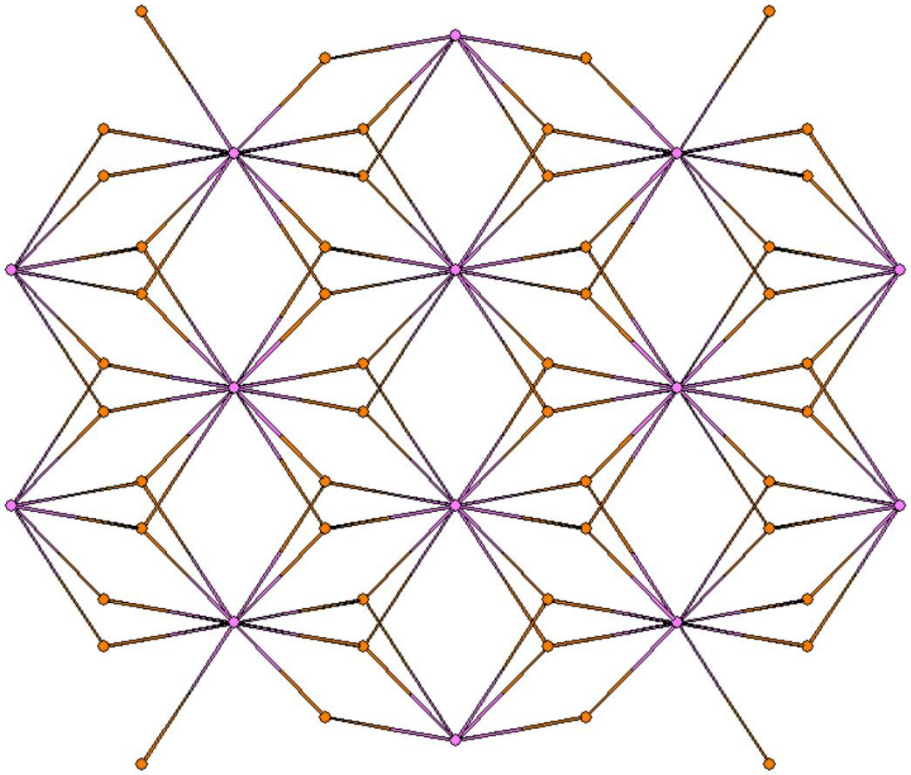

Fig. 5.9 Topological representation of **Cu-Eu-MOF**, as viewed along the crystallographic *c*-axis. Colour scheme: orange, $[Cu^{I}(2,2'\text{-DMBP})_2]^{3-}$ linker, purple, Eu^{III}dimer.

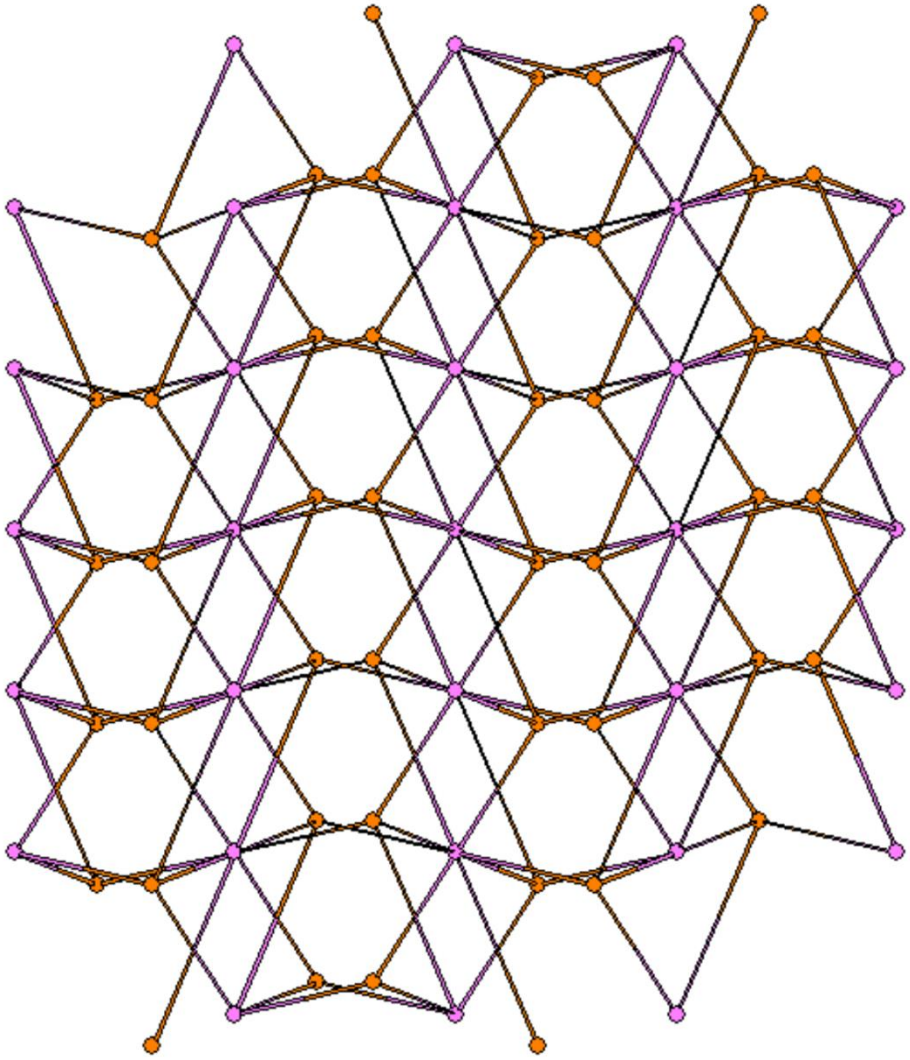

Fig. 5.10 Topological representation of **Cu-Eu-MOF**, as viewed along the crystallographic *a*-axis. Colour scheme: $[Cu^{I}(2,2'\text{-DMBP})_2]^{3-}$ linker, orange nodes, Eu^{III} dimer, purple nodes.

Bond valence sum analysis[29] was carried out to confirm the oxidation state of the Cu1 and Eu1 metal centres in **Cu-Eu-MOF** (**Table 5.6**) , using the Eu-O and Cu-N distances presented in **Table 4.2**. The R_0 value used for the Cu^{I}-N bond was 1.595.[30] BVS analysis has been used to analyse oxidation states in lanthanide ions previously,[31] including in Eu^{III} complexes. Bartczak and co-workers have calculated R_0 values for Ln^{III}-O bonds and have shown that a correlation exists between Ln^{III}-O distances and Ln^{III} coordination number.[32] The R_0 value for Eu^{III}-O bonds when Eu atoms are eight coordinate is 2.036. The results of BVS calculations for the Cu^{I} and Eu^{III} metal centres in **Cu-Eu-MOF** are shown in **Table 5.6**. The BVS calculated for Cu1 was 1.24, which is in good agreement (± 0.25) with the expected oxidation state of +I. The BVS value of 3.00 for Eu1 is in perfect agreement with the value expected for the +III oxidation state.

Table 5.6 BVS analysis of Cu and Eu atoms in **Cu-Eu-MOF**

Metal ion	R_0 (Å)	BVS	Oxidation state
Cu1	1.595	1.24	+I
Eu1	2.036	3.00	+III

5.3 Characterisation of Cu-Eu-MOF

5.3.1 Optical microscope images and powder X-ray diffraction (PXRD) studies of Cu-Eu-MOF

Samples of **Cu-Eu-MOF** synthesised according to the method described in section 6.2.1 contained both crystals which were red-orange in colour with plate morphology, and dense clusters of acicular crystals radiating from a central point, which appeared dark red-purple in colour, and formed much smaller plates (**Fig. 5.11**). PXRD analysis was carried out to investigate if the sample was a pure sample of **Cu-Eu-MOF**, or if the sample contained two distinct phases.

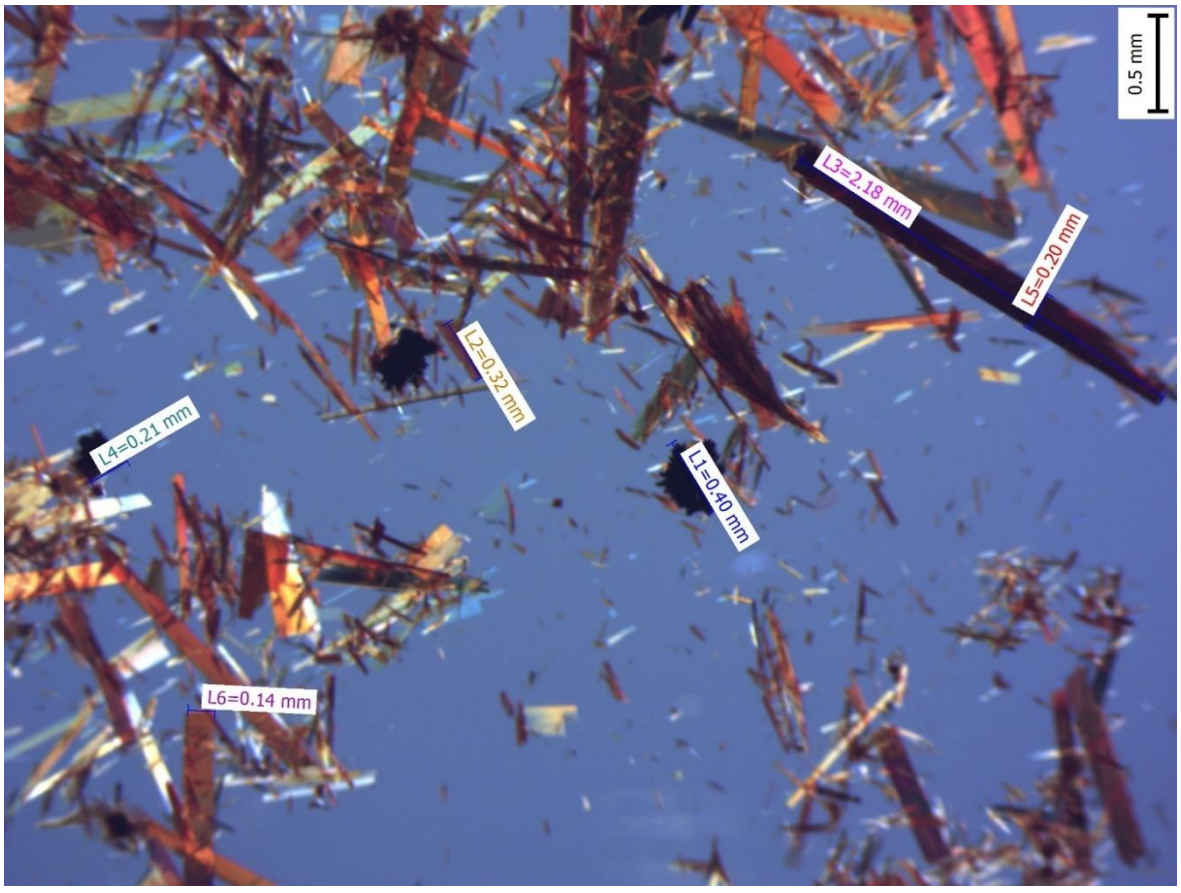

Fig. 5.11 Microscope images of **Cu-Eu-MOF** crystals, showing measurements of a selection of crystals. Both the red-purple clusters of smaller crystals and the larger red-orange needle-shaped crystals can be observed in this image.

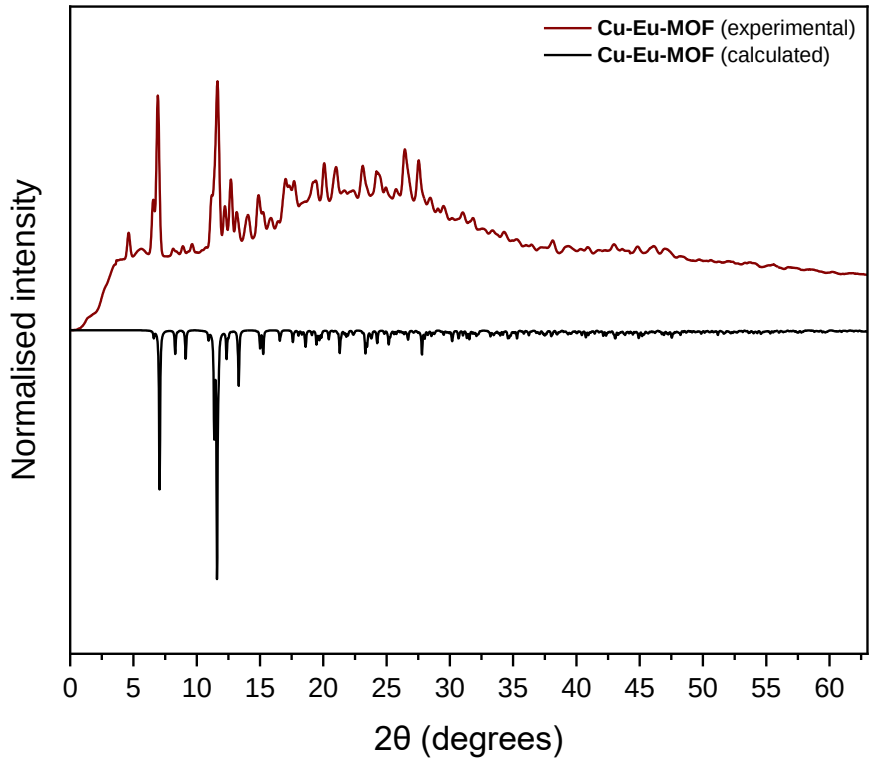

Fig. 5.12 Calculated (black) and experimental (red) PXRD pattern of **Cu-Eu-MOF**. The sample contains a mixture of the red-orange and red-purple crystals of **Cu-Eu-MOF**. The sample was synthesised with a TFA concentration of 0.43 M. The experimental powder pattern was recorded in a polyamide capillary.

A PXRD pattern was measured using a sample containing both red-orange plate crystals and clusters of red-purple needles. The sample was filtered, washed with DMF and ground to a powder, and then packed into a polyamide capillary. The experimental pattern obtained was in good agreement with that calculated from the single crystal data (**Fig. 5.12**). This indicated that the **Cu-Eu-MOF** sample synthesised was phase-pure, without any crystalline impurities. However in the experimental PXRD pattern, preferential orientation was observed, and therefore the experimental powder pattern (prior to background correction) was fit using the Le Bail method[33] within the Expo2014 software package (**Fig. 5.13**).[34] The R values obtained for the fit were R_p = 1.789 and R_{wp} = 3.254, indicating excellent agreement between the experimental and calculated PXRD patterns.

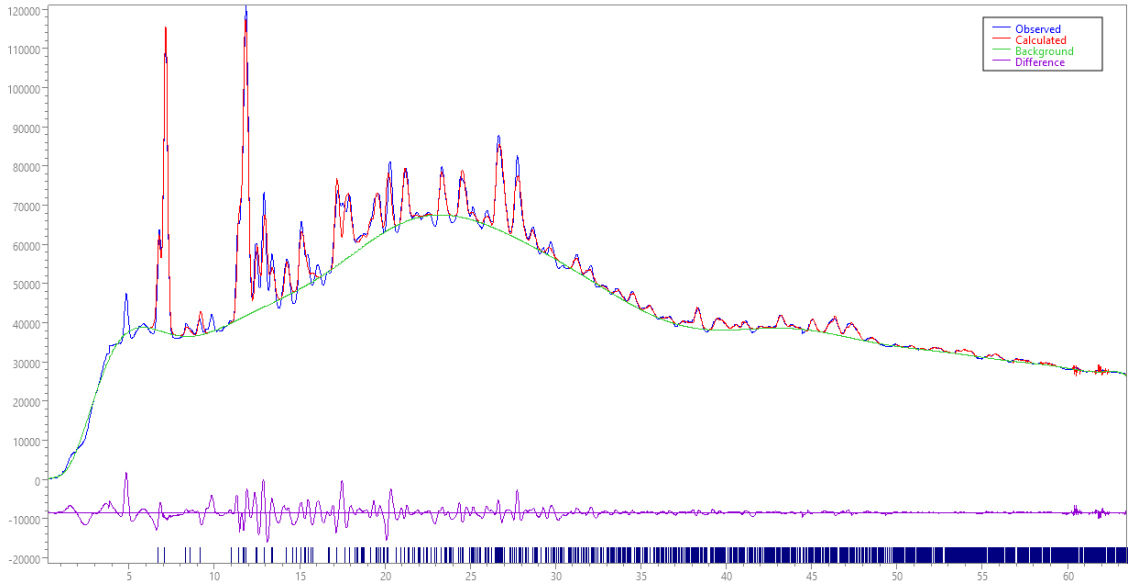

Fig. 5.13 Le Bail fits of PXRD patterns of **Cu-Eu-MOF**, showing observed (blue) and calculated (red) data, and their difference (violet). The background is shown in green, and the dark blue lines indicate the positions of reflections predicted from the unit cell. The sample used contained a mixture of the red-orange and red-purple crystals of **Cu-Eu-MOF**, was synthesised with a TFA concentration of 0.43 M. The experimental powder pattern was recorded in a polyamide capillary.

To assess whether samples of **Cu-Eu-MOF** maintain their crystallinity when handled in air, a sample of **Cu-Eu-MOF** was prepared as described above in Section 6.2.1 (TFA concentration = 0.43 M), stored in air for 3 hours, and then the powder pattern was measured in air (**Fig. 5.14**). Fitting using the Le Bail method[33] confirmed that agreement between the experimental and calculated PXRD pattern, with final R values of R_p = 4.997 and R_{wp} = 6.812 (**Fig. 5.15**). This confirmed that crystals of **Cu-Eu-MOF** can be stored in air without loss of crystallinity or decomposition of the framework.

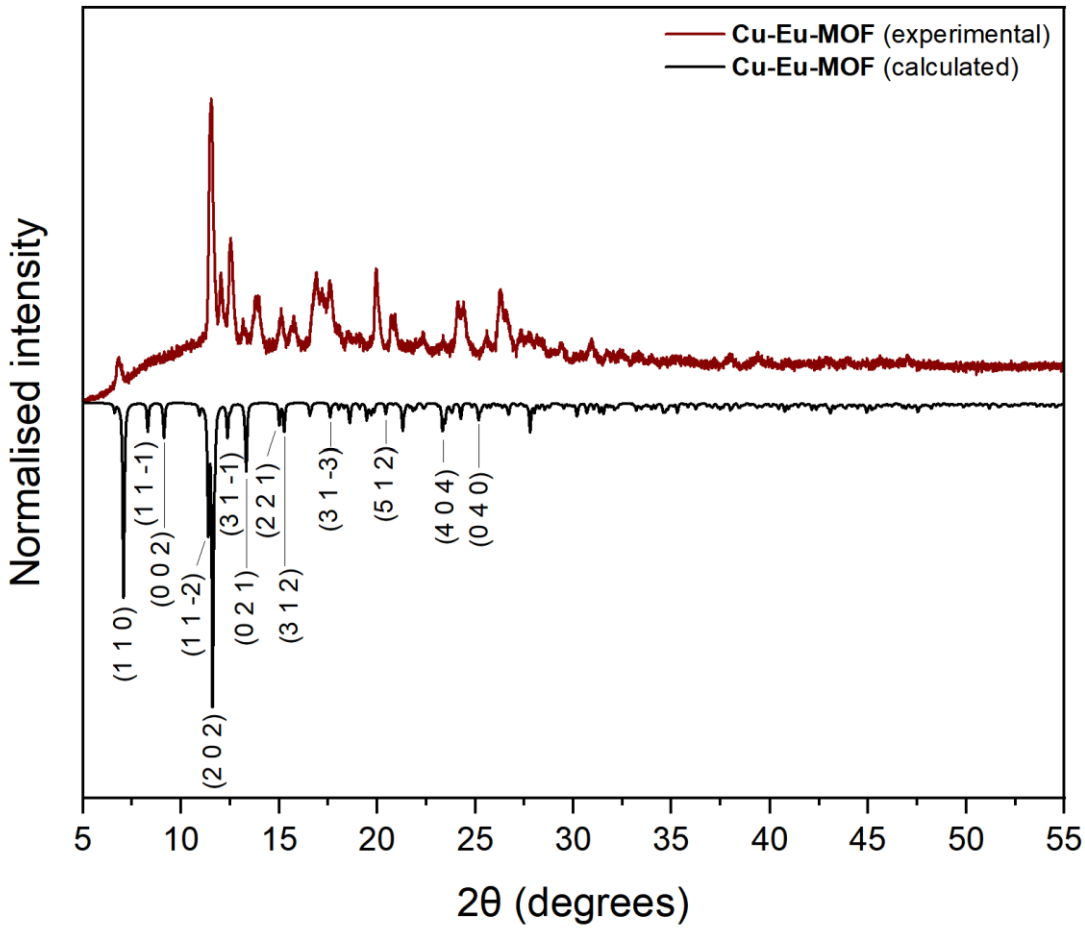

Fig. 5.14 Calculated (black) and experimental (blue) PXRD pattern of **Cu-Eu-MOF**, with indexed diffraction peaks. The sample used contained a mixture of the red-orange and red-purple crystals of **Cu-Eu-MOF**, and was synthesised with a TFA concentration of 0.43 M. The experimental powder pattern was recorded in air.

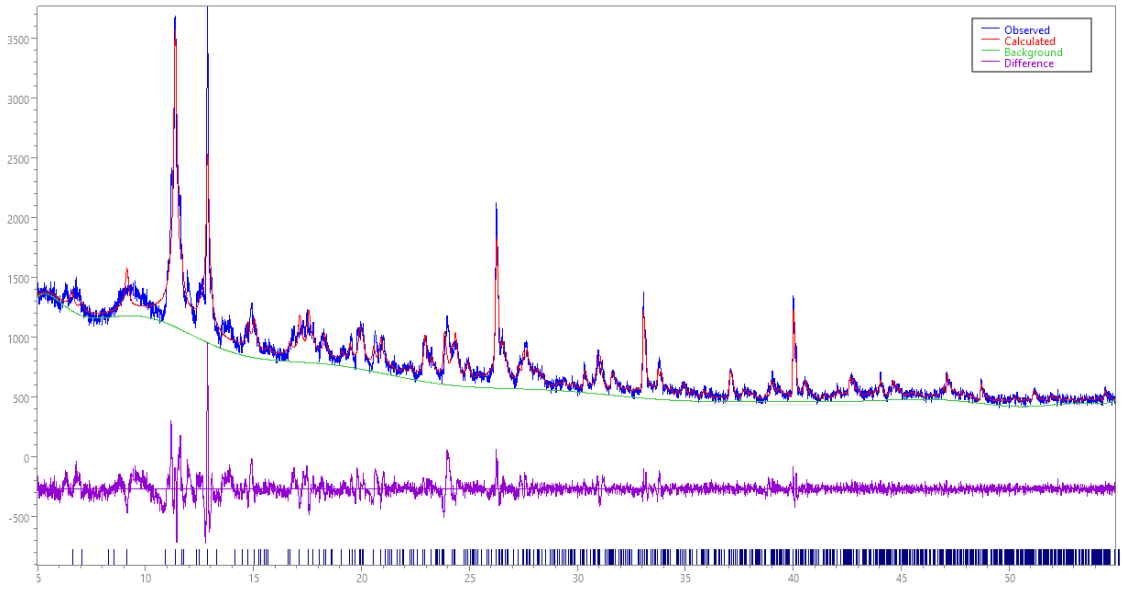

Fig. 5.15 Le Bail fits of PXRD patterns of **Cu-Eu-MOF**, showing observed (blue) and calculated (red) data, and their difference (violet). The background is shown in green, and the dark blue lines indicate the positions of reflections predicted from the unit cell. The sample used contained a mixture of the red-orange and red-purple crystals of **Cu-Eu-MOF**, and was synthesised with a TFA concentration of 0.43 M. The experimental powder pattern was recorded in air.

As previously discussed, single crystals cut from the clusters of red-purple needle-shaped crystals in **Cu-Eu-MOF** showed poor diffraction, and these crystals could therefore not be measured using single-crystal XRD analysis. To confirm that the good agreement between the simulated and experimental PXRD patterns of as synthesised **Cu-Eu-MOF** was due to phase-purity of the sample, rather than the absence of peaks corresponding to the clusters of red-purple needles due to their poor diffraction, a second PXRD measurement was carried out using a sample of the red-purple needles alone. A sample containing exclusively the red-purple crystals could be obtained by increasing the concentration of trifluoroacetic acid in the reaction system (0.57 M versus 0.43 M). The PXRD pattern of the red-purple needles (**Fig. 6.15**) confirms that the sample is phase-pure, as the experimental pattern is in good agreement with the pattern calculated for **Cu-Eu-MOF**.

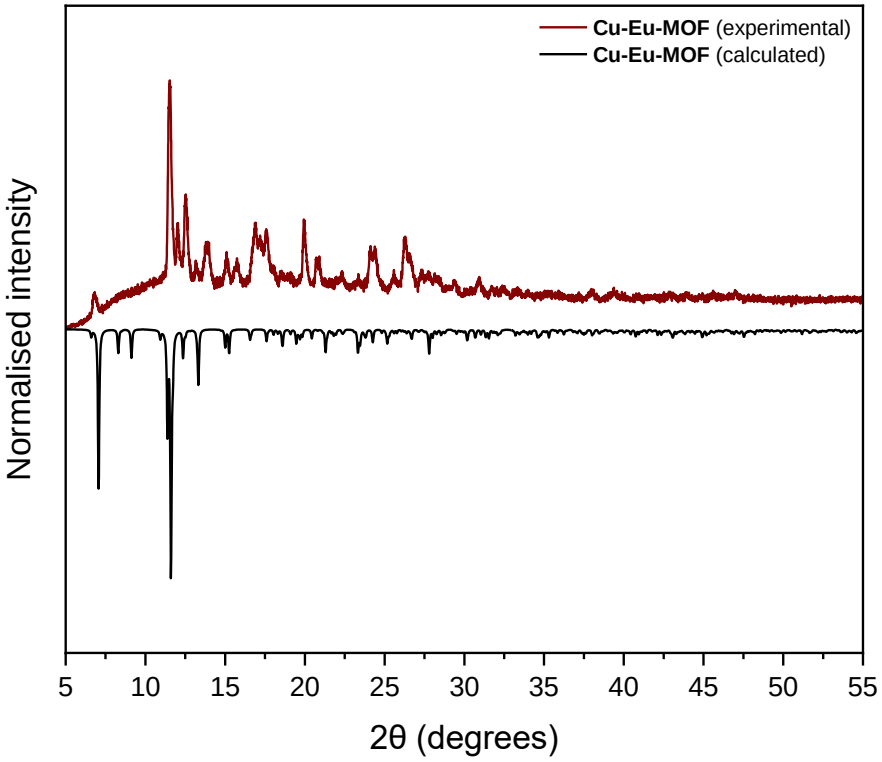

Fig. 5.16 Calculated (black) and experimental (purple) PXRD pattern of a sample of only red-purple crystals of **Cu-Eu-MOF**. The sample was synthesised by increasing the concentration of TFA in the reaction system to 0.57 M. The experimental powder pattern was recorded in air.

PXRD experiments have demonstrated that both types of crystals found in the reaction mixtures were crystals of **Cu-Eu-MOF**, and the appearance of these crystals, both in terms of size, shape and colour, is highly dependent on the concentration of TFA in the reaction system. To obtain samples of crystals for bulk analysis (FTIR spectroscopy, SEM and EDX analysis, TGA and photochemical studies, etc.), a TFA concentration of 0.43 M was used in the reactions, as this concentration was found to give a higher, more consistent yield of **Cu-Eu-MOF** crystals.

5.3.2 Fourier-Transform Infrared (FTIR) Spectroscopy of Cu-Eu-MOF

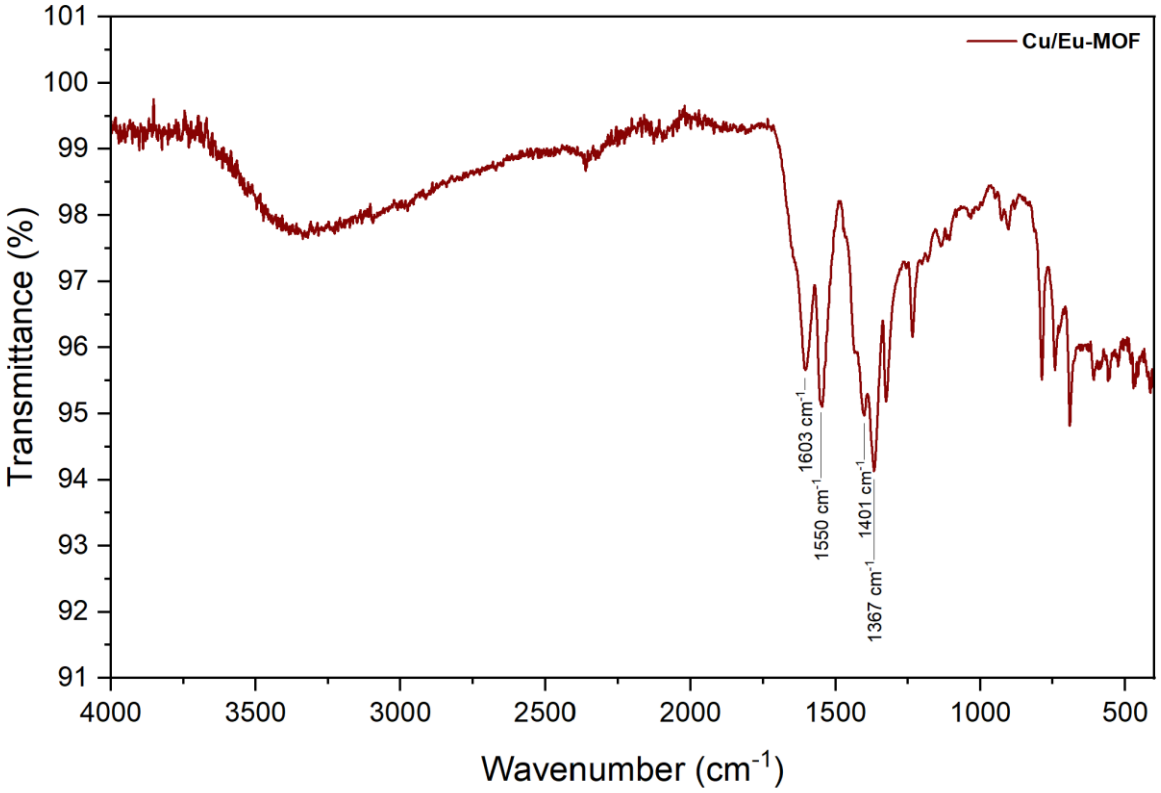

Fig. 5.17 FTIR spectrum of **Cu-Eu-MOF**, with characteristic peaks labelled.

FTIR and Raman spectroscopy were used to analyse **Cu-Eu-MOF**. The FTIR spectrum is shown in **Fig. 5.17**. A broad band from ca. 3380 cm^{-1} to 2580 cm^{-1} can be assigned to the vibrations of C-H bonds on the $[Cu^{I}(2,2'\text{-DMBP})_2]^{3-}$ metallo-linker, in addition to O-H vibrations of water molecules coordinated to the Eu^{III} metal centres. The asymmetric C=O stretches of the $[Cu^{I}(2,2'\text{-DMBP})_2]^{3-}$ carboxylate vibrations occur at 1603 and 1550 cm^{-1}, while the symmetric stretching vibrations lead to bands at 1401 and 1367 cm^{-1}. The difference between the average of the two symmetric and asymmetric carboxylate stretches, Δ, as reported by Deacon and Philips,[35] is 193 cm^{-1} (rounded to 0 decimal places). This value is in good agreement with typical values for bridging carboxylates.

5.3.3 Scanning electron microscopy and energy dispersive X-ray spectroscopy of Cu-Eu-MOF

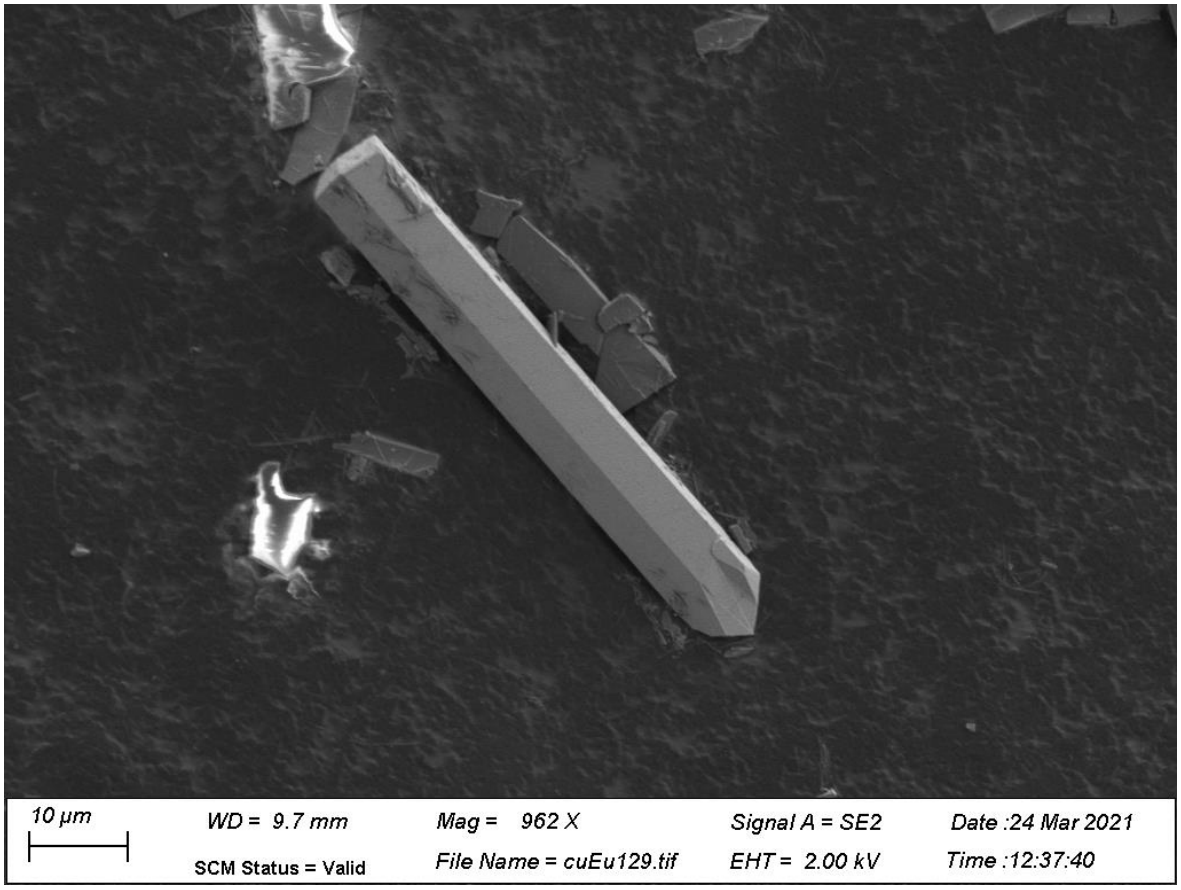

Fig. 5.18 SEM image of **Cu-Eu-MOF**.

SEM imaging was used to gain insight into the size and habit of the **Cu-Eu-MOF** crystals. **Fig. 5.18** shows an image of the larger red-orange crystals in **Cu-Eu-MOF**. The crystals possess defined needle-like shapes with varying sizes. EDX analysis was used to confirm the presence of Cu and Eu in the crystals. The elemental ratios of Cu:Eu obtained from quantitative EDX measurements are in good agreement with those expected from the molecular formula (Eu:Cu, expected ratio 1:1, observed 1:1.01).

5.3.4 Thermogravimetric analysis (TGA) of Cu-Eu-MOF

TGA was carried out to investigate the thermal stability of the **Cu-Eu-MOF**. The sample was prepared by filtering a sample of freshly synthesised **Cu-Eu-MOF** crystals, rinsing with DMF, and placing the sample onto filter paper, to remove surface solvent from the crystals, prior to transferring the crystals to the TGA crucible. The measurement was carried out in air, with a scan-rate of 5 °C per minute. The initial weight loss, between 90 °C and 150 °C is due to loss of uncoordinated constitutional solvent molecules (H_2O and DMF) in the structure (ca 5%). The second step, which occurs between 120 °C and 150 °C, occurs due to loss of coordinated solvent molecules from the Eu^{III} ions in the structure. The decomposition of the linker occurs between 300 °C and 420 °C, leading to a weight loss of approximately 55%. This is in good agreement with the temperature range of linker decomposition previously reported for coordination polymers containing this Cu^{I}

complex.[18] The remaining weight (ca. 30 %) can be attributed to Cu and Eu in the structure and is associated with the formation of oxides. The TGA curve indicates that the de-solvated structure of **Cu-Eu-MOF** retains its thermal stability up to 300 ℃, and above this point, the linkers in the MOF undergo decomposition.

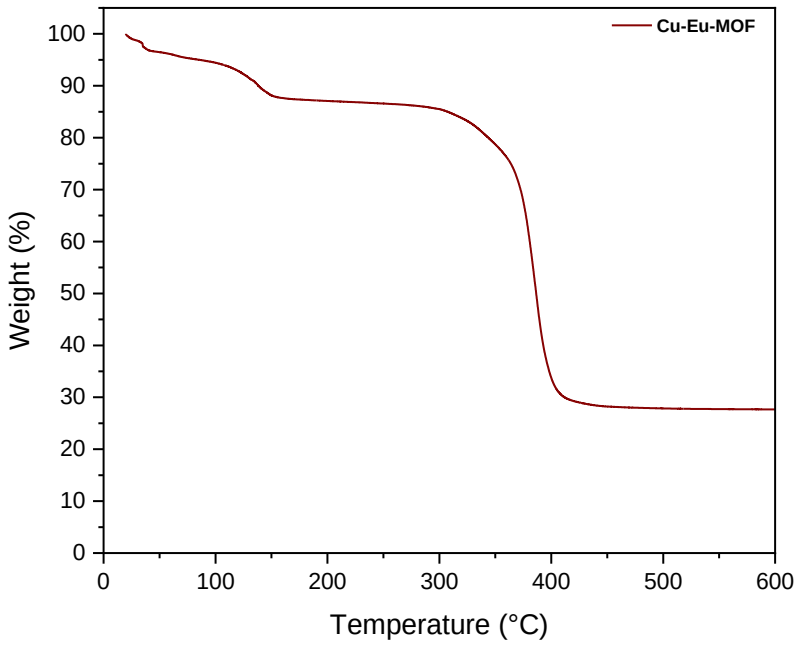

Fig. 5.19 TGA curve of **Cu-Eu-MOF**.

5.3.5 Photochemical studies

Previous studies of coordination polymers incorporating $[Cu^{I}(H_2$2,2'-DMBP$)_2]PF_6$ showed fluorescence, in which the decay rate was influenced by the metal centre in the MOF.[18] Based on this, preliminary photochemical studies of **Cu-Eu-MOF** were carried out in order to gain insight into the suitability of this MOF for photochemical applications.

The UV-vis absorption spectrum of a suspension of **Cu-Eu-MOF** crystals in acetonitrile was recorded (**Fig. 5.20**). The MOF shows broad absorption across the visible region, with two broad absorption bands, the first band has an adsorption maximum at 348 nm, while the second absorption band has a maximum at 516 nm and a shoulder at 676 nm. A fourth absorption band in the spectrum has an absorption onset at approximately 740 nm. Comparison of the absorption spectrum of the metallo-linker,[18] to that of **Cu-Eu-MOF**, allows assignment of these two bands to metal-to-ligand charge transfer interactions in the $[Cu^{I}$(2,2'-DMBP$)_2]^{3-}$ metallo-linker (**Fig. 5.20)**.

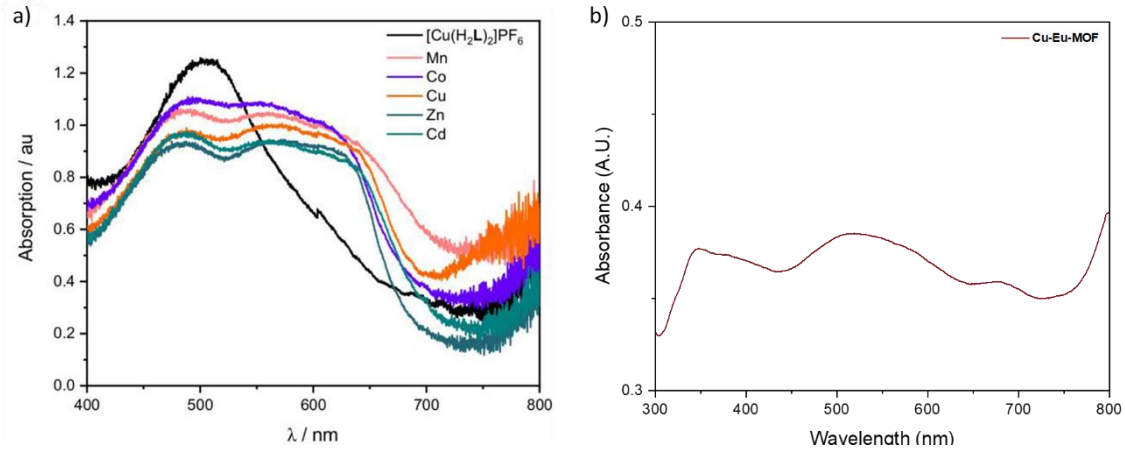

Fig. 5.20 a) Visible absorption spectrum previously reported for $[Cu^{I}(H_2$2,2'-DMBP$)_2]PF_6$ and MOFs synthesised using this metallolinker[18] **b)** UV-vis spectrum of a suspension of **Cu-Eu-MOF** in acetonitrile.

Photoluminescence studies of **Cu-Eu-MOF** were attempted using a suspension of the MOF crystals in acetonitrile, however, the spectrum did not show any emission bands when the MOF was excited at 400 nm. Similarly, the characteristic bright red luminescence associated with Eu^{III} ions could not be observed with the naked-eye when exciting crystals or suspensions of **Cu-Eu-MOF** using a 404 nm light source. The absence of both linker-based luminescence or characteristic *f-f* Eu^{III} luminescence bands in the photoluminescence spectrum of **Cu-Eu-MOF** indicates that the photoexcited $[Cu^{I}$(2,2'-DMBP$)_2]^{3-}$ metallo-linker in **Cu-Eu-MOF** does not undergo relaxation through energy transfer mechanisms. This suggests that electron transfer from $[Cu^{I}(H_2$2,2'-DMBP$)_2]^{-}$ to the Eu^{III} ions may occur in **Cu-Eu-MOF**, as luminescence quenching has been observed in other metallo-linker-based Eu^{III} MOFs, in which photoreduction of the Eu^{III} node occurs.[36]

Eu^{III} ions have a standard electrode reduction potential of -0.35 V in water, and formation of meta-stable Eu(II) can be achieved by photoreduction of Eu^{III} ions.[37] Further studies which may include electron paramagnetic resonance (EPR) spectroscopy to monitor any changes which occur in the Eu^{III} metal centres, would allow for increased insight into the photoredox characteristics of **Cu-Eu-MOF.** Importantly, electrochemical or spectro-electrochemical monitoring of redox changes in **Cu-Eu-MOF** in response to light may prove very insightful.

5.4 Conclusions

The work in this chapter built upon previous work, both in the literature and in this thesis, to give a stable Ln-MOF, **Cu-Eu-MOF** which absorbs light in the visible region of the spectrum. Though **Cu-Eu-MOF** is very densely packed, the MOF has several interesting and desirable properties, such as good stability to air, phase-purity, thermal stability and potentially open coordination sites on the Eu^{III} ions upon removal of coordinated solvent molecules. Additionally, the MOF uses an earth-abundant metallo-linker as a photosensitising ligand.

Cu-Eu-MOF is stable in air, and TGA measurements indicates that the desolvated material is thermally stable to 300 °C. **Cu-Eu-MOF** can be synthesised in high yield, and the formation of

crystals and their morphology is influenced substantially by the concentration of TFA in the reaction system.

Cu-Eu-MOF features interesting structural properties, however, the dense structure of the MOF suggests that **Cu-Eu-MOF** would not be suitable for gas sorption applications, or other applications such as dye or contaminant uptake which require accessible voids and channels in the structure.

We have presented preliminary photochemical studies of **Cu-Eu-MOF**, which indicate that the MOF absorbs light across a broad region of the UV-vis spectrum. Future work will focus on further characterising the novel **Cu-Eu-MOF**, including using electrochemical studies to explore the reduction potential of the MOF and photoresponse of this MOF in the presence and absence of light. Finally, catalytic studies may be carried out to assess if the MOF can be used as a visible-light driven catalyst for the reduction of CO_2.

References

1 I. I. Alkhatib, C. Garlisi, M. Pagliaro, K. Al-Ali and G. Palmisano, *Catal. Today*, 2020, **340**, 209–224.

2 D. Sun, L. Ye and Z. Li, *Appl. Catal. B Environ.*, 2015, **164**, 428–432.

3 Z.-M. Zhang, T. Zhang, C. Wang, Z. Lin, L. Long and W. Lin, *J. Am. Chem. Soc.*, 2015, **137**, 3197–3200.

4 A. Aziz, A. R. Ruiz-Salvador, N. C. Hernández, S. Calero, S. Hamad and R. Grau-Crespo, *J. Mater. Chem. A*, 2017, **5**, 11894–11904.

5 K. G. M. Laurier, F. Vermoortele, R. Ameloot, D. E. De Vos, J. Hofkens and M. B. J. Roeffaers, *J. Am. Chem. Soc.*, 2013, **135**, 14488–14491.

6 S. C. Fu, X. L. Zhong, Y. Zhang, T. W. Lai, K. C. Chan, K. Y. Lee and C. Y. H. Chao, *Energy Build.*, , DOI:10.1016/j.enbuild.2020.110313.

7 D. R. McMillin, M. T. Buckner and B. T. Ahn, *Inorg. Chem.*, 1977, **16**, 943–945.

8 N. Armaroli, *Chem. Soc. Rev.*, 2001, **30**, 113–124.

9 C. E. McCusker and F. N. Castellano, *Inorg. Chem.*, 2013, **52**, 8114–8120.

10 R. S. Khnayzer, C. E. Mccusker, B. S. Olaiya and F. N. Castellano, *J. Am. Chem. Soc.*, 2013, **135**, 14068–14070.

11 M. T. Miller and T. B. Karpishin, *Inorg. Chem.*, 1999, **38**, 5246–5249.

12 H. Takeda, K. Ohashi, A. Sekine and O. Ishitani, *J. Am. Chem. Soc.*, 2016, **138**, 4354–4357.

13 Y. Zhang, P. Traber, L. Zedler, S. Kupfer, S. Gräfe, M. Schulz, W. Frey, M. Karnahl and B. Dietzek, *Phys. Chem. Chem. Phys.*, 2018, **20**, 24843–24857.

14 H. Takeda, Y. Monma, H. Sugiyama, H. Uekusa and O. Ishitani, *Front. Chem.*, 2019, **7**, 1–12.

15 E. Generalic, Rare Earth Elements, https://www.periodni.com/rare_earth_elements.html, (accessed 29 August 2021).

16 Y. Pi, X. Feng, Y. Song, Z. Xu, Z. Li and W. Lin, *J. Am. Chem. Soc.*, 2020, **142**, 10302–10307.

17 X. Feng, Y. Pi, Y. Song, C. Brzezinski, Z. Xu, Z. Li and W. Lin, *J. Am. Chem. Soc.*, 2020, **142**, 690–695.

18 F. W. Steuber, J. J. Gough, É. Whelan, L. Burtnyak, A. L. Bradley and W. Schmitt, *Inorg. Chem.*, 2020, **59**, 17244–17250.

19 C. E. Housecroft and E. C. Constable, *Chem. Soc. Rev.*, 2015, **44**, 8386–8398.

20 L. J. Farrugia, *J. Appl. Crystallogr.*, 2012, **45**, 849–854.

21 G. A. Jeffrey, *An Introduction to Hydrogen Bonding*, Oxford University Press, Oxford, United Kingdom, 1997.

22 D. Herschlag and M. M. Pinney, *Biochemistry*, 2018, **57**, 3338–3352.

23 T. Steiner, *Angew. Chemie Int. Ed.*, 2002, **41**, 48–76.

24 O. C. Gagné, *Acta Crystallogr. Sect. B Struct. Sci. Cryst. Eng. Mater.*, 2018, **74**, 49–62.

25 F. W. Steuber, Trinity College Dublin, 2020.

26 O. V. Dolomanov, L. J. Bourhis, R. J. Gildea, J. A. K. Howard and H. Puschmann, *J. Appl. Crystallogr.*, 2009, **42**, 339–341.

27 S. Alvarez, P. Alemany, D. Casanova, J. Cirera, M. Llunell and D. Avnir, *Coord. Chem. Rev.*, 2005, **249**, 1693–1708.

28 V. A. Blatov, A. P. Shevchenko and D. M. Proserpio, *Cryst. Growth Des.*, 2014, **14**, 3576–3586.

29 I. D. Brown and D. Altermatt, *Acta Crystallogr. Sect. B Struct. Sci.*, 1985, **41**, 244–247.

30 W. Liu and H. H. Thorp, *Inorg. Chem.*, 1992, **31**, 1585–1588.

31 N. M. Shavaleev, S. V. Eliseeva, R. Scopelliti and J. C. G. Bünzli, *Inorg. Chem.*, 2015, **54**, 9166–9173.

32 A. Trzesowska, R. Kruszynski and T. J. Bartczak, *Acta Crystallogr. Sect. B Struct. Sci.*, 2004, **60**, 174–178.

33 A. Le Bail, *Powder Diffr.*, 2005, **20**, 316–326.

34 A. Altomare, C. Cuocci, C. Giacovazzo, A. Moliterni, R. Rizzi, N. Corriero and A. Falcicchio, *J. Appl. Crystallogr.*, 2013, **46**, 1231–1235.

35 G. B. Deacon and R. J. Phillips, *Coord. Chem. Rev.*, 1980, **33**, 227–250.

36 Z.-H. Yan, M.-H. Du, J. Liu, S. Jin, C. Wang, G.-L. Zhuang, X.-J. Kong, L.-S. Long and L.-S. Zheng, *Nat. Commun.*, 2018, **9**, 3353.

37 Y. Hasegawa, Y. Kitagawa and T. Nakanishi, *NPG Asia Mater.*, 2018, **10**, 52–70.

Chapter 6 : Conclusions and future work

In summary, this thesis focused on incorporating heterocycle-based ligands into metal-organic materials, with the aim of synthesising novel porous materials with interesting structures, which are stable, and possess interesting photoactivity.

In chapter 1, a comprehensive review of recent developments in the fields of metal-organic materials is presented. An introduction to coordination cages is provided, and this chapter also highlights examples of the applications of photoactive MOFs, with a focus on the effect of MOF components, such as organic linkers, inorganic units and framework guests, on the optical and electronic properties of the materials. Developments in utilising luminescent MOFs as chemical sensors and as light emitting materials are discussed, in addition to recent advances in designing MOF-based photocatalysts for water splitting, CO_2 reduction and organic reactions.

The first section of this thesis describes the synthesis of a novel thienothiophene-based linker, H_2**CPTT**, and the single crystal XRD structure of this linker is presented. The unusual geometry and angles in H_2**CPTT** led to a previously unreported synthetic pathway to a metal-organic hendecahedron, **Cu-TTMOP**, a Cu^{II}-paddlewheel-based coordination cage. This is the first example of a coordination cage with this geometry which is synthesised using a single organic linker. **Cu-TTMOP** contains solvent accessible pores and channels, which were used to absorb dye molecules from solution. This study highlighted the opportunities presented by heterocyclic linkers in providing synthetic pathways to fascinating and rare structures in supramolecular materials. Further chapters built on this knowledge, with the aim of synthesising stable, photoactive three-dimensional metal-organic frameworks with high surface areas.

In the second section of this work, the synthesis of new linker, H_3**TTT** is presented. This linker contains both thiophene rings, which allow unusual and flexible binding angles in the linker and a triazine ring, which has Lewis-basic nitrogen atoms which present a potential interaction site for analyte ions. H_3**TTT** was reacted with Ln^{III} ions, with the aim of synthesising stable photoactive MOFs. Three distinct series of MOFs were synthesised by reacting H_3**TTT** with Ln^{III} ions, illustrating the dependence of the structures of MOFs formed on the nature of the Ln^{III} ion used.

The first two series of Ln-MOFs synthesised with H_3**TTT** contained one-dimensional rod-shaped SBUs containing chains of Ln^{III} ions. The first series of MOFs, **La-MOF**, **Ce-MOF**, **Nd-MOF** and **Pr-MOF** contained ten-coordinate Ln^{III} ions, while the second series, **Sm-MOF** and **Eu-MOF** feature eight-coordinate Ln^{III} which form a zig-zag chain through the SBU. Both **La-MOF** and **Eu-MOF** were studied by gas sorption studies and shown to be porous materials with high surface areas.

Both **Sm-MOF** and **Eu-MOF** showed photoluminescence bands characteristic of *f-f* transitions in Ln^{III} ions. **Eu-MOF** was demonstrated to be stable to thermal activation, and chemically stable to a range of solvents, including water, and this MOF also showed bright red fluorescence under UV-

light irradiation, which could be seen with the naked eye. This luminescence was utilised to demonstrate that **Eu-MOF** can function as a selective "turn-off" luminescence sensor for metal ions in water, including toxic ions such as Pb^{II}.

When H_3**TTT** was reacted with Ln^{III} ions from the latter half of the lanthanide series, a series of two-dimensional MOFs were synthesised, which had dinuclear $\{Ln^{III}_2\}$ SBUs (Ln^{III} = Gd^{III}, Dy^{III}, Er^{III}, Yb^{III}). The structural differences between the three series of MOFs indicate that H_3**TTT** can form a wide range of metal-organic materials, the structure of which are highly dependent on the nature of the metal ion used. In future studies, it would be interesting to explore the structures and properties of metal-organic materials that can be synthesised using H_3**TTT** and transition metal ions, such as Zr^{IV}, which has previously been reported to form robust MOFs. However, the photochemical applications of MOFs synthesised using this linker are limited by the absence of visible light absorption by H_3**TTT**.

The final section of this thesis describes the use of an earth-abundant Cu^{I} photosensitiser, $[Cu^{I}(H_2$2,2'-DMBP$)_2]PF_6$, to synthesise a Eu^{III}-based three-dimensional MOF, **Cu-Eu-MOF**. Preliminary photochemical studies of this MOF showed that the material absorbs light across a broad region of the UV-vis spectrum. Future work on this material will involve assessing the reduction potential of **Cu-Eu-MOF** and studying the electrochemical photoresponse of this material. Additionally, future studies on whether this MOF can be used as a photocatalyst for light-driven CO_2 reduction. Additionally, due to the dense packing structure of this MOF, future work will focus on modifying the synthetic conditions under which $[Cu^{I}(H_2$2,2'-DMBP$)_2]PF_6$ and Eu^{III} were reacted, to see if changing the synthetic conditions would lead to more porous Eu^{III}-based MOF structures, and hence allow a broader range of applications for the resulting materials.

The novel materials presented and explored in this thesis have many promising characteristics and properties, as highlighted above, however, these materials also have limitations which would hinder their application in industrial settings. One limitation of supramolecular materials is the cost and time associated with the multistep synthesis of an organic linker, followed by subsequent high temperature solvothermal synthesis. An additional limitation is the poor stability of some metal-organic materials to air and temperature, for example, the coordination cage **Cu-TTMOP** presented in this thesis. Subsequent work in this thesis focused on designing materials, such as the series of MOFs presented in chapter 3, which, like **Cu-TTMOP**, featured a heterocyle-based linker, but possessed improved stability due to the use of lanthanide-based inorganic SBUs. This is an example of how the tunable properties of metal-organic materials allow researchers to select desirable properties from one compound or series of compounds, and incorporate these properties into new generations of materials, thus continuously improving the properties through rational design of SBUs.

Additionally, despite the challenges with cost, yield and stability, which would arise at present in utilising metal-organic materials in industrial scale processes, metal-organic materials present many

opportunities in smaller scale processes, such as is research and development. One example of this is the use of MOFs and coordination cages as crystalline sponges, which absorb molecules into their pores, allowing crystal structure elucidation without requiring crystallisation of the target molecule. Future work could explore the use of the novel porous materials presented herein for applications

A natural progression of this work would be exploring and developing a robust and efficient method of preparing the materials which were developed and explored in this thesis, for example by electrodeposition of thin films of MOFs. This would present many advantages, if successful, by leading to a fast, reproducible and energy efficient method of synthesising heterogeneous materials with promising photochemical properties.

Overall, this thesis demonstrates that utilising heterocycle-based linkers allows interesting and previously unreported structures to be accessed. Synthetic approaches to light-harvesting and photoactive materials were demonstrated, and the potential applications for these materials were explored. The limiting factors of each material for these applications were also discussed.

Chapter 7 : Experimental

7.1 Materials and methods

7.1.1 Reagents

All chemical reagents and solvents used were purchased from Sigma-Aldrich, Fluorochem, VWR Acros Organics or Santa Cruz Biotechnology. All chemicals were used without further purification. All solvents used were of HPLC grade quality. Water was deionised before use.

7.1.2 Nuclear magnetic resonance (NMR)

All NMR measurements were recorded by Dr. John O'Brien or Dr. Manuel Rüther using either a Bruker Avance II 600 MHz or Bruker Avance III 400 MHz spectrometer. Samples were dissolved in appropriate deuterated solvents. Chemical shifts are reported in ppm, with deuterated solvents used as an internal reference. All NMR spectra were carried out at 293 K. The following standard abbreviations are used to report NMR spectra: s, singlet; d. doublet; t, triplet; q, quartet; m, multiplet; br, broad singlet; *J*, coupling constant.

7.1.3 Fourier transform-infrared spectroscopy (FTIR)

FTIR spectra were recorded on a Perkin Elmer Spectrum 100 FTIP Spectrometer, equipped with a universal Attenuated Total Reflectance (ATR) sampling accessory. Samples were measured with a scan rate of 25 scans per minute, in the range 4000-400 cm^{-1}. The following abbreviations were used to describe the peaks in the spectra: w, weak; m, medium; st, strong; br, broad. Data was processed using Perkin Elmer Spectrum v5.0.1 software.

7.1.4 Mass spectrometry

Samples were dissolved in HPLC grade solvents, and undissolved solids were removed using a Teflon syringe filter with 200 μm pore size. Measurements were carried out by Dr. Martin Feeney and Dr. Gary Hessman using a Waters Micromass mass spectrometer equipped with time-of-flight analyser.

7.1.5 Thermogravimetric analysis (TGA)

TGA measurements were carried out using a Perkin Elmer Pyris 1 instrument. Measurements were carried out using between 1 and 10 mg of sample on a ceramic crucible sample holder. The measurement was carried out with a nitrogen gas flow (rate of flow: 20 mL min^{-1}) with a heating rate of 10 °C min^{-1}.

7.1.6 Single crystal X-ray diffractions

Crystals of suitable size for single crystal XRD measurements were mounted on a MiTiGen cryoloop micromount using paraffin oil. Intensity data was collected on a Bruker APEX DUO dual-source instrument using a Cu K_α (λ = 1.54178 Å) Incoatec microfocus source (multilayer optics) or a Mo (λ = 0.71073) sealed tube X-ray source (graphite monochromator). Temperature control was provided by an Oxford Cryostrem Cobra system, and the instrument was equipped with a Photon 50

CMOS detector. Where crystal twinning occurred, the unit cells and transformation matrices of samples were determined using CELL_NOW. Intensity data was processed with SAINT+ and corrected for absorption by multi-scan methods using SADABS or TWINABS as appropriate. Structure solution was achieved using Bruker SHELXT Software, using intrinsic phasing and refinement on F^2 with full matrix least squares procedures in Olex2.[1] All non-hydrogen atoms were refined anisotropically, and hydrogen atoms were included in idealised positions. Co-crystallised solvents were included and refined as rigid groups unless solvent disorder was too great to improve the model, in which case they were removed from the structure solution using the PLATON squeeze routine.[2] Single crystal XRD measurements and structure refinement were carried out by Éadaoin Whelan, Dr. Nianyong Zhu and Dr. Friedrich Steuber.

7.1.7 Powder X-ray diffraction (PXRD)

Powder XRD patterns were measured on a Bruker D2 Phaser equipped with a Cu-Kα sealed tube (λ = 1.54178 Å) and a Lynxeye detector. The measurements were carried out at room temperature. Finely ground powder samples were mounted on a silicon single crystal zero-background holder. Pattern fitting using Le Bail methods in EXPO2014.[3–5]

7.1.8 UV-Vis absorption spectroscopy

Solid-state reflectance and transmittance measurements were performed on a Perkin Elmer Lambda 1050 spectrometer using an integrating sphere accessory. Measurements were carried out in the range of 300-800 nm. A suspension of the sample in a volatile solvent (isopropyl alcohol or chloroform) was drop-casted onto a quartz slide. The transmittance of the sample was measured at the front of the integrating sphere, and the background of the quartz slide was accounted for by measuring the transmittance of a clean quartz slide in the same position. For reflectance measurements, the sample was covered with a second quartz slide. The total reflectance of the sample was measured at the rear of the integrating sphere. The data was treated for background correction by measuring the reflectance and transmittance of a blank quartz slide. All data was analysed using Origin 2019 software.

Solution-state UV-Vis spectra were measured in quartz cuvettes with an optical path length of 1 cm. Absorption spectra were measured in the range of 300-850 nm at room temperature using a Lambda35 UV/vis spectrometer. All data was analysed using Origin 2019 software.

7.1.9 Photoluminescence Spectroscopy

Solid-state photoluminescence spectroscopy was carried out in the UV/Vis region using Fluomax-4 spectrophotometer (Horiba Jobin Yvon). A suspension of the sample in a volatile solvent (isopropyl alcohol or chloroform) was drop-casted onto a quartz slide. The resulting film was then covered with a second matched quartz slide. The sample was measured using a solid sample holder in the front-facing configuration.

Solution-state photoluminescence spectroscopy was measured on a Fluoromax-4 spectrophotometer (Horiba Jobin Yvon). Samples were measured in 4-sided quartz cuvettes with an optical path length of 1 cm. When recording emission spectra, instrument-specific correction factors were applied to the data using Horiba Scientific FluorEssence software. The corrected spectrum is reported in this work as S1c/R1c (S1c = corrected detector signal, R1c = corrected detector reference).

7.1.10 Scanning electron microscopy (SEM) and energy dispersive X-ray spectroscopy (EDX)

SEM imaging was carried out using a Zeiss ULTRA plus microscope using InLens and SE2 detectors at 1 kV acceleration voltage. EDX spectra were recorded under the same microscope using a 20 mm^2 Oxford Inca EDX detector with 15-20 kV acceleration voltage. The spectra were measured for 100 seconds, and K-edge or M-edge lines were used for quantitative measurements as appropriate.

7.1.11 Gas sorption

Gas adsorption isotherms were obtained from measurements performed by Dr Sebastien Vaesen. The samples were activated under vacuum prior to analysis. Measurements were recorded in the 0 - 1 bar pressure range with a volumetric method using a Quantachrome Autosorb iQ instrument. The cryo-temperature adsorption measurements were performed at 77 K using a liquid nitrogen bath. Gas adsorption measurements were performed using N_2 and CO_2 provided by BOC Ireland.

7.1.12 Solvothermal synthesis

All solvothermal synthesis was carried out using 1.5 mL sealed vials, using a purpose-built aluminium heating block with multiple slots. The vials were cooled down over one hour after the reactions were completed. To evaluate the yield of each material, the crystals were washed with DMF, filtered, and allowed to dry in air before weighing.

7.1.13 Thin Layer Chromatography (TLC)

TLC analysis was performed on precoated $60F_{254}$ silica coated slides. The mobile phase was determined for each sample, and HPLC grade solvents were used.

7.2 Ligand synthesis

7.2.1 Synthesis of 2,4,6-tri(thiophen-2-yl)-1,3,5-triazine

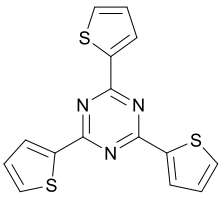

2,4,6-Tri(thiophen-2-yl)-1,3,5-triazine was synthesised according to a modified version of the procedure previously reported by Yu *et al.*.[6] Trifluoromethansulfonic acid (30 g, 0.2 mol) was added dropwise over 1 hour to a solution of thiophene-2-carbonitrile (10.9 g, 0.1 mol) in dry $CHCl_3$ at 0 °C, under argon atmosphere. The solution was stirred at 0 °C for 1 h, allowed to warm to room temperature, and stirred at room temperature for a further 16 h. The solution was quenched by addition to a dilute aqueous solution of NH_4OH. The solution was filtered and washed with water (50 mL), acetone (50 mL) then methanol (100 mL). 2,4,6-Tri(thiophen-2-yl)-1,3,5-triazine was isolated as a white product with 91 % yield (9.83 g, 0.03 mol).

^{1}H NMR and ^{13}C NMR spectra were in good agreement with those previously reported in the literature.

δ_H (400 MHz, $CDCl_3$) 8.32 (3 H, dd, J_1= 3.73 Hz, J_2=1.10 Hz), 7.65 (3 H, dd, J_1=4.96 Hz, J_2=1.01 Hz), 7.24 (3 H, dd, J_1= 4.89 Hz, J_2=3.80 Hz) ppm.

δ_C (100 MHz, $CDCl_3$) 167.6 (triazine carbon), 141.3, 132.5, 131.9, 128.5 (thiophene carbons) ppm.

FTIR (ATR): 3100-2600 (C-H, br), 3099 (w), 3063 (w), 2118 (w), 1766 (w), 1532 (m), 1500 (st), 1422 (st), 1372 (st), 1332 (w), 1313 (w), 1218 (m), 1146 (w), 1127 (w), 1084 (w), 1030 (m), 989 (w), 972 (w), 912 (w), 860 (m), 815 (st), 793 (w), 773 (m), 707 (st), 651 (w), 630 (m), 574 (m), 486 (m) cm^{-1}.

7.2.2 Synthesis of 5,5',5''-(1,3,5-triazine-2,4,6-triyl)tris(thiophene-2-carboxylic acid) (H_3TTT)

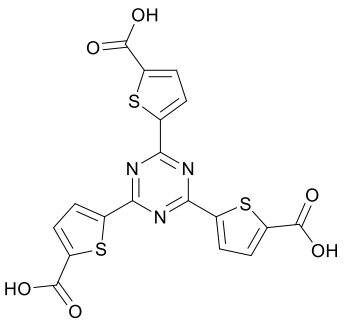

Lithium diisopropylamine was prepared by addition of *n*-butyllithium (20 mL, 2.5 M) to a solution of diisopropylamine (7.2 mL, 51.2 mmol) in dry THF (60 mL) at -78 °C under argon atmosphere. The solution was stirred for 15 minutes, after which a solution of 2,4,6-tri(thiophen-2-yl)-1,3,5-triazine (7.032 g, 21.5 mmol) in dry THF (60 mL) was added dropwise to the lithium diisopropylamine solution. After stirring the solution for 10 minutes, pellets of dry ice were added individually, resulting in a colour change from yellow to purple. The reaction was allowed to warm to room temperature and stirred under an argon atmosphere for 24 h.

The THF was removed *in vacuo*, and the resulting solid was dissolved in water. The solution was acidified to pH 1 using 1 M HCl. The yellow precipitate was filtered, and recrystallised from THF. H_3**TTT** was isolated as a pale yellow product with 53 % yield (5.23 g, 11.4 mmol).

δ_H (400 MHz, d_6-DMSO): 13.71 (3 H, br, H_C), 8.27 (3 H, d, J = 3.83 Hz, H_B), 7.86 (3 H, d, J = 3.83 Hz, H_A) ppm.

δ_C (150 MHz, d_6-DMSO) 166.9 (C1), 162.4 (C6), 144.8 (C2), 140.5 (C5), 133.9 (C3), 132.5 (C4) ppm.

FTIR (ATR): 3200-2150 (br), 2128 (br), 1670 (st), 1507 (st), 1474 (m), 1408 (m), 1366 (m), 1284 (C-O, m), 1100 (w), 1054 (w), 1025 (w), 983 (w), 912 (w), 842 (w), 806 (m), 783 (w), 748 (m), 664 (w), 572 (w), 515 (w), 485 (w), 447 (w) cm^{-1}.

UV-Vis (λ_{max}, nm): 330.

7.2.3 Synthesis of 3,4-dibromothiophene-2-carbaldehyde

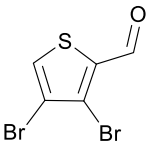

3,4-dibromothiophene-2-carbaldehyde was synthesised using a modified version of the procedure reported by Chu *et al.*[7]. Lithium diisopropylamine (LDA) was prepared by the addition of *n*-butyl lithium (28 mL, 1.6 M in hexane, 45 mmol) to diisopropylamine (9.72 mL) in dry THF (40 mL) under a nitrogen gas flow at 0°C. The reaction mixture was stirred at this temperature for 40 minutes, followed by the addition of 3,4-dibromothiophene (5 mL, 10.94 g, 45 mmol) was added. The reaction was then stirred for a further 90 minutes, at which time DMF (5.25 mL) was added to the reaction. Finally, after stirring the resulting mixture at 0°C for a further 30 minutes, the reaction mixture was poured into a saturated aqueous solution of NH_4Cl. The reaction was washed, and the product extracted with ethyl acetate (3 x 200 mL). The isolated organic phase was dried over $MgSO_4$ and concentrated under reduced pressure. The crude product was then purified using flash column chromatography with hexane: ethyl acetate (19:1, v/v) as a solvent system, giving the product as a yellow crystalline solid (5.61 g, 30 mmol, 65 % yield).

δ_H (400 MHz, $CDCl_3$), δ (ppm): 9.97 (d, J = 1.22 Hz, 1H), 7.77 (d, J = 0.30 Hz, 1H).

HRMS ($APCI^-$): 266.8120 ($[M-H]^-$, C_5HBr_2OS requires 266.8115).

FTIR (ATR): 3088 (m), 1656 (st), 1614 (m), 1490 (st), 1410 (st), 1356 (m), 1322 (st), 1256 (w), 1206 (st), 1150 (m), 1114 (w), 988 (w), 906 (m), 808 (st), 758 (m), 666 (st), 628 (m) cm^{-1}.

7.2.4 Synthesis of ethyl 6-bromothiophene[3,2-b]thiophene-2-carboxylate

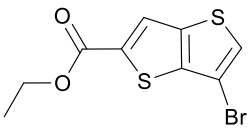

Ethyl 6-bromothiophene[3,2-b]thiophene-2-carboxylate was synthesised using a modified version of the procedure reported by Chu *et al.*.[7] Ethyl 2-sulfanylacetate (6.5 mL, 7.1 g, 60 mmol) was added to a solution of 3,4-dibromothiophene-2-carbaldehyde (10.7 g, 56 mol) and K_2CO_3 (8.20 g, 60 mmol) in DMF (50 mL) at room temperature. The reaction mixture was stirred for 72 hours, then poured into deionised water. The reaction was then extracted with ethyl acetate (3 x 300 mL), and washed with brine and an aqueous lithium chloride solution. The organic phase was then isolated, dried with anhydrous $MgSO_4$ and finally concentrated under a reduced atmosphere. The product was then purified using flash column chromatography on silica, with hexane: ethyl acetate (19:1, v/v) as an eluent. The product was obtained as a pale yellow crystalline solid (10.54 g, 55 mmol, 93 % yield). ^1H NMR spectrum is in good agreement with the literature spectrum.

δ_H (400 MHz, $CDCl_3$), δ (ppm): 8.03 (s, 1H), 7.49 (s, 1H), 4.4169 (q, J = 7.1 Hz, 2H), 1.43 (t, J = 7.1 Hz, 3H).

HRMS ($APCI^+$): 290.9143 ($[M+H]^+$, $C_9H_8BrO_2S_2$ requires 290.9149).

FTIR (ATR): 3112 (w), 3080 (w), 2988 (w), 2914 (w), 1706 (st), 1504 (m), 1450(w), 1392 (w), 1364 (m), 1346 (m), 1330 (m), 1288 (m), 1244 (st), 1156 (st), 1068 (m), 1014 (m), 940 (m), 888 (w), 858 (w), 820 (w), 810 (w), 744 (m), 736 (st), 690 (w), 652 (w), 600 (w) cm^{-1}.

7.2.5 Synthesis of butyl 6-(4-(butoxycarbonyl)phenyl)thieno[3,2-*b*]thiophene-2-carboxylate

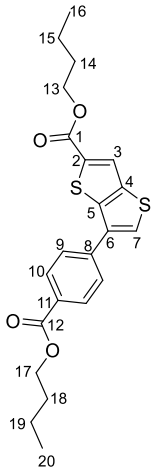

Butyl 6-(4-(butoxycarbonyl)phenylthieno[3,2-*b*]thiophene-2-carboxylate (1 g, 3.4 mmol), (4-(methoxycarbonyl)phenyl)boronic acid (0.927 g, 5.1 mol), K_2CO_3 (1.18 g, 9 mmol) and $Pd(PPh_3)_4$ (0.198 g, 0.17 mmol) were added to *n*-butanol under nitrogen gas flow. The reaction mixture was heated at 80 °C for 36 hours. The reaction mixture was then extracted with DCM (2 x 300 mL) and washed with brine (3 x 500 mL). The product was then purified by flash column chromatography over silica gel using hexane: ethyl acetate (19:1, v/v) as an eluant. The intermediate, butyl 6-(4-(butoxycarbonyl)phenyl) thieno[3,2-b]thiophene-2-carboxylate, was obtained as a pale yellow oil (0.87 g, 2 mmol, 58 % yield).

δ_H (400 MHz, $CDCl_3$), δ (ppm): 8.18 (d, J = 8.6 Hz, 2H, H-10), 8.07 (s, 1H, H-3), 7.84 (d, J = 8.6 Hz, 2H, H-9), 7.82 (s, 1H, H-7), 4.38 (m, 4H, H-13 and H-17, overlapping signals), 1.80 (m, 4H, H-14 and H-18, overlapping signals), 1.52 (m, 4H, H-15 and H-19, overlapping signals), 1.02 (m, 6H, H-16 and H-20, overlapping signals).

δ_C (100 MHz, $CDCl_3$), δ (ppm): 166.3 (C-12), 162.6 (C-1), 141.9 (C-4), 139.2 (C-5), 138.2 (C-11), 135.3 (C-2), 133.8 (C-8), 130.5 (C-10), 129.9 (C-6), 128.1 (C-7), 126.2 (C-9), 125.9 (C-3), 65.5 and 65.0 (C-13 and C-17), 30.9 (C-14 and C-18), 19.4 and 19.2 (C-15 and C-19), 13.8 (C-20 and C-16).

HRMS ($APCI^+$): 417.1189 ($[M+H]^+$, $C_{22}H_{25}O_4S_2$ requires 417.1194)

7.2.6 Synthesis of 6-(4-carboxyphenyl)thieno[3,2-*b*]thiophene-2-carboxylic acid (H_2CPTT)

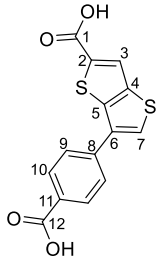

Butyl 6-(4-(butoxycarbonyl)phenylthieno[3,2-*b*]thiophene-2-carboxylate (0.8 g, 1.8 mmol) and LiOH (0.47 g, 20 mmol) were stirred in a mixture of water: THF (1:1, v/v) at room temperature for 16 hours. Aqueous HCl solution (50 mL, 1 M) was then added, and the product was isolated by filtration. The product was obtained as a white solid (0.52 g, 1.62 mmol, 90 % yield).

δ_H (400 MHz, d_6-DMSO, δ (ppm): 13.28 (br, 2H, OH), 8.46 (s, 1H, H-3), 8.24 (s, 1H, H-7), 8.07 (d, J = 11.2 Hz, 2H, H-10), 7.94 (d, J = 11.1 Hz, 2H, H-9).

δ_C (100 MHz, d_6-DMSO), δ (ppm): 166.9 (C-12), 163.2 (C-1), 140.4 (C-4), 139.3 (C-5), 137.4 (C-11), 135.7 (C-8), 132.4 (C-6), 130.5 (C-3), 130.3 (C-10), 130.0 (C-2), 126.7 (C-7), 126.1 (C-9).

FTIR (ATR): 3250-2400 (br), 3084 (br), 2974 (br), 2868 (br), 2680 (br), 2556 (br), 1674 (st), 1610 (m), 1498 (m), 1430 (m), 1398 (m), 1322 (m), 1288 (st), 1174 (w), 1148 (w), 1074 (w), 1018 (w), 914 (w), 844 (m), 798 (w) 750 (C-S-C, st), 700 (w), 670 (w), 614 (w), 546 (m), 458 (w) cm^{-1}.

7.3 Synthesis of Metal-Organic Frameworks

7.3.1 Synthesis of La-MOF

$La(NO_3)_3 \cdot 6H_2O$ (8.6 mg, 0.02 mmol) and H_3**TTT** (9.2 mg, 0.02 mmol) were dissolved in DMF (0.8 mL) and heated at 100 °C for 24 hours. **La-MOF** was isolated as clusters of pale-yellow needle-shaped crystals, which were filtered and washed with DMF (yield: 7.4 mg).

FTIR (ATR): 3500-2500 (br), 3082 (w), 1646 (st), 1524 (st), 1505 (st), 1472 (m), 1435 (w), 1386 (st), 1353 (st), 1304 (m), 1208 (w), 1104 (w), 1029 (w), 846 (w), 811 (st), 768 (st), 662 (m), 578 (m), 519 (w), 460 (st) cm^{-1}.

7.3.2 Synthesis of Ce-MOF

$CeCl_3 \cdot 7H_2O$ (7.4 mg, 0.02 mmol) and H_3**TTT** (9.2 mg, 0.02 mmol) were dissolved in DMF (1.6 mL) and heated at 100 °C for 24 hours. **Ce-MOF** was isolated as pale-yellow needle-shaped crystals, which were filtered and washed with DMF (yield: 6.3 mg).

FTIR (ATR): 3700-2200 (br), 1652 (m), 1525 (m), 1505 (st), 1471 (m), 1385 (m), 1343 (st), 1207 (w), 1099 (w), 1027 (w), 810 (st), 767 (st), 662 (m), 578 (w), 519 (w), 458 (st) cm^{-1}.

7.3.3 Synthesis of Pr-MOF

$Pr(NO_3)_3 \cdot 6H_2O$ (8.8 mg, 0.02 mmol) and H_3**TTT** (9.2 mg, 0.01 mmol) were dissolved in DMF (1.6 mL) and heated at 100 °C for 48 hours. **Pr-MOF** was isolated as white needle-shaped crystals, which were filtered and washed with DMF (yield: 8.0 mg).

FTIR (ATR): 3700-2200 (br), 1652 (m), 1505 (st), 1471 (m), 1385 (m), 1343 (st), 1207 (w), 1104 (w), 1028 (w), 811 (st), 767 (st), 662 (m), 579 (w), 518 (w), 460 (st) cm^{-1}.

7.3.4 Synthesis of Nd-MOF

$Nd(NO_3)_3 \cdot 6H_2O$ (8.8 mg, 0.02 mmol) and H_3**TTT** (9.2 mg, 0.02 mmol) were dissolved in DMF (1.6 mL) and heated at 100 °C for 72 hours. **Nd-MOF** was isolated as white needle-shaped crystals, which were filtered and washed with DMF (yield: 8.3 mg).

FTIR (ATR): 3700-2200 (br), 1652 (m), 1525 (m), 1505 (st), 1471 (m), 1385 (m), 1344 (st), 1206 (w), 1102 (w), 1026 (w), 809 (st), 767 (st), 662 (m), 578 (m), 458 (st) cm^{-1}.

7.3.5 Synthesis of Sm-MOF

$Sm(NO_3)_3 \cdot 6H_2O$ (8.8 mg, 0.02 mmol) and H_3**TTT** (9.2 mg, 0.02 mmol) were dissolved in DMF (1.6 mL) and heated at 100 °C for 24 hours. **Sm-MOF** was isolated as white needle-shaped crystals, which were filtered and washed with DMF (yield: 7.9 mg).

FTIR (ATR): 3700-2200 (br), 1655 (m), 1583 (w), 1558 (w), 1508 (st), 1476 (st), 1388 (st), 1353 (st), 1211 (w), 1111 (w), 1030 (w), 810 (st), 767 (st), 663 (m), 576 (w), 458 (st) cm^{-1}.

7.3.6 Synthesis of Eu-MOF

$EuCl_3 \cdot 6H_2O$ (7.6 mg, 0.02 mmol) and H_3**TTT** (9.2 mg, 0.01 mmol) were dissolved in DMF (1 mL) and heated at 100 °C for 48 hours. **Eu-MOF** was isolated as pale-yellow needle-shaped crystals, which were filtered and washed with DMF (10.1 mg).

FTIR (ATR): 3700-2200 (br), 3078 (w), 1705 (st), 1656 (m), 1592 (w), 1562 (w), 1505 (st), 1485 (m), 1449 (w), 1391 (m), 1363 (st), 1344 (st), 1329 (st), 1305 (m), 1287 (st), 1246 (st),

1157 (st), 1112 (m), 1068 (st), 1012 (m), 937 (m), 856 (w), 810 (st), 766 (m), 736 (st), 652 (m), 612 (w), 515 (w), 460 (st) cm^{-1}.

7.3.7 Synthesis of Gd-MOF

$Gd(NO_3)_3 \cdot 6H_2O$ (11.3 mg, 0.025 mmol) and H_3**TTT** (11.4 mg, 0.025 mmol) were dissolved in DMF (0.5 mL) and heated at 100 °C for 72 hours. **Gd-MOF** was isolated as pale-yellow crystals with plate morphology, which were filtered and washed with DMF (yield: 6.7 mg).

FTIR (ATR): 3700-2200 (br), 1649 (m), 1510 (st), 1473 (m), 1386 (m), 1351 (st), 1212 (w), 1110 (w), 1057 (w), 1029 (w), 989 (w), 810 (m), 770 (st), 662 (w), 575 (w), 454 (st) cm^{-1}.

7.3.8 Synthesis of Dy-MOF

$Dy(NO_3)_3 \cdot 5H_2O$ (11.3 mg, 0.025 mmol) and H_3**TTT** (11.5 mg, 0.025 mmol) were dissolved in DMF (0.5 mL) and heated at 100 °C for 72 hours. **Dy-MOF** was isolated as pale-yellow crystals with plate morphology, which were filtered and washed with DMF (yield: 4.4 mg).

FTIR (ATR): 3700-2200 (br), 1652 (m), 1515 (st), 1472 (m), 1386 (st), 1350 (st), 1211 (w), 1112 (w), 1053 (w), 1029 (w), 989 (w), 811 (m), 769 (st), 662 (w), 575 (w), 456 (st) cm^{-1}.

7.3.10 Synthesis of Er-MOF

$Er(NO_3)_3 \cdot 5H_2O$ (11.4 mg, 0.025 mmol) and H_3**TTT** (11.4 mg, 0.025 mmol) were dissolved in DMF (0.5 mL) and heated at 100 °C for 72 hours. **Er-MOF** was isolated as pale-yellow crystals with plate morphology, which were filtered and washed with DMF (yield: 10.1 mg).

FTIR (ATR): 3700-2200 (br), 1652 (w), 1515 (st), 1475 (m), 1435 (w), 1386 (st), 1353 (st), 1212 (w), 1111 (w), 1060 (w), 1029 (w), 990 (w), 826 (w), 810 (m), 769 (st), 677 (w), 662 (w), 574 (w), 514 (w), 456 (st) cm^{-1}.

7.3.11 Synthesis of Yb-MOF

$Yb(NO_3)_3 \cdot 5H_2O$ (11.2 mg, 0.025 mmol) and H_3**TTT** (11.5 mg, 0.025 mmol) were dissolved in DMF (0.5 mL) and heated at 100 °C for 24 hours. **Yb-MOF** was isolated as pale-yellow needle-shaped crystal, which were filtered and washed with DMF (yield: 10.57 mg).

FTIR (ATR): 3700-2200 (br), 1652 (m), 1557 (m), 1505 (st), 1471 (m), 1390 (st), 1353 (st), 1210 (w), 1117 (w), 1062 (w), 1024 (w), 988 (w), 829 (m), 811 (m), 768 (st), 678 (w), 663 (w), 579 (w), 532 (w), 477 (w), 454 (st).

7.3.16 Synthesis of Cu-TTMOP

A solution of H_2**CPTT** (3 mg, 0.01 mmol) and $Cu(NO_3)_2 \cdot 3H_2O$ (4.8 mg, 0.02 mmol) in DMF (1.5 mL) was heated in a sealed vial at 80 °C for 5 days. Blue-green crystals were obtained (yield: 3.2 mg).

FTIR (ATR): 3700-2700 (br), 3427 (br), 3090 (w), 2929 (w), 2867 (w), 2162 (w), 2039 (w), 1976 (w), 1655 (st), 1608 (w), 1507 (m), 1380 (st), 1254 (m), 1185 (w), 1169 (w), 1091 (m), 1062 (w), 1016 (w), 946 (w), 865 (w), 832 (w), 790 (w), 765 (m), 716 (w), 688 (w), 659 (m), 621 (w), 568 (w), 512 (m), 467 (w) cm^{-1}.

7.3.17 Synthesis of Cu-Eu-MOF

Cu-Eu-MOF was synthesised using a modified version of a procedure previously reported by Schmitt and co-workers for the synthesis of transition metal coordination polymers using $[Cu(H_2$2,2'-DMBP$)_2]PF_6$.[8]

$[Cu(MeCN)_4]PF_6$ (37.27 mg, 0.1 mmol) was added to $H_2$2,2'-DMBP (54.45 mg, 0.2 mmol) in DMF (20 mL), which gave a dark red solution. To an aqueous $Eu(NO_3)_3 \cdot 5H_2O$ solution (0.4 mmol, 20 mL) was added trifluoroacetic acid (TFA, 0.8 mL) and DMF (20 mL). These solutions were first combined and then divided into three 20 mL crimp vials with butyl rubber seals, and the reaction mixture was heated to 80 °C in a pre-heated oven for 16 h. The crystals obtained were needle-shaped, and red-orange in colour. The crystals were filtered and washed with DMF (yield: 25 mg).

FTIR (ATR): 3700-2200 (br), 1603 (st), 1550 (st), 1401 (st), 1367 (st), 1326 (st), 1234 (m), 1181 (w), 1137 (w), 1116 (w), 1041 (w), 948 (w), 927 (w), 903 (w), 788 (m), 742 (m), 691 (m), 609 (w), 590 (w), 559 (w), 524 (w), 472 (w), 413 (w).

7.4 Photoluminescence quenching experiments

Newly synthesised crystals of **Eu-MOF** were washed with DMF several times, soaked in deionised water for 24 hours, then removed and dried on filter paper. A 15 mL aqueous suspension of **Eu-MOF** (1 mg of **Eu-MOF** per mL of solvent) was prepared by sonication of the crystals in deionised water. Solutions of the analytes ($Cu(NO_3)_2 \cdot 3H_2O$, $Fe(NO_3)_3 \cdot 9H_2O$, $Cd(NO_3)_2 \cdot 4H_2O$, $Ni(NO_3)_2 \cdot 6H_2O$, $Pb(NO_3)_2$, $Co(NO_3)_2 \cdot 6H_2O$) in deionised water were prepared (4 mM) and 1 mL of each solution was added to 1.5 mL of the aqueous **Eu-MOF** suspension. This gave a final concentration of 2 mM for each analyte, and 0.5 mg per mL of **Eu-MOF**. A control sample was also prepared by the addition of 1.5 mL of deionised water to 1.5 mL of **Eu-MOF** suspension. The photoluminescence spectra of these solutions were measured two minutes after the addition of the analyte solution to the **Eu-MOF** suspension (λ_{ex} = 365 nm). The emission intensity of the suspensions was monitored at 592 nm.

7.5 Dye uptake experiments

In order to investigate the uptake of dyes by **Cu-TTMOP**, an aqueous solution of methylene blue (MB) (3 mL, 2.4×10^{-5} M) was prepared using deionised water. The UV-vis spectrum of this solution was measured from 300-800 nm in a quartz cuvette. A sample of **Cu-TTMOP** was washed with deionised water and dried on filter paper. The dried **Cu-TTMOP** crystals (16.3 mg) were added to the quartz cuvette containing the MB solution. The UV-vis spectrum of the solution was measured at 5 min, 10 min, 20 min, 40 min, 1 h, 2 h, 2.5 h, 3 h, 4 h and 5 h after the addition of the **Cu-TTMOP**

crystals. The decrease in concentration with time was measured as a percentage of the total concentration of MB present in the solution prior to the addition of the **Cu-TTMOP** crystals. The decrease in concentration was measured using the intensity of the MB absorption band with λ_{max} = 664 nm.

A calibration curve was obtained by preparing a series of aqueous MB solutions of varying concentrations by serial dilution (2.8×10^{-5} M, 2.1×10^{-5} M, 1.4×10^{-5} M, 7×10^{-6} M, 3.5×10^{-6} M, 1.75×10^{-6} M, 8.79×10^{-7} M). The intensity of the absorption at 664 nm was plotted against concentration and compared to the values obtained during the dye uptake experiment at various times after the addition of **Cu-TTMOP** to verify the concentration of MB remaining in the solution at each time interval.

The FTIR spectrum of **Cu-TTMOP** crystals was measured after immersion of the coordination cage in an aqueous MB solution for 72 h.

FTIR (ATR): 3700-2300 (br), 3090 (w), 1587 (m), 1530 (m), 1503 (st), 1478 (m), 1409 (m), 1378 (st), 1228 (w), 1180 (w), 1114 (w), 1017 (w), 947 (w), 840 (w), 788 (w), 749 (st), 692 (w), 678 (w), 641 (w), 616 (w), 560 (w), 495 (w), 460 (w) cm-1.

References

1 O. V. Dolomanov, L. J. Bourhis, R. J. Gildea, J. A. K. Howard and H. Puschmann, *J. Appl. Crystallogr.*, 2009, **42**, 339–341.

2 A. L. Spek, *Acta Crystallogr. Sect. C Struct. Chem.*, 2015, **71**, 9–18.

3 A. Le Bail, *Powder Diffr.*, 2005, **20**, 316–326.

4 A. Boultif and D. Louër, *J. Appl. Crystallogr.*, 2004, **37**, 724–731.

5 A. Altomare, C. Cuocci, C. Giacovazzo, A. Moliterni, R. Rizzi, N. Corriero and A. Falcicchio, *J. Appl. Crystallogr.*, 2013, **46**, 1231–1235.

6 Z. Wang, J. Liu, Y. Fu, C. Liu, C. Pan, Z. Liu and G. Yu, *Chem. Commun.*, 2017, **53**, 4128–4131.

7 S. Sun, P. Zhang, J. Li, Y. Li, J. Wang, S. Zhang, Y. Xia, X. Meng, D. Fan and J. Chu, *J. Mater. Chem. A*, 2014, **2**, 15316–15325.

8 F. W. Steuber, J. J. Gough, É. Whelan, L. Burtnyak, A. L. Bradley and W. Schmitt, *Inorg. Chem.*, 2020, **59**, 17244–17250.

Appendix 1: Gas sorption results: La-MOF and Eu-MOF

La-MOF: Data for sample activated at 150 °C

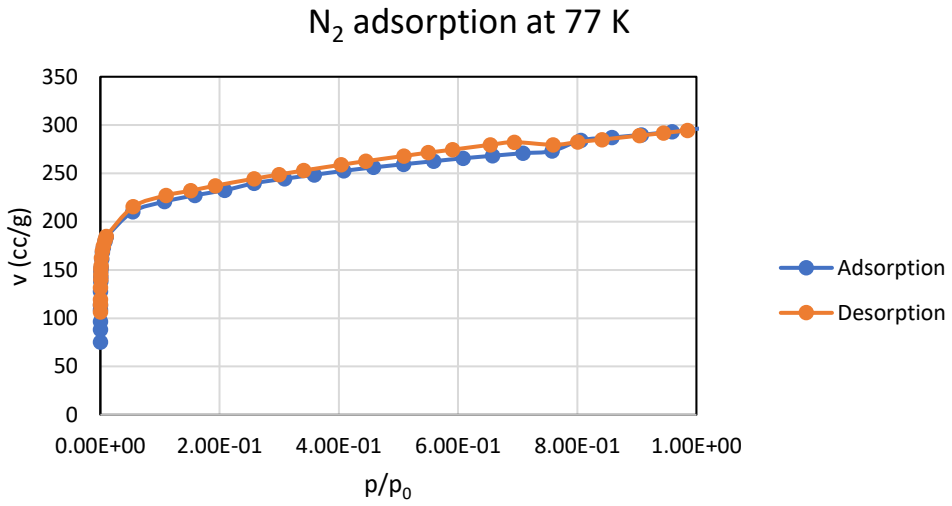

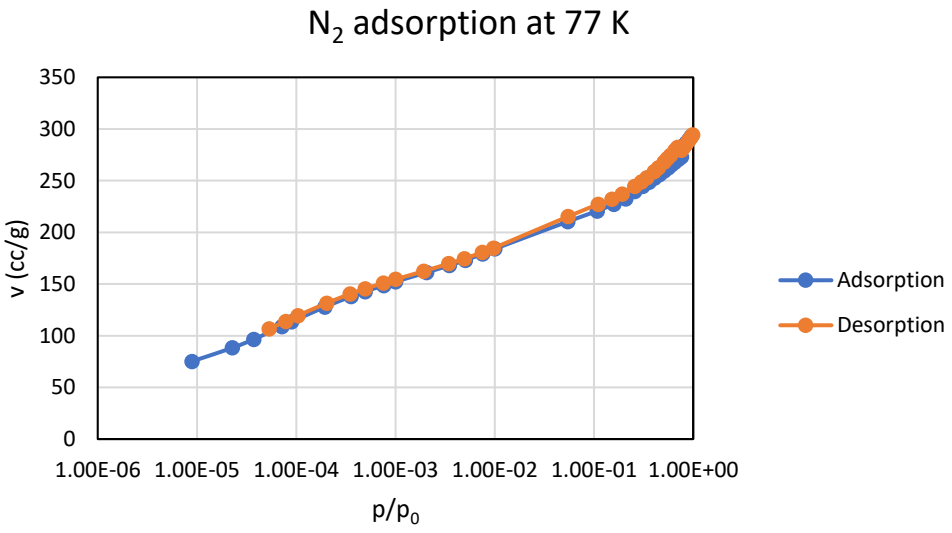

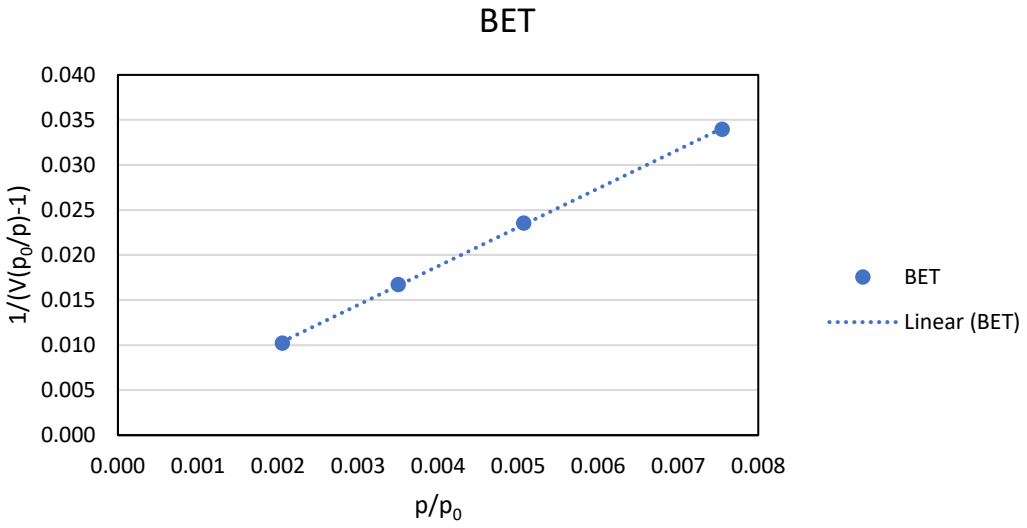

Pore size distribution: La-MOF activated at 150 °C

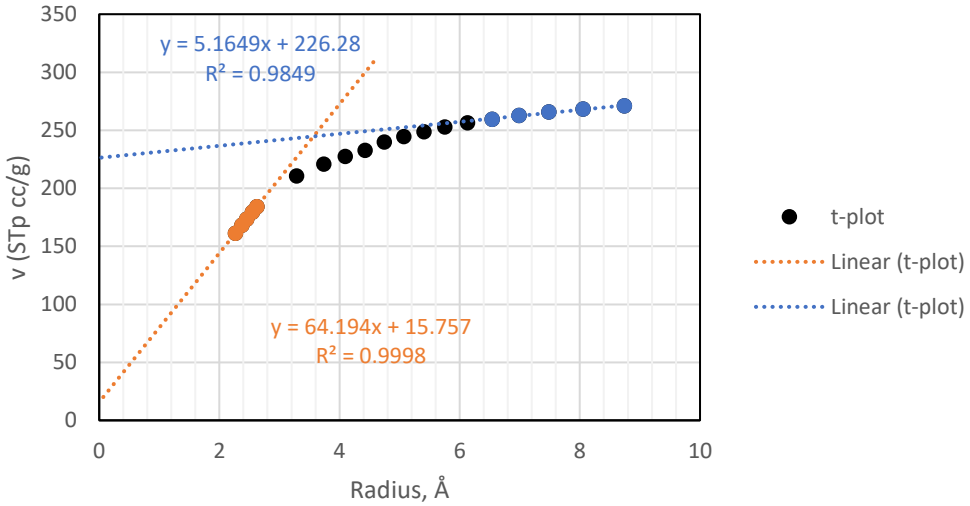

CO_2 Adsorption: La-MOF activated at 150 °C

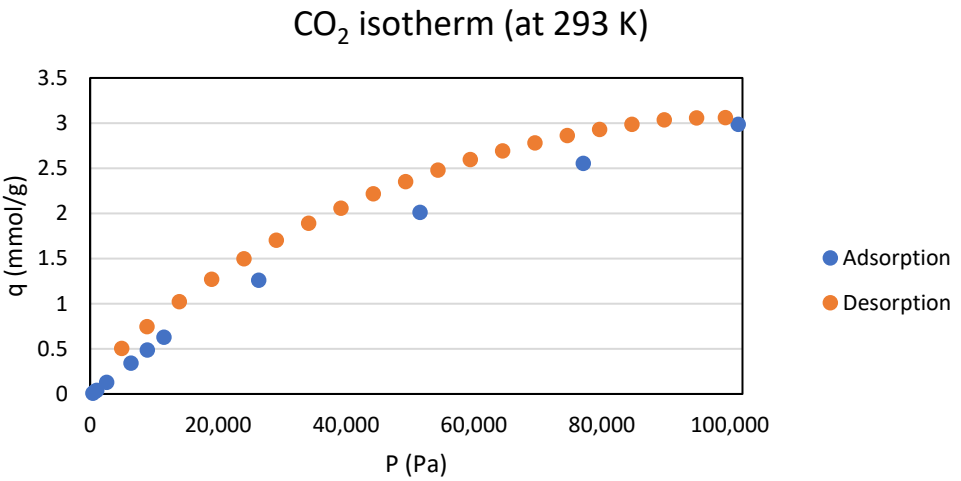

La-MOF: Data for sample activated at 300 °C

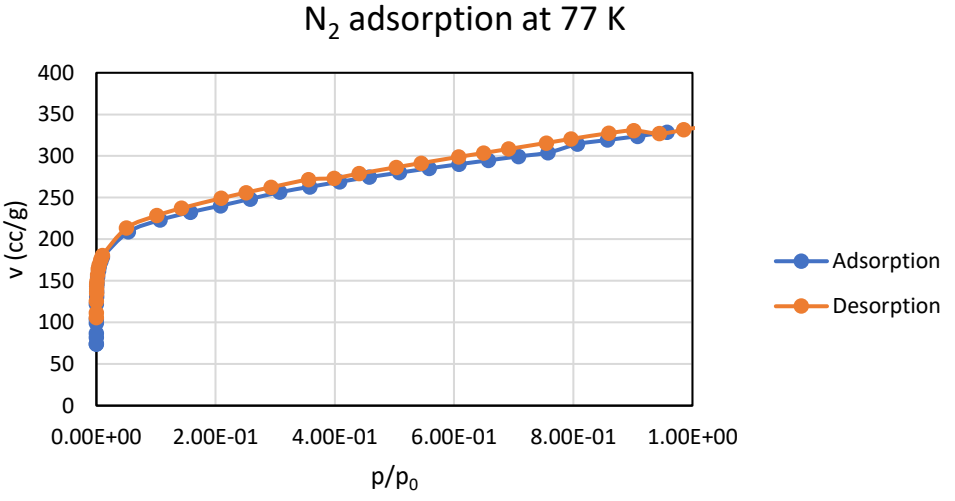

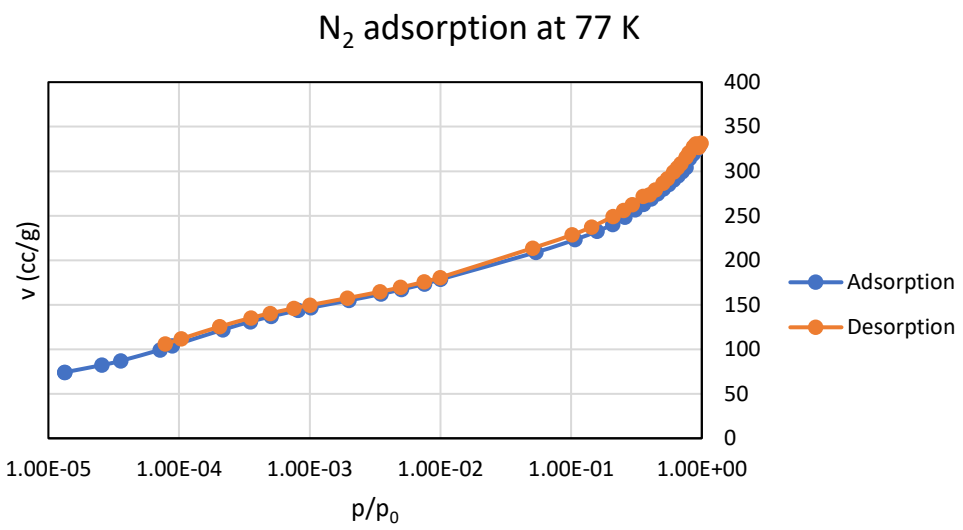
N2 adsorption at 77 K
v (cc/g)
400
350
300
250
200
150
100
50
0
1.00E-05
1.00E-04
1.00E-03
1.00E-02
1.00E-01
1.00E+00
p/p0
Adsorption
Desorption

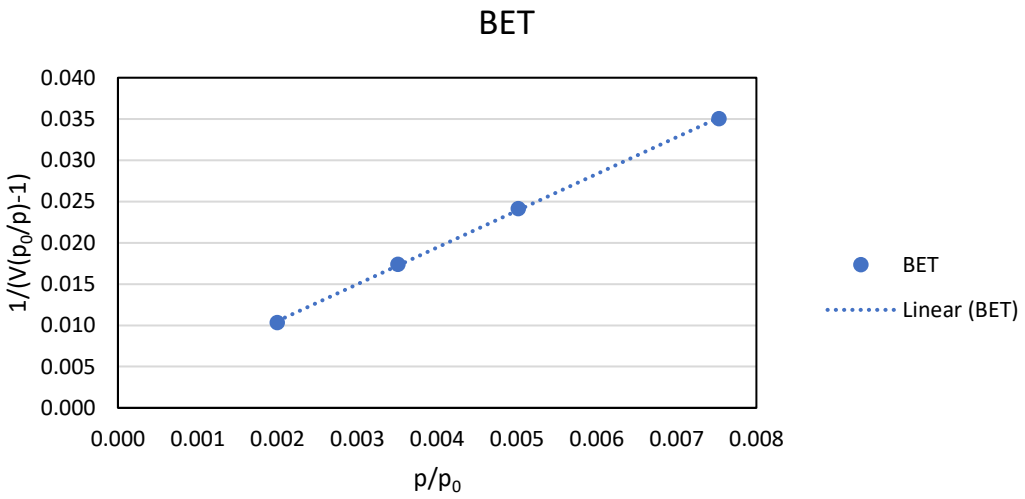
BET
1/(V(p0/p)-1)
0.040
0.035
0.030
0.025
0.020
0.015
0.010
0.005
0.000
0.000
0.001
0.002
0.003
0.004
0.005
0.006
0.007
0.008
p/p0
BET
Linear (BET)

Pore Size Distribution: La-MOF activated at 300 °C

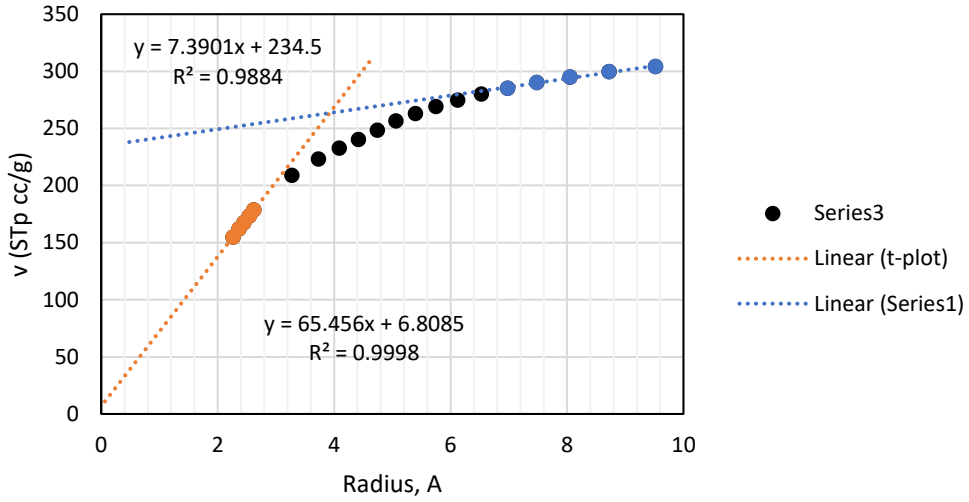

CO_2 Adsorption: La-MOF activated at 300 °C

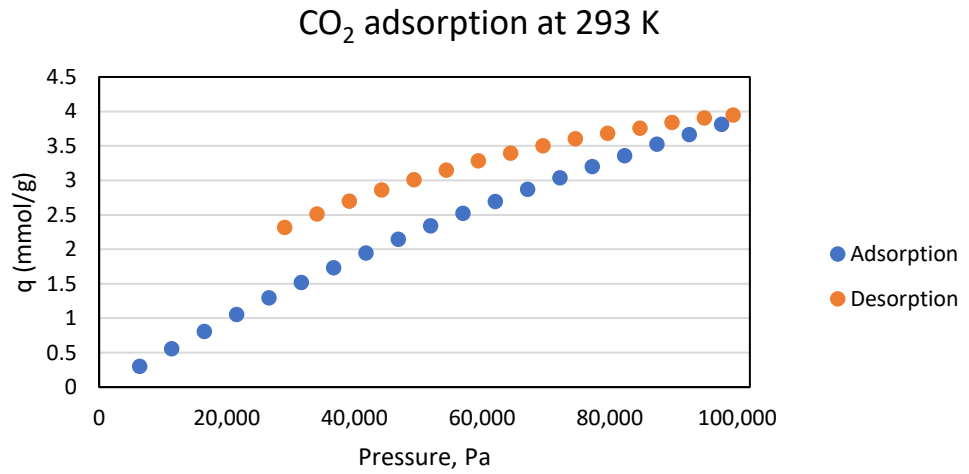

H_2 adsorption: La-MOF

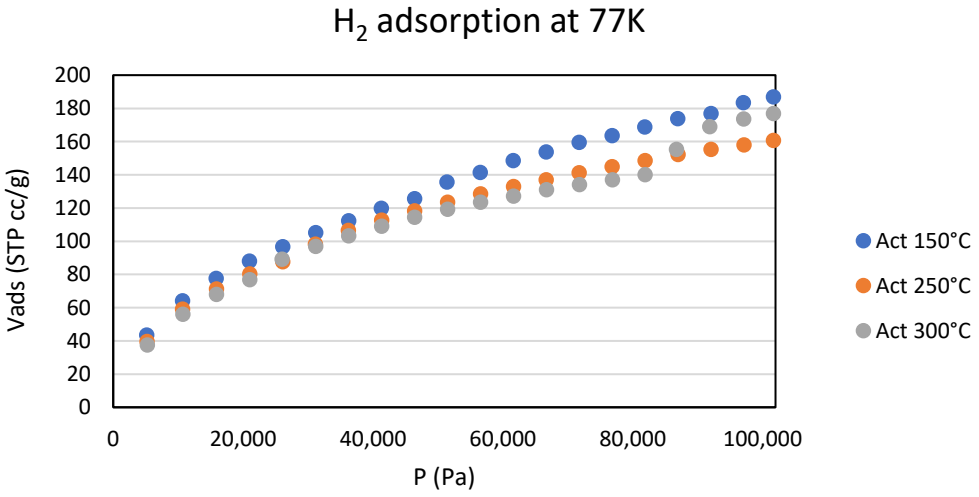

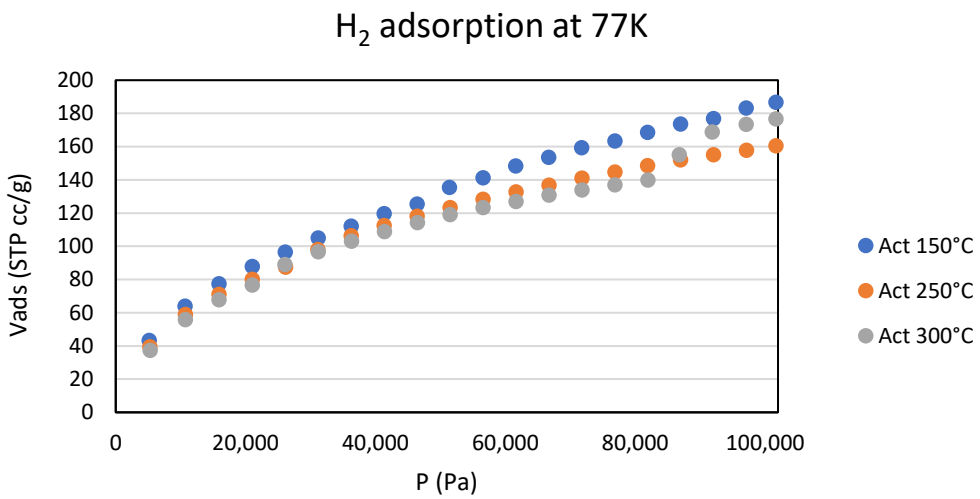

N_2 adsorption at 293 K: La-MOF

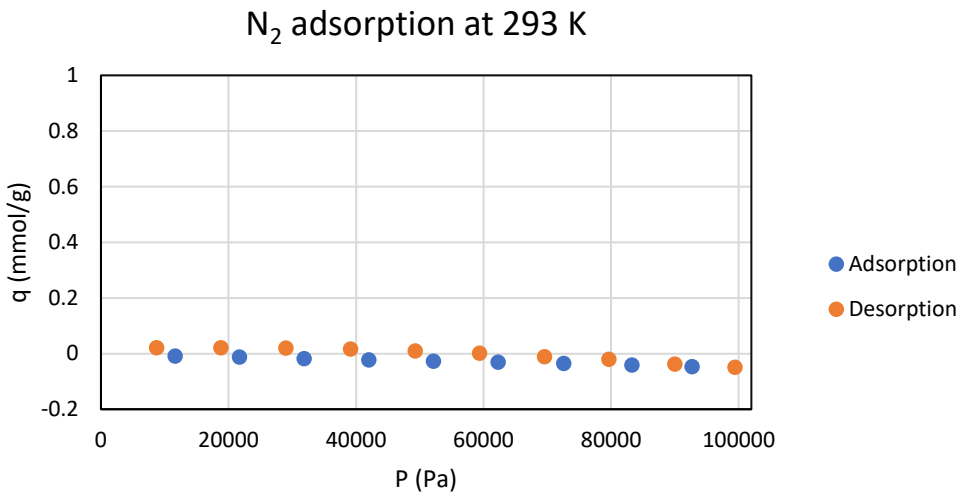

Eu-MOF: Gas adsorption data

Comparison of Eu-MOF samples activated at 120 °C and 200 °C: N_2 adsorption isotherm

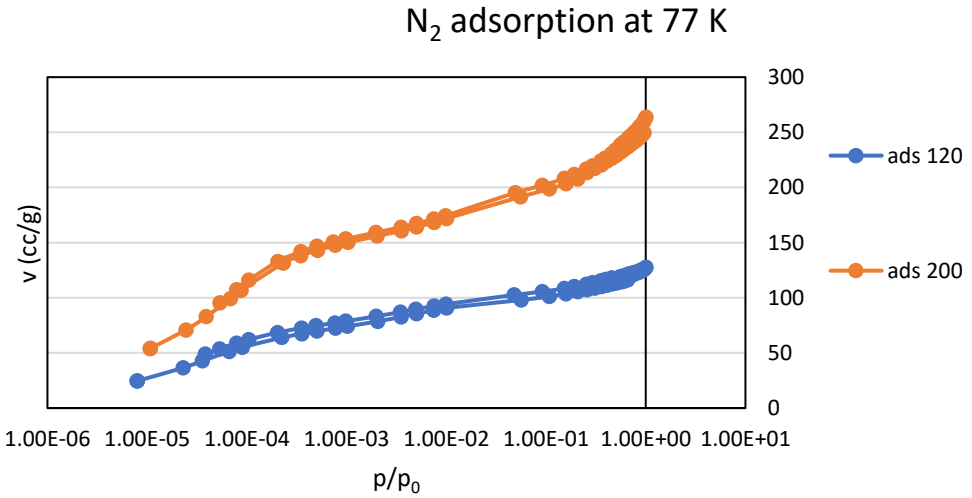

Eu-MOF: Data for sample activated at 200 °C

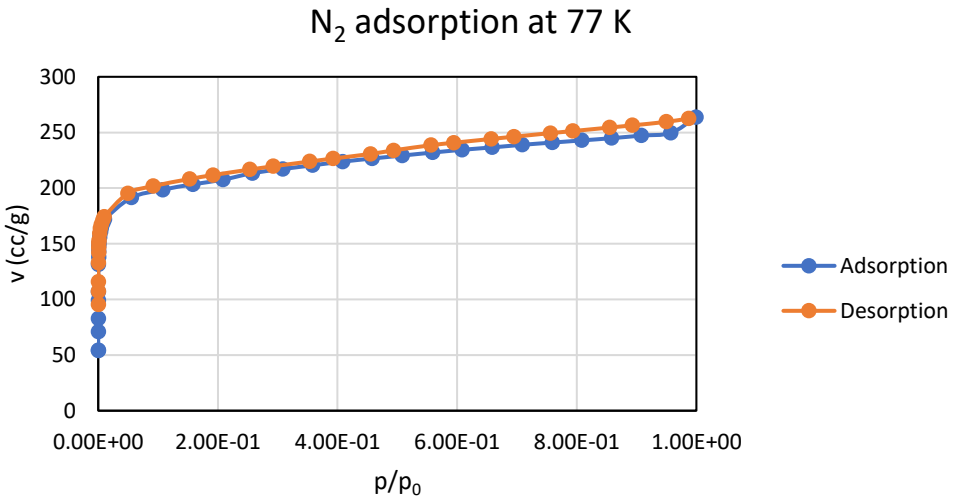

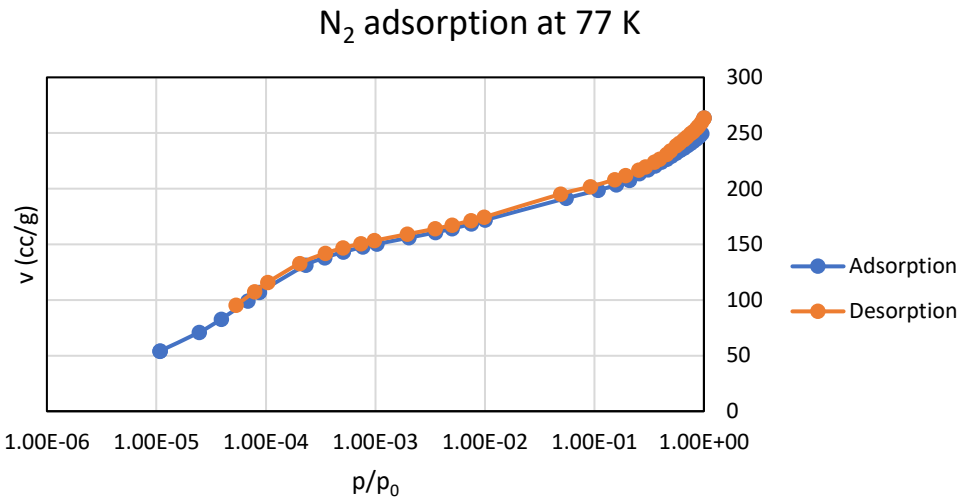

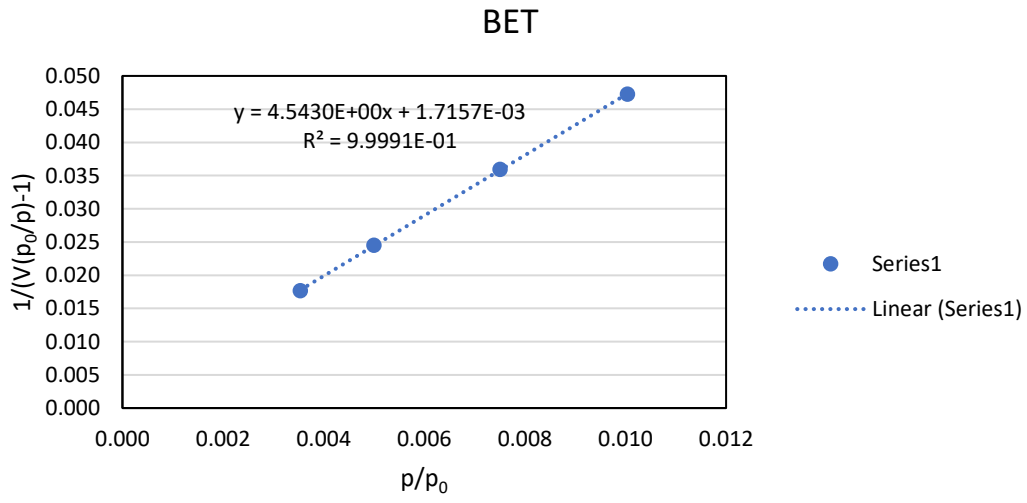

RASPA values: La-MOF and Eu-MOF

Table 7: RASPA values calculated for **La-MOF** and **Eu-MOF**

La-MOF		**Eu-MOF**	
Helium void fraction	0.45	Helium void fraction	0.446
Density	1.346 g/cc	Density	1.38 g/cc
Pore volume	0.334 cc/g	Pore volume	0.3233 cc/g
Surface area	941 m^2/g	Surface area	923.3 m^2/g

Appendix 2: Condensed Crystallographic Information Files (CIFs)

Chapter 2:

3,4-Dibromothiophene-2-carbaldehyde

```
_symmetry_cell_setting           orthorhombic
_symmetry_space_group_name_H-M   'P n m a'
_symmetry_Int_Tables_number      62
_space_group_name_Hall           '-P 2ac 2n'
loop_
_symmetry_equiv_pos_site_id
_symmetry_equiv_pos_as_xyz
1 x,y,z
2 1/2-x,-y,1/2+z
3 1/2+x,1/2-y,1/2-z
4 -x,1/2+y,-z
5 -x,-y,-z
6 1/2+x,y,1/2-z
7 1/2-x,1/2+y,1/2+z
8 x,1/2-y,z
_cell_length_a                   11.524(3)
_cell_length_b                   6.4297(13)
_cell_length_c                   9.556(2)
_cell_angle_alpha                90
_cell_angle_beta                 90
_cell_angle_gamma                90
_cell_volume                     708.06
loop_
_atom_site_label
_atom_site_type_symbol
_atom_site_fract_x
_atom_site_fract_y
_atom_site_fract_z
_atom_site_U_iso_or_equiv
_atom_site_thermal_displace_type
Br1 Br 0.11487(3) 0.750000 0.52992(3) 0.0270 Uani
```

```
Br2 Br 0.35011(2) 0.750000 0.75730(3) 0.0181 Uani
S1 S 0.44970(7) 0.750000 0.31299(7) 0.0184 Uani
O1 O 0.6756(2) 0.750000 0.4765(2) 0.0211 Uani
C1 C 0.2695(3) 0.750000 0.4692(3) 0.0178 Uani
C2 C 0.3660(2) 0.750000 0.5625(3) 0.0146 Uani
C3 C 0.4708(3) 0.750000 0.4924(3) 0.0153 Uani
C4 C 0.3018(3) 0.750000 0.3313(3) 0.0194 Uani
H4 H 0.248769 0.750000 0.255232 0.0230 Uiso
C5 C 0.5887(2) 0.750000 0.5488(3) 0.0142 Uani
H5 H 0.598015 0.750000 0.647573 0.0170 Uiso
loop_
_atom_site_aniso_label
_atom_site_aniso_U_11
_atom_site_aniso_U_22
_atom_site_aniso_U_33
_atom_site_aniso_U_23
_atom_site_aniso_U_13
_atom_site_aniso_U_12
Br1 0.01403(13) 0.0499(3) 0.01718(14) 0.000 -0.00157(10) 0.000
Br2 0.01549(13) 0.02847(18) 0.01031(12) 0.000 0.00047(9) 0.000
S1 0.0197(3) 0.0244(4) 0.0112(3) 0.000 0.0014(2) 0.000
O1 0.0171(9) 0.0283(13) 0.0180(9) 0.000 0.0034(7) 0.000
C1 0.0162(11) 0.0237(16) 0.0134(11) 0.000 -0.0012(9) 0.000
C2 0.0154(11) 0.0169(14) 0.0114(10) 0.000 0.0005(8) 0.000
C3 0.0174(12) 0.0164(14) 0.0122(10) 0.000 0.0003(9) 0.000
C4 0.0198(12) 0.0254(17) 0.0130(11) 0.000 -0.0031(9) 0.000
C5 0.0160(10) 0.0121(13) 0.0146(10) 0.000 -0.0009(9) 0.000

#END
```

Ethyl 6-bromothiophene[3,2-b]thiophene-2-carboxylate

```
_symmetry_cell_setting           monoclinic
_symmetry_space_group_name_H-M   'P 21/n'
_symmetry_Int_Tables_number      14
_space_group_name_Hall           '-P 2yn'
loop_
_symmetry_equiv_pos_site_id
_symmetry_equiv_pos_as_xyz
1 x,y,z
2 1/2-x,1/2+y,1/2-z
3 -x,-y,-z
4 1/2+x,1/2-y,1/2+z
_cell_length_a                   3.9559(4)
_cell_length_b                   38.703(2)
_cell_length_c                   13.4187(12)
_cell_angle_alpha                90
_cell_angle_beta                 92.090(7)
_cell_angle_gamma                90
_cell_volume                     2053.11
loop_
_atom_site_label
_atom_site_type_symbol
_atom_site_fract_x
_atom_site_fract_y
_atom_site_fract_z
_atom_site_U_iso_or_equiv
_atom_site_thermal_displace_type
Br01 Br 1.2193(4) -0.70042(3) 0.26801(9) 0.0369 Uani
S006 S 1.6270(9) -0.78527(7) 0.3192(2) 0.0358 Uani
S00A S 1.5124(10) -0.76514(7) 0.0150(2) 0.0404 Uani
O00E O 1.936(2) -0.84609(18) 0.4093(6) 0.0359 Uani
O00K O 2.075(3) -0.87478(19) 0.2707(6) 0.0452 Uani
C00N C 1.950(3) -0.8500(3) 0.3101(9) 0.0307 Uani
C00T C 1.370(4) -0.7336(3) 0.1776(8) 0.0358 Uani
C010 C 1.767(4) -0.8172(3) 0.1570(9) 0.0393 Uani
```

```
H010 H 1.843913 -0.834018 0.111586 0.0470 Uiso
C015 C 2.108(4) -0.8619(3) 0.5764(9) 0.0422 Uani
H01A H 2.237142 -0.840430 0.585123 0.0640 Uiso
H01B H 2.211246 -0.880007 0.618528 0.0640 Uiso
H01C H 1.874338 -0.858071 0.595716 0.0640 Uiso
C01A C 1.619(4) -0.7856(3) 0.1267(9) 0.0389 Uani
C01C C 1.352(3) -0.7297(3) 0.0769(8) 0.0314 Uani
H01D H 1.261791 -0.709827 0.044020 0.0380 Uiso
C01D C 1.536(4) -0.7654(3) 0.2096(9) 0.0373 Uani
C01F C 2.110(4) -0.8728(3) 0.4702(8) 0.0398 Uani
H01E H 2.345465 -0.875540 0.449113 0.0480 Uiso
H01F H 1.992121 -0.895211 0.461551 0.0480 Uiso
C01H C 1.789(4) -0.8210(3) 0.2546(8) 0.0427 Uani
Br03 Br 1.7796(4) -0.64976(3) 0.43554(9) 0.0384 Uani
S007 S 2.1983(9) -0.58718(7) 0.2784(2) 0.0365 Uani
S009 S 2.1114(9) -0.55075(7) 0.5689(2) 0.0396 Uani
O00D O 2.650(2) -0.50027(19) 0.2067(6) 0.0405 Uani
O00J O 2.500(3) -0.54679(19) 0.1116(6) 0.0431 Uani
C00M C 2.791(3) -0.4840(3) 0.1214(8) 0.0333 Uani
H00A H 2.611346 -0.479377 0.069813 0.0400 Uiso
H00B H 2.963522 -0.499111 0.092401 0.0400 Uiso
C00Q C 2.209(3) -0.5529(3) 0.4451(9) 0.0325 Uani
C00U C 1.951(3) -0.6065(3) 0.4724(8) 0.0311 Uani
C00W C 2.363(3) -0.5312(3) 0.3766(8) 0.0351 Uani
H00W H 2.448206 -0.508764 0.392046 0.0420 Uiso
C00X C 2.099(3) -0.5845(3) 0.4038(9) 0.0372 Uani
C00Y C 1.937(3) -0.5918(3) 0.5643(9) 0.0313 Uani
H00Y H 1.841781 -0.602864 0.619939 0.0380 Uiso
C013 C 2.514(4) -0.5322(3) 0.1908(10) 0.0444 Uani
C018 C 2.375(4) -0.5462(3) 0.2850(8) 0.0357 Uani
C01G C 2.947(4) -0.4511(3) 0.1570(10) 0.0416 Uani
H01G H 2.776427 -0.437104 0.189666 0.0620 Uiso
H01H H 3.032596 -0.438344 0.100145 0.0620 Uiso
H01I H 3.133758 -0.456146 0.204666 0.0620 Uiso
loop_
_atom_site_aniso_label
_atom_site_aniso_U_11
```

```
_atom_site_aniso_U_22
_atom_site_aniso_U_33
_atom_site_aniso_U_23
_atom_site_aniso_U_13
_atom_site_aniso_U_12
Br01 0.0558(10) 0.0291(6) 0.0265(7) -0.0029(5) 0.0112(6) 0.0016(6)
S006 0.056(2) 0.0295(14) 0.0226(16) -0.0012(12) 0.0100(15) 0.0014(14)
S00A 0.066(3) 0.0315(15) 0.0242(16) -0.0031(12) 0.0099(16) 0.0019(15)
O00E 0.051(6) 0.031(4) 0.026(4) -0.005(3) 0.007(4) 0.005(4)
O00K 0.080(8) 0.030(4) 0.026(4) 0.001(3) 0.007(5) 0.011(4)
C00N 0.035(8) 0.029(5) 0.028(5) -0.002(4) 0.001(5) -0.004(5)
C00T 0.055(10) 0.038(6) 0.015(6) 0.004(5) 0.010(6) -0.001(6)
C010 0.059(11) 0.023(6) 0.037(8) -0.002(5) 0.016(7) 0.007(6)
C015 0.051(10) 0.046(7) 0.030(7) 0.003(6) 0.006(7) 0.003(6)
C01A 0.063(11) 0.027(6) 0.028(7) -0.008(5) 0.020(7) -0.002(6)
C01C 0.041(9) 0.027(6) 0.027(7) 0.003(5) 0.011(6) 0.001(5)
C01D 0.043(9) 0.037(6) 0.033(7) 0.002(5) 0.017(6) -0.007(6)
C01F 0.056(11) 0.034(6) 0.029(7) 0.001(5) -0.002(7) 0.001(6)
C01H 0.085(13) 0.025(6) 0.018(7) 0.001(5) 0.002(7) -0.003(6)
Br03 0.0560(10) 0.0279(6) 0.0321(7) 0.0001(5) 0.0115(7) -0.0015(6)
S007 0.055(2) 0.0292(14) 0.0260(16) -0.0013(12) 0.0092(16) 0.0003(14)
S009 0.057(3) 0.0306(15) 0.0322(17) -0.0036(12) 0.0140(17) -0.0023(14)
O00D 0.061(7) 0.033(4) 0.028(5) 0.005(4) 0.010(4) -0.005(4)
O00J 0.063(7) 0.035(4) 0.032(5) 0.004(4) 0.011(5) -0.002(4)
C00M 0.041(9) 0.036(6) 0.024(6) 0.011(5) 0.017(6) -0.002(6)
C00Q 0.040(9) 0.026(5) 0.032(7) -0.006(5) 0.010(6) -0.003(5)
C00U 0.036(8) 0.031(6) 0.027(7) 0.006(5) 0.011(6) 0.001(5)
C00W 0.047(9) 0.032(6) 0.027(7) -0.009(5) 0.011(6) -0.002(6)
C00X 0.037(9) 0.044(7) 0.030(7) -0.002(6) -0.009(6) -0.002(6)
C00Y 0.029(8) 0.030(6) 0.035(7) 0.005(5) 0.003(6) -0.003(5)
C013 0.074(12) 0.029(6) 0.031(8) -0.001(5) 0.011(7) -0.003(6)
C018 0.063(10) 0.024(6) 0.021(6) 0.007(5) 0.014(6) 0.007(6)
C01G 0.040(10) 0.045(7) 0.041(8) 0.000(6) 0.017(7) -0.008(6)
```

#END

6-(4-Carboxyphenyl)thieno[3,2-b]thiophene-2-carboxylic acid (H2CPTT)

```
_symmetry_space_group_name_H-M   'P 21/c'
_symmetry_Int_Tables_number      14
_space_group_name_Hall           '-P 2ybc'
loop_
_symmetry_equiv_pos_site_id
_symmetry_equiv_pos_as_xyz
1 x,y,z
2 -x,1/2+y,1/2-z
3 -x,-y,-z
4 x,1/2-y,1/2+z
_cell_length_a                   3.8037(7)
_cell_length_b                   24.729(4)
_cell_length_c                   13.155(3)
_cell_angle_alpha                90
_cell_angle_beta                 95.50(2)
_cell_angle_gamma                90
_cell_volume                     1231.68
loop_
_atom_site_label
_atom_site_type_symbol
_atom_site_fract_x
_atom_site_fract_y
_atom_site_fract_z
_atom_site_U_iso_or_equiv
_atom_site_thermal_displace_type
S1 S 0.3718(3) 0.20689(4) 0.37269(8) 0.0323 Uani
S2 S 0.9177(3) 0.23063(4) 0.65851(8) 0.0347 Uani
O1 O 0.3857(12) 0.05081(13) 0.4129(3) 0.0567 Uani
O2 O 0.1792(10) 0.10227(12) 0.2793(3) 0.0499 Uani
O3 O -0.0586(10) 0.47049(13) 0.1946(3) 0.0511 Uani
O4 O 0.0707(13) 0.52122(14) 0.3333(3) 0.0586 Uani
C1 C 0.3331(13) 0.09668(17) 0.3662(4) 0.0371 Uani
C2 C 0.4678(12) 0.14375(16) 0.4260(3) 0.0333 Uani
C3 C 0.6492(12) 0.14577(16) 0.5197(3) 0.0341 Uani
H3 H 0.720797 0.115257 0.558947 0.0410 Uiso
```

```
C4 C 0.7163(12) 0.19964(17) 0.5504(3) 0.0313 Uani
C5 C 0.5773(11) 0.23769(16) 0.4800(3) 0.0279 Uani
C6 C 0.6262(11) 0.29255(15) 0.5137(3) 0.0276 Uani
C7 C 0.8080(12) 0.29330(17) 0.6082(3) 0.0341 Uani
H7 H 0.868907 0.325609 0.643187 0.0410 Uiso
C8 C 0.4976(11) 0.34073(16) 0.4555(3) 0.0291 Uani
C9 C 0.4396(12) 0.33900(17) 0.3496(3) 0.0333 Uani
H9 H 0.496261 0.307409 0.314969 0.0400 Uiso
C10 C 0.3011(12) 0.38248(17) 0.2947(3) 0.0360 Uani
H10 H 0.256745 0.380154 0.223281 0.0430 Uiso
C11 C 0.2268(12) 0.42980(16) 0.3447(3) 0.0337 Uani
C12 C 0.2920(12) 0.43250(17) 0.4498(3) 0.0363 Uani
H12 H 0.247337 0.464833 0.483837 0.0440 Uiso
C13 C 0.4222(12) 0.38818(17) 0.5052(3) 0.0358 Uani
H13 H 0.459702 0.390196 0.576789 0.0430 Uiso
C14 C 0.0666(12) 0.47582(17) 0.2838(4) 0.0367 Uani
H1 H 0.35(3) 0.025(4) 0.377(8) 0.1500 Uiso
H4 H -0.01(2) 0.541(4) 0.301(6) 0.1000 Uiso
loop_
_atom_site_aniso_label
_atom_site_aniso_U_11
_atom_site_aniso_U_22
_atom_site_aniso_U_33
_atom_site_aniso_U_23
_atom_site_aniso_U_13
_atom_site_aniso_U_12
S1 0.0397(7) 0.0257(6) 0.0306(6) -0.0013(4) -0.0015(4) -0.0014(4)
S2 0.0441(7) 0.0295(6) 0.0295(6) 0.0024(4) -0.0024(5) -0.0003(4)
O1 0.084(3) 0.0225(17) 0.060(2) -0.0014(16) -0.012(2) -0.0051(17)
O2 0.072(3) 0.0296(17) 0.045(2) -0.0059(14) -0.0102(17) -0.0054(16)
O3 0.078(3) 0.0311(17) 0.041(2) 0.0043(14) -0.0111(18) 0.0065(16)
O4 0.097(3) 0.0258(18) 0.050(2) 0.0009(16) -0.009(2) 0.0157(18)
C1 0.044(3) 0.025(2) 0.042(3) -0.0031(19) 0.003(2) -0.0043(19)
C2 0.039(3) 0.025(2) 0.036(2) -0.0008(17) 0.0047(19) -0.0018(18)
C3 0.044(3) 0.022(2) 0.036(2) 0.0021(17) 0.0030(19) 0.0014(18)
C4 0.036(2) 0.027(2) 0.031(2) 0.0025(17) 0.0045(18) 0.0012(17)
C5 0.028(2) 0.028(2) 0.028(2) 0.0016(16) 0.0042(16) 0.0001(16)
```

```
C6 0.027(2) 0.023(2) 0.033(2) 0.0011(16) 0.0037(17) 0.0001(16)
C7 0.043(3) 0.028(2) 0.031(2) -0.0027(17) 0.0014(19) -0.0043(18)
C8 0.029(2) 0.025(2) 0.033(2) 0.0013(17) 0.0015(17) -0.0038(16)
C9 0.041(3) 0.025(2) 0.034(2) -0.0027(17) 0.0037(19) 0.0008(18)
C10 0.046(3) 0.029(2) 0.032(2) -0.0006(17) -0.0011(19) -0.0002(19)
C11 0.039(3) 0.023(2) 0.039(2) 0.0046(17) 0.0033(19) 0.0013(18)
C12 0.046(3) 0.023(2) 0.040(3) -0.0032(18) 0.004(2) 0.0033(18)
C13 0.050(3) 0.028(2) 0.029(2) -0.0008(17) 0.0016(19) 0.0006(19)
C14 0.043(3) 0.024(2) 0.043(3) 0.0033(18) 0.003(2) 0.0010(18)

#END
```

Cu-TTMOP

```
_symmetry_cell_setting           rhombohedral
_symmetry_space_group_name_H-M   'R -3 c'
_symmetry_Int_Tables_number      167
_space_group_name_Hall           '-R 3 2"c'
loop_
_symmetry_equiv_pos_site_id
_symmetry_equiv_pos_as_xyz
1 x,y,z
2 -y,x-y,z
3 -x+y,-x,z
4 y,x,1/2-z
5 x-y,-y,1/2-z
6 -x,-x+y,1/2-z
7 2/3+x,1/3+y,1/3+z
8 2/3-y,1/3+x-y,1/3+z
9 2/3-x+y,1/3-x,1/3+z
10 2/3+y,1/3+x,5/6-z
11 2/3+x-y,1/3-y,5/6-z
12 2/3-x,1/3-x+y,5/6-z
13 1/3+x,2/3+y,2/3+z
14 1/3-y,2/3+x-y,2/3+z
15 1/3-x+y,2/3-x,2/3+z
16 1/3+y,2/3+x,1/6-z
17 1/3+x-y,2/3-y,1/6-z
18 1/3-x,2/3-x+y,1/6-z
19 -x,-y,-z
20 y,-x+y,-z
21 x-y,x,-z
22 -y,-x,1/2+z
23 -x+y,y,1/2+z
24 x,x-y,1/2+z
25 2/3-x,1/3-y,1/3-z
26 2/3+y,1/3-x+y,1/3-z
27 2/3+x-y,1/3+x,1/3-z
28 2/3-y,1/3-x,5/6+z
```

29 2/3-x+y,1/3+y,5/6+z

30 2/3+x,1/3+x-y,5/6+z

31 1/3-x,2/3-y,2/3-z

32 1/3+y,2/3-x+y,2/3-z

33 1/3+x-y,2/3+x,2/3-z

34 1/3-y,2/3-x,1/6+z

35 1/3-x+y,2/3+y,1/6+z

36 1/3+x,2/3+x-y,1/6+z

_cell_length_a 39.265(4)

_cell_length_b 39.265(4)

_cell_length_c 104.711(10)

_cell_angle_alpha 90

_cell_angle_beta 90

_cell_angle_gamma 120

_cell_volume 139809

loop_

_atom_site_label

_atom_site_type_symbol

_atom_site_fract_x

_atom_site_fract_y

_atom_site_fract_z

Cu1 Cu 0.37528(5) 0.333333 0.583333

Cu2 Cu 0.44236(5) 0.333333 0.583333

Cu3 Cu 0.44707(6) 0.11182(6) 0.69028(2)

Cu4 Cu 0.49650(6) 0.16081(6) 0.67333(2)

S1 S 0.27351(11) 0.10864(12) 0.65532(4)

S2 S 0.39370(11) 0.16586(10) 0.64969(3)

S3 S 0.27061(17) 0.1016(2) 0.51386(7)

S4 S 0.39057(13) 0.16583(11) 0.51748(4)

O1 O 0.3624(3) 0.2949(3) 0.59699(7)

O2 O 0.4168(3) 0.2921(3) 0.59620(7)

O5 O 0.3584(3) 0.2901(2) 0.57085(7)

O6 O 0.4180(3) 0.2930(3) 0.57030(9)

O13 O 0.3207(2) 0.333333 0.583333

O14 O 0.4975(2) 0.333333 0.583333

O3 O 0.4087(4) 0.1148(3) 0.68000(10)

O4 O 0.4494(3) 0.1541(3) 0.66496(9)

O15 O 0.3978(3) 0.0623(2) 0.70195(6)

O16 O 0.5396(3) 0.2011(3) 0.65957(12)

O7 O 0.4052(3) 0.1150(3) 0.48791(10)

O8 O 0.4456(4) 0.1563(3) 0.50168(9)

C1 C 0.3817(5) 0.2801(4) 0.60123(13)

C2 C 0.3703(6) 0.2513(3) 0.61083(10)

C3 C 0.3344(6) 0.2420(5) 0.61634(16)

H3 H 0.321077 0.255059 0.613706

C4 C 0.3182(3) 0.2132(5) 0.62575(16)

H4 H 0.293978 0.206825 0.629471

C5 C 0.3379(6) 0.1938(3) 0.62964(10)

C6 C 0.3738(5) 0.2032(5) 0.62413(17)

H6 H 0.387108 0.190086 0.626770

C7 C 0.3900(3) 0.2320(5) 0.61473(17)

H7 H 0.414207 0.238320 0.611005

C8 C 0.2836(6) 0.1425(4) 0.64256(12)

H8 H 0.263963 0.145061 0.638269

C9 C 0.3230(5) 0.1645(5) 0.63962(16)

C10 C 0.3455(3) 0.1525(4) 0.64780(14)

C11 C 0.3223(3) 0.1237(4) 0.65674(16)

C12 C 0.3480(7) 0.1156(4) 0.66469(11)

H12 H 0.336542 0.096157 0.671033

C13 C 0.3890(6) 0.1356(3) 0.66325(12)

C14 C 0.4161(6) 0.1336(7) 0.6708(2)

C15 C 0.3847(6) 0.2788(5) 0.56687(13)

C16 C 0.3686(5) 0.2485(3) 0.55716(10)

C17 C 0.3300(5) 0.2360(4) 0.55352(12)

H17 H 0.316266 0.247326 0.557281

C18 C 0.3119(3) 0.2069(4) 0.54431(13)

H18 H 0.285838 0.198471 0.541842

C19 C 0.3323(5) 0.1902(3) 0.53874(10)

C20 C 0.3708(5) 0.2027(5) 0.54238(14)

H20 H 0.384539 0.191398 0.538616

C21 C 0.3889(3) 0.2318(5) 0.55159(16)

H21 H 0.414967 0.240254 0.554054

C22 C 0.2815(7) 0.1349(6) 0.52701(16)

H22 H 0.261485 0.135485 0.531783

C23 C 0.3207(7) 0.1595(7) 0.52969(19)

C24 C 0.3431(5) 0.1523(7) 0.5212(2)

C25 C 0.3203(5) 0.1226(7) 0.5123(3)

C26 C 0.3375(7) 0.1099(6) 0.5030(2)

H26 H 0.323804 0.089178 0.497176

C27 C 0.3776(8) 0.1327(5) 0.50386(14)

C28 C 0.4100(7) 0.1336(6) 0.4971(2)

O9 O 0.6285(14) 0.4607(8) 0.6844(4)

O10 O 0.6226(12) 0.5030(7) 0.6962(3)

O11 O 0.491(3) 0.1945(10) 0.6847(6)

O12 O 0.4634(8) 0.1553(6) 0.7009(2)

C29 C 0.6155(16) 0.4678(9) 0.6950(4)

C42 C 0.475(3) 0.1892(12) 0.6960(4)

S5 S 0.4621(5) 0.2748(4) 0.73560(13)

S6 S 0.5052(4) 0.2680(4) 0.70010(11)

C30 C 0.5838(8) 0.4325(8) 0.6996(2)

C31 C 0.5655(9) 0.4336(8) 0.7109(3)

H31 H 0.568473 0.457555 0.713799

C32 C 0.5430(9) 0.3993(8) 0.7178(2)

H32 H 0.530605 0.400014 0.725389

C33 C 0.5386(11) 0.3639(8) 0.7135(3)

C34 C 0.5569(12) 0.3628(8) 0.7022(3)

H34 H 0.553979 0.338804 0.699301

C35 C 0.5795(10) 0.3971(9) 0.6953(2)

H35 H 0.591847 0.396344 0.687710

C36 C 0.4926(9) 0.3271(8) 0.7308(4)

H36 H 0.496709 0.349166 0.735583

C37 C 0.5084(10) 0.3276(9) 0.7188(3)

C38 C 0.4984(9) 0.2902(11) 0.7134(3)

C39 C 0.4732(8) 0.2598(12) 0.7215(2)

C40 C 0.4631(11) 0.2228(11) 0.7163(3)

H40 H 0.446440 0.200584 0.721248

C41 C 0.4750(8) 0.2159(7) 0.7048(3)

Cu1 Cu 0.666667 0.041947(50) 0.583333

Cu2 Cu 0.666667 0.109027(50) 0.583333

Cu3 Cu 0.88818(6) 0.33525(8) 0.69028(2)

Cu4 Cu 0.83919(6) 0.33569(8) 0.67333(2)

S1 S 0.89136(12) 0.16487(16) 0.65532(4)

S2 S 0.83414(10) 0.22784(15) 0.64969(3)

S3 S 0.8984(2) 0.16901(26) 0.51386(7)

S4 S 0.83417(11) 0.22474(17) 0.51748(4)

O1 O 0.7051(3) 0.0675(4) 0.59699(7)

O2 O 0.7079(3) 0.1247(4) 0.59620(7)

O5 O 0.7099(2) 0.0683(4) 0.57085(7)

O6 O 0.7070(3) 0.1250(4) 0.57030(9)

O13 O 0.666667 -0.01263(20) 0.583333

O14 O 0.666667 0.16417(20) 0.583333

O3 O 0.8852(3) 0.2939(5) 0.68000(10)

O4 O 0.8459(3) 0.2953(4) 0.66496(9)

O15 O 0.9377(2) 0.3355(4) 0.70195(6)

O16 O 0.7989(3) 0.3385(4) 0.65957(12)

O7 O 0.8850(3) 0.2902(4) 0.48791(10)

O8 O 0.8437(3) 0.2893(5) 0.50168(9)

C1 C 0.7199(4) 0.1016(6) 0.60123(13)

C2 C 0.7487(3) 0.1190(7) 0.61083(10)

C3 C 0.7580(5) 0.0924(8) 0.61634(16)

H3 H 0.744941 0.066018 0.613706

C4 C 0.7868(5) 0.1050(6) 0.62575(16)

H4 H 0.793175 0.087153 0.629471

C5 C 0.8062(3) 0.1441(7) 0.62964(10)

C6 C 0.7968(5) 0.1706(7) 0.62413(17)

H6 H 0.809914 0.197022 0.626770

C7 C 0.7680(5) 0.1580(6) 0.61473(17)

H7 H 0.761680 0.175887 0.611005

C8 C 0.8575(4) 0.1411(7) 0.64256(12)

H8 H 0.854939 0.118902 0.638269

C9 C 0.8355(5) 0.1585(7) 0.63962(16)

C10 C 0.8475(4) 0.1930(5) 0.64780(14)

C11 C 0.8763(4) 0.1986(5) 0.65674(16)

C12 C 0.8844(4) 0.2324(8) 0.66469(11)

H12 H 0.903843 0.240385 0.671033

C13 C 0.8644(3) 0.2534(7) 0.66325(12)

C14 C 0.8664(7) 0.2825(9) 0.6708(2)

C15 C 0.7212(5) 0.1059(8) 0.56687(13)

C16 C 0.7515(3) 0.1201(6) 0.55716(10)

C17 C 0.7640(4) 0.0940(6) 0.55352(12)

H17 H 0.752674 0.068940 0.557281

C18 C 0.7931(4) 0.1050(5) 0.54431(13)

H18 H 0.801529 0.087367 0.541842

C19 C 0.8098(3) 0.1421(6) 0.53874(10)

C20 C 0.7973(5) 0.1681(7) 0.54238(14)

H20 H 0.808602 0.193141 0.538616

C21 C 0.7682(5) 0.1571(6) 0.55159(16)

H21 H 0.759746 0.174713 0.554054

C22 C 0.8651(6) 0.1466(9) 0.52701(16)

H22 H 0.864515 0.126000 0.531783

C23 C 0.8405(7) 0.1612(10) 0.52969(19)

C24 C 0.8477(7) 0.1908(9) 0.5212(2)

C25 C 0.8774(7) 0.1977(9) 0.5123(3)

C26 C 0.8901(6) 0.2276(9) 0.5030(2)

H26 H 0.910822 0.234626 0.497176

C27 C 0.8673(5) 0.2449(9) 0.50386(14)

C28 C 0.8664(6) 0.2764(9) 0.4971(2)

O9 O 0.5393(8) 0.1678(16) 0.6844(4)

O10 O 0.4970(7) 0.1196(14) 0.6962(3)

O11 O 0.8055(10) 0.2965(32) 0.6847(6)

O12 O 0.8447(6) 0.3081(10) 0.7009(2)

C29 C 0.5322(9) 0.1477(18) 0.6950(4)

C42 C 0.8108(12) 0.2858(32) 0.6960(4)

S5 S 0.7252(4) 0.1873(6) 0.73560(13)

S6 S 0.7320(4) 0.2372(6) 0.70010(11)

C30 C 0.5675(8) 0.1513(11) 0.6996(2)

C31 C 0.5664(8) 0.1319(12) 0.7109(3)

H31 H 0.542445 0.110918 0.713799

C32 C 0.6007(8) 0.1437(12) 0.7178(2)

H32 H 0.599986 0.130591 0.725389

C33 C 0.6361(8) 0.1747(14) 0.7135(3)

C34 C 0.6372(8) 0.1941(14) 0.7022(3)

H34 H 0.661196 0.215175 0.699301

C35 C 0.6029(9) 0.1824(13) 0.6953(2)

H35 H 0.603656 0.195503 0.687710

C36 C 0.6729(8) 0.1655(12) 0.7308(4)

H36 H 0.650834 0.147543 0.735583

C37 C 0.6724(9) 0.1808(13) 0.7188(3)

C38 C 0.7098(11) 0.2082(14) 0.7134(3)

C39 C 0.7402(12) 0.2134(14) 0.7215(2)

C40 C 0.7772(11) 0.2403(16) 0.7163(3)

H40 H 0.799416 0.245856 0.721248

C41 C 0.7841(7) 0.2591(11) 0.7048(3)

Cu1 Cu 0.958053(50) 0.62472(5) 0.583333

Cu2 Cu 0.890973(50) 0.55764(5) 0.583333

Cu3 Cu 0.66475(8) 0.55293(6) 0.69028(2)

Cu4 Cu 0.66431(8) 0.50350(6) 0.67333(2)

S1 S 0.83513(16) 0.72649(11) 0.65532(4)

S2 S 0.77216(15) 0.60630(11) 0.64969(3)

S3 S 0.83099(26) 0.72939(17) 0.51386(7)

S4 S 0.77526(17) 0.60943(13) 0.51748(4)

O1 O 0.9325(4) 0.6376(3) 0.59699(7)

O2 O 0.8753(4) 0.5832(3) 0.59620(7)

O5 O 0.9317(4) 0.6416(3) 0.57085(7)

O6 O 0.8750(4) 0.5820(3) 0.57030(9)

O13 O 1.01263(20) 0.6793(2) 0.583333

O14 O 0.83583(20) 0.5025(2) 0.583333

O3 O 0.7061(5) 0.5913(4) 0.68000(10)

O4 O 0.7047(4) 0.5506(3) 0.66496(9)

O15 O 0.6645(4) 0.6022(3) 0.70195(6)

O16 O 0.6615(4) 0.4604(3) 0.65957(12)

O7 O 0.7098(4) 0.5948(3) 0.48791(10)

O8 O 0.7107(5) 0.5544(4) 0.50168(9)

C1 C 0.8984(6) 0.6183(5) 0.60123(13)

C2 C 0.8810(7) 0.6297(6) 0.61083(10)

C3 C 0.9076(8) 0.6656(6) 0.61634(16)

H3 H 0.933982 0.678923 0.613706

C4 C 0.8950(6) 0.6818(3) 0.62575(16)

H4 H 0.912847 0.706022 0.629471

C5 C 0.8559(7) 0.6621(6) 0.62964(10)

C6 C 0.8294(7) 0.6262(5) 0.62413(17)

H6 H 0.802978 0.612892 0.626770

C7 C 0.8420(6) 0.6100(3) 0.61473(17)

H7 H 0.824113 0.585793 0.611005

C8 C 0.8589(7) 0.7164(6) 0.64256(12)

H8 H 0.881098 0.736037 0.638269

C9 C 0.8415(7) 0.6770(5) 0.63962(16)

C10 C 0.8070(5) 0.6545(3) 0.64780(14)

C11 C 0.8014(5) 0.6777(3) 0.65674(16)

C12 C 0.7676(8) 0.6520(7) 0.66469(11)

H12 H 0.759615 0.663458 0.671033

C13 C 0.7466(7) 0.6110(6) 0.66325(12)

C14 C 0.7175(9) 0.5839(6) 0.6708(2)

C15 C 0.8941(8) 0.6153(6) 0.56687(13)

C16 C 0.8799(6) 0.6314(5) 0.55716(10)

C17 C 0.9060(6) 0.6700(5) 0.55352(12)

H17 H 0.931060 0.683734 0.557281

C18 C 0.8950(5) 0.6881(3) 0.54431(13)

H18 H 0.912633 0.714162 0.541842

C19 C 0.8579(6) 0.6677(5) 0.53874(10)

C20 C 0.8319(7) 0.6292(5) 0.54238(14)

H20 H 0.806859 0.615461 0.538616

C21 C 0.8429(6) 0.6111(3) 0.55159(16)

H21 H 0.825287 0.585033 0.554054

C22 C 0.8534(9) 0.7185(7) 0.52701(16)

H22 H 0.874000 0.738515 0.531783

C23 C 0.8388(10) 0.6793(7) 0.52969(19)

C24 C 0.8092(9) 0.6569(5) 0.5212(2)

C25 C 0.8023(9) 0.6797(5) 0.5123(3)

C26 C 0.7724(9) 0.6625(7) 0.5030(2)

H26 H 0.765374 0.676196 0.497176

C27 C 0.7551(9) 0.6224(8) 0.50386(14)

C28 C 0.7236(9) 0.5900(7) 0.4971(2)

O9 O 0.8322(16) 0.3715(14) 0.6844(4)

O10 O 0.8804(14) 0.3774(12) 0.6962(3)

O11 O 0.7035(32) 0.509(3) 0.6847(6)

O12 O 0.6919(10) 0.5366(8) 0.7009(2)

C29 C 0.8523(18) 0.3845(16) 0.6950(4)

C42 C 0.7142(32) 0.525(3) 0.6960(4)

S5 S 0.8127(6) 0.5379(5) 0.73560(13)

S6 S 0.7628(6) 0.4948(4) 0.70010(11)

C30 C 0.8487(11) 0.4162(8) 0.6996(2)

C31 C 0.8681(12) 0.4345(9) 0.7109(3)

H31 H 0.889082 0.431527 0.713799

C32 C 0.8563(12) 0.4570(9) 0.7178(2)

H32 H 0.869409 0.469395 0.725389

C33 C 0.8253(14) 0.4614(11) 0.7135(3)

C34 C 0.8059(14) 0.4431(12) 0.7022(3)

H34 H 0.784825 0.446021 0.699301

C35 C 0.8176(13) 0.4205(10) 0.6953(2)

H35 H 0.804497 0.408153 0.687710

C36 C 0.8345(12) 0.5074(9) 0.7308(4)

H36 H 0.852457 0.503291 0.735583

C37 C 0.8192(13) 0.4916(10) 0.7188(3)

C38 C 0.7918(14) 0.5016(9) 0.7134(3)

C39 C 0.7866(14) 0.5268(8) 0.7215(2)

C40 C 0.7597(16) 0.5369(11) 0.7163(3)

H40 H 0.754144 0.553560 0.721248

C41 C 0.7409(11) 0.5250(8) 0.7048(3)

Cu3 Cu 0.44515(6) 0.11374(6) 0.47639(2)

Cu4 Cu 0.49414(6) 0.16317(6) 0.49334(2)

S1 S 0.44197(12) -0.05982(11) 0.51135(4)

S2 S 0.49919(10) 0.06037(11) 0.51698(3)

S3 S 0.4349(2) -0.06272(17) 0.65281(7)

S4 S 0.49916(11) 0.05724(13) 0.64919(4)

O1 O 0.6282(3) 0.0291(3) 0.56968(7)

O2 O 0.6254(3) 0.0835(3) 0.57047(7)

O5 O 0.6234(2) 0.0251(3) 0.59582(7)

O6 O 0.6263(3) 0.0847(3) 0.59637(9)

O3 O 0.4481(3) 0.0754(4) 0.48667(10)

O4 O 0.4874(3) 0.1161(3) 0.50171(9)

O15 O 0.3956(2) 0.0645(3) 0.46472(6)

O16 O 0.5344(3) 0.2063(3) 0.50710(12)

O7 O 0.4483(3) 0.0719(3) 0.67876(10)

O8 O 0.4896(3) 0.1123(4) 0.66499(9)

C1 C 0.6134(4) 0.0484(5) 0.56544(13)

C2 C 0.5846(3) 0.0370(6) 0.55584(10)

C3 C 0.5753(5) 0.0011(6) 0.55033(16)

H3 H 0.588392 -0.012256 0.552961

C4 C 0.5465(5) -0.0151(3) 0.54092(16)

H4 H 0.540158 -0.039355 0.537196

C5 C 0.5271(3) 0.0046(6) 0.53703(10)

C6 C 0.5365(5) 0.0405(5) 0.54254(17)

H6 H 0.523419 0.053775 0.539897

C7 C 0.5653(5) 0.0567(3) 0.55194(17)

H7 H 0.571653 0.080874 0.555662

C8 C 0.4758(4) -0.0497(6) 0.52411(12)

H8 H 0.478394 -0.069370 0.528398

C9 C 0.4978(5) -0.0103(5) 0.52705(16)

C10 C 0.4858(4) 0.0122(3) 0.51887(14)

C11 C 0.4570(4) -0.0110(3) 0.50993(16)

C12 C 0.4489(4) 0.0147(7) 0.50198(11)

H12 H 0.429490 0.003209 0.495634

C13 C 0.4689(3) 0.0557(6) 0.50342(12)

C14 C 0.4669(7) 0.0828(6) 0.4959(2)

C15 C 0.6121(5) 0.0514(6) 0.59980(13)

C16 C 0.5818(3) 0.0353(5) 0.60951(10)

C17 C 0.5693(4) -0.0033(5) 0.61315(12)

H17 H 0.580659 -0.017067 0.609386

C18 C 0.5402(4) -0.0214(3) 0.62236(13)

H18 H 0.531804 -0.047495 0.624825

C19 C 0.5235(3) -0.0010(5) 0.62793(10)

C20 C 0.5360(5) 0.0375(5) 0.62429(14)

H20 H 0.524731 0.051206 0.628051

C21 C 0.5651(5) 0.0556(3) 0.61508(16)

H21 H 0.573587 0.081634 0.612613

C22 C 0.4682(6) -0.0518(7) 0.63966(16)

H22 H 0.468818 -0.071848 0.634884

C23 C 0.4928(7) -0.0126(7) 0.63698(19)

C24 C 0.4856(7) 0.0098(5) 0.6455(2)

C25 C 0.4559(7) -0.0130(5) 0.6544(3)

C26 C 0.4432(6) 0.0042(7) 0.6637(2)

H26 H 0.422511 -0.009529 0.669491

C27 C 0.4660(5) 0.0443(8) 0.66281(14)

C28 C 0.4669(6) 0.0767(7) 0.6696(2)

O9 O 0.7940(8) 0.2952(14) 0.4823(4)

O10 O 0.8363(7) 0.2893(12) 0.4705(3)

O11 O 0.5278(10) 0.158(3) 0.4820(6)

O12 O 0.4886(6) 0.1301(8) 0.4658(2)

C29 C 0.8011(9) 0.2822(16) 0.4717(4)

C42 C 0.5225(12) 0.142(3) 0.4707(4)

S5 S 0.6081(4) 0.1288(5) 0.43107(13)

S6 S 0.6013(4) 0.1719(4) 0.46657(11)

C30 C 0.7658(8) 0.2505(8) 0.4671(2)

C31 C 0.7669(8) 0.2322(9) 0.4558(3)

H31 H 0.790888 0.235140 0.452868

C32 C 0.7326(8) 0.2097(9) 0.4489(2)

H32 H 0.733347 0.197272 0.441278

C33 C 0.6972(8) 0.2053(11) 0.4532(3)

C34 C 0.6961(8) 0.2236(12) 0.4645(3)

H34 H 0.672137 0.220646 0.467366

C35 C 0.7304(9) 0.2462(10) 0.4714(2)

H35 H 0.729677 0.258514 0.478957

C36 C 0.6604(8) 0.1593(9) 0.4359(4)

H36 H 0.682499 0.163376 0.431084

C37 C 0.6609(9) 0.1751(10) 0.4479(3)

C38 C 0.6235(11) 0.1651(9) 0.4533(3)

C39 C 0.5931(12) 0.1399(8) 0.4452(2)

C40 C 0.5561(11) 0.1298(11) 0.4504(3)

H40 H 0.533917 0.113107 0.445419

C41 C 0.5492(7) 0.1417(8) 0.4619(3)

Cu3 Cu 0.66858(8) 0.55485(6) 0.47639(2)

Cu4 Cu 0.66902(8) 0.50586(6) 0.49334(2)

S1 S 0.49820(16) 0.55803(12) 0.51135(4)

S2 S 0.56117(15) 0.50081(10) 0.51698(3)

S3 S 0.50234(26) 0.5651(2) 0.65281(7)

S4 S 0.55807(17) 0.50084(11) 0.64919(4)

O1 O 0.4008(4) 0.3718(3) 0.56968(7)

O2 O 0.4580(4) 0.3746(3) 0.57047(7)

O5 O 0.4016(4) 0.3766(2) 0.59582(7)

O6 O 0.4583(4) 0.3737(3) 0.59637(9)

O3 O 0.6272(5) 0.5519(3) 0.48667(10)

O4 O 0.6286(4) 0.5126(3) 0.50171(9)

O15 O 0.6688(4) 0.6044(2) 0.46472(6)

O16 O 0.6718(4) 0.4656(3) 0.50710(12)

O7 O 0.6235(4) 0.5517(3) 0.67876(10)

O8 O 0.6226(5) 0.5104(3) 0.66499(9)

C1 C 0.4349(6) 0.3866(4) 0.56544(13)

C2 C 0.4523(7) 0.4154(3) 0.55584(10)

C3 C 0.4257(8) 0.4247(5) 0.55033(16)

H3 H 0.399351 0.411608 0.552961

C4 C 0.4383(6) 0.4535(5) 0.54092(16)

H4 H 0.420486 0.459842 0.537196

C5 C 0.4774(7) 0.4729(3) 0.53703(10)

C6 C 0.5039(7) 0.4635(5) 0.54254(17)

H6 H 0.530355 0.476581 0.539897

C7 C 0.4913(6) 0.4347(5) 0.55194(17)

H7 H 0.509220 0.428347 0.555662

C8 C 0.4744(7) 0.5242(4) 0.52411(12)

H8 H 0.452235 0.521606 0.528398

C9 C 0.4918(7) 0.5022(5) 0.52705(16)

C10 C 0.5263(5) 0.5142(4) 0.51887(14)

C11 C 0.5319(5) 0.5430(4) 0.50993(16)

C12 C 0.5657(8) 0.5511(4) 0.50198(11)

H12 H 0.573718 0.570510 0.495634

C13 C 0.5867(7) 0.5311(3) 0.50342(12)

C14 C 0.6158(9) 0.5331(7) 0.4959(2)

C15 C 0.4392(8) 0.3879(5) 0.59980(13)

C16 C 0.4534(6) 0.4182(3) 0.60951(10)

C17 C 0.4273(6) 0.4307(4) 0.61315(12)

H17 H 0.402273 0.419341 0.609386

C18 C 0.4383(5) 0.4598(4) 0.62236(13)

H18 H 0.420700 0.468196 0.624825

C19 C 0.4754(6) 0.4765(3) 0.62793(10)

C20 C 0.5014(7) 0.4640(5) 0.62429(14)

H20 H 0.526474 0.475269 0.628051

C21 C 0.4904(6) 0.4349(5) 0.61508(16)

H21 H 0.508046 0.426413 0.612613

C22 C 0.4799(9) 0.5318(6) 0.63966(16)

H22 H 0.459333 0.531182 0.634884

C23 C 0.4945(10) 0.5072(7) 0.63698(19)

C24 C 0.5241(9) 0.5144(7) 0.6455(2)

C25 C 0.5310(9) 0.5441(7) 0.6544(3)

C26 C 0.5609(9) 0.5568(6) 0.6637(2)

H26 H 0.567959 0.577489 0.669491

C27 C 0.5782(9) 0.5340(5) 0.66281(14)

C28 C 0.6097(9) 0.5331(6) 0.6696(2)

O9 O 0.5011(16) 0.2060(8) 0.4823(4)

O10 O 0.4529(14) 0.1637(7) 0.4705(3)

O11 O 0.6298(32) 0.4722(10) 0.4820(6)

O12 O 0.6414(10) 0.5114(6) 0.4658(2)

C29 C 0.4810(18) 0.1989(9) 0.4717(4)

C42 C 0.6191(32) 0.4775(12) 0.4707(4)

S5 S 0.5206(6) 0.3919(4) 0.43107(13)

S6 S 0.5705(6) 0.3987(4) 0.46657(11)

C30 C 0.4846(11) 0.2342(8) 0.4671(2)

C31 C 0.4652(12) 0.2331(8) 0.4558(3)

H31 H 0.444251 0.209112 0.452868

C32 C 0.4770(12) 0.2674(8) 0.4489(2)

H32 H 0.463924 0.266653 0.441278

C33 C 0.5080(14) 0.3028(8) 0.4532(3)

C34 C 0.5274(14) 0.3039(8) 0.4645(3)

H34 H 0.548508 0.327863 0.467366

C35 C 0.5157(13) 0.2696(9) 0.4714(2)

H35 H 0.528836 0.270323 0.478957

C36 C 0.4988(12) 0.3396(8) 0.4359(4)

H36 H 0.480876 0.317501 0.431084

C37 C 0.5141(13) 0.3391(9) 0.4479(3)

C38 C 0.5415(14) 0.3765(11) 0.4533(3)

C39 C 0.5467(14) 0.4069(12) 0.4452(2)

C40 C 0.5736(16) 0.4439(11) 0.4504(3)

H40 H 0.579189 0.466083 0.445419

C41 C 0.5924(11) 0.4508(7) 0.4619(3)

Cu3 Cu 0.88626(6) 0.33142(8) 0.47639(2)

Cu4 Cu 0.83683(6) 0.33098(8) 0.49334(2)

S1 S 1.05982(11) 0.50180(16) 0.51135(4)

S2 S 0.93963(11) 0.43883(15) 0.51698(3)

S3 S 1.06272(17) 0.49766(26) 0.65281(7)

S4 S 0.94276(13) 0.44193(17) 0.64919(4)

O1 O 0.9709(3) 0.5992(4) 0.56968(7)

O2 O 0.9165(3) 0.5420(4) 0.57047(7)

O5 O 0.9749(3) 0.5984(4) 0.59582(7)

O6 O 0.9153(3) 0.5417(4) 0.59637(9)

O3 O 0.9246(4) 0.3728(5) 0.48667(10)

O4 O 0.8839(3) 0.3714(4) 0.50171(9)

O15 O 0.9355(3) 0.3312(4) 0.46472(6)

O16 O 0.7937(3) 0.3282(4) 0.50710(12)

O7 O 0.9281(3) 0.3765(4) 0.67876(10)

O8 O 0.8877(4) 0.3774(5) 0.66499(9)

C1 C 0.9516(5) 0.5651(6) 0.56544(13)

C2 C 0.9630(6) 0.5477(7) 0.55584(10)

C3 C 0.9989(6) 0.5743(8) 0.55033(16)

H3 H 1.012256 0.600649 0.552961

C4 C 1.0151(3) 0.5617(6) 0.54092(16)

H4 H 1.039355 0.579514 0.537196

C5 C 0.9954(6) 0.5226(7) 0.53703(10)

C6 C 0.9595(5) 0.4961(7) 0.54254(17)

H6 H 0.946225 0.469645 0.539897

C7 C 0.9433(3) 0.5087(6) 0.55194(17)

H7 H 0.919126 0.490780 0.555662

C8 C 1.0497(6) 0.5256(7) 0.52411(12)

H8 H 1.069370 0.547765 0.528398

C9 C 1.0103(5) 0.5082(7) 0.52705(16)

C10 C 0.9878(3) 0.4737(5) 0.51887(14)

C11 C 1.0110(3) 0.4681(5) 0.50993(16)

C12 C 0.9853(7) 0.4343(8) 0.50198(11)

H12 H 0.996791 0.426282 0.495634

C13 C 0.9443(6) 0.4133(7) 0.50342(12)

C14 C 0.9172(6) 0.3842(9) 0.4959(2)

C15 C 0.9486(6) 0.5608(8) 0.59980(13)

C16 C 0.9647(5) 0.5466(6) 0.60951(10)

C17 C 1.0033(5) 0.5727(6) 0.61315(12)

H17 H 1.017067 0.597727 0.609386

C18 C 1.0214(3) 0.5617(5) 0.62236(13)

H18 H 1.047495 0.579300 0.624825

C19 C 1.0010(5) 0.5246(6) 0.62793(10)

C20 C 0.9625(5) 0.4986(7) 0.62429(14)

H20 H 0.948794 0.473526 0.628051

C21 C 0.9444(3) 0.5096(6) 0.61508(16)

H21 H 0.918366 0.491954 0.612613

C22 C 1.0518(7) 0.5201(9) 0.63966(16)

H22 H 1.071848 0.540667 0.634884

C23 C 1.0126(7) 0.5055(10) 0.63698(19)

C24 C 0.9902(5) 0.4759(9) 0.6455(2)

C25 C 1.0130(5) 0.4690(9) 0.6544(3)

C26 C 0.9958(7) 0.4391(9) 0.6637(2)

H26 H 1.009529 0.432041 0.669491

C27 C 0.9557(8) 0.4218(9) 0.66281(14)

C28 C 0.9233(7) 0.3903(9) 0.6696(2)

O9 O 0.7048(14) 0.4989(16) 0.4823(4)

O10 O 0.7107(12) 0.5471(14) 0.4705(3)

O11 O 0.842(3) 0.3702(32) 0.4820(6)

O12 O 0.8699(8) 0.3586(10) 0.4658(2)

C29 C 0.7178(16) 0.5190(18) 0.4717(4)

C42 C 0.858(3) 0.3809(32) 0.4707(4)

S5 S 0.8712(5) 0.4794(6) 0.43107(13)

S6 S 0.8281(4) 0.4295(6) 0.46657(11)

C30 C 0.7495(8) 0.5154(11) 0.4671(2)

C31 C 0.7678(9) 0.5348(12) 0.4558(3)

H31 H 0.764860 0.555749 0.452868

C32 C 0.7903(9) 0.5230(12) 0.4489(2)

H32 H 0.802728 0.536076 0.441278

C33 C 0.7947(11) 0.4920(14) 0.4532(3)

C34 C 0.7764(12) 0.4726(14) 0.4645(3)

H34 H 0.779354 0.451492 0.467366

C35 C 0.7538(10) 0.4843(13) 0.4714(2)

H35 H 0.741486 0.471164 0.478957

C36 C 0.8407(9) 0.5012(12) 0.4359(4)

```
H36 H 0.836624 0.519124 0.431084
C37 C 0.8249(10) 0.4859(13) 0.4479(3)
C38 C 0.8349(9) 0.4585(14) 0.4533(3)
C39 C 0.8601(8) 0.4533(14) 0.4452(2)
C40 C 0.8702(11) 0.4264(16) 0.4504(3)
H40 H 0.886893 0.420811 0.445419
C41 C 0.8583(8) 0.4076(11) 0.4619(3)
O9' O 0.6230(14) 0.4712(9) 0.6859(4)
O10' O 0.6293(12) 0.5121(8) 0.7018(2)
O11' O 0.501(2) 0.2010(9) 0.6840(6)
O12' O 0.4508(8) 0.1590(6) 0.6960(2)
C42' C 0.6095(15) 0.4786(10) 0.6964(4)
C29' C 0.476(2) 0.1946(7) 0.6931(4)
S5' S 0.5089(5) 0.3881(4) 0.73377(12)
S6' S 0.5656(3) 0.3967(3) 0.69955(10)
C30' C 0.4851(9) 0.2302(7) 0.6987(2)
C31' C 0.4769(10) 0.2310(7) 0.7116(2)
H31' H 0.467409 0.208089 0.716553
C32' C 0.4827(9) 0.2657(8) 0.7171(2)
H32' H 0.477168 0.266257 0.725816
C33' C 0.4968(8) 0.2996(7) 0.7098(2)
C34' C 0.5050(9) 0.2988(6) 0.6969(2)
H34' H 0.514452 0.321677 0.691925
C35' C 0.4991(9) 0.2641(8) 0.6914(2)
H35' H 0.504693 0.263509 0.682661
C36' C 0.4911(11) 0.3381(8) 0.7274(4)
H36' H 0.472209 0.315354 0.731614
C37' C 0.5078(11) 0.3366(8) 0.7157(3)
C38' C 0.5347(7) 0.3763(11) 0.7124(2)
C39' C 0.5397(7) 0.4067(12) 0.7202(2)
C40' C 0.5675(10) 0.4462(9) 0.7162(3)
H40' H 0.572825 0.468675 0.720873
C41' C 0.5856(10) 0.4478(7) 0.7048(3)

#END
```

```
_symmetry_cell_setting           monoclinic
_symmetry_space_group_name_H-M   'C 2/c'
_symmetry_Int_Tables_number      15
_space_group_name_Hall           '-C 2yc'
loop_
_symmetry_equiv_pos_site_id
_symmetry_equiv_pos_as_xyz
1 x,y,z
2 -x,y,1/2-z
3 1/2+x,1/2+y,z
4 1/2-x,1/2+y,1/2-z
5 -x,-y,-z
6 x,-y,1/2+z
7 1/2-x,1/2-y,-z
8 1/2+x,1/2-y,1/2+z
_cell_length_a                   25.0245(11)
_cell_length_b                   24.1040(9)
_cell_length_c                   11.6527(5)
_cell_angle_alpha                90
_cell_angle_beta                 113.748(3)
_cell_angle_gamma                90
_cell_volume                     6433.64
loop_
_atom_site_label
_atom_site_type_symbol
_atom_site_fract_x
_atom_site_fract_y
_atom_site_fract_z
_atom_site_U_iso_or_equiv
_atom_site_thermal_displace_type
C2 C 0.4667(3) 0.1479(3) 0.5804(6) 0.0613 Uani
C3 C 0.4846(2) 0.2027(2) 0.5483(5) 0.0509 Uani
C4 C 0.5245(2) 0.2778(2) 0.4647(5) 0.0440 Uani
C5 C 0.5529(2) 0.3095(2) 0.4006(5) 0.0448 Uani
C7 C 0.6061(2) 0.3144(2) 0.2843(5) 0.0451 Uani
```

C8 C 0.6371(2) 0.2860(2) 0.2176(5) 0.0457 Uani

C9 C 0.6825(2) 0.2159(2) 0.1333(5) 0.0467 Uani

C10 C 0.7030(2) 0.1632(2) 0.1027(5) 0.0528 Uani

C13 C 0.6621(2) 0.3090(2) 0.1424(5) 0.0482 Uani

C14 C 0.6879(2) 0.2682(2) 0.0941(5) 0.0489 Uani

C16 C 0.5767(2) 0.3922(2) 0.3442(5) 0.0452 Uani

C17 C 0.5761(2) 0.4536(2) 0.3515(5) 0.0497 Uani

C18 C 0.5540(2) 0.4856(2) 0.4182(5) 0.0522 Uani

C19 C 0.5632(3) 0.5423(2) 0.4064(6) 0.0611 Uani

C20 C 0.5916(3) 0.5519(2) 0.3300(5) 0.0555 Uani

C21 C 0.6093(3) 0.6072(3) 0.2976(6) 0.0570 Uani

C25 C 0.4731(2) 0.2538(2) 0.5837(5) 0.0542 Uani

C26 C 0.4956(2) 0.2971(2) 0.5354(5) 0.0492 Uani

S1 S 0.52346(6) 0.20648(6) 0.45548(13) 0.0505 Uani

S2 S 0.64489(6) 0.21507(6) 0.22846(13) 0.0489 Uani

S3 S 0.60749(6) 0.49210(6) 0.27190(13) 0.0513 Uani

N1 N 0.58107(17) 0.28263(18) 0.3421(4) 0.0434 Uani

N2 N 0.60576(18) 0.36964(18) 0.2826(4) 0.0478 Uani

N3 N 0.54896(18) 0.36543(18) 0.4046(4) 0.0477 Uani

O1 O 0.4863(2) 0.10495(19) 0.5475(5) 0.0798 Uani

O2 O 0.4336(2) 0.14784(19) 0.6352(5) 0.0786 Uani

O3 O 0.73092(18) 0.16691(17) 0.0316(4) 0.0648 Uani

O4 O 0.6934(2) 0.11884(17) 0.1447(4) 0.0688 Uani

O5 O 0.6375(2) 0.60219(17) 0.2252(4) 0.0711 Uani

O6 O 0.5978(2) 0.65034(18) 0.3348(5) 0.0780 Uani

C28 C 0.6593(3) 0.8365(3) 0.2193(7) 0.0850 Uiso

C30 C 0.6593(3) 0.7365(3) 0.2023(6) 0.0633 Uiso

C32 C 0.7002(3) 0.7903(3) 0.0816(7) 0.0748 Uiso

N6 N 0.6727(2) 0.7857(2) 0.1703(5) 0.0620 Uiso

O9 O 0.66918(19) 0.6920(2) 0.1596(4) 0.0739 Uiso

C34 C 0.7440(3) 0.0321(3) -0.0050(7) 0.0748 Uiso

C36 C 0.7875(4) -0.0195(4) -0.1239(9) 0.1030 Uiso

C37 C 0.7466(4) -0.0679(4) 0.0101(9) 0.1140 Uiso

N5 N 0.7572(2) -0.0166(2) -0.0422(5) 0.0680 Uiso

O8' O 0.7176(6) 0.0281(7) 0.0677(14) 0.0820 Uiso

O8 O 0.7590(3) 0.0764(3) -0.0452(6) 0.0670 Uiso

C38 C 0.4258(5) 0.0204(5) 0.6728(10) 0.1200 Uiso

```
C80 C 0.4216(6) -0.0815(6) 0.6892(13) 0.1630 Uiso
C81 C 0.3833(6) -0.0156(6) 0.8074(14) 0.1570 Uiso
N4 N 0.4092(4) -0.0262(4) 0.7187(8) 0.1160 Uiso
O7 O 0.4559(4) 0.0147(4) 0.6111(10) 0.1070 Uiso
O7' O 0.4007(7) 0.0585(7) 0.6902(14) 0.1040 Uiso
loop_
_atom_site_aniso_label
_atom_site_aniso_U_11
_atom_site_aniso_U_22
_atom_site_aniso_U_33
_atom_site_aniso_U_23
_atom_site_aniso_U_13
_atom_site_aniso_U_12
C2 0.065(4) 0.062(4) 0.063(4) 0.008(3) 0.032(3) -0.009(3)
C3 0.049(3) 0.057(4) 0.049(3) 0.007(3) 0.022(3) -0.002(2)
C4 0.040(3) 0.054(3) 0.043(3) -0.003(2) 0.022(2) -0.001(2)
C5 0.041(3) 0.050(3) 0.045(3) -0.003(2) 0.019(2) 0.001(2)
C7 0.040(3) 0.054(3) 0.041(3) 0.000(2) 0.016(2) -0.002(2)
C8 0.044(3) 0.050(3) 0.049(3) -0.004(2) 0.025(2) -0.007(2)
C9 0.047(3) 0.052(3) 0.047(3) 0.002(2) 0.025(2) -0.005(2)
C10 0.054(3) 0.057(4) 0.056(3) -0.001(3) 0.031(3) 0.003(3)
C13 0.050(3) 0.056(3) 0.046(3) -0.002(2) 0.027(2) 0.001(2)
C14 0.052(3) 0.052(3) 0.053(3) 0.002(2) 0.032(3) -0.003(2)
C16 0.045(3) 0.049(3) 0.046(3) -0.001(2) 0.023(2) -0.001(2)
C17 0.050(3) 0.048(3) 0.054(3) 0.001(2) 0.024(3) 0.004(2)
C18 0.058(3) 0.056(3) 0.057(3) 0.000(3) 0.038(3) 0.009(2)
C19 0.071(4) 0.057(4) 0.067(4) 0.003(3) 0.040(3) 0.011(3)
C20 0.062(3) 0.058(4) 0.053(3) 0.006(3) 0.030(3) 0.009(3)
C21 0.066(4) 0.053(4) 0.057(4) 0.003(3) 0.030(3) 0.006(3)
C25 0.055(3) 0.063(4) 0.051(3) 0.005(3) 0.028(3) 0.003(3)
C26 0.054(3) 0.052(3) 0.047(3) 0.002(2) 0.026(3) 0.000(2)
S1 0.0528(8) 0.0526(8) 0.0544(8) 0.0002(6) 0.0303(7) 0.0009(6)
S2 0.0566(8) 0.0507(8) 0.0521(8) 0.0001(6) 0.0351(7) -0.0026(6)
S3 0.0593(8) 0.0493(8) 0.0553(9) 0.0010(6) 0.0334(7) 0.0030(6)
N1 0.046(2) 0.050(3) 0.043(2) -0.0022(19) 0.027(2) -0.0033(18)
N2 0.051(2) 0.049(3) 0.053(3) -0.003(2) 0.031(2) -0.0023(19)
N3 0.049(2) 0.055(3) 0.045(2) 0.001(2) 0.025(2) 0.004(2)
```

```
O1 0.105(4) 0.057(3) 0.097(4) 0.002(2) 0.061(3) -0.003(2)
O2 0.091(3) 0.078(3) 0.092(3) 0.010(3) 0.063(3) -0.007(3)
O3 0.081(3) 0.063(3) 0.075(3) 0.006(2) 0.057(3) 0.003(2)
O4 0.095(3) 0.051(2) 0.086(3) 0.004(2) 0.063(3) -0.001(2)
O5 0.099(3) 0.058(3) 0.081(3) 0.001(2) 0.062(3) 0.006(2)
O6 0.105(4) 0.048(3) 0.100(4) -0.001(2) 0.061(3) 0.010(2)

#END
```

La-MOF

```
_symmetry_cell_setting           monoclinic
_symmetry_space_group_name_H-M   'C c'
_symmetry_Int_Tables_number      9
_space_group_name_Hall           'C -2yc'
loop_
_symmetry_equiv_pos_site_id
_symmetry_equiv_pos_as_xyz
1 x,y,z
2 x,-y,1/2+z
3 1/2+x,1/2+y,z
4 1/2+x,1/2-y,1/2+z
_cell_length_a                   22.037(9)
_cell_length_b                   16.187(8)
_cell_length_c                   8.254(5)
_cell_angle_alpha                90
_cell_angle_beta                 93.71(2)
_cell_angle_gamma                90
_cell_volume                     2938.14
loop_
_atom_site_label
_atom_site_type_symbol
_atom_site_fract_x
_atom_site_fract_y
_atom_site_fract_z
La1 La 0.30522(7) -0.01611(5) 0.47770(12)
S1 S 0.3680(2) 0.3162(3) 0.7282(6)
S2 S 0.3831(2) 0.7356(3) 0.6638(6)
S3 S 0.6003(2) 0.4965(3) 0.3476(6)
O1 O 0.3523(6) 0.0754(7) 0.6954(17)
O2 O 0.3131(6) 0.1639(7) 0.8694(16)
O3 O 0.2728(6) 0.8636(7) 0.9248(16)
O4 O 0.3390(6) 0.9047(7) 0.7516(17)
O5 O 0.7135(6) 0.6006(8) 0.0652(17)
O6 O 0.7277(5) 0.4906(7) 0.2216(16)
O7 O 0.4196(7) -0.0372(9) 0.493(2)
```

N1 N 0.3991(7) 0.4914(9) 0.6522(19)

N2 N 0.4584(7) 0.5988(8) 0.544(2)

N3 N 0.4854(7) 0.4579(8) 0.5067(17)

N4 N 0.5017(12) -0.0865(15) 0.648(3)

C1 C 0.3456(9) 0.1489(12) 0.754(3)

C2 C 0.3831(8) 0.2141(10) 0.687(2)

C3 C 0.4294(9) 0.2056(11) 0.586(3)

H3 H 0.442592 0.154923 0.549004

C4 C 0.4552(9) 0.2826(12) 0.544(3)

H4 H 0.488038 0.287767 0.479041

C5 C 0.4261(9) 0.3485(11) 0.609(2)

C6 C 0.4381(9) 0.4386(11) 0.585(2)

C7 C 0.3092(10) 0.8476(11) 0.821(3)

C8 C 0.3243(9) 0.7595(12) 0.779(2)

C9 C 0.2935(10) 0.6899(12) 0.834(3)

H9 H 0.259724 0.691593 0.895962

C10 C 0.3215(9) 0.6171(12) 0.782(2)

H10 H 0.308904 0.564345 0.808890

C11 C 0.3709(8) 0.6327(10) 0.683(2)

C12 C 0.4112(8) 0.5711(11) 0.629(2)

C13 C 0.6970(8) 0.5555(12) 0.168(3)

C14 C 0.6391(8) 0.5716(10) 0.255(2)

C15 C 0.6132(8) 0.6471(11) 0.262(2)

H15 H 0.627952 0.694202 0.213888

C16 C 0.5571(9) 0.6455(12) 0.359(3)

H16 H 0.532940 0.690484 0.382425

C17 C 0.5488(8) 0.5658(11) 0.406(2)

C18 C 0.4936(8) 0.5395(10) 0.488(2)

C19 C 0.4532(15) -0.0426(18) 0.623(4)

H19 H 0.441607 -0.011252 0.709755

C20 C 0.5391(16) -0.091(2) 0.812(5)

H20A H 0.573133 -0.127561 0.802002

H20B H 0.553610 -0.037102 0.842190

H20C H 0.514031 -0.111995 0.893508

C21 C 0.5141(16) -0.148(2) 0.512(4)

H21A H 0.550825 -0.177832 0.540175

H21B H 0.480731 -0.185860 0.497220

```
H21C H 0.518444 -0.118156 0.412365
La1 La 0.30522(7) 0.98389(5) 0.47770(12)
La1 La 0.30522(7) 0.01611(5) 0.97770(12)
La1 La 0.30522(7) 1.01611(5) 0.97770(12)
La1 La 0.80522(7) 0.48389(5) 0.47770(12)
La1 La 0.80522(7) 0.51611(5) -0.02230(12)
O1 O 0.3523(6) -0.0754(7) 0.1954(17)
O2 O 0.3131(6) -0.1639(7) 0.3694(16)
O3 O 0.2728(6) 0.1364(7) 0.4248(16)
O4 O 0.3390(6) -0.0953(7) 0.7516(17)
O4 O 0.3390(6) 0.0953(7) 0.2516(17)
O5 O 0.2135(6) -0.1006(8) 0.5652(17)
O6 O 0.2277(5) -0.0094(7) 0.2216(16)
O6 O 0.2277(5) 0.0094(7) 0.7216(16)

#END
```

Ce-MOF

```
_symmetry_cell_setting           monoclinic
_symmetry_space_group_name_H-M   'C c'
_symmetry_Int_Tables_number      9
_space_group_name_Hall           'C -2yc'
loop_
_symmetry_equiv_pos_site_id
_symmetry_equiv_pos_as_xyz
1 x,y,z
2 x,-y,1/2+z
3 1/2+x,1/2+y,z
4 1/2+x,1/2-y,1/2+z
_cell_length_a                   21.7213(9)
_cell_length_b                   16.0617(9)
_cell_length_c                   8.1106(3)
_cell_angle_alpha                90
_cell_angle_beta                 94.906(4)
_cell_angle_gamma                90
_cell_volume                     2819.27
loop_
_atom_site_label
_atom_site_type_symbol
_atom_site_fract_x
_atom_site_fract_y
_atom_site_fract_z
Ce1 Ce 0.65373(8) 1.01645(7) 0.51946(12)
S1 S 0.5921(3) 0.6830(4) 0.2737(7)
S2 S 0.3589(3) 0.5042(4) 0.6551(8)
S3 S 0.5770(3) 0.2635(4) 0.3351(7)
O1 O 0.6067(8) 0.9254(10) 0.3001(17)
O2 O 0.6462(8) 0.8377(11) 0.1281(19)
O3 O 0.2305(8) 0.5117(10) 0.782(2)
O4 O 0.2435(8) 0.3986(10) 0.9350(19)
O5 O 0.6208(8) 0.0951(9) 0.2394(16)
O6 O 0.6875(8) 0.1369(11) 0.064(2)
O7 O 0.5396(8) 1.0424(11) 0.493(2)
```

N1 N 0.4744(9) 0.5430(12) 0.499(2)

N2 N 0.5004(9) 0.3993(12) 0.455(2)

N3 N 0.5612(10) 0.5097(11) 0.355(2)

N4 N 0.4554(10) 1.0898(17) 0.336(3)

C1 C 0.6123(13) 0.8521(16) 0.243(3)

C2 C 0.5757(12) 0.7878(15) 0.311(3)

C3 C 0.5271(12) 0.7937(17) 0.414(3)

H3 H 0.511473 0.845232 0.449958

C4 C 0.5041(12) 0.7175(14) 0.457(3)

H4 H 0.470191 0.712086 0.522921

C5 C 0.5337(13) 0.6514(16) 0.399(3)

C6 C 0.5231(10) 0.5637(15) 0.418(3)

C7 C 0.4657(11) 0.4595(14) 0.515(3)

C8 C 0.4114(12) 0.4326(16) 0.599(3)

C9 C 0.3996(13) 0.3518(18) 0.647(3)

H9 H 0.423208 0.304076 0.623858

C10 C 0.3453(12) 0.3524(18) 0.739(3)

H10 H 0.329400 0.304340 0.789215

C11 C 0.3193(11) 0.4297(14) 0.746(3)

C12 C 0.2605(11) 0.4450(15) 0.832(3)

C13 C 0.5501(11) 0.4294(13) 0.378(3)

C14 C 0.5920(11) 0.3668(15) 0.314(3)

C15 C 0.6402(11) 0.3852(16) 0.223(3)

H15 H 0.653573 0.439995 0.200570

C16 C 0.6679(12) 0.3115(15) 0.168(3)

H16 H 0.702942 0.311005 0.104941

C17 C 0.6381(12) 0.2410(16) 0.215(3)

C18 C 0.6512(11) 0.1527(15) 0.178(3)

C19 C 0.5062(14) 1.0458(18) 0.364(4)

H19 H 0.518326 1.013284 0.273992

C20 C 0.4400(16) 1.151(2) 0.461(4)

H20A H 0.401559 1.133863 0.507415

H20B H 0.434526 1.205709 0.410317

H20C H 0.473489 1.152787 0.550162

C21 C 0.4186(15) 1.089(2) 0.170(4)

H21A H 0.439824 1.054968 0.092289

H21B H 0.414617 1.146362 0.127150

```
H21C H 0.377411 1.066303 0.181405
Ce1 Ce 0.65373(8) 0.01645(7) 0.51946(12)
Ce1 Ce 0.65373(8) -0.01645(7) 0.01946(12)
Ce1 Ce 0.65373(8) 0.98355(7) 0.01946(12)
Ce1 Ce 0.15373(8) 0.51645(7) 0.51946(12)
Ce1 Ce 0.15373(8) 0.48355(7) 1.01946(12)
O1 O 0.6067(8) 1.0746(10) 0.8001(17)
O2 O 0.6462(8) 1.1623(11) 0.6281(19)
O3 O 0.7305(8) 1.0117(10) 0.782(2)
O3 O 0.7305(8) 0.9883(10) 0.282(2)
O4 O 0.7435(8) 1.1014(10) 0.4350(19)
O5 O 0.6208(8) 1.0951(9) 0.2394(16)
O5 O 0.6208(8) 0.9049(9) 0.7394(16)
O6 O 0.6875(8) 0.8631(11) 0.564(2)
O8 O 0.782(2) 0.604(5) 0.478(6)
N5 N 0.7685(16) 0.691(3) 0.236(4)
C22 C 0.7661(19) 0.622(4) 0.335(6)
H22 H 0.747410 0.576006 0.276073
C23 C 0.746(2) 0.689(3) 0.061(4)
H23A H 0.780611 0.696034 -0.007370
H23B H 0.716048 0.734202 0.037344
H23C H 0.725717 0.635442 0.035545
C24 C 0.792(3) 0.770(4) 0.309(8)
H24A H 0.789736 0.767924 0.428762
H24B H 0.766590 0.815955 0.261997
H24C H 0.834835 0.777724 0.283931

#END
```

Pr-MOF

```
_space_group_name_Hall             'C -2yc'
#END
loop_
  _space_group_symop_id
  _space_group_symop_operation_xyz
 1 x,y,z
 2 x,-y,1/2+z
 3 1/2+x,1/2+y,z
 4 1/2+x,1/2-y,1/2+z

_symmetry_cell_setting             monoclinic
_symmetry_Int_Tables_number        9
_symmetry_space_group_name_H-M     'C c'
_cell_length_a                     21.866(3)
_cell_length_b                     16.0713(18)
_cell_length_c                     8.1472(11)
_cell_angle_alpha                  90
_cell_angle_beta                   93.84(4)
_cell_angle_gamma                  90
_cell_volume                       2856.62
loop_
  _atom_site_label
  _atom_site_type_symbol
  _atom_site_fract_x
  _atom_site_fract_y
  _atom_site_fract_z
 Pr1 Pr 0.30538(16) -0.01599(12) 0.4777(3)
 S1 S 0.3668(5) 0.3155(6) 0.7256(14)
 S2 S 0.3831(5) 0.7365(6) 0.6645(13)
 S3 S 0.6000(5) 0.4959(6) 0.3484(14)
 O1 O 0.3501(13) 0.0734(16) 0.690(4)
 O2 O 0.3130(13) 0.1580(16) 0.870(4)
 O3 O 0.2746(11) 0.8674(15) 0.935(3)
 O4 O 0.3369(12) 0.9073(15) 0.757(4)
 O5 O 0.7139(14) 0.5981(17) 0.059(4)
```

O6 O 0.7297(14) 0.4877(17) 0.236(5)

O7 O 0.4162(12) -0.0398(19) 0.493(4)

N1 N 0.3986(14) 0.492(2) 0.647(4)

N2 N 0.4573(18) 0.597(2) 0.540(4)

N3 N 0.4856(14) 0.4580(18) 0.505(4)

N4 N 0.4983(19) -0.086(2) 0.651(5)

C1 C 0.347(2) 0.147(3) 0.745(7)

C2 C 0.384(2) 0.213(2) 0.687(4)

C3 C 0.428(2) 0.207(2) 0.590(5)

H3 H 0.441603 0.155535 0.549498

C4 C 0.4548(19) 0.286(3) 0.551(6)

H4 H 0.489030 0.290430 0.488034

C5 C 0.427(2) 0.353(3) 0.611(5)

C6 C 0.4383(18) 0.437(2) 0.588(4)

C7 C 0.308(2) 0.851(2) 0.823(6)

C8 C 0.3243(19) 0.763(2) 0.777(5)

C9 C 0.294(2) 0.693(3) 0.831(5)

H9 H 0.259421 0.696428 0.893382

C10 C 0.319(2) 0.621(3) 0.787(5)

H10 H 0.305133 0.567887 0.818308

C11 C 0.371(2) 0.634(3) 0.681(5)

C12 C 0.413(2) 0.575(3) 0.620(5)

C13 C 0.6986(19) 0.551(3) 0.186(6)

C14 C 0.6395(17) 0.572(3) 0.254(5)

C15 C 0.6133(19) 0.647(3) 0.258(5)

H15 H 0.628439 0.694549 0.206613

C16 C 0.559(2) 0.647(3) 0.352(6)

H16 H 0.536950 0.695086 0.376473

C17 C 0.544(2) 0.566(2) 0.400(5)

C18 C 0.4949(19) 0.540(2) 0.487(5)

C19 C 0.451(2) -0.039(3) 0.614(6)

H19 H 0.443434 0.001421 0.692341

C20 C 0.537(3) -0.088(4) 0.807(8)

H20A H 0.568746 -0.129808 0.798505

H20B H 0.555267 -0.034279 0.827498

H20C H 0.511665 -0.102917 0.896056

C21 C 0.515(3) -0.147(4) 0.524(8)

H21A H 0.550800 -0.178476 0.565776

H21B H 0.481124 -0.184893 0.500101

H21C H 0.524421 -0.117859 0.424980

Sm-MOF

```
_symmetry_cell_setting           monoclinic
_symmetry_space_group_name_H-M   'C c'
_symmetry_Int_Tables_number      9
_space_group_name_Hall           'C -2yc'
loop_
_symmetry_equiv_pos_site_id
_symmetry_equiv_pos_as_xyz
1 x,y,z
2 x,-y,1/2+z
3 1/2+x,1/2+y,z
4 1/2+x,1/2-y,1/2+z
_cell_length_a                   25.810(9)
_cell_length_b                   15.987(4)
_cell_length_c                   7.041(2)
_cell_angle_alpha                90
_cell_angle_beta                 95.128(19)
_cell_angle_gamma                90
_cell_volume                     2893.66
loop_
_atom_site_label
_atom_site_type_symbol
_atom_site_fract_x
_atom_site_fract_y
_atom_site_fract_z
Sm1 Sm -0.2173(2) -0.42265(15) -0.2376(5)
S1 S -0.3942(5) -0.5363(8) -0.3304(19)
S2 S -0.5991(5) -0.7930(7) -0.6237(18)
S3 S -0.6194(5) -0.3683(7) -0.6928(18)
O1 O -0.2873(14) -0.4989(19) -0.176(5)
O2 O -0.2711(17) -0.613(2) 0.008(5)
O3 O -0.7083(13) -0.9288(17) -0.881(5)
O4 O -0.6729(13) -0.945(2) -0.601(6)
O5 O -0.6852(13) -0.217(2) -0.784(4)
O6 O -0.6287(14) -0.123(2) -0.673(5)
O7 O -0.2798(12) -0.327(2) -0.121(5)
```

N1 N -0.5259(16) -0.653(3) -0.535(6)

N2 N -0.5825(14) -0.546(2) -0.641(5)

N3 N -0.4999(16) -0.508(2) -0.495(4)

N5 N -0.3562(13) -0.2486(18) -0.170(5)

C1 C -0.297(3) -0.578(5) -0.115(10)

C1A C -0.3256(13) -0.317(2) -0.182(5)

H1A H -0.341648 -0.364019 -0.245738

C1B C -0.4099(15) -0.250(4) -0.253(9)

H1BA H -0.413783 -0.292293 -0.353775

H1BB H -0.418908 -0.194701 -0.308436

H1BC H -0.433050 -0.262772 -0.154622

C1C C -0.336(2) -0.172(2) -0.077(7)

H1CA H -0.316470 -0.186669 0.044732

H1CB H -0.364861 -0.135210 -0.053549

H1CC H -0.312791 -0.144156 -0.159391

C2 C -0.353(2) -0.609(3) -0.211(9)

C3 C -0.369(2) -0.683(3) -0.191(9)

H3 H -0.349626 -0.726909 -0.124873

C4 C -0.422(3) -0.690(3) -0.287(9)

H4 H -0.441553 -0.739990 -0.287028

C5 C -0.4410(19) -0.614(3) -0.382(9)

C6 C -0.4905(16) -0.588(3) -0.476(6)

C7 C -0.680(3) -0.901(5) -0.739(8)

C8 C -0.660(2) -0.817(3) -0.722(8)

C9 C -0.681(2) -0.742(3) -0.810(9)

H9 H -0.711094 -0.742378 -0.896403

C10 C -0.6574(17) -0.676(3) -0.769(7)

H10 H -0.671594 -0.623116 -0.802434

C11 C -0.6099(17) -0.686(2) -0.674(6)

C12 C -0.572(2) -0.627(3) -0.607(7)

C13 C -0.644(2) -0.202(3) -0.721(11)

C14 C -0.602(2) -0.267(3) -0.665(8)

C15 C -0.549(2) -0.260(6) -0.565(8)

H15 H -0.531561 -0.209401 -0.528085

C16 C -0.5304(18) -0.334(3) -0.536(7)

H16 H -0.497555 -0.341907 -0.466304

C17 C -0.5588(18) -0.404(2) -0.610(8)

```
C18 C -0.5478(17) -0.486(3) -0.590(7)
Sm1 Sm -0.2173(2) -0.57735(15) 0.2624(5)
Sm1 Sm -0.7173(2) -0.92265(15) -1.2376(5)
Sm1 Sm -0.7173(2) -0.92265(15) -0.2376(5)
Sm1 Sm -0.7173(2) -1.07735(15) -0.7376(5)
Sm1 Sm -0.7173(2) -0.07735(15) -0.7376(5)
O2 O -0.2711(17) -0.387(2) -0.492(5)
O3 O -0.2083(13) -0.4288(17) 0.119(5)
O3 O -0.2083(13) -0.5712(17) -0.381(5)
O4 O -0.1729(13) -0.445(2) -0.601(6)
O4 O -0.1729(13) -0.555(2) -0.101(6)
O5 O -0.1852(13) -0.283(2) -0.284(4)
O6 O -0.1287(14) -0.377(2) -0.173(5)

#END
```

Eu-MOF

```
_symmetry_cell_setting           monoclinic
_symmetry_space_group_name_H-M   'C c'
_symmetry_Int_Tables_number      9
_space_group_name_Hall           'C -2yc'
loop_
_symmetry_equiv_pos_site_id
_symmetry_equiv_pos_as_xyz
1 x,y,z
2 x,-y,1/2+z
3 1/2+x,1/2+y,z
4 1/2+x,1/2-y,1/2+z
_cell_length_a                   25.8127(16)
_cell_length_b                   16.1287(9)
_cell_length_c                   7.0693(4)
_cell_angle_alpha                90
_cell_angle_beta                 95.744(4)
_cell_angle_gamma                90
_cell_volume                     2928.35
loop_
_atom_site_label
_atom_site_type_symbol
_atom_site_fract_x
_atom_site_fract_y
_atom_site_fract_z
Eu1 Eu 0.21665(10) 0.42265(8) 0.2373(3)
S1 S 0.3950(3) 0.5362(4) 0.3316(10)
S2 S 0.6000(3) 0.7922(4) 0.6214(10)
S3 S 0.6213(2) 0.3693(4) 0.6955(9)
O1 O 0.2889(8) 0.5012(11) 0.173(3)
O2 O 0.2761(7) 0.6170(12) 0.008(3)
O3 O 0.7057(9) 0.9299(9) 0.882(2)
O4 O 0.6701(7) 0.9481(12) 0.593(3)
O5 O 0.6850(7) 0.2178(9) 0.781(3)
O6 O 0.6260(7) 0.1261(10) 0.667(3)
O7 O 0.2807(7) 0.3246(10) 0.122(3)
```

N1 N 0.5261(7) 0.6526(11) 0.525(3)

N2 N 0.5858(8) 0.5463(11) 0.638(3)

N3 N 0.5018(8) 0.5094(11) 0.491(3)

N4 N 0.3563(8) 0.2589(12) 0.166(3)

C1 C 0.3023(8) 0.5723(14) 0.125(4)

C2 C 0.3519(8) 0.6027(13) 0.205(4)

C3 C 0.3745(9) 0.6810(12) 0.193(4)

H3 H 0.357606 0.725961 0.125415

C4 C 0.4245(10) 0.6872(13) 0.290(4)

H4 H 0.444454 0.736763 0.300799

C5 C 0.4410(10) 0.6115(14) 0.367(3)

C6 C 0.4911(9) 0.5901(11) 0.465(3)

C7 C 0.6801(12) 0.9026(16) 0.744(4)

C8 C 0.6593(9) 0.8182(12) 0.739(4)

C9 C 0.6866(12) 0.7490(14) 0.812(5)

H9 H 0.720050 0.751456 0.881105

C10 C 0.6586(8) 0.6744(14) 0.771(4)

H10 H 0.670993 0.620987 0.809226

C11 C 0.6106(8) 0.6890(15) 0.666(3)

C12 C 0.5722(9) 0.6275(13) 0.609(4)

C13 C 0.6411(9) 0.1991(12) 0.703(4)

C14 C 0.6038(9) 0.2669(15) 0.663(3)

C15 C 0.5541(9) 0.2608(15) 0.567(4)

H15 H 0.538347 0.209301 0.529116

C16 C 0.5289(9) 0.3386(14) 0.530(3)

H16 H 0.494372 0.345081 0.471539

C17 C 0.5616(11) 0.4041(15) 0.592(4)

C18 C 0.5510(8) 0.4898(13) 0.574(3)

C19 C 0.3258(8) 0.3250(14) 0.185(3)

H19 H 0.340018 0.372942 0.248354

C20 C 0.3391(13) 0.1820(15) 0.069(5)

H20A H 0.301138 0.182403 0.042235

H20B H 0.349763 0.134425 0.149768

H20C H 0.355039 0.177683 -0.051132

C21 C 0.4109(9) 0.261(2) 0.250(4)

H21A H 0.434070 0.257771 0.148616

H21B H 0.417550 0.213720 0.336343

H21C H 0.417423 0.312718 0.321065

Eu1 Eu 0.21665(10) 0.57735(8) -0.2627(3)

Eu1 Eu 0.71665(10) 0.92265(8) 1.2373(3)

Eu1 Eu 0.71665(10) 0.07735(8) 0.7373(3)

Eu1 Eu 0.71665(10) 1.07735(8) 0.7373(3)

O2 O 0.2761(7) 0.3830(12) 0.508(3)

O3 O 0.2057(9) 0.4299(9) -0.118(2)

O3 O 0.2057(9) 0.5701(9) 0.382(2)

O4 O 0.1701(7) 0.5519(12) 0.093(3)

O5 O 0.1850(7) 0.2822(9) 0.281(3)

O6 O 0.1260(7) 0.3739(10) 0.167(3)

O8 O 0.4458(16) 0.881(3) 0.222(8)

N5 N 0.5011(12) 0.984(2) 0.308(6)

C22 C 0.4901(16) 0.903(2) 0.280(7)

H22 H 0.516714 0.862940 0.306262

C23 C 0.5527(15) 1.011(3) 0.376(8)

H23A H 0.552398 1.033657 0.504659

H23B H 0.564222 1.053579 0.291412

H23C H 0.576650 0.963550 0.379732

C24 C 0.4628(19) 1.048(3) 0.272(8)

H24A H 0.434441 1.028611 0.180844

H24B H 0.479016 1.097196 0.220286

H24C H 0.448834 1.063337 0.391617

```
_symmetry_cell_setting           monoclinic
_symmetry_space_group_name_H-M   'P 21/c'
_symmetry_Int_Tables_number      14
_space_group_name_Hall           '-P 2ybc'
loop_
_symmetry_equiv_pos_site_id
_symmetry_equiv_pos_as_xyz
1 x,y,z
2 -x,1/2+y,1/2-z
3 -x,-y,-z
4 x,1/2-y,1/2+z
_cell_length_a                   22.8462(11)
_cell_length_b                   25.8299(14)
_cell_length_c                   23.3623(12)
_cell_angle_alpha                90
_cell_angle_beta                 97.559(3)
_cell_angle_gamma                90
_cell_volume                     13666.6
loop_
_atom_site_label
_atom_site_type_symbol
_atom_site_fract_x
_atom_site_fract_y
_atom_site_fract_z
Gd1 Gd 0.14819(7) 0.51043(6) 0.75834(6)
Gd2 Gd -0.04180(7) 0.48678(6) 0.75029(7)
Gd3 Gd 0.47727(8) 0.33656(8) 0.77939(8)
Gd4 Gd 0.56165(9) 0.21142(7) 0.70010(8)
S1 S 0.1100(3) 0.8702(3) 0.4195(3)
S2 S 0.2702(3) 0.7627(3) 0.6506(3)
S3 S 0.0941(3) 0.6470(3) 0.6383(3)
S4 S 0.1246(3) 0.3579(3) 0.6281(3)
S5 S 0.1430(3) 0.1300(3) 0.4163(3)
```

S6 S 0.3030(4) 0.2663(3) 0.6342(4)

S7 S 0.5408(4) 0.4370(3) 0.6108(3)

S8 S 0.5170(4) 0.6192(3) 0.6204(4)

S9 S 0.6993(4) 0.5056(3) 0.3968(3)

O1 O 0.0040(10) 0.9480(8) 0.3082(9)

O2 O 0.1009(10) 0.9490(8) 0.3303(8)

O3 O 0.4226(9) 0.8270(11) 0.6964(12)

O4 O 0.3806(10) 0.7583(9) 0.7257(12)

O5 O 0.0728(9) 0.5533(8) 0.7062(9)

O6 O -0.0268(10) 0.5522(9) 0.6850(8)

O7 O 0.1943(13) 0.5969(10) 0.7699(13)

O8 O 0.2297(12) 0.5321(11) 0.8302(13)

O9 O -0.1231(9) 0.5437(9) 0.7589(12)

O10 O -0.1220(11) 0.4728(15) 0.6721(13)

O11 O -0.0722(13) 0.4688(10) 0.8428(10)

O12 O -0.078(2) 0.3968(13) 0.757(2)

O13 O 0.0040(11) 0.4467(9) 0.6795(9)

O14 O 0.1003(10) 0.4492(8) 0.6942(8)

O15 O 0.0416(10) 0.0516(9) 0.2986(9)

O16 O 0.1372(13) 0.0579(8) 0.3240(10)

O17 O 0.4110(12) 0.2934(10) 0.7087(13)

O18 O 0.4632(12) 0.2357(13) 0.6853(15)

O19 O 0.370(3) 0.3247(17) 0.813(2)

O20 O 0.490(2) 0.350(2) 0.8852(14)

O21 O 0.527(4) 0.416(3) 0.837(6)

O22 O 0.5207(19) 0.1219(13) 0.672(2)

O23 O 0.555(3) 0.198(2) 0.587(2)

O24 O 0.637(3) 0.227(2) 0.640(4)

O25 O 0.5113(17) 0.3602(15) 0.6979(11)

O26 O 0.5544(14) 0.2941(13) 0.6609(13)

O27 O 0.4740(16) 0.680(2) 0.7141(14)

O28 O 0.5092(12) 0.7542(7) 0.6917(17)

O29 O 0.7931(9) 0.4813(7) 0.3210(9)

O30 O 0.640(2) 0.1465(14) 0.749(3)

O31 O 0.263(2) 0.6141(15) 0.8438(18)

O32 O 0.7702(9) 0.5485(8) 0.2597(10)

N1 N 0.1549(10) 0.8085(10) 0.5201(11)

N2 N 0.1517(10) 0.7417(9) 0.5904(10)

N3 N 0.0653(9) 0.7593(8) 0.5216(8)

N4 N 0.0977(9) 0.2422(7) 0.5159(8)

N5 N 0.1883(9) 0.2000(9) 0.5129(10)

N6 N 0.1826(9) 0.2705(8) 0.5766(9)

N7 N 0.5553(10) 0.5342(9) 0.5518(10)

N8 N 0.5958(11) 0.5896(9) 0.4827(11)

N9 N 0.6136(12) 0.4983(9) 0.4796(11)

N10 N -0.0903(15) 0.4861(13) 0.9338(13)

N11 N 0.2292(12) 0.5805(11) 0.8145(12)

N12 N -0.088(2) 0.3044(17) 0.747(2)

C1 C 0.0516(11) 0.9328(11) 0.3317(13)

C2 C 0.0456(11) 0.8911(10) 0.3777(11)

C3 C -0.0034(11) 0.8644(12) 0.3859(12)

H01C H -0.041892 0.869595 0.365707

C4 C 0.0136(13) 0.8248(10) 0.4326(11)

H014 H -0.014070 0.801410 0.445370

C5 C 0.0712(12) 0.8252(10) 0.4547(11)

C6 C 0.0998(12) 0.7959(10) 0.4993(11)

C7 C 0.1786(13) 0.7792(10) 0.5661(14)

C8 C 0.2373(12) 0.7917(11) 0.5949(12)

C9 C 0.2720(15) 0.8266(16) 0.5723(17)

H6 H 0.262435 0.841087 0.534873

C10 C 0.3243(15) 0.8398(15) 0.6100(16)

H02J H 0.350494 0.867977 0.607176

C11 C 0.3273(14) 0.8026(13) 0.6500(14)

C12 C 0.3811(14) 0.7978(11) 0.6971(16)

C13 C 0.0930(12) 0.7327(9) 0.5664(10)

C14 C 0.0601(9) 0.6913(10) 0.5914(11)

C15 C 0.0018(10) 0.6825(11) 0.5800(12)

H00Z H -0.023974 0.703565 0.554573

C16 C -0.0169(11) 0.6410(10) 0.6079(11)

H01V H -0.056973 0.630413 0.604421

C17 C 0.0269(10) 0.6164(9) 0.6408(10)

C18 C 0.026(2) 0.5704(10) 0.6831(13)

C19 C 0.0501(17) 0.4302(14) 0.6738(14)

C20 C 0.0577(12) 0.3843(11) 0.6399(12)

C21 C 0.0124(11) 0.3605(10) 0.6066(12)

H01Z H -0.027666 0.370625 0.606048

C22 C 0.0301(11) 0.3189(11) 0.5727(12)

H01L H 0.004046 0.298777 0.546504

C23 C 0.0894(10) 0.3119(8) 0.5829(10)

C24 C 0.1243(11) 0.2734(9) 0.5576(10)

C25 C 0.1306(10) 0.2077(10) 0.4946(12)

C26 C 0.1017(10) 0.1728(8) 0.4493(11)

C27 C 0.0435(10) 0.1709(11) 0.4288(10)

H00X H 0.013970 0.191496 0.442818

C28 C 0.0330(11) 0.1354(10) 0.3854(12)

H018 H -0.005415 0.129380 0.365434

C29 C 0.0813(9) 0.1094(11) 0.3726(10)

C30 C 0.084(2) 0.0689(13) 0.3282(14)

C31 C 0.2123(12) 0.2322(10) 0.5540(13)

C32 C 0.2745(12) 0.2259(13) 0.5802(14)

C33 C 0.3133(16) 0.1905(19) 0.565(3)

H02G H 0.304709 0.165108 0.535450

C34 C 0.3664(18) 0.197(2) 0.598(2)

H02N H 0.399627 0.176201 0.592999

C35 C 0.3692(10) 0.2353(13) 0.6374(17)

C36 C 0.4157(19) 0.258(2) 0.683(2)

C37 C 0.527(2) 0.3435(18) 0.665(2)

C38 C 0.5557(15) 0.3712(12) 0.6111(13)

C39 C 0.5831(18) 0.3537(15) 0.5672(16)

H02S H 0.591520 0.318516 0.559683

C40 C 0.5970(17) 0.3962(11) 0.5345(14)

H02W H 0.618723 0.392845 0.502728

C41 C 0.5774(14) 0.4424(11) 0.5512(13)

C42 C 0.5822(13) 0.4952(11) 0.5259(12)

C43 C 0.5673(14) 0.5808(10) 0.5281(13)

C44 C 0.5517(17) 0.6255(13) 0.5597(17)

C45 C 0.558(2) 0.6763(13) 0.548(2)

H02Y H 0.574964 0.688642 0.516265

C46 C 0.536(2) 0.7096(16) 0.5887(18)

H02M H 0.534511 0.746208 0.584947

C47 C 0.517(2) 0.6837(16) 0.6331(19)

C48 C 0.500(3) 0.704(2) 0.683(2)

C49 C 0.6179(13) 0.5452(11) 0.4615(13)

C50 C 0.6509(14) 0.5540(11) 0.4124(14)

C51 C 0.6549(13) 0.5978(11) 0.3812(14)

H029 H 0.634820 0.629035 0.387543

C52 C 0.6913(13) 0.5917(10) 0.3393(15)

H02O H 0.695258 0.617176 0.310732

C53 C 0.7209(11) 0.5462(10) 0.3422(13)

C54 C 0.7665(12) 0.5239(12) 0.3067(14)

C55 C -0.078(2) 0.3543(15) 0.733(2)

H3 H -0.068086 0.357376 0.694469

C56 C -0.087(4) 0.2601(18) 0.709(3)

H4A H -0.071216 0.270725 0.673571

H4B H -0.126444 0.246037 0.699345

H4C H -0.060693 0.233460 0.728691

C57 C -0.105(4) 0.295(3) 0.804(3)

H7A H -0.143380 0.310251 0.806711

H7B H -0.075137 0.309623 0.833245

H7C H -0.107064 0.257116 0.810053

C58 C -0.0712(16) 0.4999(13) 0.8829(12)

H2 H -0.056926 0.533967 0.878449

C59 C -0.091(2) 0.523(2) 0.9819(17)

H5A H -0.125334 0.545663 0.973741

H5B H -0.054835 0.543076 0.986469

H5C H -0.094141 0.503274 1.017522

C60 C -0.112(3) 0.4328(16) 0.937(2)

H1A H -0.148875 0.433074 0.955040

H1B H -0.082687 0.411588 0.960223

H1C H -0.120616 0.418362 0.898035

Gd1 Gd 0.85181(7) 0.48957(6) 0.24166(6)

Gd1 Gd 0.14819(7) -0.01043(6) 0.25834(6)

Gd1 Gd 0.14819(7) 0.98957(6) 0.25834(6)

Gd2 Gd -0.04180(7) 0.01322(6) 0.25029(7)

Gd2 Gd -0.04180(7) 1.01322(6) 0.25029(7)

Gd3 Gd 0.52273(8) 0.83656(8) 0.72061(8)

Gd4 Gd 0.43835(9) 0.71142(7) 0.79990(8)

O1 O 0.0040(10) 0.5520(8) 0.8082(9)

```
O2 O 0.1009(10) 0.5510(8) 0.8303(8)
O3 O 0.5774(9) 0.3270(11) 0.8036(12)
O4 O 0.6194(10) 0.2583(9) 0.7743(12)
O15 O 0.0416(10) 0.4484(9) 0.7986(9)
O16 O 0.1372(13) 0.4421(8) 0.8240(10)
O27 O 0.5260(16) 0.180(2) 0.7859(14)
O28 O 0.4908(12) 0.2542(7) 0.8083(17)
O29 O 0.2069(9) 0.5187(7) 0.6790(9)
O32 O 0.2298(9) 0.4515(8) 0.7403(10)

#END
```

```
_symmetry_cell_setting           monoclinic
_symmetry_space_group_name_H-M   'C 2/c'
_symmetry_Int_Tables_number      15
_space_group_name_Hall           '-C 2yc'
loop_
_symmetry_equiv_pos_site_id
_symmetry_equiv_pos_as_xyz
1 x,y,z
2 -x,y,1/2-z
3 1/2+x,1/2+y,z
4 1/2-x,1/2+y,1/2-z
5 -x,-y,-z
6 x,-y,1/2+z
7 1/2-x,1/2-y,-z
8 1/2+x,1/2-y,1/2+z
_cell_length_a                   26.7959(10)
_cell_length_b                   14.1418(5)
_cell_length_c                   19.4029(7)
_cell_angle_alpha                90
_cell_angle_beta                 93.573(3)
_cell_angle_gamma                90
_cell_volume                     7338.29
loop_
_atom_site_label
_atom_site_type_symbol
_atom_site_fract_x
_atom_site_fract_y
_atom_site_fract_z
Eu1 Eu 0.46273(2) 0.11384(2) 0.54820(2)
Cu1 Cu 0.29519(3) 0.59651(7) 0.69295(5)
O1 O 0.4691(2) 0.2693(3) 0.5847(3)
O2 O 0.4579(7) 0.3762(10) 0.4879(10)
O3 O 0.47802(16) 0.8408(3) 0.5322(2)
O4 O 0.45203(16) 0.9615(3) 0.5959(2)
O5 O 0.05412(16) 0.4937(3) 0.5426(2)
```

O6 O 0.04256(18) 0.6077(3) 0.6172(3)

O7 O 0.12345(16) 0.6138(3) 0.9385(2)

O8 O 0.17516(17) 0.7155(4) 0.9947(2)

O9 O 0.45028(17) 0.1233(3) 0.6781(2)

H9A H 0.458311 0.066531 0.700668

H9B H 0.416739 0.130898 0.687168

O10 O 0.41961(18) 0.2093(4) 0.4549(3)

H10A H 0.421590 0.180875 0.412616

H10B H 0.435611 0.265894 0.448806

N1 N 0.35220(19) 0.5117(4) 0.6685(3)

N2 N 0.3388(2) 0.6969(4) 0.6514(3)

N3 N 0.22462(19) 0.5594(4) 0.6555(3)

N4 N 0.25902(19) 0.6231(4) 0.7786(3)

C1 C 0.4490(10) 0.3458(14) 0.5503(13)

C2 C 0.4246(3) 0.4100(5) 0.6055(4)

C3 C 0.3909(3) 0.3653(5) 0.6464(4)

H3 H 0.392437 0.298797 0.653383

C4 C 0.3558(2) 0.4174(5) 0.6762(4)

C5 C 0.3176(3) 0.3724(5) 0.7209(5)

H5A H 0.309282 0.416828 0.757254

H5B H 0.331564 0.314483 0.741989

H5C H 0.287240 0.357043 0.692261

C6 C 0.4213(3) 0.5071(5) 0.5971(4)

H6 H 0.443622 0.539260 0.568993

C7 C 0.3854(2) 0.5564(4) 0.6298(3)

C8 C 0.3806(2) 0.6598(4) 0.6261(3)

C9 C 0.4168(2) 0.7164(4) 0.5999(3)

H9 H 0.445129 0.689244 0.580558

C10 C 0.4110(2) 0.8135(4) 0.6024(3)

C11 C 0.4509(2) 0.8774(4) 0.5747(3)

C12 C 0.3691(2) 0.8507(4) 0.6293(3)

H12 H 0.365100 0.917266 0.632302

C13 C 0.3330(3) 0.7918(5) 0.6518(4)

C14 C 0.2853(3) 0.8287(5) 0.6805(5)

H14A H 0.293126 0.883385 0.710273

H14B H 0.270204 0.778860 0.707401

H14C H 0.261792 0.847758 0.642283

```
C15 C 0.0692(2) 0.5482(5) 0.5903(3)
C16 C 0.1245(2) 0.5459(5) 0.6155(3)
C17 C 0.1602(3) 0.5214(5) 0.5709(3)
H17 H 0.150290 0.498381 0.526074
C18 C 0.2106(3) 0.5300(5) 0.5910(3)
C19 C 0.2513(3) 0.5098(8) 0.5431(4)
H19A H 0.276022 0.560966 0.546335
H19B H 0.236859 0.505296 0.495607
H19C H 0.267672 0.449870 0.556286
C20 C 0.1392(2) 0.5739(4) 0.6810(3)
H20 H 0.115073 0.591076 0.712623
C21 C 0.1893(2) 0.5770(4) 0.7007(3)
C22 C 0.2092(2) 0.6082(4) 0.7704(3)
C23 C 0.1779(2) 0.6175(4) 0.8243(3)
H23 H 0.143544 0.601043 0.818193
C24 C 0.1978(2) 0.6517(4) 0.8879(3)
C25 C 0.1633(2) 0.6618(5) 0.9458(3)
C26 C 0.2489(2) 0.6719(5) 0.8948(3)
H26 H 0.263377 0.696181 0.937138
C27 C 0.2781(2) 0.6564(5) 0.8399(3)
C28 C 0.3335(3) 0.6763(7) 0.8459(4)
H28A H 0.350653 0.633349 0.815510
H28B H 0.346392 0.666619 0.893758
H28C H 0.339555 0.741856 0.832284
Eu1 Eu 0.46273(2) 1.11384(2) 0.54820(2)
Eu1 Eu -0.03727(2) 0.61384(2) 0.54820(2)
Eu1 Eu 0.03727(2) 0.61384(2) 0.95180(2)
Eu1 Eu 0.53727(2) 0.88616(2) 0.45180(2)
Eu1 Eu 0.03727(2) 0.38616(2) 0.45180(2)
O3 O 0.52198(16) 0.1592(3) 0.4678(2)
O4 O 0.45203(16) -0.0385(3) 0.5959(2)
O5 O 0.44588(16) 0.0063(3) 0.4574(2)
O6 O 0.54256(18) 0.1077(3) 0.6172(3)
O7 O 0.37655(16) 0.1138(3) 0.5615(2)
O2' O 0.5008(4) 0.4028(5) 0.5469(6)
C1' C 0.4708(5) 0.3567(8) 0.5783(7)
#END
```